U.S. Department of Transportation

Federal Railroad Administration

Improved Concrete Crosstie and Fastening Systems for US High Speed Passenger Rail and Joint Corridors: Volume 2

Office of Research,
Development
and Technology
Washington, DC 20590

DOT/FRA/ORD-17/23

Final Report
November 2017

REPORT DOCUMENTATION PAGE

Form Approved
OMB No. 0704-0188

1. AGENCY USE ONLY (Leave blank)	2. REPORT DATE	3. REPORT TYPE AND DATES COVERED
	November 2017	Technical Report

4. TITLE AND SUBTITLE
Improved Concrete Crosstie and Fastening Systems for US High Speed Passenger Rail and Joint Corridors: Volume 2

5. FUNDING NUMBERS
DTFR53-11-C-00023

6. AUTHOR(S)
J. Riley Edwards, Marcus S. Dersch, and Ryan G. Kernes

7. PERFORMING ORGANIZATION NAME(S) AND ADDRESS(ES)
University of Illinois at Urbana-Champaign
205 North Mathews Avenue, MC-250
1245A Newmark Civil Engineering Laboratory
Urbana, IL 61801

8. PERFORMING ORGANIZATION REPORT NUMBER

9. SPONSORING/MONITORING AGENCY NAME(S) AND ADDRESS(ES)
U.S. Department of Transportation
Federal Railroad Administration
Office of Railroad Policy and Development
Office of Research, Development and Technology
Washington, DC 20590

10. SPONSORING/MONITORING AGENCY REPORT NUMBER
DOT/FRA/ORD-17/23

11. SUPPLEMENTARY NOTES
COR: Cameron D. Stuart

12a. DISTRIBUTION/AVAILABILITY STATEMENT
This document is available to the public through the FRA Web site at http://www.fra.dot.gov.

12b. DISTRIBUTION CODE

13. ABSTRACT (Maximum 200 words)
This project used basic and applied research and experimentation to address the need for an improved railway crosstie and fastening system for high speed passenger and joint passenger and freight routes in the US. The effort provided answers several concrete crosstie and fastening system design and performance questions that apply to the US railroad industry. The results obtained from this effort will provide the rail industry with a better understanding of the factors that affect the performance of concrete crossties and fastening systems, an improved set of performance requirements for tie and fastener system design based on field and laboratory data, and a novel, mechanistic design approach to tie and fastener design. Volume 1 (the *Project Summary Report*) summarizes the activities and results from this research project. Volume 2 provides further detailed information regarding the major tasks completed for this project.

14. SUBJECT TERMS
Concrete crossties, fastening systems, flexural behavior, mechanistic design, infrastructure components, finite element modeling, finite element, FE, finite element analysis, FEA, field experimentation

15. NUMBER OF PAGES
410

16. PRICE CODE

17. SECURITY CLASSIFICATION OF REPORT	18. SECURITY CLASSIFICATION OF THIS PAGE	19. SECURITY CLASSIFICATION OF ABSTRACT	20. LIMITATION OF ABSTRACT
Unclassified	Unclassified	Unclassified	

Contents

Illustrations

Tables

Chapter Synopsis

This research project was conducted between June 2011 and December 2014 at UIUC with funding from the Federal Railroad Administration. Volume 2 of this study provided an in-depth review of several concrete crosstie and fastening system design and performance questions, outlined in Chapter 1 through 10, that apply to the US railroad industry. The following is a synopsis of the findings presented in each chapter:

Chapter 1: The primary objective of the International Concrete Crosstie and Fastening System Survey was to poll the international railway community on the use and performance of concrete crossties and elastic fastening systems. The survey aided UIUC's research team in concluding that the manufacturing process differences between the North American and international respondents may be the cause of significantly different trends in requirements and performance of concrete crossties. The results also indicated that the most critical failure concerns in North America were related to wear or fatigue on the rail seat, rail pad, or shoulder, while more critical failure concerns internationally were tamping damage, cracking from dynamic loads, and shoulder wear. Finally, the design considerations of the fastening system manufacturers were applicable to the design of concrete crossties and the entire system.

Chapter 2: The concrete crosstie and fastening system load quantification provided a framework for quantifying loads experienced at the wheel/rail interface. However, the loading spectrum at this interface was not sufficient for the design of concrete crossties and fastening systems because wheel loads were not the loads carried by these infrastructure components. Various rail seat load quantification methodologies were investigated and compared. Many factors were considered, and there may be some additional parameters that also affect this transfer of forces.

Chapter 3: The purpose of the laboratory experimental plan was to improve the current understanding of concrete crosstie and fastening system behavior under simulated loading conditions designed to replicate actual field conditions. Laboratory experiments were easier to control and provided a greater number of replicates that were possible in the field. Increasing the control of variables helped clarify how changing a given parameter (or set of parameters) affected the whole system. Additionally, by conducting multiple replicates at each set of experimental conditions, laboratory experimentation provided for larger data sets, thereby, decreasing experimental error.

Chapter 4: The laboratory experimental results led to findings regarding the most critical set of experiments. The laboratory experimentation provided further understanding of the load path through the crosstie and fastening system in two distinct manners: First, in terms of the load going through an individual crosstie and its fastening system; second, in terms of the distribution of a given load over adjacent crossties.

Chapter 5: The field experimental plan accomplished several goals including a comprehensive understanding of the characteristic deformations and displacements of concrete crosstie and fastening system components, as well as understanding the load transfer mechanics from the wheel-rail interface, through the fastening system, and into the concrete crosstie. Another goal was to obtain data used in the validation of a 3-Dimensional finite element (FE) model of the concrete crosstie and fastening system, which was used as a tool for conducting parametric analyses to aid in the design of concrete crossties and fastening systems.

Chapter 6: The purpose of this field experimentation was to enhance the rail industry's current understanding of concrete crosstie and fastening system behavior under representative loading conditions. To accomplish interaction between different components, static loadings were applied in both the vertical and lateral direction at varying magnitudes and rail seat locations, as well as dynamic loadings were applied by both passenger and freight consists passing at varying speeds and track geometries.

Chapter 7: The purpose of the objectives, methodology, and scope of work is presented for the FE modeling efforts. The goal was to advance and optimize the current design practices of concrete crosstie and fastening systems. Also, using parametric studies, the failure mechanisms of some components could be identified and suggestions to prevent such failures could be recommended. The developed concrete crosstie and fastening system models could be a useful tool to ensure the serviceability and safety of rail infrastructure, and a means to further the state of art of track infrastructure design.

Chapter 8: The detailed procedure for model validation is presented at multiple levels, as well as results from parametric studies based on the field-validated FE model. Many conclusions were drawn, such as the FE model was proven successful in capturing critical mechanisms including the distribution of wheel loads and the flexure of concrete crosstie; the frictional behavior (frictional force and relative sliding) at the bottom of the rail seat was primarily governed by the interface (i.e. rail-pad interface and plate-concrete interface) with the lowest value of coefficient of friction (COF); the elastic modulus of the fastening system insulator had little effect on the lateral load path through the fastening system; compared to the COF at the rail-pad and plate-concrete interfaces, and the elastic modulus of rail pad, crosstie spacing had a very minimal impact on the performance of the fastening system under lateral wheel load; and, the COF at the rail-pad and the plate-concrete interfaces, as well as the elastic modulus of the rail pad, significantly affected the performance of the fastening system under lateral wheel load.

Chapter 9: The Track Component Response Calculation Tool (I-TRACK) is a tool predicted to play a role in improving the current design process for track components and will aid in developing mechanistic design practices focused on optimized component and system performance. This software will provide ease of use, coupled with the capability to analyze a broad set of outputs considering multiple loading cases and different component properties.

Chapter 10: A review is presented on how the North American concrete crosstie and fastening systems have been based on an unclear understanding of failure mechanisms, their causes, and the loading environment. This design methodology led to performance challenges and service failures that cannot be adequately explained or predicted. Based on this review, a mechanistic design process can be achieved in conjunction with the existing design process for concrete crosstie and fastening systems. A mechanistic design process could provide many benefits not currently achieved by the iterative design process outlined by the American Railway Engineering and Maintenance-of-Way Association.

Chapter 1: International Survey Results

1.1 International Concrete Crosstie and Fastening System Survey Objectives

The primary objective of the International Concrete Crosstie and Fastening System Survey (hereafter referred to as the "International Survey") was to poll the international railway community on the use and performance of concrete crossties and elastic fastening systems. The survey aided the University of Illinois at Urbana-Champaign's (UIUC) research team in developing an understanding of the most common crosstie and fastening system failures, as well as the current state-of-practice regarding the design and maintenance of these systems. Finally, it enabled UIUC to continue establishing relationships and encourage collaboration with railways, researchers, and manufacturers around the world.

The International Survey provides insight to guide many aspects of the Federal Railroad Administration's (FRA) Tie and Fastener Broad Agency Announcement (BAA) project at UIUC (including modeling, laboratory instrumentation and experimentation, and field instrumentation and experimentation), ultimately leading toward improved design recommendations for concrete crossties and fastening systems. In terms of modeling, results from this survey can help determine typical loading scenarios using modeling and loading methodologies from previous research. The survey results related to modeling also provide references for literature related to previous analysis, allowing UIUC's team to incorporate past research efforts and findings into its current work. The responses from the survey also include criteria from laboratory testing performed on concrete crossties and fastening systems around the world, offering the capability to compare North American test criteria and methodologies with multiple international standards. Finally, the survey results help steer the field experimentation efforts by identifying conditions where failure most commonly occurs and developing a greater understanding of probabilistic loading conditions and failure modes.

1.2 Audience

The International Survey was distributed to professionals in many different positions and organizations within the railroad industry, including infrastructure owners, operators, or maintainers; academic, industry, or institutional researchers; and concrete crosstie or fastening system manufacturers. This breadth of coverage provides varied perspectives on the usage and performance of concrete crossties and fastening systems. Additionally, the survey's audience was geographically diverse, with responses from the international railway community in Asia, Australia, Europe, and North America.

1.3 Development

The International Survey was developed with extensive input from many of the North American experts in concrete crosstie and fastening system design, production, use, maintenance, and research. First, a list of questions was developed internally at UIUC regarding the design, usage, performance, and failure of concrete crossties and fastening systems. After researching various online survey tools and creating an initial test survey, the questions were distributed to the UIUC FRA Tie and Fastener BAA Industry Partners, FRA, and the entire UIUC research team for review and subsequent revision. The industry partners, include experts in concrete crosstie and elastic fastening system design and performance improvement in North America, provided

feedback based on North American railroading experience and what the rail industry would like to gain from such a survey. After a significant modification and revision period, the survey was distributed to the international railway community using the online survey tool Zoomerang.

A separate set of questions was distributed to fastening system manufacturers and was addressed during subsequent personal conversations. This facilitated more comprehensive answers regarding the fastening system landscape. A summary of these responses is included in Section 1.7 of this chapter.

1.4 Content

The content of the International Survey, which includes many aspects of the usage, design, production, performance, failure, recommended practices, testing, and research of the concrete crosstie and fastening system, can be explored by seeing the comprehensive question and response lists found in Appendices A, B, and C of this results report. The appendices include the following:

Appendix A – Infrastructure Owner, Operator, or Maintainer Responses

Appendix B – Academic, Industry, or Industrial Researcher Responses

Appendix C – Concrete Crosstie Manufacturer Responses

Appendix D – Definition of Critical Model Outputs

1.5 General Survey Responses

The survey was distributed to individuals at 46 organizations who the authors believed to have extensive knowledge of the performance and design of concrete crossties and fastening systems within their organization and/or their country. Of those 46 organizations invited to participate in the survey, 28 responses were received, which corresponds to a 61% response rate.

Responses were received from Asia (5 responses), Australia (5), Europe (8), and North America (10). Nine respondents were infrastructure owners, operators, or maintainers, 12 were academic, industrial, or institutional researchers, and seven were concrete crosstie manufacturers. Given the breadth of international expertise that was captured, the number of responses was considered appropriate for achieving the objectives of this survey. Although there were no responses from Africa or South America, the authors feel that the responses are representative of the concrete crosstie and fastening system community internationally.

1.6 General Survey Results

In the development of revised design recommendations, it is important to consider failure mechanisms and field performance of components and systems. Causes of failure provide insight into ways in which the concrete crosstie and fastening system can be improved. The most common failure causes, as expressed by the responses, are fastening system wear and damage, tamping damage, and concrete deterioration beneath the rail (although many of the international researchers viewed this as the least critical failure cause). It should also be noted that structural failures are viewed as critical problems by the infrastructure owners and researchers, but are not considered to be very significant relative to other failures according to the crosstie manufacturers. Figure 1 and Table 1 and Table 2 communicate some of the key findings concerning failure.

Figure 1 depicts the criticality of concrete crosstie and fastening system problems from most to least critical, as expressed by the international and North American respondents.

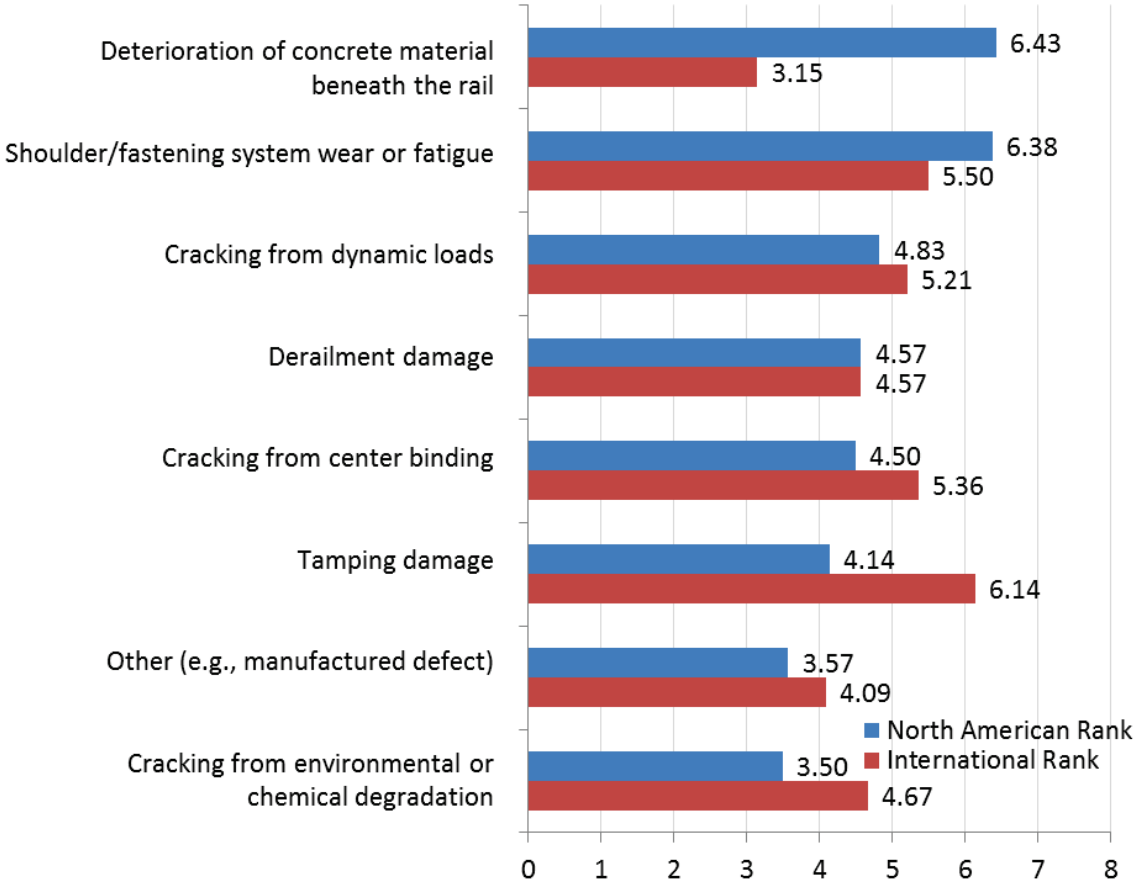

Figure 1. The Most Critical Concrete Crosstie and Fastening System Problems Ranked from 1 to 8, With 8 Being the Most Critical

According to both international and North American respondents, wear and fatigue in the shoulder and other components of the fastening system were determined to be critical problems. The international respondents expressed tamping damage as being their most critical problem, which could indicate that, comparatively, the other potential problems are not viewed as very critical. This response could also indicate that there is damage due to the tamping process or caused by infrequent or insufficient tamping. In North America, the most critical problem was determined to be rail seat deterioration (RSD). This was in sharp contrast with the international respondents, who ranked RSD as being the least critical problem.

Table 1 shows the summation of the North American responses indicating failures resulting in deficiencies of concrete crossties and fastening systems. For example, 71% of respondents indicated that concrete deterioration beneath the rail seat was a failure mechanism that was associated with their operating environment. Table 2 provides the same information according to the international respondents.

Table 1. The Most Prevalent Failure Causes Resulting in Concrete Crosstie and Fastening System Deficiencies According to North American Responses

Failure Causes Resulting in Deficiencies	Percentage of Responses (%)
Concrete deterioration beneath the rail	71
Fastening system damage	43
Poor bonding of concrete to pre-stress	43
Poor material quality or behavior (of clamp, insulator, rail pad, or crosstie)	29
Poor environmental conditions (e.g. moisture or fines intrusion)	29
Manufacturing flaws	29
Improper component design (of clamp, insulator, rail pad, or crosstie)	29
Deficient concrete strength	14
Improper pre-stress force	14
Other	14

Table 2. The Most Prevalent Failure Causes Resulting in Concrete Crosstie and Fastening System Deficiencies According to International Responses

Failure Causes Resulting in Deficiencies	Percentage of Responses (%)
Fastening system damage	50
Poor material quality or behavior (of clamp, insulator, rail pad, or crosstie)	44
Manufacturing flaws	44
Improper component design (of clamp, insulator, rail pad, or crosstie)	38
Concrete deterioration beneath the rail	38
Poor environmental conditions (e.g. moisture or fines intrusion)	31
Other	31
Poor bonding of concrete to pre-stress	25
Deficient concrete strength	19
Improper pre-stress force	6

Internationally, the most prevalent failure causes resulting in concrete crosstie and fastening system deficiencies are fastening system damage, poor material quality or behavior, and manufacturing flaws. The least prevalent causes are poor bonding of concrete to pre-stress, deficient concrete strength, and improper pre-stress force. The low prevalence of these responses can perhaps be attributed to the prevalence of the carousel manufacturing process. In

North America, RSD was the most prevalent failure cause resulting in deficiencies, followed by fastening system damage and poor bonding of concrete to the pre-stress.

Figure 2 communicates the most important concrete crosstie and fastening system topics of research from most to least critical as expressed by the international and North American responses.

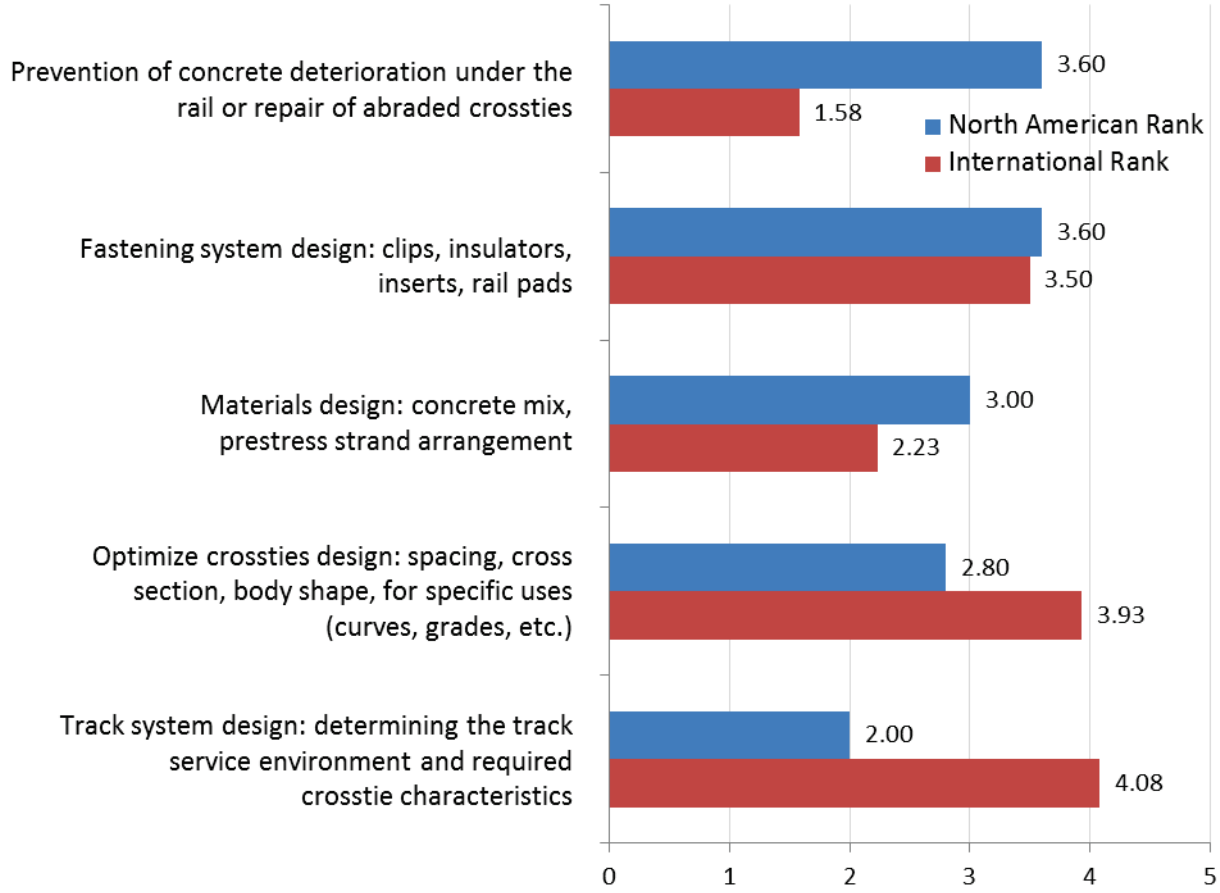

Figure 2. The Most Important Concrete Crosstie and Fastening System Research Topics; Ranked from 1 to 5, With 5 Being the Most Important

Interestingly, the international respondents indicated a reversed priority in research compared with the North American respondents. While the international respondents indicated track system design and crosstie design optimization as being the most important research topics, the North American respondents placed a high priority on RSD prevention and fastening system design. These North American research priorities are aligned with the current research thrusts at UIUC, and adjustments were made to ensure these thrusts remain consistent with the research needs identified in the International Survey. As a result, there are several projects being conducted concurrently with the FRA Tie and Fastener BAA related to mitigating RSD, and one of the primary objectives of the UIUC Tie and Fastener Research Program is to determine better mechanistic design recommendations for the crosstie and fastening systems.

Table 3 provides a summary of the total responses while comparing the international and North American responses.

Table 3. Summary of Responses to International Concrete Crosstie and Fastening System Survey

	International Responses	North American Responses
Participant Demographics		
Total number of responses	18	10
Infrastructure owner, operator, or maintainer	5	4
Academic, industry, or institutional researcher	10	2
Concrete crosstie manufacturer	3	4
Loading Environment		
Average maximum freight axle load*	29.5 tons (26.8 tonnes)	39.1 tons (35.4 tonnes)
Average maximum passenger axle load*†	21.6 tons (19.6 tonnes)	29.1 tons (26.4 tonnes)
Average annual tonnage (per track)	38.7 million gross tons (35.1 million gross tonnes)	100.0 million gross tons (90.8 million gross tonnes)
Fastening system manufacturers	Vossloh, NABLA, JIS, Pandrol, Railtech	Pandrol, Vossloh, Unit Rail/Amsted RPS**
Concrete crosstie manufacturers	Austrak, SATEBA, RAIL.ONE, KNR, Parma, Luja, SSL, BK.International, Taemyung, Samsung, IS Dongseo, Sampyo	CXT, Koppers (KSA), Rocla
Average concrete crosstie design axle load	27.6 tons (25.0 tonnes)	37.4 tons (33.9 tonnes)
Average tangent crosstie spacing	24.2 inches (61.4 centimeters)	24.0 inches (61.0 centimeters)
Average concrete crosstie and fastening system years of use	48.4	30.0
Trends in Crosstie and Fastener Performance		
Average concrete crosstie design life (years)	35.0	41.7
Abrasion plate or frame	No	Yes
Commonly failed components	Screw, clip	Pad, rail seat
Rail seat deterioration	No	Yes
Focus of research	Loading, testing, design	Life cycle cost reduction
Average minimum allowable concrete strength at transfer	6,500 psi (44.8 MPa)	4,700 psi (32.4 MPa)
Average 28-day concrete compressive strength	8,700 psi (60.0 MPa)	8,250 psi (56.9 MPa)
Concrete crosstie manufacturing process	Carousel, long line**	Long line

*Interpreted from responses due to discrepancies in axle or wheel loads
**Added by report authors for completeness
†Light rail response excluded

To better understand the complex loading conditions within the concrete crosstie and elastic fastening system, it is important to understand what types of loads are being applied to that system. The maximum freight static axle load within the responses was 44.1 tons and the average maximum freight static axle load is 32.3 tons. Internationally and domestically, the average maximum freight static axle load exceeds the design axle load based on responses from the concrete crosstie manufacturers. To include dynamic considerations in the loading environment, impact factors (IF) must also be applied to the static axle loads, ranging from 130% to 300% (with most responses around 150– 200%).

As expected, the load and tonnage values are, on average, substantially higher in North America than in the remainder of the world, according to the respondents. Also, the trends in commonly failed components and use of an abrasion frame in North America coincide with the prevalence of RSD, as shown previously in Figure 1 and Table 2.

Another significant finding displayed in Table 3 is the disparity in average minimum allowable concrete strength at transfer of pre-stress in the concrete crosstie. The concrete strength at transfer according to the North American respondents was only 72% of that reported by the international respondents, on average. This discrepancy is almost removed, however, once the 28-day compressive strength is recorded, as the North American 28-day strength is, on average, 95% of that internationally. Perhaps the difference in strength at pre-stress transfer is associated with the prevalent manufacturing processes (often carousel internationally and long line in North America).

1.7 Fastening System Manufacturer Survey

Because it was unlikely that the online survey would have been applicable to their unique global positions within the railway industry, the fastening system manufacturers were distributed a separate set of questions on an individual company basis. This list of questions was supplemented by personal conversations to discuss the current landscape of fastening systems around the world and how their organizations contribute to that landscape.

Due to the proprietary nature of the fastening system manufacturer responses, most of the results have not been included in this report. However, a few trends in the responses have been included.

For instance, in designing the fastening system, the following parameters are generally considered by the manufacturers: tonnage, daily train volume, velocity of trains, static loads, dynamic loads, the ability of the pad to evenly attenuate load to the rail seat, abrasion of the concrete rail seat by the pad or abrasion plate, and the curve radius. It is interesting to compare these considerations with those found in Chapter 30 of the American Railway Engineering and Maintenance-of-Way Association's (AREMA) recommended practices for the concrete crossties themselves, which include tonnage, train speed, static loads (with impact factor), crosstie spacing, and crosstie length.

There were also noteworthy responses to the average life of the fastening systems. Responses varied from the life of the crosstie to the life of the rail, with the pad performing the most reliably of all the fastening system components. Shortcomings are most commonly seen in the insulator materials, while most failures occur in demanding operating environments with heavy curvature and steep grades.

1.8 Summary

There were several important conclusions that can be made because of this survey. First, the manufacturing process differences between the North American and international respondents may be the cause of significantly different trends in requirements and performance of concrete crossties. There may be some testing that could be conducted to better determine the correlation between these trends. The results also indicated that the most critical failure concerns in North America are related to wear or fatigue on the rail seat, rail pad, or shoulder, while more critical failure concerns internationally are tamping damage, cracking from dynamic loads, and shoulder wear. Finally, the design considerations of the fastening system manufacturers can be applicable to the design of concrete crossties and the entire system. The fastening system manufacturers indicated that component and system interaction played a large role in their design, and this concept should be considered in the development of mechanistic design recommendations for concrete crossties and fastening systems.

This survey also played an important part in guiding research undertaken by UIUC. The results provided guidance by giving insight into specific design criteria and the variation among them. A key deliverable from this project is the development of a mechanistic design approach for concrete crosstie and fastening systems. The first step in this process is to understand how different design criteria are considered throughout the international crosstie and fastening system community. Railroads and concrete crosstie manufacturers may consider different inputs when designing the system, so understanding the process will help to combine the methods into one overarching design process.

Additionally, this survey allowed the UIUC research team to develop connections with industry professionals and provided a clear vision of the concrete crosstie and fastening system design and performance challenges faced today, both in domestic and international organizations. Insight on prevalent failure modes helped to clarify where current design processes are the most lacking. Finally, the section of the survey regarding research needs provided insight as to what types of problems may have been addressed internationally, guiding domestic researchers to results from prior research that may be relevant to the North American environment. Ultimately, avoiding overlap in research allows funding agencies to maximize the benefits of their research funding.

Chapter 2: Loading Quantification Document

2.1 Load Quantification Objectives

The performance of concrete crossties and fastening systems is largely dependent on the type and magnitude of loads travelling through the track superstructure. While a qualitative understanding of these loads is useful in interpreting fastening system component interaction and resulting failure modes, quantifying these loads is critical to determining the demands each component must withstand. There have been many efforts to quantify wheel loads and some research into how these loads transfer to the underlying infrastructure. However, there is not a clear understanding of how the load is distributed after passing from the wheel-rail interface through the rail and into the fastening system and rail seat. A better understanding of the load path, the load distribution over the rail seat, and the load path through the ballast to the subgrade is needed.

2.2 Overview of The Wheel Loading Environment

The discussion of the loading environment must begin by distinguishing between, static, quasi-static, dynamic, and impact loads. The static load is the load of the rail vehicle at rest, as if it were being weighed on a scale. The quasi-static load is "a low-frequency oscillation superimposed over the static dead weight of the train vehicle at the wheel-rail interface" (Leong 2008). More simply, the quasi-static load can be considered the combined static load and effect of the static load at speed (Standards Australia 2003), independent of time. The quasi-static load is perhaps best illustrated in curved track, where the vehicle imparts loads onto the rail due to centripetal force and curving (Andersson et al. 2013). Dynamic loads are the result of high frequency wheel/rail load interactions. Dynamic loads are affected by track component responses, including inertia, damping, stiffness, and mass, and are more complex to quantify. They are characterized by high-frequency load inputs that are dependent on time. The impact load, which often creates the highest loads seen in the track structure, is created by track and wheel irregularities, the most familiar being the flat spot on a wheel. These impacts create high-frequency, short-duration loads that travel through the infrastructure and may cause significant damage. While these distinctions regarding static and dynamic loads can be applied worldwide, their magnitudes may vary significantly across continents due to a variety of factors.

The rail operating environment in North America is unique, given the co-existence of passenger traffic and heavy axle freight traffic on shared infrastructure. As new high-speed intercity passenger service grows, it must do so while sharing infrastructure with the existing freight railways for most routes. One of the many challenges facing shared use infrastructure is the performance of critical components that were primarily designed for slower-moving, heavy-axle freight trains. To better understand the loading applied to the infrastructure, UIUC acquired significant data from Wheel Impact Load Detector (WILD) sites throughout the US from both Amtrak and the Union Pacific Railroad (UP).

These data provide insight to the varied loading distributions at representative sites throughout North America. Specific loading properties such as peak vertical load, peak lateral load, and speed are captured using strain gauge instrumentation, and these data are graphed and analyzed by creating various distributions and determining relationships between them. Figure 3 shows data that depicts a cumulative distribution of locomotive, freight car, and passenger coach peak

vertical wheel loads when about 50% of the wheels are related to freight traffic and 50% of the wheels related to passenger service, while Figure 4 shows a cumulative distribution of peak vertical wheel loads where more than 90% of the wheel loads are associated with passenger traffic. Both of these figures demonstrate widely different load levels for multiple traffic types traveling over the same infrastructure.

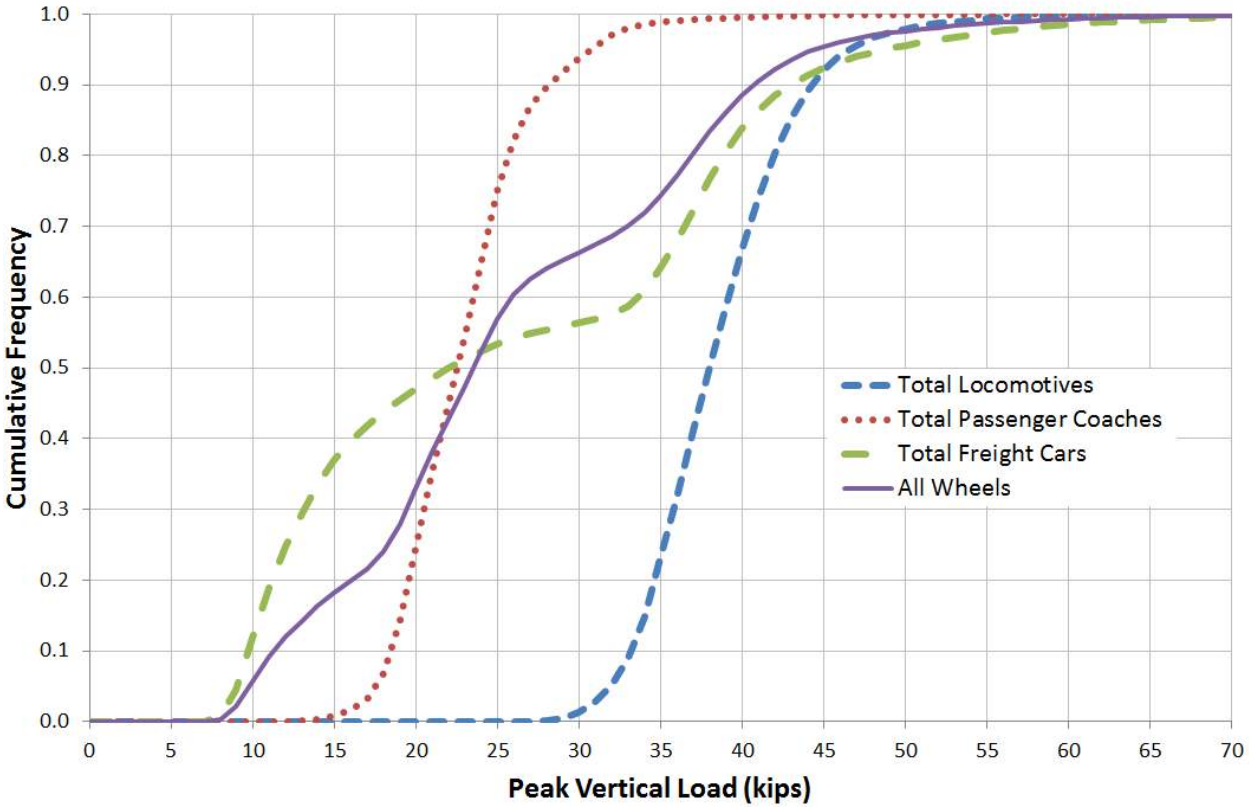

Figure 3. Freight and Passenger Peak Vertical Loads at Edgewood, Maryland (November 2010)

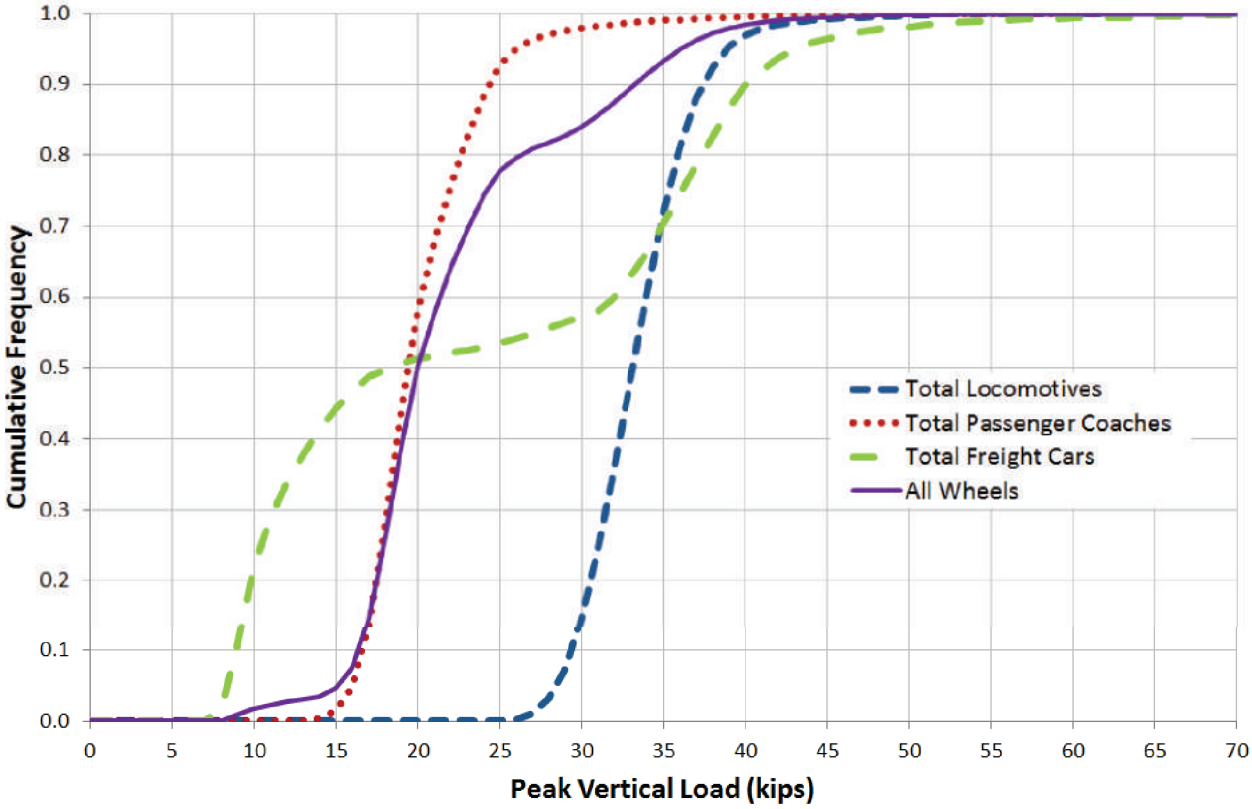

Figure 4. Passenger Peak Vertical Loads at Hook, Pennsylvania (November 2010)

The WILD data also provides information about lateral loads, but because the site is constructed on tangent track, the lateral loads are low. To monitor more significant lateral loads in curved section of track, instrumented wheel sets (IWS) can be utilized. IWS measurements on U.S. coal routes have measured lateral loads up to 31 kips (Koch 2007) toward the field side of track. However, it may be possible for even higher lateral loads to occur in areas with non-optimal rail profiles, friction management techniques, track condition, or wheel condition (Kerchof 2012).

Longitudinal forces in the track must also be considered. They most often occur because of thermal expansion or contraction of the rail and locomotive tractive effort or braking. Significant longitudinal forces can also be generated due to wheel-rail contact. In fact, with proper support conditions, four locomotives pulling a loaded train can generate longitudinal forces in excess of 225 kips (Rhodes 2013).

2.3 Lateral/Vertical Force Ratios

The lateral/vertical (L/V) force ratio is the ratio of the lateral component to the vertical component of the wheel load (Hay 1982). As this ratio increases, the lateral force against the rail increases, which can present a variety of operational and engineering challenges. High L/V force ratios can create a variety of hazards, as indicated by Table 5 (Hay 1982, Track Train Dynamics 1973). Maximum L/V force ratios in the 0.4 to 0.6 range are more typical of freight rail operation on curved track, as indicated through over-the-road IWS tests on U.S. coal routes (Koch 2007). High L/V ratios are a greater safety concern on curved track, as they are often the cause of rail rollover instances that can lead to a derailment. L/V force ratios on tangent track

are significantly lower than those on curved track, and the magnitude of this disparity will be investigated by field experimentation conducted by UIUC researchers. WILD data obtained on Amtrak's Northeast Corridor indicate that typical L/V force ratios on tangent track rarely exceed 0.2.

Table 4. Hazards Associated With Particular L/V Force Ratios (Hay 1982)

• L/V Force Ratio	• Degree of Hazard
• 0.68	• The resultant passes outside the base of the rail, indicating initial instability; an unrestrained rail may overturn
• 0.75	• A worn wheel flange may climb a worn rail
• 0.82	• The flange disengages from the rail; an outside wheel may lift from the rail on curves
• 1.29	• Derailing condition; wheel will climb a new rail; a new wheel lowers the wheel climb threshold

AREMA Chapter 30 (Ties) Test 6 for Wear and Abrasion specifies an L/V force ratio of 0.52 for testing in order to "simulate conditions for severe service testing (i.e., curves greater than 5 degrees)" (AREMA 2012). This L/V force ratio is also specified for simulating "tangent or shallow curves," but with a lesser magnitude in loading (AREMA 2012). This is generally considered to be a high L/V force ratio; however, this loading condition is specified for this test to investigate durability of the fastening components in an accelerated fashion.

As part of the FRA's Track and Rail and Infrastructure Integrity Compliance Manual, a safety limit has been established for a single wheel L/V force ratio related to the wheel's flange angle:

$$Single\ Wheel\ L/V\ Force\ Ratio \leq \frac{\tan(\delta)-0.5}{1+0.5\tan(\delta)} \quad (1)$$

Where:

δ = wheel's flange angle

According to the FRA manual, the L/V force ratio exerted by the wheel must be less than the above safety limit expression (FRA 2002).

The L/V force applied to the rail is dependent on wheel/rail interaction and track geometry variables. Some of these variables include curve radius, wheel/rail interface profiles, suspension characteristics of railcar trucks, and train speed operation (Iwnicki 2006). The wheel/rail interface is also governed by the flange angle of the wheel and the profile of the rail head, which can vary also based on the wear conditions of both the rail and wheels.

On sections of curved track, it is common that trains operate either above or below the design balancing speed of that curve. This is especially true on shared-corridors where passenger trains are operating at higher speeds and freight consists generally operate at lower speeds. The effect this has on L/V force ratios of the loads applied to the rail is that a train operating below the balance speed will cause forces to shift towards the inside of curve, possibly causing high pressures on the field sides of the low rail seats of the crossties. In the condition of trains

operating above design balance speed, forces are shifted to the outside of the curve, possibly causing high pressures on the field sides of the high rail seats (Rapp 2012).

2.4 Investigation and Comparison of Rail Seat Load Calculation Methodologies

2.5 Introduction

An important part of railway track structural analysis is the understanding the path of the load as it travels through the railcar suspension system, into the rail, onto the crossties, and down into the track substructure (ballast and subgrade). It is widely accepted that a wheel load being applied to the rail is then distributed over several crossties both in front of and behind the location of the wheel, even when the wheel is located directly above a single crosstie (AREMA 2012). An exception to this distribution might be in the case of a hanging crosstie, where there is little to no support beneath the crosstie, and the entire wheel load is supported by adjacent crossties. Using specially designed field instrumentation, wheel loads can be measured as they pass over a given section of track, thus capturing the overall input load into the track structure. The difficulty lies in understanding the distribution of these axle loads on to individual crossties at the interface of the rail pad and the concrete rail seat area. The importance of understanding this loading lies in the fact that deterioration of the concrete surface at this interface has been identified, and is believed to be a result of a crushing mechanism (Marquis 2011). Concrete crosstie deterioration at the rail seat can also be caused by the abrasion mechanism; localized high pressures with relative displacements can cause increased strain on cement particles, leading to deterioration (Kernes 2012).

To gain a better understanding of the load path from the wheel to the crosstie, an investigation of various rail seat load calculation methodologies was undertaken. The four methods presented are a means of calculating the magnitude of a rail seat load in terms of the total force applied to the rail seat area. They do not calculate the pressure or distribution of this load. The methods are sourced from AREMA, and equations developed and/or used by Arnold Kerr, Josef Eisenmann, and Arthur Newell Talbot. The methods are presented in order of increasing complexity, beginning with methods used for simplified load distribution estimation, and progressing to methods requiring a greater level of input. The strengths and weaknesses of each method are discussed, as are certain variables that may be included or excluded in each, leading to a recommendation as to which scenario a given method would be feasible to use. After discussion, a series of example calculations are presented to provide a numerical comparison of the various investigated methods. It should be noted that this analysis and discussion will focus primarily on concrete crosstie track for discussion and example calculations.

2.6 Rail Seat Load Calculation Methodologies

2.6.1 Inputs

Several of the methods require certain track characteristics as inputs to calculate rail seat loads and distributions. All methods require the applied load as the primary input, generally consisting of the axle or wheel load. Additionally, they all begin with a static load analysis, but only two allow the ability to account for dynamic and/or impact loadings of the rail seats from various speeds of train operation. Several of the methods can also account for variability in the support provided by the track structure through inclusion of a track modulus value. A lower track modulus means that the track is less stiff, and will deflect more under load. A higher track

modulus will reduce deflection, but can result in higher rail seat loads (Lu 2008). The AREMA Manual for Railway Engineering (hereafter, referred to as the "AREMA manual") provides a table of approximate track modulus values for varying crosstie types and support conditions, as shown in Table 5.

Table 5. Track Modulus Values for Various Crosstie Configurations (Adapted from (AREMA 2012))

Crosstie Configuration	Track Modulus (k, lb/in/in)
Wood-tie track, after tamping	1,000
Wood-tie track, compacted by traffic	3,000
Plastic composite-tie track, compacted by traffic	3,000
Concrete-tie track, compacted by traffic	6,000
Wood-tie track, frozen ballast and subgrade	9,000
Concrete-tie track, frozen ballast and subgrade	18,000

In several of these methods the crosstie spacing is also an input into the rail seat load calculation. The flexural rigidity of the rail, which is the product of the modulus of elasticity of the rail and the moment of inertia, is also an input for some of the calculations. The modulus of elasticity of the rail can vary depending on the material composition of the steel, but is generally considered to be 30,000 ksi for railroad applications. The moment of inertia is dependent on the size of the rail section, and a larger rail section will produce a higher flexural rigidity.

In order to simplify the scope of this investigation of rail seat load calculations, the focus will be on concrete crosstie track. The example calculations presented will use a track modulus value of 6,000 lb/in/in (except as noted), although the spreadsheet created for this analysis allows the option of changing this value. All examples are also performed using single wheel loads and negating effects of adjacent wheels.

2.6.2 AREMA Method

The AREMA manual provides recommended practices and guidelines for railway track, structures, infrastructure and passenger, and systems management (AREMA 2012). Chapter 30 of the AREMA manual covers crossties, focusing on wooden, concrete, and composite crosstie designs. The AREMA manual does not provide many details directly relating to rail seat loading or design recommendations for this area of the crosstie. However, it does include an analysis on allowable loads to be placed on a single crosstie in consideration of allowable pressure on the ballast and sub-ballast layers. The AREMA manual presents this allowable crosstie to ballast pressure information with varying center-to-center crosstie spacing values, because it is believed that this spacing value will have the largest effect on track deflections under constant crosstie, ballast, and subgrade conditions (AREMA 2012). Increasing crosstie spacing not only lowers the overall value of track modulus for a given section, but also places a higher stress on individual crossties (AREMA 2012).

The AREMA manual provides information that can be used to estimate rail seat loads given tie spacing and single tie load bearing percentage. Figure 5, which is Figure 30-4-1 from Chapter 30, Part 4 in the AREMA manual, is an estimated distribution of loads for concrete crosstie track (AREMA 2012). The purpose of this chart is to determine the percentage of an axle load that a single crosstie must carry under varying crosstie spacing. It is presented in the AREMA manual

in a section discussing the effects of axle load on the pressure imparted on the ballast by the crosstie. However, because the path of the load in the track structure travels from the wheel, through the rail and into the crosstie via the rail seats, before being distributed onto the ballast by the base of the crosstie, it seems plausible to use this chart to determine the magnitude of rail seat loads on a single crosstie. Because this chart is presented in Part 4 discussing concrete crossties, from the previously discussed track modulus values provided in the AREMA manual as shown in Table 5, it is assumed that the track modulus used in creating this distribution is 6,000 lb/in/in.

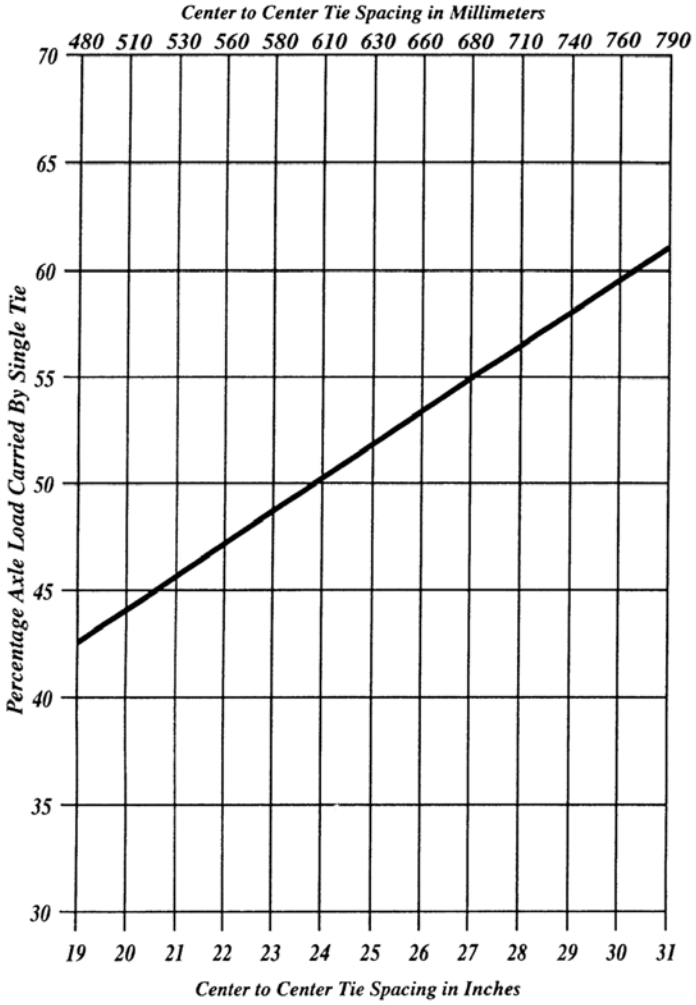

Figure 5. Estimated distribution of loads (AREMA 2012)

The distribution function of loads carried by a single crosstie as presented in this figure can be expressed as the following linear equation (AREMA 2012):

$$y = 1.5626x + 12.811 \quad (2)$$

Where:

y = percentage of axle load carried by a single crosstie

x = center to center crosstie spacing (inches)

Once the percentage of load carried by a single crosstie is calculated by using this equation, a known axle load can be multiplied by this percentage to determine the magnitude of the load carried by that crosstie. This load can then be divided by two to calculate the magnitude of the load carried by each rail seat of the crosstie. This method does not provide a means of calculating the load that is applied to crossties that are adjacent to the loaded tie, to facilitate an understanding of longitudinal load distribution.

The AREMA method is relatively simple and quick to use, and axle load, center-to-center crosstie spacing, and distribution factor are the only inputs required to obtain a rail seat load value. When this information is available for a given section of track it would seem feasible to use this method to obtain rail seat forces. Furthermore, Figure 5 accounts for track modulus, as it was formulated for the general value of stiffness for concrete crosstie track as shown in Table 5. The AREMA manual does present another figure similar to Figure 5, showing linear approximations of percent of axle load carried by a single crosstie under varying crosstie spacing for different track modulus values. This is Figure 30-1-1 in Chapter 30 Part 1 of the AREMA manual, but Figure 5 was chosen for investigation because this report focuses on concrete crosstie track. The general trend of this chart is that as the track modulus lowers, so does the percentage of the axle load carried by a single crosstie, meaning that a less stiff track will spread the load over a wider range of crossties. Whereas it would seem desirable to have a lower track modulus to reduce the impact of rail seat loads, track with a lower stiffness will experience larger magnitudes of deflection under repetitive loadings, which is a main component leading to deterioration of the track structure (Hay 1982).

One caveat to using the AREMA method is the assumption of a linear distribution of axle loads under varying crosstie spacing. This distribution was likely developed under the assumption of similar track quality conditions for all the various crosstie spacing values presented. It is possible that the track modulus can vary within given sections of track, a factor largely dependent on subgrade conditions. The AREMA manual does recognize this possibility by stating that "the percentage of wheel-to-rail load carried by an individual crosstie varies from location to location" (AREMA 2012). Nonetheless, using Figure 5 appears to be a reasonable method for calculations of approximate rail seat loads.

Talbot Equations

Equations developed by Arthur Newell Talbot at the UIUC are another method for calculating rail seat load. Talbot's equations for track analysis are presented in the *Railroad Engineering* textbook by William H. Hay (Hay 1982) and are provided in their entirety in the original Talbot reports (Chambers 1980). These equations can be used for practical track substructure and superstructure design, and are comprehensive, containing several variables not included in the two previously discussed rail seat load calculation methods (Hay 1982). Unlike the AREMA method, in which the rail seat loads are determined from a given distribution of axle load, the Talbot equations provides a method to calculate this value. The Talbot equations also include methods for determining rail deflection, as well as bending moments and stresses in the rail, from which the formula for rail seat loads is derived.

A section of rail will see its maximum deflection and bending moment at the location of a wheel load. Although this load is usually distributed by the rail to a crosstie and several adjacent crossties on either side as discussed previously, it is possible that under poor track conditions a single crosstie will carry the entirety of an axle load (Hay 1982). This is not a desired loading

scenario. A direct method for calculating a maximum rail seat load, with the ability to input rail stiffness and track condition, can provide a more accurate view of the loading of a rail seat. The Talbot equation for maximum rail seat load is as follows (Hay 1982):

$$Q_0 = \frac{0.391PS}{x_1} \quad (3)$$

Where:

Q_0 = maximum rail seat load (pounds)

P = design wheel load (pounds)

S = center to center crosstie spacing (inches)

x_1 = distance (inches) to where bending moment becomes zero

The ability to account for track modulus and rail stiffness and size in this is accounted for in the x_1 value, whose formula is as follows (Hay 1982):

$$x_1 = \frac{\pi}{4}\left(\frac{4EI}{u}\right)^{\frac{1}{4}} \quad (4)$$

Where:

E = modulus of elasticity of rail (generally assumed to be 30×10^6 psi)

I = moment of inertia of the rail (inches^4)

u = track modulus (pounds/inch/inch)

These two equations include several track condition and design variables. The user can calculate a rail seat load by incorporating the effects of the variables into a percentage of the wheel load that a single rail seat carries.

The moment of inertia of the rail is based on the rail size. Multiplying the moment of inertia by the modulus of elasticity of the rail produces a value known as the flexural rigidity of the rail, which is a factor in the rails ability to distribute a given load over various crossties. A larger rail size will increase the flexural rigidity of the rail which, according to the Talbot equation, will reduce the maximum deflection of a given section under an applied load. According to the two equations presented above, a higher flexural rigidity of the rail will also reduce the magnitude of the load on a single rail seat. The condition and type of track in question is also incorporated in the "x_1" value through means of the track modulus value. As shown previously in Table 2, this value varies for different types of track, and even within a given track type can vary based on track quality. According to the Talbot equations, a high track modulus value will result in higher rail seat loads (Chambers 1980). Therefore, a stiffer structure like concrete crosstie track must have resilient pads at the rail seat to protect from wheel impact loads and abrasive wear of the concrete material (AREMA 2012).

The Talbot equations can also be used to consider the effect of multiple wheel loads simultaneously applied at separate locations of the track structure. When considering multiple wheel loads, the location of maximum pressure is not guaranteed to be directly beneath one of the points of loading. Thus, it is necessary to evaluate the pressure intensity acting at a general distance, "x," from the point of loading. The formula is as follows (Hay 1982):

$$p_r = P\left(\frac{u}{64EI}\right)^{\frac{1}{4}} * e^{-\lambda x} * (\cos \lambda x + \sin \lambda x) \quad (5)$$

Where:

P = design wheel load (pounds)

u = track modulus (pounds/inch/inch)

E = modulus of elasticity of rail (generally assumed to be 30×10^6 psi)

I = moment of inertia of the rail (inches^4)

λ = damping factor (inches^{-1})

x = distance (inches) from point of loading

The damping factor "λ" accounts for track modulus and rail elasticity and moment of inertia, and is calculated as follows (Hay 1982):

$$\lambda = \left(\frac{u}{4EI}\right)^{\frac{1}{4}} \quad (6)$$

Where:

u = track modulus (pounds/inch/inch)

E = modulus of elasticity of rail (generally assumed to be 30×10^6 psi)

I = moment of inertia of the rail (inches^4)

Rail seat load can then be calculated from the pressure at location "x." The formula is as follows (Hay 1982):

$$q = p_r S \quad (7)$$

Where:

p_r = rail seat pressure (pounds/inch)

S = crosstie spacing (inches)

The effect of multiple wheel loads can be considered by superposing the pressures generated by each individual wheel load. The position of each load is considered relative to a reference point, typically the leftmost wheel load, and these relative positions are accounted for in determining the distance "x" for each rail seat to a given point. The rail seat pressure calculation is then iterated along the length of the rail to determine the maximum value. The maximum rail seat load is then calculated using this maximum rail seat pressure as the value of "p_r" in formula (7).

While these equations were developed using static wheel loads as input, Talbot recognized that the load on a crosstie will increase under moving and dynamic loads. Talbot, therefore, developed a formula that increases the static loads by one percent for every one mile per hour increase in speed above five miles per hour. The formula is as follows (Hay 1982):

$$P_v = P + 0.01P(V - 5) \quad (8)$$

Where:

P_v = dynamic load (pounds) at speed V

V = speed (miles per hour)

P = static load (pounds)

Compared to the AREMA method for calculating rail seat loads, the Talbot equations take into account a wider range of variables including rail stiffness, crosstie spacing, size and stiffness, stiffness of the ballast and subgrade layers, and the effect of multiple wheel loads (Hay 1982). Thus, it would seem that this method produces results of greater accuracy than the previous two approximation methods. According to Hay, the results from the Talbot equations are very similar to values obtained in field testing (Hay 1982). Recent analysis at UIUC of WILD data from Amtrak's Northeast Corridor reveals that this dynamic wheel load factor may be overly conservative for current wheel loads and train operating speeds.

Kerr and Eisenmann Equations

The textbook, *Fundamentals of Railway Track Engineering* (Kerr 2003), provides a detailed analysis of loading of the railroad track structure. The analysis of railroad track began by modeling the rail as a beam on discrete rigid supports, then evolved to be a beam on discrete elastic supports, and now is viewed to be continuously supported (Kerr 2003). In Kerr's text, many methods for determining bending stresses and deflections in a track structure are presented. He also presents a methodology for calculating rail seat loads from known wheel loads. Kerr recognizes the rail is generally viewed as being continuously supported and that the distribution of pressure on the track structure from a loaded rail is viewed as being continuously distributed. However, because rail seat forces can act only on the crossties, Kerr uses the following formula to determine the rail seat force using a continuous pressure distribution curve created by rail deflection under loading:

$$F_{max} = \frac{P\beta}{2}a \tag{9}$$

Where:

α = center-to-center tie spacing (inches)

P = wheel load (pounds)

β = variable including track modulus and rail properties (see below)

The maximum rail seat force and the applied wheel load are proportional, i.e., F_{max} will increase as wheel load increases. The β value in this equation allows for the inclusion of variables such as track modulus and rail size and modulus, and is defined as:

$$\beta = \sqrt[4]{\frac{k}{4EI}} \tag{10}$$

Where:

k = rail support modulus, or track modulus (pounds/inch/inch)

E = modulus of elasticity of rail (generally assumed to be 30×10^6 psi)

I = moment of inertia of the rail (inches^4)

This β value is derived from analysis of bending stresses and moments in rails on longitudinal tie track when a single wheel load is applied. When calculating the max rail seat force, k is taken as

three times the value of K_{summer} to account for the stiffer track during the winter months. This stiffening is due to frozen track substructure, which will cause the most severe loading on the system. Another consideration is the fact that the track ballast (and the substructure as a whole) stiffens with increasing wheel load, and the maximum rail seat load is increased by 50 percent to account for this. Any rail seat load determined using standard linear analyses should be multiplied by 1.5 in order to account for this ballast stiffening (Kerr 2003). However, when ballast is frozen this stiffness becomes less of a factor, thus only one of these assumptions should be used. Frozen ballast will have the highest stiffness, so accounting for the non-linearity of the substructure becomes unnecessary. In the sample calculations below, the winter modulus will be used in lieu of the ballast factor.

Another text that goes into a similar depth of railroad track analysis is *Modern Railway Track* (Esveld 2001). The methods for calculating rail seat loads presented by these authors are similar enough to describe jointly, and yield identical calculated static rail seat loads if the worst-case factors in Kerr aren't used (substructure stiffening under load and winter modulus). One difference between the two is that the Eisenmann method approaches rail seat force calculation using the discrete support method, rather than viewing the rail as a continuously supported beam. Each discrete rail support is meant to simulate the rail seat of a crosstie. Thus, stress in the rail created by wheel loads can be developed into forces acting on these discrete rail supports. The calculation for an average rail seat force under a wheel load is given by Esveld as:

$$F_{mean} = \frac{Q}{2}\sqrt[4]{\frac{k_d a^3}{4EI}} \tag{11}$$

Where:

F_{mean} = mean value of bearing force (pounds) on a discrete rail support in pounds

Q = effective wheel load (pounds)

k_d = half support stiffness (pounds/inch)

a = center-to-center crosstie spacing (inches)

The largest difference between the Kerr and Eisenmann methods is the presence of the half support stiffness value, k_d. In the average rail seat force calculation, the half support stiffness value is a means of determining the stiffness of a single discrete rail support, or in this instance a single crosstie, and is defined by the following equation (Esveld 2001):

$$k_d \approx k \times a \tag{12}$$

Where:

k = track modulus of elasticity (pounds/inch/inch)

a = center-to-center crosstie spacing (inches)

This value is taken to be an approximation, as the actual stiffness of the discrete supports can vary from crosstie to crosstie. This approximation simply distributes the overall track modulus value to a section of crossties based on the center-to-center spacing. An assumption made by using this simplified equation is the uniformity of track support along the section of track being analyzed. If formula (9) is substituted into formula (8), these equations that are presented by Esveld become identical to formula (6) presented by Kerr, once the β value from formula (7) has been calculated. Thus, either of these methods can be used to calculate rail seat forces; the

decision to make between the two is whether to view the rail on the track structure as a continuously supported beam, or as supported at discrete points. Kerr will have a slightly higher static input load due to the factor accounting for substructure stiffening under loads, but other than that factor the results are the same. The primary difference between the two methods is how they account for speed.

Kerr accounts for speed by varying the value of the input load used to calculate rail seat load. When considering the effect of varying train operating speed on rail seat force calculation, Kerr uses an equation to evaluate the increase in magnitude of the wheel load. The formula is given as (Kerr 2003):

$$P^{dyn} = (1 + \theta) * P^{static} \tag{13}$$

Where

θ = dynamic coefficient

P^{static} = static wheel load (pounds)

The dynamic coefficient "θ" accounts for the train speed and wheel diameter, and is calculated as follows (Kerr 2003):

$$\theta = 0.33 * \frac{v}{D} \tag{14}$$

Where:

v = speed (mph)

D = wheel diameter (in)

This increased value of P can then be used in Kerr's equation, resulting in an increased rail seat load. There are several alternative approaches to calculate the dynamic coefficient, some of which use empirical data presented in graphs, and one for speeds greater than 100 km/h. The formula above is taken from the 1996 American Railway Engineering Association (AREA) Manual (Kerr 2003). This is the most recent iteration of the dynamic coefficient, and is currently considered to be the most accurate.

The Esveld textbook presents formulas for including the effect of train speed into rail seat force calculation which differ from those used by Kerr. These equations describe an effect known as the Dynamic Amplification Factor (DAF), and the calculated value should be taken as an approximation due to the fact that variables such as geometric parameters of the track and mechanical characteristics of the track and train vehicle are not considered (Esveld 2001). The DAF, developed by Josef Eisenmann, is calculated using the following parameters:

$$DAF = 1 + t\phi \qquad if\ V < 60\ km/h \tag{11}$$

$$DAF = 1 + t\phi\left(1 + \frac{V - 60}{140}\right) \qquad if\ 60 \leq V \leq 200\ km/h \tag{12}$$

Where:

t = multiplication factor of standard deviation (depends on confidence interval)

φ = track quality factor

V = train speed (kilometers per hour) (60 kph = 37.3 mph; 200 kph = 124.3 mph)

The value for "t" in this analysis is three, given this is the assigned value for rail stresses, fastenings, and supports, and best represents the importance of the rail for safety and reliability of rail traffic (Esveld 2001). The factor depending on track quality, "ϕ," can be chosen as 0.1, 0.2, or 0.3 for track conditions of very good, good, and bad, respectively. In order to apply this amplification factor to the mean value of bearing force on a discrete rail support, the following equation is used:

$$F_{max} = DAF \times F_{mean} \quad (13)$$

Where:

F_{max} = maximum bearing force (pounds) on discrete rail support due to wheel load

F_{mean}= mean value of bearing force (pounds) on discrete rail support

In an undesired scenario, the value for "F_{max}" may be the same as the wheel load, meaning that the track condition is in such a state that a single crosstie is bearing the entire force and adjacent crossties are receiving none (Esveld 2001). An example of this scenario would be when degraded ballast under repeated loadings causes several crossties in a given section of track to be relatively unsupported, potentially leaving one well-supported crosstie to bear the entire wheel load.

Because of the ability to incorporate a large number of variables based on track quality and design, as well as the inclusion of the DAF for various train speeds, the equations presented by Esveld could be used to calculate rail seat loads with higher accuracy than the previously presented methods. The concept of the rail being a continuous beam on an elastic foundation or supported by discrete points (crossties) are common approaches for design of the railway track and understanding its responses under loading. The ability to distribute the stresses in the rail onto discrete supports simulating crossties greatly enhances the use of these equations.

Example Calculations

To numerically compare the various methodologies for calculating rail seat loads, example calculations were performed. A spreadsheet was created for two formats of input load. In one format, the input load is simply a determined applied load value, and no speed factors are involved. This format would be more beneficial to compare with modeling work or field experimentation where a given static load is applied to the rail. Other inputs include crosstie spacing, track modulus, and the selection of 115RE, 132RE, 136RE, or 141RE size rail section. For this example calculation, input loads ranging from 10,000 to 50,000 pounds were used and plotted for each of the four discussed rail seat load calculation methods. A crosstie spacing of 24 inches was used, the selected rail size was 136RE, and the input track modulus was 6,000 lb/in/in for concrete crosstie track. Table 6 shows calculated results, and Figure 6 shows them graphically. Note that Talbot and Eisenmann predict the same values for rail seat load.

Table 6. Rail Seat Loads for Various Input Load Values

	Input Load (pounds)				
	10,000	20,000	30,000	40,000	50,000
Calculation Method	Calculated Rail Seat Load (pounds)				
AREMA	5,031	10,063	15,094	20,125	25,157
Talbot	3,243	6,487	9,730	12,973	16,217
Kerr	4,268	8,537	12,805	17,074	21,342
Eisenmann	3,243	6,487	9,730	12,973	16,217

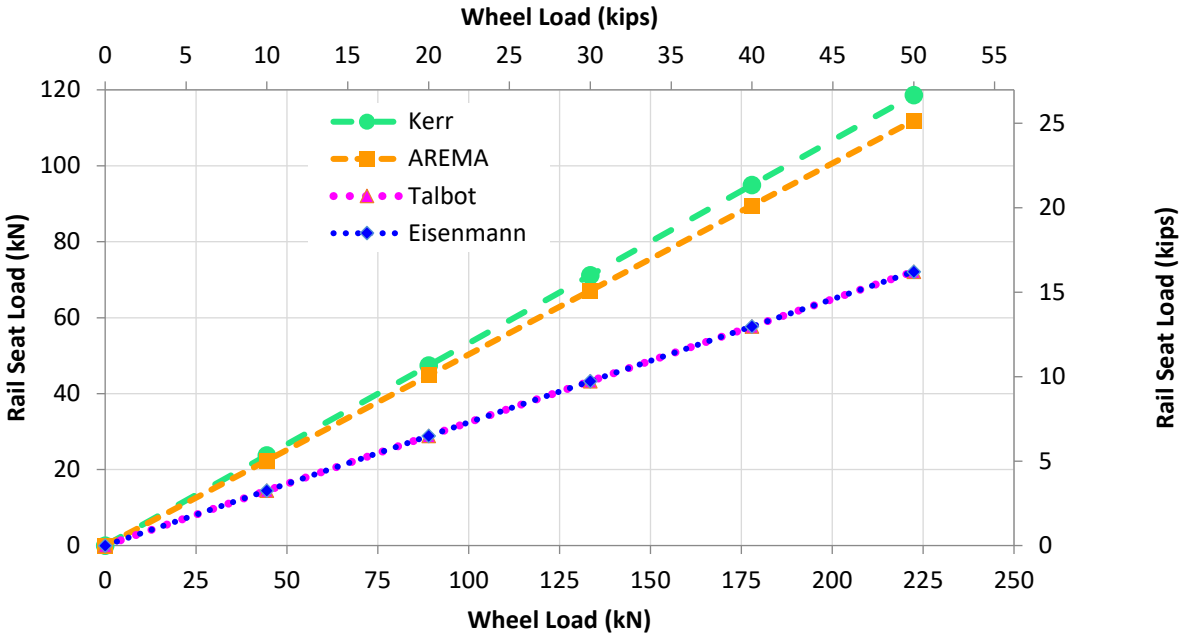

Figure 6. Multiple Rail Seat Load Calculation Methodologies

The other format of input load is based on rail car weight, and divides the total weight into applied wheel loads. In this format, speed is included as a factor and the DAFs available for the Talbot, Kerr, and Eisenmann equations are calculated based on the value of this input. A further input for the DAF applied to the Eisenmann equation is a track quality factor in addition to the track modulus value. This factor either is 0.1, 0.2, or 0.3 for very good, good, and bad track qualities, respectively. For the purpose of this calculation the very good track quality was selected. The "t" value as discussed in the section on the DAF equation is input as a value of three, which is the value for rail stresses, fastenings, and supports (Esveld 2001). All other inputs for crosstie spacing, rail size, and track modulus are the same as in the previous input format. The three different rail car gross rail loads (GRL) used as initial input loads are 263,000 lbs (263 k), 286,000 lbs (286 k), and 315,000 lbs (315 k). Table 7 shows the calculated results as well as the respective wheel load for each rail car weight, and Figure 7 is a plot of these results. The speed input for this set of data is 0 mph, thus it would simulate a static load from the various train weights. The second set of data is then presented with a 60-mph input to compare the effect

of speed into these equations versus a static load. These data are shown in Table 8 and plotted in Figure 8.

Table 7. Rail seat loads as a function of input loads at rest

Rail Car Gross Rail Load (pounds)	263,000	286,000	315,000
Wheel Load (pounds)	32,875	35,750	39,375
Calculation Method	**Calculated Rail Seat Load (pounds)**		
AREMA	16,541	17,987	19,811
Talbot	10,616	11,545	12,715
Kerr	14,032	15,260	16,807
Eisenmann	10,662	11,595	12,771

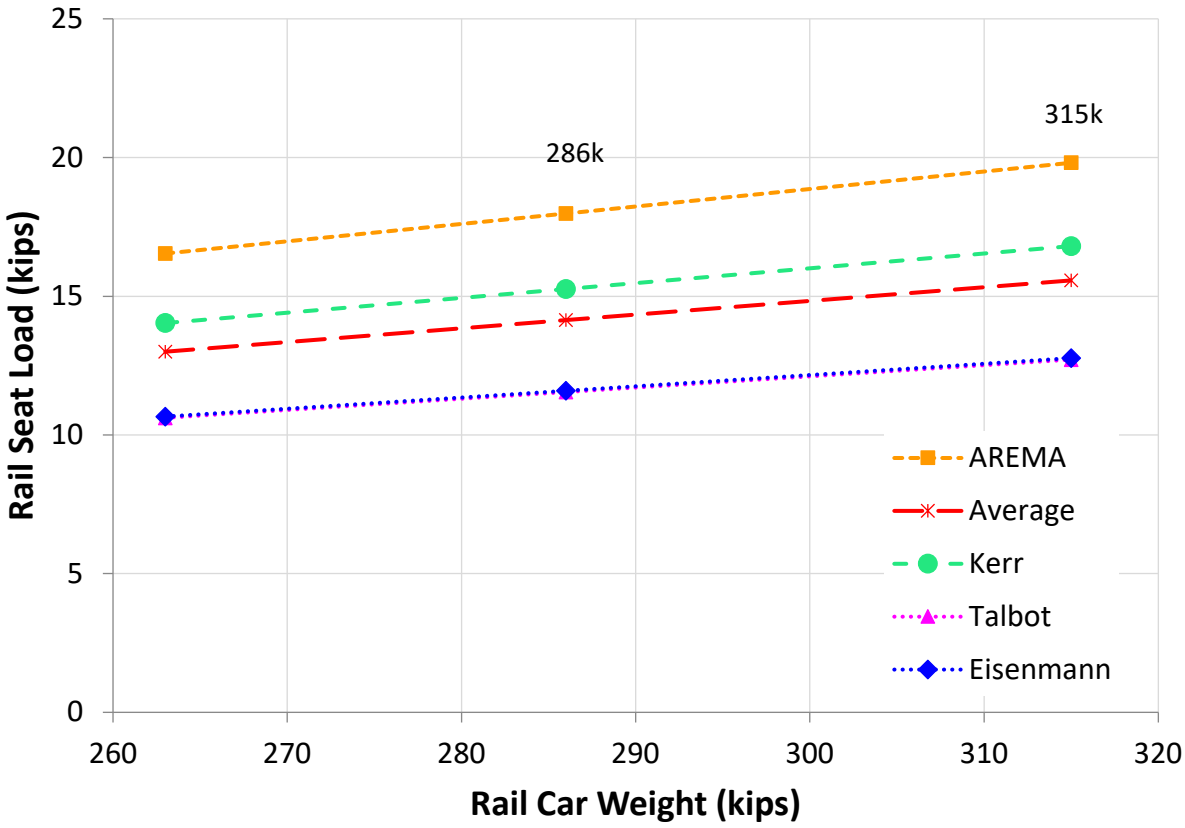

Figure 7. Rail seat loads for various rail car weights at rest

Table 8. Rail Seat Loads for Various Input Load Values at 60 mph

Rail Car Gross Rail Load (pounds)	263,000	286,000	315,000
Wheel Load (pounds)	32,875	35,750	39,375
Calculation Method	**Calculated Rail Seat Load (pounds)**		
AREMA	16,541	17,987	19,811
Talbot	16,455	17,894	19,709
Kerr	21,750	23,652	26,051
Eisenmann	14,696	15,982	17,602

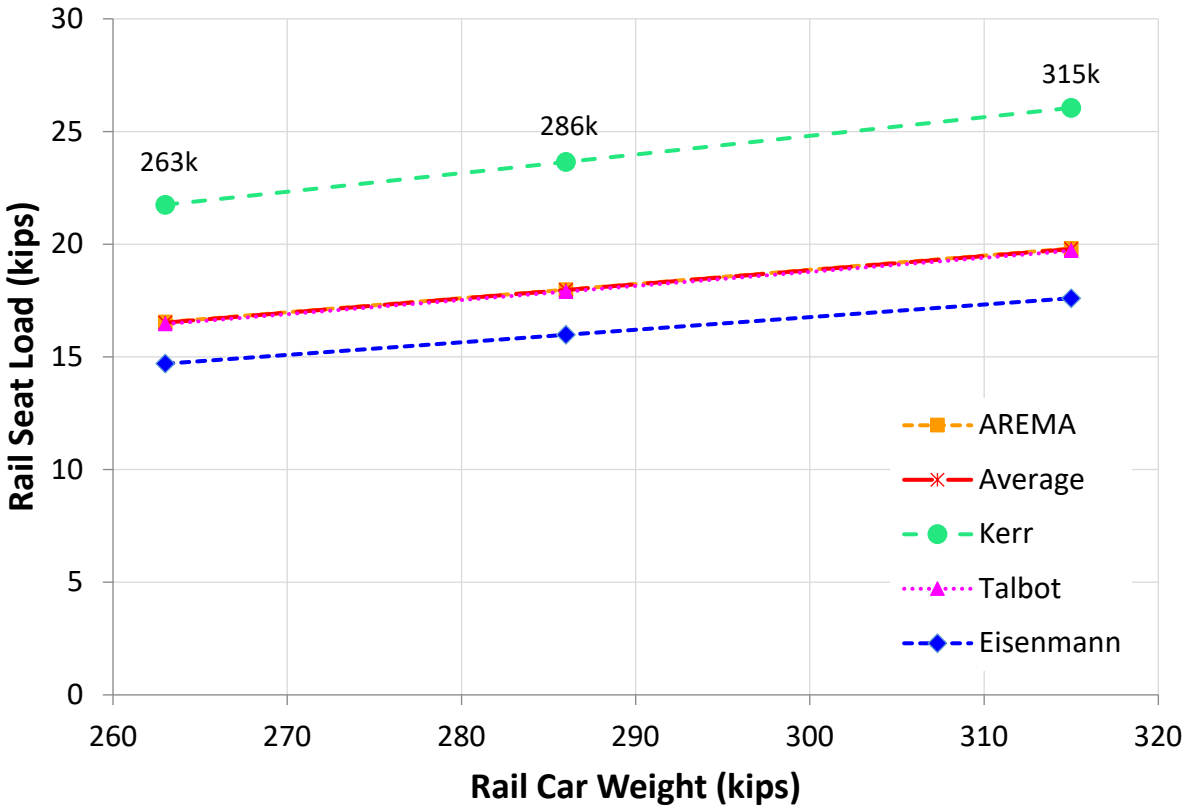

Figure 8. Rail seat loads for various rail car weights at 60 miles per hour

From these results, it can be seen that AREMA initially has the highest predicted rail seat loads. However, because the other methods include some form of a DAF, as a speed is introduced the calculated values for these three methods are increased. It can also be seen from Table 7 and Figure 7 that prior to introducing any speed variables; the calculated rail seat loads for Talbot and Eisenmann are very similar. This could be because both methods are based on the railway track model of the rail being simplified as a beam on an elastic foundation. The only major differing factors between these two methods are the formulas for calculating dynamic loading effects. This is evident in the fact that as a speed is introduced, the difference in rail seat loads between the two values increases. It should be noted that the wheel load values in Table 8 are

still based on the weight of the rail car. They may not necessarily represent the actual applied load to the rail by a wheel in this case as DAFs are included in the calculations.

2.6.3 Rail Seat Calculation Methodology Summary

There are various methods for calculating rail seat loads that range from simplified assumptions of the distribution of the wheel load onto the supporting crossties by the rails, to more complex estimations with the inclusion of several track quality variables. Under static loading conditions, the AREMA method yields maximum rail seats loads. However, as the variable of speed is included, the Talbot, Kerr, and Eisenmann calculations are increased, as only these methods use a DAF. It would appear that the values for the Eisenmann and Talbot equations are initially similar because they are both based on the concept that a track structure can be simplified and modeled as a beam on an elastic foundation. For a static wheel load (0 mph) of 35,750 pounds (286k car), the Eisenmann and Talbot equations are nearly identical, with Eisenmann yielding a rail seat force only 0.4% higher than Talbot. The results from the Kerr equation would be identical to those from Eisenmann and Talbot, but Kerr uses a higher track modulus to account for frozen ballast. The AREMA method at this input load is approximately 55% higher than the Eisenmann and Talbot equations, and about 18% higher than Kerr. With the introduction of speed into the equations, for this same wheel load at 60 mph, the Kerr method yields a higher value, being approximately 32% higher than the Talbot method. At this speed and wheel load the calculated AREMA value is only 0.5% higher than Talbot, demonstrating the effect of the dynamic factor on the rail seat load in the Talbot equations. The Kerr method uses the most severe dynamic factor, leading it to have significantly higher calculated rail seat loads under high speeds than the other methods.

The more complex methods yield more accurate results, but this cannot be fully verified until field instrumentation can allow actual data recording of rail seat loads. Nonetheless, these methods presented can be used to gain a better understanding of the loads seen by individual discrete rail seat areas.

2.7 Previous Research on Concrete Crosstie and Fastening System Load Quantification

Domestic and international railway communities have undertaken numerous modeling, laboratory, and field experimentation efforts to quantify loads, to investigate and understand specific failures, or to validate mathematical modeling. Examples of this research are summarized in this section.

2.8 Laboratory Experimental and Mathematical Modeling

In the 1970s, concurrent to the experimental efforts being performed by the Battelle Columbus Laboratories and partner organizations, a multilayer model was developed to better understand the support conditions of the track superstructure (Kennedy 1978). This model is more sophisticated than the "beam on an elastic foundation" model, yet simpler and less computationally intensive than finite element (FE) methods. The effects of rail bending, rail fastener stiffness, crosstie bending, variable ballast and subgrade material type, tie spacing, and ballast depth are included in the model and compare favorably with the experimental results described in the following section. Some recorded stresses, deflections, and track modulus

values were also compared with predicted values from the computer model GeoTrack (Stewart 1984).

In the early 2000s, researchers in India developed a mathematical model incorporating vehicle-track interaction characteristics and rail imperfections. It incorporates components of the track structure and vehicle parameters associated with Indian Railways. The dynamic interactive analysis is performed using FE methods and reaction response times in the rail seat area. Responses are evaluated based on different vehicle and track characteristics. The model output is used to create and apply suitable load amplification (impact) factors to aid in improved static design of concrete crossties (Kumaran 2002).

During the 1980s, more than half of the twin-block concrete crossties designed and installed for mixed-traffic lines in Greece developed serious cracking failure. Surprisingly, the actual field loads applied to the crossties were significantly lower than the design loads for the crossties. Greek researchers developed a mathematical model to determine the true load acting on the superstructure, including static, dynamic, and elastic considerations. It showed that more resilient fastening systems could greatly increase the superstructure's durability, a phenomenon confirmed with recent installations. The model was verified using the specific field conditions of the Greek network and is considered to be applicable to the remainder of the rail networks compliant to the interoperability specifications of the European Union (Giannakos 2010).

Researchers from the U.S. Department of Transportation's Volpe National Transportation Systems Center (Volpe) performed a theoretical study to better understand the effect of wheel and rail loads on concrete tie stresses, as well as the potential for rail rollover under excessive lateral forces (Marquis 2011). This research was performed largely in response to the deterioration of material on concrete crosstie rail seats, which is known as RSD. RSD has been observed in various levels of severity, with at least one derailment that has been attributed to severe RSD. The wear pattern in these cases was triangular, with more deterioration noted on the field side of the rail seats, Volpe researchers believe that the magnitude of the pressures being applied to the concrete surface on the field side of the rail seat is higher than the compressive strength of the concrete. It was also determined that an increasing lateral component of the resultant wheel load causes eccentric loading on the rail seat, and when the resultant force falls beyond the edge of the base of the rail, an unrestrained rail will roll. It is possible that a concrete rail seat having enough RSD that the elastic fastening clips are no longer functional can result in an unrestrained rail condition (Marquis 2011).

In a theoretical experiment, results showed that for an unrestrained rail with a 30 kilopound (kip) vertical loading an L/V force ratio of 0.60 will cause the rail to roll. This experiment was performed with an assumption of no rail cant or bending of the rail. In a similar experiment performed with a more common inward rail cant of 1:40, it was determined that an L/V force ratio of 0.65 will cause the unrestrained rail to roll. This value compares favorably to the L/V force ratio of 0.68 described in Hay that results in an unstable condition, potentially causing an unrestrained rail to overturn (Hay 1982). In the event that there is excessive deterioration of concrete material on the field side of the rail seat, the rail will likely have an outward cant. An L/V force ratio of 0.56 was found to roll a section of rail with an outward cant of 1:40. Truck-side L/V force ratios of 0.60 are not permitted by FRA as they exceed a set safety criteria, however in this experiment it was found that an L/V force ratio of approximately 0.54 applied to an outward canted rail can yield maximum stresses on the rail seat exceeding the 7,000 psi AREMA-specified minimum design compressive strength of concrete for concrete crossties.

The experiment discussed in this paper was purely theoretical using geometric principals to determine the effect of varying input loads on a section of rail; however useful insight was gained into magnitudes of L/V force ratios that could cause unsafe conditions under actual train operation (Marquis 2011).

Researchers in the Rail Transportation and Engineering Center (RailTEC) at UIUC performed a study that supports the concept of high field-side pressure values on the field side of concrete crosstie rail seats under increasing lateral loads. Matrix-based tactile surface sensors (MBTSS) were used to measure the distribution of loads onto the rail seats of concrete crossties. Various L/V force ratios were tested in a full-scale laboratory test and the results yielded that increasing the lateral component of the resultant force increases the loading that is concentrated on the field side of the rail seat. The maximum pressure value recorded in this experimentation was just above 4,000 psi, occurring at an L/V force ratio of 0.60 (32.5 kips vertical, 19.5 kips lateral). This pressure is still much lower than the 7,000 psi specified by AREMA, a value confirmed by the Volpe study as potentially resulting in degradation of concrete materials (Marquis 2011). It is possible, however, that loads in the field could exceed those chosen for the laboratory study with MBTSS (Rapp 2012).

2.9 Field Experimentation

In 1971, concrete crosstie test sections were installed on the Burlington Northern Santa Fe Railway (BNSF) mainline track in Illinois. The exterior of the crossties was outfitted with strain gauges to measure compliance with the AREA recommended practices for bending moments at the rail seat and midsection. The crossties were installed in groups with varying fastening systems (including different types of clips and pads) and concrete design strengths to determine which combinations of these design parameters performed well in accordance with the AREA recommended practices. The thorough visual inspections and strain gauge data indicated that these test sections performed very well under high axle loads up to 79 mph and after 30 million gross tons (MGT) of accumulated traffic (Weber 1976). While this testing was performed over 40 years-ago and the infrastructure components used for the testing are no longer in production, the testing methods are still relevant and represent some of the first load quantification efforts.

During the 1970s and 1980s, a very significant laboratory and field testing program was undertaken by a partnership of organizations including Battelle Columbus Laboratories, the University of Massachusetts, the Association of American Railroads (AAR), the Railway Progress Institute, and FRA. Much of the motivation for these tests involved comparing the Facility for Accelerated Service Testing (FAST) to various field locations (on Amtrak's Northeast Corridor and the Florida East Coast Railway) to determine the degree to which the facility represents the conditions found in revenue service (Harrison 1984). The significant testing performed provided great insight into the loading environment at the wheel-rail interface the concrete crosstie and fastening system, and the ballast. Forces, stresses, strains, deflections, and other measurements were measured using a variety of instrumentation techniques to investigate particular failure mechanisms and their causes. Some of the important parameters measured included track settlement, rail deflection, clip strain, pad deflection, wheel load, rail seat load, crosstie bending moment, crosstie-ballast pressure, crosstie cracking behavior, and RSD. A critical contribution of these efforts was the development of the WILD to identify impact load-producing wheel sets (Ahlbeck 1986). This development provided railroads across

the country the ability to better manage their rolling stock to effectively protect their infrastructure.

An experiment was performed at the Transportation Technology Center (TTC) in Pueblo, CO, on concrete crossties and fasteners whose results were presented in a 1990 "Workshop on Heavy Axle Loads" (Read 1990). In this experiment, concrete crossties and fasteners of various manufacturers were installed in a 5-degree section of track and a section of tangent track on the FAST as part of the heavy axle load (HAL) research program. Both 33-ton and 39-ton axle load test programs were performed to compare the performance of the concrete crossties and fasteners under various loading conditions. Data were collected from a combination of strain gauged rails, crossties, and IWS. At the 40-mph train operation speed used for this experiment, the high rail of the 5-degree curved section of track saw higher vertical and lateral loads as compared to the low rail. As expected, the magnitude of loadings between both rails did not vary significantly on the tangent track section. Also, no significant difference in track loading was measured between the 33-ton and 39-ton axle loads.

Axial strains were measured by strain gauges installed on the top surfaces of some of the crossties. The highest strains recorded on these crossties all occurred at the instrumented sections closer to the center third of the tie. This indicates that the ties all experienced negative bending between the rail seats, with strains being tensile. The magnitude of axial strains experienced by the ties during the 33-ton and 39-ton axle load programs showed little variability. Only a 13% higher strain was recorded at the 90^{th} and 95^{th} percentile levels of the distributions for the most central strain gage on the crossties under the 39-ton axle loads as compared to the 33-ton axle loads.

After 425 MGT of testing under the 33-ton axle loading program, only 7.4% of the tested crossties saw flexural cracks. For the 39-ton axle loading program, only 2.6% of crossties in one zone and 2% in another zone saw flexural cracks. The magnitude and location of cracks reported in the 39-ton axle loadings were greater than those under 33-ton axle loads, though a lower percentage of crossties experienced cracking. None of the flexural cracks that were noted appeared to significantly affect the performance of the crossties or the track, and at the time that the report was compiled, no further cracking had been noted. It should also be noted that none of crossties pulled from track for further observation saw positive bending cracks on the bottom surface of the crossties.

The fasteners were also observed during testing for signs of failure. Modes of failure that were observed included fall-out from loss of the initial toe load, and fracture of the fastener. In summary, the failure of fasteners was very low during this experiment; after 160 MGT only 5.3% of the worst-performing fasteners failed, with fall-out due to loss of toe load being the most common failure.

In Australia, significant field instrumentation and data collection efforts were undertaken to understand the vertical forces exerted on the track structure by various traffic types. The distribution of impact loads was used to predict return periods for various types of impacts. The effect of train speed proved to be significant, as doubling the speed increased the impact loads by about 140% in many cases. A probabilistic damage model was utilized to determine expected lifespan of concrete crossties according to specific impact loads. These conclusions contribute to a new limit states approach for the design of concrete crossties (Leong 2008).

Following several derailments on mainline curves involving rail rollovers, the Norfolk Southern Corporation developed a field experimentation regime in 2011 and 2012 to measure lateral wheel forces. The purpose of the experimentation effort was to determine what types of track maintenance conditions affected the lateral forces experienced at the wheel-rail interface, with the hypothesis that high lateral wheel loads are the cause of many safety and maintenance issues encountered by the Class I railroad. The study concluded that very high lateral forces (resulting in near rail-rollover conditions) can occur during particular wheel-rail contact scenarios. Certain wheel-rail interface management techniques, as well as the use of elastic fasteners, can mitigate this threat (Kerchof 2012). While this study was performed on timber crossties, the findings can also be applied to concrete crossties when trying to better understand lateral loading and its effect on particular failures.

Researchers at UIUC are aware of field experimentation that was conducted by BNSF aimed at quantifying the loads that are passed through the cast-in shoulder. The results from this work were inconclusive, and UIUC researchers are attempting to employ different technologies to answer questions about lateral load transfer through the shoulder.

2.10 Summary

While there is a fairly clear understanding of the existing static loads produced by train sets throughout the world, there must be additional information for adequate design of track components and the entire track system. It is generally well understood that the complete track loading spectrum must include forces produced from various train operating speeds, as well as forces produced at various locations within the track superstructure.

This chapter provided a framework for quantifying loads experienced at the wheel/rail interface. However, the loading spectrum at this interface was not sufficient for the design of concrete crossties and fastening systems because wheel loads were not the loads carried by these infrastructure components. Various rail seat load quantification methodologies were investigated and compared. Many factors were considered, and there may be some additional parameters that also affect this transfer of forces. Other chapters within this report describe the UIUC instrumentation and modeling efforts to provide additional insight to the conversion of wheel loads to rail seat loads.

To adequately quantify the forces and displacements within the track structure, a thorough review of previous efforts must be undertaken. Summarized in this chapter were previous efforts related to concrete crosstie and fastening system load quantification. While there were significant work performed in this area in the past, there are still excellent opportunities to learn from these efforts and improve on them to create a better understanding of the loading found within these systems. The previous literature details and modeling techniques to quantify the behavior of the concrete crosstie and fastening system, much of which was incorporated into the UIUC Instrumentation Plan and Model.

The analytical and experimental methods outlined in this chapter provided a baseline for the efforts described in the following chapters. They significantly contributed to a clearer understanding on the track structure's behaviors and interactions, providing a foundation for improved design of concrete crossties and fastening systems.

Chapter 3: Laboratory Experimental Plan

3.1 Purpose

The purpose of laboratory experimentation was to improve the current understanding of concrete crosstie and fastening system behavior under simulated loading conditions designed to replicate actual field conditions. Laboratory experiments were easier to control and provided a greater number of replicates that were possible in the field. Increasing the control of variables helped clarify how changing a given parameter (or set of parameters) affected the whole system. Additionally, by conducting multiple replicates at each set of experimental conditions, laboratory experimentation provided for larger data sets, thereby decreasing experimental error.

3.2 Objectives

To achieve the overall purpose of gaining a deeper understanding of crosstie and fastening system behavior, the laboratory experimental plan was designed to achieve the following objectives:

- **Determination of System Load Path** – Understanding load transfer mechanics of the crosstie and fastening system from the wheel-rail interface, through the fastening system, and into the crosstie.
- **Quantification of Crosstie-Fastener Response** – Analyzing the characteristic deformation and deflection of all crosstie and fastening system components.
- **Development of Analytical Model** – Providing reliable data to develop and validate the 3D FE model of the crosstie and fastening system.

3.3 Approach

Experiments were classified into material-level, component-level, and system-level analyses. In material-level experimentation, the properties of materials used to manufacture different components in the crosstie and fastening system were investigated and compared with properties supplied from manufacturers. Considering the variability of the material properties used in fastening system components, it was necessary to experimentally verify these critical material properties and focus on the range applicable to the crosstie and fastening system. Properties such as strength, elastic modulus, and the stress-strain relationship were obtained for each material.

Each component included in the crosstie and fastening system (rail, rail pad, abrasion frame, rail clip, shoulder, and concrete crosstie) was tested separately. Through individual component testing, a clear understanding of the component's behavior under an idealized loading case was accomplished. The component-level experimentation was especially important for clips and rail pads, which have non-linear behavior. During the tests, the actual loads applied to the components were recorded and strains and deflections were measured.

To understand the mechanics of the whole system and how each component interacts with the system under the actual applied load (wheel load), several system-level experiments were performed. We started with a simplified system that contained a short section of rail and one crosstie. The system was loaded statically with idealized loading and support conditions. To clarify the load sharing among adjacent crossties and the effect of changing load and support

conditions, we built a full-scale laboratory experiment and achieved more realistic load and boundary conditions.

3.4 Experimental Setup

3.5 Test Equipment

3.5.1 Uniaxial Loading Machine

The uniaxial loading machine was used to test the compression and flexural behavior of concrete crossties and fastening system components (Figure 9). The uniaxial loading machine used a hydraulically-powered actuator to apply a load up to 100,000 pound-force (100 kips) in the vertical direction, perpendicular to the loaded face of the component being tested. A ball-joint cast in the upper loading head minimized the effect of eccentric loading and the machine was adjusted to fit components with varying dimensions. A calibrated load cell was used to monitor applied load.

Figure 9. Uniaxial Loading Machine

3.5.2 Static Load Testing Machine

The static load testing machine (SLTM) was used to apply loads to a concrete crosstie and fastening system, test the behavior of rail, and calibrate strain gauge configurations installed in various locations on the rail (Figure 10). The SLTM used a hydraulic jack to apply vertical load supported by an overhead loading frame. The SLTM loading head used a simplified wheel profile to simultaneously apply a fixed combination of vertical and lateral load on both rails.

The angle between the normal direction of the contact surface of the loading head and the vertical plane is designed to be 26.5 degrees, equating to a L/V force ratio of 0.5 applied to both rails. The loading head could also be modified to apply pure vertical loads. A calibrated load cell was used to monitor applied loads.

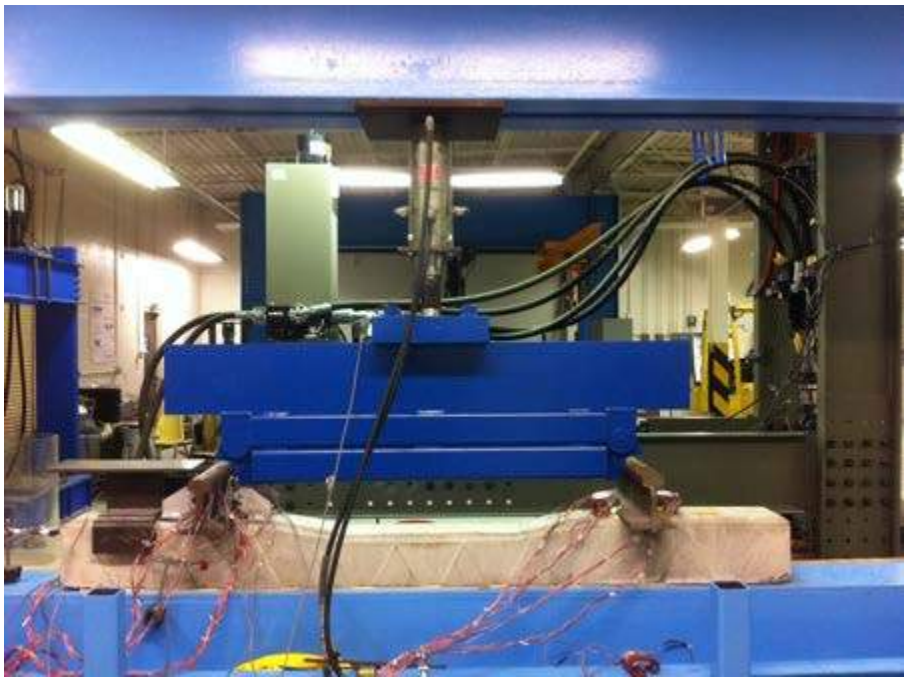

Figure 10. Static Load Testing Machine

3.5.3 Pulsating Load Testing Machine

The Pulsating Load Testing Machine (PLTM) was used to apply loads to a single concrete crosstie and fastening system and to test the magnitudes and distribution of applied forces (Figure 11). Static or dynamic vertical and lateral loads were applied to the rail on one rail seat of a full-scale concrete crosstie with a complete fastening system assembly installed. Vertical and lateral loads were adjusted separately using a control system. The PLTM used three hydraulic actuators (two vertical and one lateral) mounted on a self-reacting steel frame and a loading head. The loading head was bolted to the head of a 2-foot segment of 136RE rail. The actuators were calibrated for load and displacement prior to installation.

Figure 11. Pulsating Load Testing Machine

3.5.4 Static Tie Tester

The Static Tie Tester (STT) (Figure 12) was used to apply loads to test the flexural and compressive behavior of concrete crossties. Rail seat compression tests, rail seat positive and negative bending tests, and crosstie center positive and negative bending tests were conducted. The STT used a hydraulic cylinder to apply loads to the rail seat or center of a crosstie up to a maximum capacity of approximately 100,000 pound-force. A calibrated pressure gauge was used to monitor applied loads.

Figure 12. Static Tie Tester

3.5.5 Track Loading System

The full-scale Track Loading System (TLS) was used to apply loads to a 22-foot long section of concrete crosstie track (Figure 13). Track components were assembled on a full depth section of track that included eleven crossties spaced at 24 inches on center. Static or dynamic combinations of vertical and lateral loads were applied to the journals of a 36-inch diameter wheel set. Vertical and lateral loads were adjusted separately using a control system. The TLS used two hydraulic actuators mounted vertically and a hydraulic cylinder mounted laterally on a self-reacting steel frame. A special assembly for each journal was designed to attach one vertically-mounted actuator and the horizontally-mounted hydraulic cylinder to one journal and the second vertically-mounted actuator to the opposite journal. The actuators were calibrated for both load and displacement.

Figure 13. Track Loading System

3.5.6 Portable Track Loading Tools

Three portable track loading tools were used in the laboratory: the Delta Frame (Figure 14), the Portable Track Loading Fixture (PTLF), and a lateral load frame (LLF) provided by BNSF. The Delta Frame was used to apply loads to the rail and to calibrate instrumentation installed on the rail. Vertical loads up to 50,000 pound-force and lateral loads up to 10,000 pound-force were applied to the rail, separately. The Delta Frame used a hydraulic cylinder to apply loads. Vertical loads were applied using an upward facing steel triangular frame with loads applied in the center of the bottom side of the frame and reacting off the rail at the two bottom corners. Lateral loads were applied by disassembling the triangular frame into a straight section laid perpendicular between the two rails.

Figure 14. Delta Frame – Vertical Load Orientation

The PTLF was used to apply lateral loads up to 10,000 pounds, using a methodology similar to the Delta Frame. The PTLF used a hydraulic cylinder to apply lateral loads.

The LLF was used to apply lateral loads in a similar fashion to the Delta Frame and PTLF, with a maximum applied load of 10,000 pound-force. The LLF used a hydraulic cylinder to apply lateral loads. Calibrated load cells were used to monitor applied loads on the LLF.

3.6 Instruments

3.6.1 Strain Gauges

Strain gauges were used to measure the forces in track components induced from applied loads. Several types of strain gauges were used in this project based on the specific application. Standard 120-ohm foil type shear strain gauges (Figure 15) were used for quarter bridge circuits. Shear strain gauges in a chevron pattern with two 120-ohm gauges oriented 90 degrees to each other were used for full bridge circuits. 120-ohm concrete internal (embedment) and concrete surface strain gauges were also used. Strains were measured accurately to one microstrain. Strain bridges were calibrated using a load cell of known calibration to resolve strain measurements into forces.

Figure 15. Standard 120-ohm Foil Type Shear Strain Gauge

3.6.2 Linear Potentiometers

Displacement transducers known as linear potentiometers were used to measure relative displacement between components and global displacements of components relative to a known datum (Figure 16). These potentiometers had a maximum stroke length of 1.1 inch and were accurate to 0.001 inches. The potentiometers used a known calibration factor from the manufacturer.

Figure 16. Linear Potentiometer

3.6.3 Matrix Based Tactile Surface Sensors

Matrix based tactile surface sensors (MBTSS) were used to quantify the load magnitude and pressure distribution on the rail seat of concrete crossties (Figure 17). MBTSS use pressure-sensitive ink printed in rows and columns to form a grid. The resistivity of the ink changes as load is applied resulting in a higher voltage output to the software. Protective layers were placed between the rail pad assembly and the MBTSS as well as between the MBTSS and the rail seat to prevent shear and puncture damage. MBTSS data were recorded with software designed specifically for MBTSS instrumentation and did not require calibration.

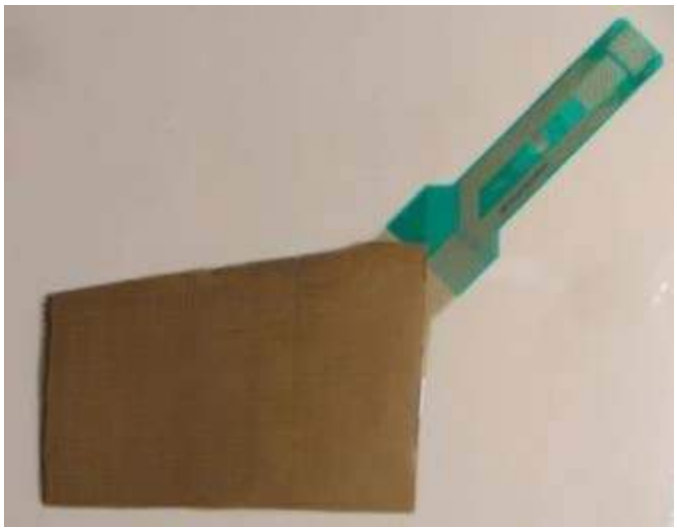

Figure 17. Matrix Based Tactile Surface Sensors

3.6.4 Compact Data Acquisition

A National Instruments (NI) compact data acquisition (cDAQ) system was used to record data from strain bridges and potentiometers (Figure 18). Strain bridges and potentiometers were connected to the cDAQ. cDAQ output signals from strain bridges and potentiometers were recorded through a NI LabView program developed for the instrumentation associated with this experimental program.

Figure 18. Compact Data Acquisition System

3.7 Experimental Methods

3.7.1 Applied Loads on the Rail

Vertical and lateral loads were measured to quantify the actual load entering the rail head, and to measure longitudinal distribution of vertical loads. Loads were measured by installing strain gauges in specific locations and orientations based on the type of load measurement (Figure 19).

Vertical loads entering the rail were measured using strain gauges applied 6 inches apart centered in the crib at the rail's neutral axis. Vertical loads entering the crosstie rail seat were measured using strain gauges applied 0.5 inches away from either side of a crosstie at the rail's neutral axis. Longitudinal loads in the rail were measured using strain gauges applied in the center of the crib on the rail's neutral axis. Vertical rail strains were measured near the base of the web using three vertical strain gauges applied two inches apart on each side of the rail, centered over the rail seat. A calibrated load cell was used to monitor applied load and calibrate all strain bridges.

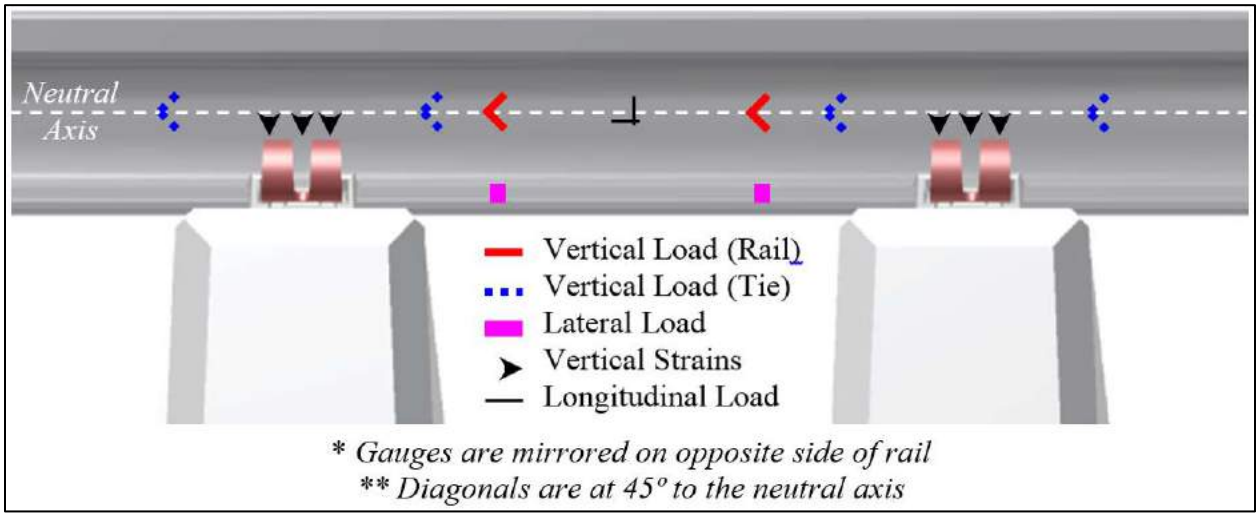

Figure 19. Strain Gauge Configuration on Rail

3.7.2 Vertical Rail Base Displacement

Vertical rail base displacements were measured to understand the behavior of the rail and fastening system under loading. Linear potentiometers were used to measure the displacements relative to the crosstie (Figure 20). These potentiometers were fixed to brackets anchored into the crosstie and were positioned perpendicular to the rail seat. The tip of the potentiometers contacted the rail base 0.5 inches from the edge of the rail base on both field and gauge sides adjacent to the cast-in shoulder.

Figure 20. Linear Potentiometers Used to Measure Vertical and Lateral Rail Base Displacement

3.7.3 Lateral Rail Base Displacement

Lateral rail base displacements were measured to understand the behavior of the rail and fastening system under loading. Linear potentiometers were used to measure the displacements relative to the crosstie (Figure 20). These potentiometers were fixed to brackets anchored into the crosstie and were positioned perpendicular to the rail and parallel to the rail seat. The tip of the potentiometers contacted the edge of the rail base on both field and gauge sides adjacent to the cast-in shoulder.

3.7.4 Vertical Crosstie Displacement

Vertical crosstie displacements were measured to understand the behavior of the crosstie and vertical support conditions under loading. Linear potentiometers were used to measure the global vertical displacement of the crosstie relative to the surface the crosstie was resting on (Figure 21). These potentiometers were positioned perpendicular to the top of the crosstie. The tip of the potentiometers contacted the crosstie one inch from both ends, or contacted a steel plate that was rigidly attached to the crosstie.

Figure 21. Linear Potentiometer Used to Measure Vertical Crosstie Displacement

3.7.5 Lateral Crosstie Displacement

Lateral crosstie displacements were measured to understand the behavior of the crosstie and lateral support conditions under loading. Linear potentiometers were used to measure the global lateral displacement of the crosstie relative to the surface the crosstie was resting on (Figure 22). The potentiometers were positioned perpendicular to the end of the crosstie. The tip of the potentiometers contacted the crosstie one inch below the top surface of the crosstie.

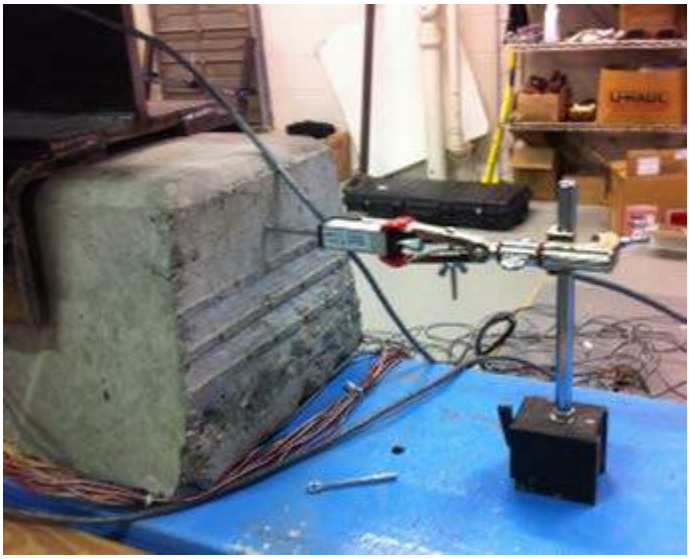

Figure 22. Potentiometers Used to Measure Lateral Crosstie Displacement on SLTM

3.7.6 External Rail Strain

External rail strains were measured to understand the bending and compression behavior of the rail under loading. Strain gauges were applied on the surface of the rail. See Section 3.7.1 for details related to the location and orientation of the strain gauges.

3.7.7 Internal Crosstie Strain

Internal crosstie strains were measured to understand the compression behavior of the crosstie beneath the rail seat area. Embedded strain gauges were used to measure rail seat forces and internal pressure distributions (Figure 23). The gauges were arranged in a two by two, 4 inch by 4-inch matrix centered 2 inches beneath the rail seat. The gauges were mounted in a steel mesh and fixed to the pre-stressing strands before the concrete was poured. Wires were secured in a wire box and pulled out after the concrete had hardened. Gauges were calibrated using load cells.

Figure 23. Mesh to Hold Embedded Crosstie Strain Gauges Prior to Concrete Being Poured

3.7.8 External Crosstie Strain

External crosstie strains were measured to understand the bending and compression behavior of the crosstie under loading. Concrete surface gauges were applied on the surface of the crosstie oriented longitudinally below the rail seats and at the center of the crosstie to measure bending moments (Figure 24). Gauges were also applied on the surface of the crosstie below the rail seats oriented vertically to measure vertical rail seat stress distribution.

Figure 24. External Crosstie Strain Gauges

3.7.9 Rail Seat Pressure Distribution

Rail seat pressure distribution was measured to understand the variance and magnitude of vertical pressures on the concrete rail seat under loading. MBTSS were used to measure the pressure magnitude and distribution. These devices were placed between the rail pad assembly and the concrete rail seat. MBTSS pressures were calculated based on the assumption that half of the vertical applied load enters the rail seat area.

3.7.10 Rail Base Bending Stress

Rail base bending stresses were measured to understand the behavior of the rail base under loading. Strain gauges were used to measure the bending strains, and were installed one inch from the edge of the rail base perpendicular to the track on the field side of the rail.

3.7.11 Insulator Post Stress

Insulator post stresses were measured to understand the compressive behavior of the insulator post under loading and help further define the lateral load path. Strain gauges were used to measure the compressive strains and were adhered to the bottom of the insulator post, perpendicular to the rail base on the field side insulator. Strains were resolved into forces using theoretical calculations.

3.7.12 Rail Clip Stress

Rail clip stresses were measured to understand the behavior of the rail clip and change in clamping force under loading. Strain gauges were used to measure rail clip stresses and were applied at specific locations on the surface of the rail clip perpendicular to the rail (Figure 25).

Figure 25. Strain Gauges on Rail Clip

3.7.13 Lateral Demands on the Shoulder – Lateral Load Evaluation Device

Lateral forces entering the shoulder were directly measured to understand the forces passing through the insulator post and further define the lateral load path. Forces were measured using UIUC's Lateral Load Evaluation Device (LLED). The LLED consisted of a small steel beam that measured bending strain from four-point bending (two points of contact with the insulator and two supports against the shoulder). Four strain gauges were adhered to the LLED. Strains measured on the LLED induced from lateral loads were resolved into forces using calibration curves generated on the uniaxial loading machine. LLEDs were installed in place of the shoulder face that had been grinded down to maintain fastening system geometry (Figure 26). The installation of the devices first required the removal of the clips and rail pad assembly from the rail seat. The shoulder faces were then manually grinded away and the LLEDs, the new rail pad assemblies, insulators, and clips were reinstalled.

Figure 26. LLED Installation Prior to Clip Application

3.7.14 Lateral Demands on the Shoulder – Lateral Axial Measurement System

An additional method was used to understand the forces passing through the insulator post. Forces were measured using UIUC's Lateral Axial Measurement (LAM) system (Figure 27). The LAM system used a plate anchored to the end of a crosstie and two cylindrical rods attached to the plate. The ends of the two rods contacted an aluminum insulator replacement component. The aluminum insulator replacement component geometry did not allow contact with the shoulder to guide all lateral loads into the rods. Strain gauges were adhered to both rods. Strains measured on the rods induced from lateral loads were resolved into a total force through theoretical calculations.

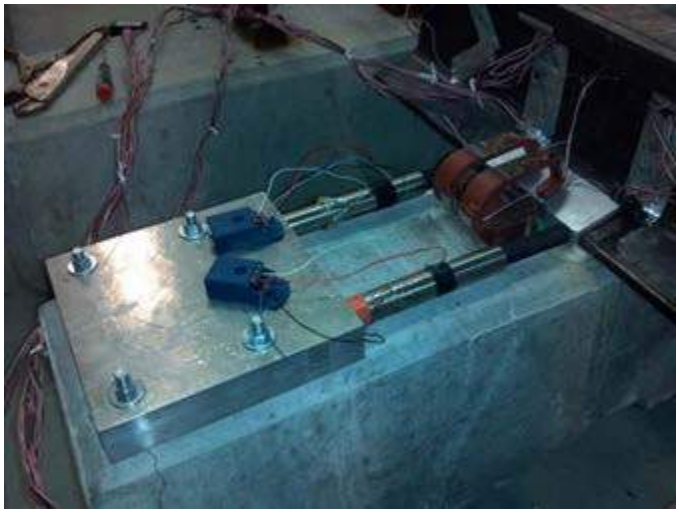

Figure 27. Lateral Axial Measurement System

3.7.15 Lateral Rail Pad Assembly Displacement

Lateral rail pad assembly displacement was measured to understand the behavior of the rail pad assembly under loading. Linear potentiometers were used to measure the lateral displacement of the rail pad assembly relative to the crosstie. The potentiometers were fixed to the crosstie adjacent to the shoulder, perpendicular to the rail (Figure 28). The tip of the potentiometers contacted the outer corner of the rail pad assembly.

Figure 28. Lateral Rail Pad Assembly Displacement

3.8 Materials-Level Experimental Plan

3.8 Compressive Stiffness of Polyurethane and Nylon 6/6

For a Safelok I type fastening system, the abrasion frame is typically made of nylon 6/6 and the rail pad is made of polyurethane. As the performance of rail pad and abrasion frame could potentially affect the vertical and lateral load path through the fastening system, it is critical to correctly define the compressive behavior of nylon 6/6 and polyurethane in the FE model. The material supplier provided data on raw material properties, but it was not clear if the material properties were altered during the manufacturing process. To obtain the compressive stiffness of the rail pad and the abrasion plate, static uniaxial compression tests of both materials were conducted on the uniaxial loading machine.

The compression tests of rail pad and abrasion frame specimens were designed to determine the compressive elastic modulus and the yielding strength of the materials. During tests, uniform compressive load was applied on the specimens, and the magnitude of compressive load and specimen deflection was measured by the loading machine. Teflon was sprayed on all the interfaces to reduce friction between the loading frame and the specimen. Two circular specimens were cut from both the rail pad and the abrasion frame for the compression tests. The geometry of the specimens, design of compression test, and material properties from the material supplier are summarized in Table 9. The circular rail pad and abrasion plate specimens used in the compression testing can be seen in Figure 29.

Table 9. Experimental Parameters and the Material Properties from Manufacturer

Component	Experimental Parameters and Results					Material Properties from Manufacturer			
	Thickness (in)	Diameter (in)	Yielding load (kips)	Test load (kips)	Load rate (in/min)	Young's Modulus (ksi)	Poisson's Ratio	Yielding Strength (ksi)	Ultimate Strength (ksi)
Rail Pad	0.236	5	23.6	30	0.015	7.5	0.49	1.2	5.2
Abrasion Frame	0.09	2	29.3	35	0.002	440	0.39	9.3	12.3

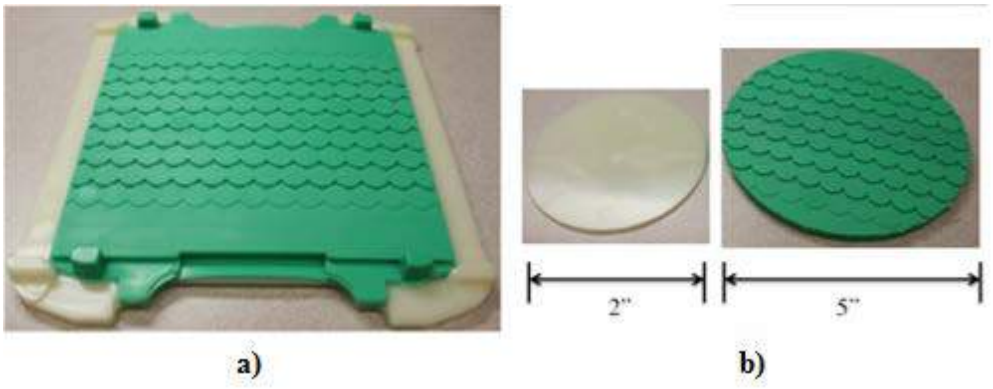

Figure 29. a) Rail Pad and Abrasion Plate; b) Specimen of Rail Pad (Polyurethane) and Abrasion Plate (Nylon 6/6) Used in Compression Test

3.9 Concrete Strength and Modulus

The concrete strength and elastic modulus were measured from concrete core compression cylinder testing. A core drill was used to obtain the concrete cylinder samples from a crosstie cast at the same time the specimens were used for other laboratory experimentation. Six concrete cylinder cores were prepared with a diameter of 3 inches and length of 4.5 inches. To measure the compressive strain during testing of the cores, three concrete surface strain gauges were installed in the vertical direction of each cylinder. Resin caps were cast on top and bottom surfaces of each cylinder to reduce stress concentrations and friction. The uniaxial compressive loading machine was used to apply a uniform compressive load to each cylinder until the cylinder reached failure (Figure 30). The experimental testing parameters and material properties from the material supplier are summarized in Table 10.

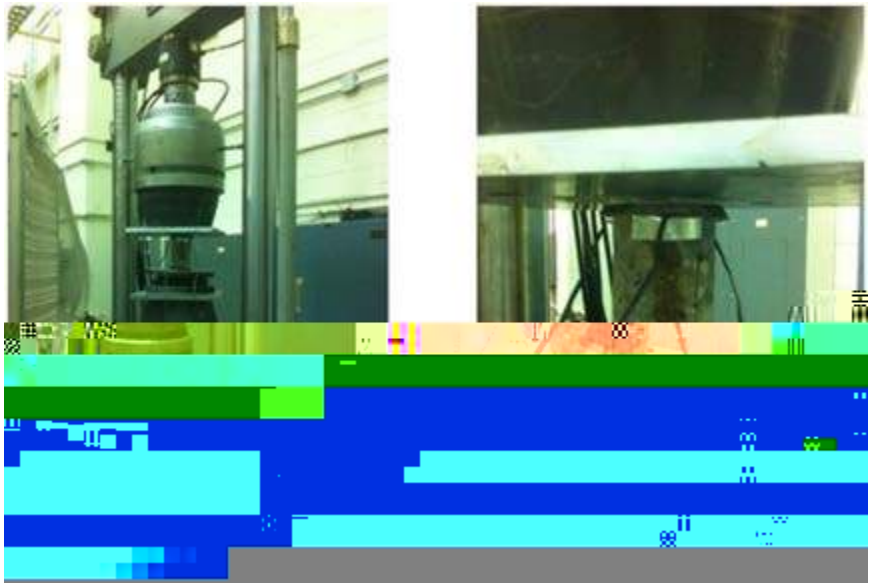

Figure 30. a) Uniaxial Compressive Loading Machine; b) Concrete Core Specimen with Three Concrete Surface Strain Gauges

Table 10. Experimental Parameters and the Material Property from Manufacturer

Component	Experimental Parameters and Results				Material Properties from Manufacturer	
	Diameter (in)	Height (in)	Crushing load (kips)	Load rate (kips/min)	Young's Modulus (ksi)	Ultimate Strength (ksi)
Concrete Core	3	4.5	>49.5	10	4,500	>7

The purpose of coring and running the material testing is to quantify the specific material properties of the concrete in the crosstie. Because many of the tests in this project were executed up to 2 years after the casting of the concrete crossties, the exact material properties were measured to increase our accuracy when analyzing the results. The elastic modulus of concrete

was also measured from center-positive bending tests conducted on the STT and compared with modulus values obtained from the concrete core cylinder compression tests.

3.10 Component-Level Experimental Plan

3.11 Rail Bending Behavior Experiment

The purpose of the rail bending behavior experiment was to:

- Understand the bending behavior of the rail under loading conditions representative of field loading conditions.
- Analyze the linearity and elasticity of the rail to design future rail bending behavior experiments.
- Evaluate the concept of using the rail as a load cell to measure forces going into the crosstie and fastening system.

The uniaxial loading machine was used to apply static vertical loads to a 24-inch rail section. The rail was tested as a simply supported beam. Eight strain gauges were installed on the rail web, with four on each side (Figure 31). A static load was applied at the center of the rail section from zero up to 35,000 pound-force at a constant load rate. Strain data recorded from the experiment was compared with theoretical calculations for validation purposes.

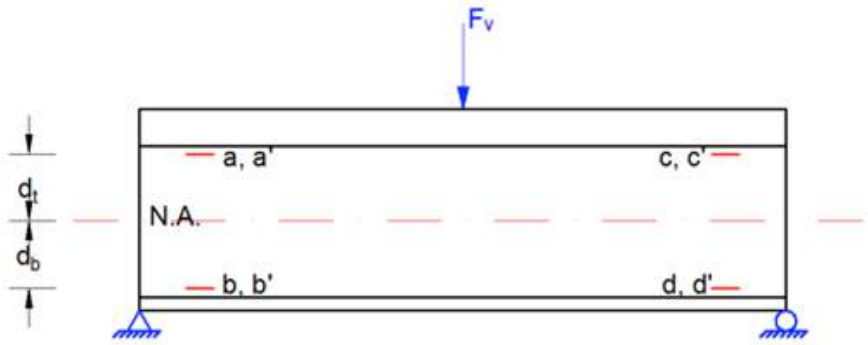

Figure 31. Profile View of Rail Bending Experiment

3.12 Rail Pad Assembly Stiffness Experiment

The compressive stiffness experiment for sample specimens of polyurethane (rail pad) and nylon 6/6 (abrasion frame) was described earlier. However, the effect of confinement brought by the friction forces at the rail base to rail pad interface, rail pad to abrasion frame interface, and abrasion frame to concrete rail seat interface was identified as a critical parameter in the behavior of the fastening system. The purpose of the rail pad assembly stiffness experiment was to measure the compression deflection of the rail pad and abrasion frame at a range of rail seat loads, and thus calculate the stiffness of the assembly.

The STT was used to apply static vertical loads to the rail seat. A 1-inch thick steel plate was placed between the STT loading head and the rail pad assembly installed on a concrete crosstie. Four potentiometers were mounted on the STT frame to measure the deflections at the four corners of the steel plate (Figure 32). A static 40-kip vertical load was applied directly to the rail

pad assembly such that it was distributed evenly over the entire rail seat. Compression deflections and rail pad assembly stiffness were compared with the material-level polyurethane and nylon 6/6 stiffness.

a) b)

Figure 32. a) Vertical Rail Seat Load Applied by STT
b) Rail Pad Assembly Deflection Measured by Potentiometers

3.13 Concrete Crosstie Behavior Experiment

3.13.1 Purpose

The stresses in a concrete crosstie were analyzed to:

- Confirm the concrete elastic modulus;
- Determine the location of the neutral axis of the crosstie;
- Clarify the load path through the crosstie from the rail seat to the crosstie's support;
- Study the effect of varying support conditions on the load path in the crosstie; and
- Calibrate embedded strain gauges to ensure measurements are not affected by eccentric loading conditions.

3.13.2 Procedure

Embedment strain gauges were installed below the rail seat area of a concrete crosstie. Concrete surface gauges were placed at the same height relative to the bottom of the crosstie on the center line of rail seat to verify the readings from the embedded strain gauges. Vertically-oriented surface strain gauges were also installed at different heights on the crosstie. This was done to study the bearing area at various heights below the rail seat, as well as to better understand the load path in the crosstie. Concrete surface gauges were placed in the longitudinal direction,

parallel to the crosstie, to quantify the bending moments in the crosstie at the rail seat and center line of the crosstie. The dimensions of the crosstie and locations of strain gauges are labeled in Figure 33.

Labels of gauges:

- E1-E8: Embedment strain gauges
- SL1-SL6: Surface gauges in longitudinal direction of concrete tie
- SV1-SV10: Surface gauges in vertical direction

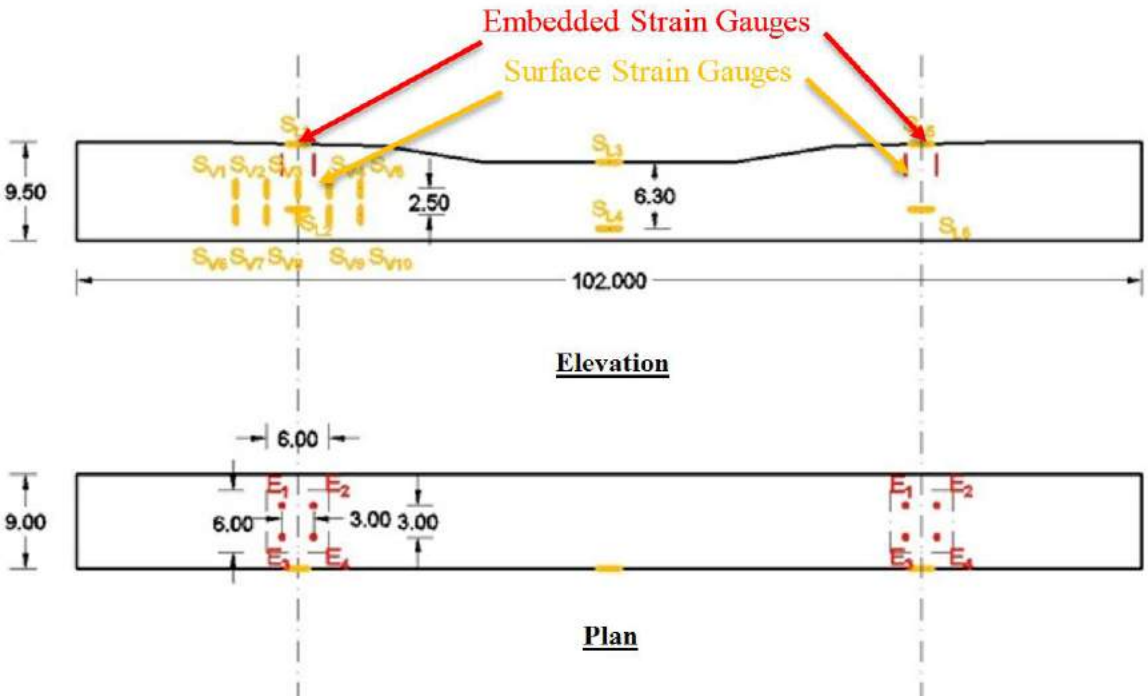

Figure 33. Dimensions of Crosstie and Location of Strain Gauges

3.13.3 Center-Positive Bending Test

Center-positive bending tests were conducted with static loads provided by the STT (Section 3.5.4). The bottom surface of both rail seats was supported by a 2-inch wide rubber pad at the center of the rail seat oriented perpendicular to the crosstie (Figure 34). A vertical static load was applied at the center of the crosstie. The vertical load started at zero and increased by 1,000-lbf increments for each step up to 5,000 pound-force (Figure 35).

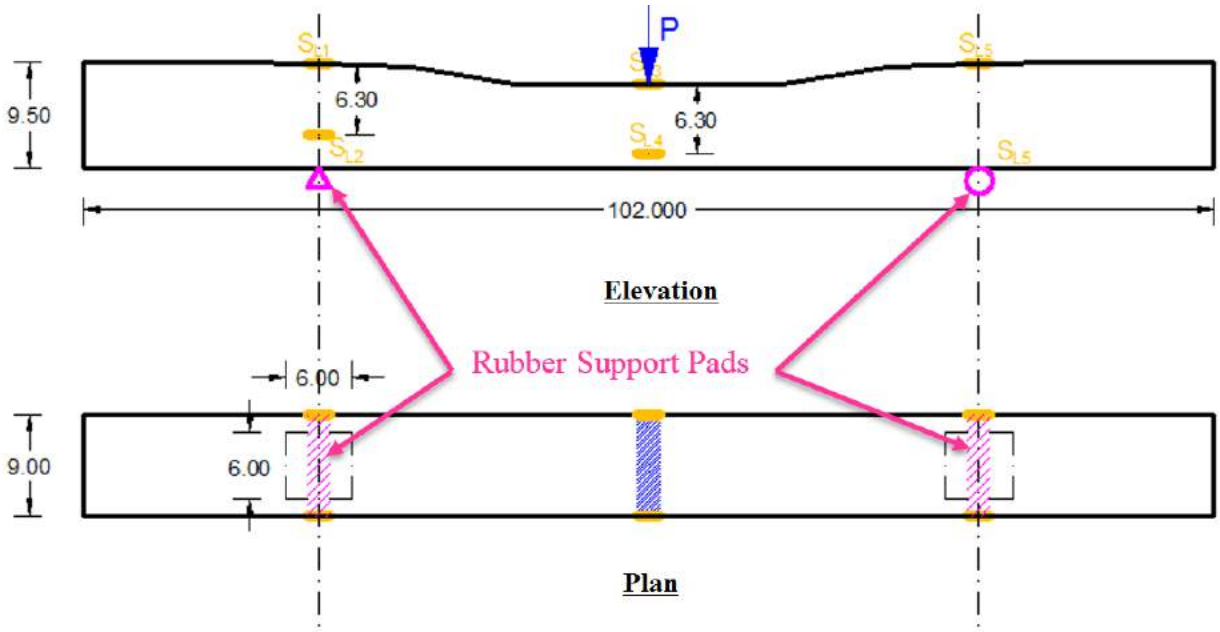

Figure 34. Load and Support Conditions for Center-Positive Bending Test

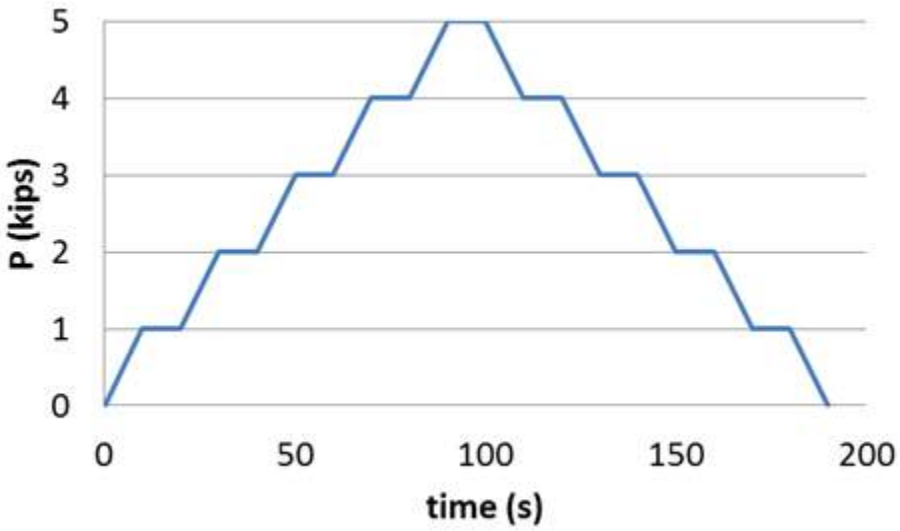

Figure 35. Loading Rate for Center-Positive Bending Test

3.13.4 Rail Seat Compression Test

Rail seat compression tests were conducted with the same instrumented crosstie used in the center-positive bending test. A static vertical load was applied with the STT (Section 3.5.4) at the rail seat at one end of the crosstie while the other end of the crosstie was supported by a roller. The vertical load started at zero and increased by 25,000-lbf increments for each step up to 50,000 pound-force (Figure 36). The length of the loading head was 6 inches, measured perpendicular to the crosstie. The width of the loading head, measured parallel to the crosstie was an independent variable in this experiment, with three cases: 6 inches, 3 inches and 1.5

inches (Figure 37 through Figure 45). The support was distributed evenly across the full width of the tie. The support length, also an independent variable, was tested with three cases: 6 inches, 12 inches and 18 inches centered about the center line of rail seat (Figure 37 through Figure 45). A rubber pad was used for the loading and support contact to prevent damage to the crosstie, and it also provided the medium to adjust the loading head contact area and support contact area.

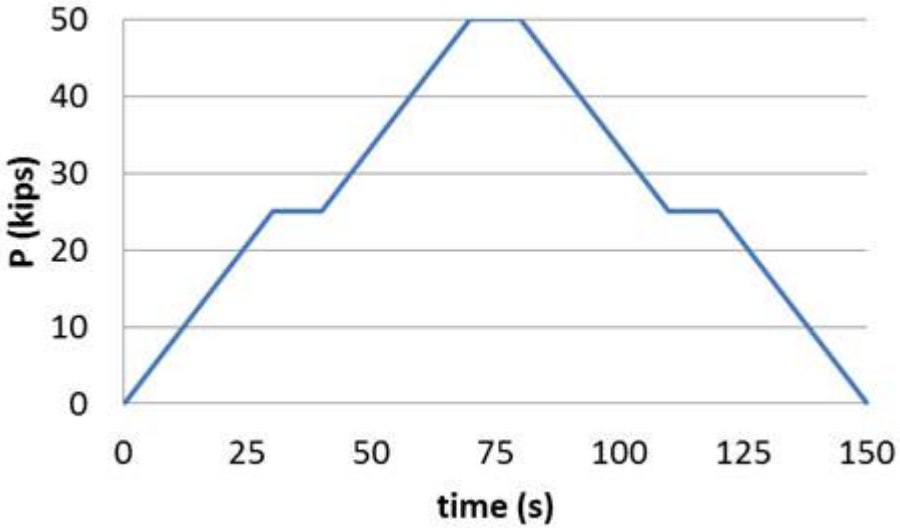

Figure 36. Loading Rate for Rail Seat Compression Test

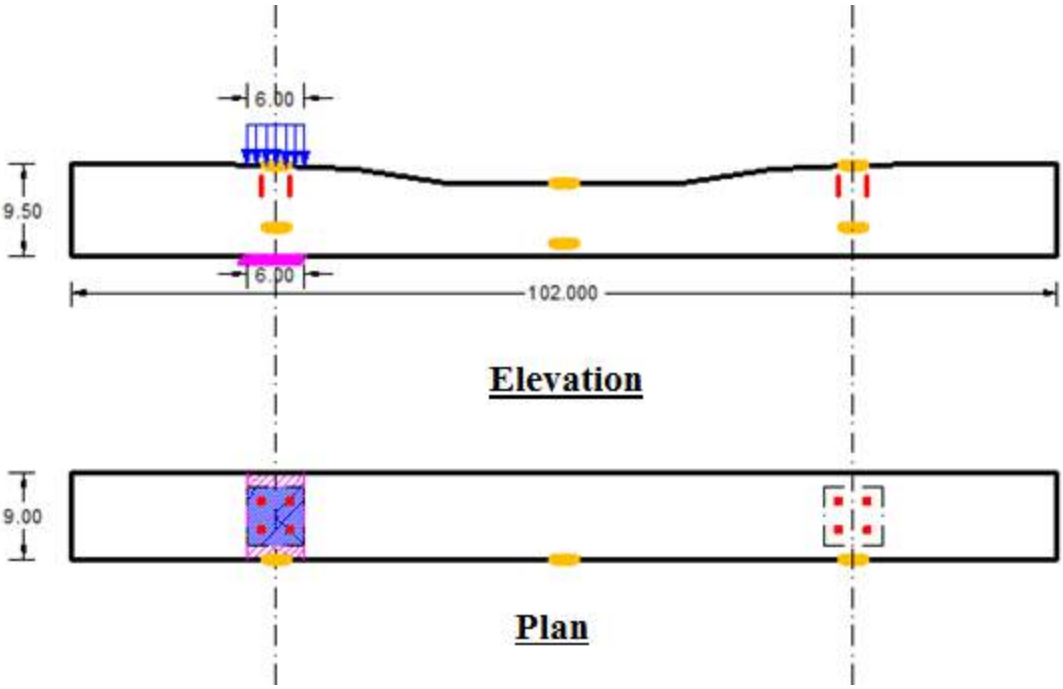

Figure 37. Load and Support Conditions for Rail Seat Compression Test – Loading Head Width: 6", Support Width: 6"

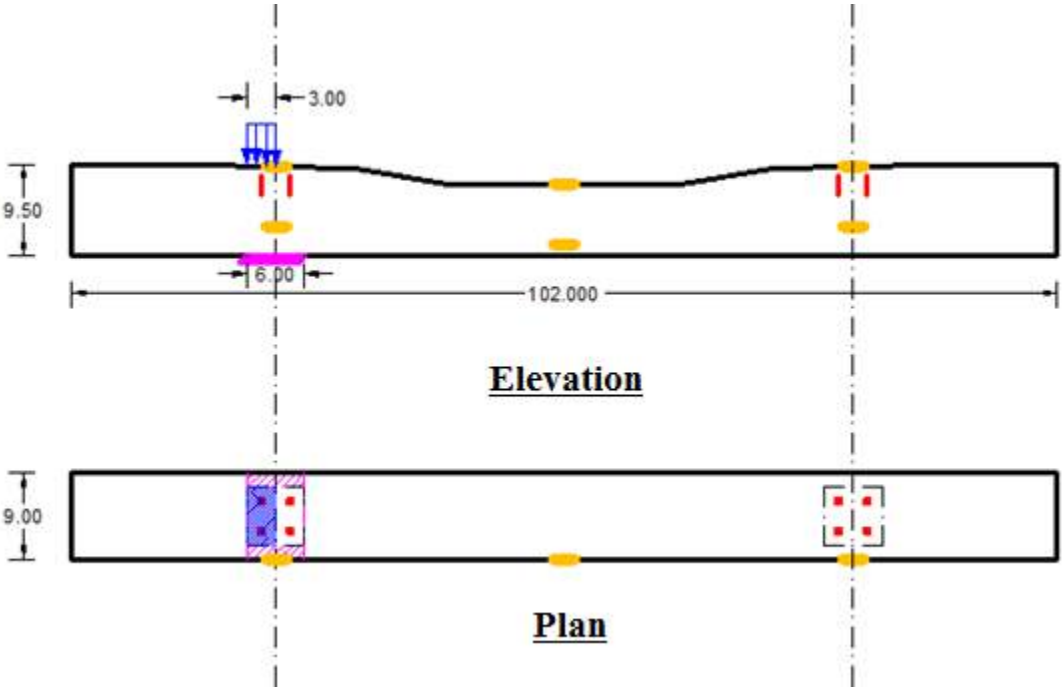

Figure 38. Load and Support Conditions for Rail Seat Compression Test – Loading Head Width: 3", Support Width: 6"

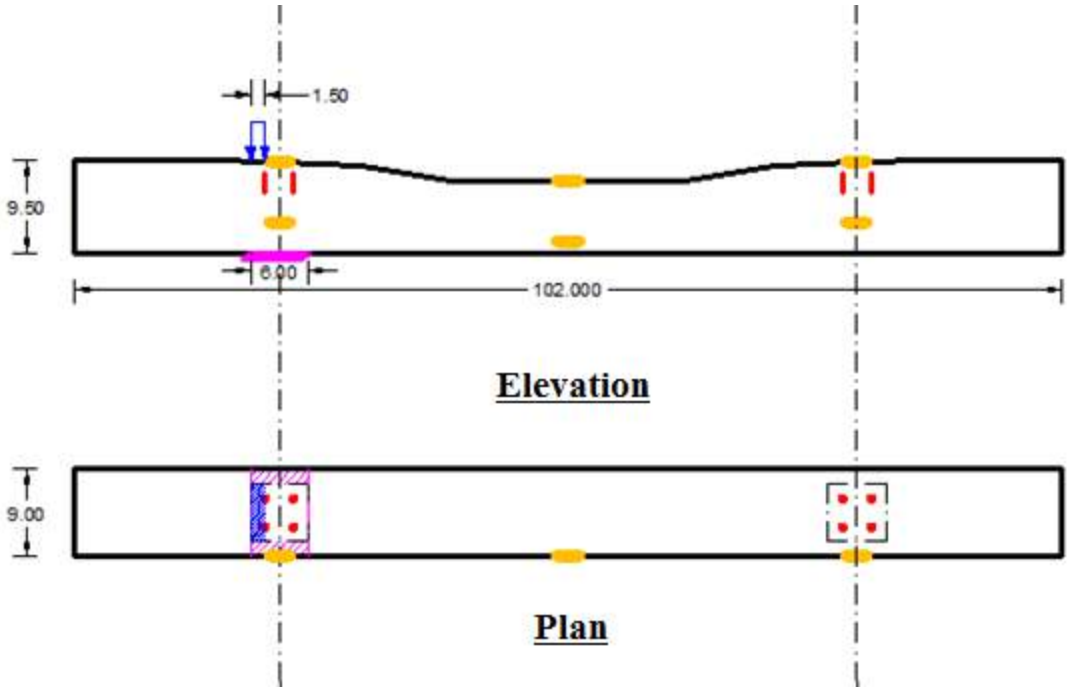

Figure 39. Load and Support Conditions for Rail Seat Compression Test – Loading Head Width: 1.5", Support Width: 6"

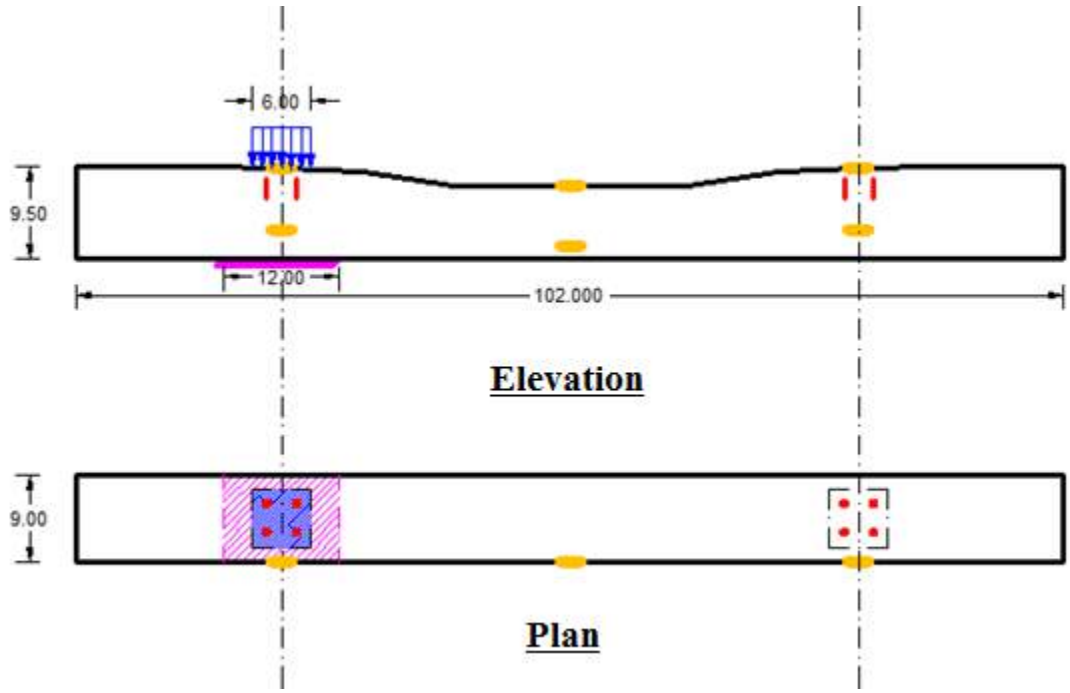

Figure 40. Load and Support Conditions for Rail Seat Compression Test – Loading Head Width: 6", Support Width: 12"

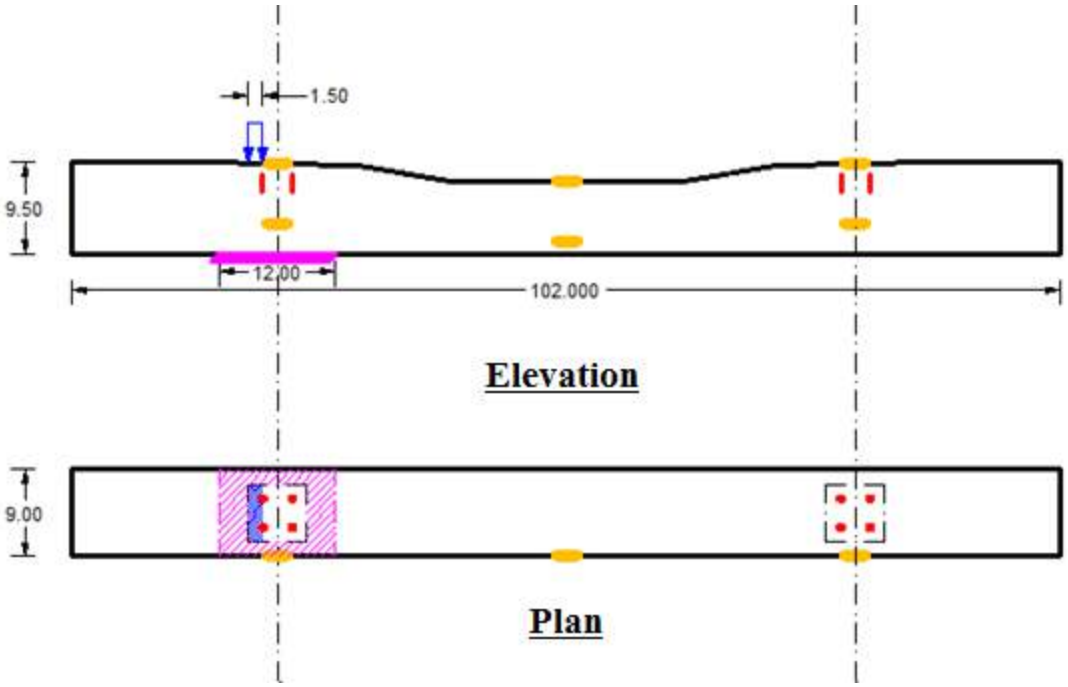

Figure 41. Load and Support Conditions for Rail Seat Compression Test – Loading Head Width: 1.5", Support Width: 12"

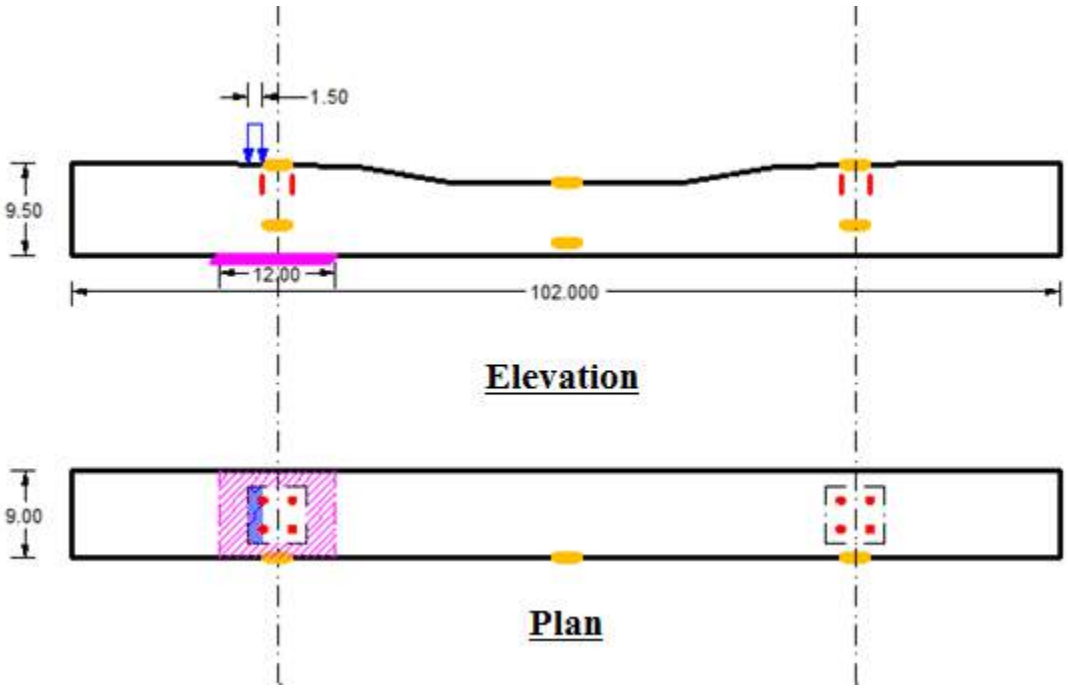

Figure 42. Load and Support Conditions for Rail Seat Compression Test – Loading Head Width: 1.5", Support Width: 12"

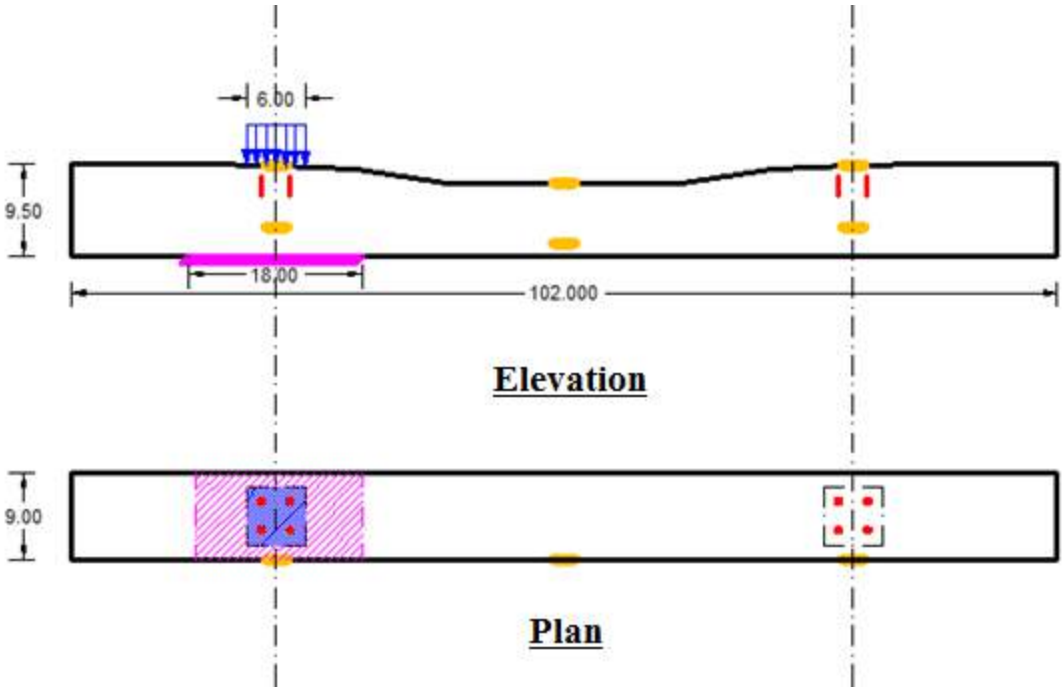

Figure 43. Load and Support Conditions for Rail Seat Compression Test – Loading Head Width: 6", Support Width: 18"

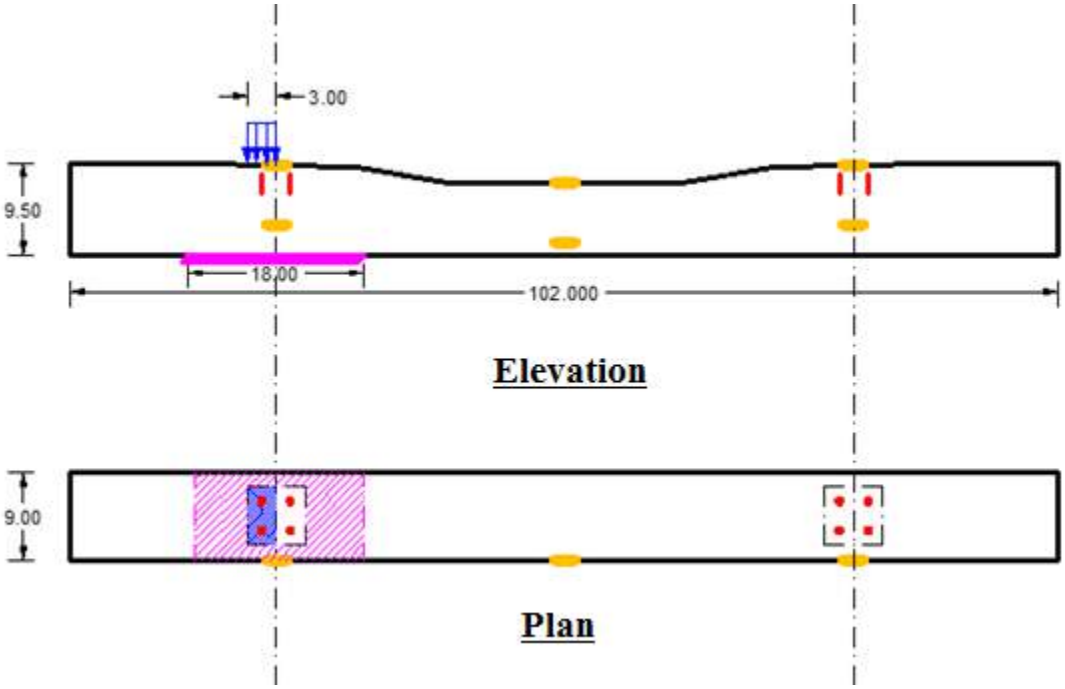

Figure 44. Load and Support Conditions for Rail Seat Compression Test – Loading Head Width: 3", Support Width: 18"

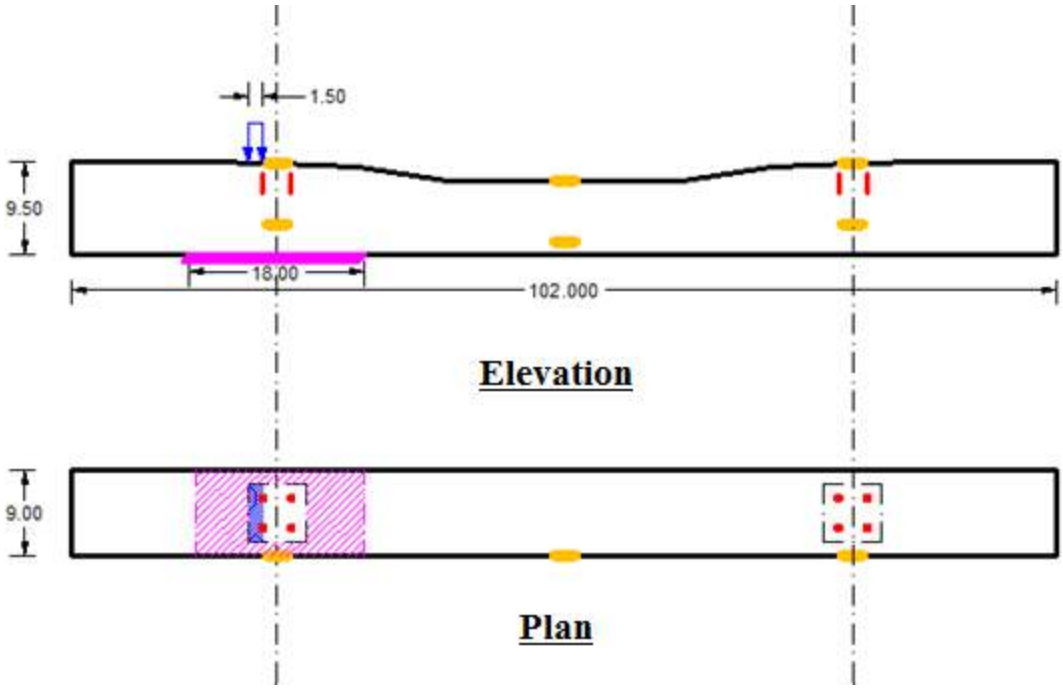

Figure 45. Load and Support Conditions for Rail Seat Compression Test – Loading Head Width: 1.5", Support Width: 18"

3.13.5 Stress Distribution Below Rail Seat Area

Vertical concrete surface strain gauges and embedment strain gauges were used to capture the stress state below the rail seat when a rail seat compressive load was applied on STT. The strain values recorded from surface gauges were compared to values recorded from embedment gauges.

3.14 System-Level Experimental Plan

3.15 Purpose

The purpose of the full-scale concrete crosstie and fastening system loading experiment was to:

- Map the vertical and lateral load paths through the rail, fastening system, and crosstie
- Validate the FE Model
- Compare system-level results with current track design standards

The rail seat reaction, lateral reaction at the shoulder, and clamping force (normal and tangential components) were used to map the load path. Some of these forces were measured directly (e.g. wheel load, rail seat vertical reaction), however, some forces were obtained indirectly by analyzing data recorded during testing (e.g. clamping force). Figure 48 shows the applied forces (vertical and lateral components of wheel load) and reactions on the rail, as well as the original and deformed shape of the rail cross-section where:

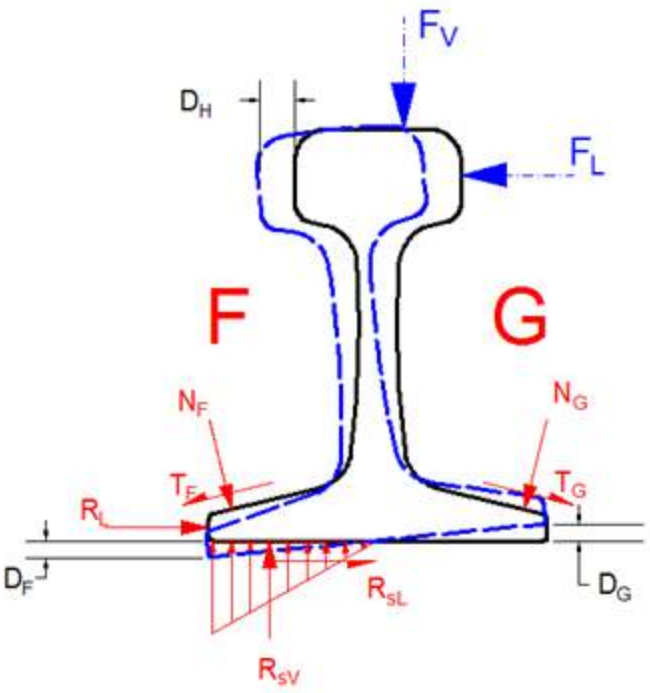

Figure 46. Idealized Load Path Through Rail Cross Section

The following describes the terms used in Figure 46:

- F_V: Vertical component of wheel load (applied load), lbf
- F_L: Lateral component of wheel load (applied load), lbf
- R_{sV}: Vertical rail seat reaction (1/3 the width of the distributed load from field side), lbf
- R_{sL}: Lateral rail seat reaction (center of the distributed load), lbf
- R_L: Lateral reaction entering shoulder, lbf
- N_F: Normal component of clamping force at field side, lbf
- T_F: Tangential component of clamping force at field side, lbf
- N_G: Normal component of clamping force at gauge side, lbf
- T_G: Tangential component of clamping force at gauge side, lbf
- D_F: Vertical displacement at field side, in.
- D_G: Vertical displacement at gauge side, in.

3.16 Loading Procedure

Three full-scale testing setups, the SLTM, PLTM and TLS were used to provide the loading and boundary conditions in the system-level experiments.

3.16.1 SLTM

Three loading conditions were applied: lateral load, a combination of lateral and vertical loads with various L/V, and a combination of lateral and vertical loads with a fixed L/V. Lateral loads were applied to the rail web using a (PTLF, Figure 47a) or to the rail head using a LLF. Lateral loads were applied from zero gradually up to a maximum of 3 kips. The combination of lateral and vertical loads with various L/V was achieved by applying a lateral force using the PTLF initially, and held on this lateral force, then applying a vertical load to the rail section at one side of the crosstie by rotating the loading frame of 90 degrees (Figure 47b). Vertical loads were applied from zero gradually up to a maximum of 40 kips. The combination of lateral and vertical loads with a fixed L/V was applied by placing the loading head over both the rails (Figure 10). Vertical and lateral loads were applied from zero gradually up to a maximum of 80 kips in at a constant L/V of 0.5.

Figure 47. a) Lateral Force Applied by PTLF b) Lateral and Vertical Forces Applied by PTLF and SLTM Loading Head

3.16.2 PLTM

Vertical loads were slowly applied using a constant loading rate up to a maximum of 40,000 pound-force. Vertical loads were applied in conjunction with lateral loads at constant L/V ratios of 0.1, 0.2, 0.3, 0.4, 0.5, and 0.6.

3.16.3 TLS

A vertical wheel load of up to 40 kips was simultaneously applied using two actuators that were connected to both sides of the wheelset. 10-kip, 20-kip, 30-kip, and 40-kip static vertical wheel loads were applied in conjunction with lateral wheel loads at L/V ratios of 0.1, 0.2, 0.3, 0.4, 0.5, and 0.6. Each test was run at various locations on the TLS with five fastening system conditions:

- All fastening system components installed correctly;
- One field side clip removed directly beneath the point of loading;
- One field side clip and one field side insulator removed directly beneath the point of loading;

- Three field side clips removed centered about the point of loading;
- Three field side clips and three field side insulators removed centered about the point of loading.

3.17 Experimental Procedure

3.17.1 Lateral Wheel Load Measurements Using Strain Gauges

The actual lateral wheel loads applied to each wheel were measured using the full strain gauge bridges installed on the rail on SLTM and TLS. The same strain gauge pattern was stated in Section 3.7.1. The actual L/V ratio of the SLTM frame that applied vertical and lateral loads simultaneously was validated through measuring the actual lateral force from the strain gauge bridges on the rail and recording the vertical force from the load cell. To form the rail strain gauge bridges, four strain gauge pairs were installed on the rail (Figure 51): the strain gauges at location #5 and #9 formed one bridge, and the strain gauges at location #6 and #8 formed another bridge. The LLF was used to calibrate the full bridges by applying 3-kip lateral loads to both rails. On the TLS, a measurable lateral force was applied to the axle of the wheel set, however, the portion of the lateral load going into each rail was measured. To achieve this goal, two strain gauge pairs were utilized to form one full bridge above each instrumented rail seat to calculate the actual lateral force applied to the rail. The locations of this strain gauge pair were at #5 and #9, as shown in Figure 51. The Delta Frame was used to provide a known lateral load for calibration.

3.17.2 Rail Seat Vertical Reaction Through Use of MBTSS

MBTSS were used on the TLS to quantify the vertical reaction and pressure distribution at the rail seat. MBTSS were placed between the rail pad assembly and the concrete rail seat. Vertical and lateral loads were applied to the track structure replicating the static loading environment used in field experimentation. The results from field experimentation were compared to corresponding results from the TLS to examine the effect of clip wear on the distribution of load at the rail seat. The pressure was calculated based on the rail seat load data calculated from embedment strain gauges beneath the crosstie rail seat.

3.17.3 Rail Seat Vertical Reaction Through Use of Embedment Strain Gauges

Embedment strain gauges were used to measure the compressive strain below rail seats and thus calculate the rail seat vertical reactions on TLS. This calculation was completed in conjunction with component level testing. The locations of the embedment strain gauges are shown in Figure 54.

3.17.4 Clamping Force Measurements using Strain Gauges

A Safelok I type clip is designed to apply 2.5 kips initial clamping force in the vertical direction normal to the rail seat. However, the 14.2 degree angle of the rail base from the rail seat plane results in 2.5 kips of clamping force applied normal to the rail base with the resultant force normal to the rail seat plane being applied to the rail seat. The tangential component of clamping force was unknown due to both the direction and magnitude being dependent on the installation procedure. Prior to clip installation, strain gauges were placed on both gauge side and field side clips. The initial reaction forces are shown in Figure 48.

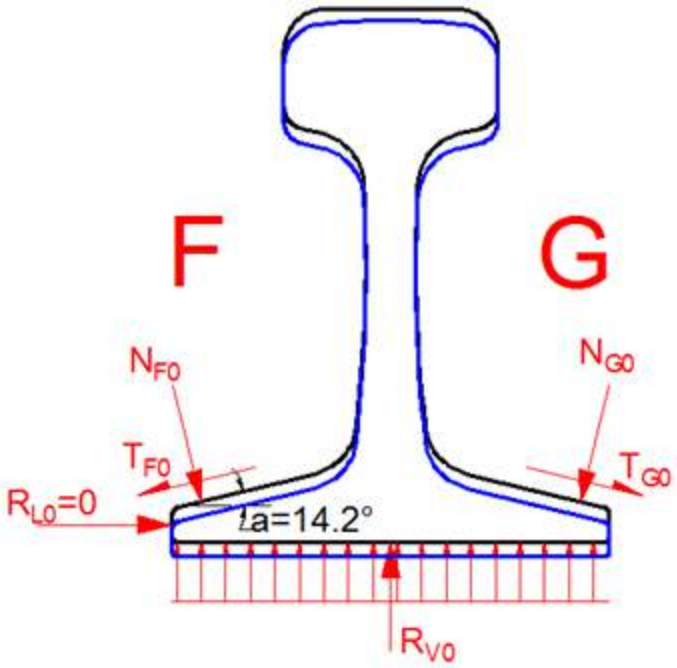

Figure 48. Initial Reaction Forces from Clips

Two strain gauge patterns were used to study the behavior of clips. Strain gauges were installed on the inner and outer surfaces of the clips at multiple locations for clamping force calculations.

Figure 49 shows the first iteration, in which seven strain gauges were placed along each leg of the clip. The distance between adjacent gauges was one inch. To protect the gauges during installation, gauges 1-3 were placed on the inner surface of the clip while gauges 4-7 were placed on the outer surface. To compensate for torsional behavior and uneven loading between each clip leg, strain gauges were installed at the same locations on both legs. The clamping force applied by each leg was calculated and summed to form a total clamping force of the clip. The distance from the center of each strain gauge, d_i, and the relevant angle, φ_i, were used to locate each gauge.

For the second iteration, a pair of stain gauges was placed on both the inner and outer surfaces of the clip to determine the bending moment (Figure 50). Strain gauges were installed on both legs of a clip to compensate for torsional behavior and uneven loading on each leg.

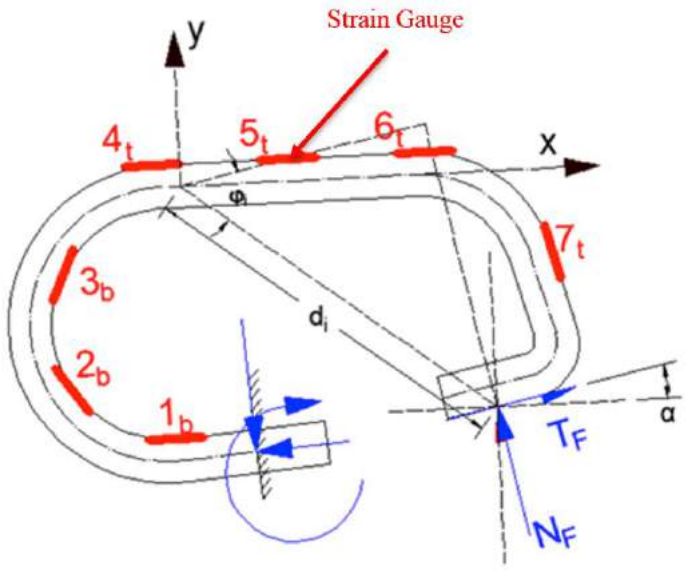

Figure 49. First Iteration of Strain Gauge Orientation on Instrumented Clips

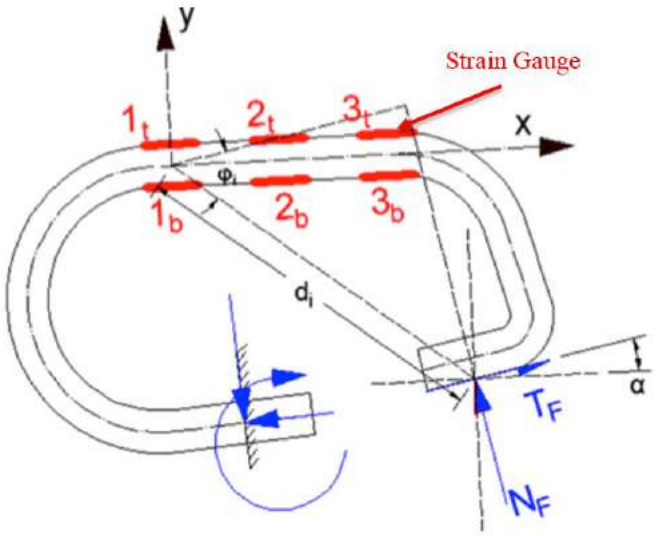

Figure 50. Second Iteration of Strain Gauge Orientation on Instrumented Clips

To measure the initial clamping force after installation, one pair of first-iteration clips were installed on one rail seat (on both field and gauge sides). To measure the change of clamping force due to lateral and vertical wheel load on the SLTM, a pair of second-iteration clips were installed at the other rail seat of the same crosstie on both field and gauge sides. The symmetry of the SLTM loading head resulted in the same loads being input into both rail seats. 36,000-lbf vertical loads were applied to each rail seat with a 0.5 L/V ratio. Strain and bending moment data from the second-iteration clip were used to validate the clamping force calculated from the first-iteration.

3.17.5 Lateral Forces Entering the Shoulder and Lateral Fastening System Stiffness

Lateral forces entering the shoulder were measured using LLEDs with loads from the PLTM and TLS. LLEDs were installed on the field side of the rail. The field side was chosen due to the majority of insulator failures being seen on the field side.

With the PLTM, static vertical loads were applied at a constant rate up to a maximum of 36,000 pound-force in conjunction with lateral loads at constant L/V ratios of 0.1, 0.2, 0.3, 0.4, and 0.5. Dynamic cyclic loads were also applied with the PLTM. Vertical and lateral loads were applied in a 3 Hz sinusoidal wave. Dynamic maximum and minimum vertical loads up to 30,000 pound-force and 1,000 pound-force, respectively, were applied in conjunction with maximum L/V ratios of 0.1, 0.2, 0.3, 0.4, and 0.5. Dynamic maximum and minimum lateral loads were applied up to 15,000 pound-force and -500 pound-force, respectively.

Lateral rail base displacements were measured in conjunction with the LLEDs on the TLS. The lateral rail base displacement, when compared with the lateral force measured at the corresponding shoulder face, describes the lateral stiffness of the fastening system. Lateral stiffness refers to the change in rail base displacement for a given change in lateral force at the shoulder as measured by the LLED. The lateral fastening system stiffness was used to analyze the variance in maximum force measured by adjacent LLEDs.

3.17.6 Rail Deformation and Deflection

Rail deformation was measured with strain gauges and loads applied with the SLTM were used to correlate the strains with the loading conditions (e.g. vertical and lateral loads). A bending moment diagram of a rail cross-section was output from these strain data. Ten strain gauges were installed in a line on each side of a 24-inch rail section. Three strain gauges were placed along the rail base and seven were in the vertical direction on rail web. The distance between adjacent strain gauges was 0.625 inches (Figure 51).

Linear potentiometers were used to measure the deflection of rail loaded with the SLTM and with the TLS. With the SLTM, a rigid frame was bolted onto the end of the crosstie, securing the potentiometers. These potentiometers measured the lateral and vertical movement of the rail with respect to the concrete crosstie (Figure 52).

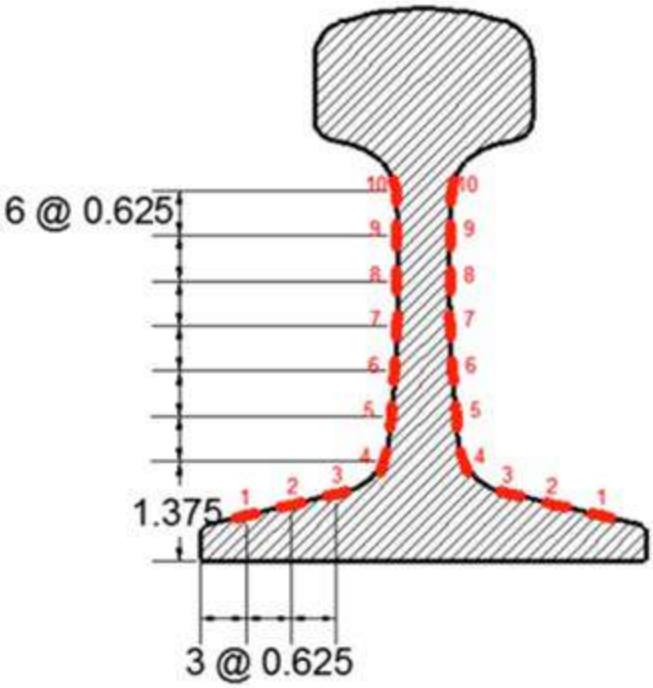

Figure 51. Strain Gauge Locations on Rail Web and Base

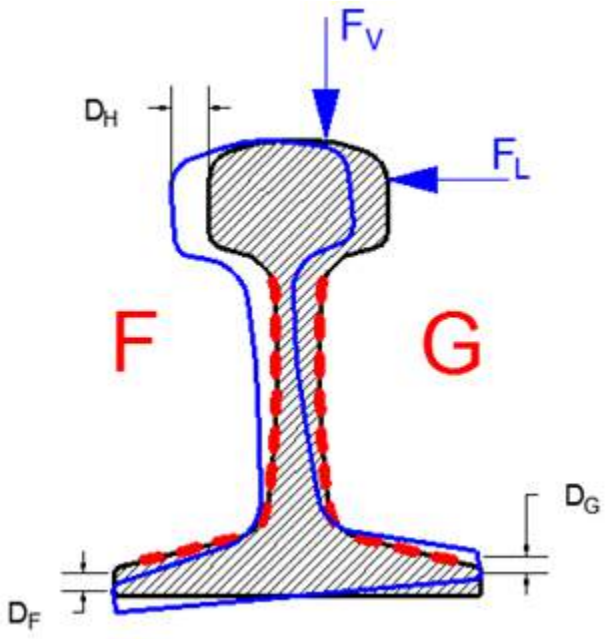

Figure 52. Rail Deflection Measurements

D_F: Vertical displacement of the field side rail base

D_G: Vertical displacement of the gauge side rail base

D_H: Lateral displacement field side face of the rail head

A linear potentiometer was placed at the center line of the rail seat parallel to the crosstie and 0.5 inches from the top of the rail head to measure lateral displacement of the field side face of the rail head. Four more potentiometers were placed at the rail base 0.5 inches from the outer most edge of the rail base and three inches from the centerline of the crosstie on each side of the rail (Figure 53).

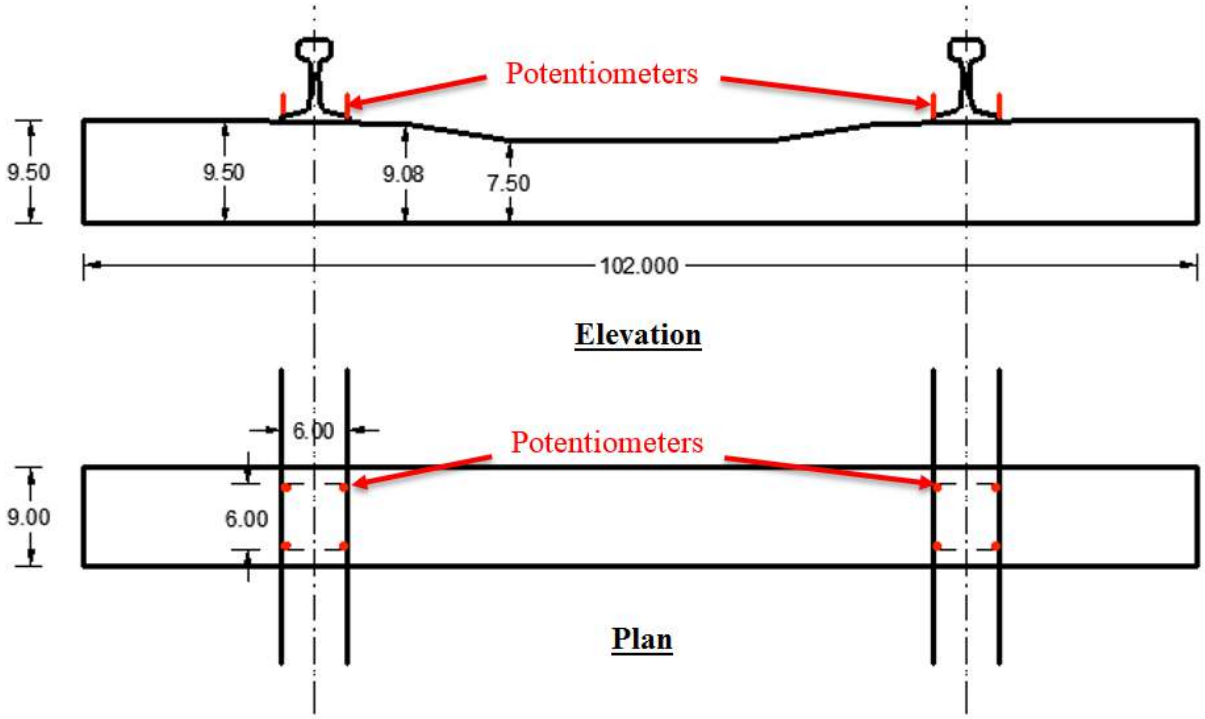

Figure 53. Potentiometer Location for Measuring Vertical Rail Base Displacement

With the TLS, potentiometers were used to measure the rail displacements relative to the crosstie (Figure 12). One potentiometer was fixed to a bracket anchored into the crosstie at the field side to measure the vertical rail base displacement. Three potentiometers were fixed to brackets anchored into the crosstie at the gauge side. One potentiometer was used to measure the vertical rail base displacement, the tip of which contacted the rail base at the same location as the field side. Two potentiometers were used to measure the lateral rail displacements at the center of the web and at the rail base.

3.17.7 Concrete Crosstie Deformation and Displacements

Concrete crosstie bending deformation was measured by concrete surface strain gauges using the TLS. Five pairs of surface strain gauges were installed on the edges of each instrumented crosstie. Five crossties were instrumented in total. Within these five crossties, all the rail seats located at the west side and the east side rail seat of the center crosstie were instrumented with embedment strain gauges. The locations of the surface strain gauges are shown in Figure 46.

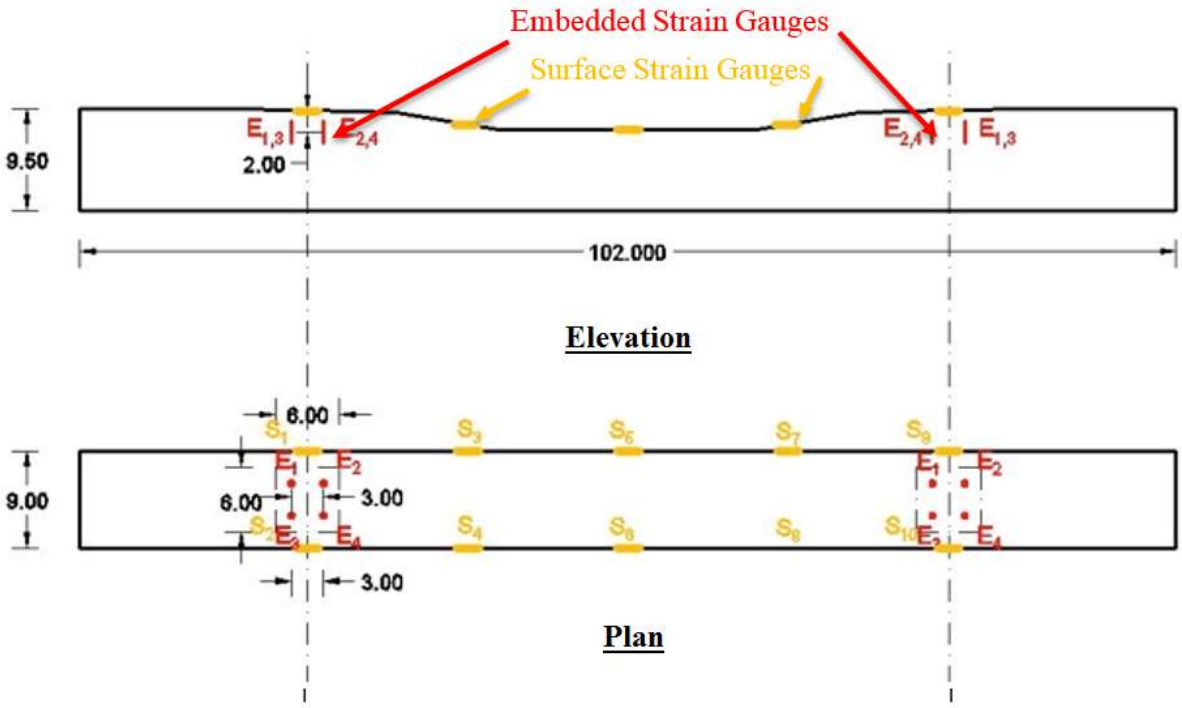

Figure 54. Dimensions of Crosstie and Location of Strain Gauges

Potentiometers were used to measure the global displacements of concrete crossties with the SLTM and with the TLS.

With the SLTM, three vertically-oriented potentiometers were attached to the loading frame to capture vertical deflection measurements of the crosstie under various loading cases. A horizontally-oriented potentiometer was fixed parallel to the crosstie and at both ends for lateral displacement measurements. In Figure 47, "Tie L_1" and "Tie L_2" show the locations of potentiometers used to measure the lateral displacement of the crosstie. "Tie V_1", "Tie V_2" and "Tie V_3" show the locations of potentiometers to measure vertical crosstie deflection.

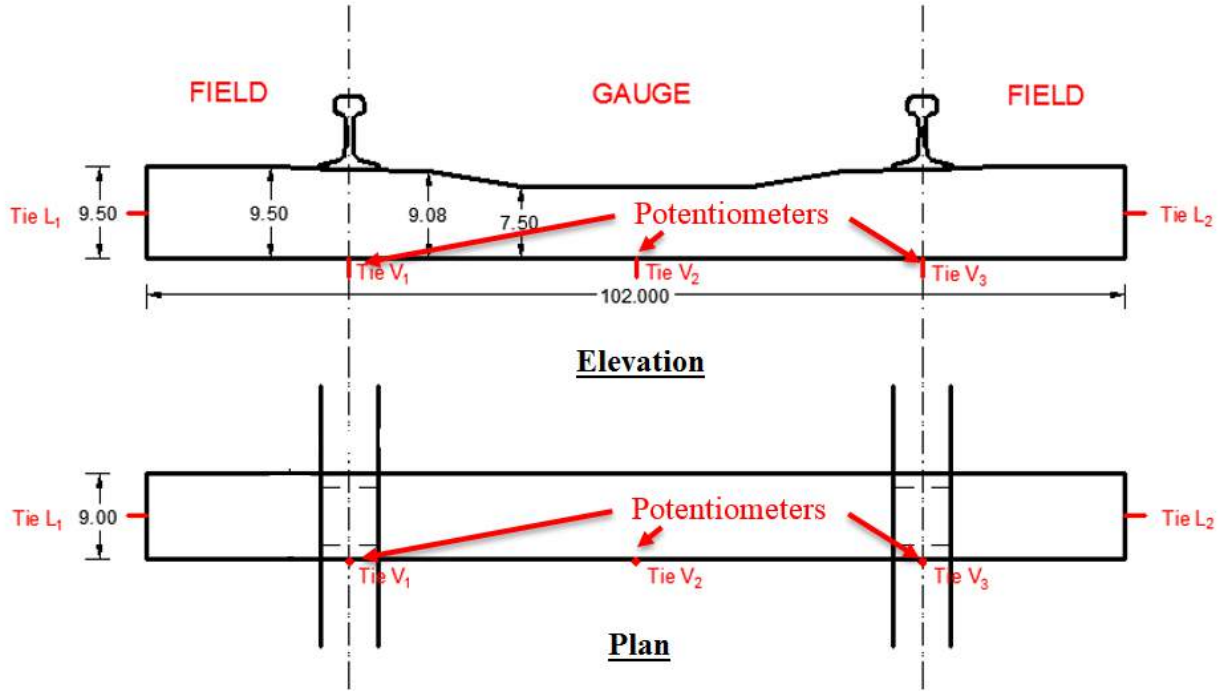

Figure 55. Displacement Measurements of Concrete Crosstie

With the TLS, the global displacements of the five instrumented crossties were measured. For each crosstie, one horizontally-oriented potentiometer was used to measure the lateral global displacement from the west end, the location of which was the same as "Tie L_1" shown in Figure 48**.** One vertically-oriented potentiometer was used to measure the vertical global displacement from the west end. The tip of this vertically-oriented potentiometer touched the center line of the crosstie 1-inch away from the end surface.

Chapter 4: Laboratory Experimental Results

4.1 Laboratory Experimentation Overview

The purpose of the laboratory experimental results is to provide a detailed summary of the findings from the most critical set of laboratory experiments. Laboratory experimentation deepened our understanding of the load path through the crosstie and fastening system in two distinct manners. First, we gained an understanding of the load going through an individual crosstie and its fastening system. Secondly, we were able to understand the distribution of a given load over adjacent crossties. During the laboratory experimental phase, the load path going into each crosstie and fastening system was examined under known loading conditions and the behavior of each component was evaluated. The demand and capacity of each component, the support conditions provided by the ballast, and the stability of the system due to changing load and boundary conditions were evaluated and are discussed in this chapter. Results from laboratory experimentation are discussed at the material, component, and system level.

4.2 Materials-Level Experimental Results

4.3 Compressive Stiffness of Polyurethane and Nylon 6/6

To determine the compressive elastic modulus and yield strength of the polyurethane rail pad and nylon 6/6 abrasion frame, we conducted a compression test using circular specimens. Two specimens from each both polyurethane and nylon 6/6 were tested as described in Chapter 3, Section 3.12. Figure 56 summarizes the results of the compression test. No significant inelastic behavior was observed in the range of the design and service loads. As a result, we further increased the loading to the capacity of the loading machine. For the test with the nylon 6/6, the loading was stopped when the specimen deflection was near the original thickness of the abrasion plate specimen.

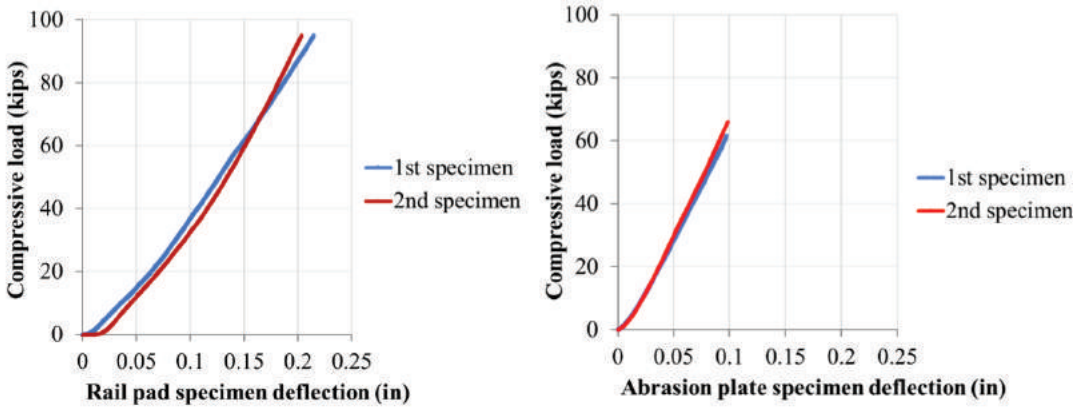

Figure 56. Relationship Between Compressive Load and Specimen Deflection of Rail Pad and Abrasion Plate Specimens

As seen in Figure 56, all specimens remained elastic throughout the compression test, with similar outcomes observed between replicates. Images of the final specimens after the

compression tests were conducted are shown in Figure 57, and evidence of Poisson's effect was observed. Specifically, the specimens expanded horizontally under vertical compressive load, and contracted back to the original size during the unloading process. The Teflon sprayed on the loading frame was partially worn away due to the expansion and contraction of the specimens, as shown by the gray ring in Figure 57.

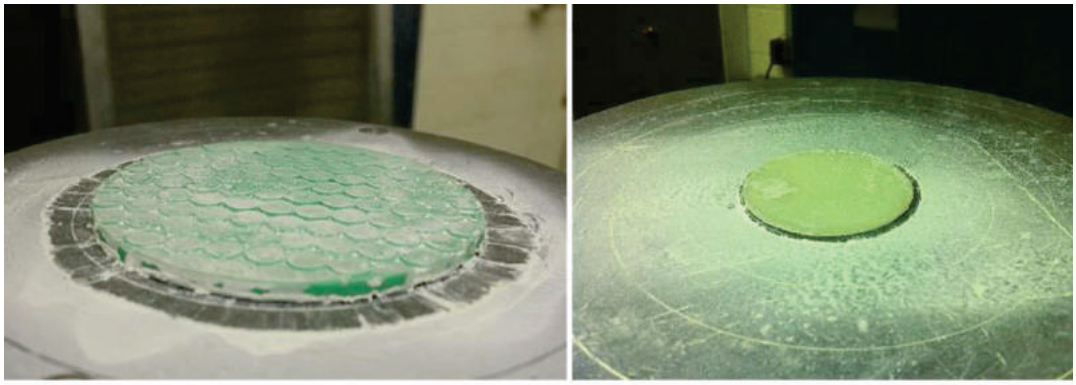

a) b)

Figure 57. Specimens of a) Rail Pad and b) Abrasion Frame After Compression Test

A comparison between material properties measured during the compression test and data provided from the manufacturer is shown in Table 11. The measured elastic moduli of nylon 6/6 and polyurethane were lower than the values provided by the manufacturer. No plastic behavior was observed at stress levels that were considerably higher than the yielding strength provided from the manufacturer. As a result, yield strength was not determined in these experiments. The material properties provided from the manufacturer were confirmed through tension tests, and the difference in loading scenarios (compression and tension) could contribute to the observed differences between the test results and the manufacturer-supplied data. The confinement of the material specimen may have also contributed to the difference in the measured stiffness. Ideally, the compression test should be conducted with no friction between the loading frame and the test specimens. For our experiments, Teflon was sprayed on the interfaces to reduce confining friction, but the frictional characteristics of this interface were not clear. Considering these factors, the test results were not incorporated into the material property definitions contained within the FE model, and the data from the material supplier was used.

Table 11. Comparison Between Compression Test Results and Data from Material Supplier

	Experimental Test Result		Manufacturer-Supplied Data	
Component	Young's modulus (psi)	Maximum elastic stress (psi)	Young's modulus (psi)	Yield strength (psi)
Abrasion plate	23,258	20,510	440,000	12,000
Rail pad	5,520	4,762	7,500	1,900

4.4 Concrete Strength and Modulus

The concrete strength and elastic modulus were measured at the crosstie manufacturing plant by the crosstie manufacturer. The average strength f'_c and Young's modulus E_c are shown in Table 12.

Table 12. Concrete Properties

Days from casting	f'_c (psi)	E_c (psi)
1 day	--	3.68×10^6
7 days	--	4.00×10^6
28 days	11,730	4.26×10^6

The concrete strength (f'_c) of cores drilled from the crossties one year after fabrication was tested. A core drill was used to remove cylinder samples from concrete crossties. Six specimens that were 3 inches by three inches were tested, and the average concrete strength obtained from the compressive test was converted to American Concrete Institute (ACI) standardized uniaxial concrete strength. The 1-year strength was found to be 11,000 psi, which was 6.2% lower than the reported 28-day strength. The slightly lower strength could be due to the small sampling size. The Young's modulus was found to be 4.50×10^6 psi, which was 5.6% greater than its 28-day modulus. The tensile strength (cracking stress) of the concrete cores was not measured directly but was obtained using the equation recommended by ACI 318 as shown below:

$$f'_t = 7.5\sqrt{f'_c} = 7.5\sqrt{11{,}000} = 787 \text{ psi}$$

The material properties obtained from the concrete cylinder core testing were used in the subsequent analysis of concrete crossties.

4.5 Component-Level Experimental Results

4.6 Rail Bending Behavior Preliminary Experiment

To understand the bending behavior of the rail and the linearity and elasticity of rail material, a center-positive bending test was conducted on a 24-inch rail section (Figure 58). The loading and boundary conditions, loading procedure, and the locations of strain gauges are included in Section 3.13 of Chapter 3.

Figure 58. 24-Inch Rail Section Loaded by Uniaxial Compression Machine

The strain measurements recorded under various center positive loadings were compared to the analytical strain values obtained by applying the Euler-Bernoulli beam theory (Figure 59). In Figure 59, the experimental and analytical strain measured from the upper and lower strain gauges were labeled as "e_t" and "e_b". The values for average strain measured from strain gauges a, a', c and c' (Figure 23 in Section 3.11 in the Laboratory Experimental Plan of Chapter 3) were used as "e_t (experimental)"; and the average strain measured from strain gauges b, b', d and d' from the same figure were used as "e_b (experimental)".

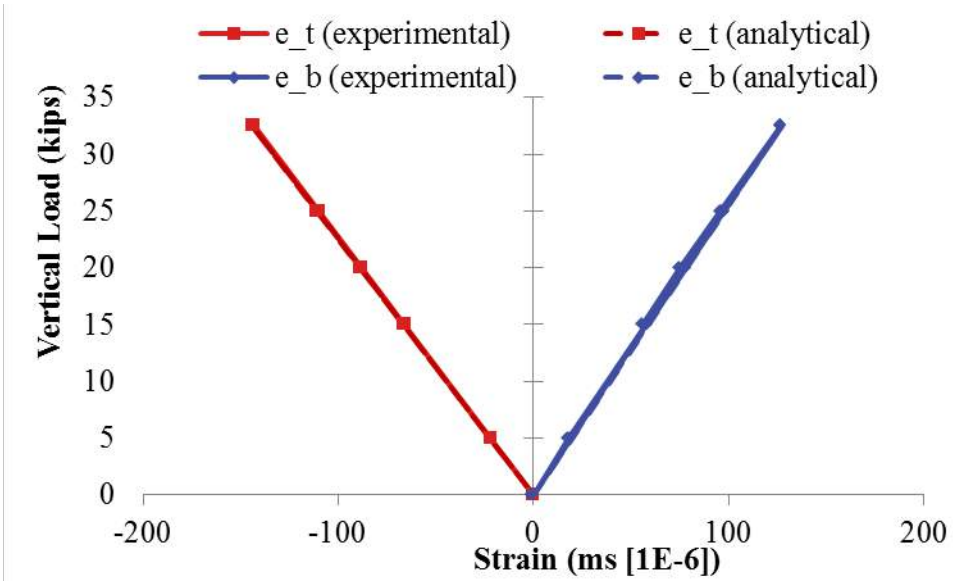

Figure 59. Experimental and Analytical Strain Measurements Under Center-Positive Bending Test

The results show that the experimental strain values matched the analytical strain values very well, and the maximum error for the top and bottom strain was only 0.8% and 0.3%. The results

also revealed that the rail strain remained linear under the static loading up to 32.5 kips. The straight plane assumption made in the Euler-Bernoulli beam theory can be applied to rail 2.5 inches away from the testing rig supports (the lateral distance from the strain gauges to the testing rig supports). In summary, the most notable finding from this experiment is that the rail deformed elastically under the range of applied static loads.

4.7 Rail Pad Assembly Stiffness Experiment

An experiment was executed to obtain the rail pad assembly stiffness and is described in Chapter 3, Section 3.12 of the Laboratory Experimental Plan. Because the nominal elastic modulus of polyurethane (7,500 psi) is known to be far less than that of nylon 6/6 (440,000 psi), and the thickness of pad (0.236 inch) is about 4 times greater than the thickness of abrasion frame (0.055 inch), the compression deformation of the abrasion plate was neglected.

A comparison of rail pad assembly deflection and stiffness from the nominal material properties and assembly laboratory experiments is shown in Table 13. The compression deflection of the rail pad was only 23% of the deflection calculated using its nominal Young's modulus. This is likely due to the confinement provided by the shoulders and friction between top and bottom interfaces. This result revealed that the effect of the friction confinement was great. In design and analysis, the stiffness of the pad assembly should be used lieu of its Young's elastic modulus.

Table 13. Comparison of Nominal Material Properties and Assembly Test Result

	Nominal material properties		Assembly experimental results	
Component	Young's modulus (psi)	Deflection at 40 kips rail seat load (in)	Stiffness (psi)	Deflection at 40 kips rail seat load (in)
Rail pad	7,500	0.035	21,850	0.012

4.8 Concrete Crosstie Behavior Experiment

The instrumented concrete crosstie was tested using the STT (Chapter 3, Section 3.5.4 in the Laboratory Experimental Plan). First, the bending behavior concrete crosstie was evaluated through the center-positive bending test (Figure 34 in the Laboratory Experimental Plan). The testing specimen was not loaded to the point of flexural tension cracking, but the bending strains acquired from the crosstie surface strain gauges were used to compare with the analytical strain values.

The vertical load used in this experiment was calculated to make sure the crosstie would not crack when the loading was applied (Table 14). The cracking moments at the rail seats and center were calculated using the Euler-Bernoulli beam theory. The concrete tensile strength was obtained in Chapter 3, Section 3.9, and the crosstie dimensions and the locations of the pre-stressed wires were provided by the manufacturer. The calculated cracking moments at rail seats and the crosstie center are shown in Table 14. The positive cracking moment was 196.8 kip-inches at the crosstie center, and the critical loading was calculated as 13.1 kips. In the center-positive bending test, the maximum vertical load was limited to 10 kips, and no cracking was found.

Figure 60. Vertical Rail Seat Loading Applied Using the STT

As is explained in the Laboratory Experimental Plan, six strain gauges were installed on one side of the crosstie. The pair of strains recorded from the crosstie center was used for analysis. Theoretically, the lateral strain immediately above the support should be zero, and the strain was indeed very small (<10 ms). This test specimen and the recorded strains were used in the subsequent full-scale TLS experiment (Section 3.5.5 in the Laboratory Experimental Plan).

Table 14. Concrete Crosstie Cracking Moments (values in kip-inches)

Moment	Rail seat	Crosstie center
Positive	405.6	196.8
Negative	219.6	256.8

In the concrete crosstie center-positive bending test, strains were recorded from the pair of gauges (S_{L3} and S_{L4} in Figure 33 in the Laboratory Experimental Plan) located at the center of the crosstie is shown in Figure 61. When 10 kips of vertical load was applied, the top strain was -82 ms in compression and the bottom strain was 43 ms in tension. The load versus strain relationship was relatively linear throughout the loading process, and the strain went back to zero when the load was removed. Using the Euler-Bernoulli beam theory, the centroid axis was found to be 3.8 inches below the top surface or 3.7 inches above the bottom surface of the crosstie. This experimental result agreed with the location of the actual centroidal axis of the transformed cross-section. Young's modulus of the concrete was calculated as 4,525 ksi.

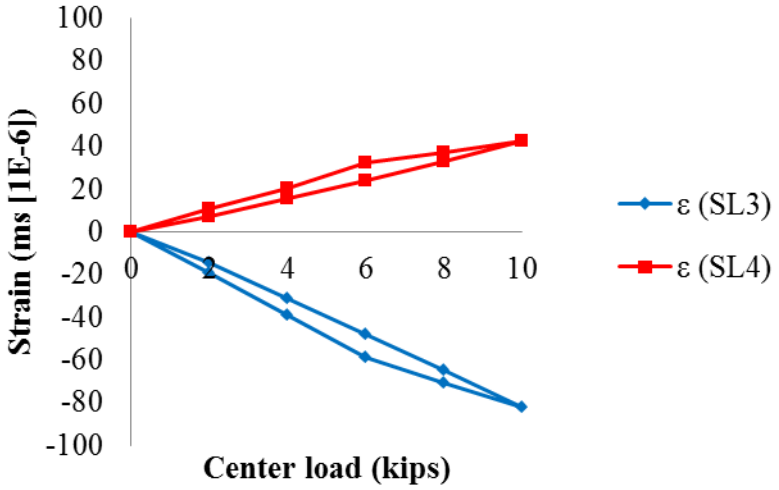

Figure 61. Crosstie Strain Recorded from Center-Positive Bending Test

The compressive strain measured below the rail seat was used to validate the effective load distribution assumption made in International Union of Railways (UIC) 713 (2002). The assumed support condition is shown in Figure 62a (or Figure 1a in UIC 713 (2002)). The effective load distribution and lever arm defined in UIC 713 are shown in Figure 62b (or Figure 2 in UIC 713 (2002)). The effective width of the reaction force distribution was derived from the rail seat width and the crosstie depth, and the assumed distribution angle was 45 degrees.

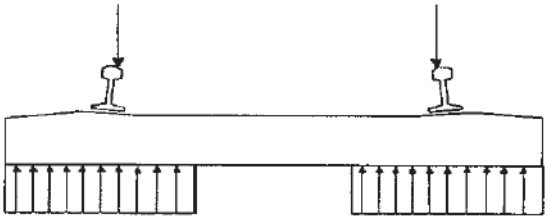

a)

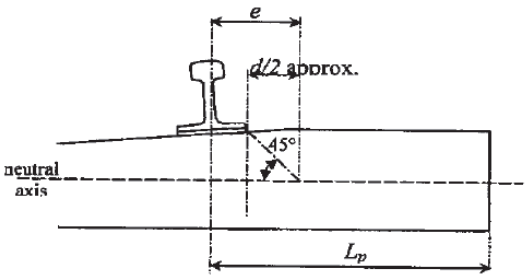

b)

Figure 62. Support Condition and Calculation Methodology Used in UIC 713 (2002) for a) Crosstie Reaction Distribution for Newly Tamped Track and b) Assumed Load Distribution and Lever Arm Derivation for Rail Seat Bending

Concrete embedment and surface strain gauges were used to quantify the strain distribution and the load path in the concrete below the rail seat. Four concrete embedment strain gauges were installed two inches below the surface of the rail seat before casting. The locations of the embedment and surface strain gauges are shown in Figure 33 in the Laboratory Experimental Plan.

Using the STT (Chapter 3, Section 2.1.4) three support conditions with different support widths were evaluated. The compressive strain measured from the concrete surface below the rail seat is shown in Figure 63, Figure 64, Figure 65, Figure 66, Figure 67, and Figure 68 for the three support conditions. The x-axis represents the distance from the location of the strain measurement to the center of the rail seat. Figure 63, Figure 64, and Figure 65 show the strain measured 5 inches above the bottom surface of the crosstie (S_{V1} – S_{V5} in Figure 33 in the Laboratory Experimental Plan). Figure 66, Figure 67, and Figure 68 show the strain measured from 2.5 inches above the bottom surface (S_{V6} – S_{V10} in Figure 33 in the Laboratory Experimental Plan).

By comparing the three unique support conditions, the wider support led to a slightly lower compressive strain when there was no eccentricity for the rail seat loadings. When the support width was 6 inches, the center strain at a point 5 inches above the bottom surface of the crosstie was -157 ms (“6″×6″” in Figure 63). The center strain was -111 ms for the 12-inch support (“12″×6″” in Figure 65), and -105 ms for the 18-inch support (“18″×6″” in Figure 67). The support width had a large effect on the strain measured 2.5 inches above the bottom of crosstie. The compressive strain measured from 2.5 inches above the bottom at the center line of the rail seat was -130 ms (“6″×6″” in Figure 64), -110 ms (“12″×6″” in Figure 66) and -61 ms (“18″×6″” in Figure 68). These results show that the bottom of the crosstie sees significantly lower compressive strain values due to wider support conditions.

When eccentric loading was applied to the rail seat, the strain distribution drifted from the centerline of the rail seat toward the side with eccentric loading (field side in this test). For example, when the support width was 18 inches, and the rail seat load was applied with a large eccentricity (Figure 67 and Figure 68, case “18″×1.5″”), the peak of the distributed strain below the rail seat drifted towards the field side. Based on this result, the common assumption of evenly distributed crosstie reaction forces may not be valid. Additionally, as shown in these data, the 45 degree assumption found in UIC 713 may not be accurate under some loading scenarios.

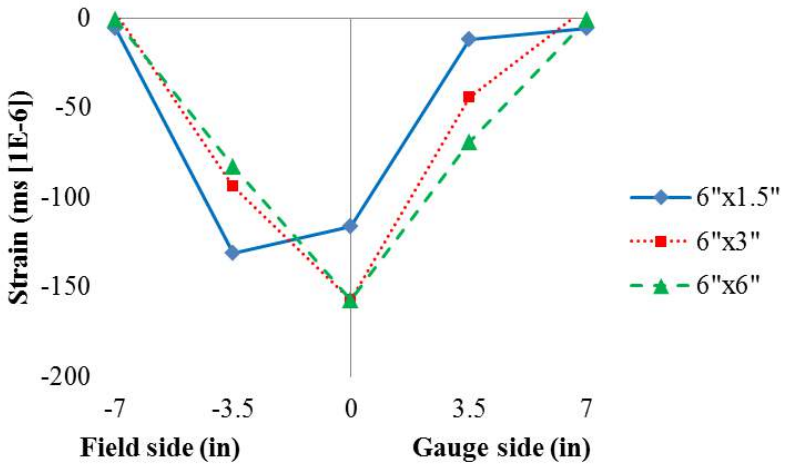

Figure 63. Compressive Strain Distribution 5 Inches Above the Crosstie Bottom (Support Width = 6")

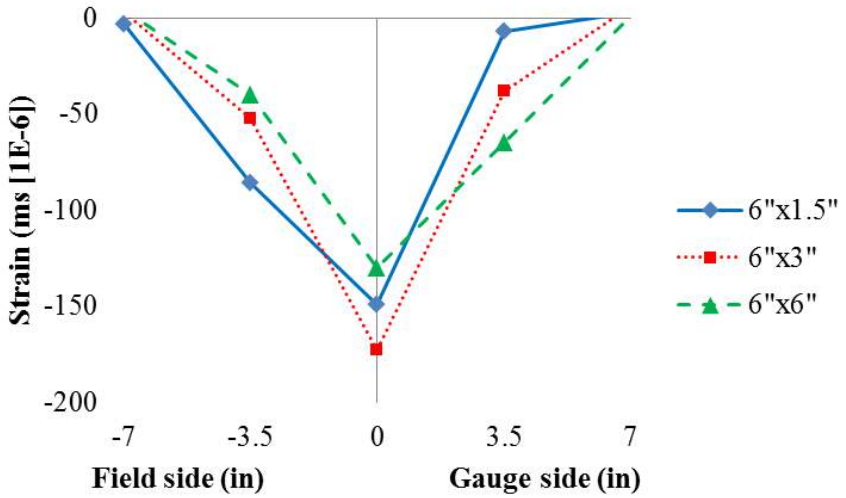

Figure 64. Compressive Strain Distribution 2.5 Inches Above the Crosstie Bottom (Support Width = 6")

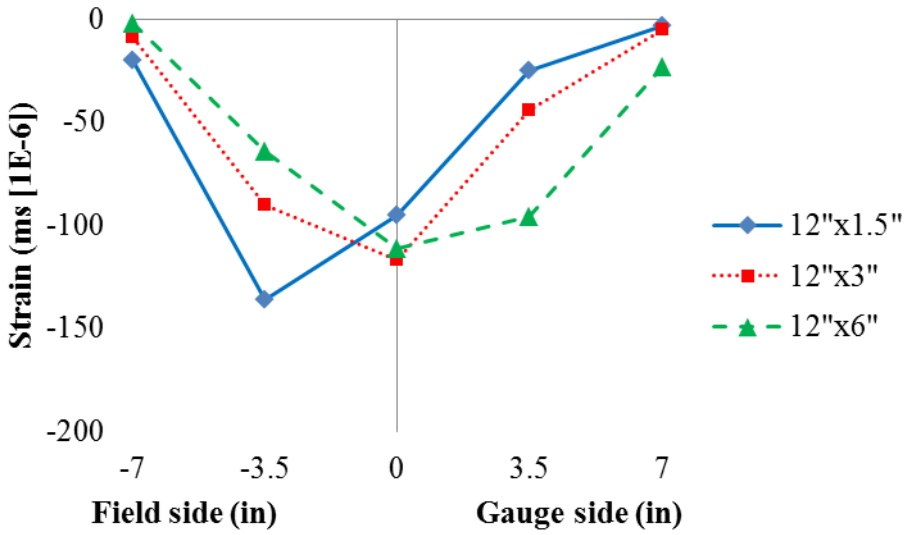

Figure 65. Compressive Strain Distribution 5 Inches Above the Crosstie Bottom (Support Width = 12")

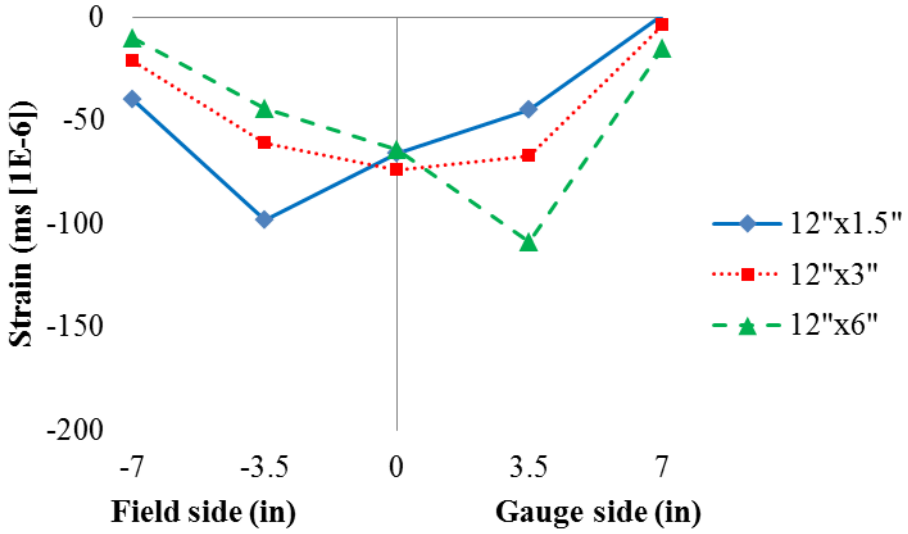

Figure 66. Compressive Strain Distribution 2.5 Inches Above the Crosstie Bottom (Support Width = 12")

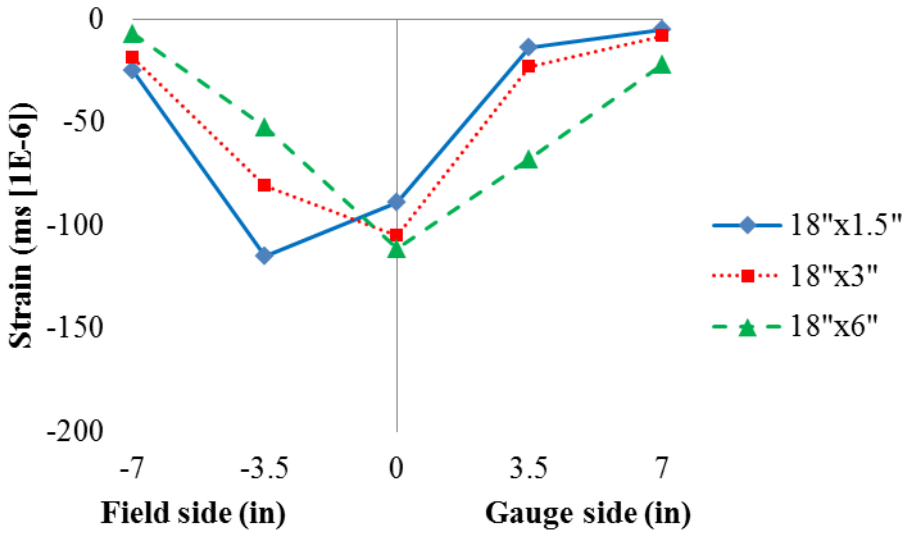

Figure 67. Compressive Strain Distribution 5 Inches Above the Crosstie Bottom (Support Width = 18")

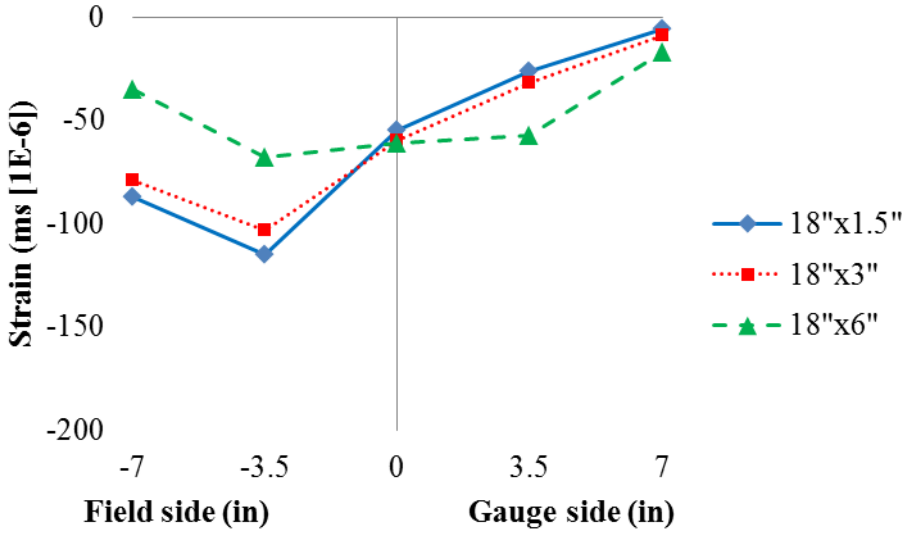

Figure 68. Compressive Strain Distribution 2.5 Inches Above the Crosstie Bottom (Support Width = 18")

The internal compressive strain measured from the embedment strain gauges is shown in Figure 69, Figure 70, and Figure 71 for the three cases of support conditions. The internal strain distribution agreed with the concrete surface strain measurements where the maximum strain was measured on the field side of the rail seat under eccentric loads. Using the cases shown in Figure 69 as an example (6-inch support width), the internal compressive strain was measured as -146 ms and -150 ms from the field and gauge sides when there was no loading eccentricity (case "6"×"6"). The measured internal compressive strain was -327 ms and -33 ms from the field and gauge side when the largest eccentricity was applied (case "6"×1.5"").

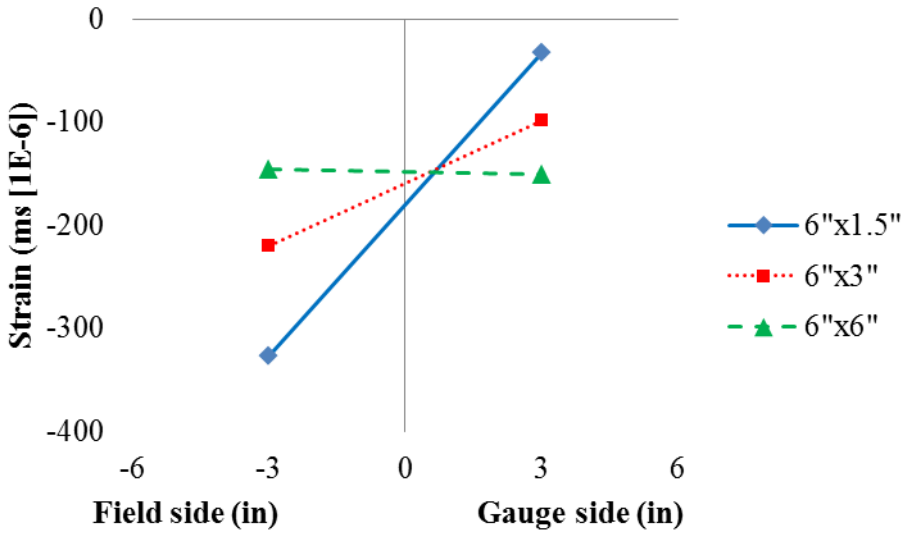

Figure 69. Compressive Strain Measured from Embedment Strain Gauges (Support Width = 6")

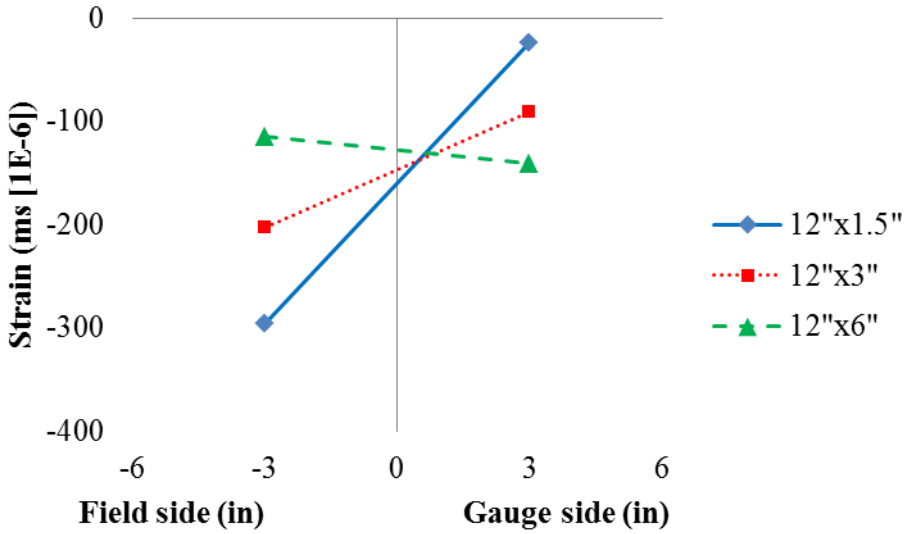

Figure 70. Compressive Strain Measured from Embedment Strain Gauges (Support Width = 12")

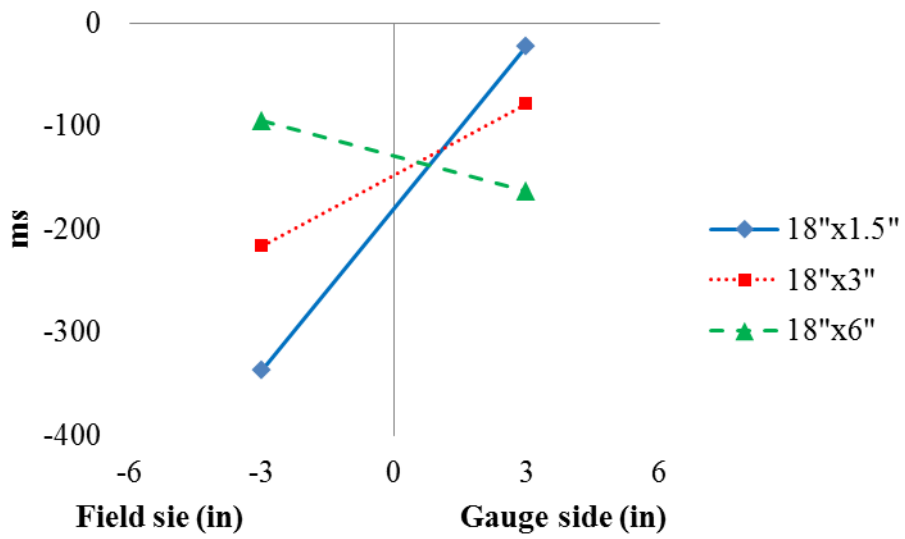

Figure 71. Compressive Strain Measured from Embedment Strain Gauges (Support Width = 18")

Crosstie designers should consider modifying the methodology provided in UIC 713 (2002) to calculate the design bending moment to accommodate eccentric loadings, such as those that have been shown to be common on heavy-axle freight rail infrastructure where high L/V load ratios are present. More research is needed to include various cases of loading and support conditions in a revised approach to crosstie flexural design.

4.9 System-Level Experimental Results

Three full-scale testing setups were used to provide the loading and boundary conditions for system-level experiments; the SLTM, PLTM and TLS. These setups allowed us to answer questions that include the rail seat reaction, lateral force transfer, clamping force variation, and crosstie flexural behavior.

The applied wheel load, rail seat vertical reaction, lateral reaction at the shoulder (lateral friction force going to rail seat can be calculated consequently), and clamping force (normal and tangential components) were measured. Figure 72 shows the applied forces (vertical and lateral components of wheel load) and reactions on the rail as well as the original and deformed shape of the rail cross-section where:

- F_V: Vertical component of wheel load (applied load), kips
- F_L: Lateral component of wheel load (applied load), kips
- R_{SV}: Vertical rail seat reaction (1/3 the width of the distributed load from field side), kips
- R_{SL}: Lateral rail seat reaction (center of the distributed load), kips
- R_L: Lateral reaction entering shoulder, kips
- N_F: Normal component of clamping force at field side, lbf
- T_F: Tangential component of clamping force at field side, lbf

- N_G: Normal component of clamping force at gauge side, lbf
- T_G: Tangential component of clamping force at gauge side, lbf
- D_{VF}: Vertical displacement at rail base at field side, in.
- D_{VG}: Vertical displacement at rail base at gauge side, in.
- D_{LH}: Lateral displacement at rail head, in.
- D_{LW}: Lateral displacement at rail web, in.
- D_{LB}: Lateral displacement at rail base, in.

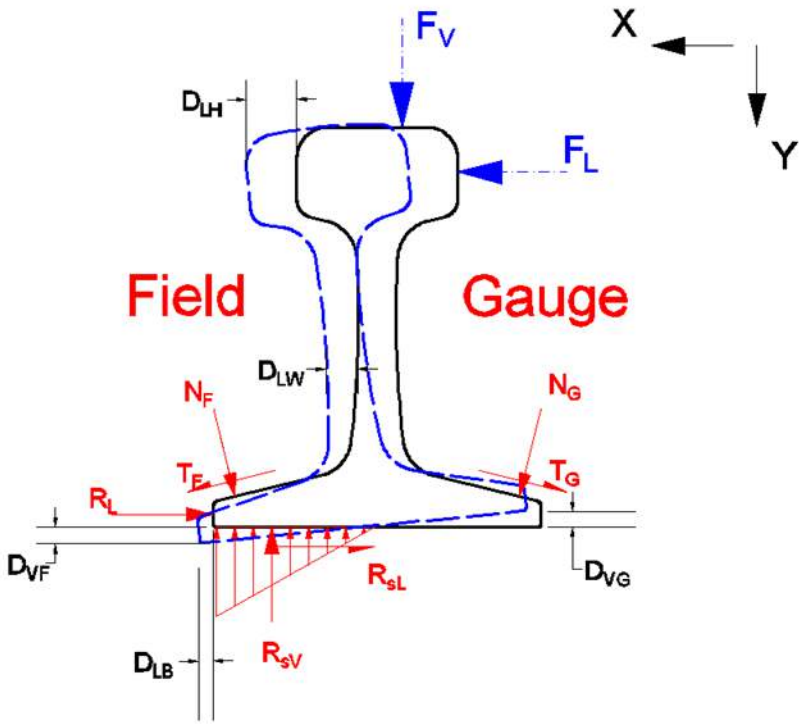

Figure 72. Idealized Load Path Through Rail

The positive position for all the forces and displacements in the lateral (X) direction is directed to the field side. The positive direction for the vertical (Y) direction is pointing downward perpendicular to the rail seat. The global displacements of a concrete crosstie and positive directions are given in Figure 73.

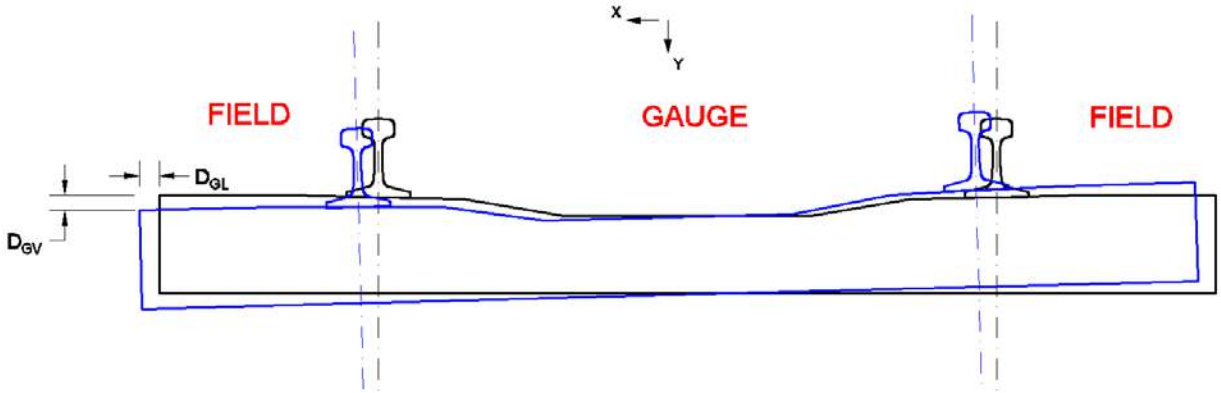

Figure 73. Undeformed/Deformed Shape of a Concrete Crosstie

D_{GL}: Global lateral displacement of a crosstie, in.

D_{GV}: Global vertical displacement of a crosstie, in.

The positive position for the global lateral displacement (X) is pointing to the near side of the track. The positive direction for the global vertical displacement (Y) is pointing downward perpendicular to the crosstie's centroid axis.

4.10 Rail Seat Reaction and Pressure Distribution with Matrix Based Tactile Surface Sensor

Matrix Based Tactile Surface Sensor (MBTSS) field experimentation performed for this report has indicated that the rail seat load distribution may become highly concentrated under the application of lateral load, with up to half of the total rail seat load distributed over an area of the rail seat just one inch in width. Although the rail pad assemblies and insulators were replaced prior to field experimentation, the clips were not. At the time of experimentation, the clips had been subjected to 5 MGT of traffic and three cycles of removal and reapplication. It was hypothesized that the wear on the fasteners, especially due to the three reapplications, significantly reduced the applied toe load. This reduced the ability of the fastening system to resist rail rotation under lateral load, which has been shown to lead to significant rail seat load concentrations.

Laboratory experimentation was conducted using the TLS. During experimentation, any clips that were removed were replaced with new clips to maintain an unworn condition. Although other sources of variation exist between the TLS and the field, it is believed that the health of the fastening system had the greatest effect of the possible variables relating to the rail seat load distribution for identical loading environments.

Figure 74 compares the qualitative effect of the lateral to vertical (L/V) force ratio under a constant 40 kip (178 kN) vertical load for three separate cases. The first case represents the common design assumption that the rail seat load is distributed uniformly across the entire rail seat. This distribution is not affected by L/V force ratio. The second case represents a typical rail seat load distribution for a rail seat with new fasteners, as illustrated by data from experimentation on the TLS. Although there is some concentration of load on the field side of the rail seat, the fasteners are able to restrict rail rotation to 0.31 degrees or less. This results in very little change in rail seat load distribution. The final case represents a typical rail seat load

distribution for a rail seat with worn fasteners, as illustrated by data from experimentation on the railroad test track (RTT) using the track loading vehicle (TLV). The ability of the clips to restrict rail rotation is reduced, allowing rail rotations up to 0.52 degrees, which results in significant concentration of the rail seat load along the field side of the rail seat. Furthermore, this excessive rail rotation results in a complete unloading of the gauge side of the rail seat at high L/V ratios. Figure 74 also shows the change in pressures exerted on the rail seat: the increased rail rotation in the worn fastener case results in higher pressures than the new fastener case, as illustrated by the accompanying pressure scale.

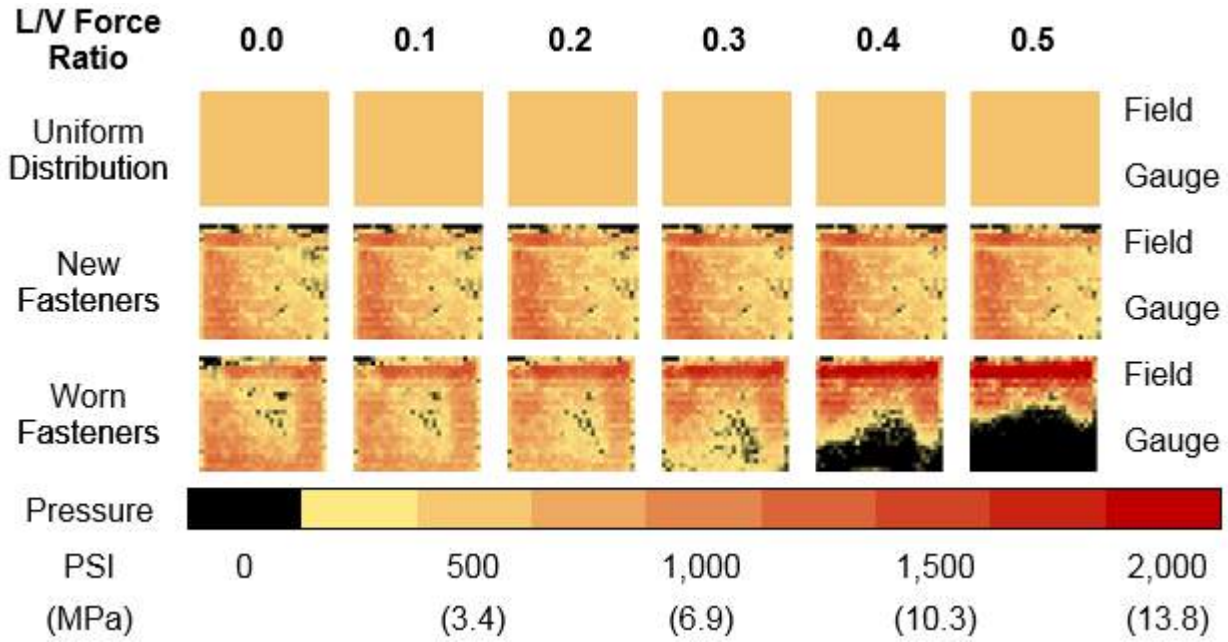

Figure 74. Three Rail Seat Pressure Distributions Under 40 Kip (178 kN) Vertical Wheel Load at Varying L/V Force Ratios

Figure 75 illustrates the quantitative effect of L/V force ratio and fastener health on contact area, the area of the rail seat that is engaged in load transfer. The data has been normalized to the contact area seen under a 40 kip (178 kN) vertical and 0 lb lateral loading environment. Therefore, the percent of contact area at a 0.0 L/V force ratio describes the effect of vertical load, while the change in percent contact area for each data series describes the effect of L/V force ratio for each vertical load magnitude. The new fastener case results in a consistent increase in contact area for all vertical load magnitudes between 0.58% and 1.75%. It is hypothesized that this increase is due to deformation of the rail pad assembly as the rail rotates under higher L/V force ratios. By contrast, the worn fastener case exhibits a loss of up to 42% of initial contact area once the L/V force ratio exceeds a critical "threshold" value (Greve et al. 2014). These data support the hypothesis that the ability of the worn fasteners to restrict rail rotation was reduced, which resulted in the observed lower contact areas under worn fasteners.

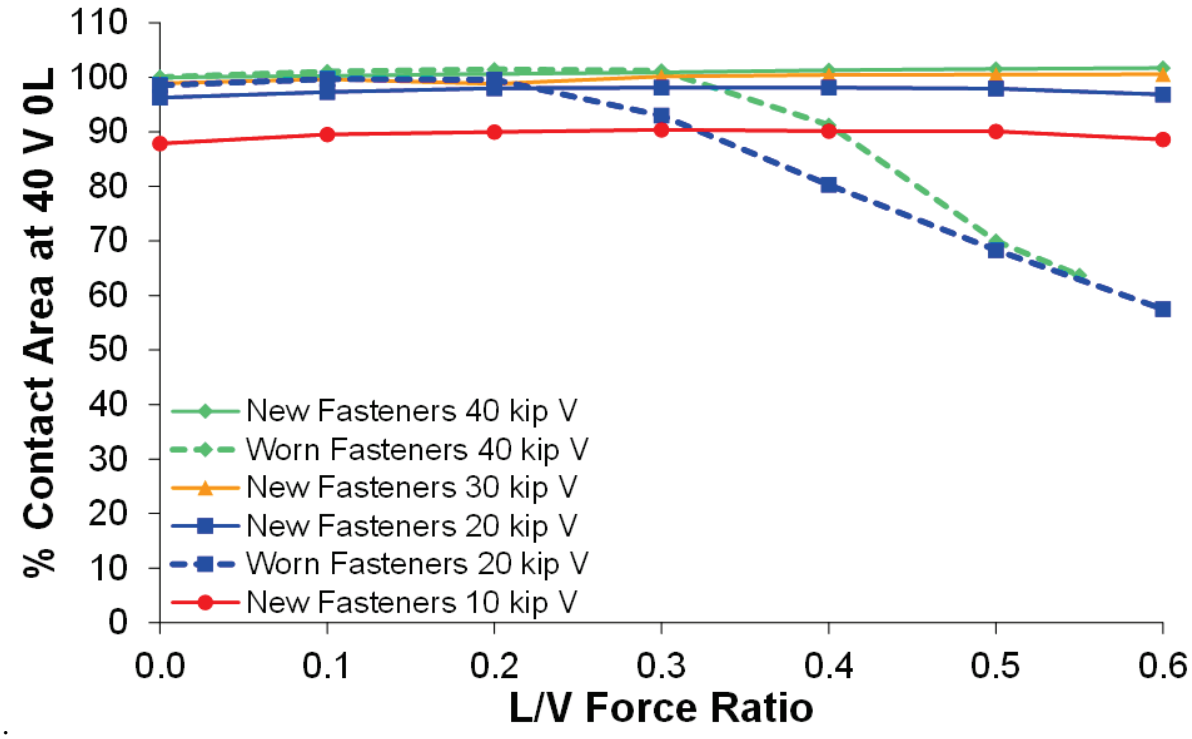

Figure 75. Effect of L/V Force Ratio on Contact Area

To examine the effect of fastener wear and loading environment on pressures, it is necessary to determine the total load applied to each rail seat. For the new fastening system investigated in the laboratory, the rail seat load was calculated from internal strain gauges embedded below the crosstie rail seat. For the worn fastener case (data collected in the field), these embedment gauges were not present on rail seats instrumented with MBTSS. It was therefore necessary to estimate the rail seat load directly below the point of loading. The rail seat load in this case was estimated to be half of the vertical wheel load, based on both an extensive literature review and data acquired from strain gauges used in field.

Figure 76 and Figure 77 illustrate the effect of loading environment on the pressures exerted on the crosstie rail seat. There are three primary metrics used to characterize the pressures at the rail seat interface. The first is the theoretical uniform pressure, which represents conventional design methodology. It assumes that the rail seat load is evenly distributed across the rail seat and is not affected by L/V force ratio, analogous to the uniform pressure distribution case illustrated in Figure 73. The second is the average pressure, which is calculated by dividing the rail seat load by the measured contact area. The third pressure metric is the maximum pressure observed for a given combination of vertical load and L/V force ratio.

Figure 76 compares the uniform, average, and maximum pressures for the new and worn fastener cases under a 20 kip (88.9 kN) vertical load, and Figure 77 compares the uniform, average, and maximum pressures for the same cases under a 40 kip (178 kN) vertical load. In both figures, the new fastener average pressures plot within 50% of the theoretical uniform pressure, even under L/V force ratios as high as 0.6. This indicates that almost all the contact area is utilized in load transfer. The worn fastening system average pressures plot close to the theoretical uniform

pressure below the aforementioned "threshold" L/V force ratio. Above this critical point, the reduction of contact area increases these pressures by up to 80% of their original value.

The maximum pressures observed for the new fastener case were approximately 325% higher than the theoretical uniform pressure under a 20 kip (88.9 kN) vertical wheel load, experiencing no net change from 0 to 0.6 L/V. Under a 40 kip (178 kN) vertical wheel load, the new fastener maximum pressures are inversely related to L/V force ratio, ranging from 211% to 177% higher than the theoretical uniform pressure. By contrast, the maximum pressures observed in the worn fastening system case for both vertical wheel load magnitudes exhibited strong positive correlation with L/V force ratio. Again, the magnitude of maximum pressure relative to the theoretical uniform pressure is greater under the 20 kip vertical load, ranging from 350% to 660% greater than the theoretical uniform pressure, than under the 40 kip vertical wheel load, ranging from 160% to 370% greater than the theoretical uniform pressure. It is important to note that although none of the observed pressures approach the design strength of the concrete (i.e. 7,000 psi), the increase in pressure will change the characteristics of failure mechanisms associated with RSD (e.g. increased frictional force leading to more severe abrasion). Figure 77 shows a higher maximum pressure for the new fastening system case than was observed in the worn fastener case under a 40 kip vertical wheel load. It is hypothesized that this is due primarily to increased rail seat load on the instrumented rail seats resulting from stiffer support conditions relative to adjacent crossties.

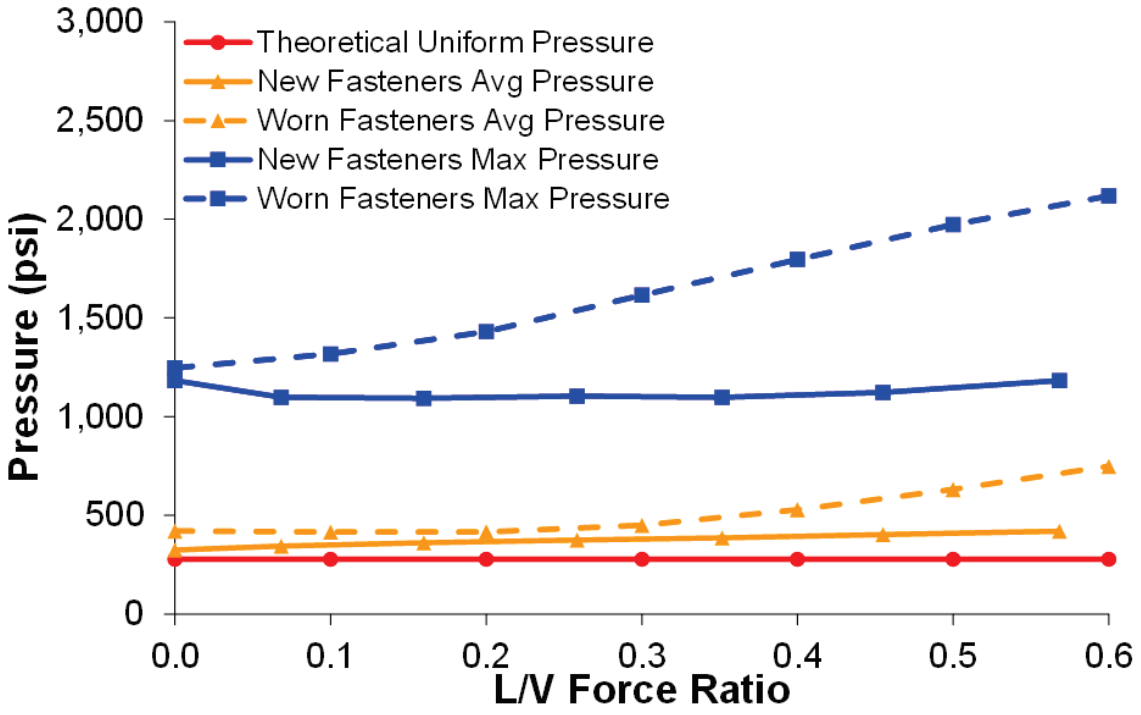

Figure 76. Effect of L/V Force Ratio on Pressure (20 Kip (88.9 kN) Vertical Wheel Load)

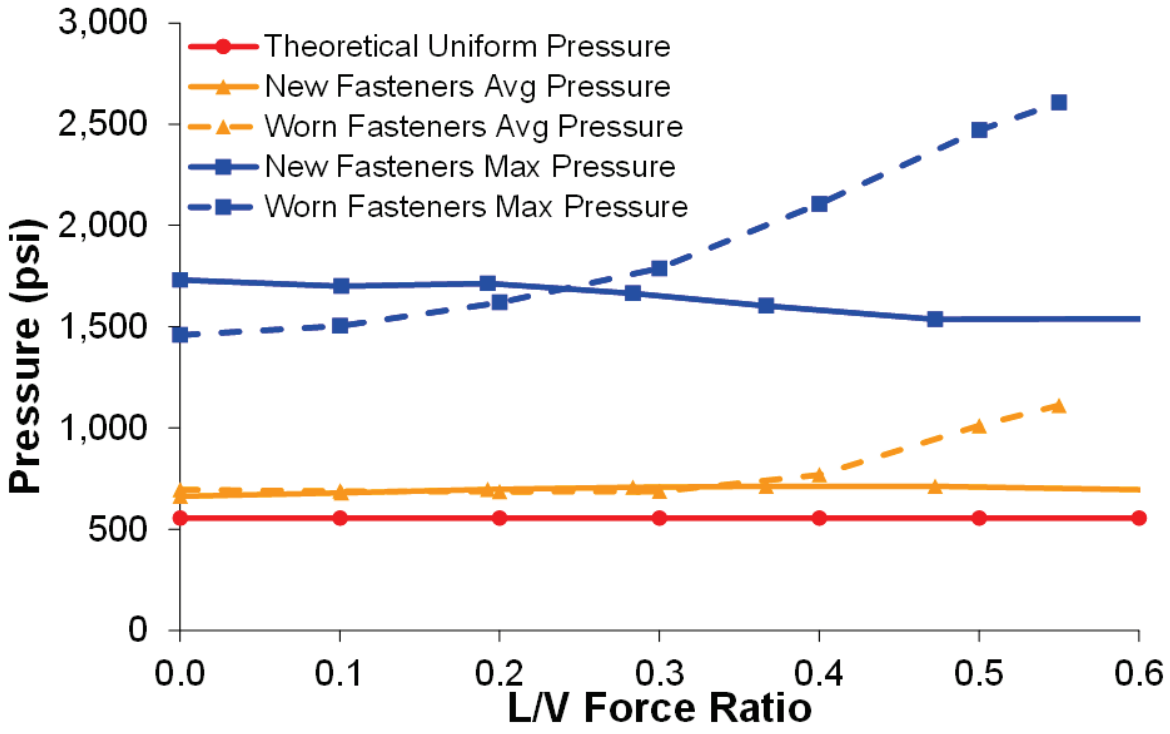

Figure 77. Effect of L/V Force Ratio on Pressure (40 Kip (178 kN) Vertical Wheel Load)

4.11 Rail Seat Vertical Displacement

Vertical rail seat displacements were measured to provide a reference for FE modeling, and to calculate the magnitude of the rail seat vertical reaction force.

Using the SLTM, four linear potentiometers were installed at each corner of one rail seat (Figure 78) to measure the vertical deflection. To compare with rail seat compressive stress calculated from the deflection data, MBTSS was placed at the other rail seat between the bottom surface of the abrasion plate and the top surface of the concrete crosstie.

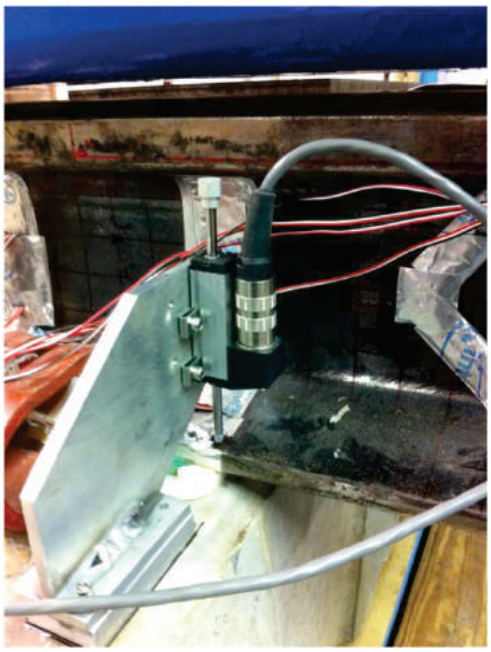

Figure 78. Potentiometers and Aluminum Fixture Used to Measure Rail Seat Vertical Displacement

Three loading cases were examined and average rail seat vertical displacements are shown in Table 15.

Table 15. Rail Seat Vertical Displacements for Various Loading Cases

	Case 1		Case 2		Case 3	
	Lateral load		Lateral & Vertical Load		Lateral & Vertical Load	
Loading	L	V	L	V	L	V
	PTLF	--	--	Overhead frame	Overhead frame	Overhead frame
	3 kips	--	--	36 kips	18 kips	36 kips
Δ_{VF} (in)	0.008		0.0011		0.021	
Δ_{VG} (in)	-0.105		0.0011		-0.044	

Given the rail pad assembly stiffness and the vertical displacements measured at the four corners of a rail seat, it is possible to calculate the rail seat vertical reaction. When concrete strain measurement is not available, this will provide an alternative method to obtain the rail seat loads. To improve the validity of this calculation, two assumptions were made:

1) The rail base movement can be treated as rigid body motion (i.e. the rail base remains plane or the deformation remains linear in both directions along the crosstie and in the direction along the rail).
2) The distributed rail seat reaction can be expressed by a linear function, $FV = kADavg/t$, where k is the polyurethane pad assembly stiffness (obtained through experiments

described in Section 3.13.2), A is the distributed area, D_{avg} is the average vertical deflection in the rail seat reaction area, and t is the thickness of the pad (0.236 inch).

Using these two assumptions, a linearly distributed vertical reaction from the rail pad was expected. When the load applied to the rail was with a large L/V ratio (Case 3 in Table 15**),** the gauge side of the rail base saw uplift. During uplift of the gauge side there was no reaction force in that area of the pad due to a loss of contact between the rail and the rail pad.

To verify the above assumptions, the curvature at rail base was calculated from the strain measurements at the rail base. In SLTM testing, strain gauges were installed on the rail (Figure 52 in the Laboratory Experimental Plan). Strain gauges #1 - #3, applied at both the field and gauge side, were used for this analysis.

The three loading cases in Table 15 were used to validate these assumptions. Under loading Case 3, the deflection of the rail base is shown in Figure 79. The x-axis shows the distance to the field side edge of the rail ("0" is for the field side edge, and "6" is for the gauge side). The "rigid deflection" was generated by drawing a line between the average displacement measurements from the field side and the gauge side. Considering the curvature of rail base due to bending, the rigid deflection was corrected to more accurately represent the deformed shape of the rail base. The "corrected deflection" was the real deflection of the rail base calculated using both the displacement and strain measurements. From Figure 79, it can be seen that the rigid deflection of the rail base was close to the corrected deflection. The maximum error was found at a point 1.875 inches from the field side edge, which was 0.00078 inches or 1.2% of the total deflection. The results from loading Cases 1 and 2 also allowed us to reach the same conclusion, that the bending of the rail base was negligible and the rigid body assumption held.

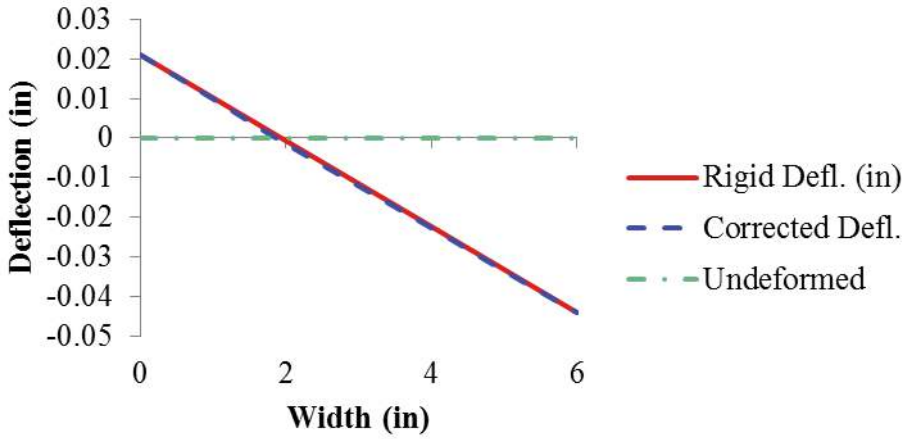

Figure 79. Deformed Shape of Rail Base (F_L=18 Kips F_V=36 Kips)

The vertical rail base deflection is needed to calculate the clamping force, which is due to both the compression of the polyurethane pad and the compression of the nylon 6/6 abrasion plate. The properties of these two layers of material between the rail and the concrete crosstie are shown in Table 16.

Table 16. Properties of the Rail Pad and Abrasion Plate

Component	Material	Thickness (in)	Assembly stiffness (ksi)
Rail pad	Polyurethane	0.236	32.8
Abrasion plate	Nylon 6/6	0.055	439

To compare the rail base deflection contributed by the rail pad and the abrasion plate, the following equation is used:

$$\frac{\Delta t_{pad}}{\Delta t_{frame}} = \frac{E_{frame}}{E_{pad}} \cdot \frac{t_{pad}}{t_{frame}} = \frac{439}{32.8} \cdot \frac{0.236}{0.055} = 57.4$$

where t is the thickness of the component and E is the stiffness. The deflection of the abrasion plate was significantly smaller than the deflection of the rail pad, and could be neglected. In other words, the rail base deflection measured from the test can be treated as the rail pad vertical deflection. To calculate the rail seat vertical loading by utilizing the rail base vertical deflection measurements, the equation stated in assumption two was used.

To calculate the full load path in the vertical direction, the change of the clamping force at both the field and gauge sides was calculated. Similarly, as used in Assumption (2), $N=k_cD$ was used, where k_c is the clip stiffness, which was determined by the manufacturer to be 8.65 kips/in, and D is the field and gauge side rail clip vertical deflection at 0 and 6 inches (Figure 79).

For the three loading cases listed in Table 15, the comparison of the applied rail seat vertical load, the calculated rail seat reaction force, and the calculated change of the clamping force are shown in Table 17. The magnitude of the change of the clamping force was much smaller than the applied vertical rail seat load (no more than 1.2%). When comparing the applied load to the calculated reaction force, the change of the clamping force could be neglected.

Table 17. Comparison of the Applied Load and the Calculated Reaction Force

Loading Case	Applied rail seat load (kips)	Rail seat reaction force (kips)	Δ clamping force (field side) (kips)	Δ clamping force (gauge side) (kips)
1	0	1.40	-0.07	0.91
2	36	36.7	-0.06	-0.06
3	36	33.4	0.42	-0.23

When there was no eccentric loading (Case 2), the calculated rail seat reaction force was found to be almost exactly equal to the applied load. For the same magnitude of vertical load, when a large lateral force (18 kips) was introduced, the error was as great as 7.2%. This conclusion reveals that the rail base deflections can be used to calculate the vertical rail seat reaction force. The average of rail base vertical deflection from the four corners should be used, because uneven compression of rail pad may be experienced.

A reduced number of rail base vertical displacement measurements were applied during TLS experimentation. One potentiometer was placed at both the field and gauge sides of the rail.

Each of them was located 0.5 inch from the outer most edge of the rail base and 3 inches from the centerline of the crosstie. When zero lateral force and various vertical wheel loads were applied directly over each crosstie, the average rail base vertical displacement measured from both the gauge and field sides is shown in Figure 80.

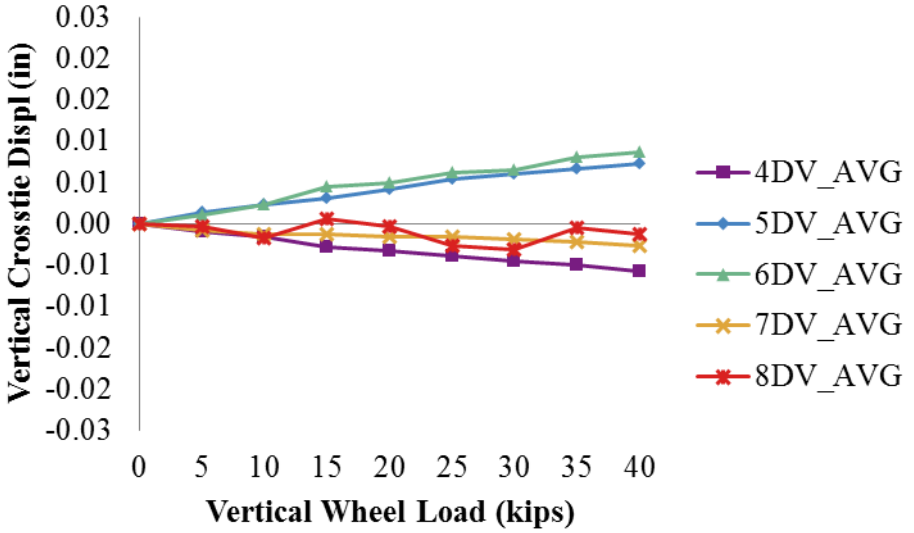

Figure 80. Average Rail Base Vertical Displacement Under Various Vertical Wheel Loads

Under cyclical vertical loading (50 loading cycles ranging from 0 to 40 kips), a hysteresis loop was observed for the vertical deflection measurements from both the field and the gauge side (Figure 81). The area of the loop represents the energy dissipation.

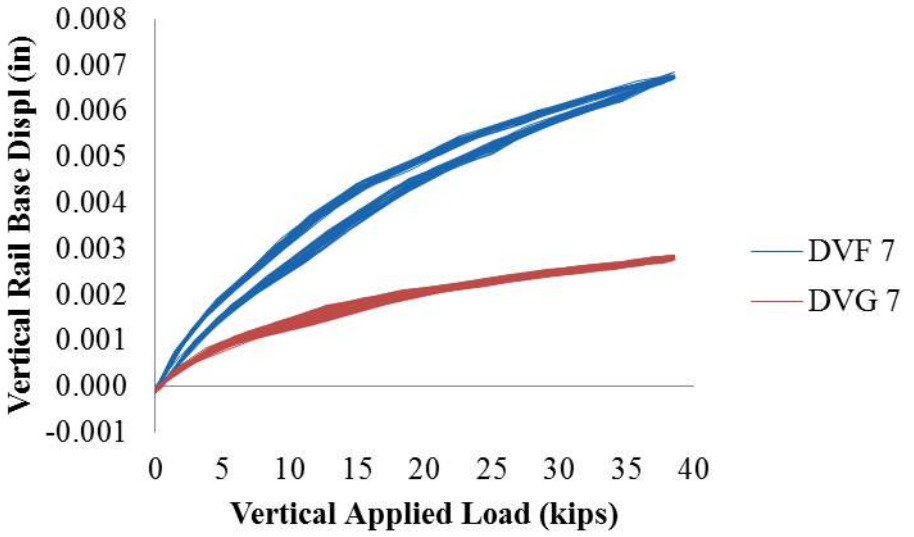

Figure 81. Vertical Displacements at Field/Gauge Side Under Cyclical Loading

When the maximum applied vertical wheel load (40 kips) was held constant, increased increments of lateral forces were applied. The rail base vertical displacement measured from gauge and field side is shown in Figure 82 and Figure 83.

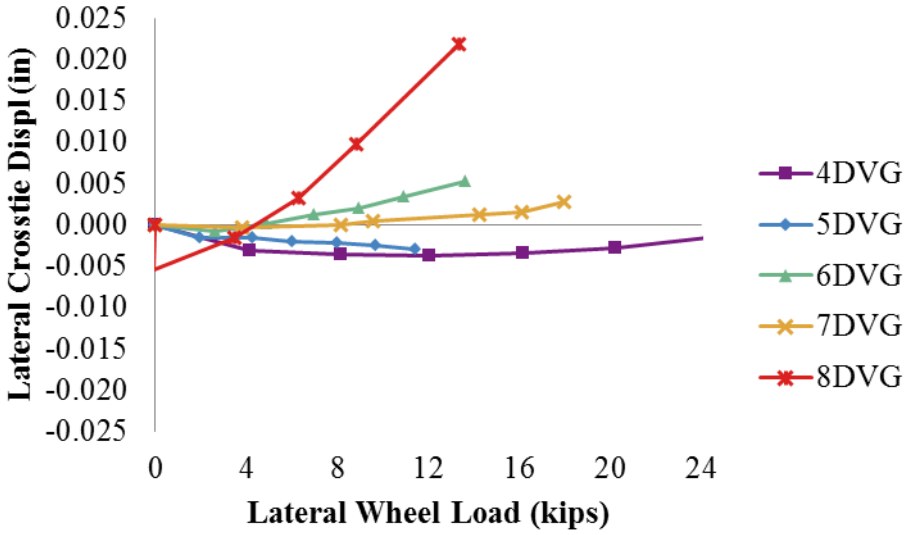

Figure 82. Rail Base Vertical Displacement at Gauge Side Under 40 kip Vertical and Various Lateral Wheel Loads

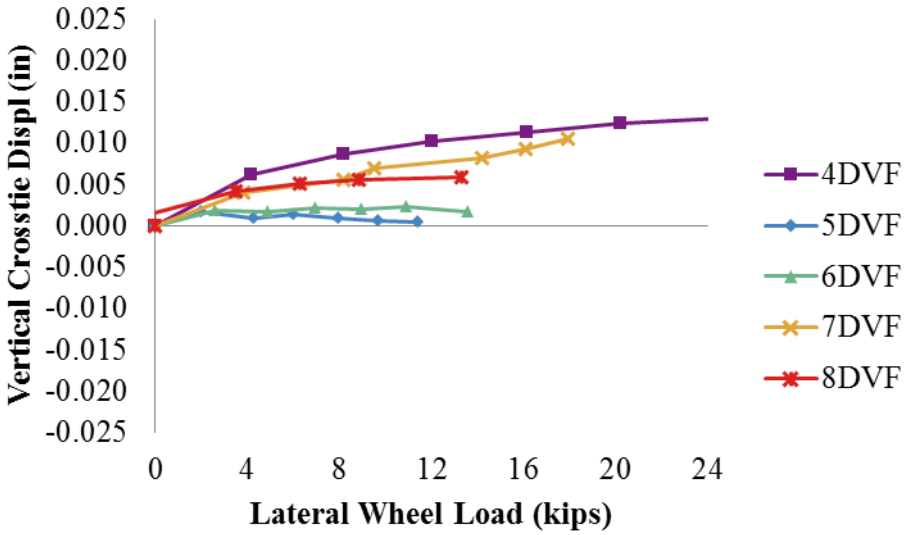

Figure 83. Rail Base Vertical Displacement at Field Side Under 40 kip Vertical and Various Lateral Wheel Loads

4.12 Clamping Force

Measurement of clip strains and the clamping force calculation methodology were described in Chapter 3, Section 3.7.12 in the Laboratory Experimental Plan. Relevant material properties are listed in Table 18.

Table 18. Material Properties of Rail Clip

Manufacturer/Design	Elastic Modulus (E)	Yield Stress (fy)	Yield Strain (ey)
Amsted RPS UAB 2000	23,000 ksi	183 ksi	7,957 ms

4.12.1 Initial Clamping Force

When the clips were properly installed, there was 2.375 kips of clamping force applied to both field side and gauge side perpendicular to the rail. However, the tangential component of the clamping force was not defined in the design. Both the sign and the magnitude of the tangential component of the clamping force is dependent on the installation procedure. Prior to clip installation, strain gauge patterns were placed on both the gauge side and field side of clips. The strain gauge pattern was referred to the first iteration in Figure 51 in the Laboratory Experimentation Plan. By analyzing the data read from these strain gauges, initial clamping forces were determined.

The initial stress level on the clips was examined and compared with the yield stress shown in Table 18. A MATLAB program was developed to calculate the initial clamping force and to plot the strain diagram. In this program, a single contact point was used to simulate the contact condition between the clip toe and insulator. This contact point was located at 0.3 inches from the edge of the rail clip's toe.

Figure 84 shows the analytical strain distribution in micro-strain (ms) along the clip after installation. A 2.5-kip normal force and no tangential force were assumed. Strains at the inner surface and outer surface of the clip were calculated and labeled in Figure 84a and Figure 84b. The difference between the absolute value of strain at the clip inner and outer surface was no more than 100 ms due to axial deformation. The maximum strain was found at the left transition area, which was 7,206 ms at the inner surface and -7,259 ms at the outer surface, both of which were above 90% of the yield strain (7,957 ms). This finding reveals that the safety margin is quite small (approximately 10%). When the normal or tangential component of the clamping force increases under the wheel load, the maximum strain might exceed the yielding limit.

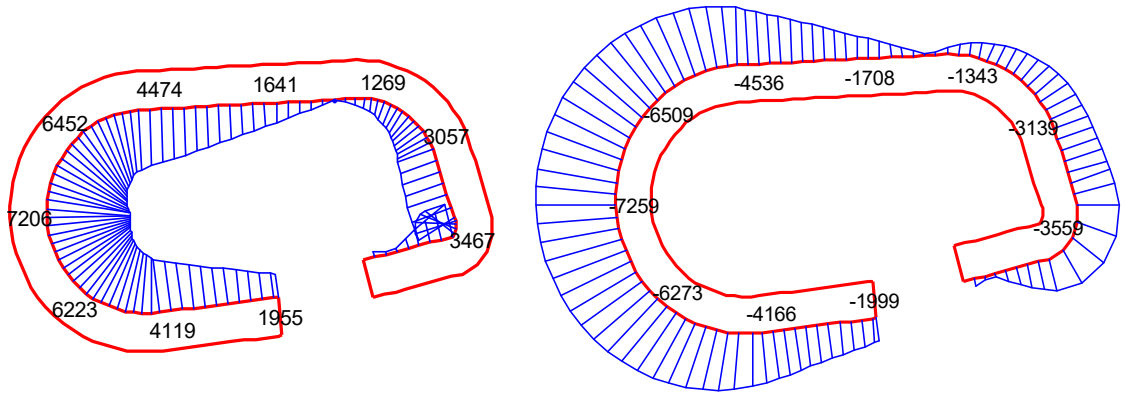

a) b)

N = 2.375 kips, T = 0

Figure 84. Strain Distribution of Inner (Left) and Outer (Right) Surface in Micro-strain

Figure 84 shows the strain distribution of the case with 0 tangential force. Even though the tangential force was not defined in the clip design, evidence of a tangential force exists. The actual installation tangential force was calculated using the strain measurements. The change of strain recorded from gauge #2 to #6 after the clip installation is listed in Table 19.

Table 19. Initial Strain (ms) After Clip Installation

Gauge #	2	3	4	5	6
Toe 1	6,993	5,510	-3,338	-1,651	355
Toe 2	6,845	6,378	-3,518	-1,937	88
Average	6,919	5,944	-3,428	-1,794	222

6,919 ms was recorded from strain gauge #2, which fell on the location where the maximum strain was found with the linear elastic analysis (Figure 84). Several replicates were conducted in both the laboratory and field, all showing similar results.

Theoretically, any combination of the two strains readings from the same leg of a clip can be used to calculate the normal and tangential forces applied at each clip toe. Linear elastic theory and the free body diagram as shown in Figure 51 in the Laboratory Experimental Plan were used. The equations used to address the normal forces (N) and tangential forces (T) are written below:

$$N = \frac{a_{22} \cdot e_t - a_{12} \cdot e_b}{a_{11} \cdot a_{22} - a_{12} \cdot a_{21}}$$

$$T = \frac{-a_{21} \cdot e_t + a_{11} \cdot e_b}{a_{11} \cdot a_{22} - a_{12} \cdot a_{21}}$$

where,

$$a_{11} = \frac{-d \cdot A \cdot (t/2) \cdot \cos\varphi - I \cdot \sin\alpha}{E \cdot A \cdot I},$$

$$a_{12} = \frac{-d \cdot A \cdot (t/2) \cdot \sin\varphi + I \cdot \cos\alpha}{E \cdot A \cdot I}$$

$$a_{21} = \frac{d \cdot A \cdot (t/2) \cdot \cos\varphi - I \cdot \sin\alpha}{E \cdot A \cdot I},$$

$$a_{22} = \frac{d \cdot A \cdot (t/2) \cdot \cos\varphi + I \cdot \sin\alpha}{E \cdot A \cdot I}$$

where E is elastic modulus of steel used for the clips, A is area of the cross-section of each toe, and I is the moment of inertia of the cross-section of each leg.

However, as the dimensions of the clip were not substantially longer than the length of the strain gauge used in the test, the strain reading was affected by the location of the gauges. To obtain an accurate result, all five strain measurements were used to find the actual clamping force applied to each leg of the clip.

To achieve this goal, a MATLAB program was developed to search for the N and T that best matched the five strain measurements. The N and T output from this program were found to be 2.230 kips and 0.280 kips. Figure 85 shows the comparison between the strain distributions of the clip calculated from linear elastic theory and the actual strains measured from the test. In Figure 85, the blue shaded areas express the analytical strain distributions at the inner surface (left) and outer surface (right) of the clip due to this pair of normal and tangential forces. The strain values are shown in black along the clip body. The red markers and values are for the strains recorded from the test. The error for the maximum strain was 4.1%.

Even though the actual installation normal force was lower than the design value, the maximum clip strain could approach the yield strain. Based on these findings, the tangential component of clamping force needs to be considered in clip design, and the increment of the normal and tangential force under wheel loads should be investigated to calculate the actual strain profile.

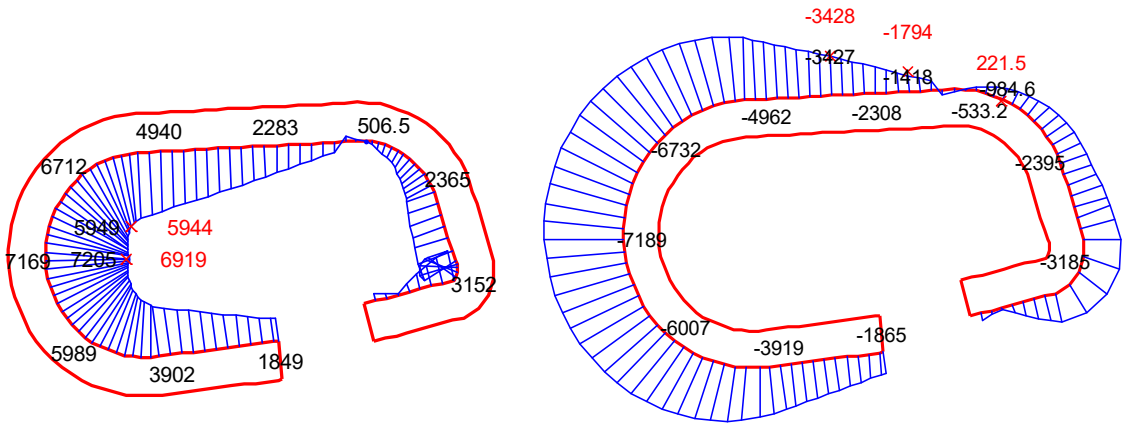

N = 2.230 kips, T = 0.280 kips

Figure 85. Comparison of Strain from Theoretical Calculation and Laboratory Measurement

4.12.2 Change of Clamping Force

The change of the normal and tangential component of clamping force under wheel loads was examined with the SLTM loading frame (Figure 86).

Figure 86. Instrumented Clips Used in SLTM Experimentation

Three loading cases were tested. Figure 87 shows the change of the normal and tangential component of clamping force under a lateral force up to 2 kips applied by the portable track loading frame (PTLF). In general, the change of normal and tangential forces was linear, and corresponded to the increase in the lateral force. When the lateral force was applied, the field side normal force decreased with the downward movement of the rail base. Also, due to the rail

rotation, the gauge side normal force increased with the lifting of the gauge side rail base. When the lateral wheel load was 2 kips, the increment of the gauge side normal force was 66 pound-force. The change of all the other forces was less than 25 pound-force. Due to the limitation of the lateral load capacity of the single crosstie-rail system with the SLTM, no higher loads were examined. The change of the clamping force under a greater lateral wheel load is discussed in the Field Experimentation section.

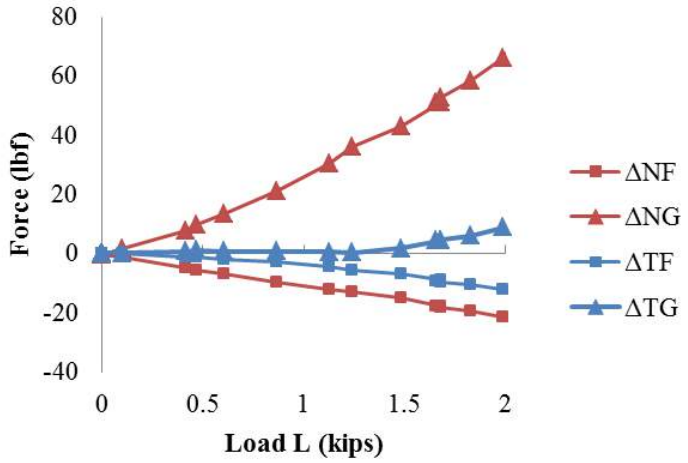

Figure 87. Change of Normal and Tangential Forces at Varying Lateral Wheel Loads

With a 2-kip lateral force applied by PTLF, the vertical load was increased to 36 kips (Figure 88). Due to the loading eccentricity introduced by the SLTM loading head, the rail section rotated, and the gauge side normal force increased. The change of the gauge side normal force reached 163 pound-force, and the change of the field side normal force decreased 73 pound-force.

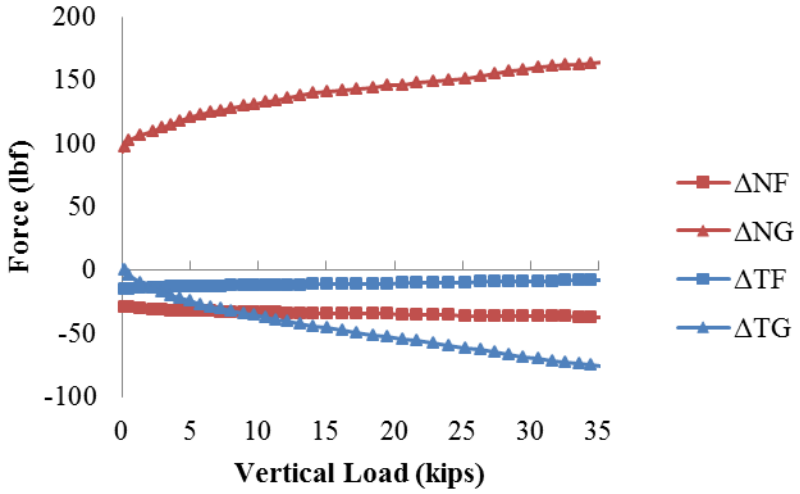

Figure 88. Change of the Normal and Tangential Force Under 2 kip Lateral and Various Vertical Wheel Loads

4.13 Lateral Forces Entering the Shoulder and Lateral Stiffness

To investigate the lateral demands on the cast-in shoulder, UIUC conducted experiments to formulate a realistic testing regime to simulate forces in the fastening system as described in Chapter 3, Sections 3.7.13 and 3.17.5.

Initial static testing was conducted on the PLTM to validate the LLED technology for future field tests. However, valuable data was collected during the design and evaluation process. Because separate data acquisition systems were used to record applied loads and LLED forces, time is presented on the x-axis of Figure 89.

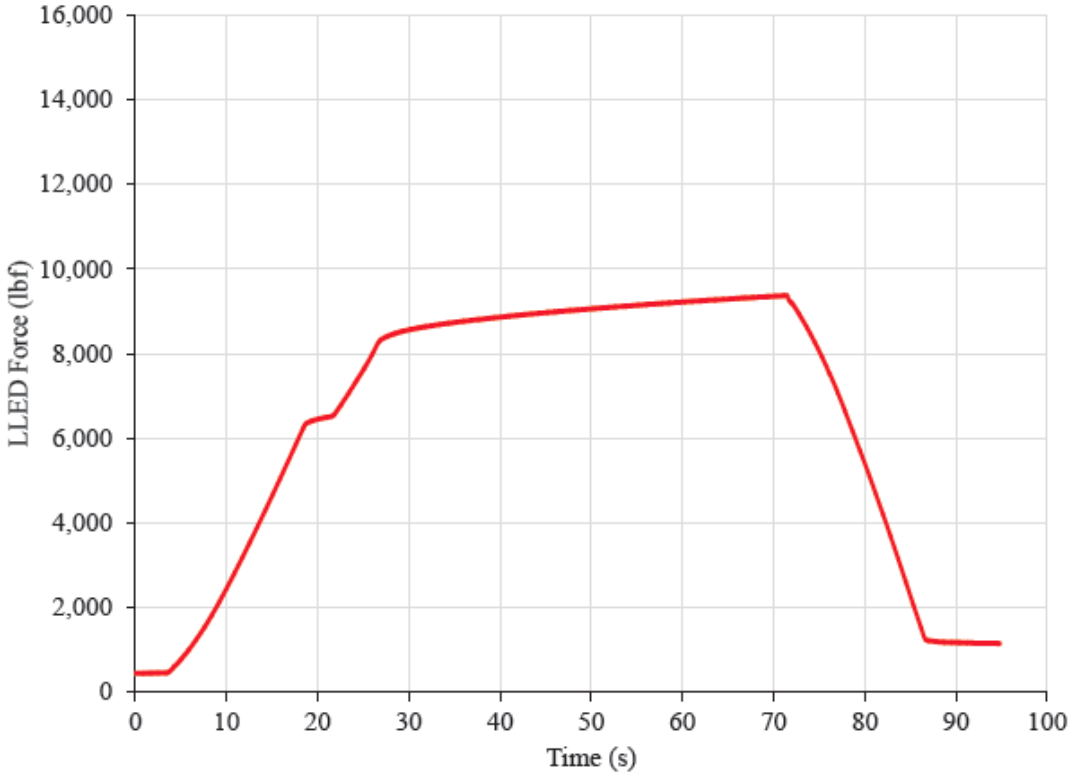

Figure 89. LLED Forces Measured on PLTM, L=15,000 lbf, V=30,000 lbf, L/V=0.5

The small plateau in Figure 89 beginning at 19 seconds and in Figure 90 at 10 seconds is due to a safety measure of the hydraulic system control program that causes the applied load to dwell at 80% of the maximum applied load before proceeding to the maximum load. The maximum applied load was reached at 28 seconds and lasts until 71 seconds. The slight increase in LLED force over the duration of the maximum applied lateral load of 15,000 pound-force is due to the rail translating toward the shoulder and bearing more on the shoulder. This phenomenon should not occur on the field due to the short duration of applied wheel loads.

When the maximum applied lateral load was 15,000 pound-force at a L/V ratio of 0.5, the maximum LLED force was 7,817 pound-force, or 52.1% of the applied lateral load. Due to the single-tie setup, the percentage of the applied lateral load transferred to the shoulder is higher than what is expected to occur in the field with multiple ties.

LLEDs were also tested in conjunction with MBTSS (Chapter 3, Section 3.17.5). MBTSS have a much lower coefficient of friction (COF) than the concrete rail seat. Static tests were run with

LLEDs and MBTSS installed and similar loading conditions as Figure 89. Figure 90 shows LLED forces measured when MBTSS was installed. When the maximum applied lateral load was 15,000 pound-force at a L/V ratio of 0.5, the maximum LLED force with MBTSS installed was 15,240 pound-force, or 102% of the applied lateral load. The low COF of the MBTSS allowed for a much higher percentage of the applied load to be transferred to the shoulder. The increase of over 100% is likely due to the cant of the rail instituting a lateral component of the applied vertical load.

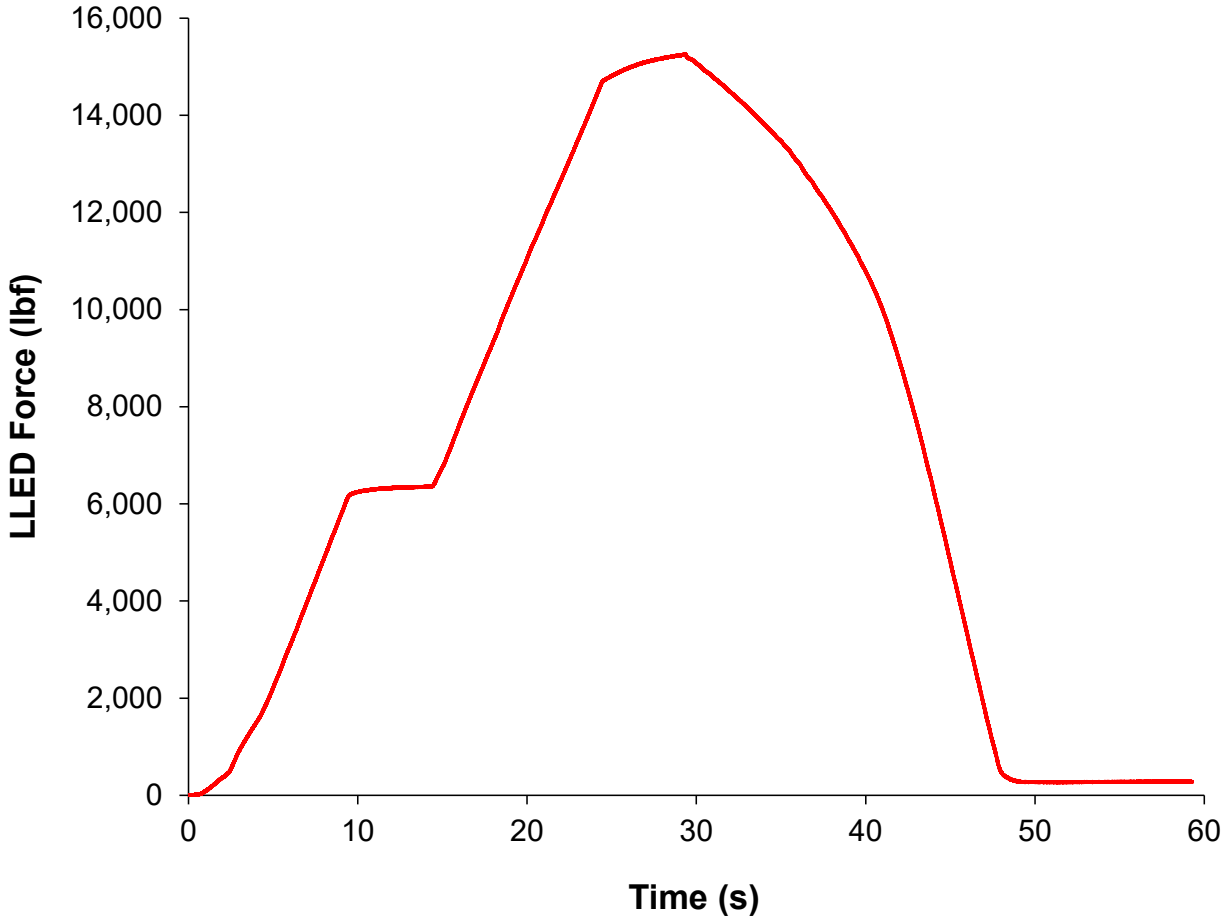

Figure 90. LLED Forces Measured on PLTM with MBTSS Installed, L=15,000 lbf, V=30,000 lbf, L/V=0.5

Dynamic testing was also conducted on the PLTM at 3 Hz and a maximum applied lateral load 15,000 pound-force at a L/V ratio of 0.5 without MBTSS installed, and a maximum applied lateral load 12,500 pound-force at a L/V ratio of 0.5 with MBTSS installed. The minimum force applied for both tests was -1,000 pound-force, in the direction towards the gage. Figure 91 shows a two second segment of dynamic test data without MBTSS installed. The maximum LLED force measured under dynamic loading was approximately 8,300 pound-force (55.3% of the applied lateral load) without MBTSS installed. The minimum LLED force measured under dynamic loading was approximately 2,250 pound-force (15% of the applied lateral load) without MBTSS installed. Figure 92 shows a two second segment of dynamic tests with MBTSS installed. When MBTSS was installed, the maximum LLED force measured under dynamic loading was approximately 10,500 pound-force, 84% of the applied lateral load. The minimum

LLED force measured under dynamic loading was approximately 0 pound-force without MBTSS.

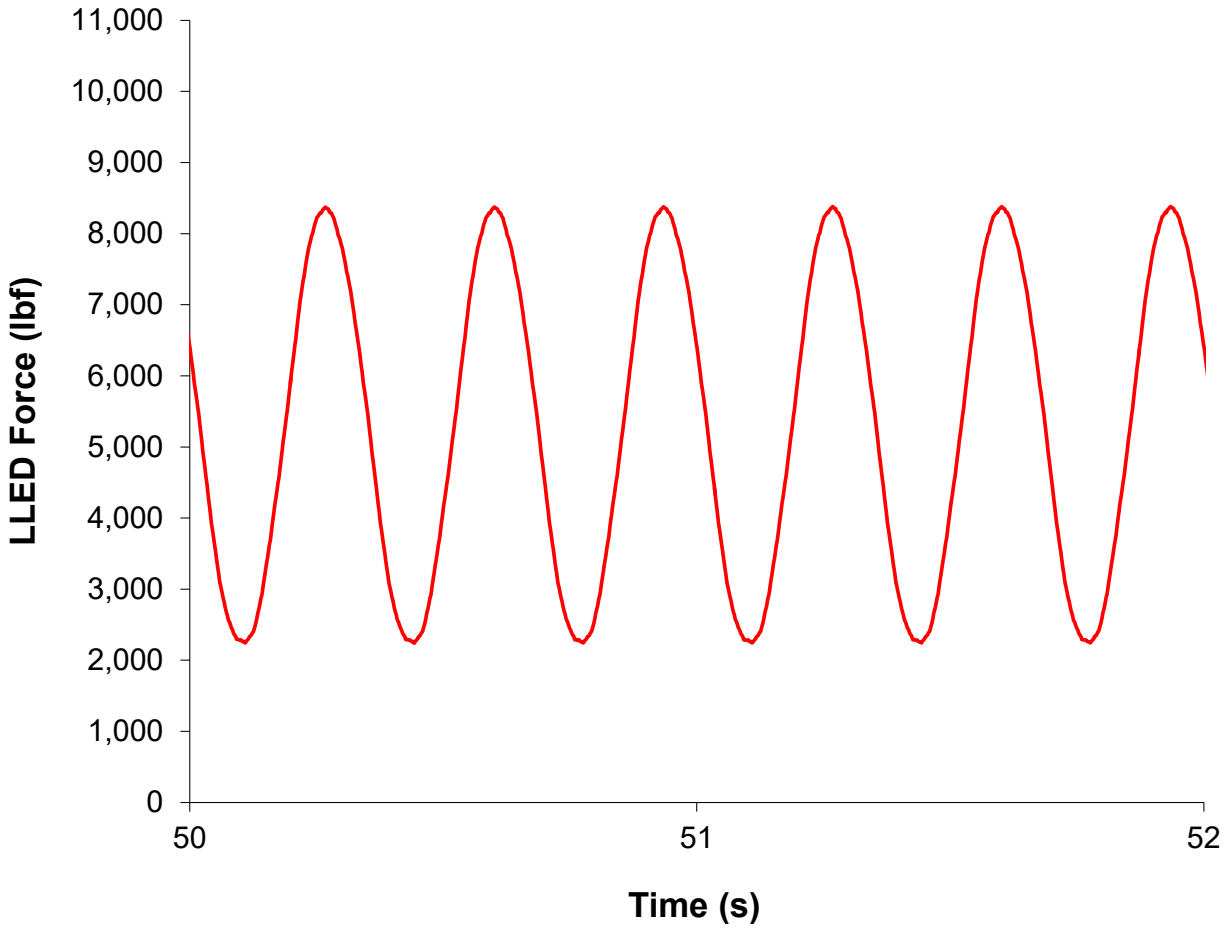

Figure 91. Dynamic LLED Forces Measured on PLTM, L=15,000 lbf, V=30,000 lbf, L/V=0.5, Frequency = 3 Hz

The dynamic data indicates that a higher COF will allow for a portion of the applied lateral load to be resisted by friction. Additionally, data shows that the movement is resisted during unloading causing a continuous force to be applied on the shoulder and insulator. A low COF at the rail seat interface will ultimately produce higher forces on the shoulder, but will allow for complete unloading of the shoulder and insulator before and after train passes.

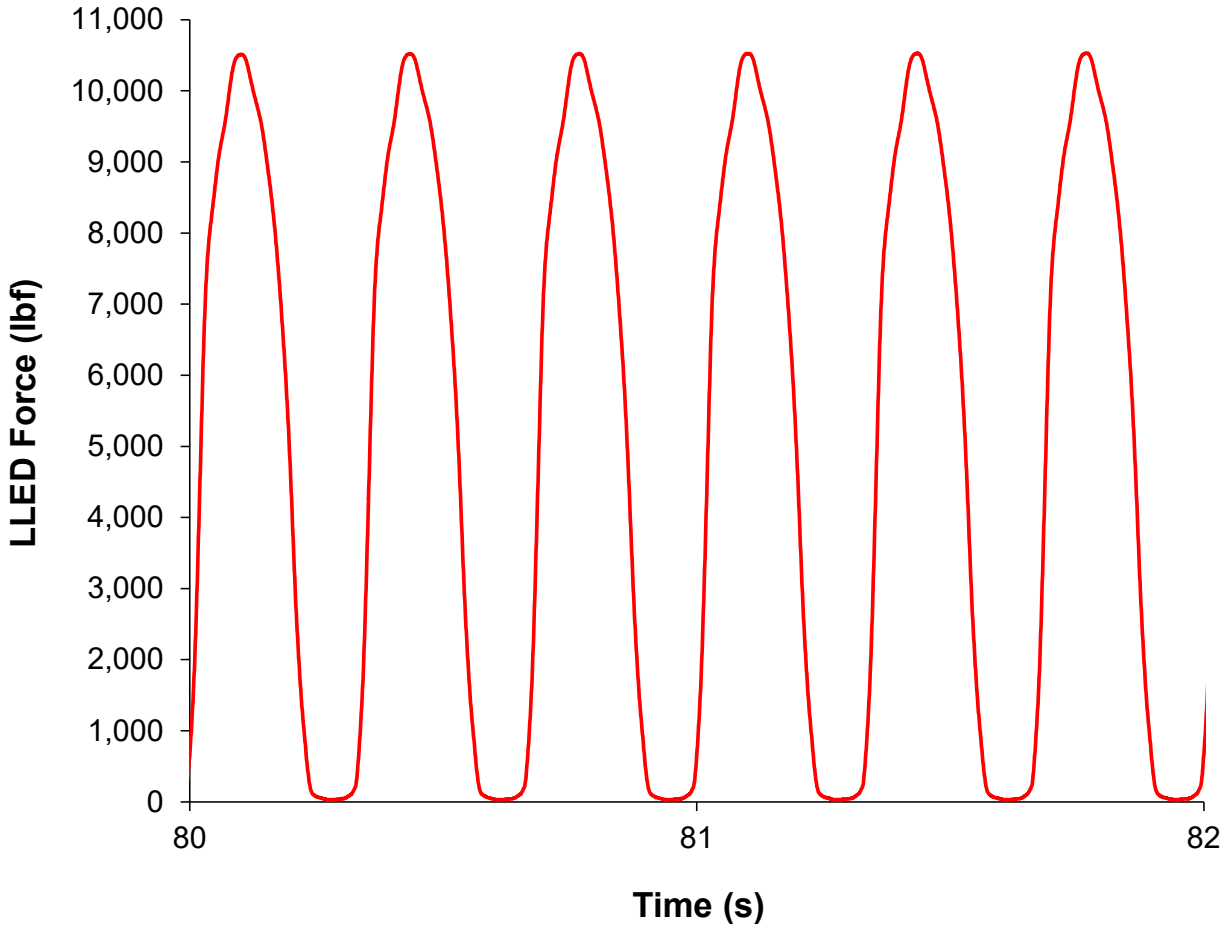

Figure 92 Dynamic LLED Forces Measured on PLTM with MBTSS Installed, L=12,500 lbf, V=25,000 lbf, L/V=0.5, Frequency = 3 Hz

As a part of TLS testing, the lateral force going through each shoulder was measured (Figure 93). This figure shows the variability from shoulder to shoulder, which is related to the lateral stiffness of individual rail seat fastening systems.

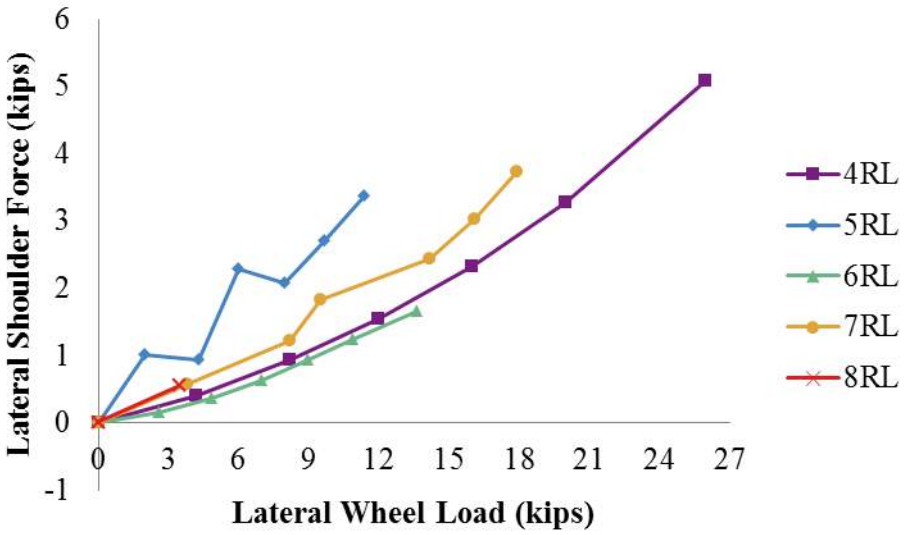

Figure 93. Static LLED Force Measured From TLS

4.14 Rail Deformation and Deflection

4.14.1 SLTM Testing

Strain gauges were used for measuring the deformation of the rail section. The strain gauge pattern can be seen in Figure 52 of the Laboratory Experimental Plan. Two sets of this strain gauge pattern were installed parallel to each other, 3 inches away from the rail seat center line (Figure 94). In this case, the deformation of the rail at the centerline can be expressed as an average.

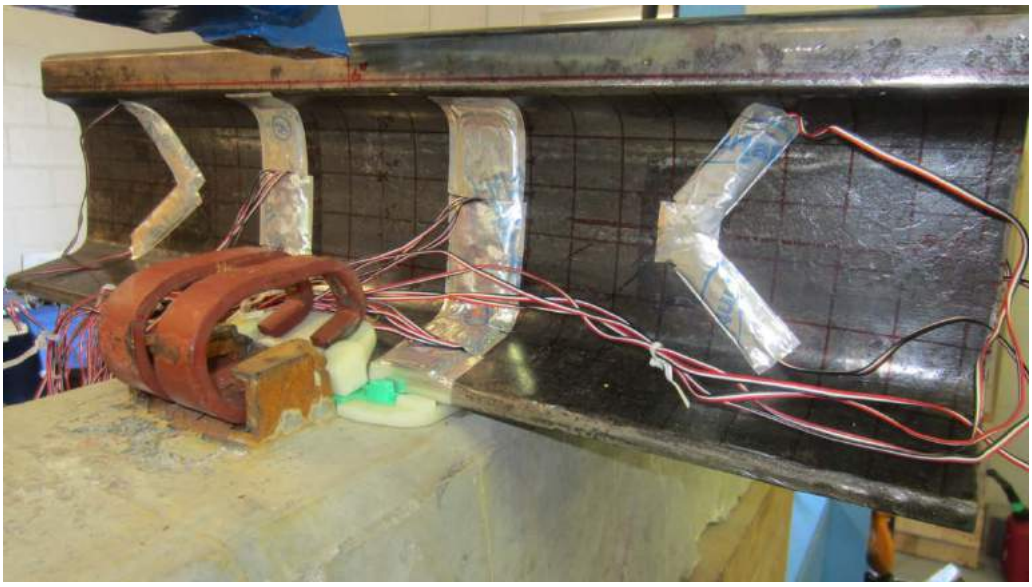

Figure 94. Strain Gauges Installed on a 24 Inch Rail Section

Another purpose of analyzing the strain measurements from the rail was to measure the actual lateral force applied by the loading head. The methodology of calculating the actual lateral applied force was stated in the Laboratory Experimental Plan.

Three loading cases were tested with the SLTM. For the third case, a fixed combination of lateral and vertical force was applied to both rails with a L/V of 0.5. The strain measured from the field and gauge side of the rail in this loading case is shown in Figure 95 and Figure 96.

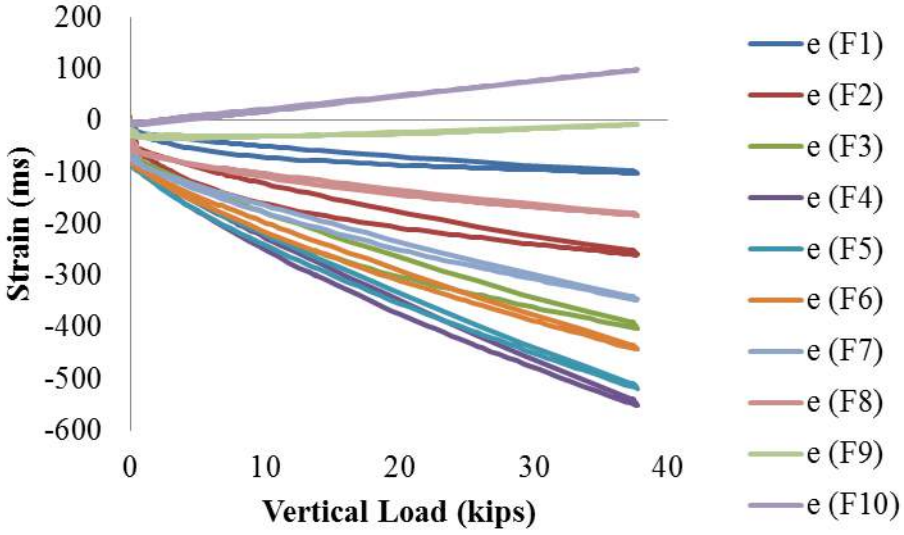

Figure 95. Strain Measured from the Field Side of Rail (L=18 kips, V=36 kips)

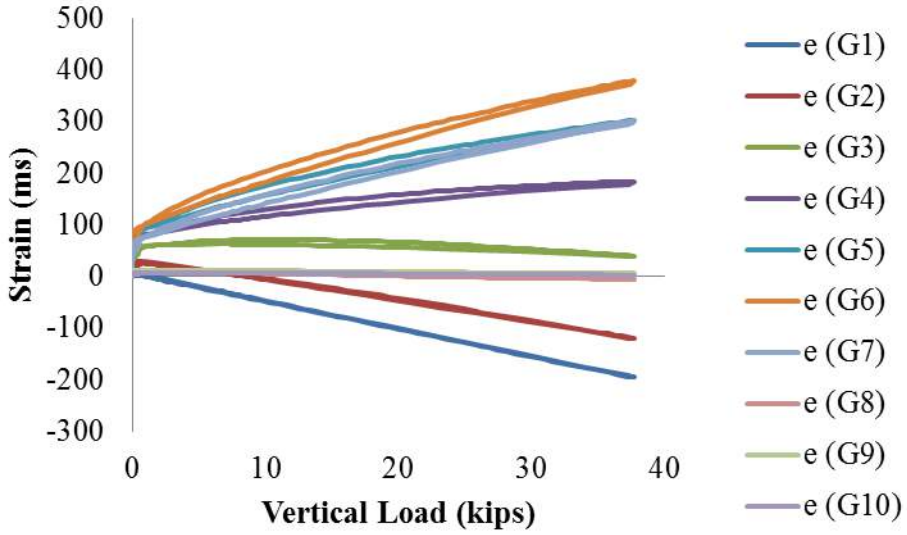

Figure 96. Strain Measured from the Gauge Side of Rail (L=18 kips, V=36 kips)

Combining the deflections measured from both sides of rail base (Case 3 in Table 15) with strain measured from rail surfaces, the deformed shape of the rail cross-section is shown in Figure 97. For better visualization, an amplification factor of 50 was used in this plot, generated with MATLAB using linear elastic theory. In Figure 97, the blue line shows the un-deformed shape and the red line shows the deformed shape of the rail cross-section. As the wheel load was not

applied at the centerline of the rail base, two directions of curvature can be seen at the rail web. The first curvature was found at the transition area between the rail head and the rail web due to the moment created by the eccentric loading. The second curvature was referred at the middle of the web due to the lateral force applied to the rail head.

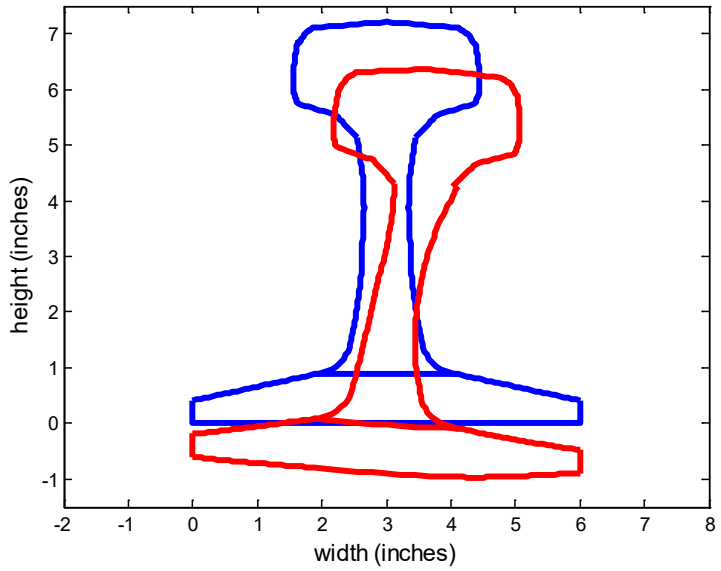

Figure 97. Deformed Shape of Rail Cross Section Shown With an Amplification Factor of 50 (L=18 kips, V=36 kips)

The validation of the designed L/V is shown in Figure 98. The solid green line is for the design lateral force. The dashed blue and red lines are the lateral force measured from the two strain gauge bridges described in Section 3.17.6 in the Laboratory Experimental Plan. At first, the SLTM loading head pushed both rails towards the field side. When the lateral force reached approximately 3 kips, it started to apply the lateral and vertical force simultaneously. The actual applied lateral force and the design lateral force converged when the vertical applied force was 38 kips, and the error was 5.5%.

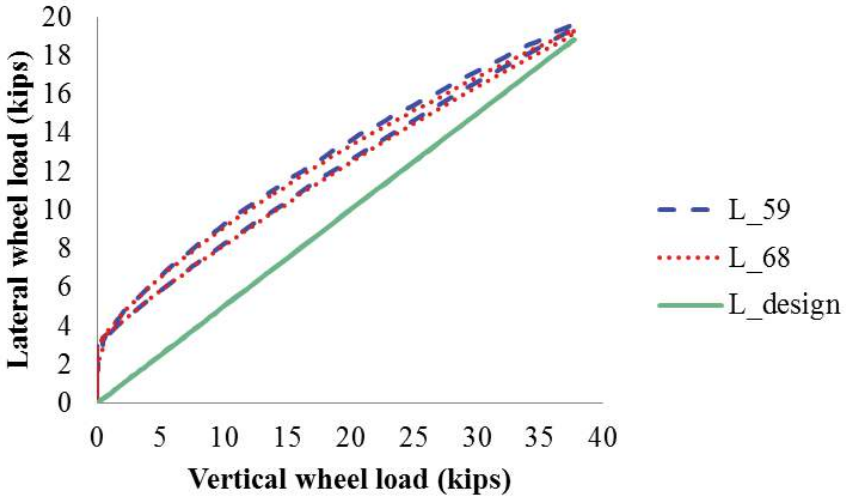

Figure 98. Lateral Applied Load Measurement

4.14.2 Full Scale Track Loading System Testing

TLS rail base vertical displacements measured at both the field and gauge sides were discussed in Section 4.13. The lateral rail base and web displacements under 40 kip vertical and various lateral wheel loads are shown in Figure 99 and Figure 100. Good agreement is shown among the experimental results.

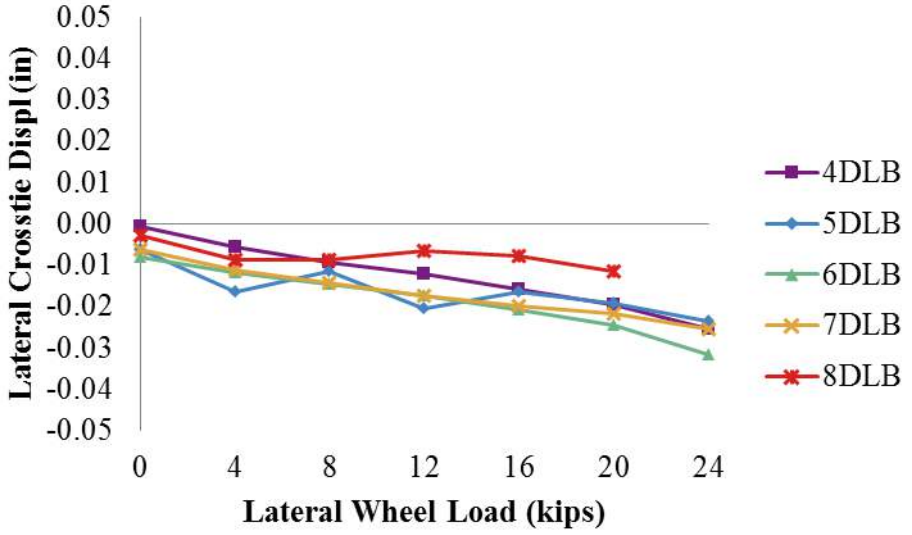

Figure 99. Lateral Rail Base Displacement Measured at Each Rail Seat Under 40 kip Vertical and Various Lateral Forces with the TLS

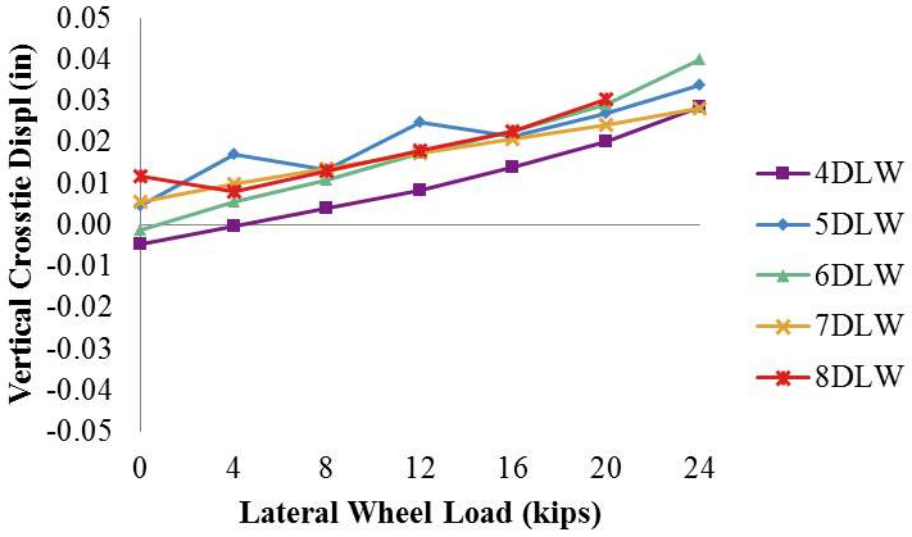

Figure 100. Lateral Rail Web Displacement Measured at Each Rail Seat Under 40 kip Vertical and Various Lateral Forces with the TLS

4.15 Rail Pad Assembly Displacement

To generate data to investigate the relative displacement between rail pad and crosstie rail seat, an experiment was conducted to simulate forces and motions generated through the fastening system. The experiments were conducted on the PLTM.

A potentiometer mounted on a metal bracket was attached to the gage side cast-in shoulder to capture the lateral motion of the pad assembly. The potentiometer was in direct contact with the abrasion frame. In this case, the rail pad assembly consisted of a polyurethane rail pad and a nylon 6/6 abrasion frame manufactured by Amsted RPS (Table 20 and Figure 101).

Table 20. Material Properties of the Experimental Rail Pad Assembly

Component	Material	Young's Modulus (psi)	Poisson's Ratio	Area (in^2)	Mass Density (lb/in^2)
Abrasion Frame	Nylon 6/6	440,000	0.350	38.250	0.049
Rail Pad	Polyurethane	7,500	0.394	36.600	0.068

Figure 101. Rail Pad Assembly

Lateral and vertical loads were applied to the rail during the tests on the PLTM, with L/V force ratios varying from 0.1 to 0.5. The maximum lateral load applied was 18,000 pound-force (80 kN). Initially, only static loads were applied, beginning with a low L/V ratio. Next, lateral loads were increased for each constant vertical force (18 kips, 30 kips, and 32.5 kips). The dynamic test used the same loading protocol, and the loading rate was 3 Hertz (Hz). The measured maximum displacement was 0.042 inches (1.05 mm) for a 0.5 L/V ratio with a 36,000-lbf (160 kN) vertical load.

The displacement increased linearly with variation in lateral load (Figure 102). Even for a lateral load less than 2 kips displacements were recorded, indicating the potential of relative slip between the rail pad assembly and the rail seat even under loading scenarios commonly associated with less demanding track geometry (e.g. tangent or shallow curves). As expected, the magnitudes of these displacements were small compared to the dimensions of the rail seat, since there are very small gaps between the rail pad assembly and the shoulders in the rail seat

area that allow the rail pad to displace (Figure 102). When this test was repeated with different crossties, there was a variation in the maximum displacement higher than 50% based on the geometry and manufacturing differences. Therefore, it is likely that manufacturing tolerances and the resulting fit of components have a measurable impact on displacements.

Although, the magnitude of the vertical loads applied in the system have a large impact on the longitudinal elastic deformation of the rail pad assembly (Rhodes 2005, Rhodes 2013), their effects on the lateral displacement behavior are not evident when lateral loads of less than 6.3 kips (28 kN) were applied. For lateral loads up to 6,300 pound-force (28 kN), vertical forces ranging from 18,000 pound-force (80 kN) to 32,500 pound-force (145 kN) did not exhibit differences in the pad assembly lateral displacement. The results recorded for these three different vertical loading cases were similar for lateral loads up to 6,300 pound-force (28 kN) despite the 14,500 pound-force (65kN) difference between the minimum and maximum vertical force applied (Figure 102). However, given the results obtained from this experiment, it is plausible that for lower lateral loading cases, the pad assembly is capable of overcoming the static frictional forces present at the rail pad assembly to rail seat interface. In contrast, for higher lateral loads, the vertical forces reduced the magnitude of the lateral displacement, pointing to the influence of friction on the shear behavior of the pad assembly. This is more evident when comparing the inclination of the curves, where the tests that were carried out using a vertical load 18 kips presented a much steeper curve compared to the other results.

Under severe loading cases, where high L/V ratios and high lateral loads are encountered, the magnitude of the wheel load will likely affect the lateral displacement of the pad assembly (Figure 103). It is also important to notice that the lateral and longitudinal motion of the rail pad assembly is restrained by the shoulders and is highly dependent on the condition of the rail seat. Based on the results from laboratory testing, large lateral and longitudinal displacements are less likely to occur when the rail pad assembly fits tightly within the rail seat.

Comparing the displacements obtained by the laboratory experiments and the imposed displacements used to run large scale abrasion experiments (Kernes 2013), it is possible to conclude that relative translation between the rail pad and crosstie rail seat equal to 0.125 inches (3.175 mm) is unrealistic for new components, since the maximum displacement measured, 0.04 inches, corresponds to only 30% of the large-scale abrasion test (LSAT) motion. It is important to emphasize that the objective of setting a large displacement in the LSAT was to simulate a deteriorated fastening system where insulators or clips were missing, providing a larger gap and less restraint to the rail pad motion.

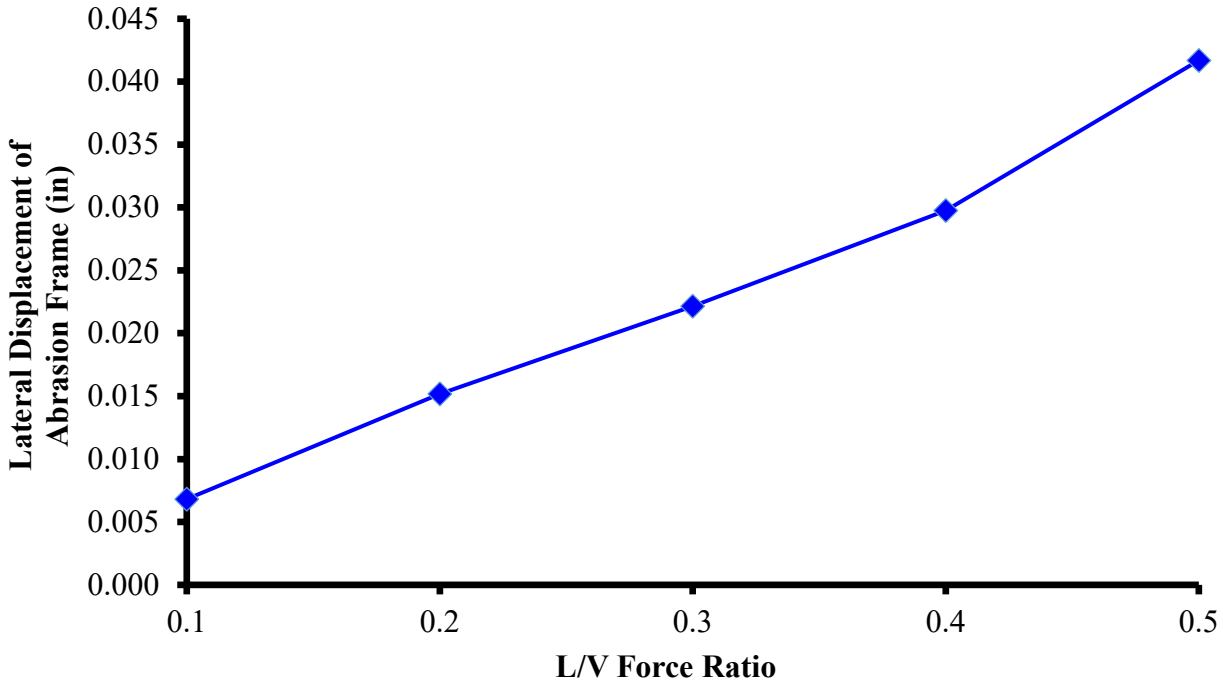

Figure 102. Lateral Displacement of the Abrasion Frame with 36,000 lbf (160kn) Vertical Load for Increasing L/V Force Ratio

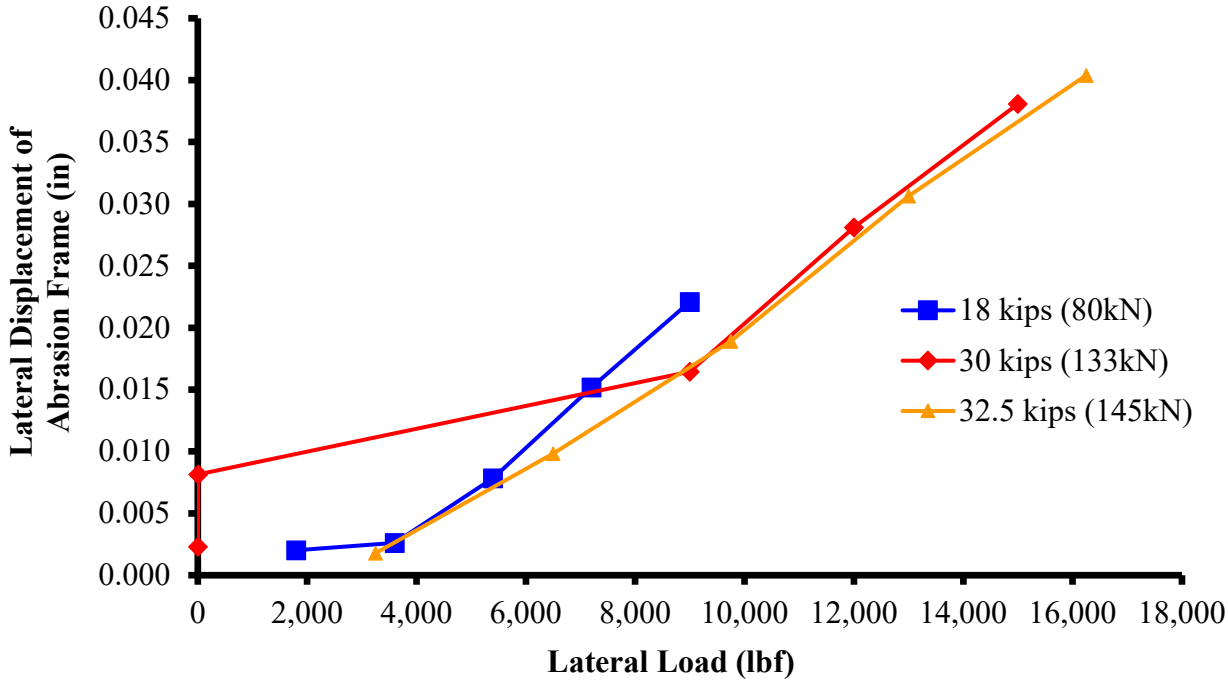

Figure 103. Lateral Displacement of the Abrasion Frame for Increasing Lateral Loads and Constant Vertical Loads (18 Kips, 30 Kips, and 32.5 Kips)

4.16 Crosstie Global Displacements

With the TLS, under vertical loading, vertical (DGV) and lateral (DGL) crosstie global displacements were measured from the end of each crosstie (Figure 104 and Figure 105). The deflections (both in vertical and lateral directions) measured from crosstie 6-17 and 8-19 were found to be higher than the others, although no rail seat reaction force was recorded. This observation implied that the rail seat load doesn't necessarily correlate with DGV. The large deflections were resulted by the poor support conditions below these two rail seats. When a 40-kip vertical wheel load was applied, the vertical crosstie displacement varied between 0.030 inch (crosstie 4-15) and 0.134 inch (crosstie 8-19). The crosstie lateral displacements were oriented toward the field side, and ranged from 0.008 inch (crosstie 4-15) to 0.057 inch (crosstie 8-19).

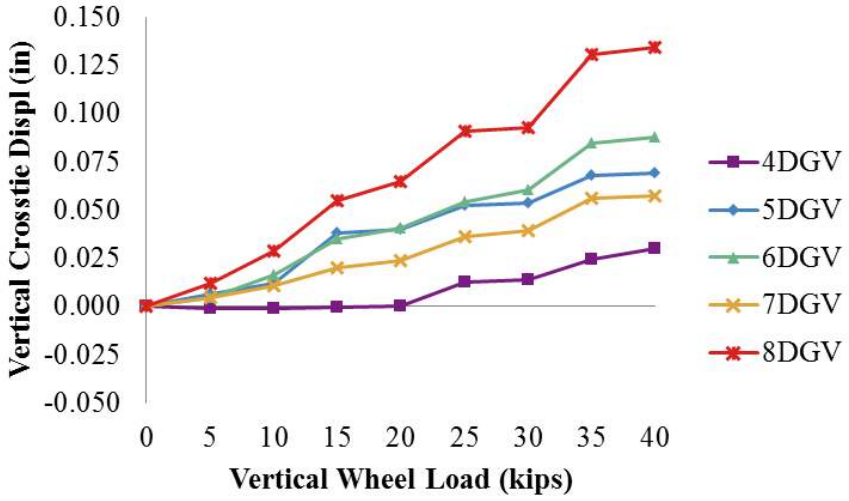

Figure 104. Crosstie Vertical Deflection Under Vertical Wheel Load Applied Directly Over Each Crosstie

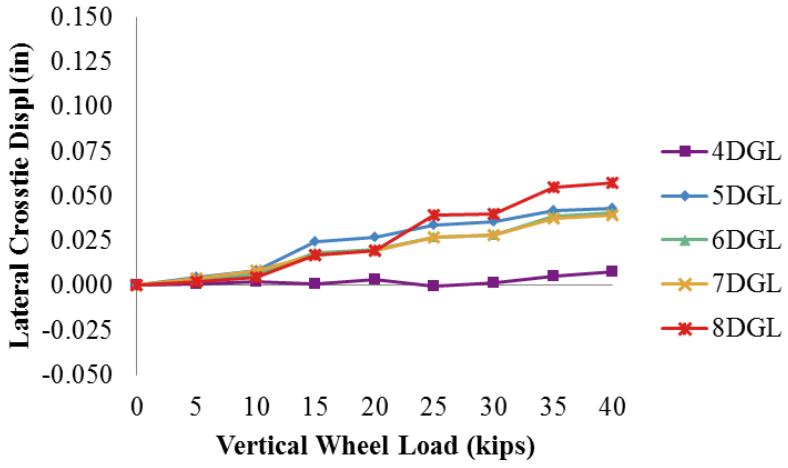

Figure 105. Crosstie Lateral Deflection Under Vertical Wheel Load Applied Directly Over Each Crosstie

Similar to that shown in Figure 77, under cyclical vertical loading (range from 0 to 40 kips), a hysteresis loop was observed for the crosstie global measurements for both the vertical and lateral directions (Figure 106). Again, the area of the loop represents energy dissipation.

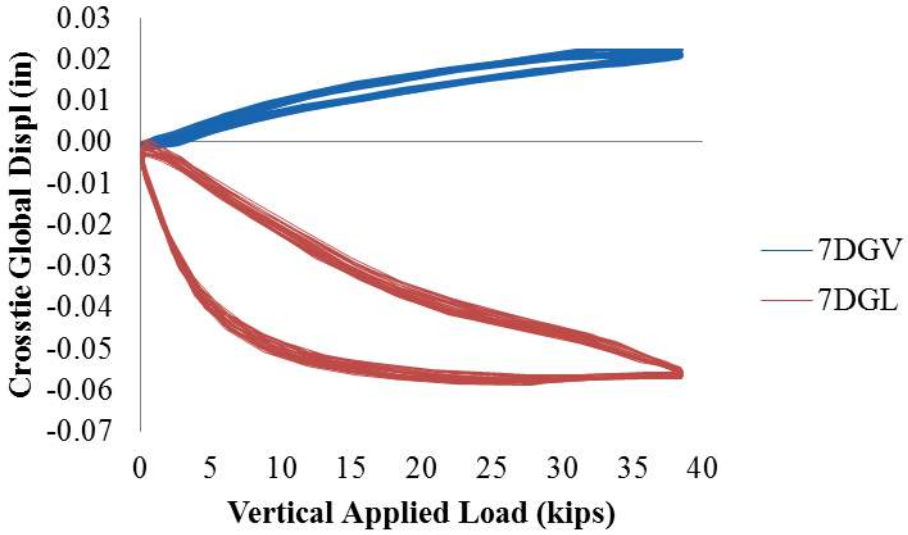

Figure 106. Crosstie Global Displacements at Field/Gauge Sides Under Cyclical Vertical Loading

While holding on 40 kips vertical load and increasing lateral applied loads, the change of DGV and DGL are shown in Figure 107 and Figure 108. The existence of lateral force resulted in all the crossties globally translating downward and shifting toward the near side.

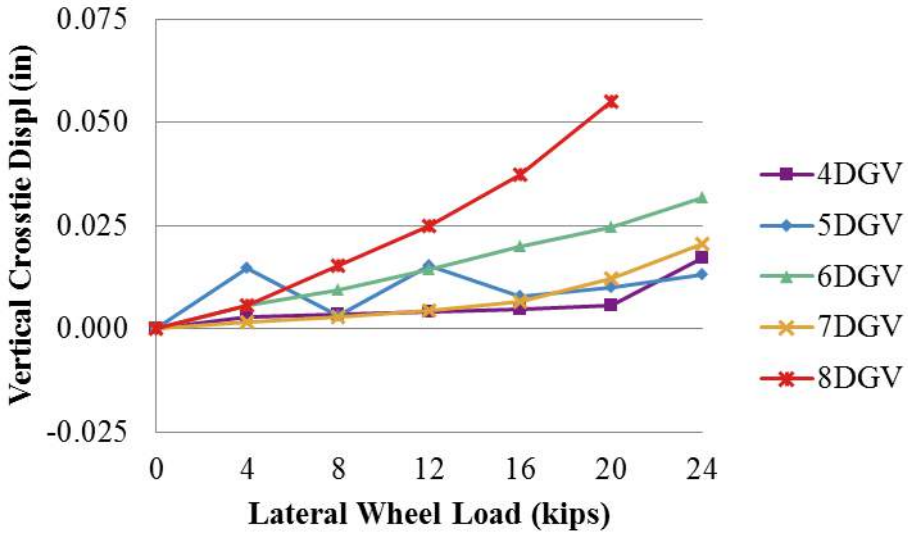

Figure 107. DGV Under 40 kips Vertical and Various Lateral Wheel Load Directly Applied Over Each Crosstie

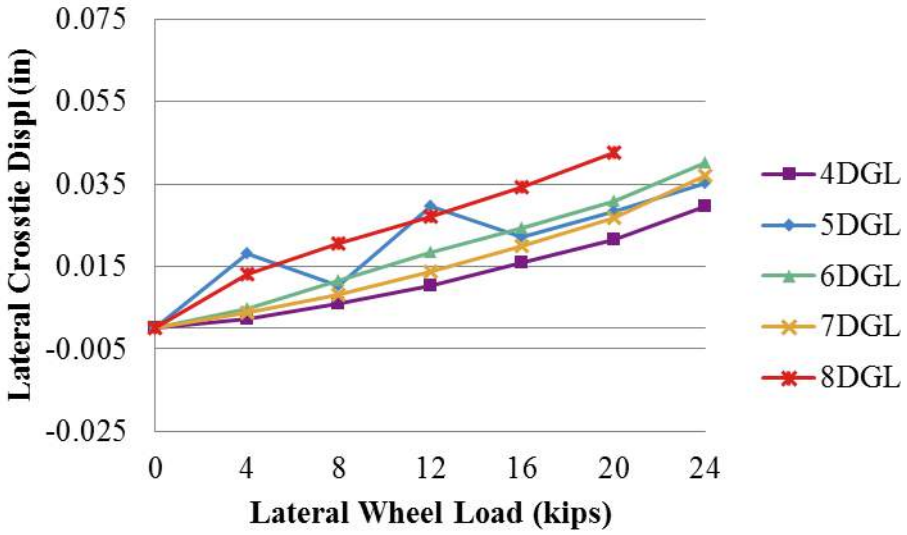

Figure 108. DGL Under 40 kips Vertical and Various Lateral Wheel Load Directly Applied Over Each Crosstie

4.17 Concrete Crosstie Bending Behavior

Crosstie bending stain was measured by concrete surface strain gauges (Figure 55 in the Laboratory Experimental Plan). Using the following equation, the bending moment corresponding to each pair of strain measurement was calculated:

$$M = (e_{Sa} - e_{Sb}) E_c I_{ab} / d$$

$$a = 2, 4, 6, 8, 10$$

$$b = 1, 3, 5, 7, 9$$

Where:

- e_{Sa}-e_{Sb} are the strains recorded from each pair of concrete surface strain gauges as noted in Figure 106
- E_c is the elastic modulus of concrete material
- I_{ab} is the moment of inertia of the concrete cross section at the location of each strain gauges pair
- d is the vertical distance between the two strain gauges in each pair

The distribution of the bending moments along a crosstie was drawn from the five moment measurements measured by the embedment strain gauges. Figure 109 presents the measured moment diagram of crosstie 7 under 40-kips vertical wheel loads as an example (blue dots connected with straight segments). This bending diagram reflects the crosstie bending behavior when the loading was directly applied above it. Using these measured moments as well as the measured rail seat loads (shown in blue in Figure 110), the support conditions underneath the crosstie were back-calculated (Figure 55). To achieve this simulation, a numerical program was developed with Matlab. As the comparison, the measured bending moments were found far below the theoretical cracking moments listed in Table 14. This suggests that there is no

cracking occurring under the given loading and support conditions. The crosstie bending diagram and the calculated support conditions for other well supported crossties were found similar as crosstie 7. This work will be further developed under future research funding.

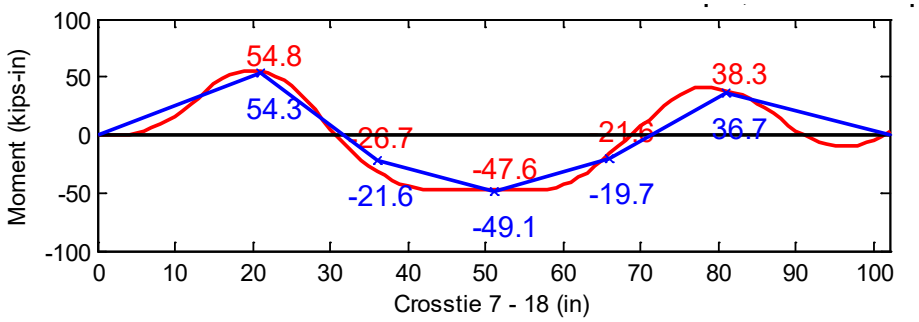

Figure 109. Measured (Blue) and Simulated (Red) Moment Diagram

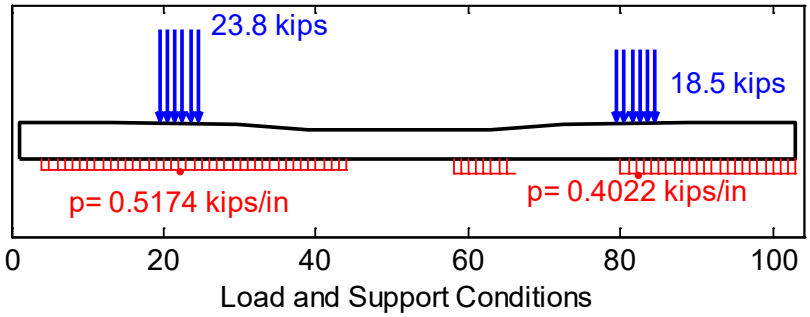

Figure 110. Simulated Support Conditions Using the Bending Moment Measurements

Chapter 5: Field Experimental Plan

5.1 Objectives

Researchers executed significant field experimentation aimed at both filling voids in the current understanding of concrete crossties and fastening systems and aiding future designers by obtaining quantifiable data regarding the expected loading environment for these components. The overall objective of the field experimentation was to quantify the loading demands placed on the individual crosstie and fastening system components as well as the system as a whole under a variety of operational conditions. This data will aid in providing answers to critical questions about the design and performance of concrete crossties and fastening systems, providing a baseline for mechanistic design.

This field experimentation plan accomplished the following primary goals:

- **Quantification of Crosstie and Fastening System Response** – The instrumentation of the concrete crosstie and fastening system components during testing under known applied loads led to a comprehensive understanding of the characteristic deformations and displacements of these components.
- **Determination of System Mechanics** – The instrumentation of the concrete crosstie and fastening system components during testing under known applied loads also led to a comprehensive understanding of the load transfer mechanics from the wheel-rail interface, through the fastening system, and into the concrete crosstie.
- **Development of Analytical Model** – The data obtained from the field experimentation were used in the validation of a 3D FE model of the concrete crosstie and fastening system which was used as a tool for conducting parametric analyses to aid in the design of concrete crossties and fastening systems.

5.2 Experimental Locations

The field experimental plan was conducted at TTC in Pueblo, CO. Field experiments and results were conducted on a segment of tangent track on the RTT and a segment of 5-degree curved track on the High Tonnage Loop (HTL) with 4 inches of superelevation, and a 33 mph (53 kph) balance (Figure 111). Both test track sections consisted of a 136RE rail section, concrete crossties spaced at 24-inches center-to-center, Safelok I type fastening systems, and premium ballast.

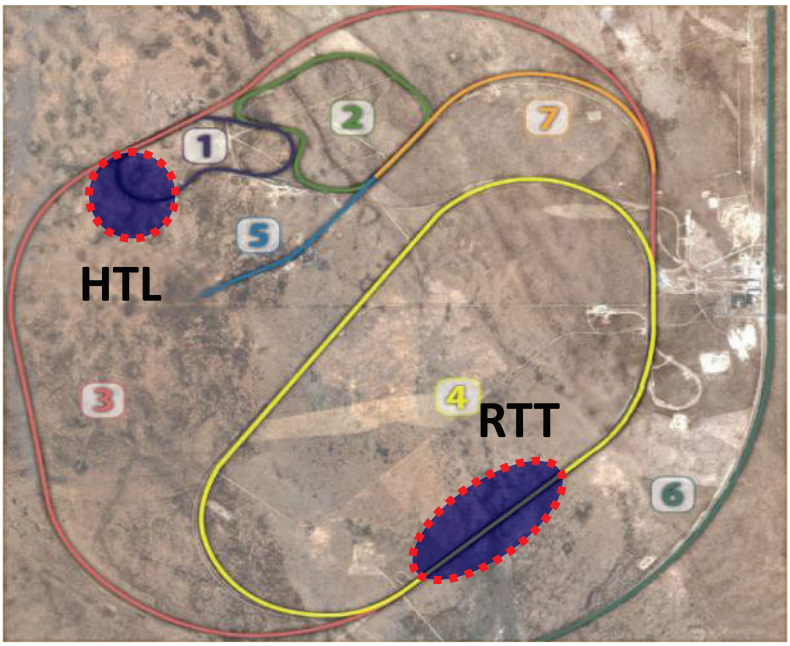

Figure 111. Experimental Testing Locations at TTC

5.3 Load Application Devices

Various devices were used to apply loads during experimentation. Vertical and lateral load magnitudes and combinations were chosen by researchers based on typical loading scenarios experienced in field conditions.

5.3.1 Track Loading Vehicle

The TLV (Figure 112) was used to apply controlled loading scenarios to the track structure. Static and dynamic loads were applied using the TLV. The TLV uses a deployable axle and wheelset capable of applying various combinations of vertical and lateral wheel loads to simulate typical loading conditions and true wheel-rail contact.

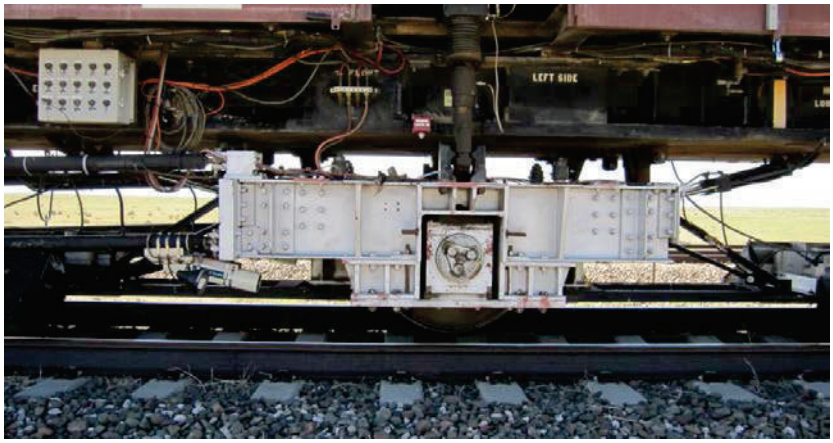

Figure 112. Track Loading Vehicle

5.3.2 Delta Frame

The Delta Frame (Figure 113) was used during the May 2013 experimentation to calibrate vertical and lateral strain bridges used to measure vertical and lateral wheel loads, respectively. Vertical loads up to 50,000 pound-force and lateral loads up to 10,000 pound-force were applied to the rail, separately. The delta frame used a hydraulic cylinder to apply loads. Vertical loads were applied using an upward facing steel triangular frame with loads applied in the center of the bottom side of the frame and reacting off the rail at the two bottom corners. Lateral loads were applied by disassembling the triangular frame and laying the central upright perpendicular to and between the two rails to apply a gauge-widening force.

Figure 113. Delta Frame – Vertical Load Orientation

5.4 Passenger and Freight Train Consists

Passenger and freight train consists were run over each test section to simulate actual train passes that can occur on a shared-rail corridor in the field. Table 21 shows the make-up and car rolling stock weight for each consist as tested at each location. Two runs at the same speed were run in at each location. On the RTT, the passenger consist was run at 2 mph, 15 mph, 30 mph, 60 mph, 80 mph, 90 mph, and 105 mph while the freight consist was run at 2 mph, 15 mph, 30 mph, 45 mph, 60 mph, and 70 mph. On the HTL, the passenger consist was run at 2 mph, 15 mph, 30 mph, and 40 mph while the freight consist was run at 2 mph, 15 mph, 30 mph, 40 mph, and 45 mph.

Table 21. Train Consist Make-up and Car Weights as Tested at Each Location

	Tangent Track (RTT)		Curved Track (HTL)	
Location in Consist	Freight (lbs)	Passenger (lbs)	Freight (lbs)	Passenger (lbs)
1	259,600	259,600	390,000	390,000
2	286,440	88,025	398,000	86,200
3	285,325	86,475	397,000	87,050
4	285,700	87,100	267,980	87,300
5	262,300	86,750	317,125	86,450
6	315,370	86,150	315,075	86,150
7	315,370	86,450	315,370	86,750
8	317,125	87,300	262,300	87,100
9	267,980	87,050	285,700	86,475
10	266,550	86,200	285,325	88,025
11	43,900		266,550	
12			286,440	
13			43,900	

Locomotive Freight Car Passenger Car

5.5 Summary of Experimental Measurements and Instruments

Measurements were acquired to meet the objectives described in Section 4.10. These measurements were captured during two large-scale field experimental programs conducted at TTC in Pueblo, CO. Some measurements were collected using well-established instrumentation methodologies, while novel approaches were used to collect data that have not been reliably captured to date. The following measurements were captured in one or both experimental programs. In addition, we described how each of these measurements was captured and the intended use of the data.

5.6 Experimental Measurements

5.6.1 Vertical Wheel Loads

Vertical wheel loads were determined using an arrangement of strain gauges on the web of the rail (Figure 114). Weldable strain gauges were assembled in a Wheatstone bridge and calibrated with a TLV. The forces recorded were used as inputs into the system which would result in stresses in most of the components within the system.

5.6.2 Vertical Rail Seat Loads

Vertical rail seat loads were determined using the same arrangement of strain gauges on the rail web as in Section 4.14.1, but directly above the rail seat area (Figure 114). Weldable strain gauges were assembled in a Wheatstone bridge and the calibration from Section 4.14.1 was used to capture the load transferred into the crosstie. These forces were used as inputs imparted into the pad assembly and crosstie rail seat.

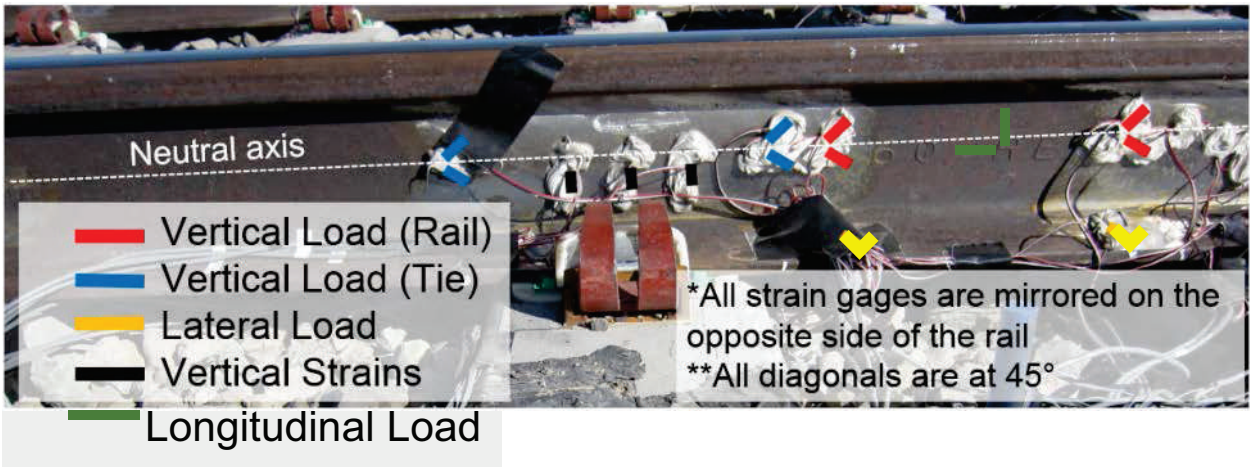

Figure 114. Strain Gauge Configurations for Test Measurements 1, 2, 3, 4 and 15

5.6.3 Lateral Wheel Loads

Lateral wheel loads were determined using an arrangement of strain gauges on the web of the rail (Figure 114). Weldable strain gauges were assembled in a Wheatstone bridge and calibrated with the TLV. These forces were used as inputs into the system to determine the influence they impart on the components in the lateral direction

5.6.4 Longitudinal Rail Loads

Longitudinal rail loads were determined using an arrangement of strain gauges on the web of the rail (Figure 114). Weldable strain gauges were assembled in a Wheatstone bridge and the strains resolved into forces. These forces were measured to understand how the train braking and acceleration influence the components in the longitudinal direction.

5.6.5 Vertical Rail Base Displacements

Vertical rail base displacements were measured at one location on the rail base, 1.5 inches from the edge of the gauge-side rail base. These measurements were acquired with linear potentiometers, mounted to the crosstie to provide relative rail uplift to the crosstie. These measurements were used to further define the vertical stiffness at this interface and, when coupled with other measurements, quantify rail rotation.

5.6.6 Lateral Rail Displacements

Lateral rail displacements were measured at the rail base and at the neutral axis of the rail relative to the crosstie using linear potentiometers. These measurements, in conjunction with lateral force measurements, were used to define the lateral stiffness of the system at this interface.

5.6.7 Vertical Crosstie Global Displacements

Vertical crosstie global displacements (DGV) were measured at each end of the crosstie relative to the ground using linear potentiometers affixed to a rod driven to refusal. These measurements, when coupled with other measurements, were used to determine the support

stiffness of each rail seat. These displacement values were also used to validate the UIUC FE model.

5.6.8 Lateral Crosstie Global Displacements

Lateral crosstie global displacements were measured at the end of the crosstie relative to the ground using linear potentiometers affixed to a rod driven to refusal. These measurements, when coupled with other measurements, were used to determine the lateral support stiffness of each crosstie.

5.6.9 Crossties Strains (Measured Internally)

Internal crosstie strains were measured using embedment strain gauges. These strains were than used to calculate the rail seat force imparted onto the crosstie rail seat. These measurements were also used to determine the compressive forces and pressure distribution at the rail seat.

5.6.10 Crossties Strains (Measured Externally)

External crosstie strains were measured by concrete surface strain gauges. These longitudinally placed gauges provide crosstie bending moments. These measurements were used to determine the bending moments under load as well as the support conditions of each crosstie.

5.6.11 Rail Seat Pressure Distribution

Load distribution at the rail seat was measured using matrix based tactile surface sensors (MBTSS). These measurements were used to determine the longitudinal distribution of the applied load as well as the uniformity and intensity of the compressive stresses applied to the crosstie rail seat.

5.6.12 Rail Base Bending Stresses

Rail base bending stresses were measured transverse to the field side of the rail using weldable strain gauges located 1 inch from the edge of the rail base. These gauges measured the bending of the rail base and these measurements were used to help determine the longitudinal distribution of the applied load.

5.6.13 Insulator Post Stresses

Insulator post stresses were measured on the field and gauge side of the rail using strain gauges located on the bottom surface of the insulator post; the stresses were then used to calculate the applied load. These measurements were used to further define the lateral load path and determine the demands placed on the insulator post.

5.6.14 Fastening Clip Stresses

Fastening clip stresses were measured on the field and gauge side of the rail using strain gauges located on the surface of the fastening clips; the strains were then used to calculate the change in the normal and tangential components of clamping force applied to the base of the rail. These measurements were used to further define the load transfer path within the fastening system and determine the demands placed on the clips. These strain values were also used to validate the FE model.

5.6.15 Vertical Rail Strains

Vertical rail strains were measured near the base of the web (Figure 114) using three vertical strain gauges applied 2 inches apart on each side of the rail, centered over the rail seat. Using these measurements across seven crossties, the strain values assessed the load distribution of the applied load longitudinally along the track. These strain values were also used to validate the model.

5.6.16 Lateral Forces Entering the Shoulder – Method 1

Lateral forces entering the shoulder face were determined using measurements from (LLED, see Chapter 3, Section 3.7.13). This measurement, in conjunction with the lateral rail base displacement measurement, was used to further define the load path within the fastening system, determine the lateral stiffness at the rail base-shoulder interface, and determine the demands placed on the insulator post and shoulder.

5.6.17 Lateral Forces Entering the Shoulder – Method 2

Lateral forces entering the shoulder face were also determined using a plate with two strain gauged rods contacting a replacement aluminum insulator. This plate was anchored into the concrete crosstie behind the shoulder. The strain values measured were resolved into a force. This measurement, in conjunction with the lateral rail base displacement, was used to further define the load path within the fastening system, determine the lateral stiffness at the rail base-shoulder interface, and determine the demands placed on the insulator post and shoulder.

5.6.18 Pad Lateral Displacements

The lateral rail pad displacement was measured relative to the crosstie using linear potentiometers. These measurements were used to further define the load path and lateral stiffness of the fastening system as well as the demands placed on the pad assembly.

5.6.19 Pad Longitudinal Displacements

The longitudinal rail pad displacement was measured relative to the crosstie using linear potentiometers. These measurements were used to further define the load path and determine the demands placed on the pad assembly.

5.6.20 Pad Temperatures

Pad temperatures were measured both at the abrasion frame and rail pad using a K type thermocouple inserted inside each component. These measurements were used to define the thermal changes in the pad assembly resulting from train passes.

5.7 Instrumentation

All strain gauges, LLEDs, and potentiometers were plugged into a National Instrument's (NI) compact data acquisition (cDAQ) system using the relevant modules needed. This system was connected to a laptop and ran in conjunction with a LabVIEW program to record all the data. The data was recorded at 2000Hz for all loading scenarios. MBTSS and thermocouples were plugged into separate data acquisition systems described in more detail in their respective sections below.

5.7.1 Strain Gauges

Four types of strain gauges were used in this project based on the application. Standard 120-ohm foil type shear strain gauges were used for quarter bridge circuits. Shear strain gauges in a chevron pattern with two 120-ohm gauges oriented 90 degrees to each other were used for full bridge circuits. 120-ohm concrete internal and concrete surface strain gauges were also used. All strains could be measured accurately to one ms.

5.7.2 Potentiometers

Displacement transducers called linear potentiometers were used to measure relative displacement between components. The transducers used had a maximum stroke length of 1.1 inches. Displacements could be measured accurately to one-thousandth of an inch.

5.7.3 Matrix Based Tactile Surface Sensors

MBTSS can record pressure distribution on a surface. In this experimentation, MBTSS were used to capture the pressure distribution at the rail seat. Data from MBTSS was recorded at 100Hz for both static and dynamic loading using a separate data collection program designed specifically for use with MBTSS.

5.7.4 Lateral Load Evaluation Devices

LLEDs have two defined points of contact with the shoulder that act as outer supports and two defined points of contact with the insulator that are narrower than the outer supports. Under load, this specific geometry induces four-point bending of the beam. The beam contains four strain gauges which are wired into a full Wheatstone bridge to measure bending strain under load. Two strain gauges are applied horizontally 1 inch from the center of the beam to measure compressive strains (Figure 115a). The locations of the gauges are between the points of contact with the insulator to minimize damage to the gauges. The other two strain gauges used to measure tensile strains are applied horizontally 1 inch from the center of the beam between the two supports (Figure 115b). The face of the fastening system shoulder is ground away using a handheld grinder and straight edge to ensure the original dimensions after placement of the LLED are maintained.

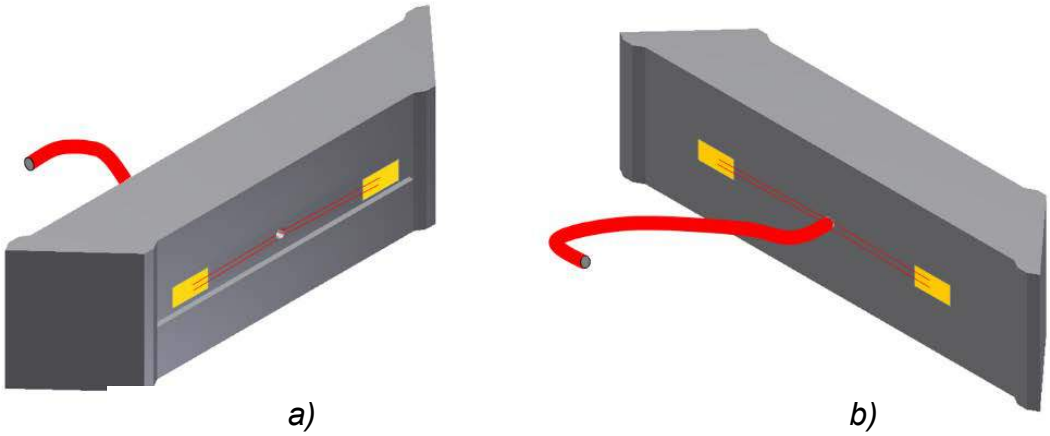

Figure 115. LLED Strain Gauge Location and Orientation

5.7.5 Thermocouples

K-type thermocouples were used to measure temperature changes within the rail pad and abrasion frame. Temperature date was recorded through PicoLog data acquisition software and within a range of -103 °F to +482 °F. Temperatures could be measured accurately to approximately 0.3 °F.

5.8 Naming Conventions

The following is the direction of the coordinates from the test set-up (Figure 116):

X – Transverse direction of the track

Y – Vertical direction (gravity)

Z – Longitudinal direction of the track

Figure 116. Coordinate Naming Convention

5.9 July 2012 Field Testing at TTC

Two sections of track were investigated at the TTC in Pueblo, CO. One section was on a tangent segment of the RTT while the other was on a curved segment of the HTL with a curvature of approximately 5 degrees. For both sections, 15 new concrete crossties were installed and tamped prior to testing (Figure 117).

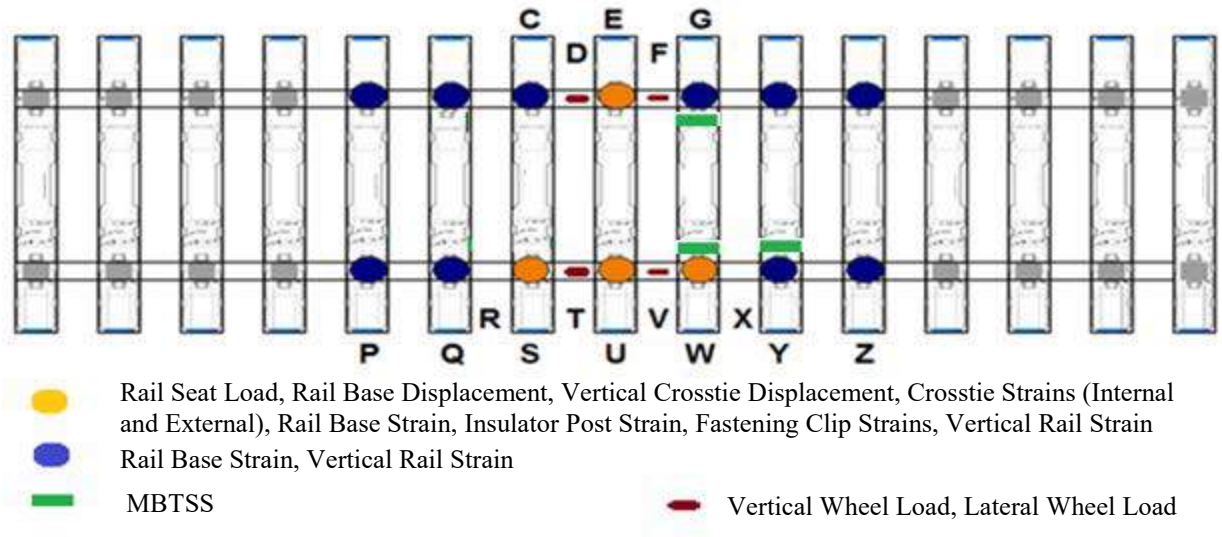

Figure 117. Locations of Fully (Orange) and Partially (Blue) Instrumented Ties

There were two levels of instrumentation densities that were deployed at each of the two locations. A dense set of instrumentation was deployed on three adjacent rail seats and the opposite rail seat of the center crosstie (labeled orange in Figure 117). Additional rail seats in the section were partially instrumented with vertical strain gauges on the rail (labeled blue in Figure 117). The instrumentation methodologies employed during field experimentation, their specific locations, and the reference section within this chapter are shown in Table 22. Unless otherwise noted, the same instrumentation plan was deployed on both the RTT and HTL.

Table 22. Measurements Recorded in July 2012 Field Instrumentation with Locations

Test Methodology	Reference Section	Location (Fig. 3)
Vertical Wheel Loads	4.5.1	D, F, T, V
Vertical Rail Seat Loads	4.5.2	E, S, U, W
Lateral Wheel Loads	4.5.3	E, S, U, W
Vertical Rail Base Displacements	4.5.4	E, S, U, W
Lateral Rail Displacements	4.5.5	E, S, U, W
Vertical Crosstie Displacements	4.5.6	Ties C/S, E/U, G/W
Internal Crosstie Strains	4.5.7	E, S, U, W
External Cosstie Strains	4.5.8	Ties C/S, E/U, G/W
Rail Seat Pressure Distributions	4.5.9	G, W, Y
Rail Base Bending Stresses	4.5.10	E, S, U, W
Insulator Post Stresses	4.5.11	E, S, U, W
Fastening Clip Stresses	4.5.12	E, S, U, W
Vertical Rail Strains*	4.5.13	ALL
Pad Temperatures	4.5.14	E, S, U, W

*The two end strain gauges were only measured at rail seats E, S, U, and W

Additional wheel load measurements were taken by the Transportation Technology Center, Inc.'s personnel using an IWS. These results were used to supplement the data analysis.

5.10 July 2012 Field Measurements

5.10.1 Vertical Wheel Loads

Gauges were placed in the chevron pattern (Figure 118 and Figure 119) about the neutral axis of the rail section as shown, oriented at 45 degrees to the neutral axis. Four gauges were mirrored on each side of the rail. The centers of the two groups of gauges were measured at 5 inches from each side of the center of the crib

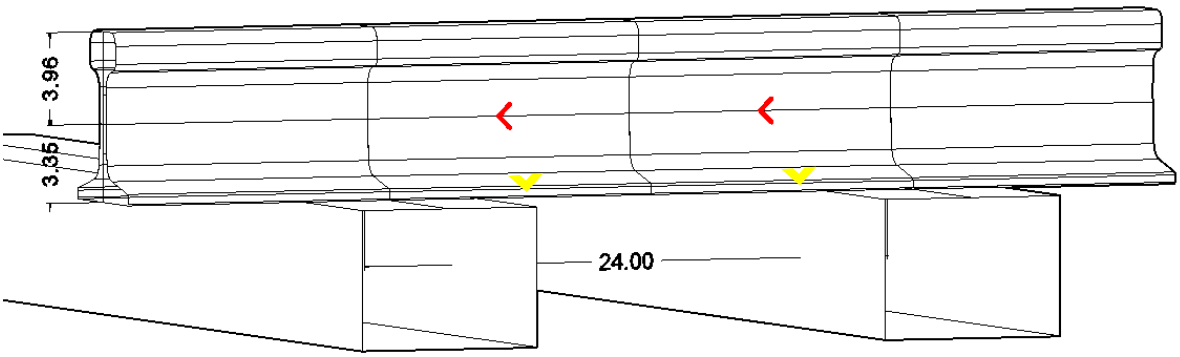

Figure 118. Gauge Locations for Vertical Load (Red) and Lateral Load (Yellow)

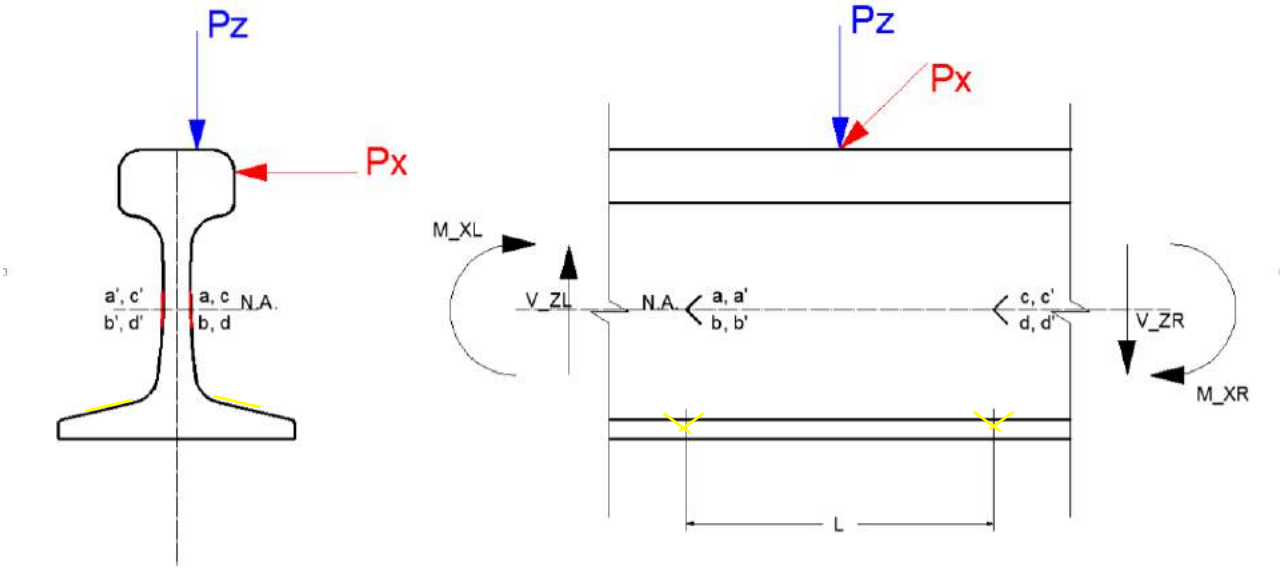

Figure 119. Vertical Applied Load Calculation

The vertical load, P_z, can be determined using the following equations and methodology:

$$P_Z = V_{ZL} - V_{ZR} \quad \textbf{(Eq. 1)}$$

$$V_{ZL} = \frac{EI}{(1+\nu)Q}\varepsilon_1, V_{ZR} = \frac{EI}{(1+\nu)Q}\varepsilon_2 \quad \textbf{(Eq. 2)}$$

$$\varepsilon_1 = \varepsilon_a - \varepsilon_b + \varepsilon_{a'} - \varepsilon_{b'}, \varepsilon_2 = \varepsilon_c - \varepsilon_d + \varepsilon_{c'} - \varepsilon_{d'} \quad \textbf{(Eq. 3)}$$

$$P_Z = \frac{EI}{(1+\nu)Q}(\varepsilon_1 - \varepsilon_2) \quad \textbf{(Eq. 4)}$$

Where:

- V_{ZL} and V_{ZR} are shear forces at the left and right sections of the rail as in Figure 119
- $\varepsilon_a, \varepsilon_b, \varepsilon_c, \varepsilon_d, \varepsilon_{a'}, \varepsilon_{b'}, \varepsilon_c, \varepsilon_d$ are strains measured at a, b, c, d, a', b', c' and d' respectively
- E, ν, I and Q are the elastic modulus of the rail, poisson's ratio of rail, Moment of Inertia of the section of the rail and moment of the area of the rail above the neutral axis of the rail respectively

Strains $\varepsilon_1 \; and \; \varepsilon_2$ can be measured separately by using the Wheatstone bridge connection shown in Figure 120 (left); $\varepsilon_1 - \varepsilon_2$ can be measured directly by using the Wheatstone bridge connection shown in Figure 120 (right).

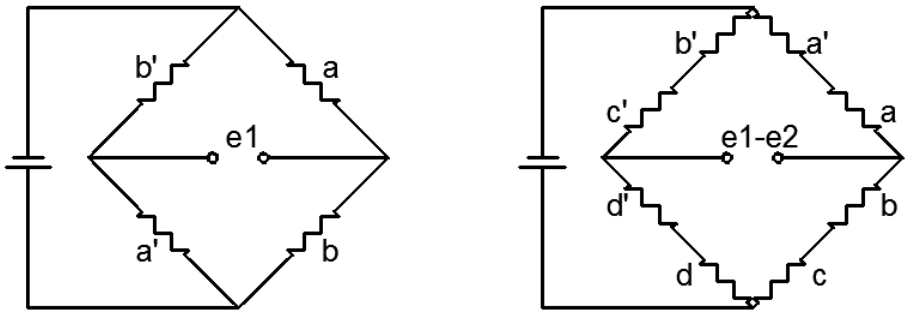

Figure 120. Diagram Showing Wheatstone Bridge Connections

5.10.2 Calibration

A TLV owned and operated by the AAR is equipped with actuators and load cells was used for the calibration of both the vertical and lateral load gauge patterns. The calibration was conducted as follows for all full-bridge circuits:

1. The TLV deployable axle is positioned above the center of the crib with the strain gauge assembly (Figure 121).

2. Output is recorded from "vertical load" strain gauge bridge.

3. Vertical loads were applied in increments of 5 kips, until a maximum of 40 kips is reached.

4. The gain factor is recorded for the vertical load strain gauge bridges, using measurements of each vertical load step.

5. Initiate recording of output from “lateral load” strain gauge bridge.

6. Increments of 2-kip lateral load are then applied, while sustaining the vertical load, until a maximum of a 20 kip lateral load.

7. The gain factor is recorded for the lateral load strain gauge bridges, using measurements of each lateral load step.

Figure 121. TLV in Operation

5.10.3 Vertical Rail Seat Loads

Similar to the measurement of vertical wheel loads, the chevron gauges (with identical geometry) on the rail above the rail seat (Figure 114) were installed. Using the calibration from Chapter 3, Section 3.17.1, measurements were made of the difference of shear over the crosstie (the wheel-rail load subtracted by the reaction at the rail-crosstie interface). Taking the difference of this measurement and the vertical wheel load we determined the reaction force (the load transferred into the crosstie).

5.10.4 Lateral Wheel Loads

Similar to the measurement of vertical wheel loads, chevron gauges were installed and used on the rail base (Figure 114). The configuration and working principle of these strain gauges is exactly same as the vertical wheel load, the only difference being the location of the gauges. To measure forces in a perpendicular plane the strain gauges are placed on the base of the rail (Figure 114**,** Figure 118, and Figure 119) the full Wheatstone bridge, which records the shear in the x-axis. These strain gauge bridges were adequately calibrated to read lateral loads.

5.10.5 Vertical Rail Base Displacements

Vertical displacements were measured with linear potentiometers, which are screwed into aluminum fixtures (Figure 122 and Figure 123-2) that were epoxied to the crosstie. The potentiometers were positioned 1 in from the face of the tie and 0.5 in from the edge of the rail base on the gauge side of the rail on one side of the clip. This displacement was measured to determine average vertical displacement (i.e. pad compression).

Figure 122. Aluminum Fixture for Potentiometer Placement

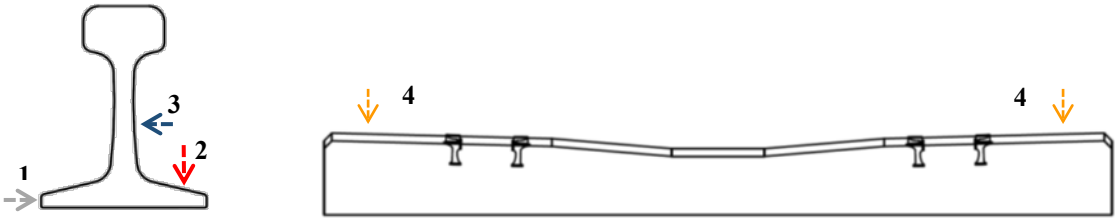

Figure 123. Vertical (2) and Lateral Displacements (1, 3) of Rail Base and Web [left]; Global Displacements of the Crosstie (4) [right]

5.10.6 Lateral Rail Displacements

Lateral displacements were measured with linear potentiometers, which were screwed onto one of the aluminum fixtures. The lateral displacements at two locations were measured; one at the rail base (Figure 123-1) and one at the neutral axis (Figure 123-3) to determine the average lateral displacement as well as the rotation and bending of the rail, about the z-axis.

Figure 124. Position of Lateral Displacement at Rail Web [left]; Lateral Displacement at Rail Base [right]

5.10.7 Vertical Crosstie Global Displacements

Global displacements of the crosstie were measured with linear potentiometers, which were clamped onto two rods driven into the subgrade, one at each end of the crosstie (Figure 125).

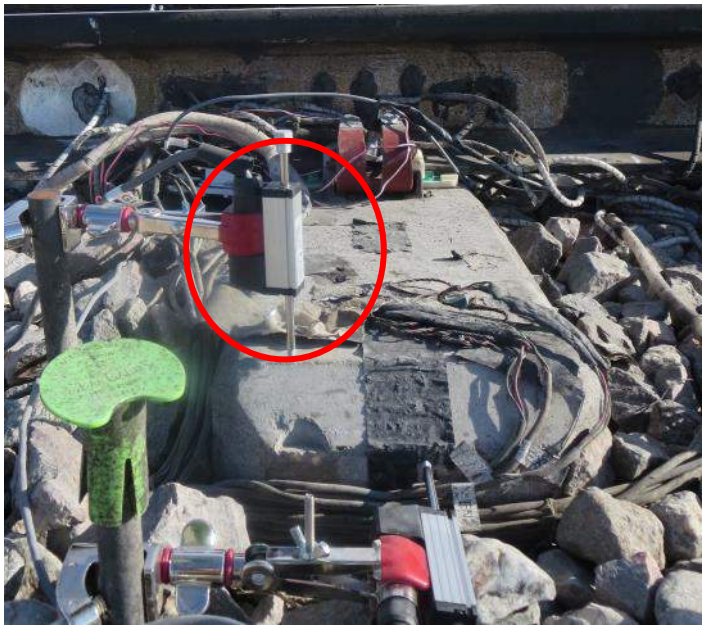

Figure 125. Vertical Crosstie Displacement Potentiometer

5.10.8 Internal Crosstie Strains at the Rail Seat

Internal crosstie strains are measured approximately 1.5 in below the surface of the rail seat using embedment gauges (Figure 126). Embedment gauges were installed during crosstie manufacturing in a 2 x 2 pattern. These strains determined are the average compression and stress distribution (in the x and z-directions).

$$V(kips) = e_{AVG} \cdot E_c \cdot A \cdot Q_1 \cdot Q_2 \cdot Q_3 \quad \textbf{(Eq. 5)}$$

Equation 5 gives the calculation of rail seat vertical loading.

Where,

- e_{AVG} is the average strain recorded from the four embedment sensors
- E_c is the elastic modulus of the concrete material
- A is the area of rail seat
- Q_1 is the correction factor for bearing area in concrete at the height of embedment strain gauges
- Q_2 is the correction factor for loading eccentricity
- Q_3 is the correction factor for support length below concrete crosstie
- Q_1, Q_2, Q_3 were obtained through laboratory calibration; see 5.10.9 below

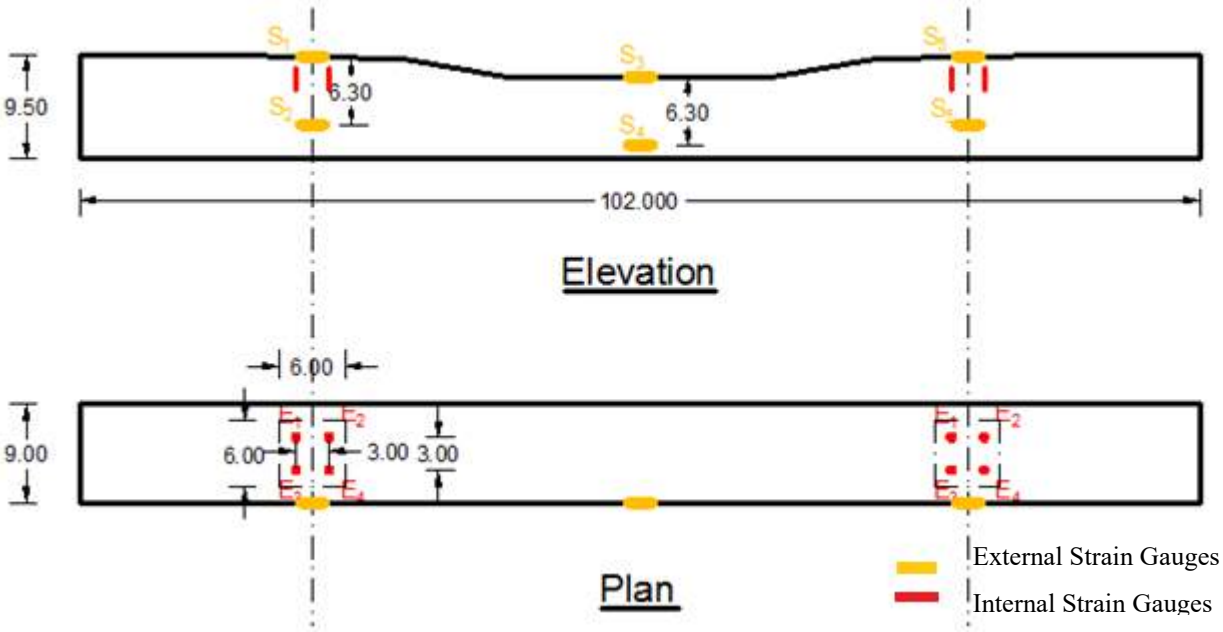

Figure 126. Crosstie Strain Gauge Locations

5.10.9 Calibration of Internal Crosstie Strains

By applying a uniform distributed load on the rail seat, the internal strains can be associated with compressive loads. Given, it was difficult to apply a known uniform compressive load to each rail seat in the field environment; work was performed in the lab to convert the strain in concrete into rail seat loads Equation 5.

Q_1 was measured with no loading eccentricity and Q_3 was standardized as 1 for 6-inch support width. Q_3 was calculated with no loading eccentricity and varying support widths. Q_3 for each rail seat was determined by the ratio of moment diagram of each crosstie obtained from the concrete surface strain gauges. Q_2 was calculated with various loading eccentricity and standardized support width (6 inches). The correction factors used for rail seats E, S, U and W at RTT are listed in Table 23.

Table 23. Correction Factors Used for Rail Seats E, S, U and W at RTT

E		S		U		W	
Q_1	2.075	Q_1	2.075	Q_1	2.075	Q_1	2.075
Q_2 (α)	0.175	Q_2 (α)	0.175	Q_2 (α)	0.175	Q_2 (α)	0.175
Q_3	1	Q_3	1	Q_3	1	Q_3	1
e_{DIFF_MAX}	600	e_{DIFF_MAX}	400	e_{DIFF_MAX}	400	e_{DIFF_MAX}	400

In September 2013, Crosstie CS, EU, GW were removed from RTT and shipped to UIUC. The calibration work for these three crossties was done and the correction factors were obtained as shown in Table 23. However, none of the crossties at HTL were calibrated in the laboratory. In this case, the averages of the correction factors of all the crossties calibrated in the laboratory were used for crossties from HTL. The correction factors for rail seats E, S, U and W at HTL are listed in Table 24.

Table 24. Correction Factors Used for Rail Seats E, S, U and W at HTL

E		S		U		W	
Q_1	2.075	Q_1	2.075	Q_1	2.075	Q_1	2.075
Q_2 (α)	0.175	Q_2 (α)	0.175	Q_2 (α)	0.175	Q_2 (α)	0.175
Q_3	1.15	Q_3	1.15	Q_3	1.15	Q_3	1.15
e_{DIFF_MAX}	400	e_{DIFF_MAX}	400	e_{DIFF_MAX}	400	e_{DIFF_MAX}	400

5.10.10 External Crosstie Strains

External crosstie strains were used to determine the moment at the integral sections of the crosstie (at the rail seat and tie center). All the external strain gauges were positioned longitudinally to the crosstie. A pair of strain gauges was applied on the crosstie below each rail seat and the tie center. Within each strain gauge pair, the upper gauge was installed at the narrow-inclined surface at the top of concrete crosstie, the other should be 6 in below the upper one.

The following equations show the calculation to obtain the bending moments at each real seat as well as at concrete crosstie center.

$$M(railseat1) = (e_{S2} - e_{S1})E_c I_{12} / d$$
$$M(center) = (e_{S4} - e_{S3})E_c I_{34} / d$$
$$M(railseat2) = (e_{S6} - e_{S5})E_c I_{56} / d$$

Where:

- eS1~eS6 are the strains recorded from concrete surface strain gauges S1~S6 (Figure 126)
- Ec is the elastic modulus of concrete material
- I12~I56 are the moment of inertia of the concrete cross section at the location of each strain gauges pair
- d is the vertical distance between the two strain gauges in each pair

5.10.11 Rail Seat Pressure Distribution

MBTSS were installed on both rail seats of the crosstie about which full instrumentation of strain gauging took place, with the purpose of measuring the distribution of the load onto the concrete rail seat surface. A single rail seat on an adjacent crosstie was also instrumented with MBTSS, to collect data from successive crosstie rail seats during train operation.

Sensor installation and removal were accomplished by temporarily raising the rail to a height adequate for accurately placing and removing the sensor. During instrumentation, the track structure was not disturbed. Figure 127 shows a profile view of the fully instrumented crosstie with all components of the MBTSS installation. Figure 128 shows a plan view of the MBTSS as it was installed on the rail seats.

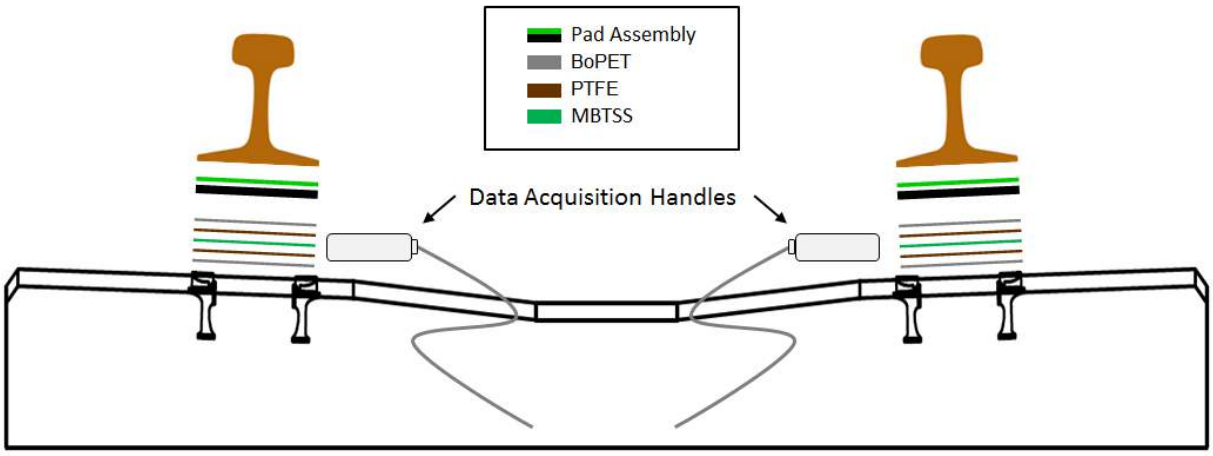

Figure 127. Profile View of MBTSS Installation on Crosstie

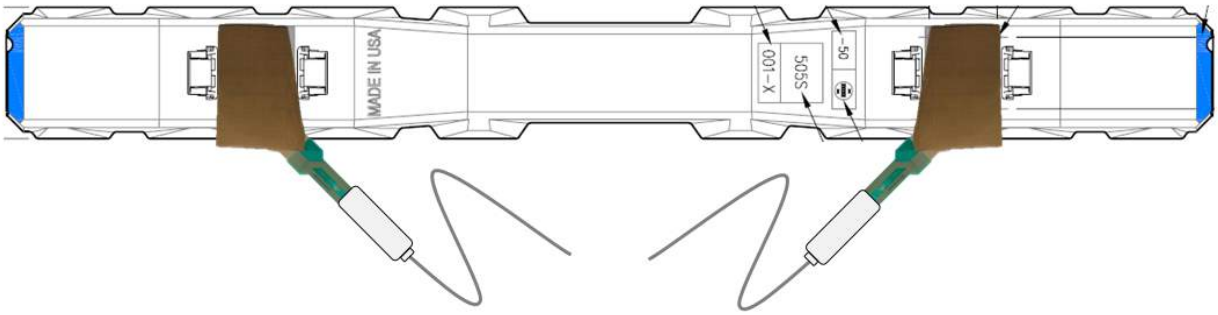

Figure 128. Plan View of MBTSS Installation on Crosstie

5.10.12 Calibration of MBTSS

Because MBTSS data is collected in nominal raw sum units, pre-experiment calibration was not necessary. A value of 50% was assumed for the percentage of the vertical wheel load transferred to the rail seat. The assumed vertical rail seat load data was used in conjunction with the nominal raw sum unit output data during data analysis to quantify the rail seat pressure distribution on a given rail seat.

5.10.13 Rail Base Bending Stresses

Gauges were placed in the transverse direction (x-direction) on the rail base (Figure 129). The gauge was centered 1 in from the face of the crosstie in the y-direction and 1 in from the edge of the rail base in the x-direction. These strains were used to analyze the bending action of the rail base. The strains recorded were used to determine if the rail base was behaving as a rigid body of if significant bending occurred in the rail base.

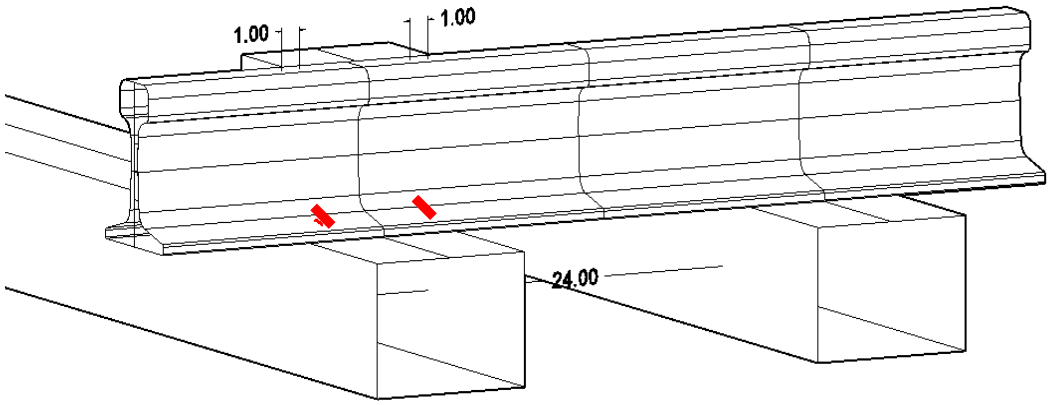

Figure 129. Transverse Gauges

5.10.14 Insulator Post Stresses

Insulator post stresses were determined by attaching a miniature strain gauge to the bottom surface of the insulator, oriented in the x-direction (Figure 130) and the insulator was trimmed by 0.5 mm to allow clearance for the wires. This gauge would measure the stresses placed on the

insulator post and the lateral load being transferred into the cast-in shoulder.

Figure 130. Insulator Post Compression; Location of Strain Gauges; Direction of Strain (left to right)

5.10.15 Fastening Clip Stresses

To measure clamping forces, a pair of strain gauges was installed on the inner and outer surfaces of each clip toe of a clip. The free body diagram of the clip and the locations of the strain gauges are shown in Figure 131.

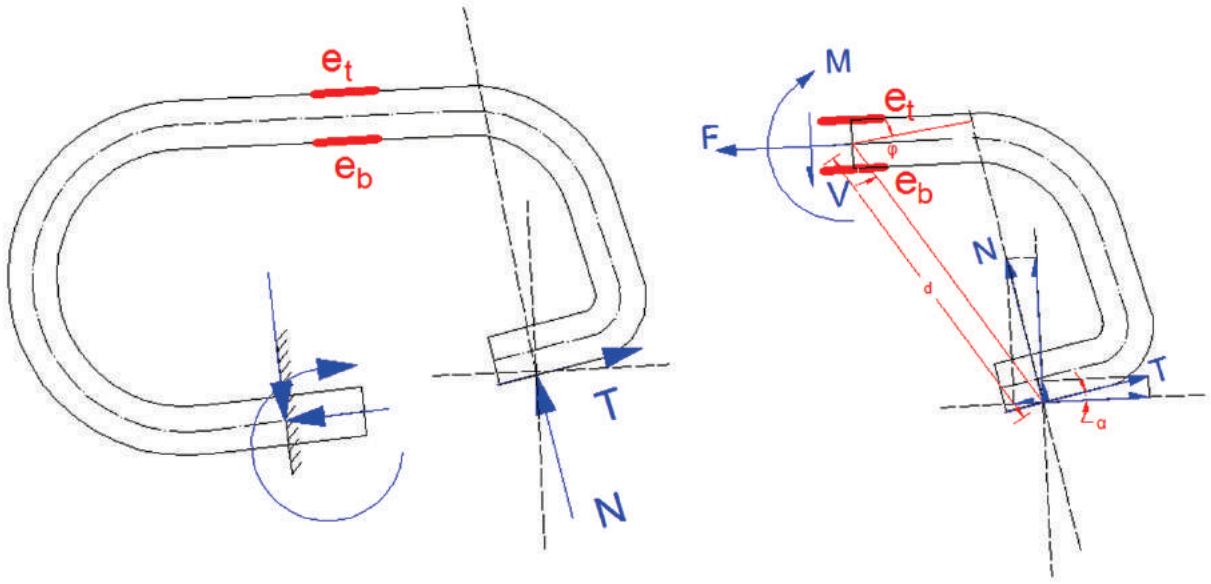

a b

Figure 131. Strain Gauge Pattern and Free Body Diagram of the Clip

Linear elastic analysis was used to analyze the clip's behavior. In Figure 131b, F, M, and V are used to show the resultant axial force, bending moment, and shear force at the location of the strain gauge pair. N and T are the actual normal and tangential force applied to the clip tip. d, α, and φ are the geometric properties of the clip. The contact point between the clip and the insulator is assumed to be 0.3 inches from the edge of the clip toe, which agreed with findings from FE modeling, methodology, and development.

Strain at inner and outer surface of the clip e_b and e_t can be theoretically calculated using the following equations (shear deformation is neglected):

$$e_t = -\frac{M(t/2)}{EI} + \frac{F}{EA}$$

$$e_b = \frac{M(t/2)}{EI} + \frac{F}{EA}$$

where,

$$M = Nd\cos\varphi + Td\sin\varphi$$

$$F = -N\sin\alpha + T\cos\alpha$$

Strain measurements are used to calculate the clamping force components N and T. The strain reading was easily affected by the hand installation of the gauges due to the relative dimensions of the stain gauge and the clip. To obtain an accurate result, an alternative way was developed by applying two assumptions:

1) The contact point between the clip toe and the insulator was assumed to be 0.3 in from the edge of the clip toe.
2) Because a standard clip installation process had been followed, a 2,500-lbf normal force was assumed to be applied to each clip.

Using these assumptions, a numerical program was developed with Matlab to calculate the normal and tangential components of the clamping force. The normal force for each instrumented clip was set to be 2,500 pound-force and the tangential force was an output.

The change of normal and tangential forces can be calculated using the equations below:

$$\Delta N = D_G \cdot (1250lbs / 0.289in)$$

$$\Delta T = \left(\frac{-e_t + e_b}{2} - \frac{\Delta N d(t/2)\cos\varphi}{EI}\right) \cdot \frac{EI}{d(t/2)\sin\varphi}$$

Where,

- ΔN is the change of normal force N
- ΔT is the change of tangential force T
- e_t and e_b are the strains measured from strain gauges
- φ is the angle shown in Figure 131
- d is the distance shown in Figure 131
- E is the elastic modulus for steel used for the clips
- A is the area of the cross-section of each toe
- I is the moment of inertia of the cross-section of each toe
- t is the thickness of the clip

- D_G is the vertical rail base deflection

The assumptions used for calculating N and T are listed below:

1) The normal component of clamping force can be expressed by $\Delta N=kD_G$ (in linear range), where k is the clip opening stiffness, which was obtained from the manufacturer manual and FE model analysis, or from simple component testing. For AmstedRPS P 2000 clips, k is designed to be 8650 lbf/in, and the initial clamping force (normal component) is 2500 pound-force.
2) Vertical displacement of the clip toe was measured relative to the crosstie at the tip of the rail base. As the inclination of rail base is 14.2°, cos(14.2°)=0.97~1, it is reasonable to use the vertical rail base displacement during calculation.

There is a relative movement between the clip toe and the rail along the rail base when the tangential component of the clamping force is greater than the maximum static friction force. The vertical displacement of the clip toe due to siding up the rail base is assumed to be negligible compared to the vertical rail base displacement.

5.10.16 Vertical Rail Strains

Vertical rail strains were measured on the web, as close to base as possible without transitioning into the fillet, at seven adjacent crossties (Figure 132). One strain gauge was welded to each side of the rail, centered above the crosstie. The average of the gauges on each side provided a relative measurement of vertical loading, while the difference of strains on each side provided a relative measurement of lateral loading

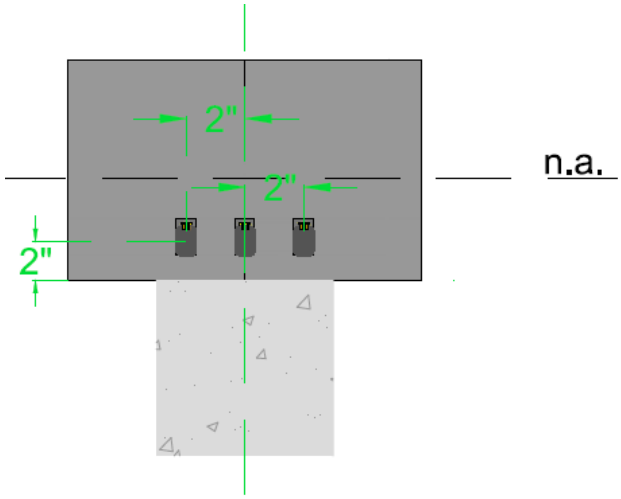

Figure 132. Location of Vertical Strain Gauge Above Rail Seat

5.10.17 Pad Temperatures

A thermocouple wire was installed inside the nylon abrasion frame and the polyurethane rail pad (Figure 133). The instrumented rail pad assemblies were then installed on the test section. These thermocouples measured the temperature at 1-second intervals.

Figure 133. Instrumented Rail Pad with Thermocouple Wires on the Side

5.11 May 2013 Field Testing at TTC

The same two sections of track were investigated at the TTC in Pueblo, CO as in July 2012. Since the July 2012 instrumentation, the 15 new concrete crossties and fastening systems on the curved section (HTL) experienced approximately 110 MGT. However, the track was tamped several times during this period. The section had been subjected to approximately 5 MGT of traffic prior to experimentation in 2013. The tangent section (RTT) was subjected to 5 MGT total and was not tamped between tests.

Apart from the instrumentation used on the section in July 2012 certain new instrumentation techniques were used which are discussed in the following section. A large set of measurements was collected on three adjacent rail seats and the opposite rail seat of the center tie (labeled orange in Figure 134). Additional rail seats in the section were also instrumented with a lower density of instrumentation as labeled in Figure 134 below.

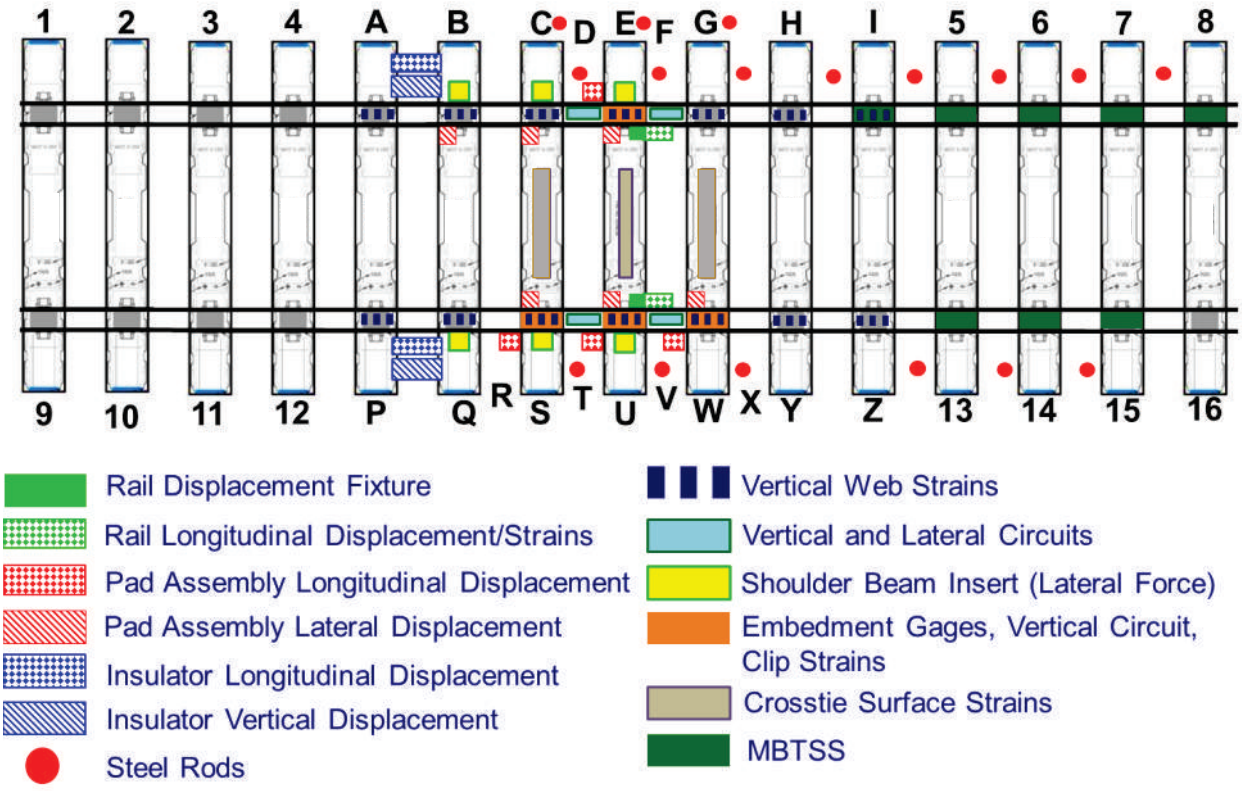

Figure 134. Locations of All Instrumentation Technologies Used During May 2013

All measurements recorded during the field experimentation along with their locations are also included in Table 23. Unless otherwise noted all the instrumentation was installed at both the sections of the test track.

Table 25. Measurements Recorded in May 2013 Field Instrumentation with Locations

Test Methodology	Reference Section	Location
Vertical Wheel Loads	4.9.1	D, F, T, V
Vertical Rail Seat Loads	4.9.2	E, S, U, W
Lateral Wheel Loads	4.9.3	E, S, U, W
Longitudinal Rail Loads	4.9.4	F, V
Vertical Rail Base Displacements	4.9.5	E, S, U, W
Lateral Rail Displacements	4.9.6	E, S, U, W
Vertical Crosstie Displacements	4.9.7	Ties C/S, E/U, G/W
Lateral Crosstie Displacements*	4.9.8	C, E, G
Internal Crosstie Strains	4.9.8	E, S, U, W
External Crosstie Strains	4.9.9	Ties C/S, E/U, G/W
Rail Seat Pressure Distributions	4.9.10	I, 5, 6, 7, 8, 13, 14, 15
Rail Base Bending Stresses	4.9.11	E, S, U, W
Insulator Post Stresses	4.9.12	E, S, U, W
Fastening Clip Stresses	4.9.13	E, S, U, W
Vertical Rail Strains	4.9.14	ALL
Lateral Force In Shoulder – Method 1	4.9.15	B, C, E, Q, S, U
Lateral Force In Shoulder – Method 2**	4.9.16	n/a
Pad Lateral Displacement	4.9.17	B, C, E, S, U, W
Pad Longitudinal Displacement	4.9.18	E, S, U, W

*Only HTL ** Not used in 2013

5.12 New or Revised Test Measurements for May 2013 Test

5.12.1 Longitudinal Rail Loads

Longitudinal rail loads were determined using an arrangement of surface strain gauges on the rail

web in between adjacent concrete crossties (Figure 4). Weldable gauges were assembled in a Wheatstone bridge and the strain values were theoretically converted to load values to understand the system.

The longitudinal stresses in the rail were measured on both sides of the rail using a strain bridge in the center of the crib. The full Wheatstone bridge uses the longitudinal strains at the neutral axis of the rail, as well as the vertical strains on each adjacent leg. The configuration of strain gauges is shown in Figure 135 and Figure 136. Each of the chevrons shown in the figures has two gauges at 90 degrees. The Wheatstone bridge connection is shown in Figure 137.

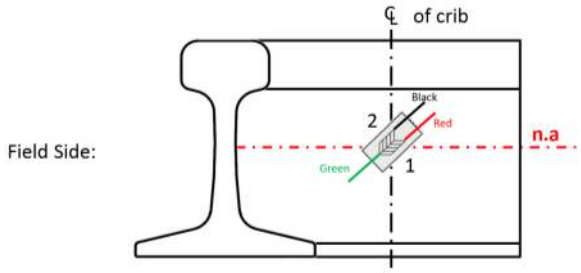

Figure 135. Strain Gauge Configuration for Longitudinal Stress Circuit (field-side)

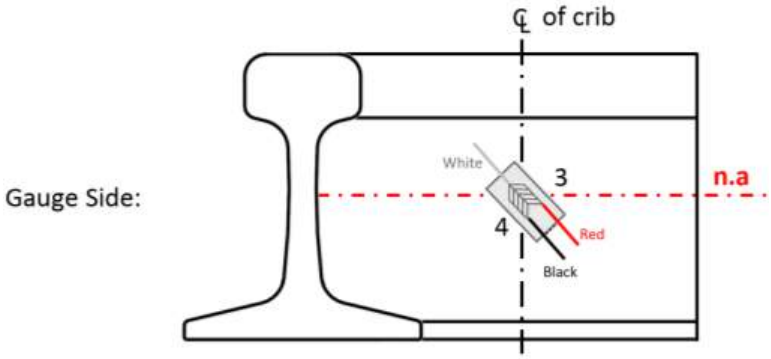

Figure 136. Strain Gauge Configuration for Longitudinal Stress Circuit (gauge-side)

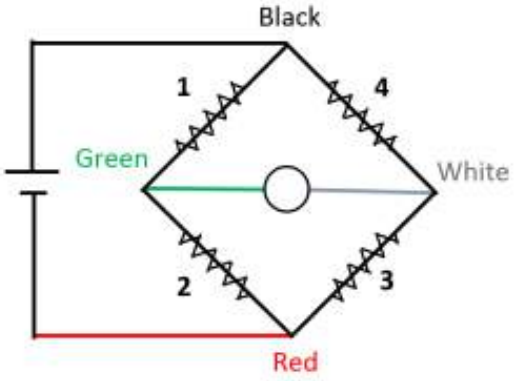

Figure 137. Wheatstone Bridge Connection for Longitudinal Stress Circuit

5.12.2 Vertical Rail Base Displacements

This measurement was the same as previously described. However, rather than affixing the aluminum fixture to the crosstie with an epoxy, as was the procedure in 2012, the fixture (Figure 138) was screwed onto the crosstie to reduce the noise and improve the accuracy of the displacement measurements. The potentiometers were positioned 1 in from the face of the tie and 1 in from the edge of the rail base on the gauge side of the rail on one side of the clip.

Figure 138. Aluminum Fixture for Potentiometer Placement

5.12.3 Lateral Rail Displacements

This measurement was the same as described previously. However, rather than affixing the aluminum fixture to the crosstie with an epoxy, as was the procedure in 2012, the fixture (Figure 139) was screwed onto the crosstie to reduce the noise and improve the accuracy of the displacement measurements. Similarly, as in July 2012, two points were measured (one at the neutral axis [1] and one at the base [2],) to determine lateral displacement, rotation and bending of the rail, about the z-direction.

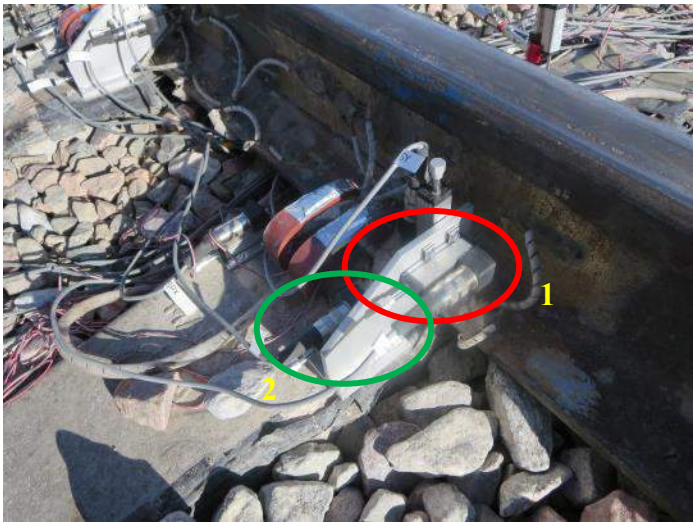

Figure 139. Lateral Displacement Potentiometers on Web (1) and Base (2)

5.12.4 Lateral Crosstie Displacements

Lateral crosstie displacements were measured at the HTL only (Figure 140) on the high rail side using linear potentiometers affixed to rods driven to refusal into the track structure.

Figure 140. Lateral Crosstie Displacement Measuring Potentiometers

5.12.5 Rail Seat Pressure Distribution

Because including MBTSS between the rail pad assembly and rail seat significantly altered the lateral load path, its implementation was offset to not affect the lateral force measurement technologies (Figure 134). Additionally, eight rail seats were outfitted with MBTSS to provide a clearer understanding of load distribution. Five adjacent rail seats were instrumented with MBTSS, with three additional rail seats instrumented on the opposite rail (Figure 134).

5.12.6 Vertical Rail Strains

The vertical rail strains were measured similarly to the July 2012 instrumentation. However, only one strain gauge was utilized on the field and gauge side to measure vertical strain at the center of the rail seat, compared to three gauges in July 2012.

5.12.7 Lateral Forces into Shoulder – Method 1

Lateral forces at the shoulder face-insulator interface were measured using LLEDs.

5.12.8 Lateral Forces into Shoulder – Method 2

The transfer of lateral force into the cast shoulder was measured at the shoulder face-insulator interface with this technology as well. An aluminum load-bearing plate was anchored to the end of the concrete crosstie. Two rods, each instrumented with strain gauges in a Wheatstone bridge, were threaded into the plate on one end and were in contact with a fabricated aluminum insulator on the other end (Figure 141). These rods acted as cylindrical load cells and were placed on either side of the cast shoulder. Strain readings from the rods were resolved into a force using theoretical calculations of axial loads acting on a cylinder. The aluminum insulator was milled out where it contacts the shoulder to ensure the entire load is being transferred through the rods.

Note that this technology was *not* used during the May 2013 test due to poor performance and results in lab and abbreviated field testing.

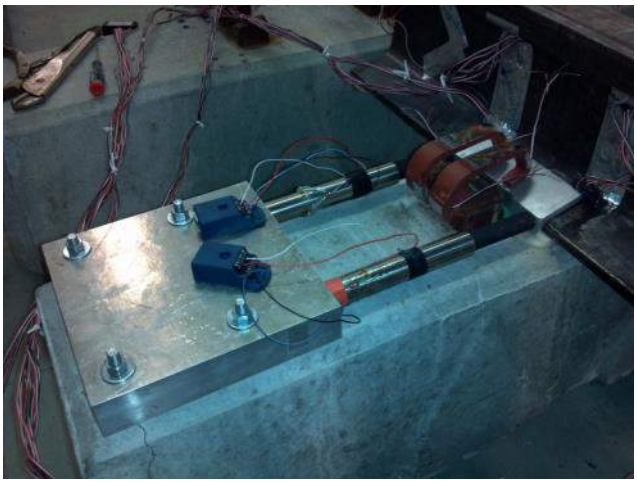

Figure 141. Plate and Rod System

5.12.9 Pad Lateral Displacements

The lateral displacement of the rail pad assembly was measured using linear potentiometers mounted on aluminum brackets and installed adjacent to the clip shoulders. The installation process consists on drilling four holes on the concrete crosstie and then tightening up the aluminum brackets and potentiometers on the crosstie with screws and nuts. The potentiometers were used oriented along the X axis, touching the abrasion frame, to measure the lateral displacement. Figure 142 shows the final configuration of the instruments used to measure the lateral displacement of the pad assembly.

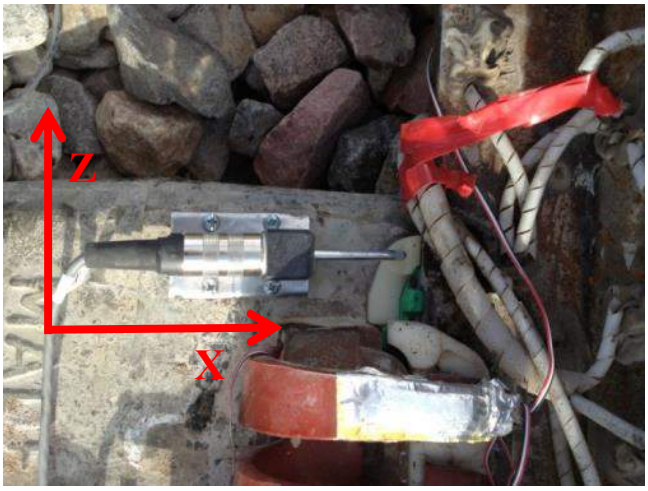

Figure 142. Potentiometer Placed to Measure the Lateral Displacement of the Rail Pad Assembly

5.12.10 Pad Longitudinal Displacements

The longitudinal displacement of the rail pad assembly was measured using linear potentiometers mounted on aluminum brackets and installed on the body of the concrete crosstie. The potentiometers were placed pointing towards the z axis (see Section 4.14 of Chapter 4), touching the abrasion frame. The installation process consisted of fixing the potentiometer on the top of the bracket and then fixing the assembly on the body of the concrete crosstie. The final configuration of the potentiometer and bracket can be observed on Figure 143.

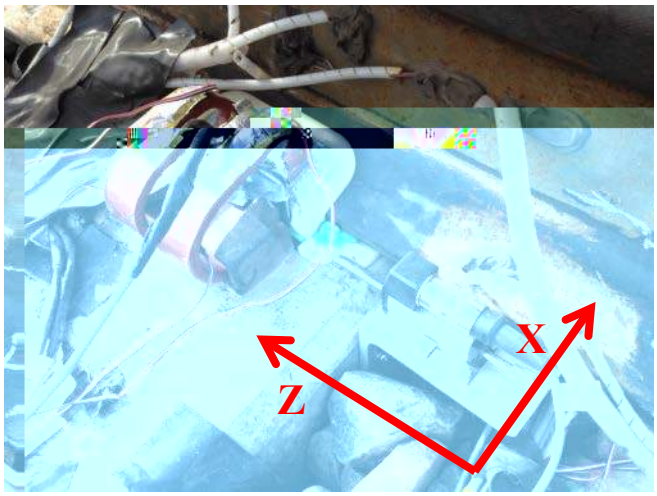

Figure 143. Potentiometer Placed to Measure the Longitudinal Displacement of the Rail Pad Assembly

Chapter 6: Field Experimental Results

6.1 Purpose

The purpose of this field experimentation was to enhance the rail industry's current understanding of concrete crosstie and fastening system behavior under representative loading conditions. This experimentation was not as controlled as the laboratory experimentation, but expected to better simulate the loading environment seen in the field. However, since testing was conducted at TTC, some variables could be controlled, which helped to better understand the effect of these parameters on the system. Additionally, testing at the TTC facilitated the installation of extensive instrumentation to collect data about the crosstie and fastening system, which would not be easily implemented in revenue service.

6.2 Objectives

To achieve the overall purpose of gaining a deeper understanding of concrete crosstie and fastening system behavior, the primary objectives of this field experimental plan were:

- **Investigation of Dynamic Loading Effects** – To understand how dynamic and impact loads differ in magnitude, distribution, and load path from static loads.
- **Characterize the Effect of Loading Environment on System Load Path** – To determine the flow of forces through the rail, fastening system, and crosstie vary under different vertical and lateral loadings.
- **Collect Representative Validation Data for Analytical Model** – To provide realistic data to develop and validate the 3D FE model of the crosstie and fastening system.

In summary, field experimentation facilitated a comprehensive study of the entire concrete crosstie and fastening system under realistic service conditions. To accomplish this, the interaction between different components was analyzed by applying static and dynamic loadings on both tangent and curved track. Static loadings were applied in both the vertical and lateral direction at varying magnitudes and rail seat locations. Dynamic loadings were applied by both passenger and freight consists passing at varying speeds and track geometries.

6.3 Methodology

6.3.1 Location/Zones

Field experimentation was conducted at the TTC in Pueblo, CO. Field experiments and results described in this report were conducted on a segment of tangent track on the RTT and a segment of curved track on the HTL at the TTC. The curvature on the HTL section was approximately 5 degrees. The RTT and HTL sections are shown as track number 3 and 1, respectively, in Figure 143 below. For both sections, 15 new concrete crossties were installed and tamped prior to experimentation. The test sections used a 136RE rail section, concrete crossties spaced at 24-inches center-to-center, Safelok I fastening systems, and premium ballast.

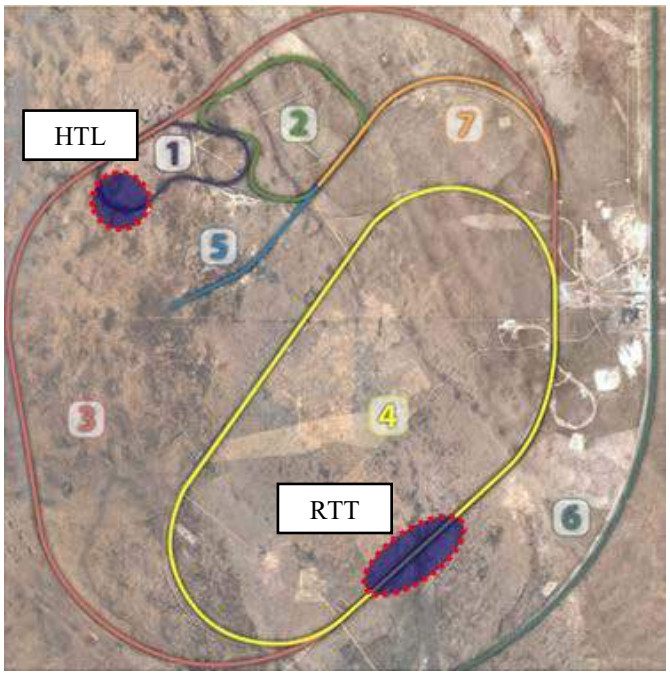

Figure 144. Map of Test Tracks at the TTC

Experimentation was conducted and data was collected at the same locations in July 2012 and May 2013. Instrumentation maps for July 2012 and May 2013 are shown below in Figure 144 and Figure 145, respectively. Detailed information behind the instrumentation setup of the July 2012 testing can be found in Volume 2, Chapter 5, Field Experimental Plan, Section 5.10. The May 2013 testing used the existing instrumentation from July 2012 and added several new technologies to take new measurements. This is explained further in the Field Experimental Plan.

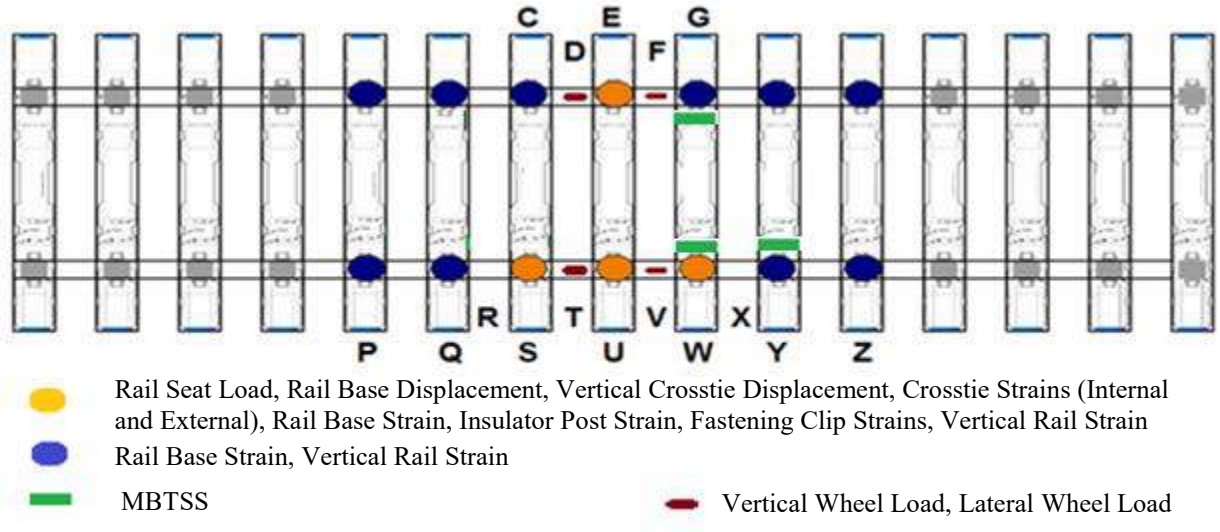

Figure 145. Instrumentation Map for July 2012 Experimentation

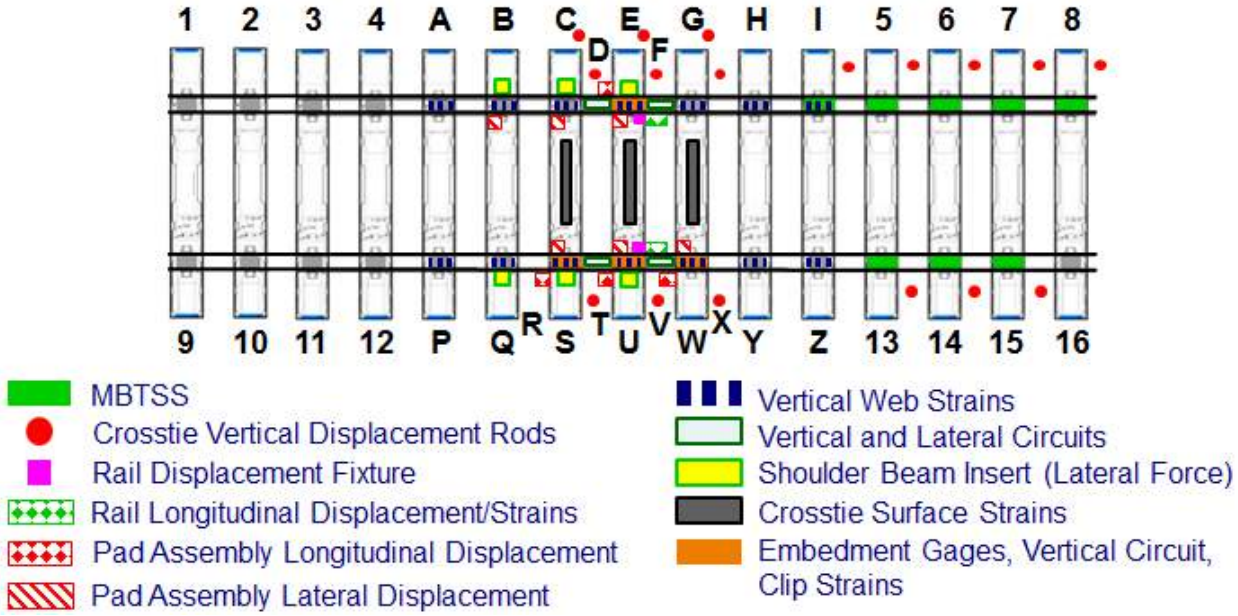

Figure 146. Instrumentation Map for May 2013 Experimentation

6.3.2 Loading/Procedure

Static loading scenarios (e.g. load magnitudes, L/V force ratios, etc.) were applied to the track using the AAR TLV. The TLV uses a deployable axle capable of applying various combinations of vertical and lateral loads to simulate typical track loading conditions. Loads were applied to the track directly above the instrumented crossties, as well as in the crib between crossties. For both July 2012 and May 2013 experimentation, applied vertical loads ranged between 0 and 40 kips and applied lateral loads ranged between 0 and 24 kips. This allowed testing to be performed at L/V force ratios of 0.0 to 0.6.

Dynamic loading scenarios were applied by using passenger and freight consists. The passenger consist had a locomotive weighing 263 kips and nine passenger cars weighing 87 kips. The freight consist had a locomotive weighing 263 kips and ten freight cars weighing 263, 286, and 315 kips. On the RTT, the passenger consist was operated at 2, 15, 30, 60, 80, 90, and 105 mph and the freight consist was operated at 2, 15, 30, 60, 70 mph. On the HTL, the passenger consist was run at 2, 15, 30, and 40 mph and the freight consist was run at 2, 15, 30, 40, 45 mph. A single flat spot was present on one 263-kip car in the freight consist to simulate impact loadings seen from wheel/rail imperfections.

6.4 Wheel/Rail Vertical and Lateral Input Loads

6.5 Background

The purpose of this field experimentation was to enhance the current understanding of the crosstie and fastening system component behavior under representative loading conditions. Therefore, it is the objectives of this section to verify that the loading conditions applied to both test sections were indeed representative of revenue service loading conditions. Additionally, experimentation was designed to quantify the wheel-rail loads to use as inputs into the FE model and the laboratory experimentation.

Wheel loads vary due to many factors, including, but not limited to, static load, speed, temperature, location, position within the train, vehicle characteristics, track geometry and quality, curvature, and grade (Van Dyk 2014). Previous research has shown that the nominal (static) wheel load is the best indicator of the load expected to enter into the track structure and is highly dependent on the type of vehicle passing over the track. It was shown that, in general, vehicles with higher nominal wheel loads produce higher peak wheel loads. However, there is a wide distribution beyond the most highly concentrated data, suggesting there are other factors affecting the peak load entering the track structure (Van Dyk 2014, Scheppe 2015).

For the purposes of this field experimentation, it is hypothesized that the change in vertical dynamic factor due to speed can be expressed by Equation 1 (Van Dyk 2013a):

$$Peak/_{Nominal} = 1.099 + 0.00386\ (Speed(mph)) \qquad (1)$$

While many of the wheel loads do exceed the predicted dynamic factor in revenue surface, it is likely not a result of speed, but one of the other variables discussed earlier. The wheel loads that do exceed this predicted dynamic factor can more appropriately be incorporated into an impact factor (Van Dyk 2013a). Generally, impact forces are caused by imperfections in the moving vehicles (e.g. wheel flats), track geometry imperfections, and variations in track stiffness (Van Dyk 2013b).

6.6 Methodology

Vertical and lateral wheel loads were quantified under freight and passenger trains using the instrumentation and methodology described in Volume 2, Chapter 5, Section 5.10. The experimental matrix described within Section 5.4 was executed and provided dynamic data at speeds varying from 2–105 mph on tangent and curved track.

It is important to note that there was one known flat spot on a wheel within the freight consist, which is pictured in Figure 146. Due to the configuration of the instrumentation deployed, it was not possible to capture this flat spot on every train pass, but it was frequently captured by a variety of instrumentation types. While the sample size collected for impact loads was too small to make accurate generalizations, some conclusions relevant to crosstie and fastening system design and performance can be drawn.

Figure 147. Large Flat Spot on the Wheel of Freight Consist

6.7 Vertical Loads

Figure 147 is a plot of the peak and nominal wheel loads observed at the WILD site at Gothenburg, NE, as well as all the wheel loads recorded during experimentation on the RTT at the TTC. Lines representing impact factors (IF) of 1.5, 2, 3, 4, and 5 have been included in Figure 147 to further describe the data distribution. Through visual inspection of the data, the wheel loads measured during the experimentation on the RTT fall in-line with the data collected at UP's Gothenburg WILD site.

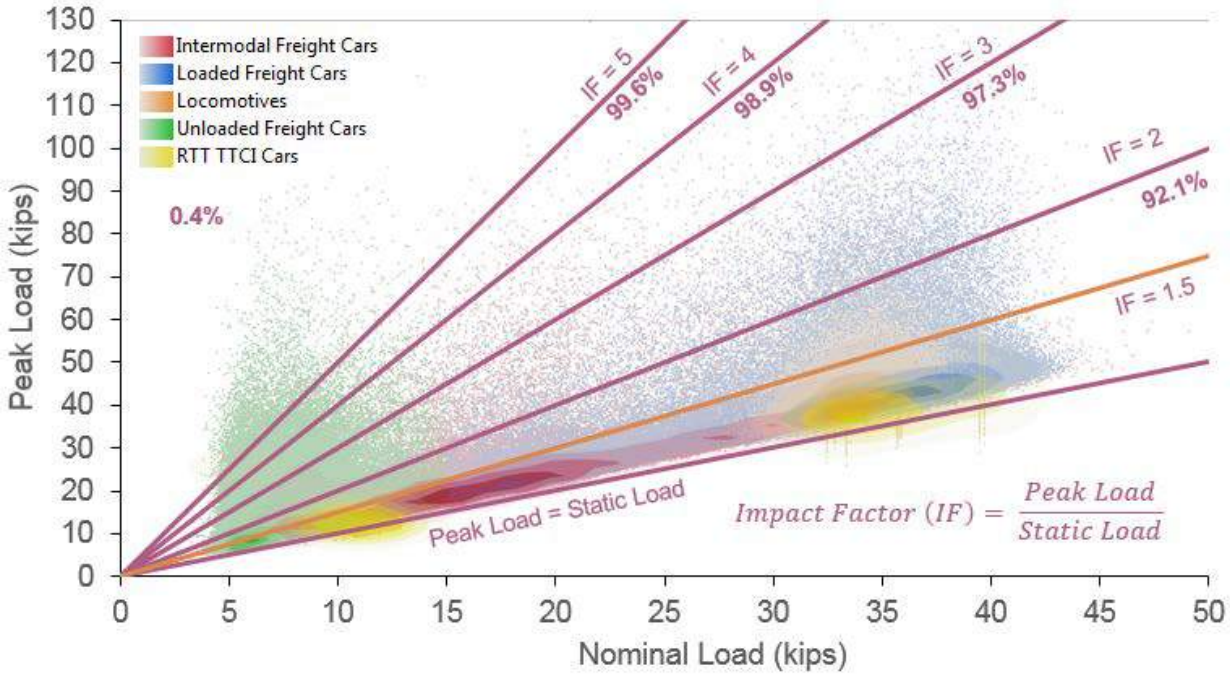

Figure 148. Relationship Between Peak and Nominal Wheel Loads on UP at Gothenburg, NE, (WILD Data from January 2010) and Design IF

Table 26 shows the results from a more detailed analysis of the wheel-loads measured on the RTT at the TTC compared to the UP Gothenburg WILD site.

Table 26. Dynamic Factors Measured on RTT

Speed	263K Cars*	286K Cars*	315K Cars*	Passenger Cars*	Predicted**
2	1.11	1.09	1.06	1.05	1.11
15	1.12	1.10	1.09	1.09	1.16
30	1.15	1.12	1.11	1.16	1.21
60	1.36	1.25	1.29	1.21	1.33
70	1.38	1.25	1.27	n/a	1.37
80	n/a	n/a	n/a	1.26	1.41
90	n/a	n/a	n/a	1.32	1.45
105	n/a	n/a	n/a	1.34	1.50

*Dynamic factors were calculated based on the 99% peak confidence values.
**Predicted values were calculated using Equation 1.

Table 26 shows that though the freight vertical loads were expected to increase by a factor of 1.37 at 70 mph, the 263K cars exhibited the largest dynamic increase of 1.38, followed by the 315K cars at 1.27, and 286K cars at 1.25. Furthermore, although the passenger car vertical loads were expected to increase by a factor of 1.5 at speeds of 105 mph, they only exhibited a factor of 1.34. In fact, when analyzing all values within Table 26, it was evident that the predicted values were almost always greater than the recorded values, with the only outlier being the 263K cars. One reason for this can likely be attributed to the method in which wheel loads were characterized on the RTT (e.g. only two vertical load bridges were installed and the highest peak load was not always recorded). Additionally, the overall wheel and track health was better on the RTT compared to WILD sites. Even so, the difference between predicted and actual dynamic factors never exceeded 10%. Therefore, the loading environment was considered to be representative of revenue service.

The measured vertical wheel loads (99% confidence peak values) are listed below in Table 27. Additionally, these loads have also been plotted against speed and compared to their static car weight wheel loads in Figure 148**.**

Table 27. Vertical Loads Measured on RTT

Speed	263K Cars*	286K Cars*	315K Cars*	Passenger Cars*
2	36.5	39.0	41.8	11.4
15	36.9	39.2	43.0	11.8
30	37.9	40.0	43.7	12.5
60	44.7	44.8	50.6	13.2
70	45.4	44.7	50.2	n/a
80	n/a	n/a	n/a	13.7
90	n/a	n/a	n/a	14.4
105	n/a	n/a	n/a	14.6

*Vertical loads calculated based on the 99% peak confidence values

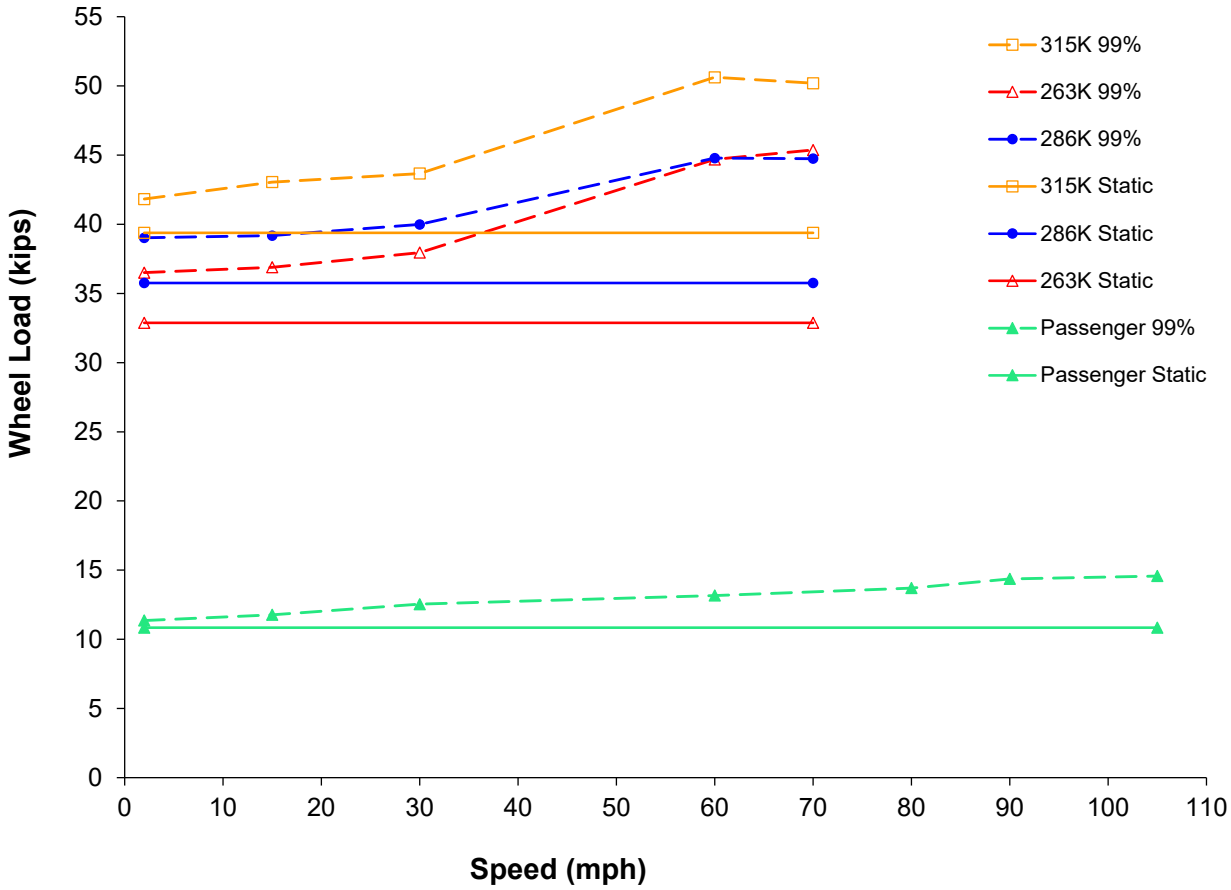

Figure 149. Vertical Wheel Loads (99% confidence) of Freight and Passenger Cars at Various Speeds on Tangent Track (RTT)

Figure 148 illustrates the expected behavior of increased wheel load magnitudes at increasing speed. The 263K cars continued to be an outlier in the data set. This is evident at 70 mph when the measured loads were larger than the 286K cars at the same speed. This can be attributed to that fact that the wheel rail loads are effected by, but not limited to, static load, speed, temperature, location, position within the train, vehicle characteristics, track geometry and quality, curvature, and grade. Therefore, because the loads are influenced by many factors, and the sample size is relatively small, no general conclusions can be made as to why this occurred. Nevertheless, the general conclusion drawn by previous researchers is that the nominal (static) wheel load is the best indicator of the load expected to enter into the track structure was confirmed.

6.8 Lateral Loads

A similar analysis, compared to the RTT vertical load quantification, was performed with the wheel load data acquired on the HTL. The focus of this analysis was on the lateral loads and L/V force ratio. The lateral wheel loads (99% confidence peak values) are provided in Table 28 while the data is presented graphically in Figure 149 below. The maximum lateral load recorded throughout the duration of this experimentation was 21.3 kips under the 315K car at 45 mph on the high rail.

Table 28. Lateral Loads Measured on HTL

Speed	263K Cars High Rail	263K Cars Low Rail	286K Cars High Rail	286K Cars Low Rail	315K Cars High Rail	315K Cars Low Rail	Passnger Cars High Rail	Passenger Low Rail
15	8.56	12.29	9.09	13.61	7.23	11.99	1.77	3.89
30	12.24	12.15	14.45	12.96	11.89	12.08	2.30	4.11
40	13.86	11.64	13.90	13.98	14.06	11.78	3.74	3.35
45	15.38	12.24	16.77	12.63	16.12	11.84	4.26	3.08

*Vertical loads calculated based on the 99% peak confidence values

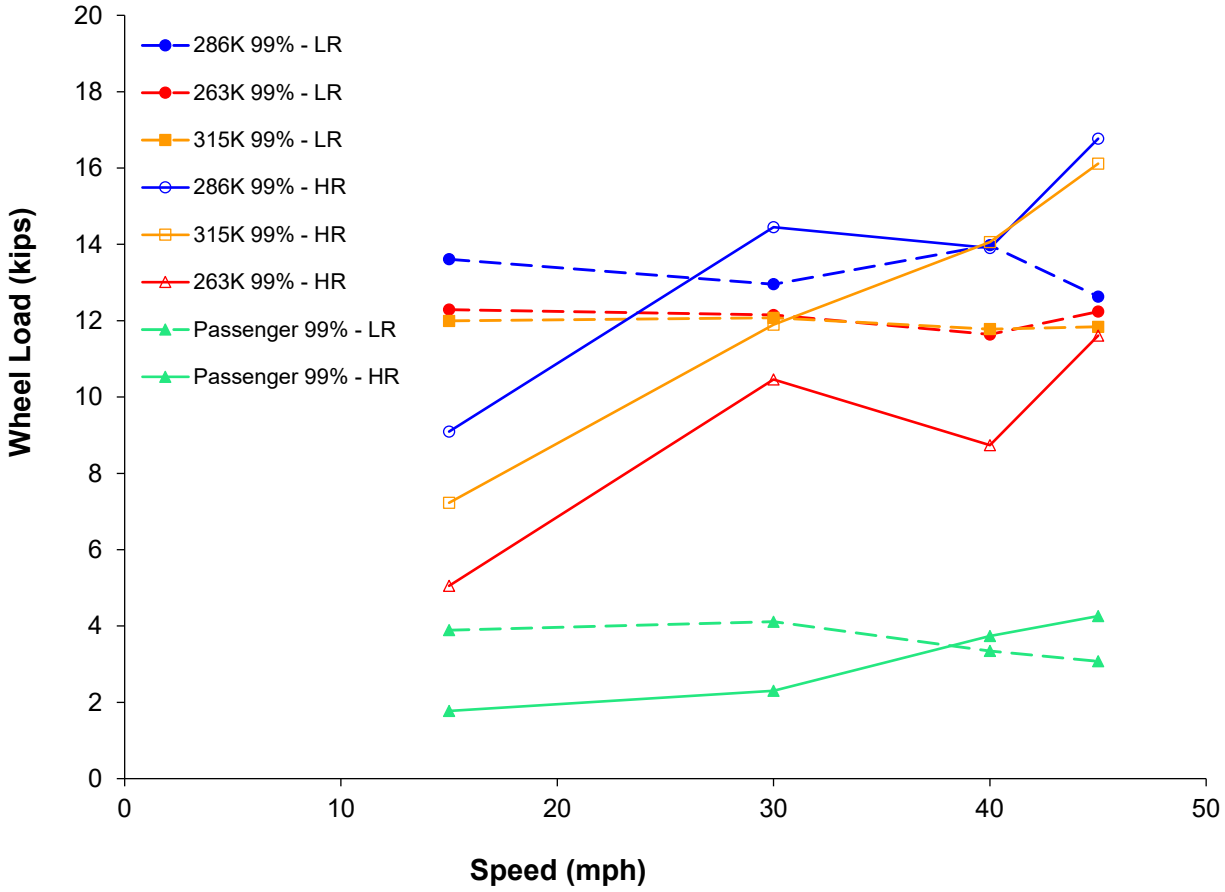

Figure 150. Lateral Wheel Loads (99% confidence) of Freight and Passenger Cars at Various Speeds on High and Low Rails of Curved Track (HTL)

Figure 149 illustrates that the wheel loads on the high rail increased with increasing speed, as expected. Table 29 quantifies the effect of speed on the increase in lateral load on the high rail by providing the dynamic load factors, assuming 15 mph as the baseline load. From this data, for these specific curves and car types there was an increase in lateral loading of up to 2.23 for freight cars and 2.4 for passenger equipment. Furthermore, when looking only at the freight data, there appears to be a general trend of increased dynamic lateral load factor with increased nominal load.

Previous research has found that, in general, vehicles with higher nominal wheel loads produce higher peak wheel loads. However, the data recorded on the HTL does not confirm this trend.

In fact, while the dynamic load factors presented in Table 29 do agree with this statement, the lateral load magnitudes do not. Though the 263K cars did exhibit the smallest lateral loads, the 286K cars exhibited the largest lateral load, while the 315K cars were in between. Due to the size of the sample size, no reason for this can be provided.

Table 29. Lateral Load Dynamic Factors on HTL, High Rail

Speed	263K Cars	286K Cars	315K Cars	Passenger Cars
15	1.00	1.00	1.00	1.00
30	1.43	1.59	1.65	1.30
40	1.62	1.53	1.95	2.11
45	1.80	1.84	2.23	2.40

*15 mph was arbitrarily considered to be the base loading scenario

Another point of interest regarding Figure 147 is the behavior of the loads on the low rail. It was hypothesized, and has typically been seen in data, that as speed increases, the low rail force will decrease. However, as can be seen, the freight loads on the low rail stay relatively constant at all speeds, compared to the high rail. Because of this anomaly, the dynamic lateral load factors for the low rail were also investigated and are provided below in Table 30. This table shows that the freight cars exhibited, at most, a decrease to 0.93 and the passenger cars exhibited, at most, a decrease in load factor to 0.79. Though, no conclusions can be made as to the specific reason for why this occurred, it is known that the wheel profile used in conjunction with the freight cars on the HTL is significantly different (i.e. conformal) compared to standard wheel profiles of cars in revenue service.

Table 30. Lateral Load Dynamic Factors on HTL, High Rail

Speed	263K Cars	286K Cars	315K Cars	Passenger Cars
15	1.00	1.00	1.00	1.00
30	0.99	0.95	1.01	1.06
40	0.95	1.03	0.98	0.86
45	1.00	0.93	0.99	0.79

*15 mph was arbitrarily considered to be the base loading scenario

Finally, the freight data was analyzed to better quantify and understand the L/V force ratios as a function of train speed on the HTL. Figure 150 shows that for the specific curve instrumented and the equipment used, L/V ratios on the low rail deviated on average by only 4% and did not deviate by more than 15%, as in the case for the 315K car at 30 mph. L/V ratios on the high rail meanwhile deviated from the 15-mph loading scenario, by 14% and experienced a maximum reduction in L/V of 26%. Therefore, when comparing this data to Table 29 and Table 30 above, we see that the lateral load on the high rail increases at a greater rate than the vertical load and that the vertical and lateral loads on the low rail remain relatively constant at all speeds. Additionally, Figure 150 shows no relationship between nominal car weight and L/V ratio. Therefore, it is hypothesized that wheel profile has a greater effect on lateral loads, and the resulting L/V force ratio, than nominal car weight.

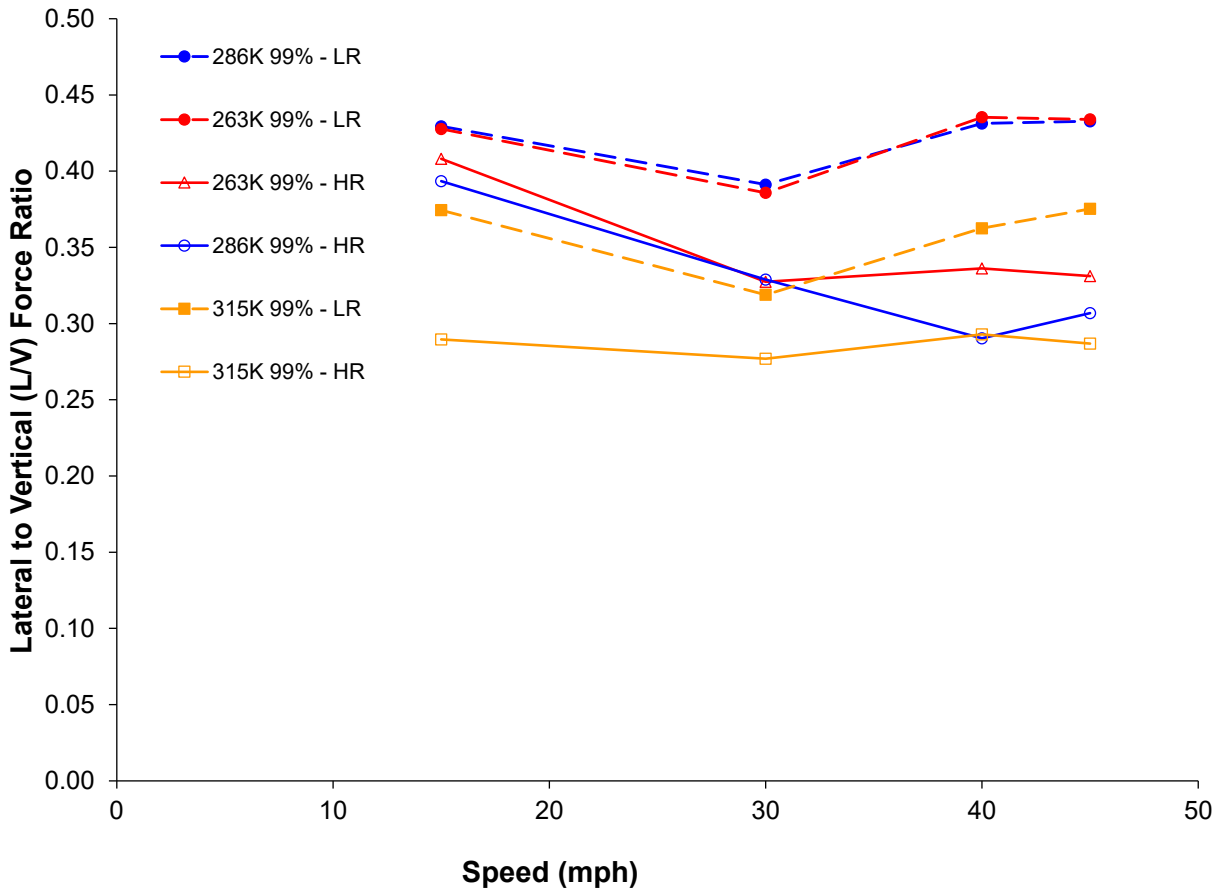

Figure 151. Relationship Between Nominal Car Weight and L/V Load Ratio as a Function of Train Speed

6.9 Summary

The lateral and vertical wheel load data collected from field experimentation yielded several critical findings:

- Dynamic vertical wheel load factors ranged from 1.05 to 1.50 and were, in general, below the predicted values, but the difference was never greater than 10%. The loading environment was, therefore, considered to be representative
- There is a relationship between car weight and vertical load (i.e. as car weight increases, vertical wheel load increases). This confirms previous research in this area.
- There was no trend between nominal car weight and lateral load in the curve studied. This contradicts previous research and conventional wisdom in this area.
- The high rail freight and passenger lateral loads were significantly affected by speed, relative to the low rail. The lateral load dynamic factors were 2.23 for freight and 2.40 for passenger.
- The low rail freight car lateral loads were not significantly affected by speed, relative to the high rail. The lateral load dynamic factor decreased from 1.00 to 0.93.

- The maximum L/V force ratio recorded under freight equipment was 0.60, and typically ranged between 0.29 and 0.44.
- There was no relationship between L/V force ratio and nominal car weight.

6.10 Normal and Tangential Clamping Forces

6.11 Background

The fastening system is designed to attach the rail to the crosstie as well as to maintain gage (Hay 1982). Additionally, the components that make up these systems should be resistive to wear and fatigue (Armstrong 2008). Couple this with the fact that fastening system fatigue is considered one of the most critical areas for research by members of the North American rail industry (Volume 2 Chapter 1, International Survey Results, Section 1.6), the mechanics of the elastic clip under load were investigated.

The principle objectives of this experimentation were to quantify: 1) how the strain within the clip is affected by a change in clamping force, 2) how the clamping force is affected when subjected to static and dynamic wheel loading, 3) the longitudinal length of track in which clamping force is significantly affected by load. To reach these goals and the objectives of field experimentation, instrumentation was developed and deployed to quantify the magnitude and distribution of lateral fastening system forces.

6.12 Methodology

Two sets of field experiments were conducted at the TTC in Pueblo, CO. For both sets of experiments, instrumented clips were placed on three adjacent rail seats, S, U, and W on the low rail and one rail seat, E, on the high rail. Additionally, linear potentiometers were positioned at each instrumented rail seat to capture vertical rail base deflection. The data gathered was analyzed using the methodology and assumptions presented within Chapter 5. The track was loaded using the TLV as well as passenger and freight consists. More information about the equipment used and speeds tested at can be found within Chapter 5.

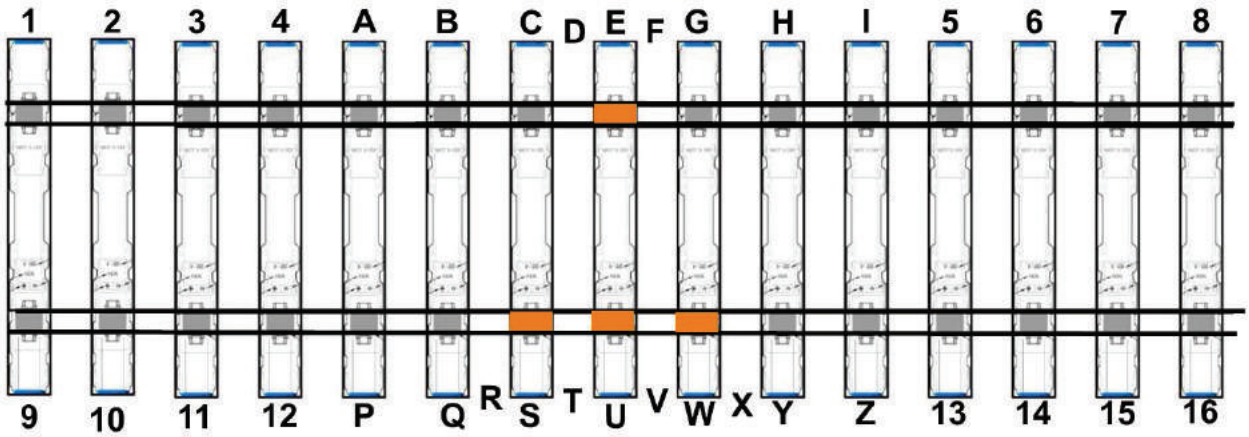

Figure 152. Locations of Instrumented Clips at RTT/HTL (May 2013, TTC)

To better characterize the mechanics of the clip, it was determined that the clamping force that is commonly reported, should be broken into its normal and tangential components. The normal

component of clamping force is perpendicular to the top of the rail base while the tangential component is parallel to the top of the rail base. These components are defined and presented in Figure 152.

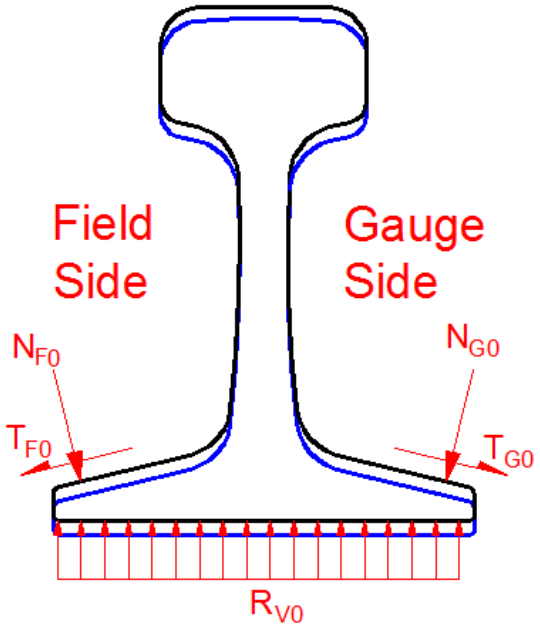

Figure 153. Initial Clamping Force Applied to Rail Base

Where:

- $N_{F0/G0}$: Normal component of clamping force at field/gauge side
- $T_{F0/G0}$: Tangential component of clamping force at field/gauge side
- R_{V0}: Rail seat reaction force

Safelok I type clips have been extensively used in North America on heavy haul railroads and the detailed properties of this type of clip are provided in Table 31. The clips used during experimentation had a pair of 2,375-lbf clamping forces when installed properly applied to both the field and gauge side of rail; and a 4,750-lbf nominal force applied normal to the rail seat. From this information, the normal component of the force applied to the clip tip can be calculated as 2,500 pound-force. However, the tangential component cannot be calculated because the sign and the magnitude depend on installation.

Table 31. Clip Properties

Thickness (in)	Weight (lb)	Material	Toe Load
0.315	1.5	Amsted RPS UAB 2000	4,750 lbf/ Seat Nominal

High strength steel was used to produce the clips and the material properties of the high strength steel used for analysis are listed in Table 32. The elastic modulus of the steel is 23,000 ksi which is slightly lower than typical structural steel. The yield stress and strain are 183 ksi and 7,957 ms respectively.

Table 32. Material Properties of the Clip

Material	Elastic Modulus (E)	Yield Stress (fy)	Yield Strain (y)
Amsted RPS UAB 2000	23,000 ksi	183 ksi	7,957 ms

6.13 Effect of Change in Clamping Component Force on Clip Strain

Referring to the Laboratory Experimental Results, the maximum strain found at the clip after installation might surpass 90% of the yield strain of the steel. Because it appears there is a small safety margin in the design, a change in normal or tangential force could result in exceeding the clip yield limit in strain, which would lead to plastic deformation of the clip.

If a clip plastically deforms, there is a resulting loss of clamping force. A loss of clamping force could lead to accelerated wear and fatigue of other fastening system components. Therefore, to understand the relationship between the change in clamping force components and strain (tensile/compressive) along the clip, a Matlab program which uses Euler-Bermoulli theory was developed. The minimum and maximum clip strains under various combinations of normal and tangential force are shown in Figure 153.

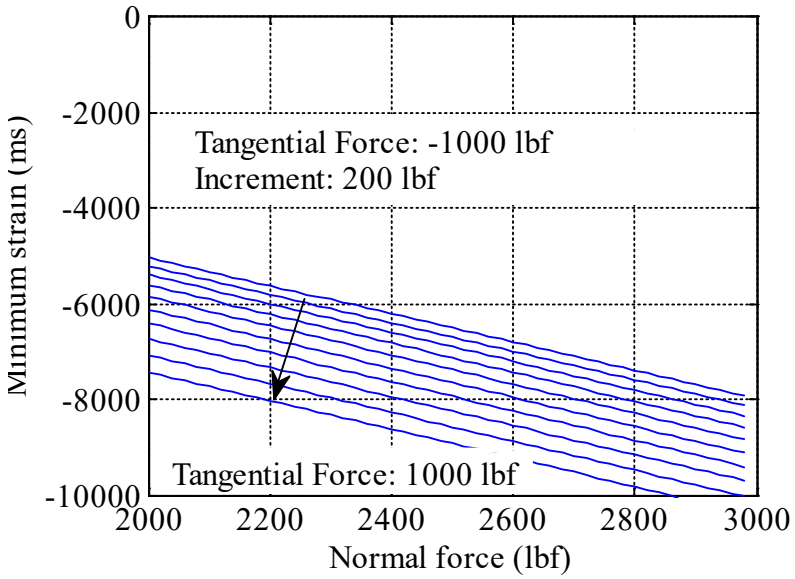

a)

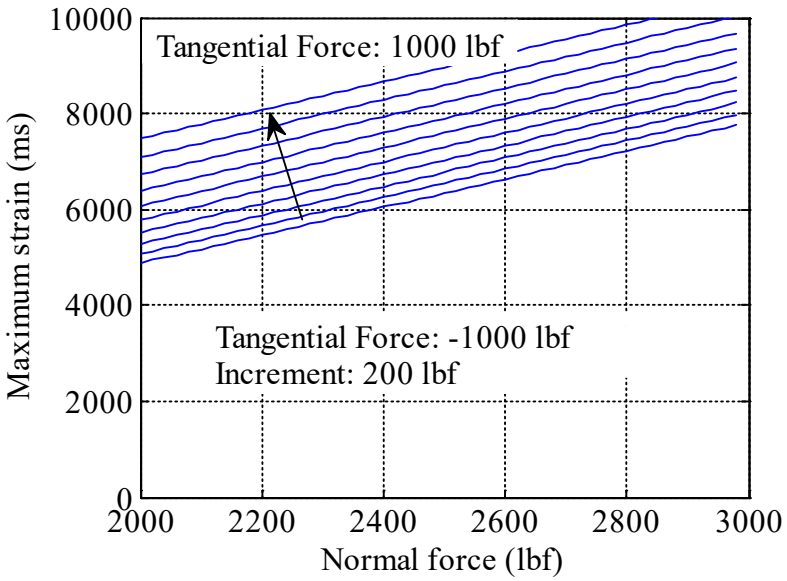

b)

Figure 154. a) Minimum strain (compressive) on outer surface of a clip under various normal and tangential forces; b) Maximum strain (tensile) on inner surface of a clip under various normal and tangential forces.

Figure 153 shows that as normal or tangential force increase there is an increase in the maximum strain on the clip. Furthermore, when the normal force is 2500 pound-force, a 200-lbf tangential force would cause the clip to surpass the material yielding limit.

6.14 Clamping Force and Clip Strains Due to Installation

The motivation for measuring the initial clamping forces in the field tests was to find the actual clamping forces applied to clips and to determine if these clamping forces would result in plastic deformation.

In May 2013, TTC tested instrumented clips that were installed at both field and gauge sides of rail-seats E, S U and W for both RTT and HTL (Figure 151). Before and after the clip installation, the strain values were recorded from each gauge manually using the NI strain gauge indicator box. Clip strains due to the installation process have been subtracted afterwards.

The initial tangential force applied to each clip tip was calculated and shown in Figure 154, in which the x-axis is the average of the absolute strain value measured from the four strain gauges installed on each clip.

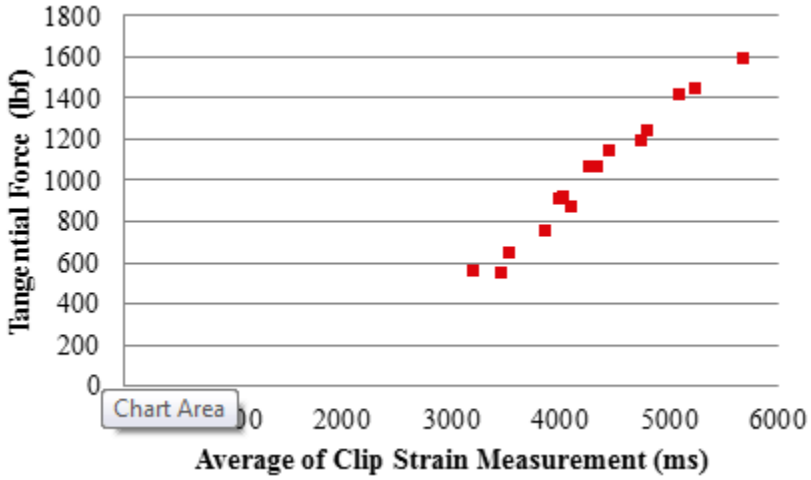

Figure 155. Initial Tangential Force at RTT and HTL

From Figure 154, it was found that the range of the tangential force varied from 551 pound-force to 1,588 pound-force, which was approximately 20-60% of the normal force. The maximum tangential force recorded was located at the gauge side of rail seat U at the RTT, the maximum tangential and compressive strain under this pair of clamping forces (2,500 pound-force for normal force, 1,588 for tangential force) were calculated as 10,600 ms and -10,500 ms, which were 32% higher than the calculated yielding strain. These observations reveal that the clip design might be inadequate even when only considering installation, and further investigation is warranted.

In addition to the magnitude, the tangential component was found to be always positive, which means after the clip installation process, there was a tangential force pulling the clip tip and holding it in place. It should be noted that the clips tested in this field study were installed by hand. It is also known that there is significant variability in clip strains and forces depending on the installation procedure.

6.15 Effect of Static Wheel Loads on Clamping Force Components

The normal component of clamping force was anticipated to decrease under a purely vertical wheel load, while when subjected to vertical and lateral loads, the gauge side clamping force was

expected to increase. Using the current analysis methodology, only the change of clamping force at the gauge side can be determined.

When only vertical wheel load was applied by the TLV, the rail pad was compressed as if the vertical load was applied right above the center of the rail seat. The average normal and tangential components of clamping force when subjected to 0-40-kip vertical wheel load on the RTT is shown in Figure 155**,** when the TLV static wheel load was applied directly above each rail seat.

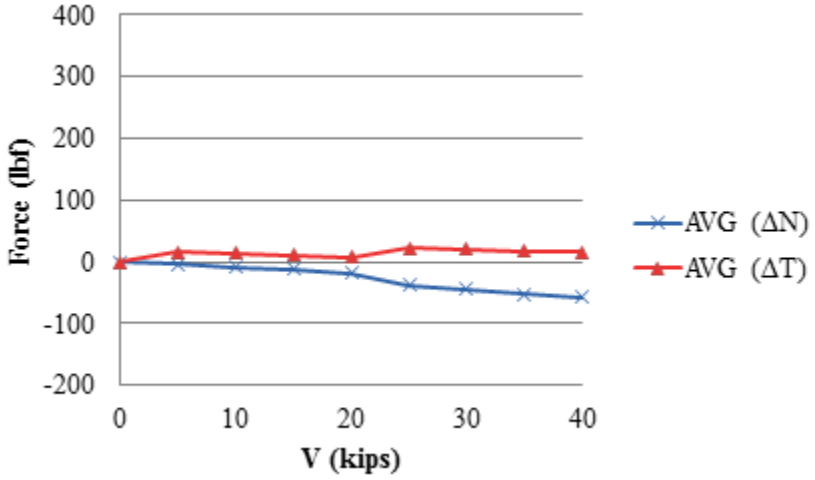

Figure 156 Change in normal and tangential force under various vertical wheel loads

The compression of the rail pad is equivalent to the action of spring relief to the clips. From Figure 156**,** the normal component of clamping force decreased slightly, which agrees with this spring relief action. Under a 40-kip vertical wheel load, the average change in the normal component of clamping force was -57 pound-force which was -2.3% of initial normal force, and the change of tangential force was only 15 pound-force. This observation revealed that there was practically no lateral translation of rail base under pure vertical wheel load. Therefore, the change in normal and tangential forces was considered to be very small, relative to the initial clamping force values.

Because the normal force always decreased and the tangential force remained relatively constant, clips subjected to a purely vertical force, would not be harmful to the clips when referring to the trend displayed in Figure 153.

When the vertical wheel load applied by the TLV was 40 kips on both rails (at RTT), a lateral force was applied to the gage side of both rails while maintaining the 40-kip vertical load. Figure 156 shows the average normal and tangential forces due to the application of lateral wheel loads.

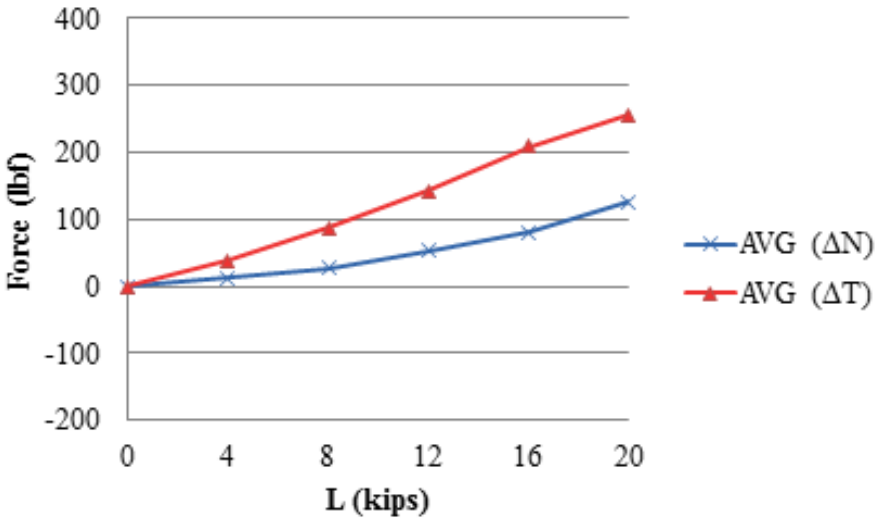

Figure 157. Change in Normal and Tangential Forces Under 40 kip Vertical and Various Lateral Wheel Loads

The rail rotation and translation which occurred as a result of the lateral load led to an increase in the normal and tangential component of the clamping force as shown in Figure 156. The gauge-side clip at rail seat E experienced the greatest change in normal clamping force; an average increase of 127 lbf, or 5.1% of the initial normal force. The greatest change in tangential clamping force was 256 lbf in average under a 20-kip lateral force. The tangential forces measured ranged from 230 lbf to 270 lbf.

Figure 153 reveals that an increase in normal and tangential clamping force leads to an increase in the maximum clip strain (both in tensile and compressive). Therefore, if one assumes that the normal clamping force is 2,500 lbf and there is zero tangential force, then when a 40-kip vertical and 20-kip lateral wheel load is applied to the rail, the normal and tangential forces were 2,578 lbf and 219 lbf for the gauge side clip at E, 2,537 lbf and 129 lbf for S, 2,534 lbf and 192 lbf for U, 2,630 lbf and 199 lbf for W. This would lead to tensile and compressive strains of +/-8,200 ms, +/-8,000 ms, +/-8,100 ms and +/-8,400 ms, which were 3.1%, 1.0%, 1.8% and 5.6% higher than the yielding strain calculated using the assumptions presented in Chapter 5 Section 5.10.15.

6.16 Effect of Dynamic Wheel Load on Change of Clamping Force Components

Under constant speed wheel load

In this section, the change in clamping force under constant speed wheel loads was examined. From the static analysis, the change of clamping force was found to be highly dependent on the lateral wheel load. In the following discussion, the vertical wheel load was held constant at 40 kip as various lateral loads were applied. The speed of the TLV was held constant at 15 mph. Given the TLV provided the same loading for both rails, it was assumed that the clip behavior at the high rail and the low rail would not differ greatly. Only the data recorded from RTT is presented here. Figure 157 shows the normal and tangential components of the clamping force.

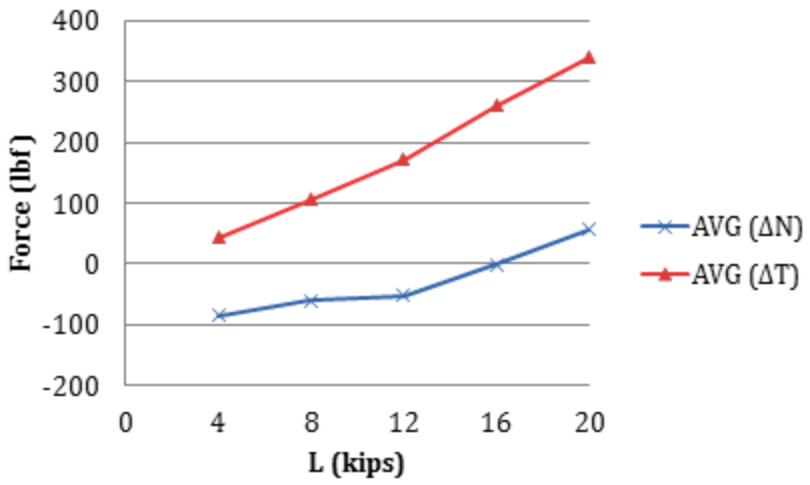

Figure 158.Change in Normal and Tangential Force at Gauge Side Clips Under 40-kip Vertical Load and Various Lateral Loads (TLV speed = 15 mph)

A greater variation was found in both the normal force and the tangential force. A similar trend was found, and the magnitude of the change of normal force decreased from 127 lbf to 57 lbf under 20-kips lateral force; while the tangential force increased from 256 lbf to 339 lbf.

Comparison between passenger and freight consist

Figure 158 and Figure 159 show the correlation between the change of normal and tangential component of clamping force with the lateral wheel load.

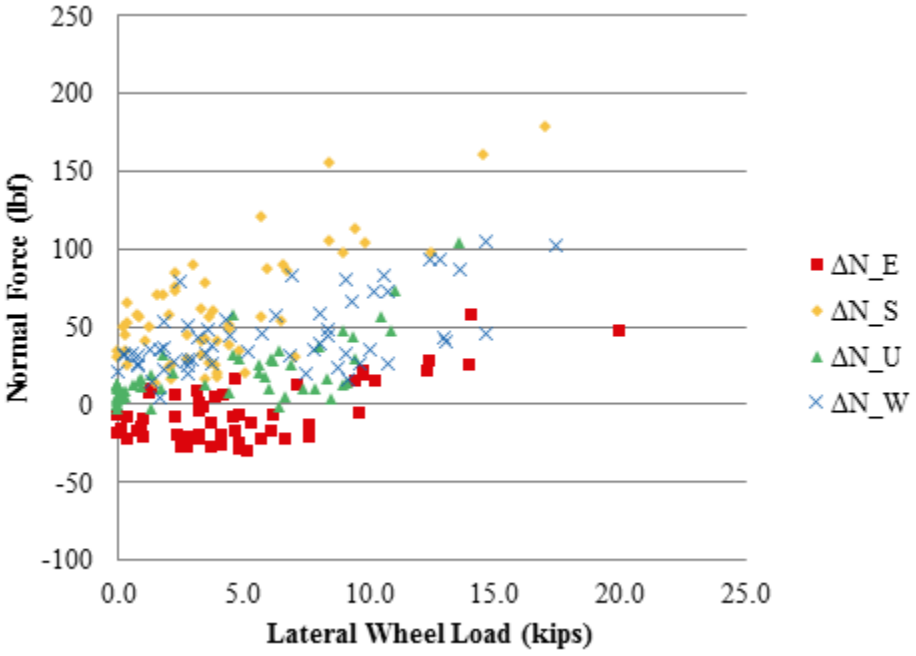

Figure 159. Change of Normal Force of Gauge Side Clips Under 45 mph Train Traffic (HTL)

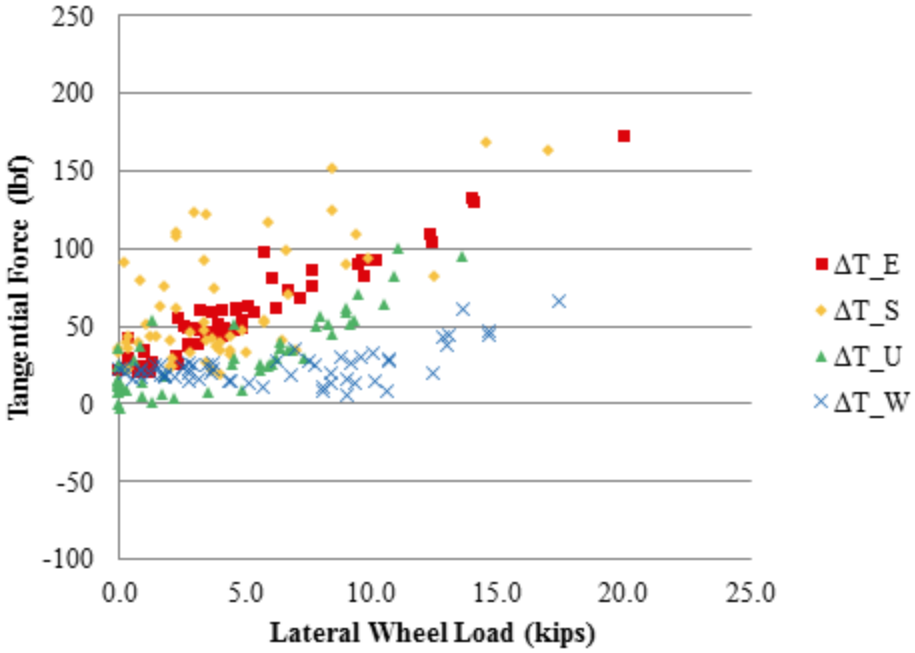

Figure 160. Change of Tangential Force of Gauge Side Clips Under 45 mph Train Traffic (HTL)

Generally, there was a stronger positive correlation between lateral wheel load and the change in tangential clamping force as compared to the change in normal clamping force. The gauge side clip at the center rail seat in the testing section (rail seat U) will be focused on in the following discussion.

Figure 160 and Figure 161 show the normal and tangential components of the clamping force with respect to the train speed for the passenger consist. Figure 162 and Figure 163 show the normal and tangential components of the clamping force measured from this clip with respect to the train speed and car weight for the freight consist.

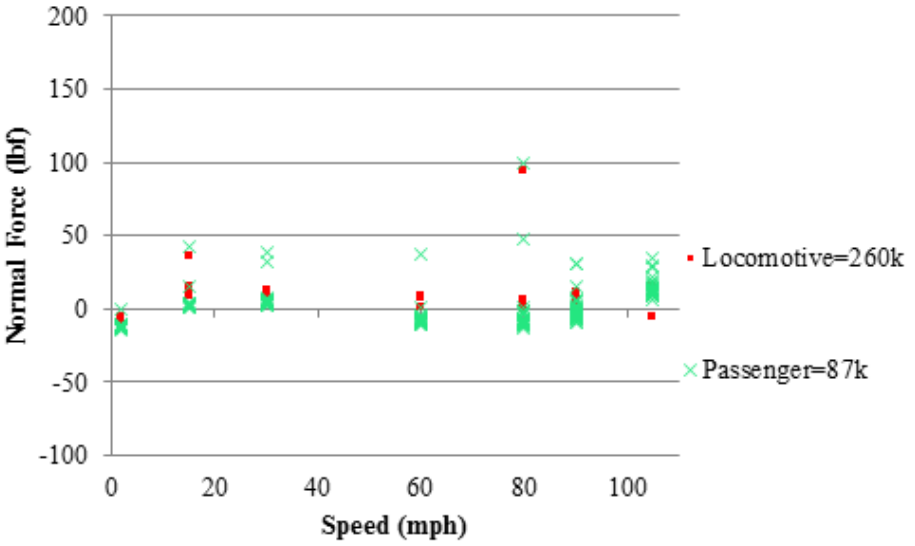

Figure 161. Change of Normal Force of Gauge Side Clip at Rail Seat U (RTT)

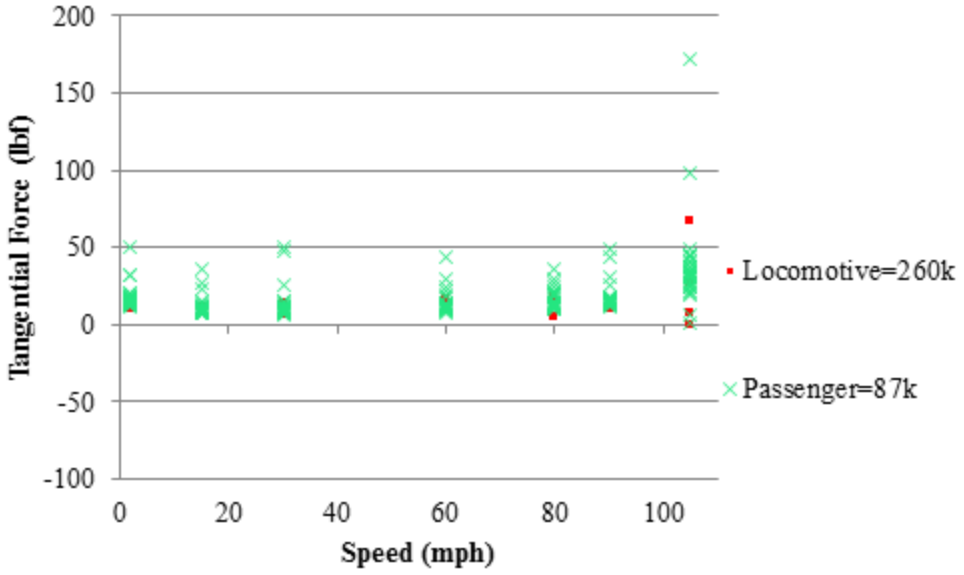

Figure 162. Change of Tangential Force of Gauge Side Clip at Rail Seat U (RTT)

As seen Figure 160 and Figure 161, the maximum change of both normal and tangential forces was below 200 pound-force. Typical normal values recorded were near zero pound-force, though the highest value recorded was 100 pound-force. Typical tangential values recorded were below 50 pound-force, though the highest value recorded was 175 pound-force. The effect of train speed was not as significant as the magnitude of the change of forces when compared to the effect of lateral force. Though the scatter of data increased with increasing speed, there was no direct relationship between speed and tangential force. This analysis was completed for all rail seats and the data was compared and similar conclusions were made.

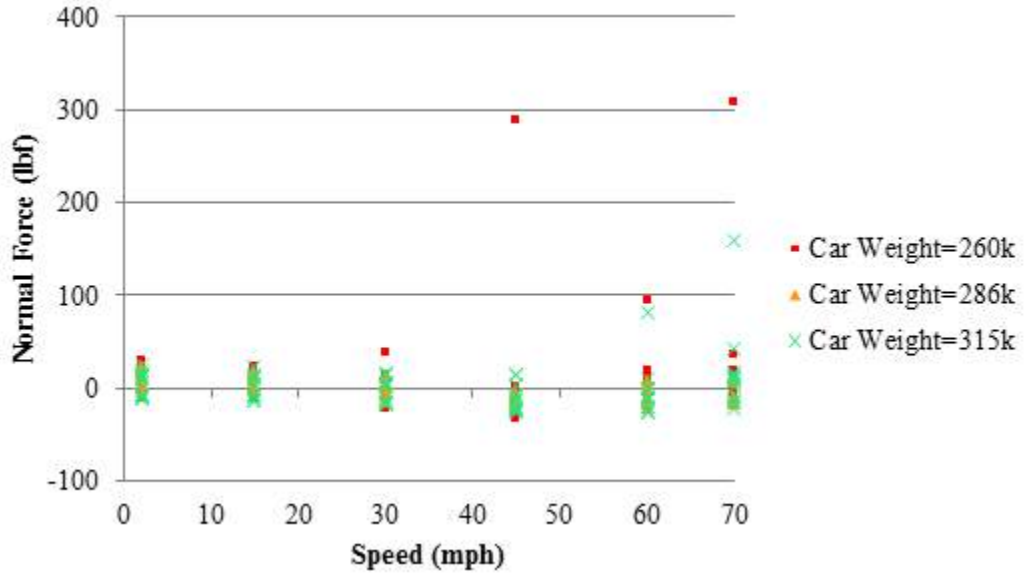

Figure 163. Change of Normal Force of Gauge Side Clip at Rail Seat U (RTT)

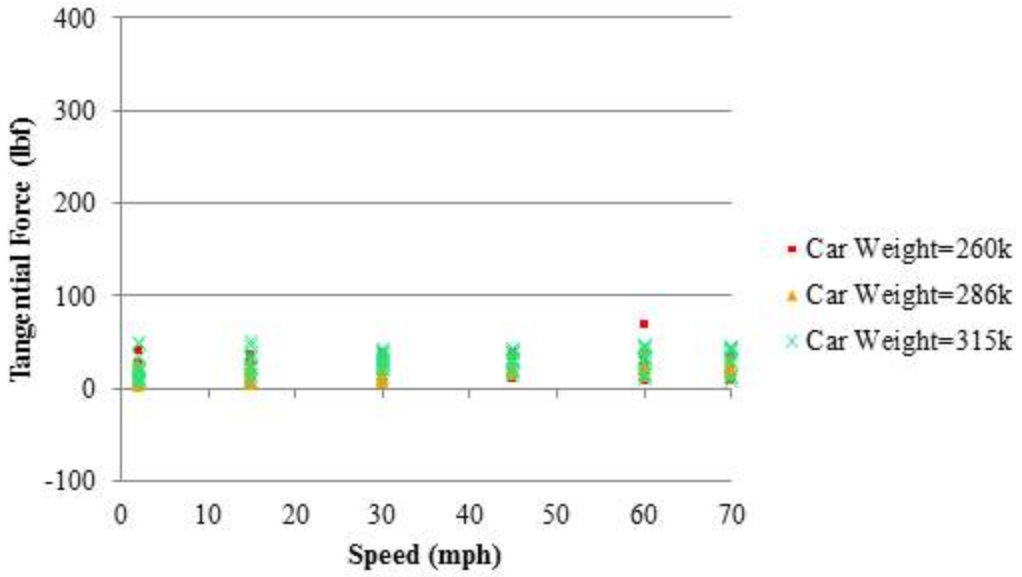

Figure 164. Change of Tangential Force of Gauge Side Clip at Rail Seat U (RTT)

From Figure 162 and Figure 163, it is evident that on average the maximum change of both normal and tangential forces was below 100 pound-force. Typical normal values recorded were near zero pound-force, though the highest value recorded was 308 pound-force. Typical tangential values recorded were below 50 pound-force, though the highest value recorded was 68 pound-force. The effect of train speed again was not as significant to the magnitude of the change of forces when compared to the effect of lateral force. Though the scatter of data increased with increasing speed, there was no direct relationship between speed and tangential force.

The extreme value for the change of the normal force was 308 pound-force, which was from the 260 kip car running with a speed of 70 mph. This value can be attributed to a dynamic wheel impact due to a wheel with a flat spot.

A similar analysis was performed on the data collected from the HTL. The maximum change of normal forces was found to be 142 lbf, which was less than half the 310 lbf on the RTT. The typical magnitude in the change in normal and tangential forces was higher than the RTT. This can be attributed to the increase in lateral forces. However, until more instrumented clips can be tested from both the low rail and high rail, any conclusion drawn from the comparison between the clips on the HTL should be considered premature.

6.16.1 Effective Longitudinal Area of Clamping Force Change

The distribution of the change of clamping force is discussed in this section for when the wheel load was applied over a specific rail seat. Referring to the field instrumentation map shown in Figure 151, the TLV applied static loading (both in vertical and lateral directions) over crossties BQ, CS, EU, GW and crib FV and DT. The data presented in this section will focus on when the static loading was applied at crosstie EU on the RTT.

When a 40 kip vertical wheel load was applied at crosstie EU, the change of normal and tangential forces are shown in Figure 164.

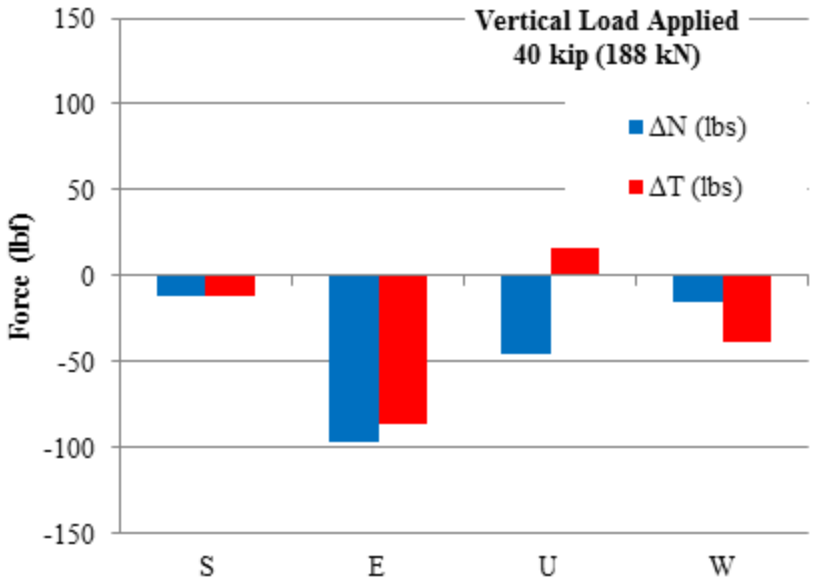

Figure 165. 40-kip Vertical Load Applied by TLV at Crosstie EU

In general, the maximum change of the normal force took place at the rail seat directly beneath the point of load. The adjacent gauge side clips recorded less than 50% of the change in normal force. It is believed that crosstie skewing and varying support conditions led to the differences in magnitude of the change in normal force at the same crosstie. When a 40-kip vertical and a 20 kip lateral wheel load were applied at crosstie EU, the change in clamping force is shown in Figure 166.

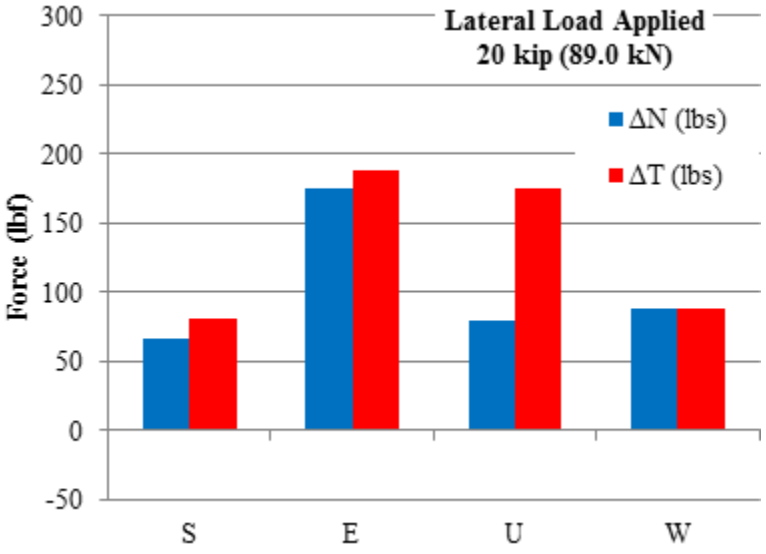

Figure 166. 20-kip Lateral Load Applied by TLV at Crosstie EU

As seen in Figure 165, the change in normal and tangential forces was 175 lbf and 188 lbf for the gauge side clip E, and 80 lbf and 176 lbf for clip U, which were both directly beneath the loading. For the clips at adjacent crossties, the change in normal and tangential forces was approximately 50%.

The experimental inspection from HTL brought a similar result; approximately 50% of both normal and tangential components of clamping forces were recorded from the clips on the crossties adjacent to the loading.

6.16.2 Summary

Data collected from this experimentation yielded critical findings concerning the effect of load on the normal and tangential components of clamping force:

- An increase in the normal or tangential component of clamping force will increase the strain within the clip.
- When subjected to vertical loading only:
  - There is a strain reduction within the clip due to the decrease in the normal clamping force component.
  - There is a negligible effect on the strain within the clip due to the relatively constant tangential clamping force component.
- There is a direct relationship between change in normal and tangential clamping force components and change of lateral load:
  - The relationship is dependent on the specific fastening system and affected by tolerances, support conditions, etc.
- The change in the normal clamping force component is, in general, lower when subjected to dynamic loads than static loads:
  - Impact loads can lead to an increase in the normal force by a factor of up to eight.
- The change in the tangential clamping force component is, in general, greater when subjected to dynamic loads than static loads:
  - Dynamic loads can lead to an increase in the tangential force by a factor of up to 1.3.
- There appears to be a three crosstie longitudinal distribution in change of clamping force components:
  - Crossties directly adjacent to the point of loading experience approximately 50% of the change in normal and tangential clamping forces as the point of loading.

The findings from this experimentation have been used to guide both further experimentation in the lab and efforts to introduce mechanistic principles to the design of crossties and fastening systems.

6.17 Rail Seat Loads

6.18 Background

RSD is one of the most critical areas for research by members of the North American rail industry. To address RSD, it is critical to understand the loading environment at the crosstie rail seat because of its effect on failure mechanisms associated with RSD (Greve et al 2014). The current AREMA design methodology for crosstie flexure treats the rail seat load as a point load. In keeping with the objectives of the field experimentation to better quantify the load transferred

into the crosstie and fastening system, instrumentation was deployed to quantify the load exerted on the crosstie rail seat.

Rail seat load is an important input parameter in the design of concrete crossties and fastening systems. Estimating this value is critical to the efficiency of the design. Currently, a 50% distribution factor is assumed when ties are properly supported, including AREMA Chapter 30 (Ties). However, it is also understood that differing crosstie support conditions will lead to differing rail seat loads. Therefore, it is important to characterize the effect support condition plays on rail seat load. Finally, this section will try to characterize the common rail seat loads experienced today.

6.19 Methodology

Two sets of field experiments were conducted at the TTC in Pueblo, CO. For both sets of experiments, strain gauge bridges were installed on the rail at cribs T, V, D, and F to measure the wheel-rail load. Strain gauge bridges were also installed on the rail above rail seats S, U, W, and E to be utilized in the calculation of the rail seat load at each respective rail seat; an instrumentation strategy that has been regularly employed within the rail industry. A second instrumentation strategy consisting of strain gauges cast into the concrete rail seat was also deployed to directly quantify the rail seat loads at S, U, W, and E. In addition to the strain gages, potentiometers were attached to rods driven to refusal at the ends of each crosstie rail seat S, U, W, and E in an effort to quantify the global vertical crosstie displacement at each instrumented rail seat.

The instrumentation was deployed in this manner in an effort to quantify the longitudinal distribution of loading along the track as well as the variability of loading of two rail seats on the same crosstie. The data gathered was analyzed using the methodology and assumptions presented within Chapter 5. The track was loaded using the TLV as well as passenger and freight consists.

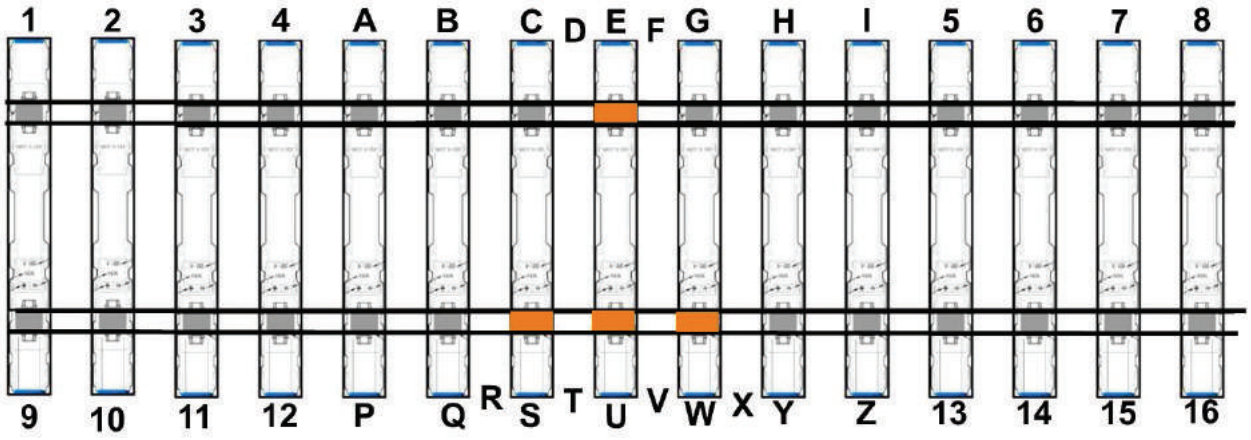

Figure 167. Locations of Instrumented Clips at RTT/HTL (June 2012/May 2013, TTC)

6.20 Comparison of Rail Strain Gage Bridges and Internal Crosstie Strain Gages

Two instrumentation strategies were deployed to quantify the rail seat load and the data collected via these methods was compared. Figure 167 below shows a representative plot of the outputs from these two methods as recorded in the lab under varying vertical wheel loads.

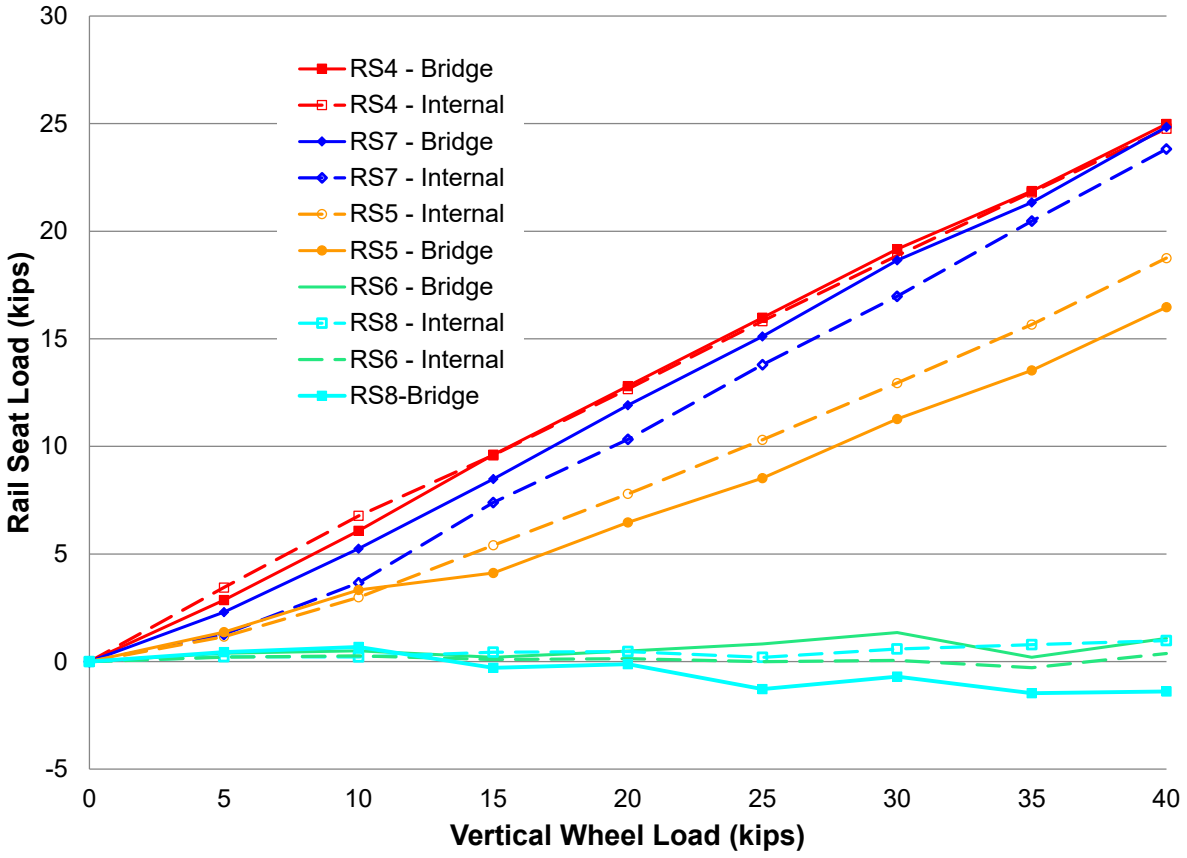

Figure 168. Comparison of Rail Seat Load Instrumentation Methodologies Via Comparing Static Vertical Wheel Load to Rail Seat Load Data (2012, HTL)

Analysis of the laboratory data recorded via these methods showed that when a 40-kip wheel load was applied to the rail, the difference in the recorded rail seat loads at rail seats 4, 5, and 7 was, on average, 6.2% and had a standard deviation of 4.7%. It should be noted that the percentage difference of rail seats 6 and 8 were not included in this analysis because the percentage differences were outliers while the difference in loading magnitude was considered to be negligible. Therefore, these two methods were expected to produce values around 10% of one another in the field.

A brief analysis of the field data recorded via these methods revealed that the difference in the recorded rail seat loads ranged on average from 16 to 148% and displayed standard deviations of 6 to 82%. Therefore, it was determined that the measurement techniques were not producing similar results given the range in rail seat load differences was between 8 and 200% when considering a 99.5% confidence interval.

It is believed that the embedded internal strain gages provided more repeatable and accurate rail seat loads given they were calibrated in the lab and exhibited similar behavior in the laboratory

and field. Therefore, it was concluded that the internal strain gage methodology was more accurate and thus was exclusively used in the discussion below.

6.21 Rail Seat Load, Support Condition, and Modulus

An effort was made to quantify the effect of support condition on rail seat load. It was determined that the amount of data captured was not sufficient to make focused conclusions and thus researcher will be conducted in the future. Additionally, the data that was collected yielded results that were unexpected. Figure 169 and Figure 170 below shows the static and dynamic rail seat load plotted against the global vertical deflections measured at one speed for three consecutive rail seats on the HTL in 2012. This data is representative of the data recorded at other speeds and from the RTT. The static data represents the rail seat load and tie end deflection data while the load applied by the TLV was directly above the crosstie being measured. Therefore, if the support conditions were constant, then the load versus displacement graphs would be the same.

The static data presented appears to show that rail seat S and W are not supported as well as Rail Seat U. That is, there is approximately 0.05 inches of displacement before the rail seats take any appreciable load. Additionally, the data shows that when a 40-kip wheel load was applied, rail seat U takes load before both rail seat S and W and also takes the largest rail seat load of 20.3 kips and displaces 0.15 inches. When the 40-kip wheel load was applied above rail seat S and W, rail seat S took 9.7 kips and displaced 0.14 inches while rail seat W took 12.9 kips and displaced 0.13 inches.

An analysis of the modulus supporting the tie was also conducted. Two sets of assumptions were made to determine the modulus values. The first set of assumptions assumed that the ballast section was 12 inches thick, the bottom of crosstie contact area was 1,100 square-inches, and the rail seat load recorded was evenly distributed along half of the crosstie. The second set of assumptions assumed the same ballast section and tie surface area, but that the rail seat load was half the wheel load. Furthermore, Equation 2 was used to determine the modulus.

Eq. 2. $$u = {}^{\sigma}/_{\epsilon}$$

Where:

- σ = stress
- ϵ = strain

and

Eq. 3. $$\sigma = {}^{Rail\ Seat\ Load}/_{(0.5 \times bottom\ of\ crosstie\ area)}$$

and

Eq. 4. $$\epsilon = {}^{Global\ Crosstie\ Deflection}/_{Ballast\ Depth}$$

The data appears to show that once the "gap" beneath the crosstie was closed, the modulus of the track substructure beneath each crosstie varied by approximately 1,700 psi. That is, when wheel loads increased from 25 to 40 kips, the tie end displacements increased 0.037, 0.039, and 0.045 inches for rail seat S, U, and W respectively or moduli values of 5,000, 6,100, and 6,700 psi. This is critical because when modulus values vary greatly, as in the vicinity of bridges, crossings,

and mud spots (Zakeri 2009), dynamic forces are imposed on the track increase. It should be noted that when one calculated the modulus of the support beneath the tie using the total displacement values and the wheel load applied, the values only ranged from 6,000 – 6,600 psi, or typical values of concrete crosstie track modulus. However, because the displacement of each crosstie was measured at different magnitudes, the gap under the crossties was quantified. It is hypothesized that the ballast will breakdown at an accelerated rate under the well supported tie while the crosstie will abrade at an accelerated rate when moving relative to the ballast.

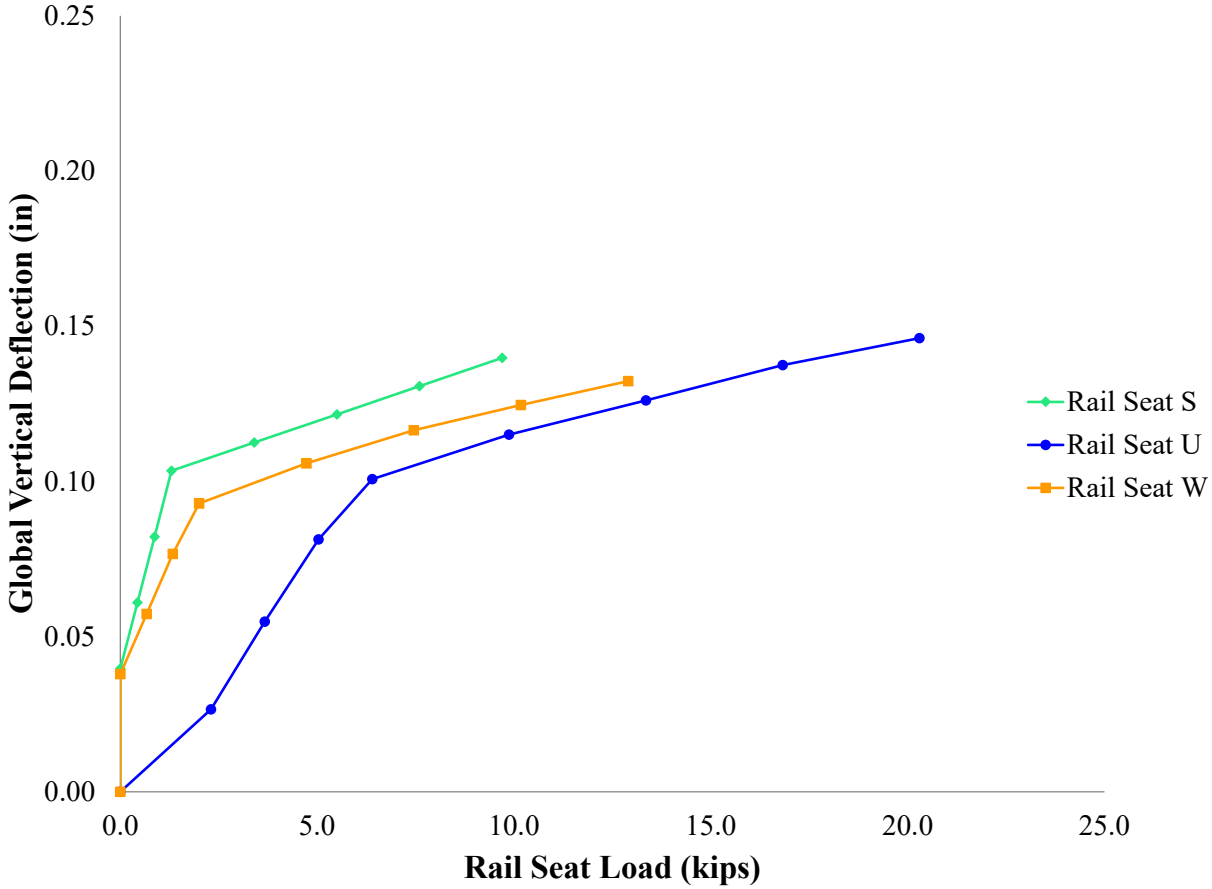

Figure 169. Global Vertical Crosstie End Deflection Versus Rail Seat Load of Three Adjacent Rail Seats Under Static Vertical Wheel Load Increased from 0 – 40 kips Above Each Rail Seat (HTL, 2012)

From Figure 169 one can see that there is a linear relationship between global vertical crosstie displacement and rail seat load. However, this relationship is only applicable to each crosstie. This is hypothesized to be the case because of the support conditions under each crosstie. Rail seat U consistently exhibits the largest displacement as well as records the highest rail seat loads on average. Rail seats S and W exhibit similar behavior to one another, but displace approximately 0.05 inch less than rail seat U. From this analysis, one can see that a crosstie can record the same rail seat load at various displacements. Therefore, one cannot simply determine the rail seat load by quantifying the crosstie displacement.

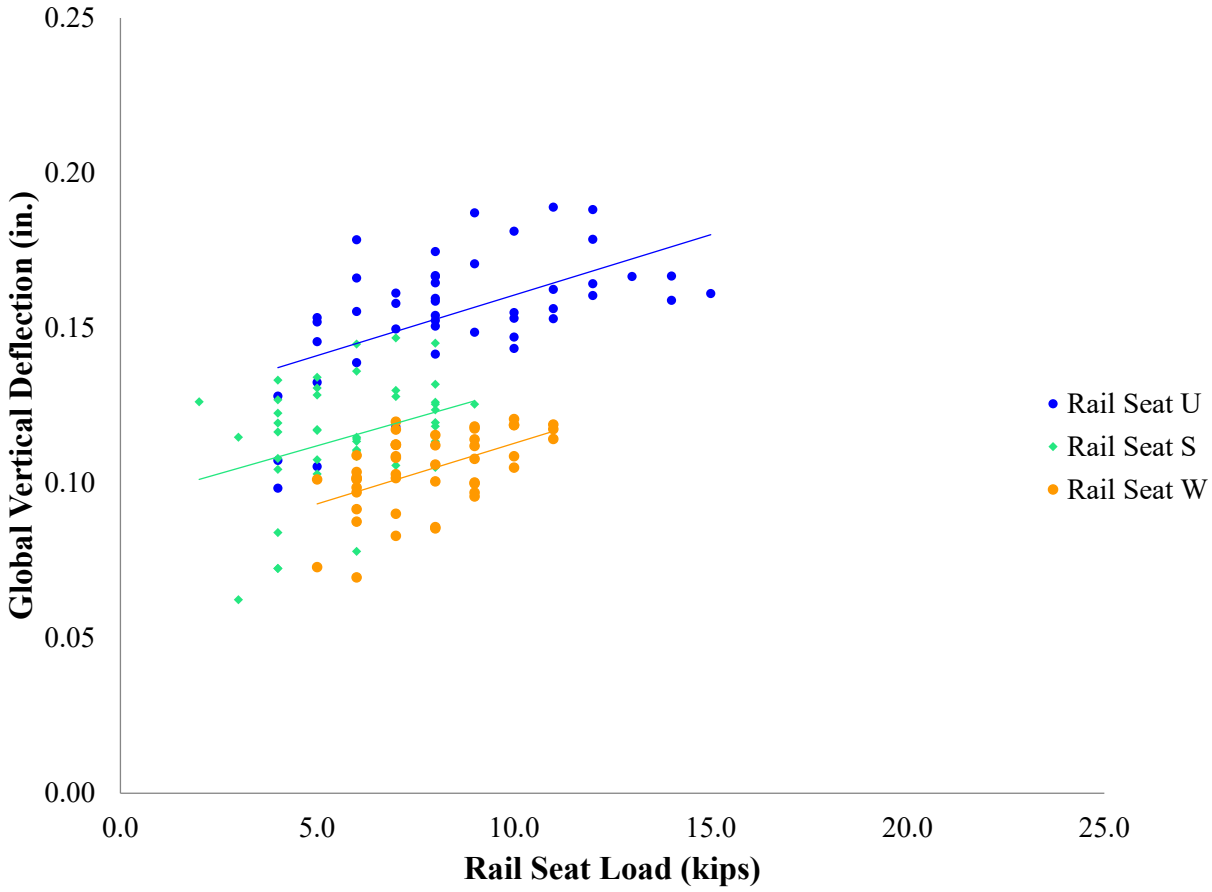

Figure 170. Global Vertical Crosstie End Deflection Versus Rail Seat Load of Three Adjacent Rail Seats Under Dynamic Vertical Wheel Loads from Train Passes at 45 mph (HTL, 2012)

6.22 Effect of Static Vertical Wheel Load on Rail Seat Load

Under static wheel load, the rail seat directly below the wheel set is hypothesized to support a constant ratio of vertical load (i.e. the rail seat load is expected to grow proportionally with the increasing of wheel load). However, the attenuation of the vertical load supported by each rail seat is expected to be highly dependent on the vertical stiffness of the track and support conditions from ballast, and therefore it is highly variable. Additionally, the existence of lateral force is expected to have a negligible effect on the magnitude of rail seat loading and rail seat load distribution.

Figure 170 and Figure 171 show the vertical rail seat load under 0 - 40 kips vertical wheel load, when the TLV applied the loads directly above each rail seat.

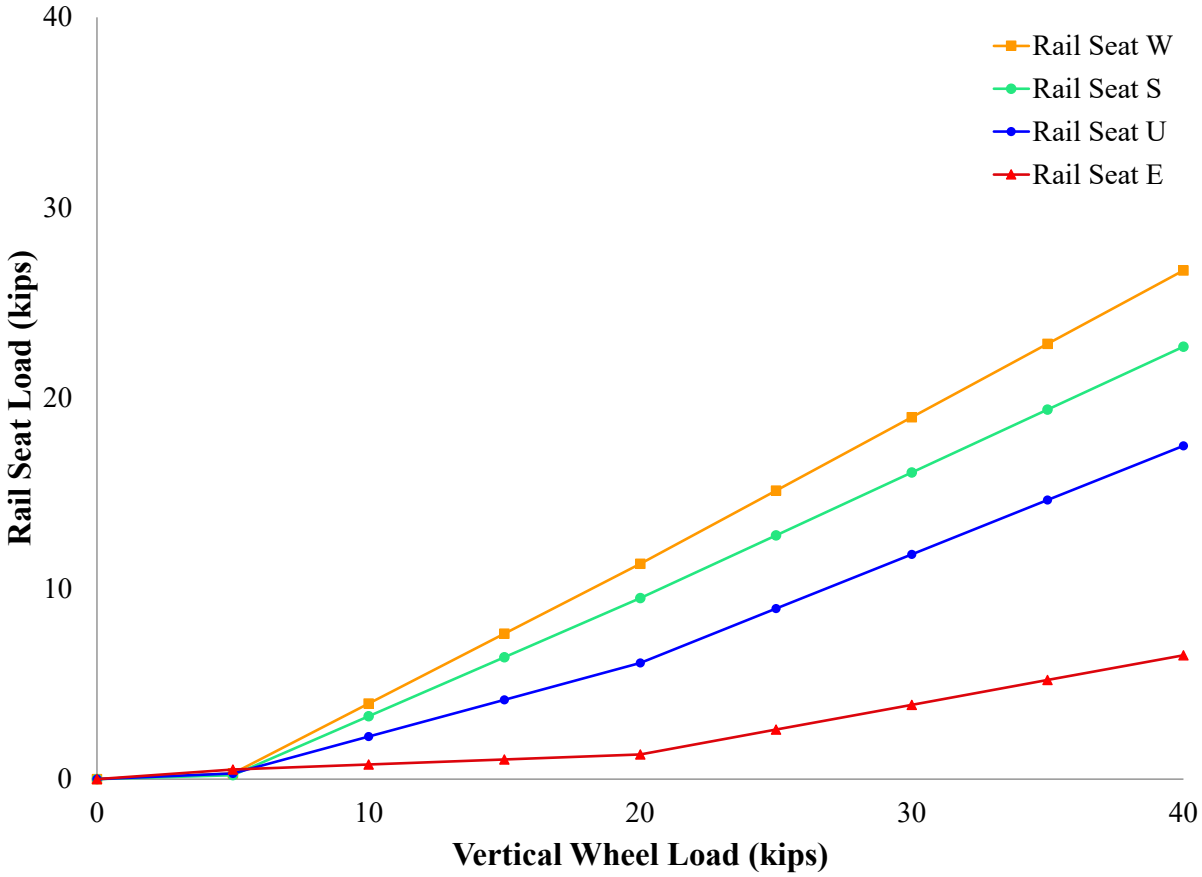

Figure 171. Rail Seat Loading Under Various Static Vertical Wheel Loads (RTT, 2012)

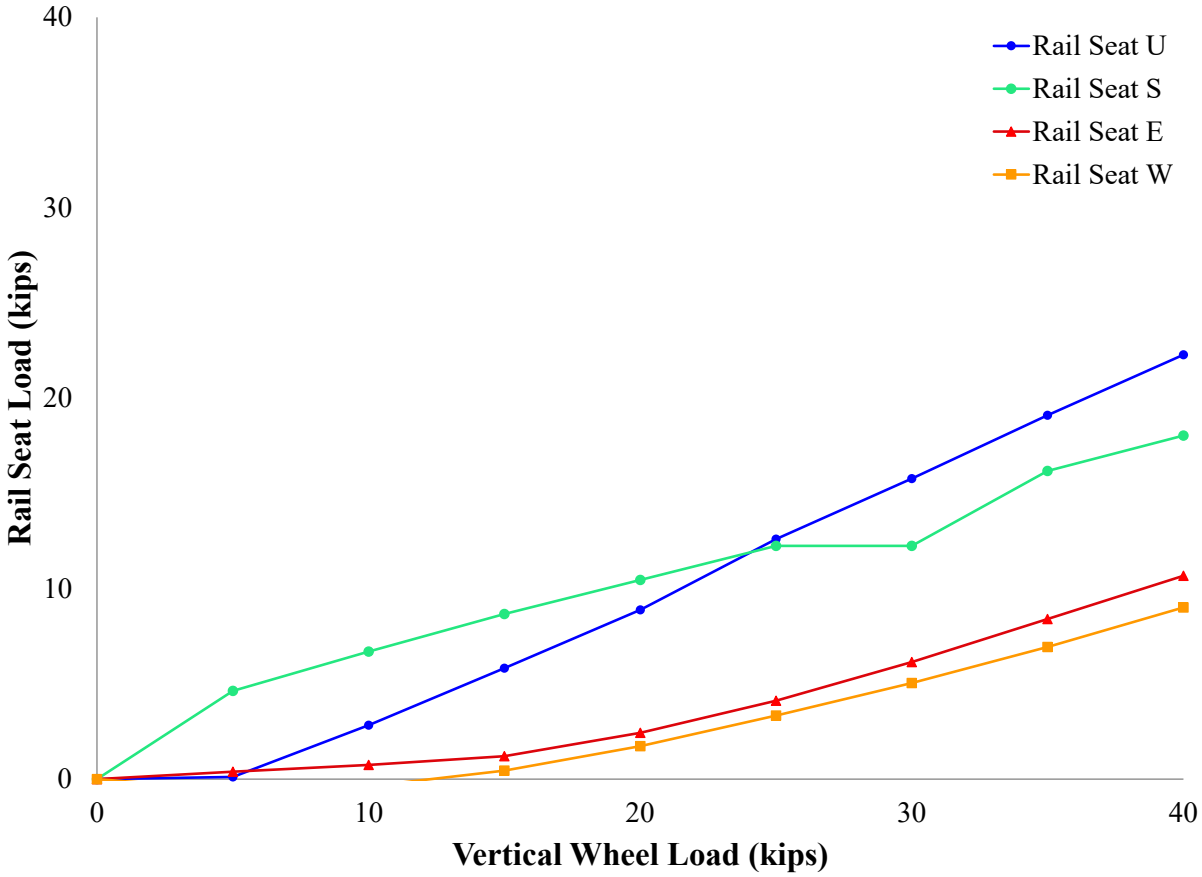

Figure 172. Rail Seat Loading Under Various Static Vertical Wheel Loads (RTT, 2013)

In the 2012 tests at the TTC, the data was zeroed for all sensors at 5 kips of vertical load. In this case, the 5-kip vertical applied load should be taken as a pre-loading, and all rail seat loadings recorded in 2012 increased from 5 kips. Both Figure 171 and Figure 172 show that the rail seat load is not uniform under a predicted vertical wheel load. In the testing conducted at RTT in 2012, Figure 171, under a 40-kip vertical wheel load, the rail seat load varied from 6.5 kips to 26.7 kips, or 16% to 67% of the wheel load. For the data collected from 2013, Figure 171, the rail seat load varied from 9.0 kips to 22.3 kips, or 22% to 56% of the vertical wheel load.

Upon further analysis of the 2013 data, it appears that rail seat S was the only instrumented rail seat in direct contact with the ballast with no load applied; that is, when 5-kips vertical wheel load was applied, rail seat S recorded a 4.6-kip rail seat load, or 92% of the wheel load. Rail seat U was not in contact with the ballast until approximately a 5-kip wheel load was applied while rail seats E and W did not contact the ballast until a 15 kip wheel load was applied. Though each rail seat exhibited a linear response to load after it was seated, the rate of rail seat load increase was not constant as expected. Both rail seats S and U exhibited nearly linear response in rail seat load as the vertical wheel load increased beyond the seating load. However, rail seat S increased at approximately a rate of 380 pounds per kip of wheel load while rail seat U increased at approximately a rate of 630 pounds per kip of wheel load. Furthermore, rail seats E and W did not exhibit linear responses; the response rate ranged from 250 to 450 pounds per kip of wheel load.

A comparison between 2012 and 2013 data (Figure 170 and Figure 171) shows that the rail seat load can vary significantly as the track experiences load and as a result support conditions change. For example, under a 40-kip wheel load, the rail seat load recorded at rail seat W was 26.7 kips in 2012 and 9.0 kips in 2013. The track had experienced approximately 5 MGT of traffic and had not undergone any maintenance activities or tamping between tests. Therefore, this shows that as a result of a relatively small volume of traffic, the rail seat load was significantly changed. It is hypothesized that the reason for this change is directly related to changing crosstie support conditions.

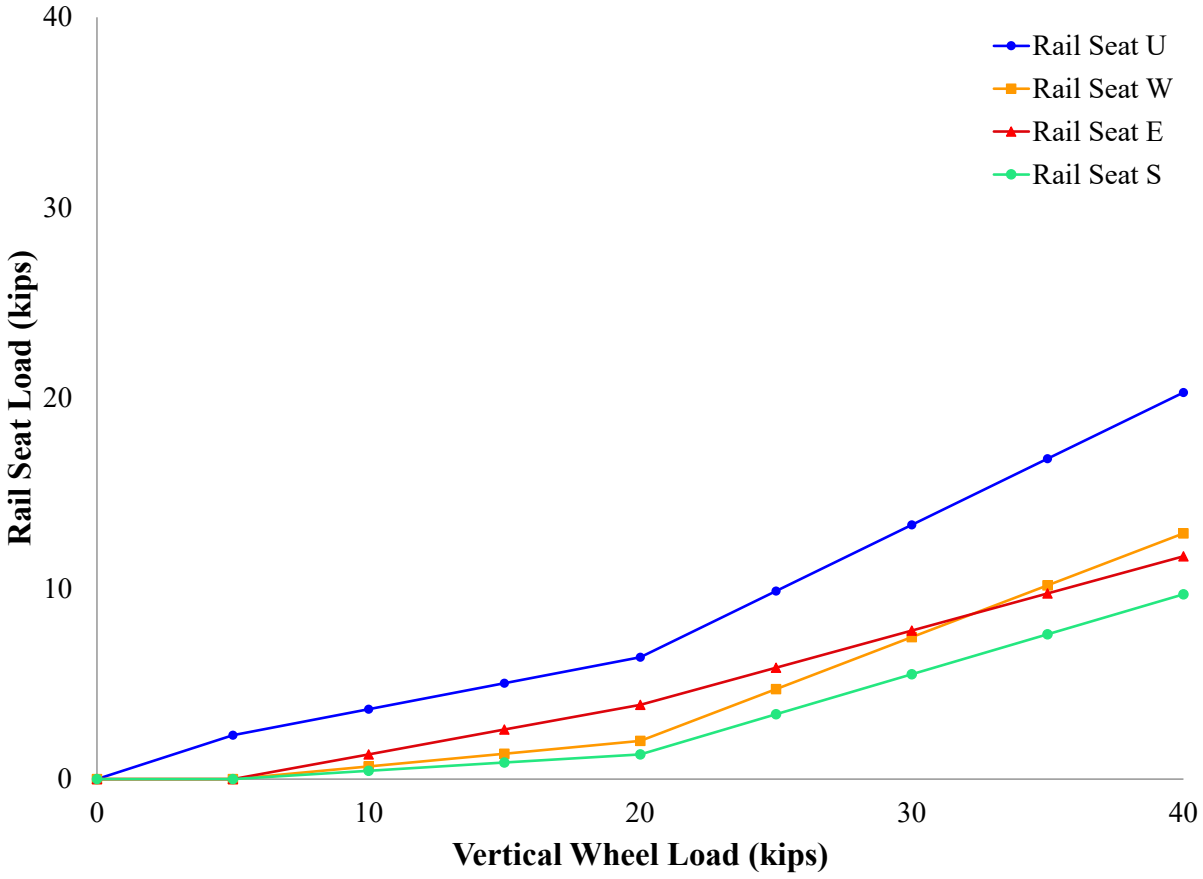

Figure 173. Rail Seat Loading Under Various Static Vertical Wheel Loads (HTL, 2012)

As shown in Figure 172 for the reaction force measurements from each rail seat, evidence was provided for investigating the effect of a hanging crosstie at the curved section (HTL). Clearly, the portion of the wheel load supported by each rail seat was lower when the applied wheel load was below 20 kips. A preload of about 20 kips was required to initiate a full reaction from the ballast. This illustrates how the distribution of rail seat load is affected by its support conditions. If the crosstie placed directly below the wheel set hangs, the crossties located one or more away from the point of load must provide higher reaction forces.

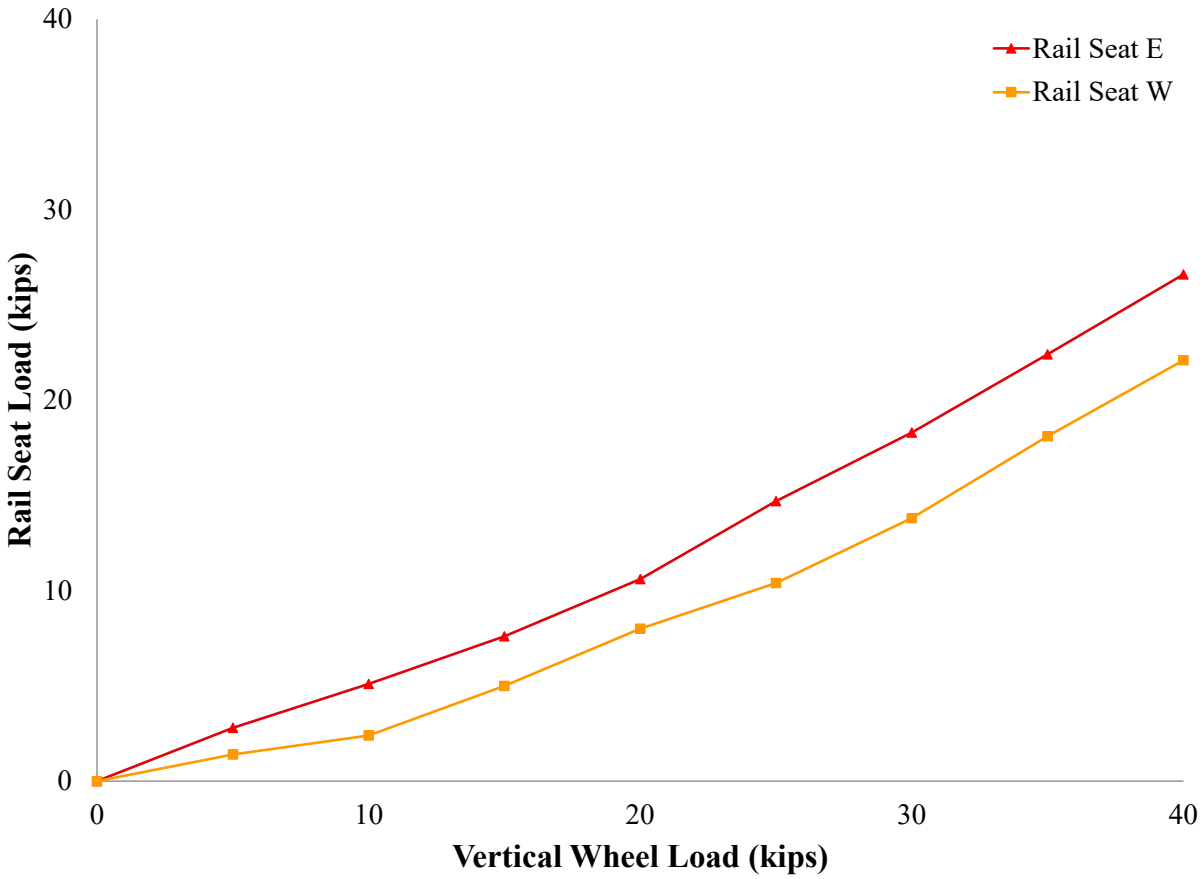

Figure 174. Rail Seat Loading Under Various Static Vertical Wheel Loads (HTL, 2013)

The support conditions for the hanging crosstie might be improved by tamping the track. Figure 173 shows the rail seat loading measured from the same testing section at HTL one year later (2013), after the track was re-tamped. The sensors below the rail seats S and U were damaged and did not give readings, but the vertical reaction forces measured from the remaining two rail seats increased immediately upon application of wheel load and took significantly higher load.

The hypothesis that rail seat load grows proportionally with increasing wheel load can be accepted based on these results. Once adequate contact was made with the ballast, the rail seat loading increased in a nearly linear manner. This loading increase is highly dependent on support conditions, however, as ballast contact and stiffness are primarily responsible for the changes in rail seat loading.

6.23 Rail Seat Load Distribution – Static Wheel Load

The distribution of rail seat loading is how the rail seat loads distribute over the adjacent crossties when the wheel load was applied over a specific rail seat. Referring to the field instrumentation map shown in the field instrumentation plan section, the TLV applied static loading (both in vertical and lateral directions) over crosstie CS, EU, GW and crib FV and DT. Figure 174 shows the rail seat loading when 0–40-kips vertical wheel loads were applied above the center crosstie EU.

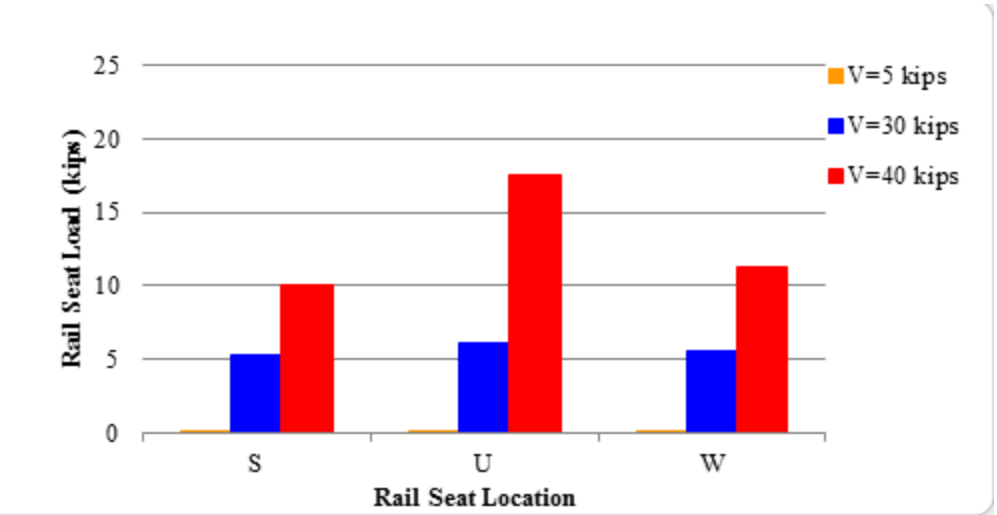

Figure 175. Rail Seat Load Distribution Under Various Static Vertical Wheel Loads Applied Over Crosstie EU (RTT, 2012)

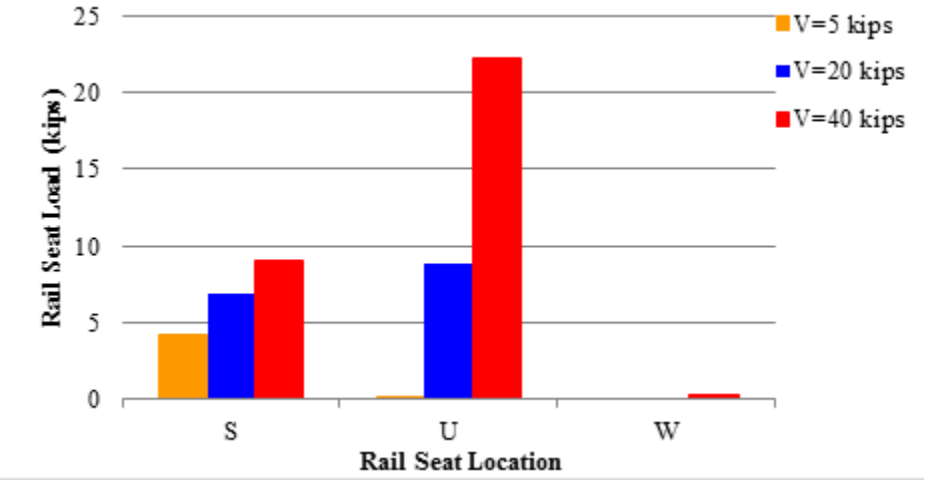

Figure 176. Rail Seat Load Distribution Under Various Static Vertical Wheel Loads Applied Over Crosstie EU (RTT, 2013)

It can be clearly seen in the 2012 data (Figure 174) that rail seat load increases with increasing applied vertical load. Figure 175 provides a good example of similar support conditions under the crossties. The tie being directly loaded (U) takes about than twice the load as the adjacent ties (S and W), and about 50% of the total applied vertical load. The adjacent ties take about 25% of the total vertical applied load each. Together, at 40 kips total vertical loading, crossties S, U, and W take almost the entire applied 40 kips. This supports the AREMA load distribution factor specified in Figure 30-4-1 (50% of total vertical load to tie directly beneath wheel load for 24-inch spacing).

The rail seat loading distribution from the 2013 data (Figure 175) provides further evidence of the importance of a hanging crosstie. When the wheel set was placed over the center crosstie EU, rail seat U only began to take load after the vertical wheel load exceeded 5 kips. Instead, an adjacent rail seat (S) took most of the vertical load. When 5-kips wheel load was applied, rail

seat S was bearing 4.6 kips, or 92% of the vertical wheel load. Once vertical loads exceeded 5 kips, the distribution of rail seat loads changed, and the other rail seat U began to take a higher percentage of vertical wheel load. This shows the drastic changes in the load distribution as a result of support conditions, especially hanging crossties. In many cases, there is a certain vertical load that is required to engage the ballast and cause a reaction from the supports. This is seen from rail seat W, where the rail seat takes no load because ballast engagement is not achieved. Additionally, once this ballast reaction was engaged the rail seat under direct loading took a higher percentage of the total vertical load than the adjacent crossties. When comparing these distribution percentages, it is evident that the three instrumented rail seats did not take the full 40-kip vertical load that was applied. The tie directly under the applied load (U) still takes about 50% of the total load, the adjacent crosstie that takes load takes about 25% (S), but since the other adjacent tie (W) takes practically no load the vertical load must be spread to the next set of adjacent ties to satisfy vertical equilibrium. In short, the distribution of loads under is highly dependent on support conditions, but if a full ballast interaction is achieved this distribution can be estimated in Figure 30-4-1 from the AREMA Manual for Railway Engineering.

However, this data again illustrates the extreme importance that support conditions have on load distribution. Rail seats with good contact with the ballast take load initially until the hanging rail seats make contact with the ballast. Contact needs to be made with ballast before any load bearing can occur, and some rail seats may not ever engage with the ballast. This is clearly seen in the above 2013 data, as rail seat S takes initial load due to good initial contact with ballast and rail seat W barely takes any load because it is never forced into good contact with ballast.

6.24 Effect of Dynamic Wheel Load on Rail Seat Load

An analysis was performed to further quantify the rail seat loading environment under dynamic train passes (passenger and freight). Figure 176 and Figure 177 below show the rail seat loads measured for three adjacent rail seats under freight and passenger trains at 45 mph and 60 mph respectively. The rail seat loads did vary as speed varied, but more as a result of the wheel loads. The wheel loads were measured from rail strain gauge bridges as discussed in in Volume 2, Chapter 5. The data is presented from the RTT to eliminate the effect of track geometry (e.g. curvature).

Figure 176 shows that there was very little difference between rail seat U and rail seat S under the freight train. The average rail seat load for rail seat U was 20.9 while the average rail seat load for rail seat S was 20.5 kips. At the same time, the rail seat load measured at rail seat W was always substantially lower. The average load was 7.3 kips. However, Figure 176 shows that the rail seat loads measured at all three rail seats under the passage of the passenger trains were similar. The average rail seat loads recorded were 10.7, 8.6, and 9.3 kips for rail seat U, S, and W respectively. Given ballast is a non-homogeneous and unbound material, it is possible that the ballast particle could have shifted between these two runs resulting in rail seat W taking a greater load. A comparison of the values recorded under a freight train and passenger train show that the loaded freight train will, on average, impart rail seat loads double in magnitude compared to passenger cars. It should be noted that this data falls in-line with what was expected looking at Figure 172 above; that is, rail seats U and S recorded the highest rail seat loads under static load.

The percentage of wheel load imparted into the rail seat was also calculated. Though the conventional wisdom assumes that 50% of the wheel load is imparted onto the crosstie under the

freight cars rail seat S recorded values that were on average 92% of the wheel loads. Nevertheless, rail seat U recorded values that were 53.3% while rail seat W only recorded values of 19%. The values were also looked at under the passenger cars and rail seat U recorded values that were on average 87% of the wheel loads. Furthermore, rail seat S on average exhibited the lowest transfer percentage of 67%. This change in percentage carried by each crosstie further leads one to believe that the support conditions under each crosstie had indeed changed as a result of train loading within a short period of time and low amount of tonnage.

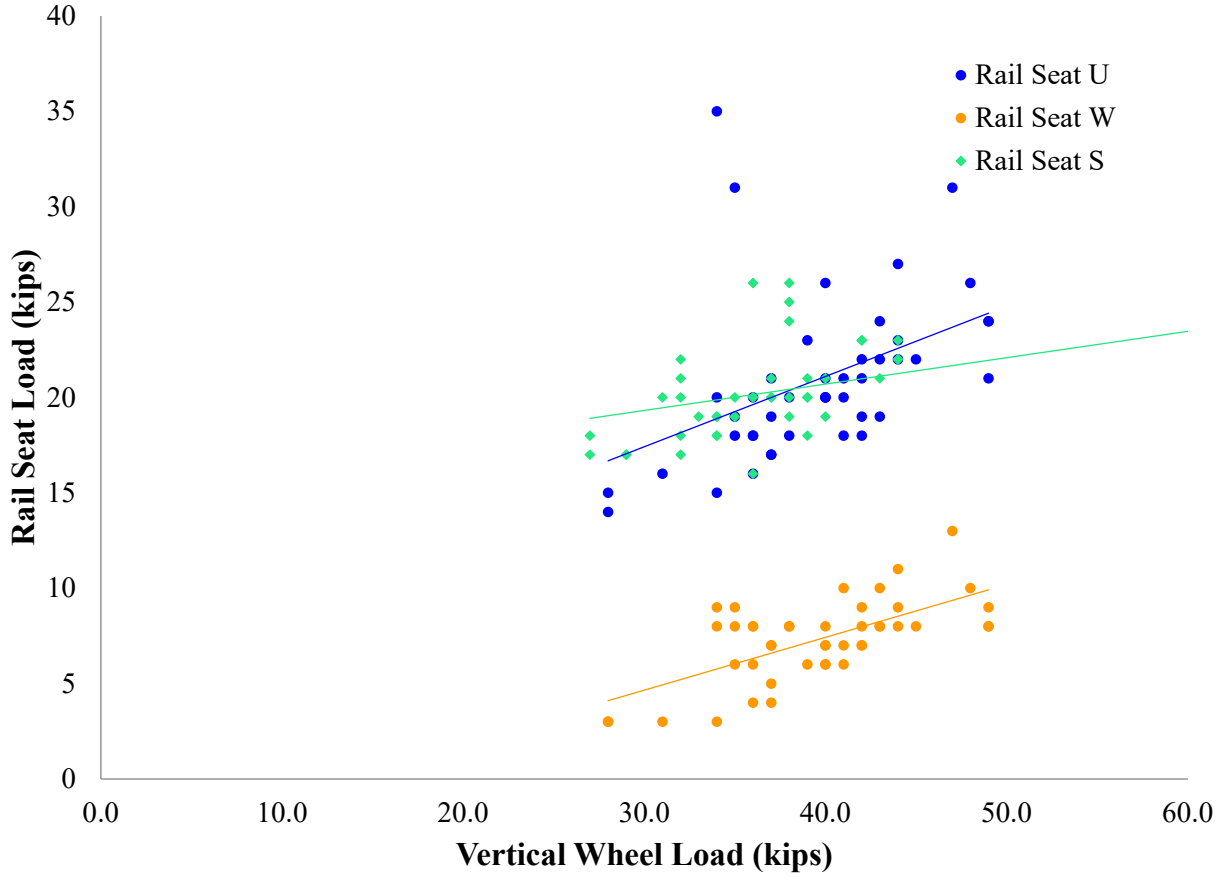

Figure 177. Rail Seat Load Versus Vertical Wheel Load Under 45 mph Freight Train Passes (RTT, 2013)

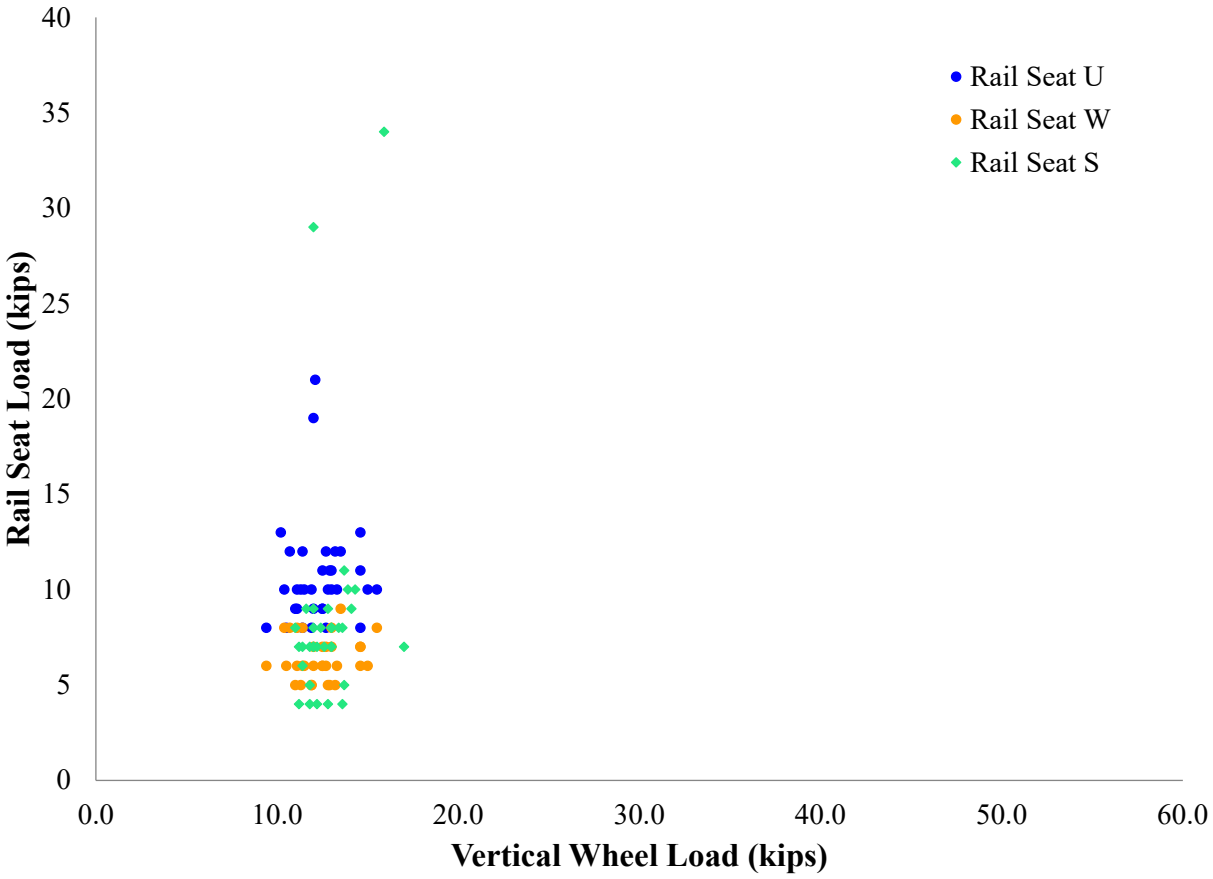

Figure 178. Rail Seat Load Versus Vertical Wheel Load Under 60 mph Passenger Train Passes (RTT, 2013)

6.25 Summary

Data collected from this experimentation yielded five critical findings concerning the rail seat load:

- A new method to accurately quantify the rail seat load was developed:
  - This method was compared to previous methods in the lab and field and was considered to have less variability.
- There is a relationship between global crosstie displacement and rail seat load:
  - Each crosstie exhibits its own relationship which is highly variable and relates to the support conditions of each crosstie.
- The percentage of wheel load that is imparted into the rail seat under a static analysis is approximately 50%, confirming what has typically been documented in the literature.
- The percentage of wheel load that is imparted into the rail seat under dynamic loading can vary significantly:
  - The range of values recorded from a single day of trains ranges from 19 – 92%.

- Tamping and traffic have significant impacts on the load imparted into the rail seat.

6.26 Uniformity of Rail Seat Load Distribution

6.27 Background

RSD is considered one of the most critical areas for research by members of the North American rail industry. To address RSD, it is critical to understand the loading environment at the crosstie rail seat because of its effect on failure mechanisms associated with RSD (Greve et al 2014). Current design methodology assumes a uniform distribution of load at the crosstie rail seat. In keeping with the objectives of the field experimentation to better understand the load transfer mechanics within the fastening system and crosstie, instrumentation was deployed to quantify both the uniformity of load distribution and the pressures exerted on the crosstie rail seat.

6.28 Methodology

Two sets of field experiments were conducted at TTC in Pueblo, CO. For the first set of experiments, conducted in July 2012, Matrix Based Tactile Surface Sensors (MBTSS) were placed on two adjacent rail seats, A and C, on the low rail and one rail seat, B, on the high rail, as shown in Figure 36, between the rail pad assembly and concrete rail seat surface. For the second set of experiments, conducted in May 2013, MBTSS were installed on five adjacent rail seats, 1N through 5N, on the near rail and three adjacent rail seats, 2F through 4F, on the far rail, as shown in Figure 36, between the rail pad assembly and concrete rail seat surface. In May 2013, linear varying displacement transducers (LVDTs, or potentiometers) were positioned at each rail seat instrumented with MBTSS to capture crosstie vertical deflection.

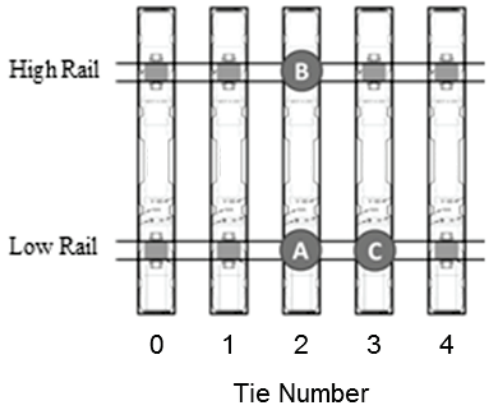

Figure 178. MBTSS Field Installation for July 2012 Experimentation

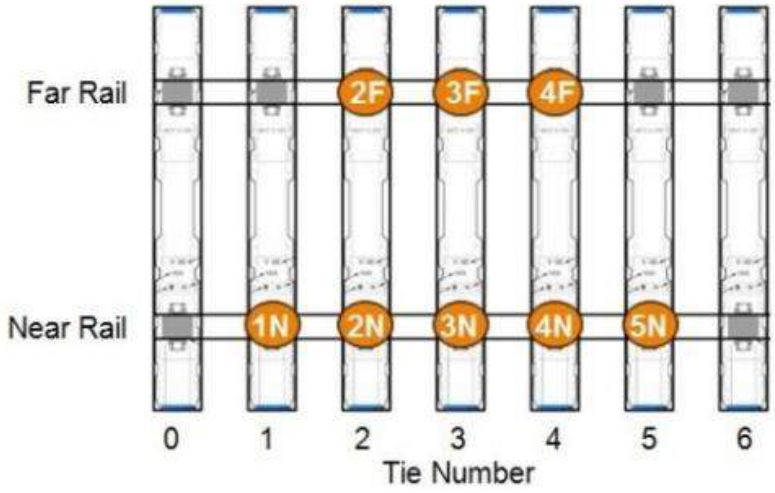

Figure 179. MBTSS Field Installation for May 2013 Experimentation

6.29 Effect of L/V Force Ratio

Current design methodology assumes that the rail seat load is uniformly distributed across the entire rail seat area, and that lateral load does not affect the distribution of the load. It was determined that for this design assumption to be an acceptable approximation, the maximum pressure exerted on the rail seat could increase by no more than ten percent as a result of an increase in L/V force ratio from 0.0 to 0.5 at a constant vertical load of 40,000 lb (178 kN). A tangent section of the RTT was chosen to minimize variability due to vehicle-track dynamics which would be induced by a curved alignment. The pressure distributions collected from the three instrumented rail seats under varying L/V force ratios with a constant 40,000 lb (178 kN) vertical load can be seen in Figure 180 with a scale depicting the severity of pressure being imparted on to each rail seat.

The distributions for rail seats A and B are oriented such that the field sides of each are facing opposite directions to show the effect of the outward forces applied by the TLV loading frame under increasing L/V force ratios. Rail seat C is oriented with rail seat A, as these were adjacent to each other on the low rail. A qualitative observation that none of the three rail seats are uniformly loaded is apparent, though rail seat C did not vary as significantly under the various loads as did A and B. All three rail seats show increased pressures on the field and gauge edges, with a decrease in loading in the center. This trend is especially evident in rail seats A and B, where little to no force was registered in the center of the rail seats by the MBTSS. While a slight decrease in load in the center of the rail seat can be seen on rail seat C, the MBTSS on this rail seat shows that it was more uniformly loaded than rail seats A and B.

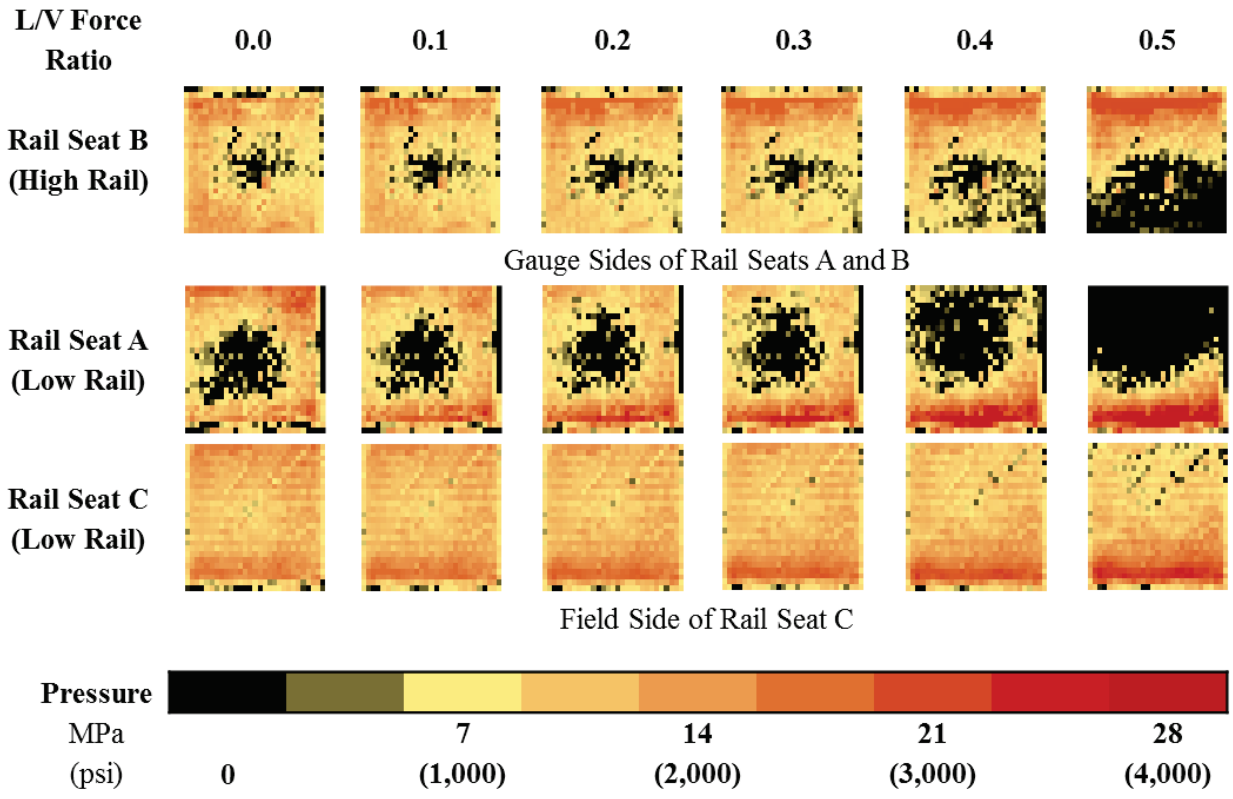

Figure 180. Rail Seat Pressure Distributions - Varying L/V Force Ratios

Quantitative analysis can be performed on the pressure distributions shown in Figure 180. The effect of increasing L/V force ratio on maximum and average pressures imparted onto the rail seats, as well as the area of the rail seat engaged in load transfer, are considered in the following analysis. Table 37 summarizes the maximum pressures imparted onto each of the three rail seats under the various L/V force ratios applied by the TLV with a constant 40,000-lb (178 kN) vertical load. For rail seat A, the maximum pressure imparted onto the rail seat at a 0.5 L/V force ratio of was approximately 34% higher than at a zero lateral load. For rail seats B and C, these percent increases in the maximum pressures at 0.5 L/V force ratios were approximately 11% and 57% higher than at a zero lateral load, respectively. The maximum pressure seen in this experimentation was on rail seat A under a 40,000 lb (178 kN) vertical load and 20,000-lb (89 kN) lateral load (L/V force ratio of 0.5), reaching approximately 3,640 psi (25.1 MPa). Therefore, we reject our hypothesis and conclude that the prescribed loading environment increases the maximum rail seat pressure by more than 10%.

Table 33. Maximum Pressures in PSI (MPa) of Rail Seat Loads at Various L/V Force Ratios

	L/V Force Ratio					
Rail Seat	0	0.1	0.2	0.3	0.4	0.5
A	2,715 (18.72)	3,336 (23.00)	3,368 (23.22)	3,453 (23.81)	3,609 (24.88)	3,640 (25.10)
B	2,410 (16.62)	2,266 (15.62)	2,282 (15.73)	2,339 (16.13)	2,469 (17.02)	2,673 (18.43)
C	1,401 (9.66)	1,437 (9.91)	1,545 (10.65)	1,622 (11.18)	1,856 (12.80)	2,199 (15.16)

We can also examine the change in average pressure as a second indicator of rail seat load uniformity. Table 38 summarizes the average pressure imparted onto the rail seat at each loading. The value shown was calculated considering the loaded area of the rail seat, rather than the entire rail seat area. For rail seat A, the average pressure imparted onto the rail seat at a 0.5 L/V force ratio was approximately 83% greater than at zero lateral load. For rail seats B and C, these percent increases in the average pressures at 0.5 L/V force ratios were approximately 46% and 0.1%, respectively. As with maximum pressure, rail seat A yielded the highest average pressure observed in this experimentation: under a 40,000 lb (178 kN) vertical load and 20,000 lb (89 kN) lateral load (L/V force ratio of 0.5), the average pressure exerted on rail seat A was 1,546 psi (10.66 MPa).

Table 34. Average Pressures in PSI (MPa) of Rail Seat Loads at Various L/V Force Ratios

	L/V Force Ratio					
Rail Seat	0	0.1	0.2	0.3	0.4	0.5
A	847 (5.84)	817 (5.63)	811 (5.59)	829 (5.72)	1001 (6.90)	1546 (10.66)
B	709 (4.89)	701 (4.83)	707 (4.87)	706 (4.87)	740 (5.10)	1037 (7.15)
C	693 (4.78)	690 (4.76)	688 (4.74)	688 (4.74)	689 (4.75)	694 (4.78)

For all three rail seats, there was an increasing trend in maximum pressure as the L/V force ratio is increased, as the rail seat loads become more concentrated towards the field side. This behavior supports the study performed by Marquis (2011) showing increased field side pressures under higher L/V ratios, as well as the laboratory experimentation performed by Rapp (2013) with single crossties. By contrast, although the highest average pressures for all three rail seats were observed at 0.5 L/V force ratio, the rail seat experiences a slight reduction of average pressure between 0 and 0.3 L/V force ratio, before increasing with the reduction in contact area visible in Figure 180. It is hypothesized that the rail pad assembly deforms under the increasing lateral load in this range, leading to an increase in contact area and therefore a decrease in average pressure.

The difference in the pressure values recorded for the three rail seats can primarily be explained by the differences in the contact areas on each rail seat. Not coincidentally, rail seat A, having experienced the highest pressure values, consistently showed lower contact areas compared to

rail seats B and C. Table 39 summarizes the contact areas on each rail seat under the various L/V force ratios applied by the TLV with a constant 40,000-lb (178 kN) vertical load.

Table 35. Contact Areas in in^2 (cm^2) of Rail Seat Loads at Various L/V Force Ratios

	L/V Force Ratio					
Rail Seat	0	0.1	0.2	0.3	0.4	0.5
A	29.53 (190.5)	30.6 (197.4)	30.81 (198.8)	30.15 (194.5)	24.97 (161.1)	16.17 (104.3)
B	35.28 (227.6)	35.67 (230.1)	35.39 (228.3)	35.43 (228.6)	33.77 (217.9)	24.1 (155.5)
C	36 (232.6)	36 (233.9)	36.35 (234.5)	36.35 (234.5)	36.3 (234.2)	36.01 (232.3)

Rail seat C had the most consistent contact areas, with a decrease of 0.13% between L/V force ratios of 0 and 0.5. Rail seat A had a decrease of approximately 45% from the initial loading to the most extreme case, while this value was approximately 32% for rail seat B. Figure 181 summarizes the ratio of contact areas at the various L/V force ratios to the initial contact areas recorded at the pure vertical loading for each respective rail seat.

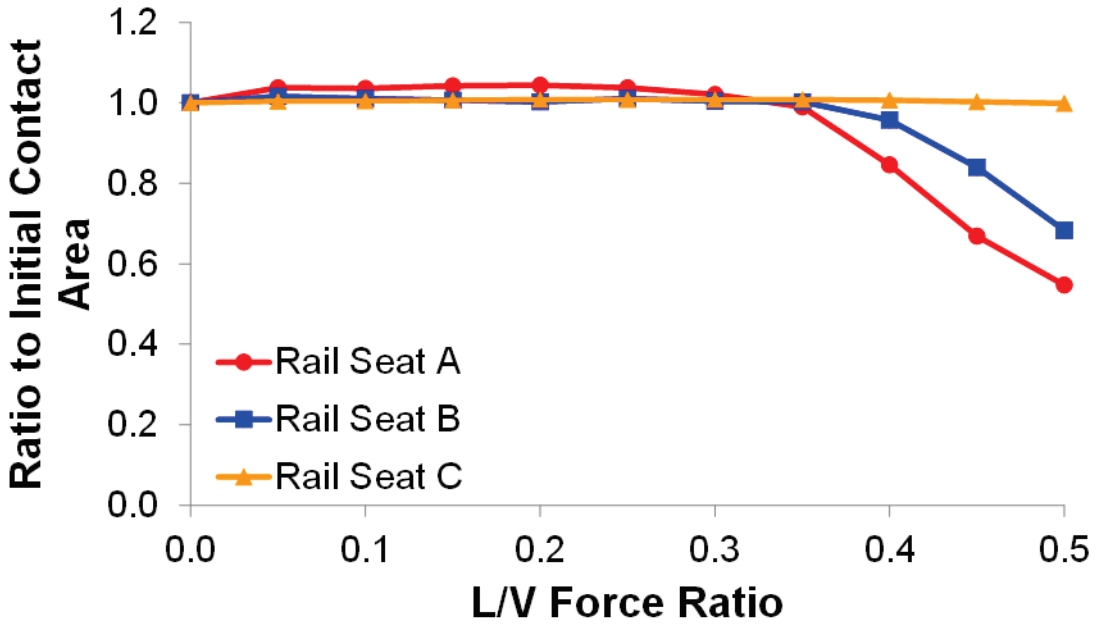

Figure 181. Contact Area per L/V Force Ratio with 40,000 lb (178 kN) Vertical Wheel Load

Figure 181 illustrates a common trend in all three rail seats: the contact areas remain relatively constant through an L/V force ratio of 0.35, when a 14,000-lb (62.3 kN) lateral load was applied. It is hypothesized that this is the lateral load at which significant rail base rotation began to occur, given that at L/V force ratios from 0.35 to 0.5 rail seats A and B show nearly linear decreases in contact area. The pressure distributions shown in Figure 180 also reflect this trend: both rail seats show a significant decrease in contact on the gauge side between the L/V force ratios of 0.3 and 0.4. Rail base rotation is also likely occurring on rail seat C under increased

lateral loading, but not as significantly as on rail seats A and B. At rail seat C, the contact area remains constant and the pressure distributions in Figure 180 show very small unloading of the gauge side at higher L/V force ratios. It is possible that a greater rail base rotation occurred on rail seats A and B because the fastening clips were not driven on properly or had experienced more wear than those installed at rail seat C, resulting in a reduction in clamping forces compared to rail seat C.

In summary, all three measurements—maximum pressure, average pressure, and contact area—indicate that the rail seat load is not uniformly distributed across the rail seat, even under a pure vertical load. Moreover, the data indicate that the lateral load has a significant, added effect on the rail seat load distribution, resulting in a concentration of the load on the field side of the rail seat. Thus, we see that the original design assumption, that the rail seat load is uniformly distributed over the entire rail seat, does not accurately describe the field loading environment, and that a more representative design standard should be developed. An improved standard should facilitate the establishment of mechanistic failure criteria which, ultimately, would promote crosstie and fastening system designs more resistant to failure mechanisms associated with RSD, which is affected by the non-uniformity of the rail seat load distribution.

6.30 Effect of Support Conditions

In well-maintained track with proper geometry and support conditions, a load that is applied to the rail is generally distributed over several crossties. Because of this, the percentage of the load transferred to the crosstie centered under the TLV loading axle was assumed to calibrate the MBTSS data. Strain gauge data from this field experimentation showed a load transfer of approximately 50% into the rail seat when subjected to dynamic loads, with the rest being distributed across adjacent crossties; therefore, this percentage of load was used for data calibration (Grassé 2013). Depending on the crosstie spacing, the percentage of an axle load that a crosstie carries is often considered to fall within the range of 40 to 60%, further confirming the assumption of a 50% transfer for this field experimentation (Hay 1982). Other methods found in literature for calculating rail seat loads also agree with this range of percentages, with variables such as track stiffness and rail size, among others, having an effect on the actual percentage of an axle load carried by a single crosstie.

While this assumption provides a sensible average value for rail seat load, the support conditions under individual rail seats will cause variations in the actual rail seat load experienced by any individual rail seat. In extreme cases, a crosstie may carry an entire axle load, if support conditions of adjacent ties are inadequate (Hay 1982, Grassé 2013). Inversely, a crosstie may carry almost no axle load if its support conditions are weak relative to adjacent crossties. Thus, it is important to examine the effect of support conditions. Theoretically, the vertical deflection of the crosstie, as a response to increased vertical load, is correlated to the stiffness of the ballast below the rail seat. Thus, higher deflections should correlate to lower ballast stiffness and therefore lower rail seat loads. Similarly, lower deflections should correlate to higher ballast stiffness and therefore higher rail seat loads. The rail seat load, in turn, should affect the maximum pressure exerted on the rail seat. In summary, if the assumption of 50% load transfer accurately predicts the load imparted to the rail seat directly below point of loading, it will result in an inverse relationship between crosstie displacement and maximum pressure.

Figure 181 illustrates the relationship between vertical crosstie displacement and maximum pressure using data from experiments conducted in tangent track on the RTT at the TTC in May

2013. As a baseline for comparison, the aforementioned assumption of a 50% load transfer is assumed. Contrary to the hypothesis detailed above, no clear relationship between crosstie displacement and maximum pressure is discernable from the data. The high- and low-bound pressure data series correlate to displacements in the middle of the observed range, while the high- and low-bound displacement data series yield nearly identical maximum pressures above 25 kips. It is evident that the assumption of the average case, 50% load transfer, is not appropriate for examining the results from discrete rail seats and in fact confounds the results of this analysis.

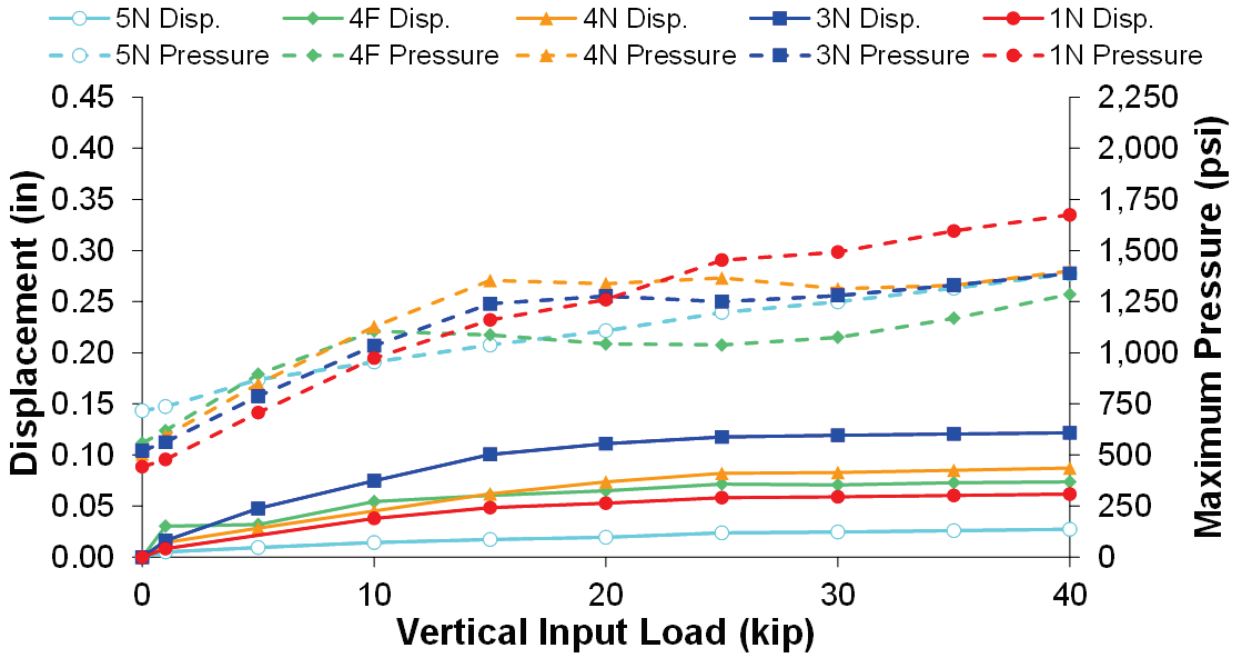

Figure 182. Vertical Crosstie Displacement and Maximum Pressure at Various Levels of Vertical Load (50% Wheel Load Assumption)

Although the rail seats on which MBTSS were used were not instrumented to capture rail seat loads, the data can be presented with more meaning by estimating the percent of load transfer at each rail seat. It was assumed that as the crosstie deflections increased, the support conditions improved (as evidenced by reduced change in vertical deflection at higher loads). Thus, it was assumed that the percentages of load transfer would increase with increasing vertical load. The position of the data series relative to one another were also considered to determine the percentages of load transfer at high vertical loads. Finally, as the vertical deflection of each rail seat became constant, it was assumed that the percentage of load transfer remained constant as well. The results of these estimations are illustrated in Figure 183.

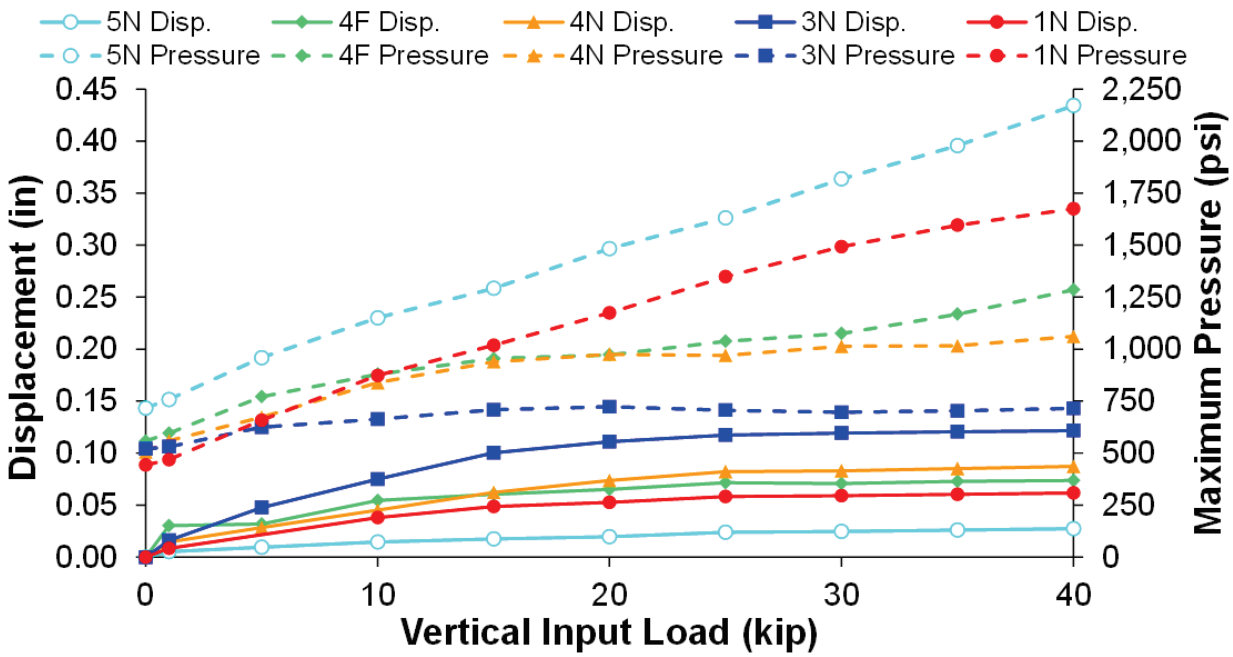

Figure 183. Vertical Crosstie Displacement and Maximum Pressure at Various Values of Vertical Load (Estimated Load Transfer)

By correlating higher percent load transfer with less change in displacement (corresponding to stiffer support conditions), we see that the maximum pressures now behave as predicted by the thought experiment. Therefore, we can conclude that while an assumption of 50% load transfer may accurately represent the average load applied to a rail seat, it is not appropriate for use in determining the exact load applied to a specific rail seat. To properly examine the effect of crosstie support conditions on the rail seat load distribution, further experimentation is required in which the exact rail seat load is recorded and used to analyze data from MBTSS.

6.31 Summary

Data collected from this experimentation yielded five critical findings concerning the distribution of loads at the crosstie rail seat:

- The rail seat load distribution is highly non-uniform, even on well-behaved rail seats.
- L/V force ratio plays a significant role in RSD failure mechanisms due to its effect on rail seat load distribution.
- Rail seat load distribution may lose more than 40% of contact area under high L/V force ratios, depending on fastening system health.
- Although the average pressure exerted may be substantially lower, the maximum pressure may exceed 3,600 psi in extreme cases.
- The 50% load transfer assumption is not appropriate for analyzing the performance of specific rail seats.

The findings from this experimentation have been used to guide both further experimentation in the lab and efforts to introduce mechanistic principles to the design of crossties and fastening systems.

6.32 Quantifying Rail Pad Displacement

6.33 Background

The purpose of the field experimentation throughout this project was to enhance the understanding of the crosstie and fastening system component behavior under representative in-service loading conditions. Therefore, it is the objectives of this section to quantify the lateral displacement of the rail pad assembly and rail base as well as better understand the effect of lateral load magnitude on these displacements to address the concerns related to RSD which is widely considered to be one of the most critical areas for concrete crosstie research by members of the North American rail industry.

Today, the most common rail pad assemblies used by North American heavy haul railroads are two-part assemblies; a polyurethane rail pad on top of a nylon 6/6 abrasion frame. The primary purpose of this design is to provide both impact attenuation and abrasion resistance and though the rail pad assembly design has improved over the past thirty years, some of these assemblies continue to fail prior to their design life due to a variety of failure mechanisms. Based on previous research conducted at UIUC focusing on the failure mechanisms leading to RSD (Zeman 2010, Kernes 2013), it is hypothesized that the failure of these assemblies can not only accelerate the RSD abrasion progression rate due to additional displacement within the fastening system (do Carmo 2013), but ultimately lead to undesirable track geometry and reduced network velocity due to slow orders.

Abrasion occurs as frictional forces act between two surfaces that move relative to one another, and a harder surface cuts or ploughs into the softer surface resulting in the removal of a portion of the softer material (Bayer 2004, Williams 1997, Kernes 2013). In concrete crosstie rail pad assemblies, abrasion can be caused by relative slip between fastening system components and usually manifests itself as three body-wear and involving the concrete crosstie rail seat, rail pad assembly, and abrasive fines (Bayer 2004, Williams 1997, Kernes 2013). Therefore, the lateral displacements of the rail pad assembly and rail base of newly installed concrete crossties and fastening systems were quantified. These values could also then be compared to values used in previous abrasion research and testing.

6.34 Field Instrumentation Setup

Two sets of field experiments were conducted at the TTC in Pueblo, CO. In May 2013, the lateral displacements of the rail base and rail pad assemblies were measured and recorded using linear potentiometers mounted to the concrete crossties with metal brackets at six different rail seats as shown in Figure 184 and Figure 185. Lateral forces exerted on the rail were captured simultaneously using the lateral load strain gage bridge. These strain gauges were installed in the cribs between rail seats C-E, E-G, S-U, and U-W. Both the HTL and RTT track sections had the same instrumentation layout and naming convention (Figure 184). This study will only reference the instrumented crossties (BQ, CS, EU, and GW).

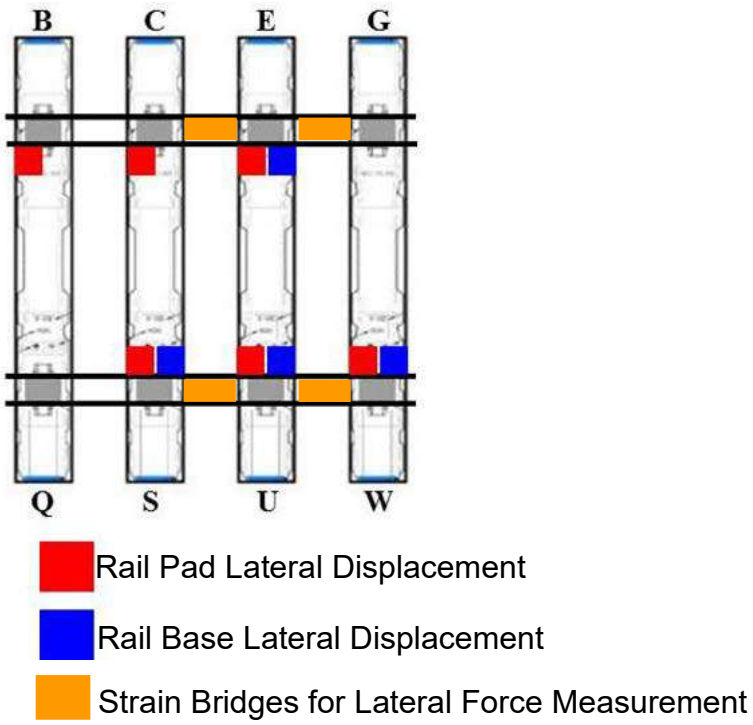

Figure 184. Location of Instrumentation and Naming Convention for Rail Seats and Cribs Located in the RTT and HTL Track Sections

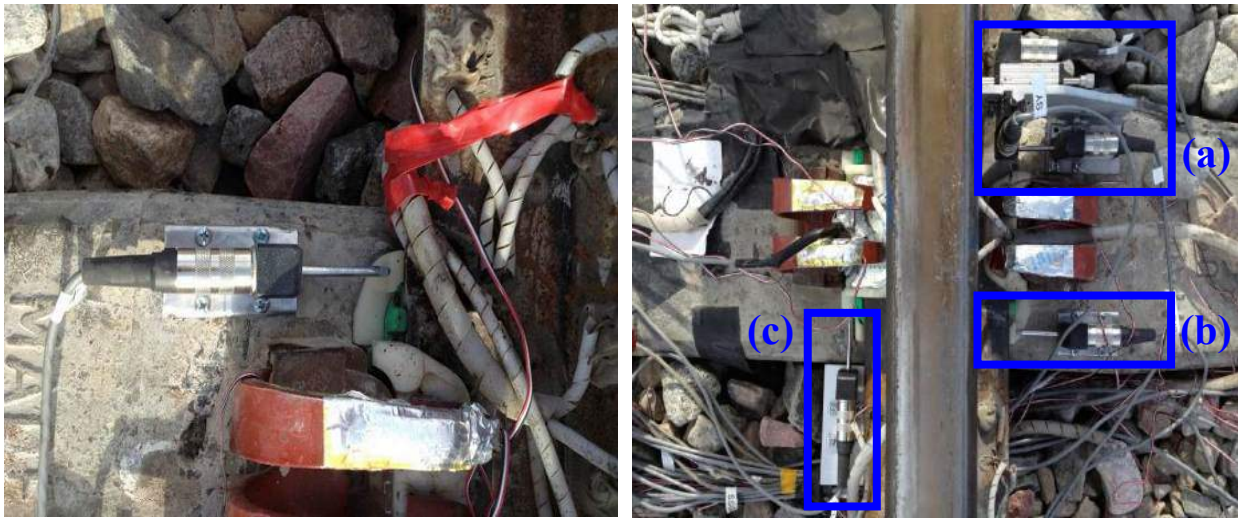

Figure 185. Field Experimental Setup Showing Instrumentation to Measure (a) Rail Base Translation, (b) Rail Pad Lateral Translation, and (c) Rail Pad Longitudinal Translation

6.35 Effect of Static Load on Lateral Rail Base and Rail Pad Assembly Displacement

It was hypothesized that an increase of lateral wheel load will result in larger displacements of the rail pad assembly. To test this, as described previously, the displacements of the rail base

and the pad assembly were recorded at rail seats E, S, U, and W. Figure 186 displays the displacements recorded when crosstie C-S was subjected to a 40-kip vertical load and varying lateral loads.

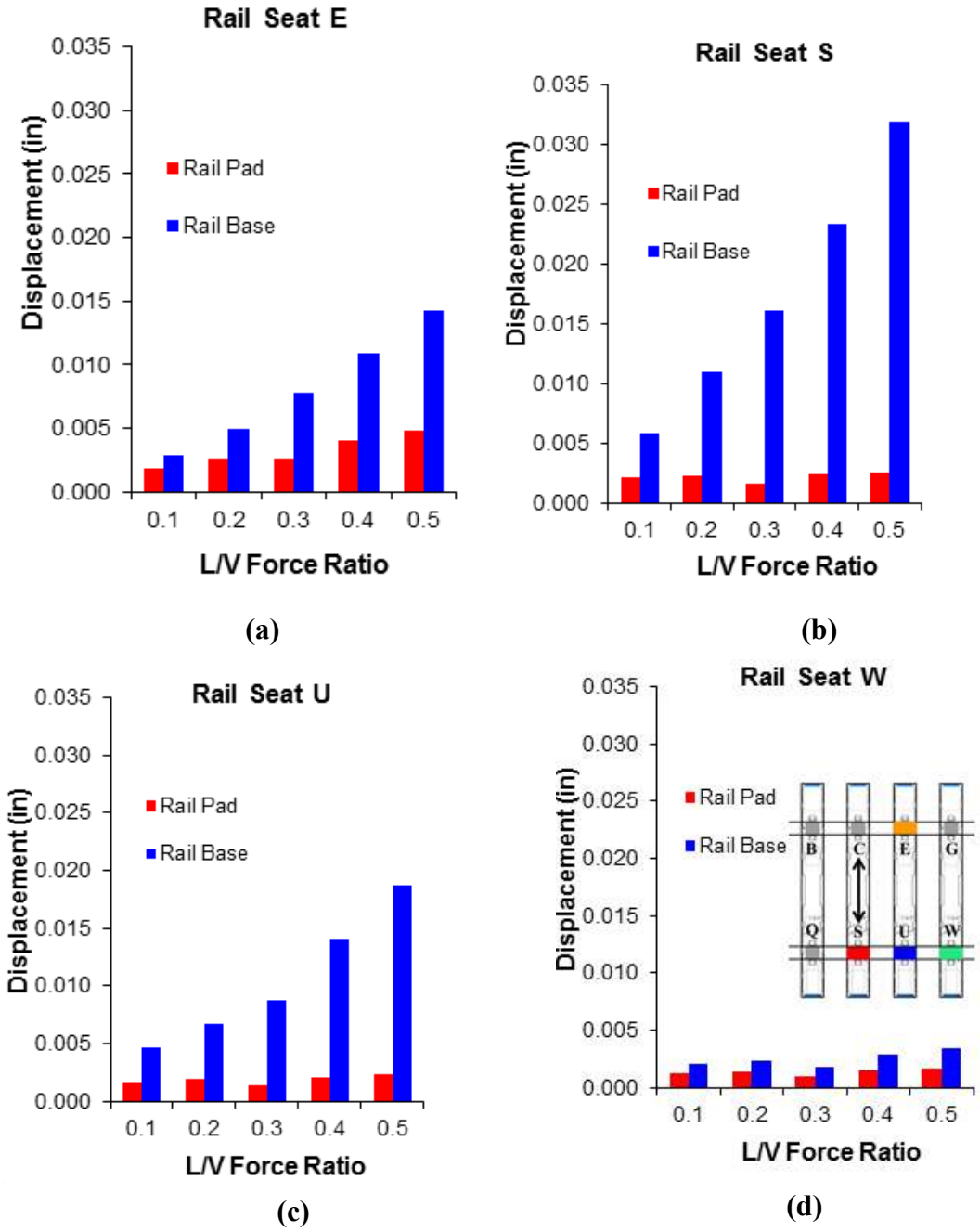

Figure 186. Rail Pad Assembly and Rail Base Displacements for Varying L/V Force Ratios at 40 kips Vertical Load Applied at Crosstie CS

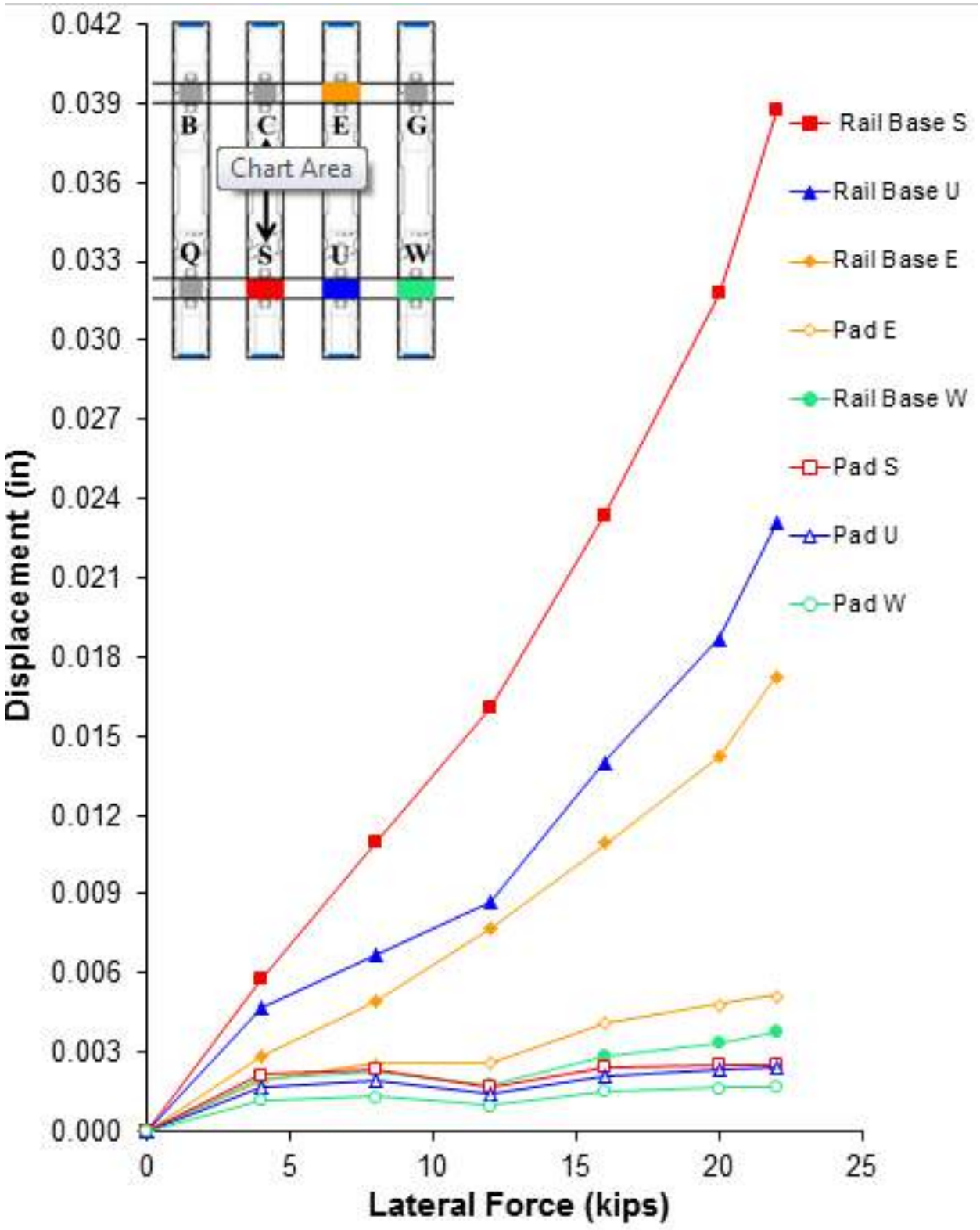

Figure 187. Rail Base and Rail Pad Assembly Lateral Displacement for Increasing Lateral Loads with A 40 kip (178 kN) Vertical Load (RTT, Tangent Track)

Upon analyzing the data, there was a relationship between the lateral wheel load and the lateral rail base displacement; as the lateral wheel load increased, the rail base lateral displacements increased. Specifically, rail seat S displacements increased from 0.006 inches to 0.030 inches as the lateral load increased from 4,000 to 20,000 pounds respectively. Rail seats E and U, one crosstie away, displacements increased from 0.003 and 0.005 inches to 0.0142 and 0.019 inches, respectively. On average, the rail base at both rail seats displaced approximately 50% of rail seat S. Rail seat W, two crossties away, displacements increased from 0.002 to 0.003 inches.

The relationship between lateral wheel load and lateral pad displacement was not as evident as the rail base lateral displacement. In fact, the lateral pad displacement at rail seat S stayed relatively constant at a magnitude of 0.002 inches. The lateral pad displacement at rail seat E increased from 0.002 inches to 0.005 inches as the lateral load increased from 4,000 to 20,000 pounds respectively. The lateral pad displacement at rail seat U also remained fairly consistent at a value of 0.002 inches. The lateral displacement at rail seat W ranged from 0.001 to 0.002 inches.

The lateral rail base and pad assembly displacement were considered to be negligible at distances greater than 48 inches (1220 mm) (Figure 186d). Therefore, it appears that the track was able to transfer most of the lateral load to three crossties (24 inches in either direction from point of load application).

Upon further analysis of the data, it was clear that the lateral rail base displacement magnitude was always greater than the pad displacement, thus leading to a relative displacement between the rail base and rail pad assembly. The difference in relative displacement increased as the lateral force on the system increased. The relative slip between the rail base and pad assembly indicates a possible occurrence of shear at the rail pad assembly interfaces, which supports the feasibility of the hypothesis. This relative slip at this interface also would more likely lead to the deterioration of the pad assembly, rather than the crosstie rail seat.

The magnitude of the displacements observed in the field was smaller than the measurements recorded in the laboratory. This result is likely due to lateral load distribution throughout the track structure provided by adjacent fastening systems, whereas, in the laboratory, the lateral force was resisted by only one rail seat. Furthermore, comparing the displacements obtained in the lab to the imposed displacements used in previous abrasion experimentations at UIUC (Kernes 2013), the maximum measured rail pad displacement of 0.005 inches (0.13 mm) consisting of new fastening system components, corresponded to only 4% of the simulated motion [1/8 inch (3.18 mm)].

Despite the reduced displacement magnitude, the high frequency recurrence of the relative displacement throughout the rail pad service life may be harmful to the integrity of this component and the crosstie rail seat. Additionally, the displacements will only increase throughout the life of the system as other components wear. Therefore, further experimentation should focus on analyzing the relationship between the measured relative displacement and the severity and/or rate of abrasion.

6.36 Effect of Dynamic Load on Lateral Rail Pad Assembly and Rail Base Displacement

It was hypothesized that the freight consist would impart the highest demands on the track components, resulting in higher displacements in the rail base and pad. This section will focus on results from 315,000 pound-force (1,400 kN) rail cars with vertical wheel loads of approximately 40 kips (178 kN). Rail seats "S" and "U" on the low rail are highlighted because these two locations had the necessary overlapping instrumentation necessary to simultaneously measure the rail pad displacement, rail base lateral displacement, and the lateral wheel loads imposed on the rail. During the freight train runs, the speed was increased from 2 mph up to 45 mph.

The potentiometers placed at rail seat "U" captured a maximum lateral rail pad assembly displacement of approximately 0.004 inches (0.10 mm), which presented an increase in magnitude for increasing lateral wheel loads. The behavior of rail pad "S" also showed a trend of increasing in magnitude with respect to the increase in wheel load, though the displacements were smaller as compared to rail seat U seen in Figure 189. Furthermore, the dynamic lateral rail pad assembly displacements were greater than static displacements.

The behavior of the rail base lateral displacement also presented a direct relationship with the increase in lateral wheel load Figure 191. The maximum rail displacement was close to 0.022 inches (0.55 mm), a value that is 5.5 times greater in magnitude than the displacements recorded for the rail pad assemblies. Unlike the rail pad assembly, the dynamic rail base lateral displacements were smaller than the static displacements.

The difference in displacement magnitude between rail pad assembly and rail base is likely related to the bearing restraints. Cast-in shoulders confine the rail pad assembly while insulators confine the rail base, and shoulders are stiffer than insulators. Additionally, the rail pad assembly is subjected to frictional forces at most of its surfaces, which forces this component to interact within the fastening system on its top and bottom surfaces, reducing its movements.

Loads of similar magnitudes resulted in different displacements of the rail pads on rail seats "U" and "S." This variation is likely due to the inherent crosstie-to-crosstie variability in support conditions and geometric variations in the rail seats that may lead to differences in gaps between rail pad and shoulders. This last parameter is a function of the manufacturing tolerances.

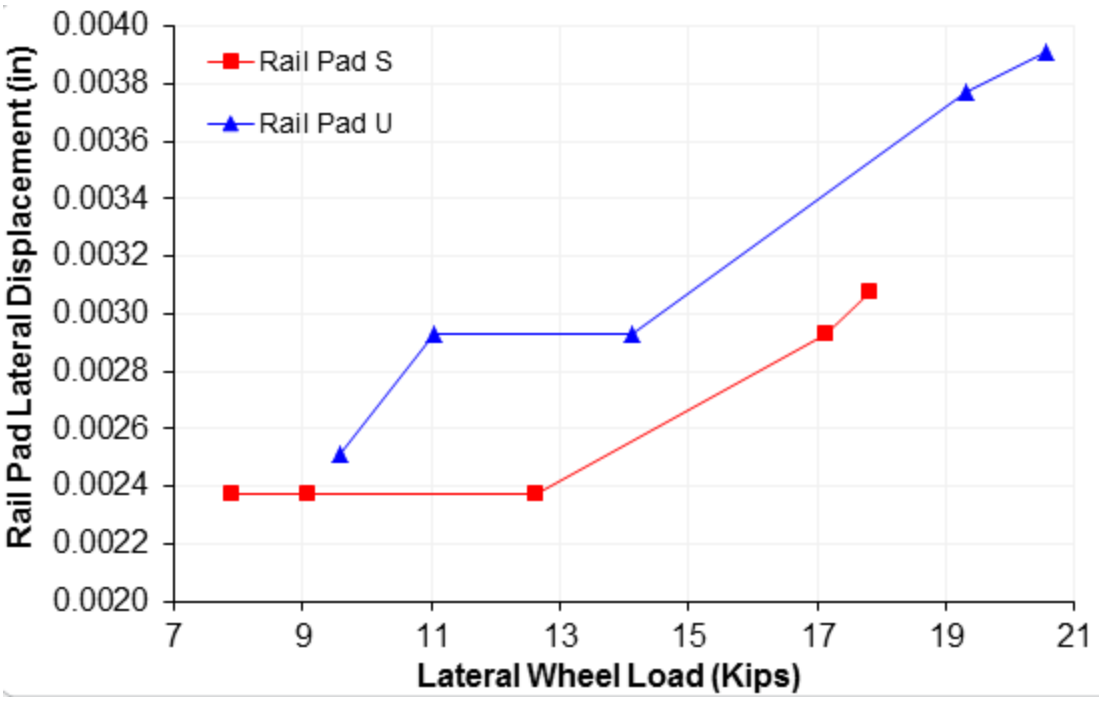

Figure 188. Rail Pad Lateral Displacement for Increasing Lateral Wheel Load

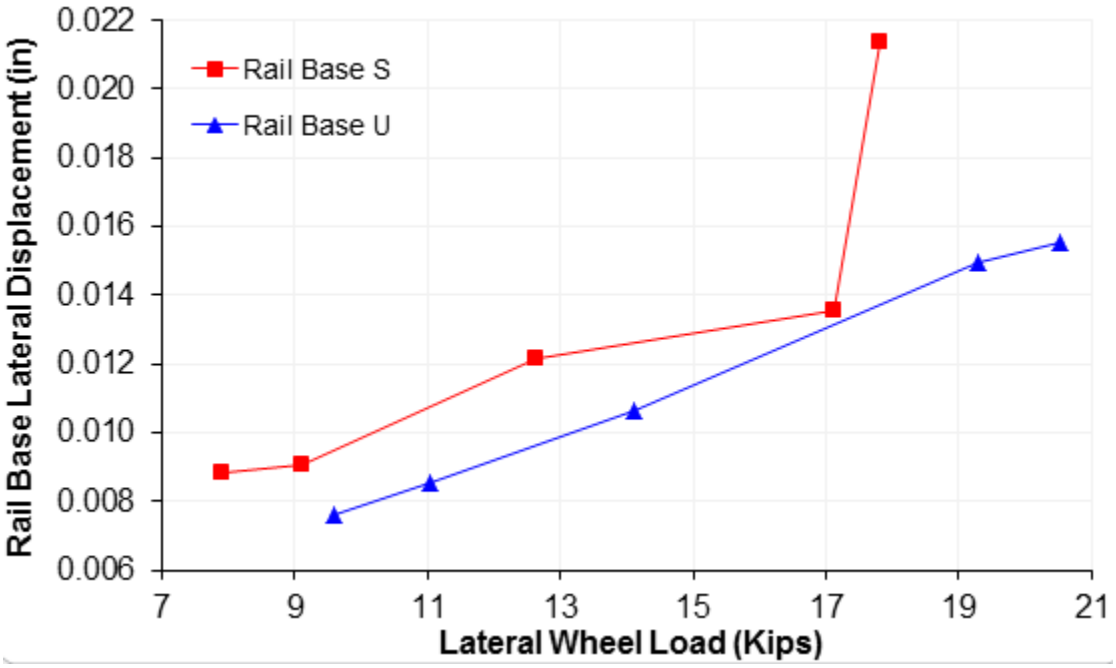

Figure 189. Rail Base Lateral Displacement for Increasing Lateral Wheel Load

6.37 Summary

Data collected from this experimentation yielded eight critical findings concerning the distribution of loads at the crosstie rail seat:

- There is a direct relationship between lateral wheel load and lateral rail base displacement.
- There was not a direct relationship between lateral wheel load and lateral pad assembly displacement.
- The lateral rail base and pad assembly displacement were considered to be negligible at distances greater than 48 inches.
- The lateral rail base displacement magnitude was always greater than the pad displacement.
- The difference in relative displacement increased as the lateral force on the system increased.
- Rail pad assembly lateral displacements increased when subjected to dynamic loading.
- Rail base lateral displacements decreased when subjected to dynamic loading.
- All displacements quantified were smaller than those used in previous research.

6.38 Crosstie Bending

6.39 Background

As a material, concrete is very weak in tension, but very strong in compression. Because of this, concrete crossties must be held in compression, or "pre-stressed," with tensioned steel (Zeman 2010). This can be achieved by tensioning steel wires or strands before or after the concrete is cast; members made this way are referred to as "pre-tensioned" and "post-tensioned", respectively. Pre-tensioning is the more common practice for the manufacture of pre-stressed concrete crossties in the United States. Pre-stressing significantly increases concrete's flexural strength, ductility, and resistance to cracking. With this improved strength and ductility, pre-stressed concrete crossties can withstand the demanding dynamic loading environment imparted by passing trains (Zeman 2010, Jimenez 2004).

The primary purpose of the crosstie is to maintain track geometry (e.g. gauge, cross level, etc.) and to transfer applied wheel loads to the track substructure (Hay 1982). When a concrete crosstie supported on ballast is loaded vertically, the load is transferred from the wheel to the track system through the rail, fastening system, crosstie, ballast, sub-ballast, and subgrade. The ballast support conditions play a critical role in the type and severity of bending that the crosstie will experience under loading from a passing train (Wolf 2015). The ballast support is affected by a variety of factors that include loading during train operations, tamping, fouling, and voids (Kaewunruen 2007). Common failure modes for concrete crossties, as ranked by six Class I railroads, include rail seat deterioration, cracking from center binding (center negative bending), and cracking from dynamic loads (Zeman 2010).

Because cracking from center binding and rail seat cracking are among the primary challenges facing concrete crossties, it is critical to understand the effect of loading and support conditions on the induced crosstie bending moments. The current AREMA design criteria mandates that

cracking should not occur under the design wheel load (AREMA 2014). Therefore, to determine if this criteria is satisfied, the bending moments were measured and compared with the cracking moments found for a specific crosstie using Response 2000, a linear elastic analysis program.

Table 36. Concrete Crosstie Cracking Moments (kip-in)

	Rail seat	Center
Positive (top in compression)	405.6	196.8
Negative (top in tension)	219.6	256.8

6.40 Methodology

Two sets of field experiments were conducted at the TTC in Pueblo, CO. For the both sets of experiments, crosstie surface strains gages were placed on three adjacent crossties, CS, EU, and GW as shown in Figure 190. These strain gages were used to quantify the bending moment at critical locations along the length of the crosstie. The track was loaded using the TLV as well as passenger and freight consists.

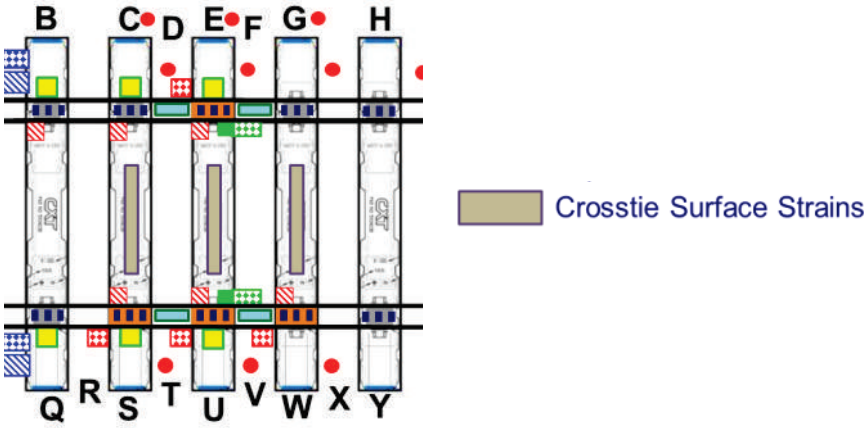

Figure 190. Locations of Crossties with Concrete Crosstie Surface Strain Gauges

As described in the field experimental plan, six strain gauges were installed on each crosstie to measure the moments at both rail seats and at the crosstie center. Due to the limitation of the number of the channels available, only the strain gauges on crosstie CS and EU were connected to the NI DAQ. The locations for the surface strain gauges are shown in Figure 190**.**

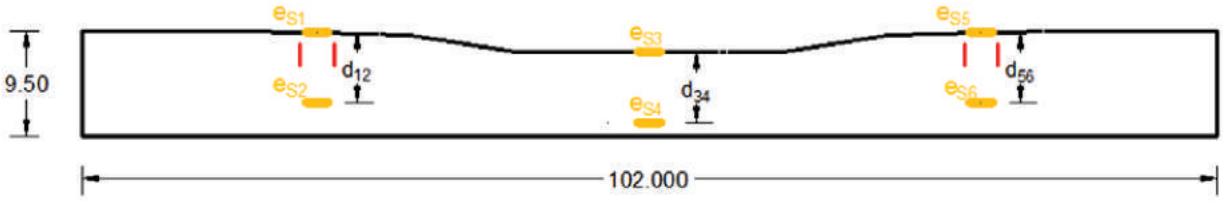

Figure 191. Locations of Concrete Crosstie Surface Strain Gauges on Crosstie

The following equations are used to calculate the bending moments:

$$M(railseat1) = (e_{S2} - e_{S1})E_c I_{12} / d$$
$$M(center) = (e_{S4} - e_{S3})E_c I_{34} / d$$
$$M(railseat2) = (e_{S6} - e_{S5})E_c I_{56} / d$$

Where:

- e_{S1}-e_{S6} are the strains recorded from concrete surface strain gauges
- E_c is the elastic modulus of concrete material
- I is the moment of inertia of the concrete cross section at the location of each strain gauge pair
- d is the vertical distance between the two strain gauges in each pair

6.41 Effect of Static Vertical Wheel Load on Crosstie Bending Moment

For the following analysis, rail seat load was assumed to be directly at the center of the rail seat. Thus, the wheel load is modelled as a point load occurring at the center of the rail base. Figure 192 and Figure 193 show the rail seat and center bending moments measured from crossties CS and EU under 0-40-kips vertical wheel load, when the TLV static wheel load was applied directly above each crosstie.

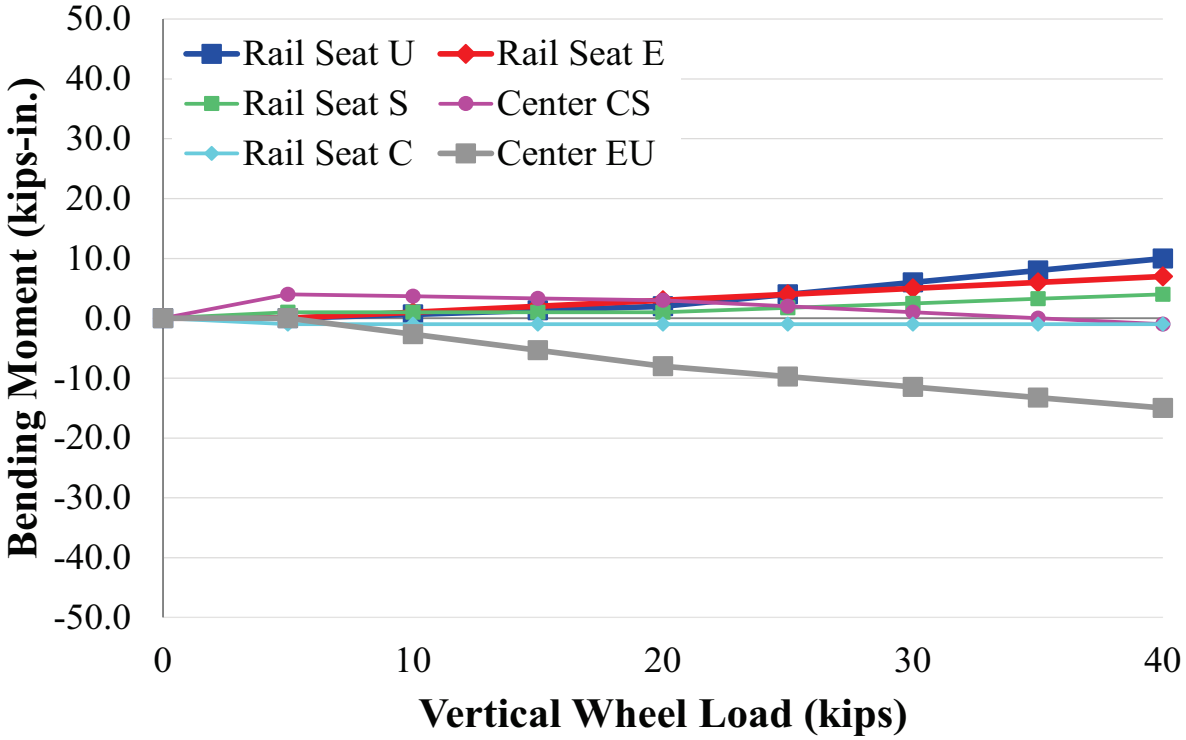

Figure 192. Crosstie Bending Moments Under Various Vertical Wheel Loads (RTT, 2012)

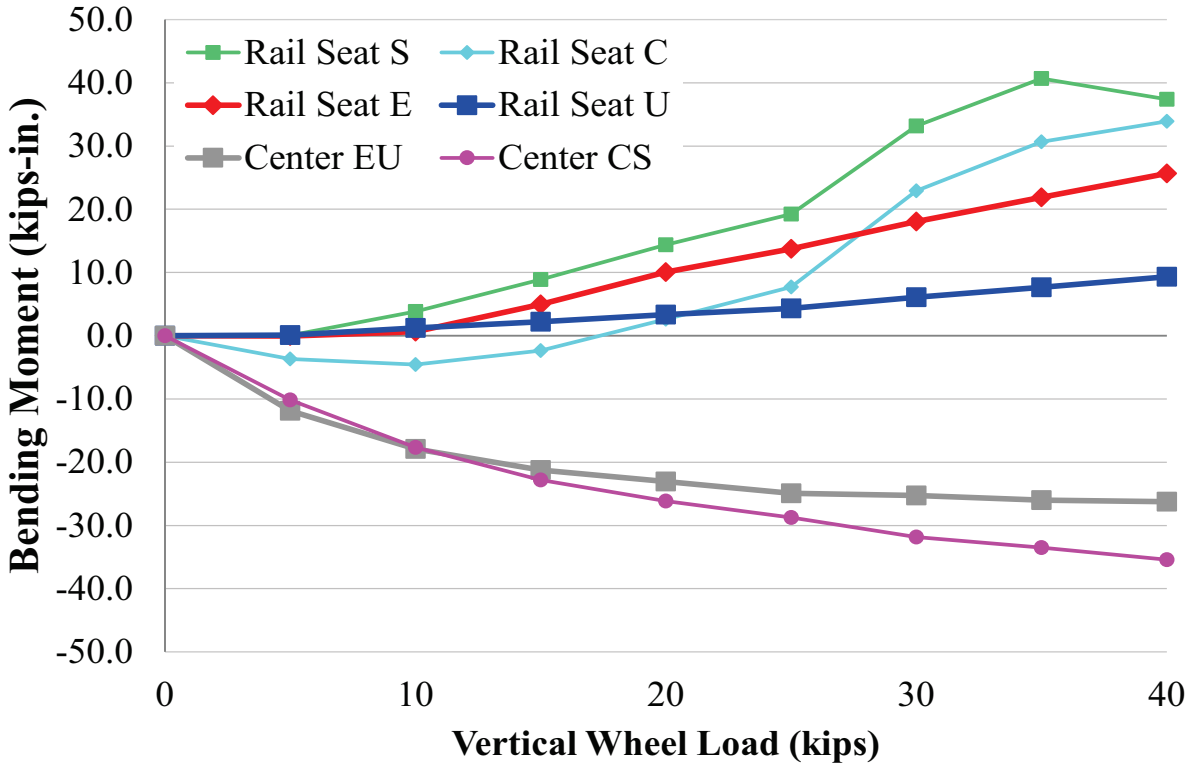

Figure 193. Crosstie Bending Moments Under Various Vertical Wheel Loads (RTT, 2013)

In both 2012 and 2013, rail seat and center bending moments increased with increased applied vertical load. The bending moments measured were considerably lower than the crosstie cracking moments provided in Table 40. Therefore, under these support and loading conditions there is no expectation of cracking in the crosstie.

Upon further analysis, the 2012 rail seat bending moments recorded (E, U, C, S) were always positive and did not exceed 10 kip-in. The crosstie center bending moments were always negative and did not exceed -15 kip-in. The 2013 bending moments recorded from crossties showed a similar trend, but the magnitude for both positive and negative bending moments exhibited a greater magnitude. The rail seat bending moments reached a maximum of 47 kip-in while the crosstie center moments were as high as -33 kip-in.

One interesting point shown in Figure 195 was that the bending moments at rail seats U and E did not start to increase until the vertical wheel loads reached 10 kips. For rail seat C, the bending moment was measured to be negative at relatively low vertical loads, returning to positive between 15 and 20-kips vertical load. This suggests that there was some separation between the bottom of the tie and the ballast and a pre-load was required to engage the ballast and cause tie bending. A brief analysis was conducted to investigate if there was a relationship between rail seat load and rail seat and center bending moments (Figure 196)

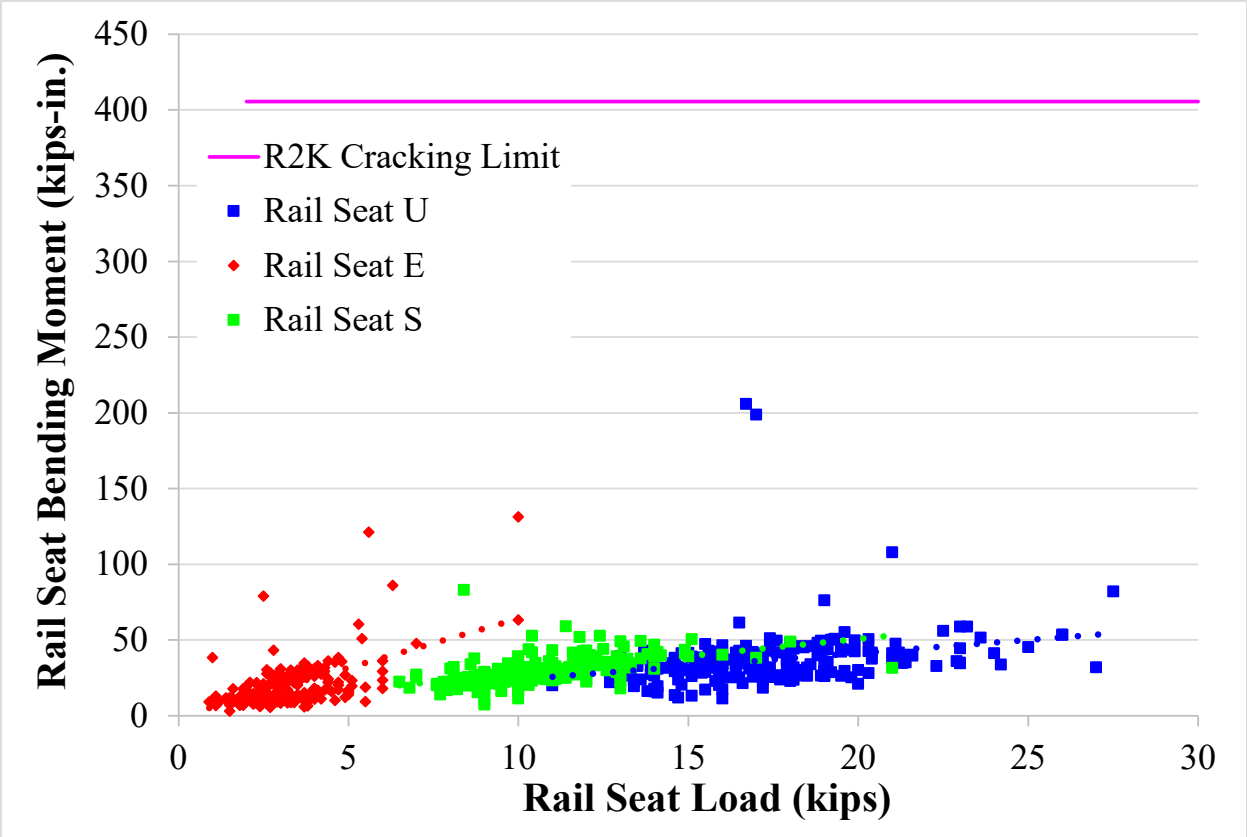

Figure 194. Rail Seat Bending Moments Under Various Rail Seat Loads (RTT, 2012)

Figure 194 does show that there is a general relationship between rail seat load and rail seat bending moment for each rail seat. However, when comparing rail seat to rail seat, there does not appear to be a trend (e.g. there is a wide range of rail seat loads that exhibit the same rail seat bending moment). Therefore, one cannot predict the bending moment solely from understanding the rail seat load.

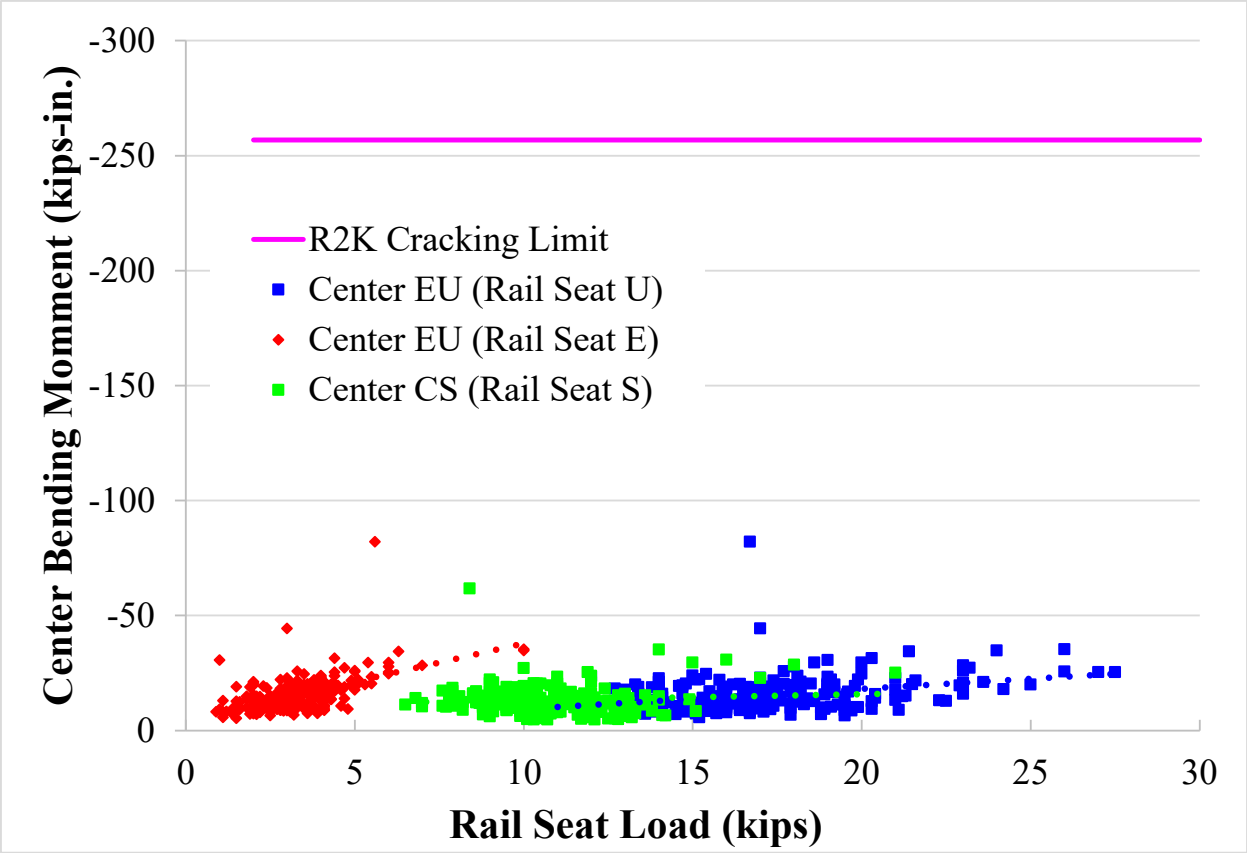

Figure 195. Crosstie Center Bending Moments Under Various Rail Seat Loads (RTT, 2012)

Figure 195 also shows that there is a general relationship between rail seat load and center bending moment for each crosstie; the bending moment increases as rail seat load increases. However, there does not appear to be a trend when looking at all crossties (e.g. there is a wide range of rail seat loads that exhibit the same center bending moment). Therefore, one cannot predict the bending moment solely from understanding the rail seat load. This finding is not a surprise in and of itself given there are many variables that effect the change in crosstie bending moments. One additional note about Figure 194 and Figure 195 is that rail seat E did exhibit the lowest rail seat load, yet the highest rate of increase in bending moment as rail seat load increased. Therefore, it is hypothesized that as these poorly supported crossties will be more apt to be damaged when load is transferred to them.

6.42 Effect of Static Lateral Wheel Load on Crosstie Bending Moment

Figure 196 and Figure 197 show the rail seat and center bending moments measured from crossties CS and EU, when the TLV was directly above each crosstie, under 40-kip vertical wheel load while increasing the lateral load applied to both rails from 0–20 kips.

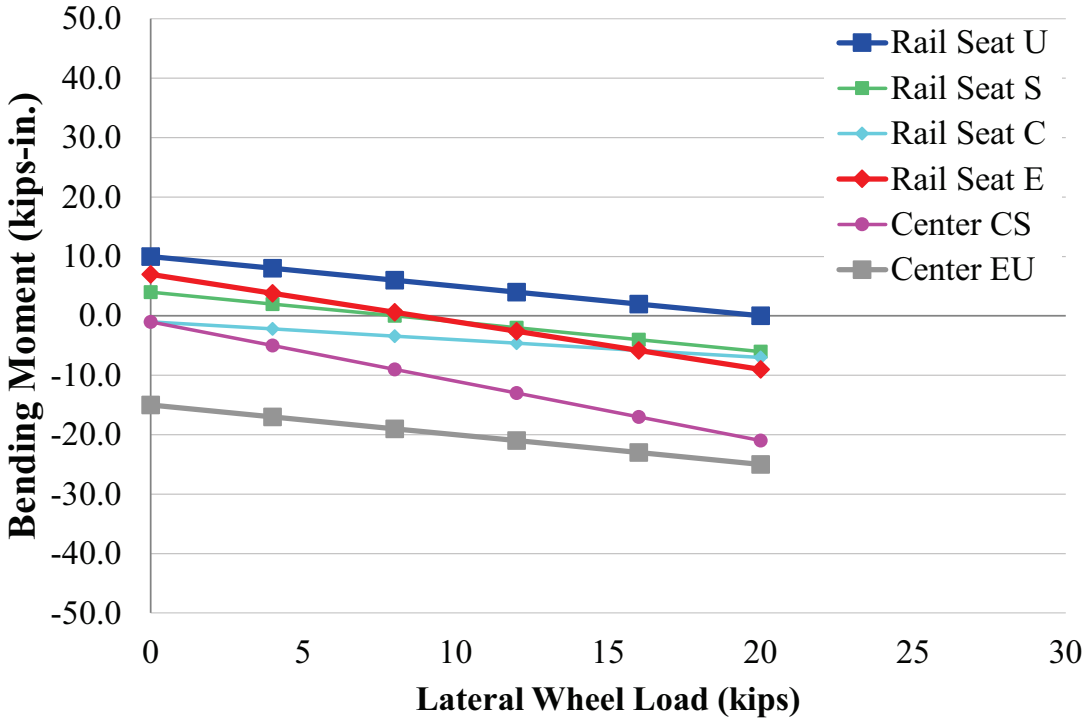

Figure 196. Crosstie Bending Moments Under Various Lateral Wheel Loads (RTT, 2012)

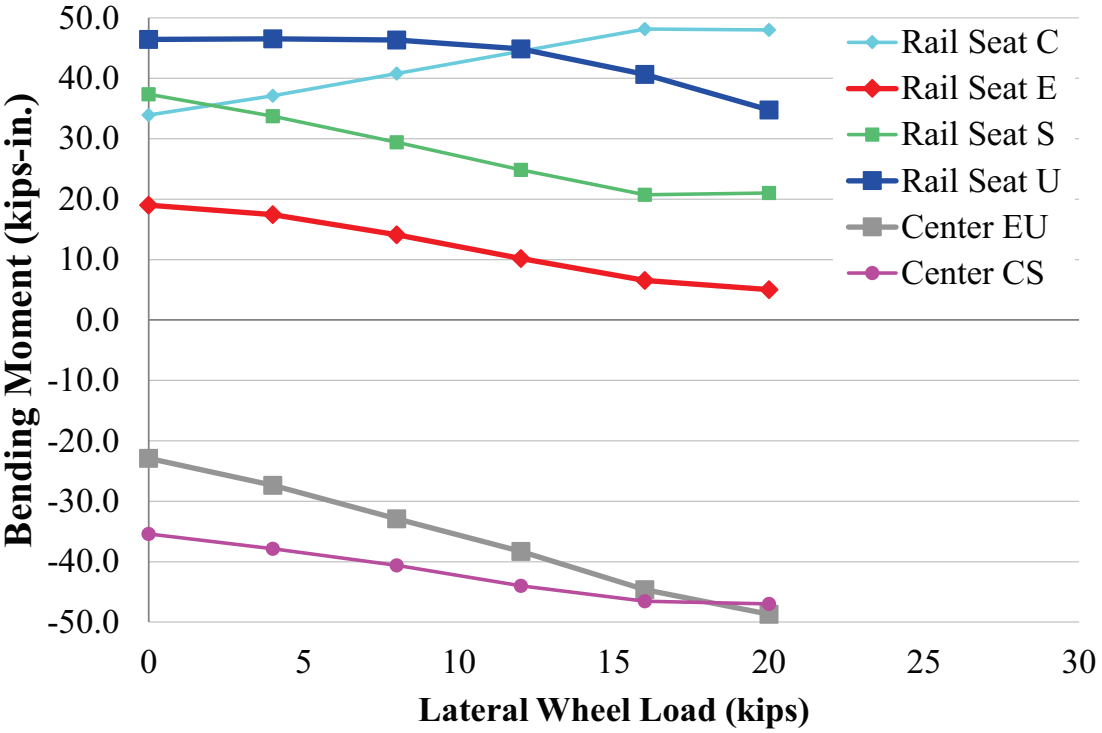

Figure 197. Crosstie Bending Moments Under Various Lateral Wheel Loads (RTT, 2013)

Figure 196 and Figure 197 show that the application of lateral forces did lead to a change in the magnitude of the rail seat bending moments. Rail seat C notwithstanding, when a lateral load

was applied, the rail seat bending moments decreased in magnitude. Given rail seat positive cracking is of concern to the industry, this data confirms that the addition of lateral load should not be the cause for seat positive cracking. Similar results were found during testing on the HTL.

Figure 196 and Figure 197 also show that the application of lateral forces also leads to a change in magnitude of the center bending moments. In each case, when lateral load was applied, the center moment increased in magnitude. Given center negative cracking is one of the primary concerns in the rail industry, this data shows that the addition of lateral load could produce moments greater in magnitude than expected under purely vertical loads and induce higher rates of center negative cracking. Similar results were found during testing on the HTL.

6.43 Rail Seat Bending Moment under Dynamic Wheel Load

An analysis of the RTT dynamic data from 2012 was performed and the findings are presented below. The analysis was performed in an effort to understanding the effect of dynamic loading on the crosstie rail seat bending moments. The effect of crosstie support, car weight, and speed were investigated. All bending moments recorded were below the AREMA design requirement. All data was captured within a couple hours on well-maintained track and thus high bending moments were not expected.

Figure 197, Table 37, and Table 38 focus on determining how each individual crosstie exhibits varying rail seat bending moments when subjected to the same loading.

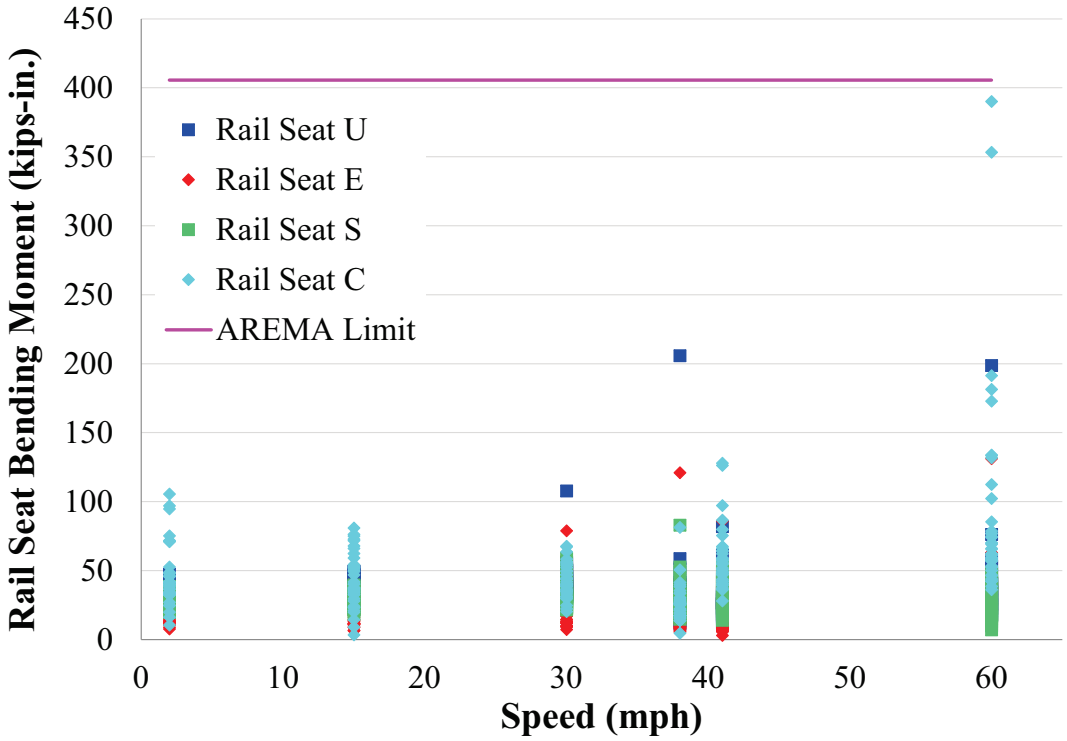

Figure 198. Rail Seat Bending Moments of Each Rail Seat Under 263, 286, 315k Freight Car Dynamic Loading Ranging from 2 mph to 60 mph (RTT, 2012)

Table 37. Mean, Median, Standard Deviation, and Maximum Rail Seat Bending Moments (kip-in) of Each Rail Seat Under 263, 286, 315k Freight Car Dynamic Loading Ranging from 2 mph to 60 mph (RTT 2012)

Rail Seat	C	S	E	U
Mean	50.3	29.8	22.8	36.6
Median	41.8	28.5	17.8	34.4
Standard Deviation	42.6	8.9	30.5	19.6
Maximum	390.1	82.9	131.2	205.8

Table 38. Standard Deviation of Rail Seat Bending Moments (kips-in.) of Each Rail Seat Under 263, 286, 315k Freight Car Dynamic Loading Ranging from 2 mph to 60 mph (RTT 2012)

Rail Seat	C	S	E	U
All	42.6	8.9	30.5	19.6
263k	52.2	9.3	16.0	31.2
286k	55.2	5.7	8.0	7.1
315k	22.8	9.0	16.3	9.9

When comparing the rail seat bending moments of all traffic, the standard deviation was 42.6 kips-in. for rail seat C, 8.9 kips-in. for rail seat S, 30.5 kips-in. for rail seat E, and 19.6 kips-in. for rail seat U. When looking at the data presented within Figure 197, Table 37, and Table 38, one can see that rail seat C consistently exhibited the most variable bending moments. Rail seat C also recorded the highest recorded bending moments of 390.1 kips-in. Rail seat S consistently exhibited the lowest standard deviation and recorded the lowest maximum rail seat bending moment of 82.9 kips-in. Table 38 provides a means of comparing the standard deviation of each rail seat under each type of car (263, 286, and 315k).

Figure 198 and Table 39 focus on determining the effect of car weight on rail seat bending moment when considering all rail seats. This data was analyzed to understand if car type had a larger effect when compared to individual crosstie support.

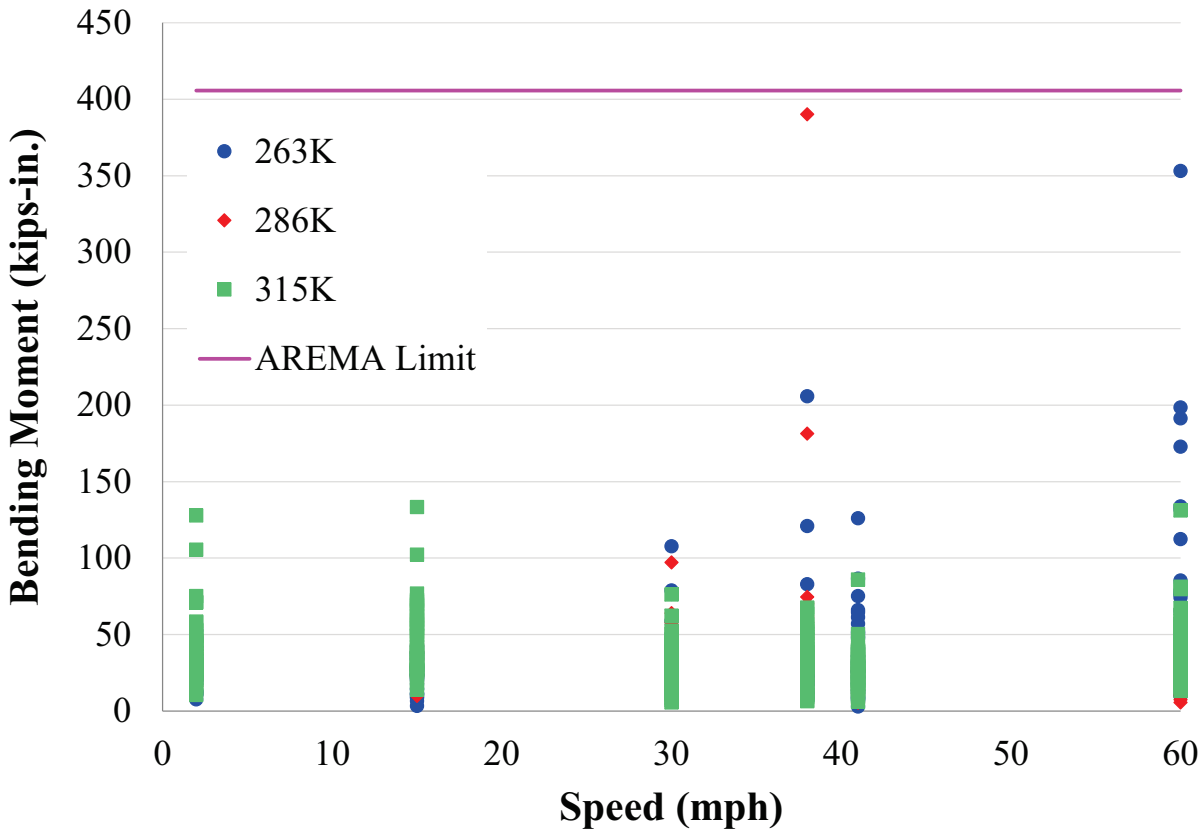

Figure 199. Rail Seat Bending Moments of All Rail Seats Under 263, 286, 315k Freight Car Dynamic Loading Ranging from 2 mph to 60 mph (RTT, 2012)

Table 39. Comparison of Rail Seat Bending Moments (kip-in.) to Car Weight Under Dynamic Loading Ranging from 2 mph to 60 mph (RTT, 2012)

Nominal Car Weight (k)	263	286	315
Mean	32.7	32.6	36.5
Median	26.2	28.8	34.3
Standard Deviation	33.8	30.9	17.9
Maximum	353.2	390.1	133.5

The standard deviation for 263k and 286k cars were 33.8 and 30.8 kip-in., respectively while the standard deviation for the 315k cars was only 17.9 kip-in. Therefore, it would appear that the wheel health of the 315k cars was better than that of the 263k cars given the mean and median rail seat bending moment were higher. The 315k cars also lead to the lowest maximum bending moment of 133 kip-in.

6.44 Crosstie Center Bending Moment under Dynamic Wheel Load

An analysis of the RTT dynamic data from 2012 was also performed in an effort to understand the effect of dynamic loading on the crosstie center bending moments. The effect of crosstie support and car weight. All bending moments recorded were below the AREMA design

requirement. All data was captured within a couple hours on well-maintained track and thus high bending moments were not expected.

Figure 199 and Table 40 below focus on determining how each individual crosstie exhibits varying crosstie center bending moments when subjected to the same loading.

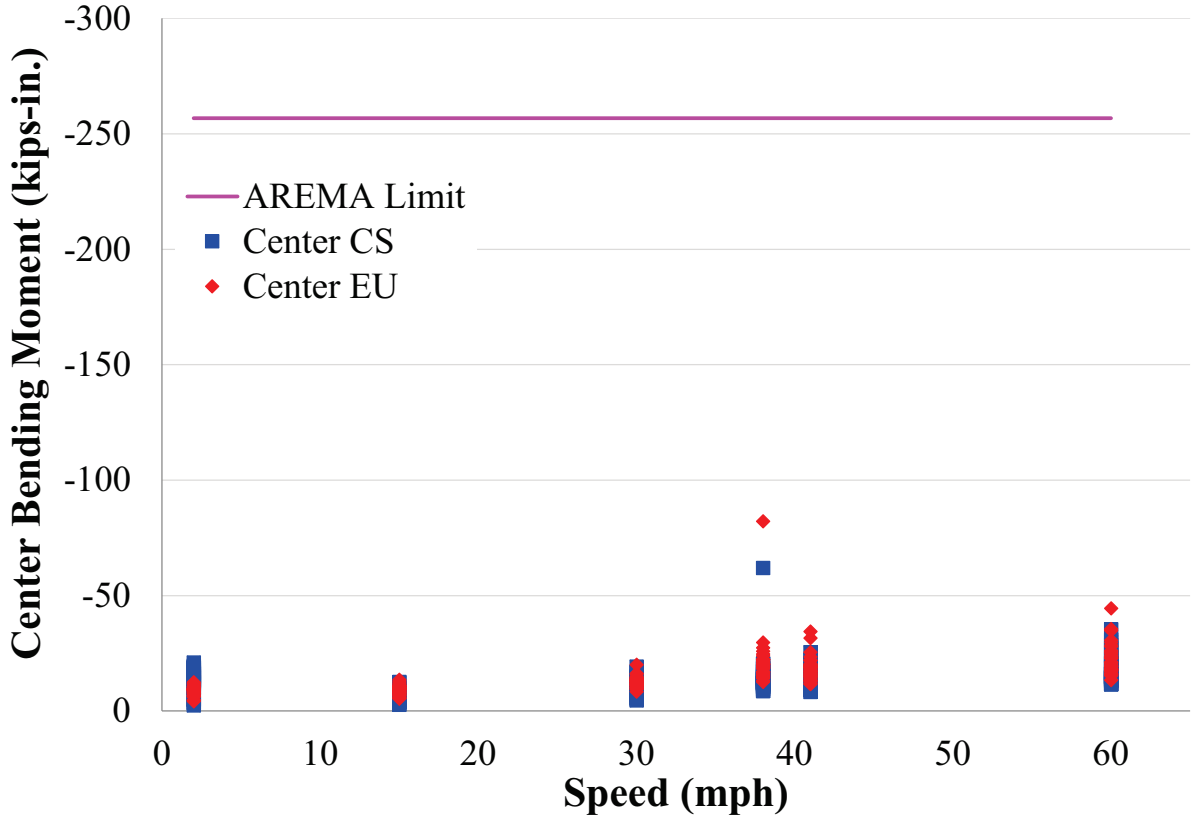

Figure 200. Center Bending Moments of Each Crosstie Under 263, 286, 315k Freight Car Dynamic Loading Ranging from 2 mph to 60 mph (RTT, 2012)

Table 40. Mean, Median, Standard Deviation, and Maximum Center Bending Moments (kips-in.) of Each Crosstie Under 263, 286, 315k Freight Car Dynamic Loading Ranging from 2 mph to 60 mph (RTT 2012)

Crosstie	CS	EU
Mean	-13.4	-15.7
Median	-12.8	-14.2
Standard Deviation	6.0	7.8
Maximum	-61.8	-82.1

The mean center bending moments for crossties CS and EU were -13.4 and -15.7 kip-in respectively. The standard deviations were 6.0 and 7.8 kip-in, respectively. Though these differences were small, crosstie EU, which exhibited the greatest standard deviation, also exhibited the highest maximum center moment of -82.1 kip-in. This trend is similar to what was found when analyzing the rail seat bending moment data. When qualitatively analyzing the data from Figure 199, one can see an increasing trend in the center bending moment with increasing speed. One additional comment about the data presented within Table 40 is that though rail seat C consistently exhibited the highest bending moments, crosstie CS does not yield the highest center negative moment.

Figure 200 and Table 16 focus on determining the effect of car weight on center bending moment when considering both crossties. This data was analyzed to understand if car type had a larger effect when compared to individual crosstie support.

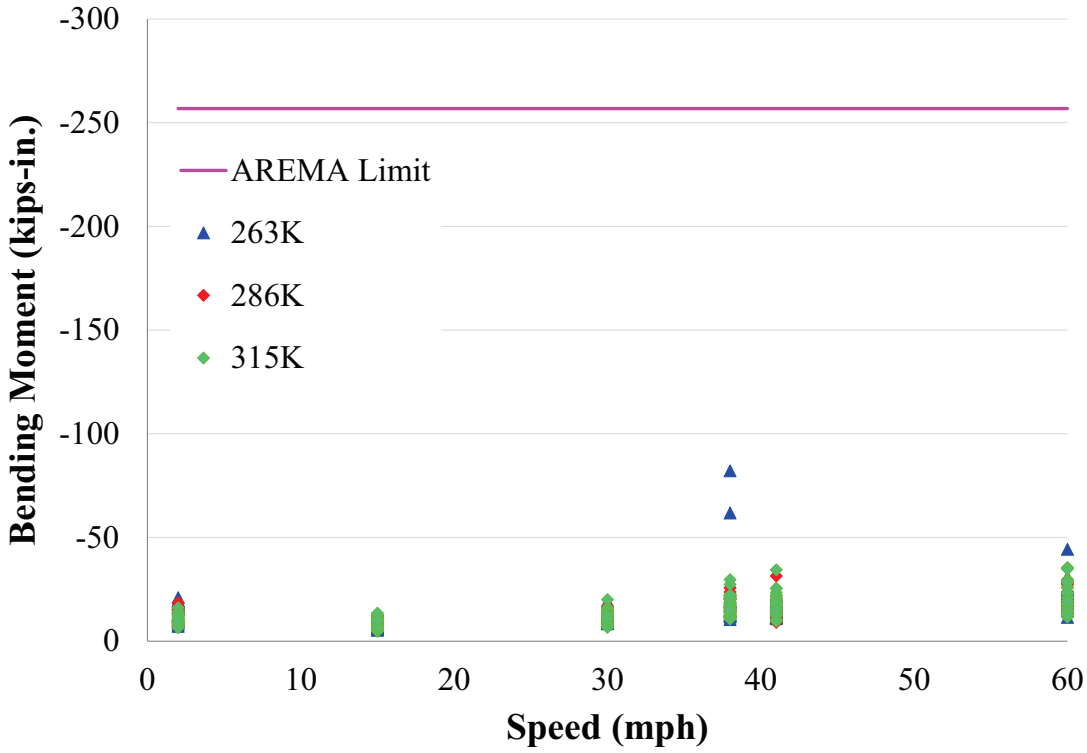

Figure 201. Center Bending Moments of all Crossties Under 263, 286, 315k Freight Car Dynamic Loading Ranging from 2 mph to 60 mph (RTT, 2012)

Table 41. Comparison of Center Bending Moments (kips-in.) to Car Weight Under Dynamic Loading Ranging from 2 mph to 60 mph (RTT, 2012)

Nominal Car Weight (k)	263	286	315
Mean	-15.4	-14.2	-14.2
Median	-13.7	-13.3	-12.9
Standard Deviation	8.8	5.3	6.2
Maximum	-82.1	-31.5	-35.4

The standard deviation for all car types was below 9 kip-in which was significantly less than the standard deviation found in the similar analysis of the rail seat bending moment data. Additionally, the mean and median values of all car types were all within 1.2 kip-in.

6.45 Summary

Data collected from this experimentation yielded the following four findings concerning the crosstie rail seat and center moments:

- A static analysis of tie bending can lead to a basic understanding of trends, but most likely will not lead to the maximum moments a crosstie will experience.

- Though there is a trend between bending moment (rail seat and center) and rail seat load for an individual rail seat or crosstie, one cannot quantify the bending moment solely from the rail seat load.

- The mean and median dynamic crosstie rail seat and center bending moments were always greater than the static bending moments.

- Individual crosstie support, plays a greater role in rail seat crosstie bending moments than nominal car weight.

The findings from this experimentation have been used to guide both further experimentation in the lab and efforts to introduce mechanistic principles to the design of crossties and fastening systems. It is recommended that additional work focus on further understanding the relationship between crosstie bending moments and tonnage as well as the effect of tamping in well-maintained and poorly-maintained track.

6.46 Lateral Shoulder Forces

6.47 Background

Wear and fatigue of the shoulder in fastening systems is considered one of the most critical areas for research by members of the North American rail industry (Volume 2, Chapter 1, International Survey Results, Section 1.6). To gain a better understanding of how and why this wear occurs, it is important to understand the characteristics of lateral loads entering the shoulder face because of their potential effect on failed fastening system components in that area. The current design methodology does not account for the magnitudes or distribution lateral fastening system forces. To contribute to reaching the goals and objectives of field experimentation (Volume 2, Chapter

4, Field Instrumentation Plan, Section 4.10), instrumentation was developed and deployed to quantify the magnitude and distribution of lateral fastening system forces.

6.48 Field Experimental Setup

Field experimentation was conducted at the TTC in Pueblo, CO. Field experiments and results described in this report were conducted on a segment of tangent track on the RTT and a segment of curved track on the HTL at the TTC. Different loading scenarios (e.g. load magnitudes, L/V ratios, etc.) were applied to the track using the TLV. The test section used a 136RE rail section, concrete crossties spaced at 24 inches (610 mm) center-to-center, and premium ballast.

LLEDs deployed at the TTC were installed on the field side of the rail on both rail seats of three adjacent concrete crossties. The field side was chosen due to the vast majority of fastening system component failures are seen on the field side. Figure 202 shows the location and naming convention of LLEDs on both test sections. The installation first required removing the clips and rail pad assemblies from each rail seat. Next, the shoulder face was ground away, and new Safelok I type rail pad assemblies, insulators, and clips were installed. The LLED was then installed in place of the shoulder face. To ensure an adequate number of samples were collected during both static and dynamic tests, a sampling rate of 2,000 Hertz was used.

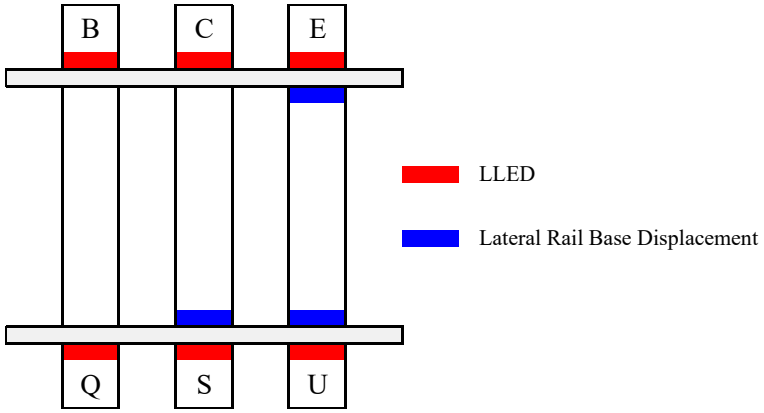

Figure 202. Lateral Load Instrumentation Location at the TTC

Lateral rail base displacements were also measured in conjunction with the LLEDs. This displacement, when compared with the lateral force measured at the corresponding LLED, describes the lateral stiffness of the fastening system. Lateral stiffness measurements were captured at three of the six LLED locations, since they overlapped with lateral rail base displacement measurements. The term lateral stiffness refers to the change in rail base displacement for a given change in lateral force as measured by LLEDs.

6.49 Influence of Lateral and Vertical Wheel Loads

6.49.1 Static Tests

The RTT was chosen for static testing to minimize variability due to vehicle-track dynamics in the curve. The LLED at rail seat Q on the RTT was compromised during static testing, making any data gathered from the LLED unreliable. However, rail seats B, C, E, S, and U functioned properly (Figure 201). Data from the five functioning rail seats were analyzed to understand the

influence of lateral wheel loads on lateral fastening system forces. Figure 202 shows the average magnitude of lateral forces measured by the LLEDs for given lateral wheel loads and a 40,000-lbf (40 kip) vertical wheel load applied by the TLV directly over a rail seat.

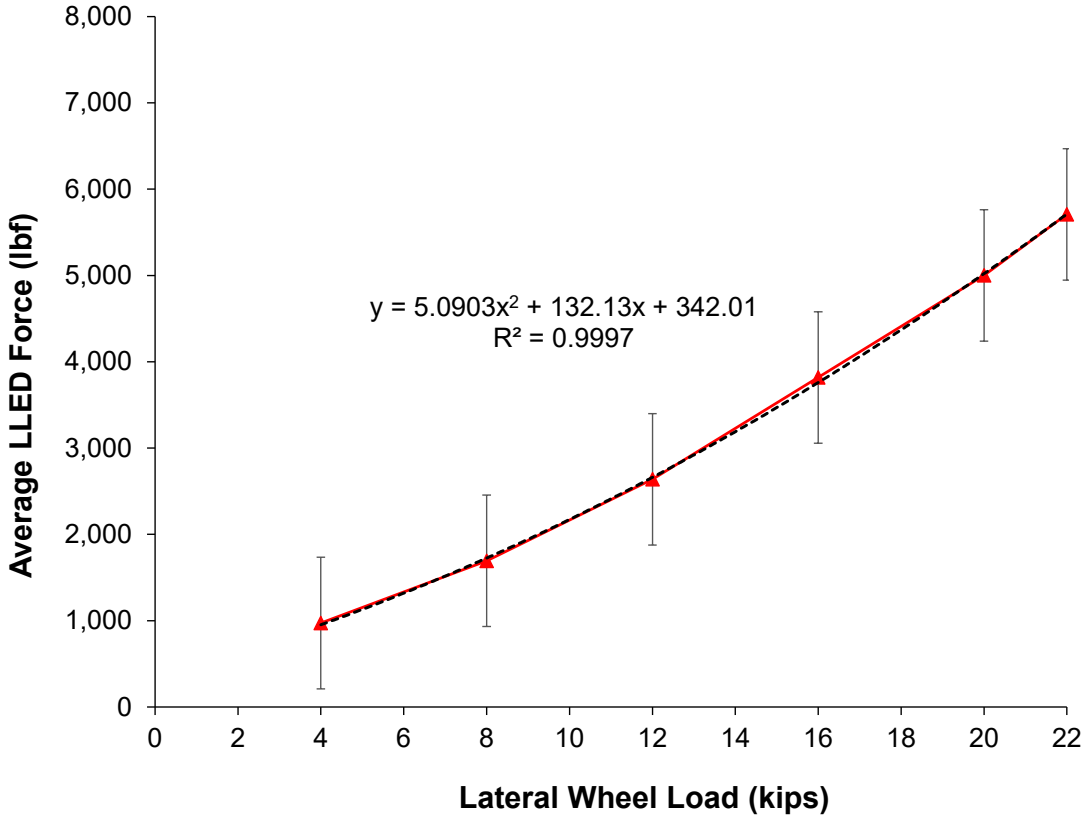

Figure 203. Average LLED Force Under Static 40-kip Vertical Wheel Load

The average LLED force from static TLV loading was plotted against various lateral wheel loads under a constant 40-kip vertical wheel load to determine the load transfer characteristics of the fastening system (Figure 202). As lateral wheel loads increased, the average LLED force on the rail seat directly beneath the point of loading increased in an upward trend. A quadratic trend line of the average LLED force data shows that as the lateral wheel load increases, the percentage of that lateral wheel load transferred into the shoulder increases. The data also appear to indicate, when extrapolated for zero kips of lateral wheel load, that an initial load on the shoulder is present. An applied load on the shoulder and insulator when no wheel load is applied (i.e. no trains are present) may indicate that creep or fatigue in the form of slow plastic deformation of the insulator could occur over time.

The average LLED force from static TLV loading was also plotted against various lateral wheel loads under constant 20 kip and 40-kip vertical wheel loads to determine the load transfer characteristics of the system under varying vertical wheel loads (Figure 203). As lateral wheel loads increased, the average LLED force under both magnitudes of vertical wheel load on the rail seat directly beneath the point of loading also increased in an upward trend. A quadratic trend line of the average LLED force data for all data points shows that as the lateral wheel load increases, the percentage of that lateral wheel load transferred into the shoulder increases, similar

to Figure 202. Also, similar in behavior to the data collected under only a 40-kip vertical load, the data appear to indicate, when extrapolated for zero kips of lateral wheel load, that an initial load on the shoulder is present.

When comparing the trends for 20 and 40 kip vertical loads on Figure 203, a minimal effect is seen by varying the vertical wheel load. When interpolated for a 10-kip lateral wheel load under a 40 kip vertical wheel load, the average LLED force is 1,923 lbf. At 10 kips of lateral wheel load under a 20-kip vertical wheel load, the average LLED force is 2,405 lbf, a difference of only 482 pound-force. This indicates that under equivalent lateral loading conditions in this experiment, when the vertical wheel load increases by 100% (e.g. increases force normal to rail seat that contributes to friction), the force on the shoulder decreases by 20%.

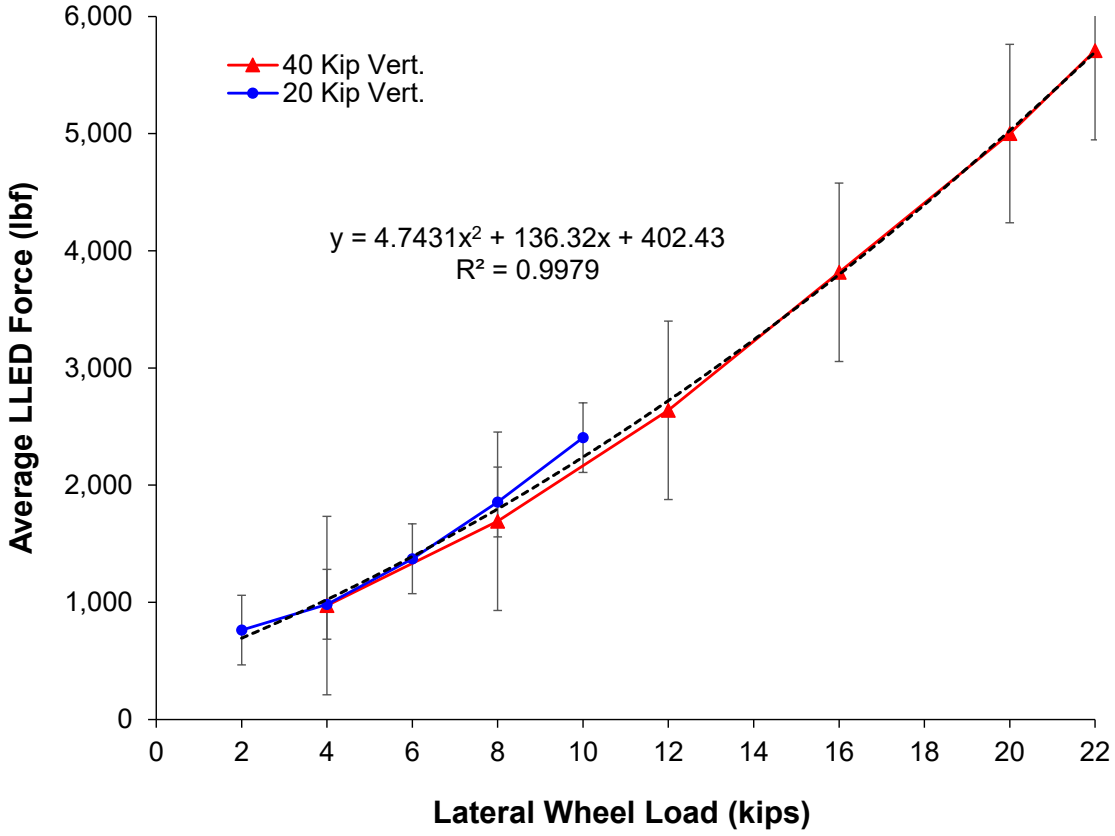

Figure 204. Average LLED Force Under Static 20 kip and 40-kip Vertical Wheel Load

6.49.2 Dynamic Tests

All dynamic train test data described in this report is from rail seat U on the low rail and rail seat E on the high rail of the HTL test section. Rail seats U and E were chosen to maintain a constant location while being able to compare rail seats on the same crosstie under varying dynamic loading scenarios. The peak LLED forces from axles of dynamic freight car loading were also plotted against the corresponding applied lateral wheel loads under speeds ranging from 2 mph to 45 mph to determine the load transfer characteristics of the system under varying speeds and car weights (Figure 203). As lateral wheel loads increased, the corresponding peak LLED forces from the axles of the freight train increased in an upward trend similar to static results. A

quadratic trend line of the peak LLED force data for both rail seats shows that as the lateral wheel load increases, the percentage of that lateral wheel load transferred into the shoulder increases. The data indicate that different rail seats may have different load transfer characteristics, yet still exhibit the same upward trend as lateral wheel load increases. A variety of factors could have led to the difference between rail seats E and U. Differences in loading conditions (i.e. static vs. dynamic) can have an effect on the magnitudes of the LLED forces, as well, and likely contribute to the varied trends between Figure 202 through Figure 204. Differences in track geometry (i.e. tangent vs. curved) will also have an effect on the vehicle-track interaction causing variances in magnitudes of the LLED forces.

Although the static and dynamic data cannot be directly compared due to different testing locations (RTT vs. HTL), it can be noted that rail seat U on the low rail of the HTL behaved similarly to the averaged data from the RTT. However, rail seat E on the high rail of the HTL produced much higher magnitudes of lateral forces on the shoulder than the remaining data. The quadratic relationship between the force imparted into the shoulder and applied lateral wheel load under dynamic loading shows that for zero kips of lateral wheel load, an initial load on the shoulder is present, also similar to the data recorded from static tests.

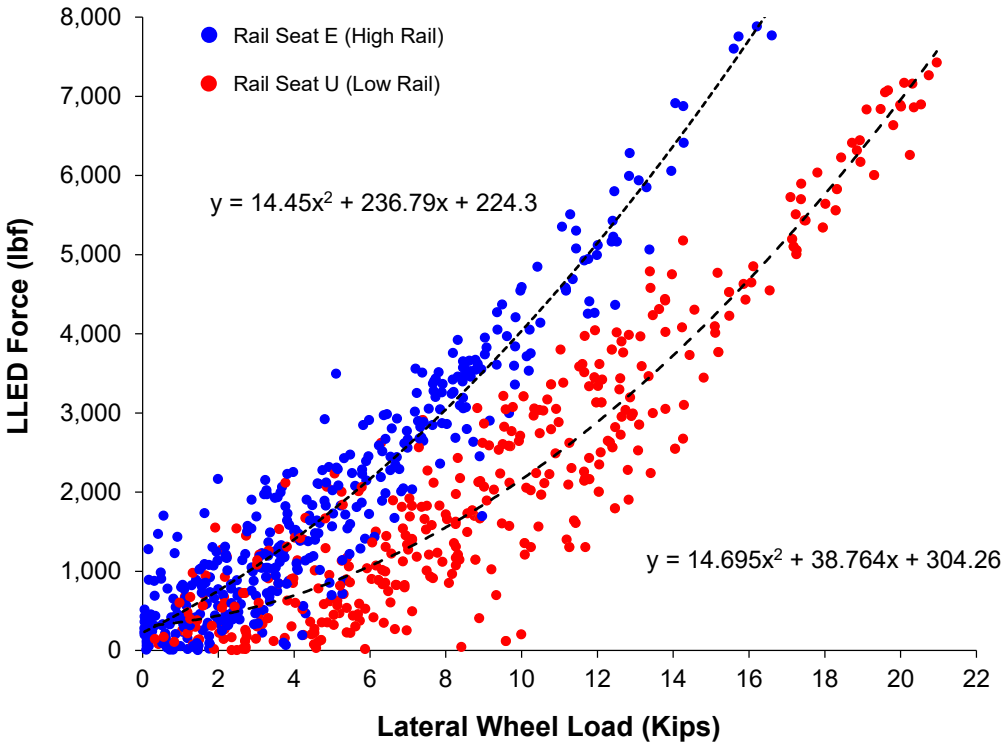

Figure 205. Peak LLED Forces Under Freight Train as a Function of Wheel Load

6.50 Influence of Train Consist Type

By definition, shared corridors see a variety of rolling stock types. To better understand the lateral demands on the shoulder that different types of rolling stock impart on the track, passenger and freight consists are compared. Figure 205 shows peak LLED forces from various speeds during dynamic freight and passenger train tests. The maximum LLED forces for

passenger cars were consistently significantly lower than the magnitudes measured from freight cars (Figure 205). All lateral forces measured by the LLED were less than 1,000 pound-force. At 15 mph, lateral forces measured by the LLED on rail seat U on the low rail were 618 pound-force for the passenger consist while the freight consists yielded 6,637 pound-force, more than an order of magnitude higher than the passenger consist. Lower magnitudes of loads from passenger trains were consistent at all speeds. The lower magnitudes indicate that passenger trains impart lateral demands on the fastening that are significantly lower than freight trains. Although the forces from the freight consist were about ten times larger than those from the passenger consist, the freight car weights were only approximately 3.7 times heavier than the passenger cars. The disparity indicates that an increase in car weight of approximately 400% could result in an increase in lateral fastening system forces of approximately 1,000%. The disparity also indicates that due to their inherently higher car weights, freight consists impart much higher forces in the fastening system than passenger consists.

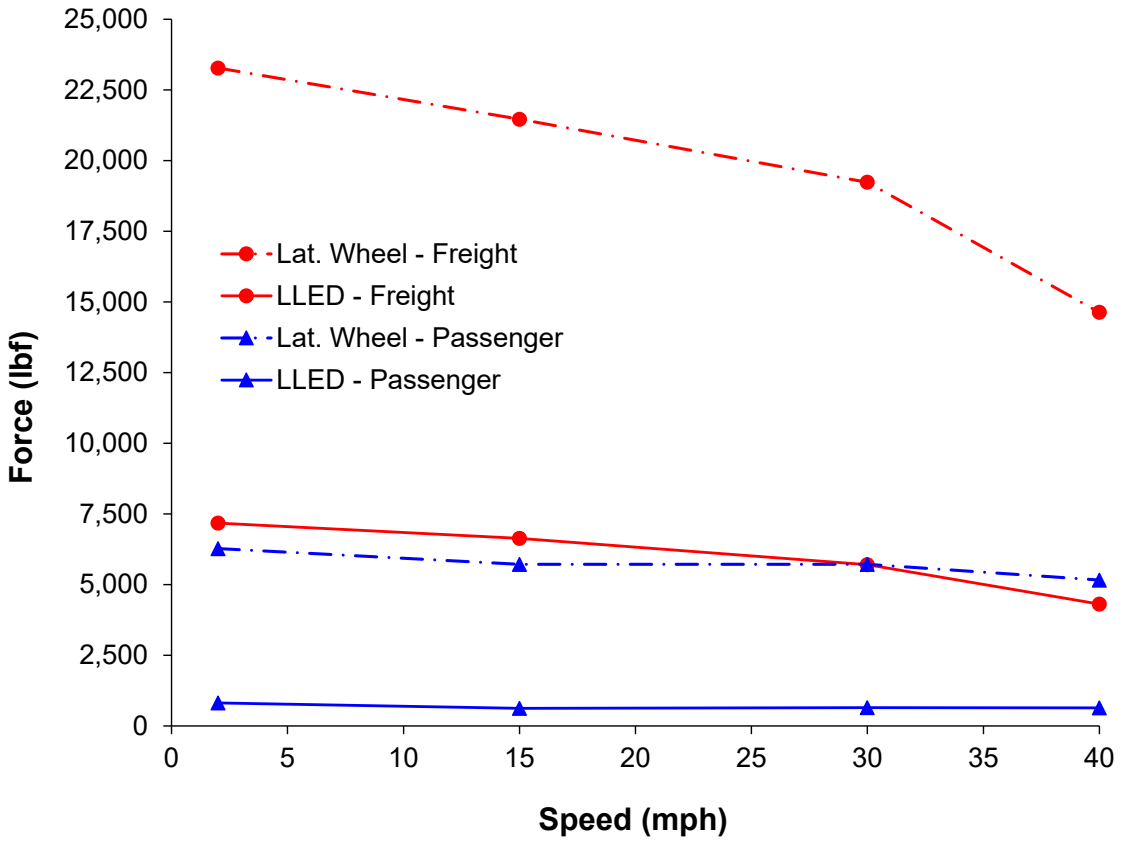

Figure 206. Maximum Lateral Wheel Loads and LLED Forces as A Function of Speed

The decreasing trend in the data is due to the location of the instrumentation. Because rail seat U is on the low rail of the curve, the increasing outward force of the train with increasing speed causes the low rail to withstand lower forces. Train dynamics will govern the steering charactersitics of a train through a curve, which warrants addional discussion that is outside the scope of this report and project. However, the data can still be investigated. As speed increased, both lateral wheel loads and LLED forces decreased. Figure 205 indicates rail seat U exhibited an upward trend of lateral wheel loads tranferred into the shoudler as lateral wheel load increased. Although the trend as speed increases is a downward trend from Figure 206, the same

upward trend of lateral wheel loads tranferred into the shoudler can be observed. The percentage of lateral wheel loads transferred to the shoulder at 45, 40, 30, 15, and 2 mph was 30.8%, 31.5%, 32.8%, 33.5%, 34.5%, respectively. The percentages show that as speed decreased and lateral wheel load increased, the percentage of the lateral wheel load transferred into the shoulder increased, as well.

6.51 Longitudinal Distribution of Lateral Forces

Lateral wheel loads are hypothesized to be distributed to three crossties (i.e. the crosstie directly beneath the point of loading and the two adjacent crossties). The test matrix for TLV loading on the RTT included many unique loading scenarios (e.g. varying L/V ratios, load magnitudes, etc.). For the purpose of this section, a 40-kip vertical and 20-kip lateral loading scenario resulting in a 0.5 L/V force ratio will be discussed to provide a means of comparison between the rail seats. Additionally, the focus will be on load application at three discrete locations on the test section: crosstie E-U, crosstie C-S, and crosstie B-Q (Figure 202). When a 20-kip lateral load was applied at crosstie E-U, the measured LLED forces on rail seat E and U were 5,520 lbf and 3,782 lbf, respectively (Figure 207**,** Table 21). Likewise, the measured LLED forces on rail seat C and S were 4,315 lbf and 3,420 lbf, respectively (Figure 206**,** Table 42). The measured LLED force on rail seat B was 35 lbf (Figure 206**,** Table 42), a negligible amount relative to the adjacent rail seats. The lack of force measured at rail seat B (i.e. two crossties away) indicates that lateral loads are distributed to the crosstie directly beneath the point of loading and to the two adjacent crossties (i.e. a three crosstie distribution). While the difference between lateral force measured at adjacent rail seats E and C is 1,205 lbf, the difference between adjacent rail seats U and S is only 362 lbf (Figure 206**,** Table 42). However, when the loading location is moved to crosstie C-S, the distribution of lateral forces changes dramatically from what is seen when loaded at crosstie E-U.

Table 42. Summary of Measured LLED Forces

	Force (lbf) When Loaded at Crosstie:		
Rail Seat	B-Q	C-S	E-U
B	2,407	1,600	35
C	1,450	6,380	4,315
E	26	1,325	5,520
S	2,258	6,980	3,420
U	12	540	3,782

When a 20-kip lateral load was applied at crosstie C-S, the measured LLED forces on rail seat C and S were 6,380 lbf and 6,980 lbf, respectively (Figure 206**,** Table 43). Likewise, the measured LLED forces on rail seat E and U were 1,325 lbf and 540 lbf, respectively (Figure 206, Table 43). The difference between LLED forces measured at adjacent rail seats C and E and adjacent rail seats S and U are much higher when loaded at crosstie C-S than when loaded at crosstie E-U. The difference between LLED forces measured at adjacent rail seats C and E is 5,055 lbf, while the difference between adjacent rail seats U and S is 6,440 lbf (Figure 206**,** Table 43). The distribution of lateral forces when loaded at crosstie C-S changes significantly when loaded at crosstie E-U. The difference between adjacent rail seats C and E when loaded at crosstie C-S was three times larger than when loaded at crosstie E-U. Similarly, the difference between

adjacent rail seats U and S when loaded at crosstie C-S was 17 times larger than when loaded at crosstie E-U. The distribution of lateral forces continued to change when the loading location was moved to crosstie B-Q.

When a 20-kip lateral load was applied at crosstie B-Q, the measured lateral LLED force on rail seat B was 2,407 lbf (Figure 206**,** Table 43). The measured LLED forces on rail seat C and S were 1,450 lbf and 2,258 lbf, respectively (Figure 206**,** Table 43). The measured LLED forces on rail seat E and U were 26 lbf and 12 lbf, respectively (Figure 206, Table 43), negligible amounts relative to the adjacent rail seats. The lack of force measured at rail seat E and U (i.e. two crossties away) further indicates that lateral loads are distributed to the crosstie directly beneath the point of loading and to the two adjacent crossties (i.e. a three crosstie distribution). The difference between lateral forces measured at adjacent rail seats B and C was 957 lbf.

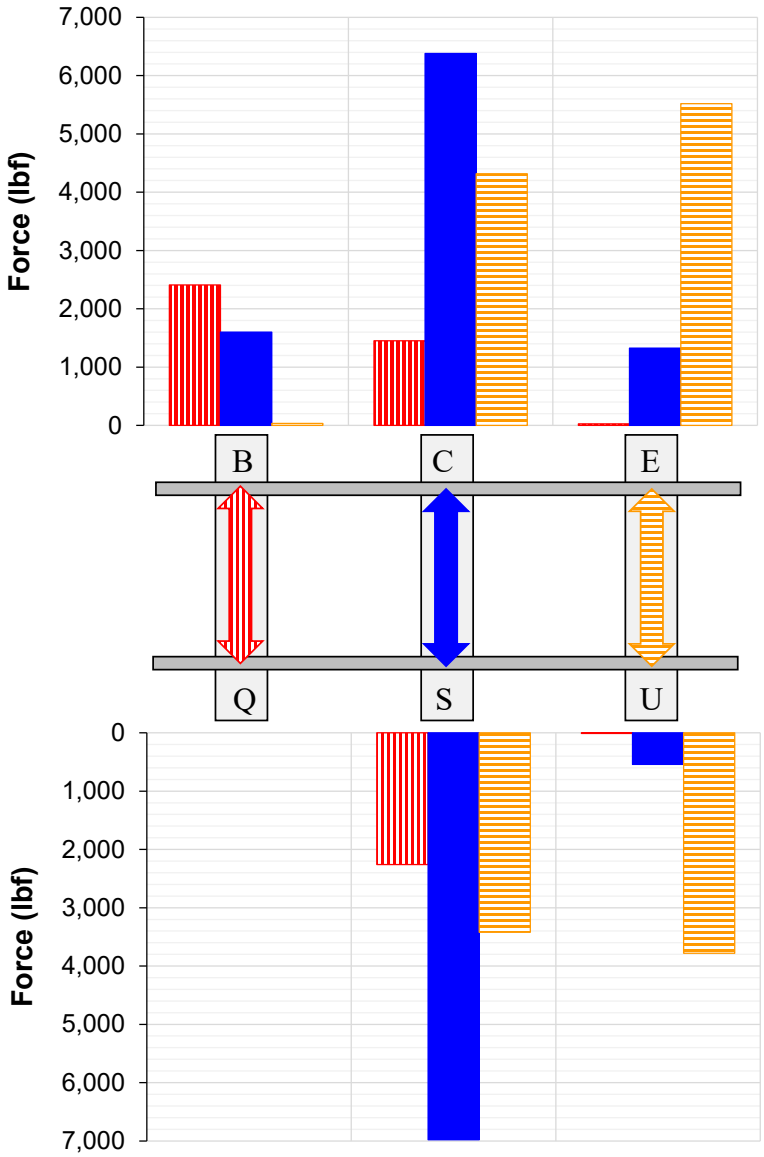

Figure 207. LLED Forces Due to 20-kip Gauge-Widening Force at Specified Crosstie

Although rail seat Q was inactive, it can still be noted that the difference between lateral forces measured at rail seats C and S (same crosstie) was 808 pound-force (Figure 206**,** Table 42). The difference between lateral forces measured at rail seats C and S indicated that rail seats at equivalent distances from the point of loading location, yet on the same crosstie, can have dissimilar magnitudes of lateral forces in the fastening system. To better understand why this variance of lateral force distribution among adjacent rail seats exists, the lateral stiffness of adjacent rail seats S and U was investigated.

6.52 Influence of Lateral Fastening System Stiffness

The magnitudes of lateral fastening system forces are hypothesized to increase with increasing lateral fastening system stiffness. The lateral rail base displacement measurement at rail seat S, E, and U was used in conjunction with the LLED at the corresponding rail seat on the RTT to generate force-displacement curves. Additionally, these measurements allowed for quantification of the lateral stiffness of the fastening system at the insulator-shoulder interface. When load was applied at crosstie E-U, rail seat E had a lateral stiffness of 155,369 lbf/in, while rail seat U had a lateral stiffness of 146,322 lbf/in (Figure 207**,** Table 43). In comparison, when load was applied at crosstie C-S, rail seat S had a lateral stiffness of 192,498 lbf/in (Figure 207**,** Table 43), which is 32% stiffer than rail seat U. There was not an LLED at rail seat C. Referring to the load magnitude data, when load was applied at crosstie E-U, rail seat U shared roughly equal magnitudes of lateral force with adjacent rail seat S. However, when the loading location was moved to crosstie C-S, rail seat S carried about 6,500 more than adjacent rail seat U. The change in distribution indicates that rail seat S carried more lateral force than rail seat U due to increased lateral stiffness.

Table 43. Linear Trend Line Data for Lateral Stiffness of Rail Seats S, E, and U on RTT

Rail Seat	Equation of Linear Trend Line	R2 Value	Stiffness (lbf/in)	Max. Force
E	y = 192,498x + 747.32	0.9819	192,498	7,828
S	y = 155,369x + 988.07	0.9964	155,369	5,582
U	y = 146,322x + 57.37	0.9962	146,322	4,632

The magnitude of lateral force measured at rail seat S when loaded at crosstie C-S was 104% more than the lateral force measured at rail seat U when loaded at crosstie E-U. The increase in magnitude indicates that a lateral stiffness increase of about 30% can increase the lateral load carried by a rail seat by more than 100% (i.e. a factor of two).

The data from rail seats E, S, and U can be explained by two different explanations. First, because the measured lateral forces increased significantly with increasing lateral stiffness, larger lateral forces at a particular rail seat may indicate that the rail seat has a higher lateral stiffness. The lateral stiffness of the fastening system is a function of fastener design parameters (e.g. insulator and rail pad material properties, clamping force, etc.) and can affect the lateral forces at the insulator-shoulder interface. However, variances in stiffness among adjacent rail seats are likely to occur in the field due to factors associated with manufacturing and installation procedures, such as gaps between fastening system components. Since the fastening system was held constant for this experiment, factors due to manufacturing and installation were the likely cause of variation. Figure 170 shows the maximum lateral forces measured by LLEDs at each

rail seat under a 22-kip lateral load and a 0.55 L/V ratio, the maximum load application during testing.

The lateral stiffness at rail seat E was 155,369 lbf/in, 6% higher than the lateral stiffness at rail seat U. The 5,585 lbf measured at rail seat E is also 20% higher than the 4,635 lbf measured at rail seat U, showing us that a relatively small increase in lateral stiffness will ultimately result in a larger increase in load carried. The data further show that lateral stiffness at rail seat S is 24% higher than the lateral stiffness at rail seat E, while the maximum lateral force measured at rail seat S is 40% higher than rail seat E.

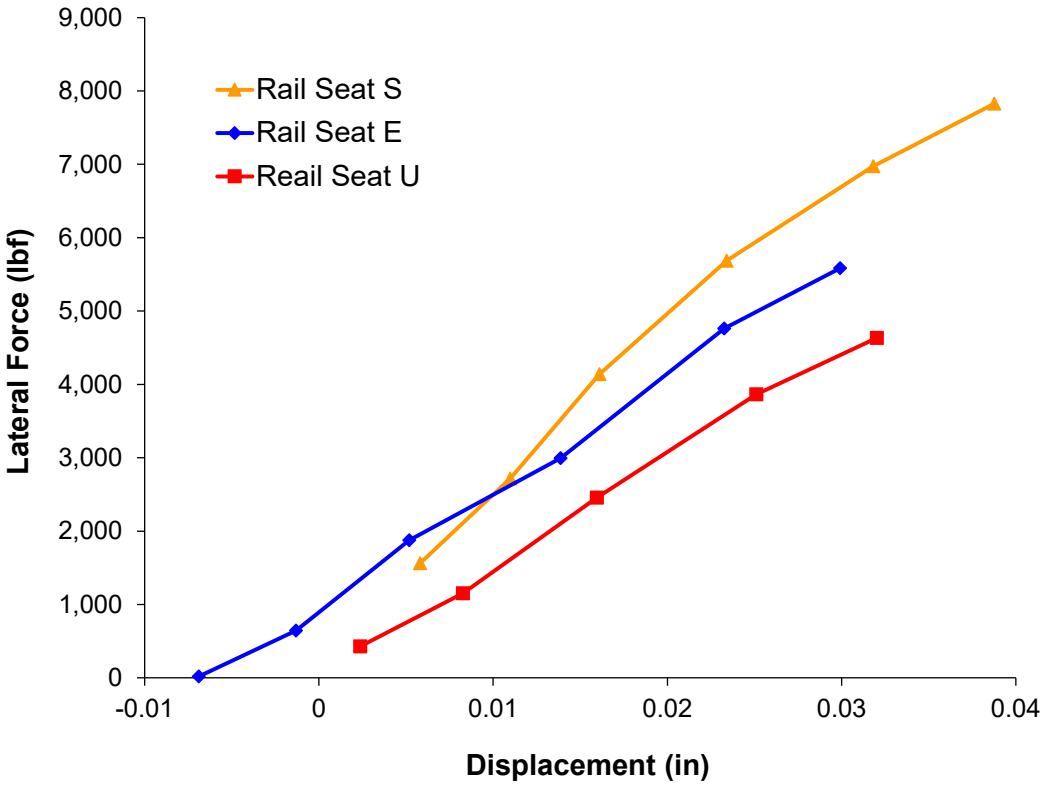

Figure 208. Lateral Fastening System Stiffness at Rail Seats S, E, and U on RTT

6.53 Effect of Friction and Applied Vertical Wheel Load

For the Safelok I fastening system, it is assumed that the majority of the lateral forces from wheels are restrained by bearing forces (e.g. acting on the shoulder) and frictional forces (e.g. acting between the rail and rail pad and the rail pad and rail seat). This relationship is expressed in Equation 5.

$L_R = \Sigma L_B + \Sigma L_F$ **Eq. 5**

Where:

- L_R = Total lateral restraining force
- ΣL_B = Summation of lateral bearing forces

- ΣL_F = Summation of lateral frictional forces

All lateral bearing forces within a fastening system are measured by the LLED because there are no other surfaces for lateral forces to bear on in a Safelok I type fastening system. Lateral bearing restraint forces are affected by geometric tolerances within the track structure and fastening system as well as the lateral fastening system stiffness as shown above. Lateral frictional restraint forces occur at the interfaces between the rail and rail pad as well as the rail pad and rail seat. Lateral frictional restraint forces are affected by the vertical wheel load, fastening system component material properties, and their frictional characteristics relative to one another. Lateral frictional restraint forces are assumed to be the difference between the applied lateral wheel load and the sum of all consecutive LLEDs (i.e. lateral bearing forces). Frictional forces require a force normal to the plane of the interface between two surfaces, and the relationship is expressed in Equation 6.

$L_F = \mu N$ **Eq. 6**

Where:

- L_F = Lateral frictional forces
- μ = COF between rail pad and rail seat
- N = Vertical wheel load (i.e. force applied normal to frictional planes)

Figure 208 from Section 6.537 shows the average magnitude of lateral bearing restraint forces measured by the LLEDs for given lateral wheel loads under constant 20 kip and 40-kip vertical wheel loads applied by the TLV directly over the specified rail seat. Each data point represents five replicates and the error bars represent one standard deviation.

The trend of the curves for 20 kip and 40 kip applied vertical wheel loads are similar. As the applied lateral wheel load increases under a constant vertical wheel load, an upward trend of lateral bearing restraint forces (i.e. forces measured by the LLED) can be seen. This is likely due to the theoretically constant frictional force from the constant vertical wheel load under all lateral loading conditions. However, the rate at which the slope of the curve increases appears to be greater under a 20-kip applied vertical wheel load. At four kips of applied lateral wheel load, the LLED force is approximately 1,000 lbf for both vertical loading conditions. As the lateral wheel load increases to eight kips, the LLED forces increase to approximately 1,850 lbf and 1,700 lbf under a 20 kip and 40-kip vertical wheel load, respectively, a difference of 150 lbf. As the lateral wheel load increases to ten kips, the LLED forces increase to approximately 2,400 lbf under a 20-kip vertical wheel load and 2,150 lbf when interpolated under a 40 kip vertical wheel load, a difference of 250 lbf. The increase in the difference between LLED forces under equivalent lateral loads with varied vertical loads indicates that the lower magnitude of vertical wheel load may result in higher lateral bearing restraint forces due to the lower magnitude of force applied normal to the frictional planes. However, this increase in the difference between LLED forces under equivalent lateral loads with varied vertical loads is not in accordance with Equation 6. If the vertical wheel load doubles from 20 kips to 40 kips, the frictional forces should theoretically double, as well, causing the bearing forces at similar lateral loads to decrease.

A reasonable conclusion cannot be drawn from Figure 3 about the effect of vertical wheel loads on both the lateral bearing and frictional restraint forces. This behavior is further confirmed through Figure 67 which shows the sum of lateral forces from rail seats B, C, and E as a function of lateral wheel load under constant 20 kip and 40-kip vertical wheel loads applied by the TLV. Based on Equation 5 and Equation 6, the difference between the lines for total frictional and bearing forces under a 20-kip vertical load should be smaller than under a 40-kip vertical wheel load (i.e. bearing forces should increase and frictional forces should decrease). However, both 20 kip and 40-kip vertical wheel load plots appear to produce similar results for both frictional and bearing force. Because these circumstances do not agree with the theoretical equations, this is an area for future research.

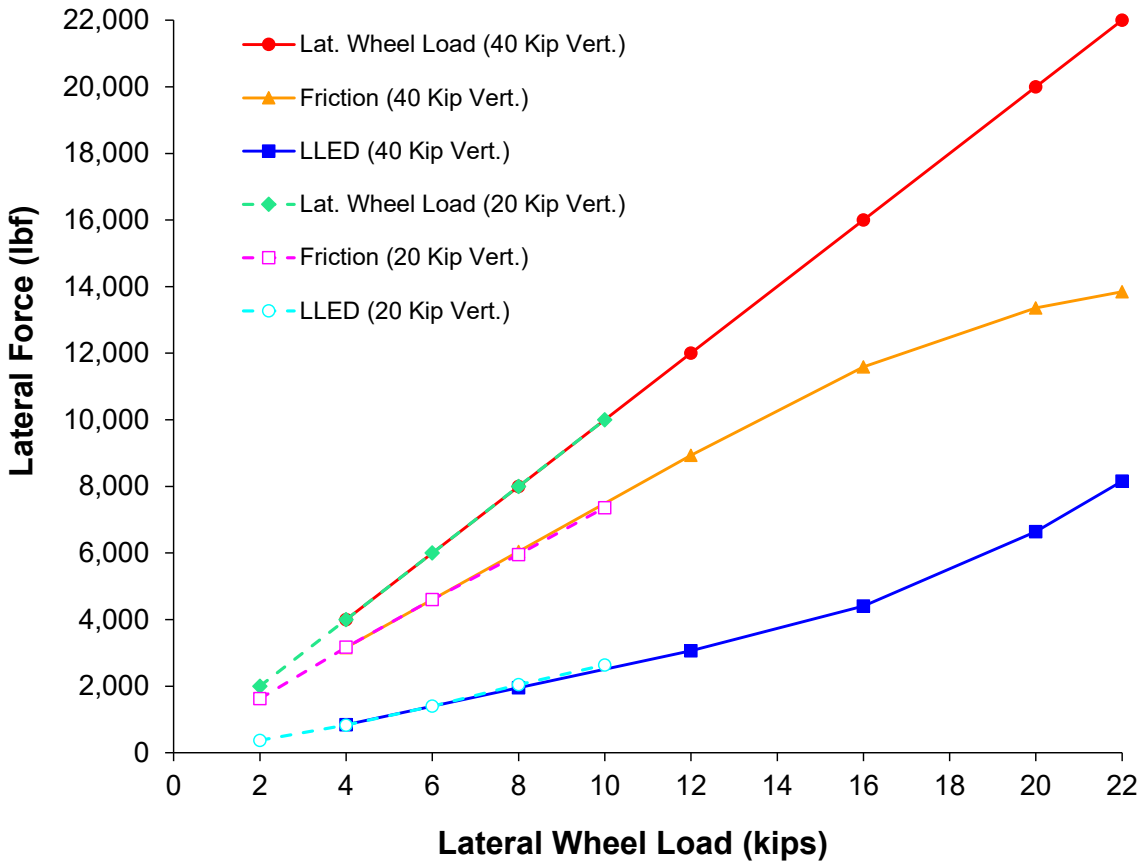

Figure 209. Sum of Lateral Fastening System Forces on Rail Seats B, C, and E as A Function of Lateral Wheel Load

6.54 Percentage of Lateral Restraint Forces

As previously mentioned, lateral frictional restraint forces are assumed to be the difference between the applied lateral wheel load and the sum of all consecutive LLEDs (i.e. lateral bearing restraint forces). As the applied lateral wheel load increases, the lateral frictional and bearing restraint forces begin to converge (Figure 66). A similar converging trend has also been observed through the analysis of results from UIUC's 3-D FE model of the same crosstie and fastening system used in the field (Chen 2013). The similar results from both field

experimentation and FE model data show the converging trend is what occurs within the fastening system as lateral wheel load increases. The trend indicates that the percentage of applied lateral wheel load restrained by frictional forces decreases while the percentage of applied lateral wheel load restrained by bearing forces increases, imparting a higher load on the insulator.

Figure 67 shows the change in lateral restraint forces as a function of lateral wheel load in two ways: the ratio of frictional forces to bearing forces and lateral bearing restraint forces as a percentage. As the applied lateral wheel load increases, the ratio of frictional forces to bearing forces decreases from approximately 3.7 at 4 kips of lateral wheel load to 1.7 at 22 kips of lateral wheel load, a decrease of 54%. The percentage of the applied lateral wheel load restrained by lateral bearing restraint forces increases from approximately 21% at 4 kips of lateral wheel load to 37% at 22 kips of lateral wheel load, an increase of 16%. This indicates that as the lateral wheel load increases, the demands on the insulator and shoulder increase due to more of the lateral wheel load being restrained by bearing forces.

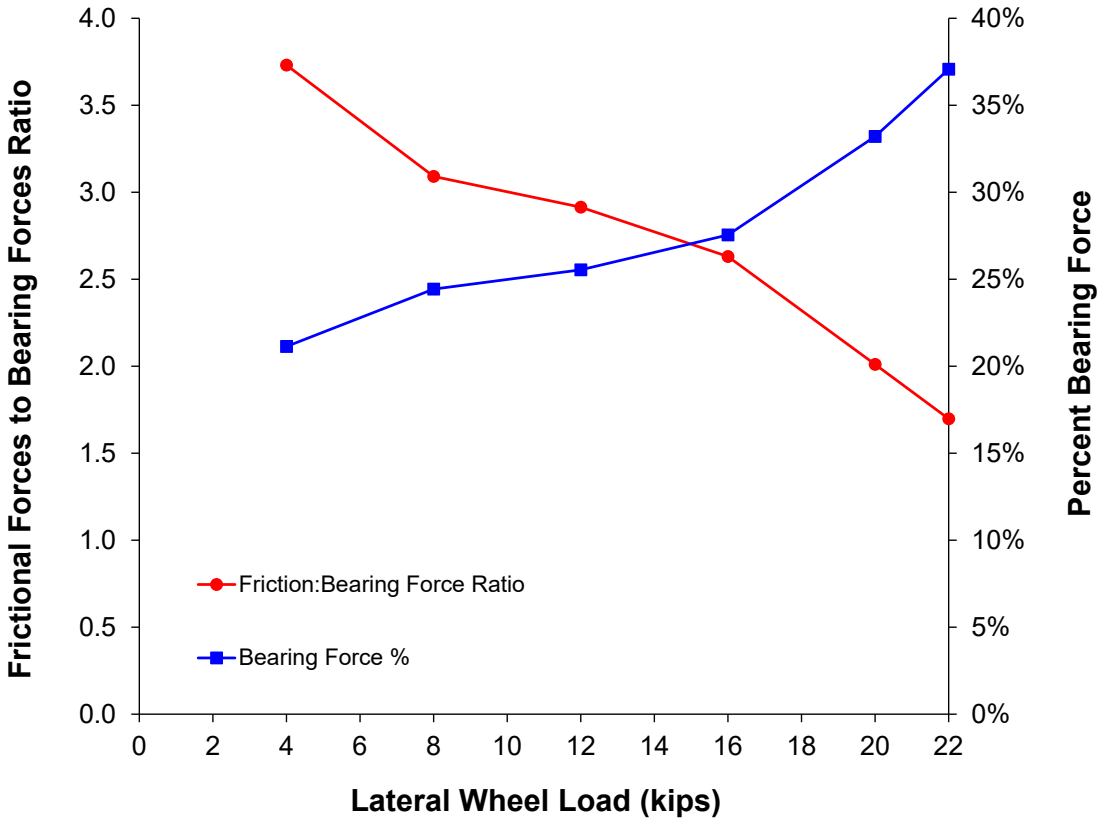

Figure 210. Change in Lateral Restraint Forces as A Function of Lateral Wheel Load Sum of Rail Seats B, C, and E

6.55 Summary

Data collected from this experimentation produced the following findings regarding the magnitude and distribution of lateral fastening system forces:

- As lateral wheel load increases, the percentage of that lateral wheel load transferred into the shoulder increases. Different rail seats may have different load transfer characteristics, yet still exhibit the same upward trend as lateral wheel load increases.
- Under equivalent lateral loading conditions, when the vertical wheel load increases by 100% (e.g. increases force normal to rail seat that contributes to friction), the force on the shoulder decreases by only 20%.
- An increase in car weight of approximately 400% could result in an increase in lateral fastening system forces of approximately 1,000%.
- An increase in lateral stiffness of approximately 30% can increase the lateral load carried by a rail seat by more than 100% (i.e. a factor of two).
- As lateral wheel load increases, the ratio of frictional forces to bearing forces decreases from approximately 3.7 at 4 kips of lateral wheel load to 1.7 at 22 kips of lateral wheel load, a decrease of 54%.
- The percentage of the applied lateral wheel load restrained by lateral bearing forces increases from approximately 21% at 4 kips of lateral wheel load to 37% at 22 kips of lateral wheel load, an increase of 16%.

The findings from these results have been used to guide both laboratory experimentation and efforts to move toward the mechanistic design of crossties and fastening systems.

Chapter 7: FE Modeling Methodology and Development

Detailed FE modeling of the concrete crosstie and fastening system was conducted at UIUC to quantify the loading demands that originate at the wheel-rail interface and are transferred to the individual components and improve the current level of understanding of the vertical, lateral, and longitudinal load path. The purpose of this chapter is to communicate the objectives, methodology, and scope of work for the FE modeling efforts. The critical inputs and outputs of FE models are listed along with a summary of the functionalities of the models, model validation strategies, and the approach to conducting parametric analyses.

7.1 Modeling Methodology and Strategy

FE modeling serves as an important analytical means to examine the behavior of complex systems under multiple loading scenarios. In the initial stage of this project, critical input and output parameters that serve as guidelines for FE analysis were determined based on existing literature and experience from within the railroad industry. Laboratory and field instrumentation techniques were designed to extract measurements of the critical outputs in the laboratory and field environment, and the FE model was employed to predict responses of the track system. After the collection of test data, the modeling predictions were compared with the experimental data to verify the assumptions and simplifications included in the model. To improve the credibility of the FE models, the model validation was conducted in a hierarchical fashion based on experiments at different levels. After the validation of models, parametric studies based on the critical inputs and outputs were conducted. In this process the correlation between inputs and outputs were evaluated, and possible alternatives to the current design of concrete crosstie and fastening system were compared. The results of the parametric analyses serve as the basis for the proposed mechanistic design approach. In addition, the output of the parametric studies based on the validated models served as the input data for I-TRACK, which is a simplified tool for estimating the response of concrete crosstie and fastening system under various loading conditions, material choices, and geometric design configurations. Additionally, a specific FE model was developed to conduct an analysis of the longitudinal load path, but this model has yet to be validated with experimental data.

7.2 Critical Input and Output Parameters

The critical inputs and outputs of the FE models were determined based on FRA's Track Safety Standards Compliance Manual, research work published by peers, and engineering judgment of industrial partners with field experience. Table 44 summarizes the critical input list of the FE models and Table 45 includes supplementary explanations for the input frictional behavior parameters. The location of the interaction definition for COF is shown in Figure 210. In addition, Table 46 shows a summary list of output parameters of the FE models. The definition for the critical model outputs are listed in the appendix. In Table 44 and Table 45 the critical inputs are classified based on the component that they are related to. Although the focus of this research was the concrete crosstie and fastening system, the modeling of the rail and substructure was also included in the analysis as they are closely related to the performances of the system. The rail was defined according to its actual cross section (136RE rail) and material properties, while the track substructure was simplified into a general support layer. The stiffness of the

support layer was calibrated based on field displacement measurements, and it represented the system behavior of multiple support layers.

Table 44. Critical Modeling Inputs

Component	Input	Component	Input
Load	Vertical loading	Abrasion Frame	Young's modulus
	Lateral loading		Frame geometry
Rail	Rail geometry	Shoulder	Young's modulus
	Location of contact patch		Shoulder geometry
	Young's modulus		Yielding strength
Insulator	Insulator geometry	Reinforcement	Pre-stress force
	Yielding strength		Young's modulus
	Young's modulus		Strand diameter
Clip	Young's modulus		Strand distribution
	Yield strength		Number of reinforcement
Crosstie	Compressive strength	Support	Track modulus
	Tie spacing	Rail Pad	Young's modulus
	Geometry of crossties		Pad geometry
	Bond-slip behavior		Poisson's ratio
		Wheel	Acceleration

Table 45. Critical Friction Input

Component	Frictional Interaction	COF
Pad	Pad-frame interface	0.3
	Pad-rail interface	0.3
Abrasion Frame	Frame-concrete interface	0.3
Insulator	Insulator-rail interface	0.15
	Insulator-clip interface	0.15
	Insulator-shoulder interface	0.15
Shoulder	Shoulder-clip interface	0.5
Crosstie	Crosstie-ballast interface	0.7
Wheel	Wheel-rail interface	0.5

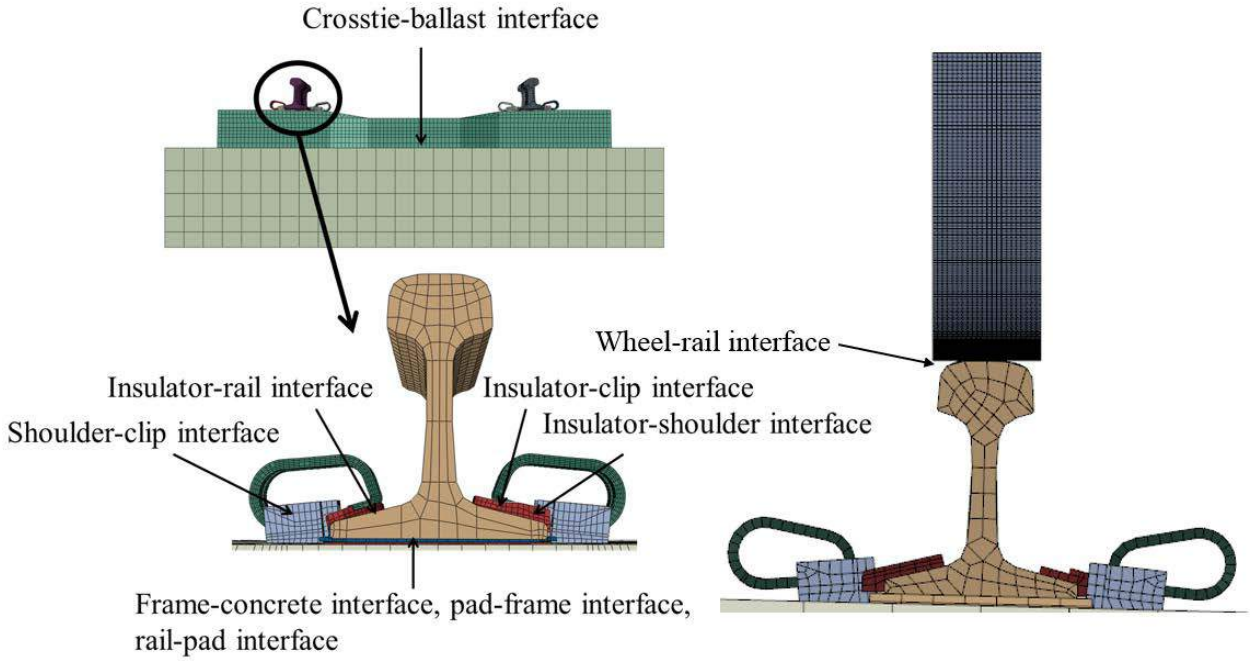

Figure 211. Illustration of Frictional Interface Locations

Table 46. Critical Modeling Output

Critical Modeling Output	
Track vertical deflection	Rail base rotation
Track lateral deflection	Shoulder bearing force
Rail-base lateral displacement	Rail pad frictional force
Abrasion frame lateral translation	Crosstie rail-seat moment
Vertical rail-seat load	Crosstie center moment
Lateral rail-seat load	Vertical rail-seat load at adjacent crossties
Gauge-side clamping force	Lateral rail-seat load at adjacent crossties
Field-side clamping force	Relative sliding between rail and rail pad
Maximum rail-seat pressure	Relative sliding between abrasion frame and rail seat

7.3 Modeling of Concrete Crosstie, Fastening System, and Wheel

Various designs of fastening systems and pre-stressed concrete crossties have been placed in revenue service in North America. Modeling every possible combination of fastening system and concrete crosstie would be impractical. Therefore, the UIUC model focused on a prevalent type of concrete crosstie and fastening system in North America, the Safelok I system (Figure 211). As shown in Figure 211, the fastening system is cast into the concrete crosstie to transmit wheel load from the rail to the concrete and maintain uniform track geometry. The modeled fastening system includes embedded cast iron shoulders, rail clips, nylon insulators, and a rail

pad assembly consisting of a polyurethane rail pad for load attenuation and a nylon 6/6 abrasion frame to mitigate abrasion of the concrete. Rail clips are assembled into the shoulder with initial deformation, and the resulting clamping force prevents longitudinal and lateral displacements of the rail. Insulators were placed between the clip and the rail to insulate the two rails electrically. When modeling the components of the fastening system, the geometries of the components were simplified. Figure 212 shows FE models of the individual fastener components in the isometric view.

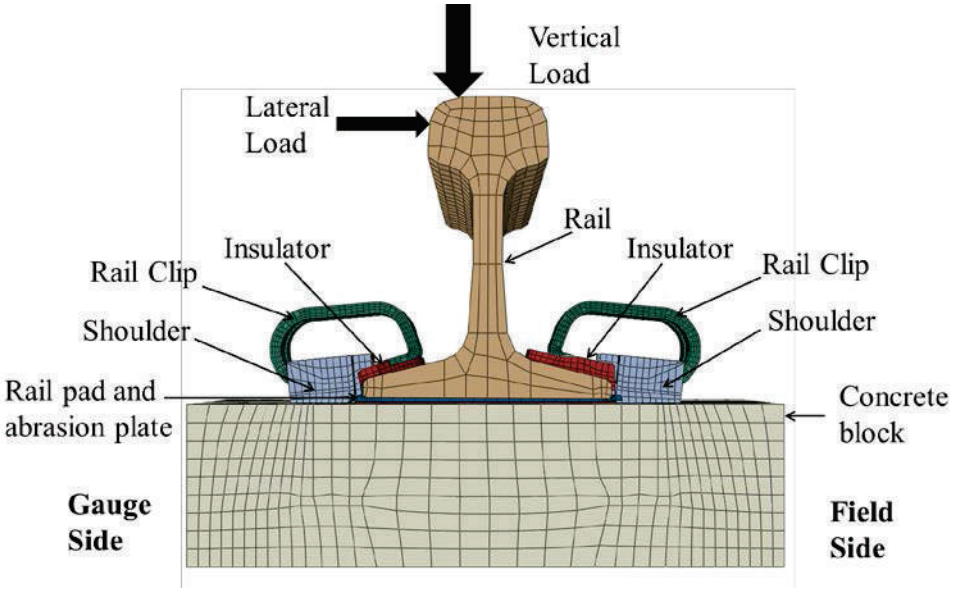

Figure 212. Schematic of the Fastening System Model

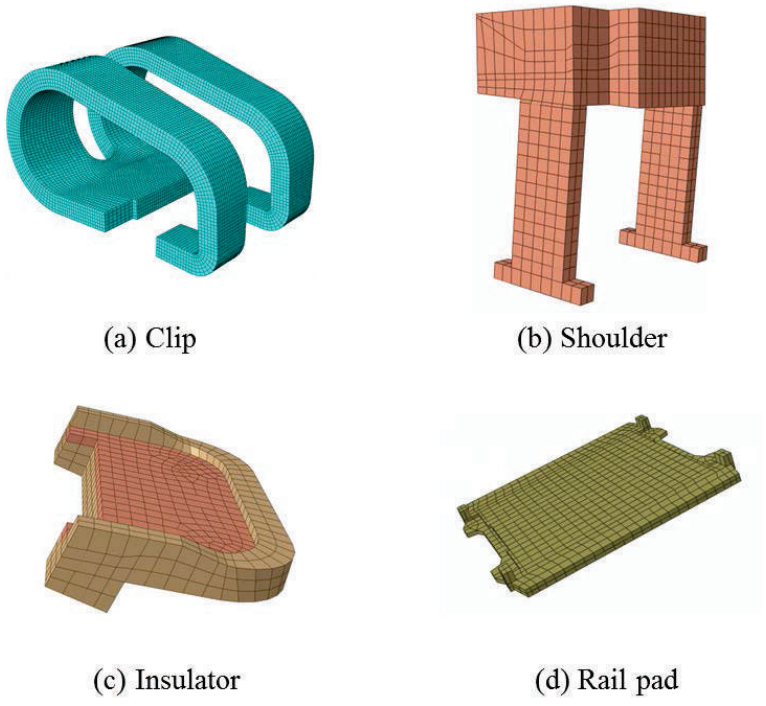

Figure 213. Components of the Fastening System: (a) Clip, (b) Shoulder, (c) Insulator, and (d) Rail Pad

The engineering drawings of the concrete crosstie included in the FE model is shown in Figure 213. Figure 214 shows a single pre-stressed concrete crosstie model with fastening systems assembled on each rail seat. The dimensions of the crosstie are 102 in (length) x 11 in (width) x 9.5 in (height). Twenty steel wires of 0.21 in diameter are embedded in the crosstie to provide pre-stressing forces.

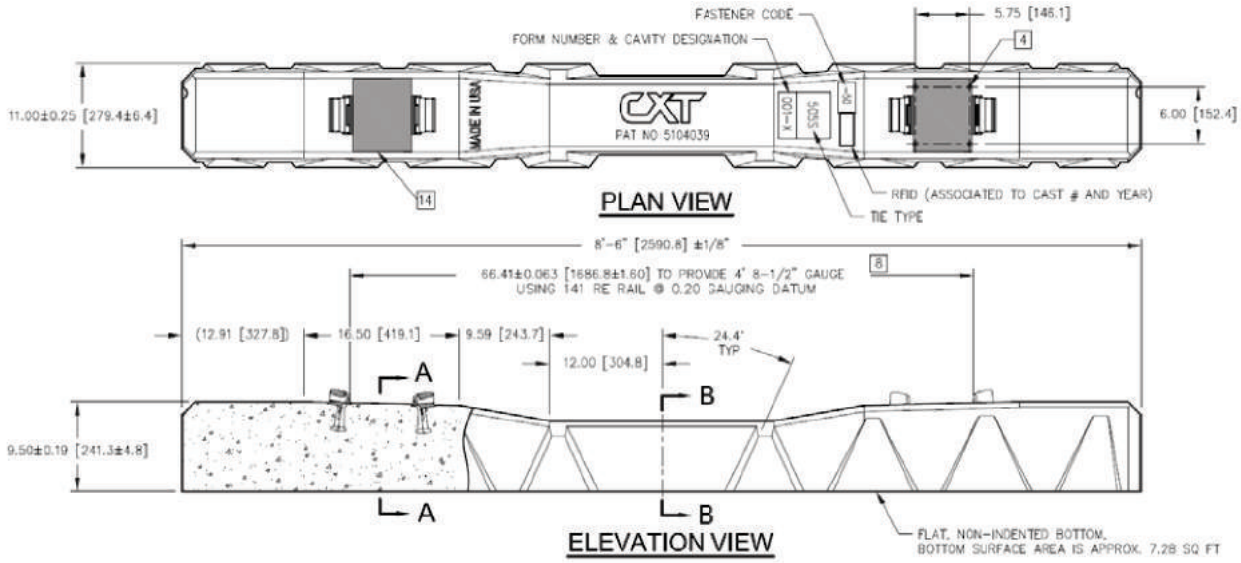

Figure 214. Engineering Drawing for the Concrete Crosstie Simulated in the FE Model

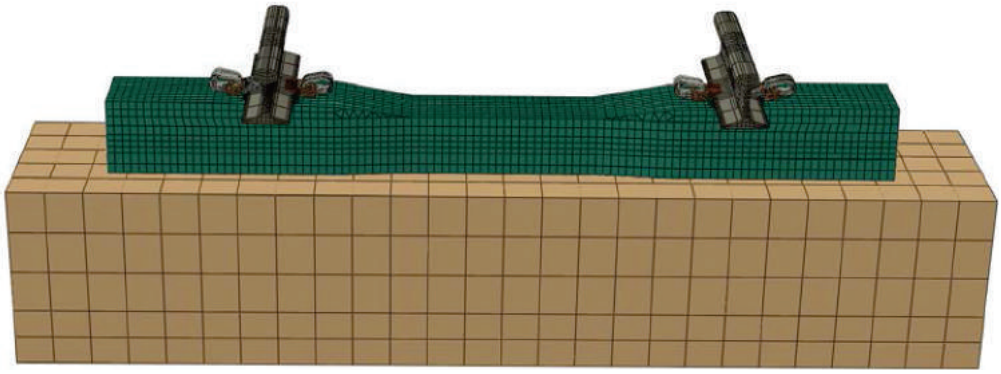

Figure 215. Configuration of 3D Concrete Crosstie, Rail, Fastening System, and Substructure FE Models

To investigate the distribution of vertical and lateral wheel load among multiple rail seats, and the load path through an individual fastening system and rail seat, a static finite element analysis (FEA) is conducted. The modeling work was carried out using FE program, ABAQUS (Dassault Systemes Simulia Corp. 2011). The rail, fastening system, concrete crosstie, and substructure were all modeled with eight-node brick elements, which have three translational degrees of freedom (DOF) at each node, and the pre-stressing wires were modeled with 1-D truss elements that only have stiffness along the crosstie's longitudinal direction (i.e. the longitudinal direction of the crosstie). Based on the geometry of the components, unique mesh densities were assigned to different components. A dense mesh was assigned to the clips as they went through large deformation during installation, and the component response was shown to be sensitive to mesh density. In contrast, the ballast was coarsely meshed to reduce the calculation time of the model.

The mesh densities of all the components were determined with mesh sensitivity analysis, and the mesh sensitivity of the clip is shown as an example in Figure 215. It can be observed that a finer mesh does not significantly affect the behavior of clip, and the clip mesh with 10,292 elements was used in further studies.

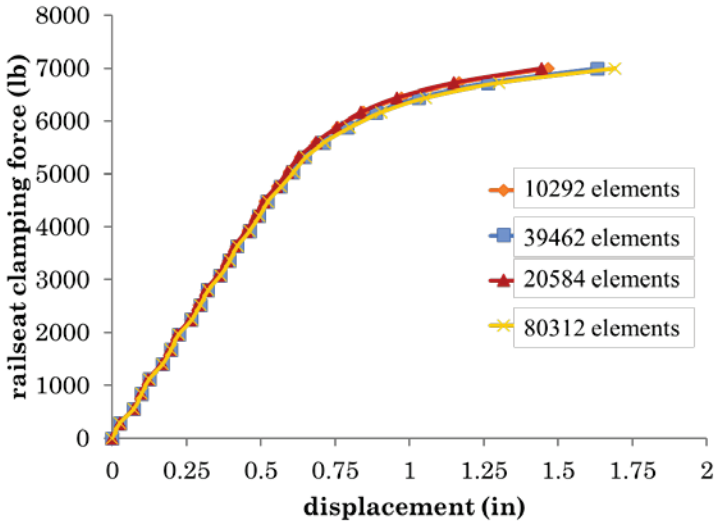

Figure 216. Comparison of the Clamping-Force Displacement Relationship Between Clips of Different Mesh Densities

In addition, a similar investigation of the distribution of longitudinal loads and the longitudinal load path was performed using dynamic FEA. The dynamic FE model incorporates a locomotive wheel. A locomotive wheel is driven by torque from its axle while a railcar wheel is driven by a translational force resulted from the translational movement of the railcar (Figure 216). The same mesh densities that were used in the static model were implemented on all components except for rail and wheel. For these components, mesh sensitivity analyses were carried out. As the accuracy of wheel-rail contact force was sensitive to mesh size on the contact interface, a very dense mesh was assigned to the center of the head of the rail and the perimeter of the wheel. In order to reduce computational demand, the portions of the rail and wheel that were not in contact were meshed with four-node tetrahedron elements to generate a smooth mesh transition from fine to coarse mesh.

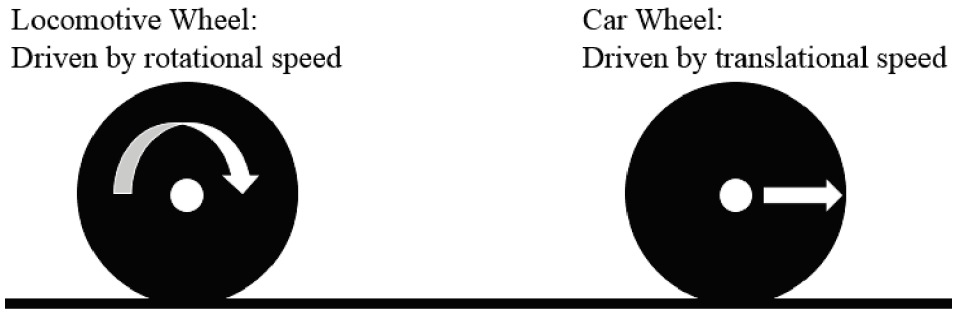

Figure 217. Comparison of the Driving Mechanisms Between Locomotive and Railcar Wheels

7.4 Constitutive Relationships

The concrete damaged plasticity model was used to define the concrete material properties. This material model can represent both tensile and compressive failure mechanisms in concrete. Under uniaxial tension, concrete first goes through a linear elastic stage. When the tensile stress reaches the tensile strength limit, it gradually reduces with increasing tensile strain. Under uniaxial compression, the initial response is linear until the yielding stress is reached. In the plastic stage the response is first characterized by strain hardening and then strain softening after the compressive ultimate strength is reached.

For rail and all the components of the fastening system including the shoulder, rail clip, rail pad, abrasion frame and insulator, and rail, elasto-plastic material models were assigned. In the beginning, it follows an elastic relationship, and the plastic stage consists of a strain-hardening range. As the static loading scenarios were considered in the models, the effect of loading rate was not defined for the given material property. These components are modeled with 3D solid elements. The wheel was simplified as a rigid body as its behavior is not within the scope of this research effort, therefore, it is modeled with 2D rigid elements. Critical parameters used in the definitions of the constitutive relationships for concrete, rail steel, and fastening system components are summarized in Table 47.

Table 47. Material Properties of Concrete, Rail and Fastening System Components

Component	Young's Modulus (ksi)	Poisson's Ratio	Yielding Strength (ksi)	Ultimate/Peak Strength (ksi)	Cracking Strength (ksi)
Concrete	4,347	0.20	N/A	7	0.8
Clip	23,000	0.29	183	202	
Rail	30,000	0.30	150	150	
Insulator	440	0.39	9.3	12.3	
Rail Pad	7.5	0.49	1.2	5.2	
Shoulder	24,500	0.30	45	65	
Abrasion Frame	440	0.39	9.3	12.3	

To provide realistic support for the concrete crosstie, a substructure section of 24 in depth was included in the model. However, the track substructure itself was quite complex to model, as it consisted of multiple layers of granular materials and soils (i.e. ballast, subballast, and subgrade) of heterogeneous material properties. Discrete element method (DEM) provides an alternative to accurately capture the response of track substructure, and relevant research work has been published (Huang and Tutumluer 2011). However, DEM simulation is often computationally expensive. Additionally, as the emphasis of this research work lies in the modeling of concrete crosstie and fastening system, the ballast model herein mainly served as a general representation of the track substructure, and the material property was defined based on the support stiffness measured during field experimentation at TTC in Pueblo, CO.

7.5 Component Interaction

Interactions among different components of the fastening system were defined with contact pairs in ABAQUS. For each contact pair, a master and a slave contact surface, often of different mesh densities, were identified. Some coefficients of friction defined in the model (Table 45) were based on a series of large-scale abrasion resistance tests that were conducted recently at the UIUC, and others were based on literature (Friedrich 1986, Kernes et al. 2012, Wang et al. 2011, Yamaguchi 1990).

To avoid numerical singularity and to simplify the mesh of concrete, the "embedded region" constraint in ABAQUS was used to model the interaction between the shoulder and concrete (Dassault Systemes Simulia Corp. 2011). With this constraint, the translational DOF of the embedded element is restrained by the corresponding DOF of the host element, and with the "embedded region" constraint, the tensile and compressive stress between the concrete and shoulder insert can be reasonably represented until damage occurs between them.

Based on the range of manufacturing tolerances, the gap between an insulator and shoulder could not be explicitly determined, as it is related to the load history of the system. In the model, the range of the gap was set to be 0.002 in, which is consistent with the relative sliding between the concrete and abrasion frame that was observed in laboratory testing.

In the static model, connector elements were used to define the interaction between the concrete and the pre-stressing wires. The concrete was meshed in a way that the element nodes along the

line of the wires coincided with the wire nodes, and a connector element connected the coincident concrete and wire nodes. A Cartesian connector section was assigned to the connector element, and the connector element acted as a spring based on the relative displacements of the connected nodes. To simplify a bond-slip behavior, an elastic force-displacement relationship was defined for all the connectors. The stiffness along the direction of the wires was defined based on the pull-out test results of similar materials, and it was determined as 20,000 lb/in/in (Almeida Filho et al. 2007, Du et al. 2010, Ertzibengoa et al. 2012, Gambarova and Rosati 1996, Mitchell and Marzouk 2007). In addition, the connection in the other two directions of connector elements was infinitely stiff relative to the stiffness along the wires. In the dynamic model, as the behavior of concrete crosstie is not the primary emphasis, and the "embedded region" constraint is utilized to simulate the interaction between crosstie and pre-stressing wires with no bond slip behavior.

7.6 Sequence of Loading and Boundary Conditions in the Static Model

At the beginning of an analysis, a pre-stress force of 7 kips was defined for each of the 20 wires, and then the pre-stress forces were released. At the same time, clips were lifted with pressure while the clip base was restrained by the boundary condition. In the second step, clips were inserted into shoulders with displacement boundary controls. As the pressure was gradually reduced, clip toes started to contact insulators and apply clamping force to the rail base. In the next three steps, the initial boundary conditions and loads were gradually removed from the model. At the end of the fifth step, the model was ready for input loads. Figure 217 illustrates the loadings and boundary conditions applied in different steps.

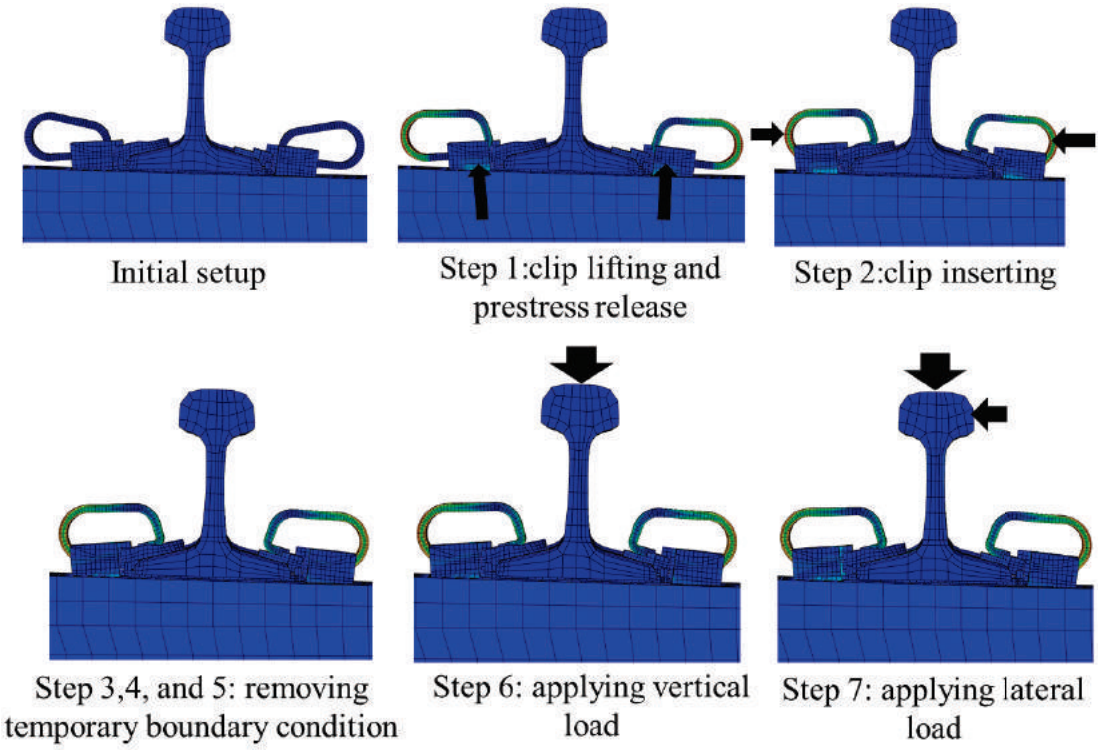

Figure 218. Illustration for the Loadings and Boundary Conditions Applied in Different Steps in the Static Model

7.7 Sequence of Loading and Boundary Conditions in the Dynamic Model

The dynamic analysis consisted of two phases; a static phase followed by a dynamic phase. In the static phase, a same approach was taken to apply pre-stressing forces and install clips. However, after temporary boundary conditions were removed as illustrated in Figure 217, the loading sequence was different. A gravity load was applied to the track superstructure to simulate the resistance to upward deflection resulting from the vertical wheel load, and a wheel load was applied to the centroid of the wheel. A dynamic analysis in which a constant rotational acceleration was applied to the wheel was initiated upon the completion of the static phase.

ABAQUS provides two types of integration schemes for dynamic simulation; explicit and implicit time integration schemes. An explicit dynamic analysis is computationally efficient for analyzing large models with relatively short dynamic response times. They are also efficient for analyzing events or processes that are discontinuous. Explicit dynamic analyses take small time increments and are typically chosen when performing transient time dynamic analyses such as an impact analysis. In contrast, an implicit dynamic analysis usually gives acceptable solutions with time increments typically larger than explicit schemes by one or two orders of magnitude (Dassault Systemes Simulia Corp. 2011). As the total dynamic simulation time was relatively long, implicit time integration schemes were selected. Figure 218 illustrates the loadings and boundary conditions applied in each step of the implicit time integration scheme.

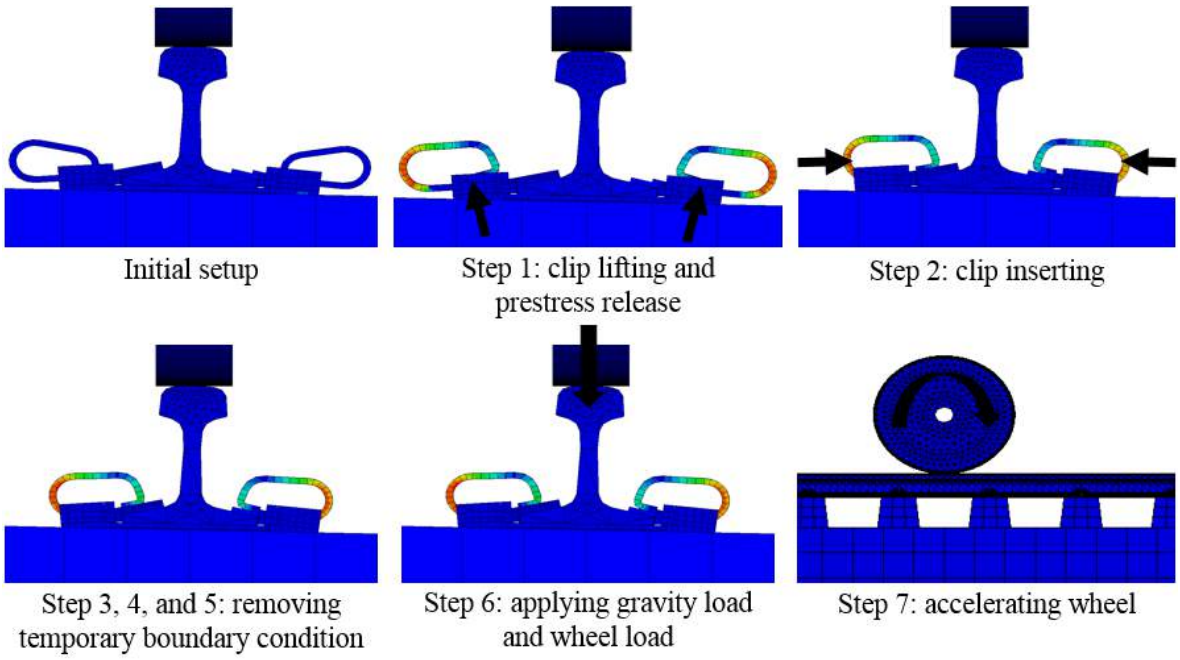

Figure 219. Illustration for the Loadings and Boundary Conditions Applied in Each of the Different Steps in the Dynamic Model

7.8 Single-Tie Model, Multiple-Tie Model, and Dynamic Model

Single-tie models and multiple-tie models were developed to accomplish multiple objectives. Two types of single-tie models have been built according to the settings of laboratory experiments, and they were used to investigate the vertical and lateral load paths through the

system, and the demand on each component. Figure 219 and Figure 220 show the two single-tie models for the following laboratory experiments: PLTM experimentation and SLTM experimentation. At a given loading condition, responses such as the lateral displacement of railhead, vertical displacements of the rail base, web strains of the rail, and strains of the clip surfaces were compared. The Portable Track Loading Frame (PTLF) was used to apply known lateral load, and the PLTM was used to apply a controlled vertical and lateral load with a specific L/V ratio.

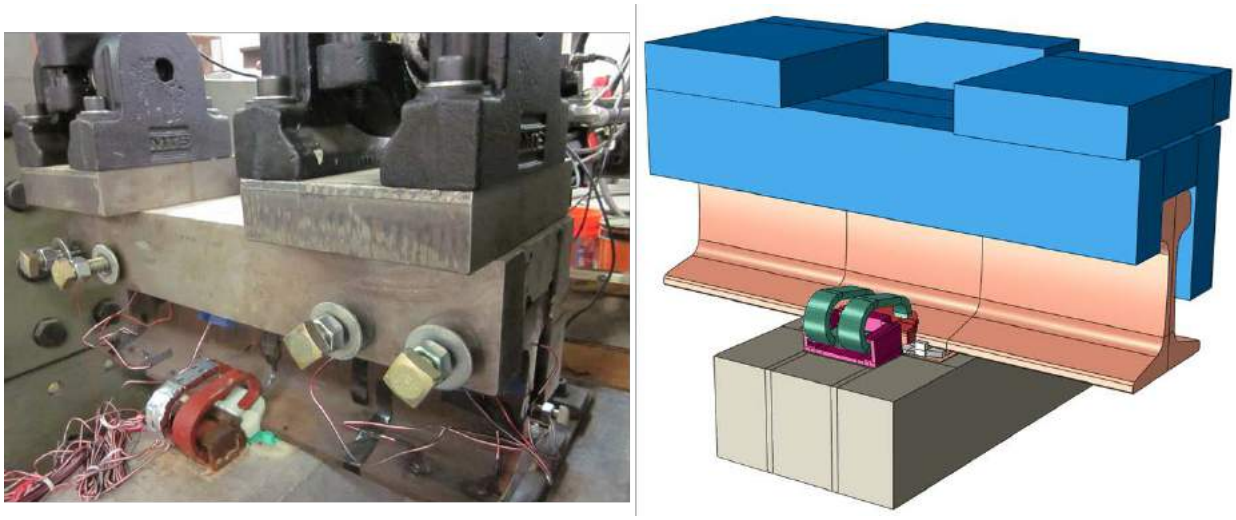

(a) **(b)**

Figure 220. (a) PLTM Test Setup (Loading Head), and (b) PLTM FE Model

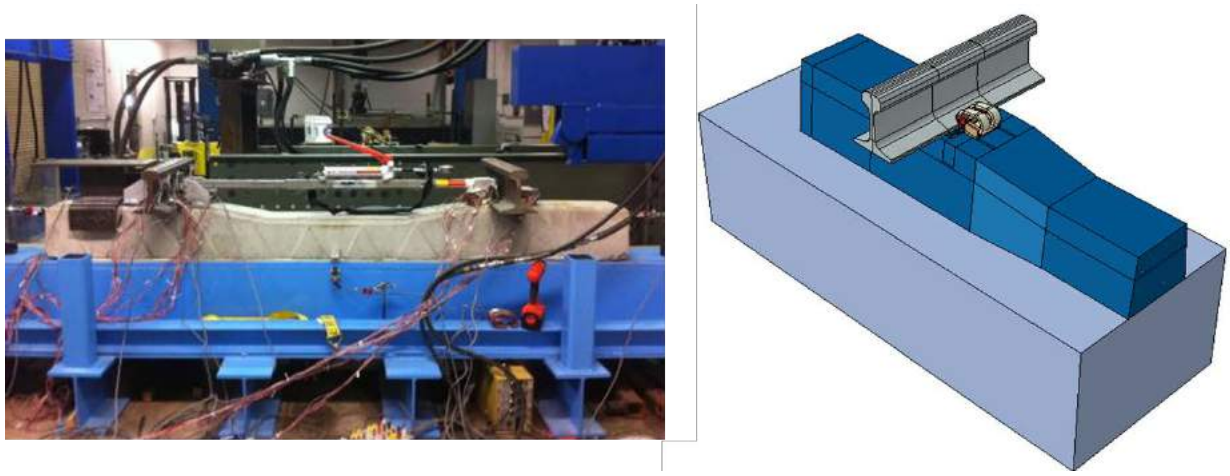

(a) **(b)**

Figure 221. (a) SLTM Test Setup, and (b) Symmetric SLTM FE Model

To accurately simulate the track structure in the field, a multiple-tie model was developed, and Figure 221 shows the developed multiple-tie model. One of the key features related to modeling the track structures in the field is to incorporate realistic support conditions. The simulation results were validated with various measurements collected from field tests conducted at the TTC in Pueblo, CO.

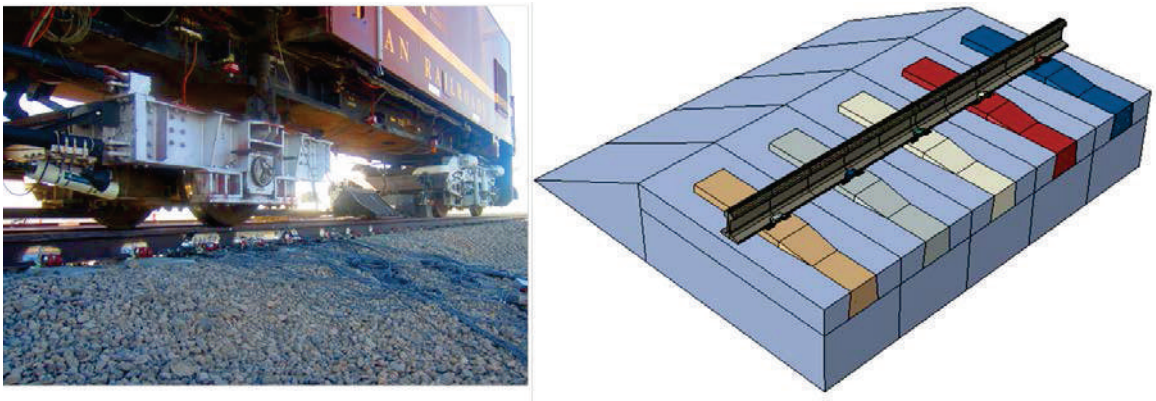

Figure 222. Field Test Setup Using the Track Loading Vehicle and Simplified Multiple-Tie FE Model

The multiple-tie model is computationally expensive, and it is not computationally efficient to use the multiple-tie model to run the parametric analyses. Submodeling is an alternative modeling technique to simulate the track structure with a global model and a detailed model. Figure 222 shows a diagram of the submodeling approach. In the detailed model that includes the single crosstie and fastening system, the boundary conditions applied at each end of the rail was extracted from the global track model. The global model was calibrated based on the field test results to represent the support conditions of the testing track section. The rail displacement in the global model served as the boundary condition in the detailed single-tie model, which was used for system parametric studies.

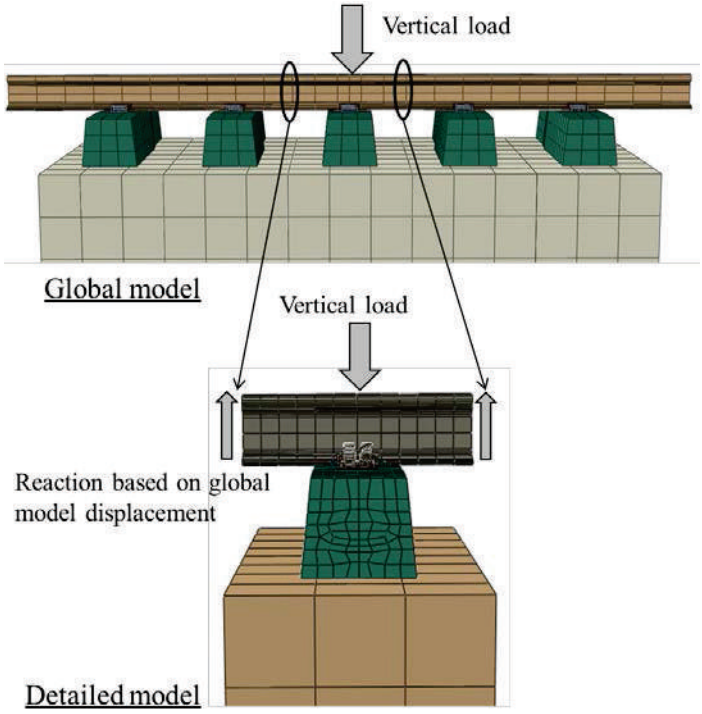

Figure 223. Sub-modeling of Track Structure to Represent Field Conditions

The dynamic model was developed based on the multiple-tie FE model. The intention of the model is to provide insight into the longitudinal load distribution among multiple rail seats and

load path under dynamic wheel loads. The length of the dynamic model was modified several times during its development so that the length was sufficient for the longitudinal load to dissipate among rail seats. The finalized dynamic model consisted of 43 crossties with 24-inch spacing, resulting in a total track length of 86 feet. As the major computational demand was caused by the dense mesh of the rail and wheel, the rail section with refined mesh only extended over seven rail seats located at the center of the track. The segments of rail connected to the center segment were modeled with coarse elements to reduce computational time. Figure 223 shows a profile view of the track that was used for the dynamic model.

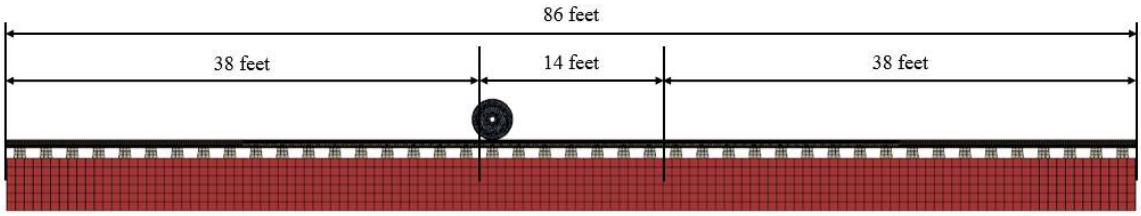

Figure 224. Profile View of 43-Crosstie Dynamic Model Setup

7.9 Model Validation

Validation of the FE models was accomplished in several phases: component model validation, laboratory test model validation, and field test model validation. In each phase, FE models were developed to represent the actual experimental setups. Numerical results such as concrete and steel surface strains, concrete embedded strains, displacements, and load distributions were compared with corresponding experimental measurements to validate the FE models. The difference between numerical results and test measurements were mainly related to unrealistic assumptions, simplifications in the FE model, or measurement error during the experiments. The first error type was corrected by checking the definitions of the FE model with the experiment setup, and by updating the models accordingly. Simplifications in the model were clarified through comparison with theoretical calculations. The component level validation of the clip was based on the clamping force-displacement relationship provided by the manufacturer. The concrete crosstie model was validated with the test result from the crosstie flexural test on the STT at UIUC, as shown in Figure 224. Then the validated components were assembled to build system models. Single-tie models were validated by examining the lateral force transmitted to the shoulder through the rail and insulator, displacement-load relationships, component responses such as strains, and displacements of the rail pad assembly. After validating the models in the laboratory experiments, the models were validated with field experimental data by comparing the distributions of the vertical and lateral wheel load, and the results of other types of instrumentation (e.g. displacement of rail and crosstie).

Figure 225. STT at UIUC Used in the Laboratory Experiment and FE Model Validation

7.10 Parametric Analyses

Based on experimental field experience, the conceptual correlations between the model inputs and the outputs were summarized. The correlations were prioritized based on the range of input influence and the relative importance of the output. The parametric studies were conducted based on this prioritized list and are described in Volume 2, Chapter 8. For each input, a realistic range of the parameter was determined based on representative values chosen to verify the parametric sensitivity for the validated model. A standard set of model definitions were determined including applied load, component geometry, material properties, and component interaction. By changing the input within the determined range, cases of the parametric analysis were defined, and outputs of the cases were compared to evaluate the effect of the input. To screen out the critical input, a fractional factorial design was used in the design of experiment. Based on the result of preliminary regression analysis, more cases were designed at additional levels to improve the statistical model.

The goal, herein, is to advance and optimize the current design practices of concrete crosstie and fastening systems. Also, using parametric studies, the failure mechanisms of some components can be identified and some suggestions to prevent such failures can be recommended. The developed concrete crosstie and fastening system models can be a useful tool to ensure the serviceability and safety of rail infrastructure, and a means to further the state of track infrastructure design.

Chapter 8: FE Modeling Results and Conclusions

8.1 Validation of Component Models

Extensive FE analysis of concrete crossties and fastening systems was executed at UIUC. Detailed FE models were built and validated at multiple levels using data supplied by manufacturers and data obtained through laboratory and field experimentation. The validated FE models were used for parametric studies to further investigate the load path and design of concrete crossties and fastening systems. The purpose of this chapter is to provide details of FE model validation, results of the parametric studies based on the validated FE model, and a summary the conclusions associated with the FE analysis.

8.2 Validation of Clip Model

To verify the functionality of the fastening system components, single component models were developed, and the model outputs were compared with performance information supplied by the manufacturer. Figure 225 shows the comparison between the rail clip and the rail clip FE model. The rail clip is a critical component of the fastening system as it provides the lateral and longitudinal resistance for the rail. In the fastening system, the rail clip works as a spring, and the force-displacement relationship for two clips at a rail seat was compared with the manufacturer information. As shown in Figure 226, the behavior of the clip component model shows good agreement with the manufacturer's data.

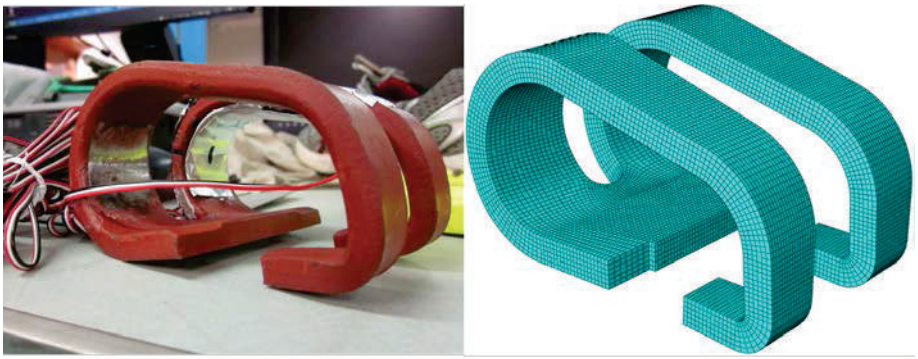

a) b)

Figure 226. Comparison Between a) the Rail Clip and b) the Rail Clip FE Model

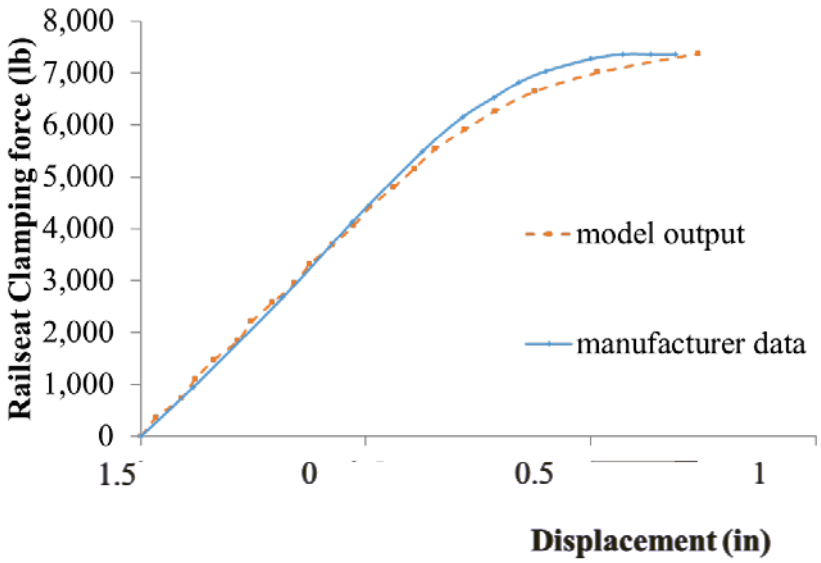

Figure 227. Comparison Between the Force-Displacement Relationship of the Clip Component FE Model and Manufacturer-supplied Data

8.3 Validation of Concrete Crosstie Model

To validate the concrete crosstie component model, flexural testing of concrete crossties was conducted using the STT. Figure 227 shows the STT, the loading protocol, and the location of the concrete surface strain gauges. More details about this specific flexural test are contained in Chapter 3, Section 3.5.4. For the flexural test, the concrete crosstie was supported under the rail seat region, and a vertical static load was applied at the center of the top surface of the crosstie. Figure 228 shows the component model of the concrete crosstie that was validated with the flexural test. As shown in Figure 228, 2-inch wide blocks were placed at the supports and loading positions of the tested crosstie as point loads and point supports. The blocks were also simulated in the FE model.

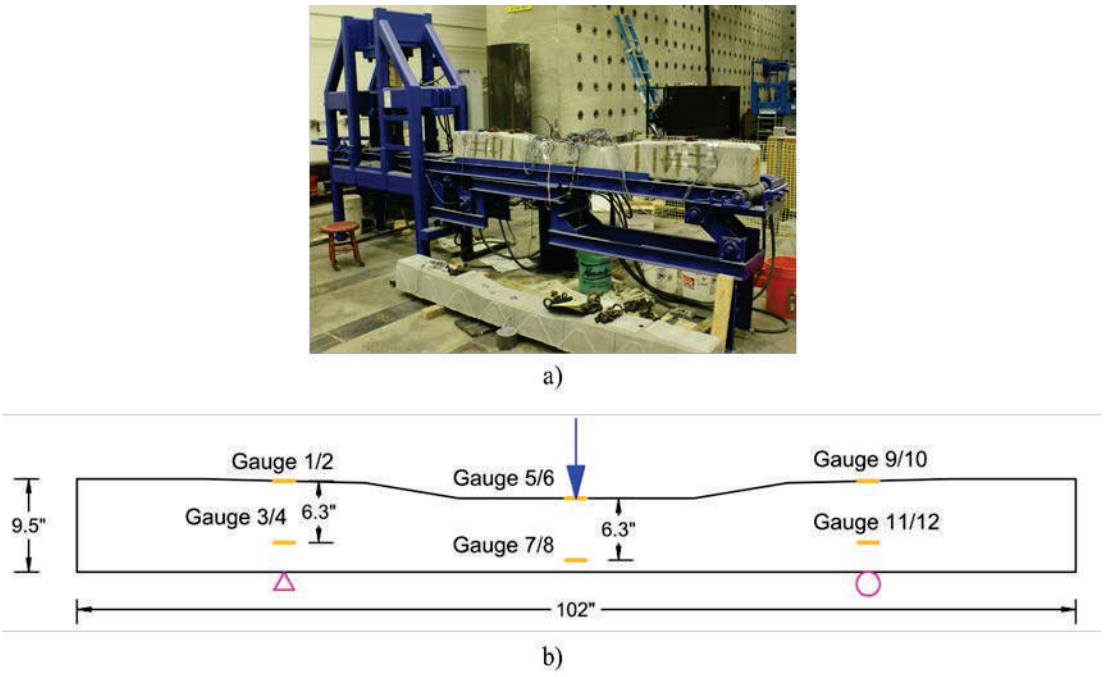

Figure 228. a) The STT Used for Crosstie Bending Testing, b) the Loading Scenario for the Concrete Crosstie and the Location of the Longitudinal Strain Gauges

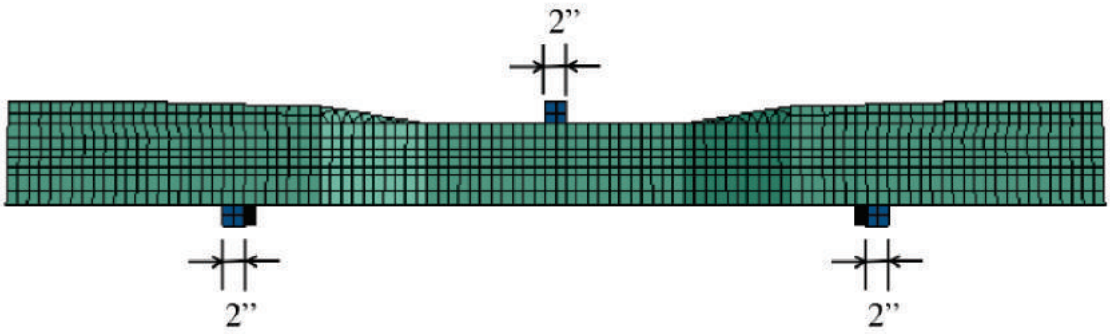

Figure 229. Component FE Model of Concrete Crosstie for Use in Conjunction with Flexural Testing

In the flexural test, a static load of 5 kips was applied to the top surface of the crosstie center to examine the flexural response of the concrete crosstie in the elastic range. The magnitude of the applied load was measured by a load cell, and the flexural strain of concrete crosstie was measured with concrete surface strain gauges. Given that the maximum moment was generated at the midspan of the crosstie, the measurement of surface strain gauges 5, 6, 7, and 8 were used for model validation. The comparison between model prediction and laboratory measurement for the relationship between applied load and concrete flexural strain is summarized in Figure 229. As strain gauge pair 5 and 6 and pair 7 and 8 were attached at symmetric positions on the two sides of the crosstie, the model prediction was combined into one line and compared with each of the pairs. As the crosstie was in positive bending, tensile strain was observed close to the bottom surface (strain gauges 7 and 8), and compressive strain was observed close to the top

surface (strain gauges 5 and 6). As pairs of strain gauges were attached in symmetric positions, minor differences were observed between the measurements of strain gauge pairs (strain gauges 5 and 6, 7 and 8). Good agreement was observed in the comparison between model prediction and laboratory measurement, but the FE model predicted slightly larger flexural strain. It can be observed that the component model of the concrete crosstie was able to capture its flexural behavior as observed through laboratory experimentation.

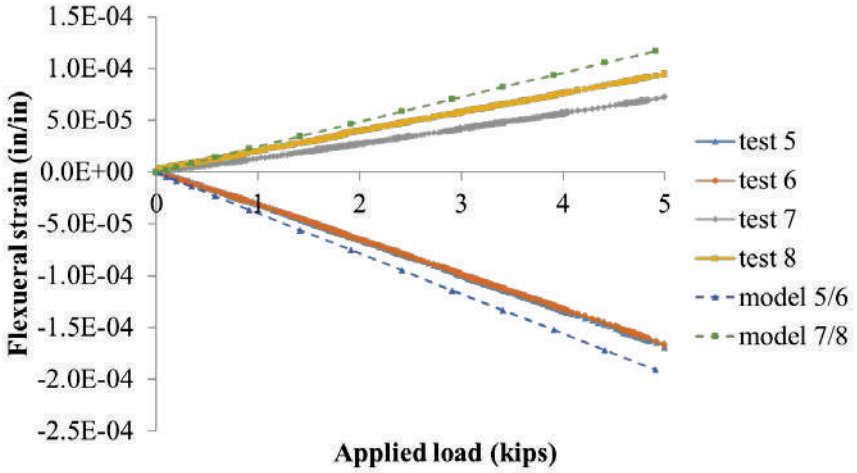

Figure 230. FE Model Prediction and Laboratory Measurement for the Relationship Between Applied Load and Concrete Flexural Strain

8.4 Validation of System Models

8.5 Validation of Single-Crosstie Model

8.5.1 Laboratory Test Setup

To examine the load path through the fastening system and validate the single-crosstie model, laboratory testing was conducted using a pre-stressed concrete crosstie and two sets of fastening systems. As shown in Figure 230, the concrete crosstie was placed on a steel frame, and a thin wooden pad was inserted between the bottom surface of the tie and the loading frame. Two sets of fastening systems and two 24-inch segments of rail were used. Most of the instrumentation was placed on the left rail seat, and a load cell was placed between the portable track loading frame (PTLF) loading head and the rail on the right side to record applied lateral load. By using the PTLF, the lateral load was applied to the rail web, and the response of the system was measured during the test using strain gauges and potentiometers.

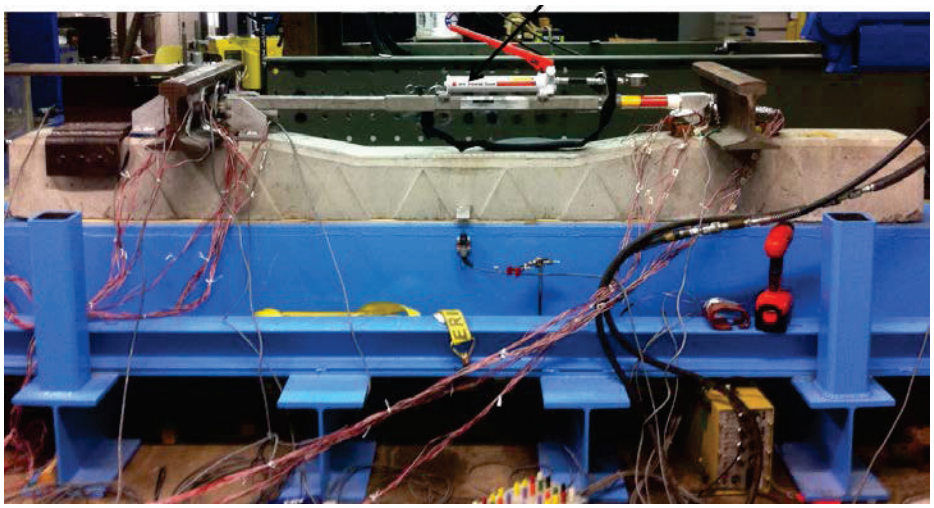

Figure 231. Laboratory Test Setup Using the PTLF

The PTLF was used to apply a lateral load to the two rails. The capacity of the PTLF was 5 kips, and a lateral load of 2.2 kips was applied during the test. The location of contact point between the PTLF loading head and the rail web was at the centerline of rail seat, one inch higher than the top surface of the rail clips.

As shown in Figure 231, strain gauges in the vertical direction were attached to the surface of the rail web to measure the vertical flexural strain of the rail due to lateral loading. Two lines of 10 strain gauges were attached to each side of the rail. Strain measurement from gauges 4 through 10 and 14 through 20 are used as a basis of comparison with the results of the FE model.

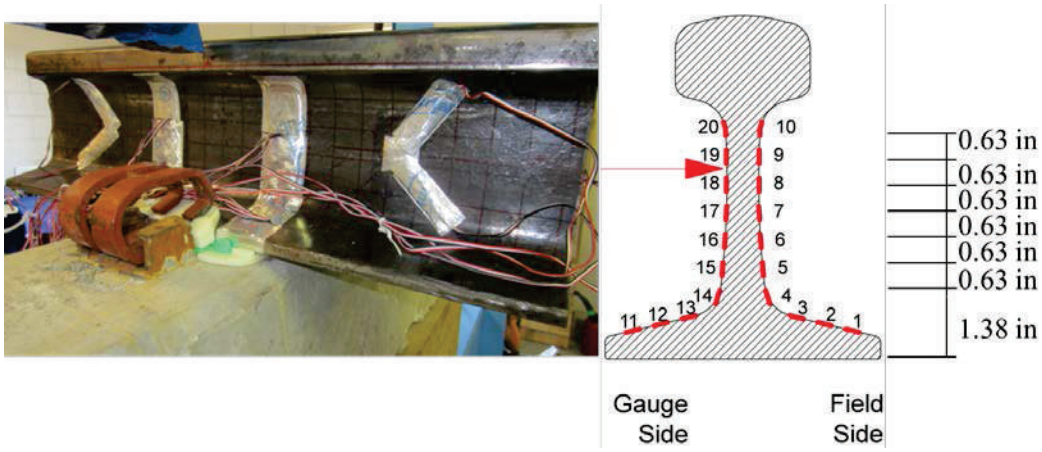

Figure 232. Rail Used in the Laboratory Test with Strain Gauges Attached and Schematic Showing Strain Gauge Naming Convention

During the experiment, seven strain gauges were attached to each clip toe. The instrumented clips were installed at both field and gauge sides of the rail seat. The positions of the strain gauges were marked with red lines in Figure 232, and were numbered 0-6. Along the central line of the clip (dashed line in Figure 232), the distance from the fixed end to the strain-gauged section increased from one inch (gauge 0) to 7 inches (gauge 6).

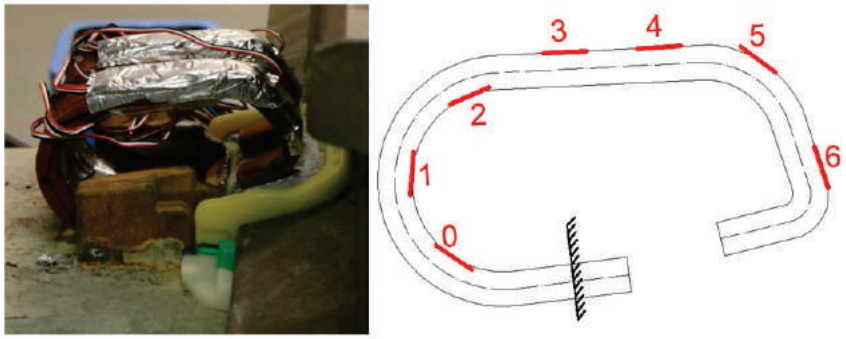

Figure 233. Layout of the Strain Gauges Attached to the Rail Clips

As shown in Figure 233, five linear potentiometers were used to measure the displacement of the rail under lateral loading, and they were all fixed to a steel frame that was connected to the crosstie. Potentiometers 1 through 4 measured the vertical displacement at rail base, while potentiometer 5 measured the lateral displacement at railhead. The positions of potentiometers 1 through 4 are shown in Figure 233, and potentiometer 5 was aligned with the applied lateral load at a height of 0.165 m from the rail base.

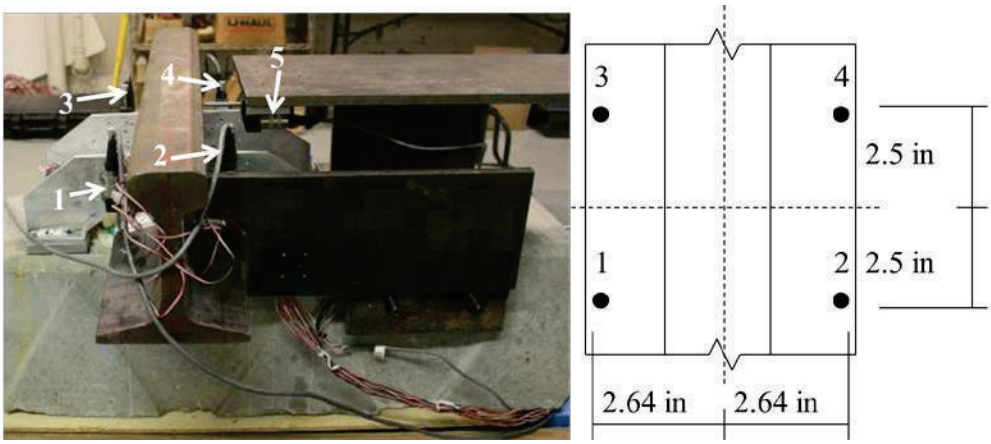

Figure 234. Image and Layout of the Linear Potentiometers to Measure Rail Displacement

8.5.2 Comparison between Model Output and Test Data

Based on the specific attributes of the laboratory test setup, slight modifications were made to the FE model. As shown in Figure 234, a steel cube was in contact with the rail web to represent the loading head of PTLF. This is due to the surface of the loading head (which is parallel to the ground) and the rail web surface (which is almost perpendicular to the canted rail base) are not parallel. The resulting contact stress concentration was simulated through the interaction between the loading head and rail web (Figure 234).

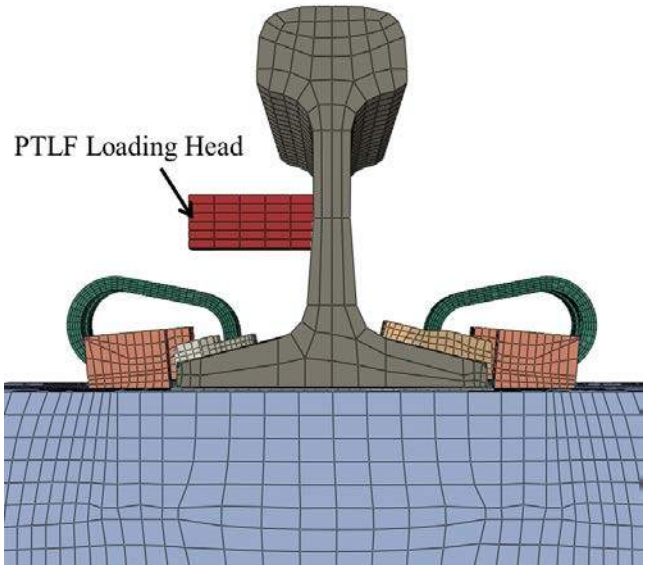

Figure 235. Modified Version of FE Model Designed to Accurately Represent the PTLF Laboratory Test Setup

The comparison between the numerical FE model results and experimental measurements of rail-web vertical strain on the field side and gauge side are shown in Figure 235 and Figure 236, respectively. The vertical strain gauges attached to the rail web at different heights (Figure 235 and Figure 236). Since the PTLF applied lateral load at a height close to strain gauge 18, the strain reading from gauges 8 through 10 at field side and 18 through 20 at gauge side are very small. Strain measured from gauges 5 through 7 and 15 through 17 was negative at field side and positive at gauge side, and larger strain measurements were observed at lower position. This result indicates clear bending behavior of the rail, which was similar to the behavior of a cantilever beam, where the field side of the rail web is in compression and the gauge side is in tension.

In Figure 235 and Figure 236, every set of strain comparisons (model output and experimental measurements) are shown using the same line type. The vertical rail strains increased linearly with lateral load, and good agreement was observed between the numerical and experimental results. Different degrees of agreement in strain were observed at different positions. Close to the middle of rail web (strain gauges 6, 7, and 8), where the surface was relatively flat, better agreement is observed than other positions close to the railhead or rail base, where the rail surface is curved.

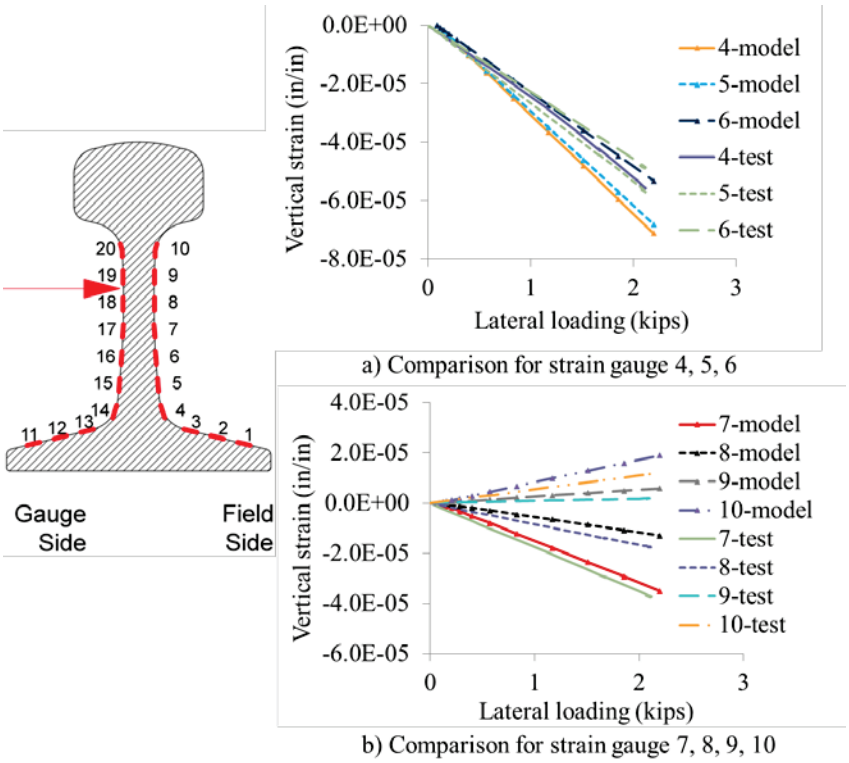

Figure 236. Comparison of FE Model Versus Experimental Field-side Rail Vertical Strain Data

In addition, the location in which the lateral load was applied was between strain gauges 18 and 19 (gauge side) and strain gauges 8 and 9 (field side). FE model output showed that the sign of strain changed at higher gauge positions (strain gauges 9 and 10). This change is due to the rail is of a considerable length in the longitudinal direction, and performs as a combination of both a beam and a plate. The geometry of the rail was correctly captured in the FE model, and the experimental measurement of rail strain on the field side agreed with the FE model output with respect to the fact that the sign of rail strain changed at higher positions than the load.

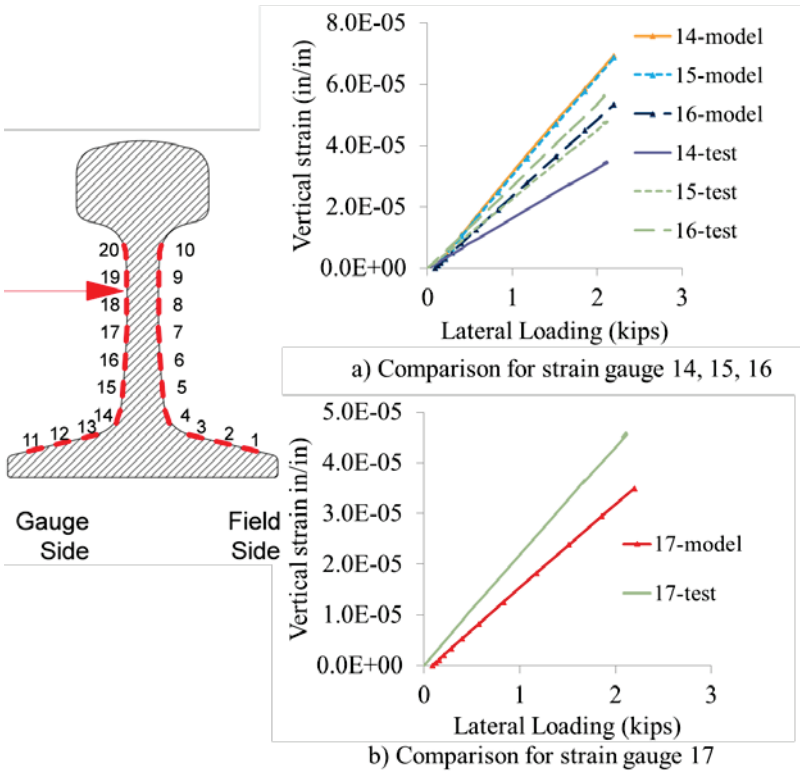

Figure 237. Comparison of FE Model Versus Experimental Gauge-side Rail Vertical Strain Data

Comparisons between the numerical and experimental strain results of field and gauge side clips are shown in Figure 237 and Figure 238, respectively. In each set of comparisons, the FE model output was compared with the two strain gauge measurements at the same position on the rail clip toes. Some gauges were damaged during installation and testing and they are not shown in the comparison. To focus on the behavior of the clip after installation, the strain data was compared after initialization, so that zero strain was observed before load was applied. It can be observed that the strain measurements at the same position of the two rail clip toes are not identical; suggesting that the behavior of the two rail clip toes could be different. The strain prediction based on FE model was close to the experimental strain measurement. In both the model output and test measurement, the clip surface strain increased linearly with lateral load, and minor nonlinear behavior was observed in the experimental data. The nonlinear behavior could be due to post-processing conducted by the manufacturer and the clip installation process. It was confirmed by the manufacturer that the clip was hardened by generating a large deflection, and this process was not captured in the FE model. In addition, the clips were installed with a clip installation tool, and the manual installation process could introduce some effects that are difficult to capture in the FE model. Moreover, the clip surface strain was sensitive to the position of strain gauges, and minor difference in the position of strain gauges between the FE model and the test setup may also result in error.

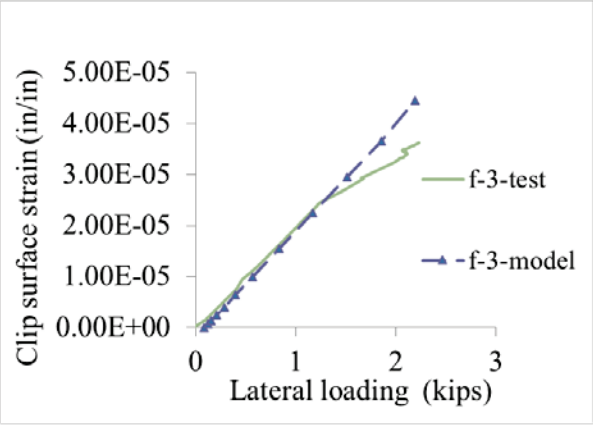

a) Comparison for strain gauge 3

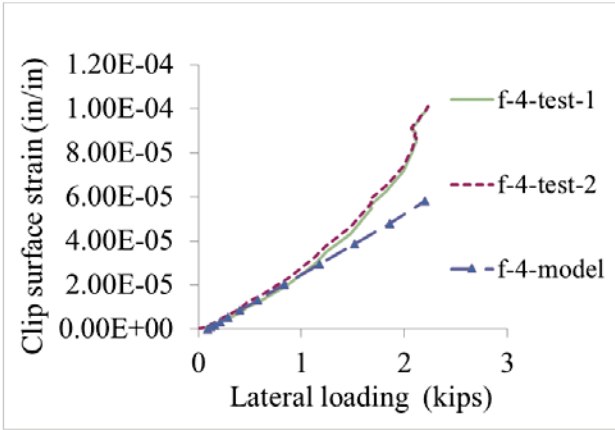

b) Comparison for strain gauge 4

Figure 237. Comparison of FE Model Versus Experimental Field-side Clip Strain Data

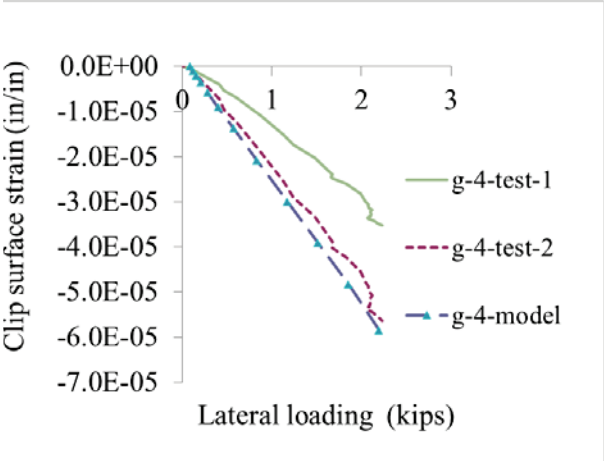

a) Comparison for strain gauge 4

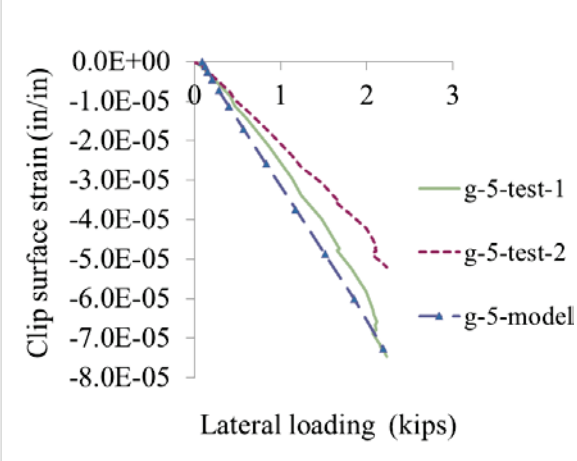

b) Comparison for strain gauge 5

Figure 238. Comparison of FE Model Versus Experimental Gauge-side Clip Strain Data

In addition, under increasing lateral load, increasing compressive strain was observed in the gauge-side clip, while decreasing compressive strain was observed on all strain gauges on the field-side clip. As the gauges were on the outer surface of the clips, it was noticed that under lateral loading the clamping force on the gauge side was increasing while the clamping force on the field side was decreasing. This was validated through further investigation into the interaction of output between the clips and the insulators using the FE model. Theoretically, this was because the rail base on the gauge side lifted upward, leading to larger deflections of the clip and a larger clamping force. Likewise, since the rail base on the field side moved down, this reduced the deflection of the clip and induced smaller clamping forces.

As shown in Figure 233, five linear potentiometers were used in the experiment to measure the displacement of the rail. The comparison between the output of the FE model and the experimental measurements of rail displacement are shown in Figure 239. For rail-base vertical

displacements, positive measurements indicate that the rail base moved upward. Also, for rail head lateral displacements, positive measurements indicate that the rail displaced toward the field side. Some comparisons between FE model output and experimental measurements are shown as examples. Figure 239 illustrates that the field side of the rail base moved downward due to the lateral load, and the rail head moved toward the field side. With 2.2 kips of lateral load applied at rail web, the rail base vertical displacement at field side was about 0.005 in and the railhead lateral displacement was about 0.024 inches. Negative displacement was observed at potentiometer 2 and potentiometer 4, and positive displacement was observed at potentiometer 5. It was observed that the two displacements measured at the field side varied. As the positions of potentiometer 2 and potentiometer 4 were approximately symmetric in the longitudinal direction about the loading point, the difference in test measurement indicates possible difference in the installation of the potentiometers.

The output of the FE model shows smaller displacements at all three positions than that of the experimental measurements, which indicates that there was more rotation of the rail than was observed in the laboratory experiment. Possible sources of variation include the material property definition of the rail pad and the abrasion frame. This is due to the material property of the raw material was used in the model, and unique material treatment in the manufacturing process was not considered in the FE model.

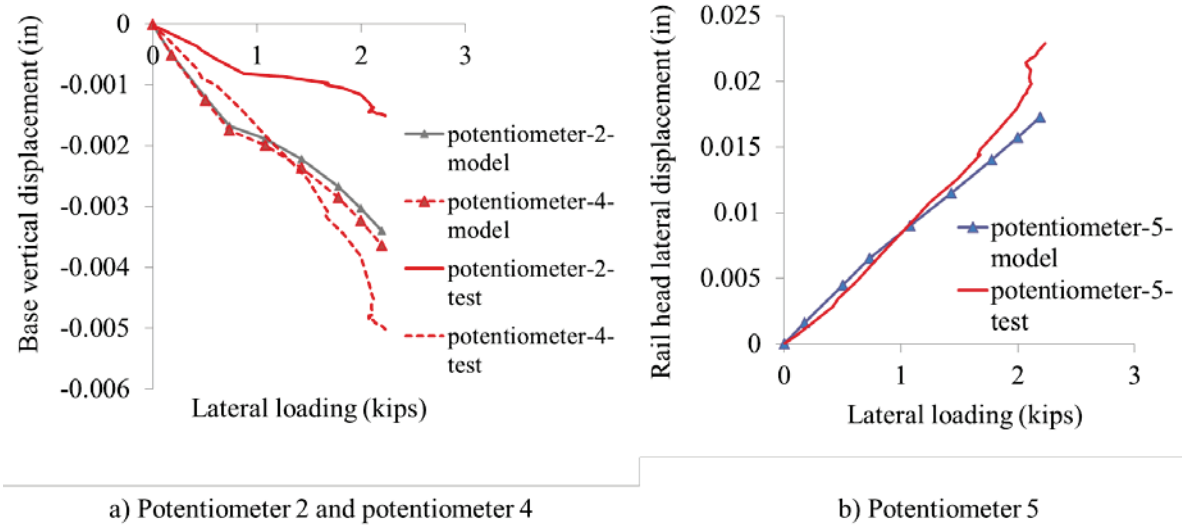

a) Potentiometer 2 and potentiometer 4

b) Potentiometer 5

Figure 239. Comparison of FE Model Versus Experimental Rail Base Vertical Displacement and Rail Head Lateral Displacement

As illustrated by the results in this section, there was good agreement between the FE model and laboratory experimental results in terms of rail vertical strain, rail clip surface strain, and rail displacements. Although the magnitude of load applied in this experiment was relatively low compared to that of field loading scenario, the objective was to compare and validate the FE model of the fastening system in the elastic stage under lateral loading. Field experiments were used for further model validation at higher loading regimes.

8.6 Calibration of Multiple-Crosstie Model Based on Field Experimentation

Field experimentation was performed at TTC in Pueblo, CO, in May 2013, and the detailed field experimental plan is provided in Volume 2, Chapter 5. The FE model of a single concrete crosstie and fastening system was validated with laboratory experimentation, and the field experimentation was performed to investigate the distribution of wheel loads among multiple rail seats and the effects of track substructure support stiffness. The FE model was calibrated and validated with static experimentation using the AAR TLV. On the tangent section of RTT at the TTC, controlled static wheel loads were applied using TLV. At each concrete crosstie, symmetric vertical wheel loads were applied on the two rails and the magnitude was gradually increased from 0 to 40 kips. While the vertical wheel load is maintained at 40 kips, symmetric lateral wheel load (i.e. a gauge-spreading load) was incrementally applied from 0 to 20 kips.

8.6.1 Calibration of Vertical Support Stiffness

Appropriate support stiffness for the track substructure is critical to the performance of railroad track. As track substructure consists of multiple layers of inhomogeneous materials including ballast, subballast, and subgrade, the support stiffness of track substructure is often determined through field experimentation (Selig and Li 1994). Linear potentiometers were installed on multiple concrete crossties to measure the vertical crosstie displacement under different loading scenarios (Figure 240). Figure 241a summarizes the relationship between vertical crosstie displacement, measured with linear potentiometers, and vertical wheel load at different rail seats. The support stiffness (increment vertical load divided by increment vertical deflection of concrete crosstie) varied considerably among rail seats. For two out of five rail seats, the support stiffness has an abrupt change under increasing vertical wheel load. This is likely due to the fact that voids of different sizes were noted between crossties and ballast at certain crosstie locations. After the vertical wheel load increased to a certain critical magnitude, the voids were closed and higher support stiffness was observed as vertical loads were further increased. For the other three rail seats, the support stiffness gradually increased with higher vertical wheel load, demonstrating strain-hardening behavior.

As the emphasis of this research lies in the modeling of concrete crosstie and fastening system, and the ballast model mainly served as a general representation of the track substructure. The material property was defined based on the support stiffness measured at the TTC. The multiple-crosstie model was developed to represent an ideal uniform track with realistic support characteristics. As a result, the material property of the support block in the FE model was uniformly calibrated with the measurement of one rail seat. The field measurement at rail seat C was used for model calibration, as it was more representative of the track condition. As such, different measurements at rail seat C were used for model validation. To capture the change of support stiffness, a hyper-elastic model was used to define the material property of the support block in the FE model. This material model is usually used for nonlinear elastic materials with little compressibility. In ABAQUS, the field experimental test results were used as input to define the hyper-elastic model. After calibration, the comparison between model output and field test data for vertical crosstie displacement is shown in Figure 241b, and good agreement was observed. It is shown that the FE model is able to capture the nonlinear support stiffness of the track substructure.

Figure 240. a) TLV Applying Controlled Wheel Load and b) Linear Potentiometers Installed to Measure Vertical Crosstie Displacement

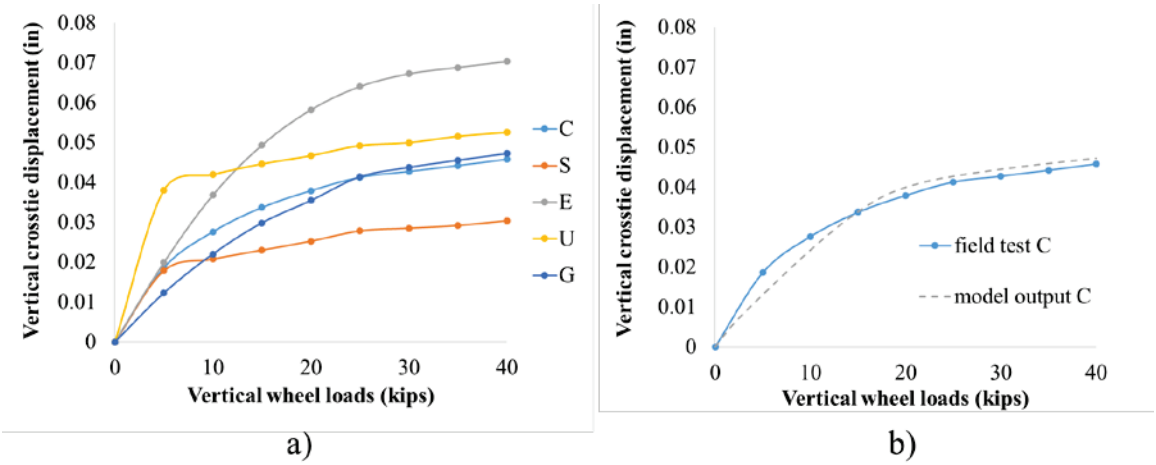

Figure 241. a) Relationship Between Vertical Crosstie Displacement and Vertical Wheel Load at Different Rail Seats and b) Comparison Between FE Model Output and Experimental Measurement of Vertical Crosstie Displacement

8.6.2 Calibration of Concrete-shoulder Connection

To avoid numerical singularity and to simplify the mesh of concrete, an "embedded region" in ABAQUS was used to model the concrete-shoulder interaction. With this constraint, the translational DOF of the embedded element (shoulder element) are restrained by the corresponding DOF of the host element (concrete element), and the stiffness of the concrete-shoulder connection was determined with the area of shoulder that the constraint was defined on. To realistically capture the interaction between the shoulder and the concrete, the constraint definition in the FE model was calibrated with field experimental data. As shown in Figure 18, linear potentiometers were attached to the crosstie to measure the rail web and rail base lateral displacement relative to the crosstie. As the geometry and material property of the rail and the fastening system were known, the shoulder-concrete connection can be calibrated based on the rail lateral displacement data. Figure 243a compares the rail base lateral displacement measurement of two rail seats, and minor difference was observed between the measurements of

the two rail seats. The rail lateral displacement measurement at rail seat S was used to uniformly calibrate the concrete-shoulder connection in the model, and the comparison between model output and field measurement is shown in Figure 243b.

a) b)

Figure 242. Linear Potentiometers Installed to Measure a) Rail Base Lateral Displacement and b) Rail Web Lateral Displacement

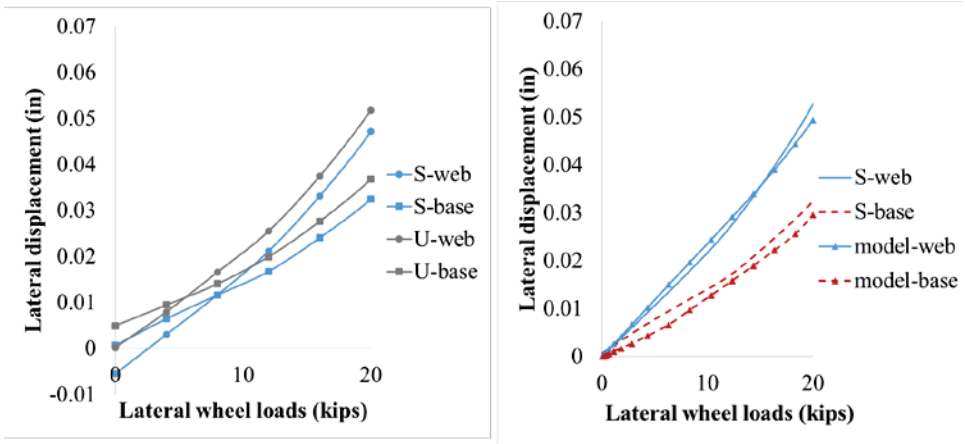

a) b)

Figure 243. a) Comparison of Rail Lateral Displacement of Different Rail Seats and b) Comparison Between Field Measurements and Model Output

8.7 Validation of Multiple-Crosstie Model Based on Field Experimentation

Both the calibration and validation of the multiple-crosstie model were based on static field experimentation on tangent track using the TLV. Some field measurements were used to calibrate the model, and others were used to validate the calibrated model. The detailed field experimental plan is provided in Volume 2, Chapter 5. As the same fastening system was validated in the laboratory experimentation, not all the field measurements were used for model validation, and the discussion focused mainly on the distribution of wheel load among multiple rail seats, the performance of the crosstie, and some new data that were not included in the laboratory experimentation.

8.7.1 Vertical Rail Seat Load

As a part of field experimentation, Chevron gauges were installed around multiple rail seats to measure the vertical rail seat load. As previously shown in Figure 241, the support stiffness varied considerably from one crosstie to another in the field. However, the support stiffness of different crossties in the FE model were uniformly calibrated based on the measurement of vertical crosstie displacement at one rail seat. As a result, there was some level of disagreement between the vertical rail seat load in the field experimentation and that predicted by the FE model. In field experimentation, a vertical wheel load of 40 kips was applied over different crossties, and Figure 244 summarizes the vertical rail seat load at different rail seats and the output from FE model. In the field, when a vertical wheel load of 40 kips was applied, the vertical rail seat load of the loaded crosstie varied from 10 kips to 25 kips. Under the same wheel load, the vertical rail seat load from the FE model was 23.2 kips, which was within the range of field measurement.

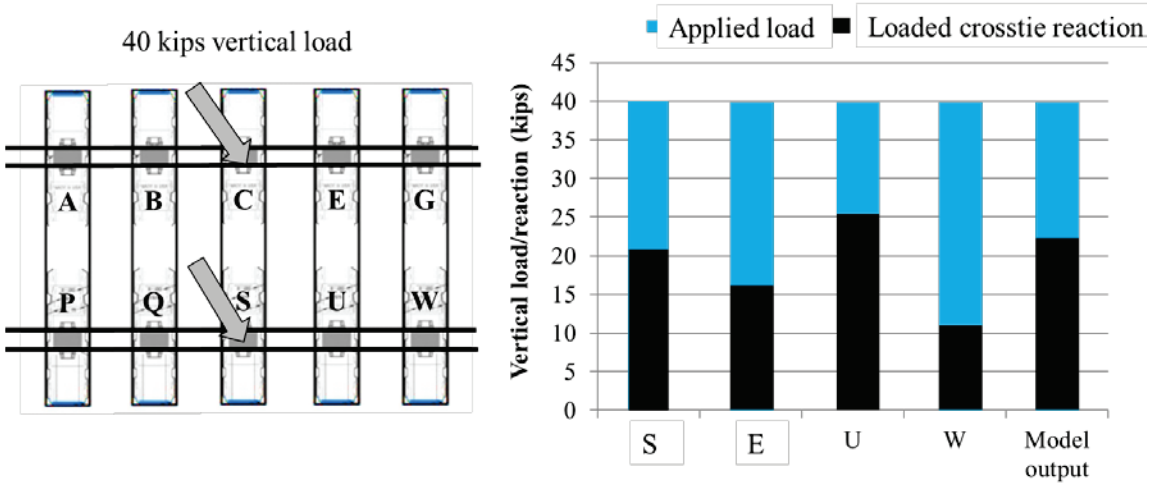

Figure 244. Rail Seat Vertical Reaction When the Wheel Load Was Applied Over Different Crossties and Rail Seats

8.7.2 Lateral Force into Shoulder

Instrumented steel beams were installed in place of the shoulder face to measure the interaction force between field-side shoulder and insulator. One loading scenario was selected to validate the FE model, in which a vertical wheel load of 40 kips and a lateral wheel load of 20 kips were symmetrically applied over crosstie C-S. The comparison of shoulder bearing forces between FE model output and field experimental data at rail seats B, C, and E are shown in Figure 245 and Figure 246. At rail seat C, the shoulder bearing force measured in field experimentation was slightly higher than that in the model output. At rail seats B and E, the shoulder bearing force predicted at the two rail seats by the FE model were identical given that rail seats in the FE model were uniformly calibrated. However, shoulder bearing forces measured at rail seat E were much smaller than those measured at rail seat B, which indicated lower lateral stiffness or larger shoulder-insulator gap at rail seat E. Due to the anomaly at rail seat E that was noted in the field data, the FE model predicted lower lateral loads. In addition, both the field measurements and model output show that under lateral wheel loads, the shoulder bearing force was only captured at the three adjacent rail seats (rail seats B, C, and E). This indicated that in the configuration

used for field experimentation, the lateral wheel load was solely resisted by the three adjacent crossties. In the comparison, it was shown that the FE model was able to capture the distribution of lateral wheel load among multiple rail seats.

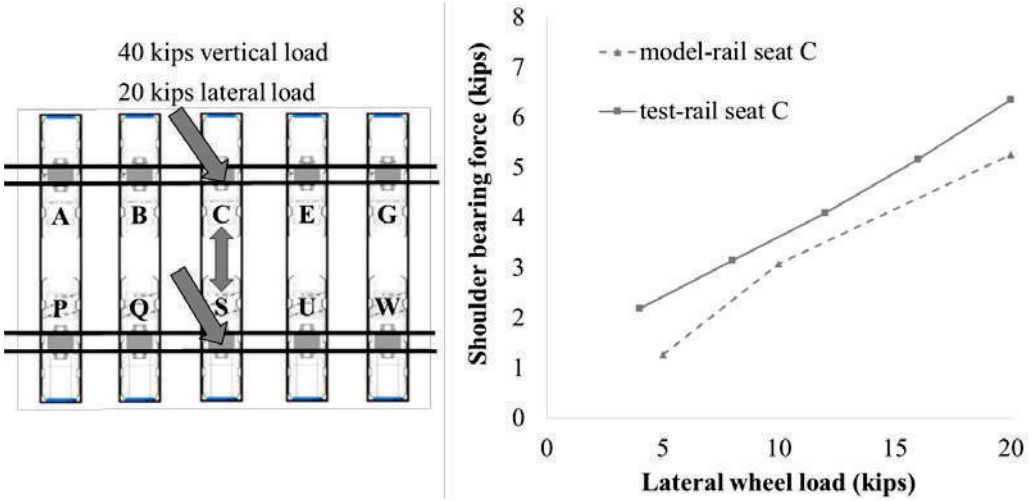

Figure 245. Comparison of FE Model Versus Experimental Data Showing Shoulder Bearing Force at Rail Seat C

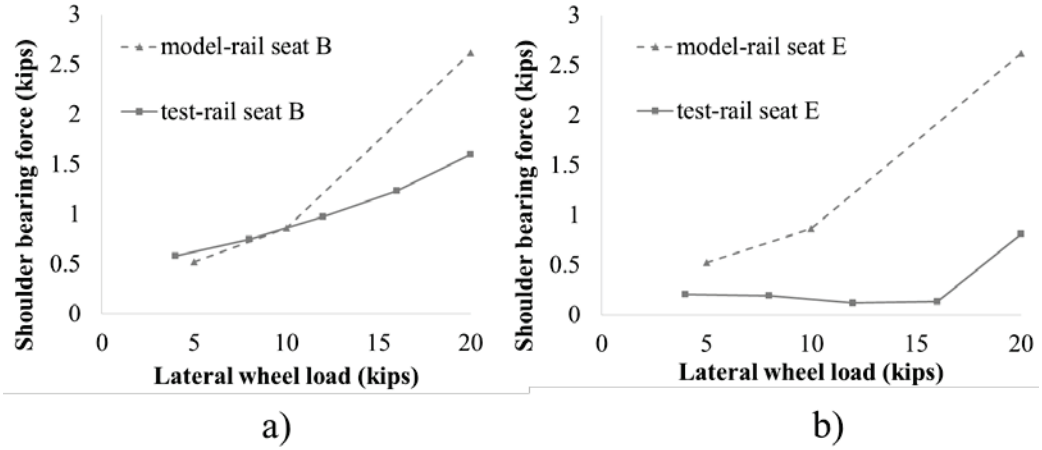

Figure 246. Comparison of FE Model Versus Experimental Data Showing Shoulder Bearing Force a) at Rail Seat B and b) Rail Seat E

8.7.3 Internal Crosstie Strain at Rail Seat

Strain gauges were embedded into concrete crossties to measure the internal strain of concrete. The location of embedded strain gauges is shown in Figure 247. For each rail seat, four strain gauges were embedded into concrete to measure the vertical concrete strain in the rail seat region, and the measurement at rail seat S was used for model validation.

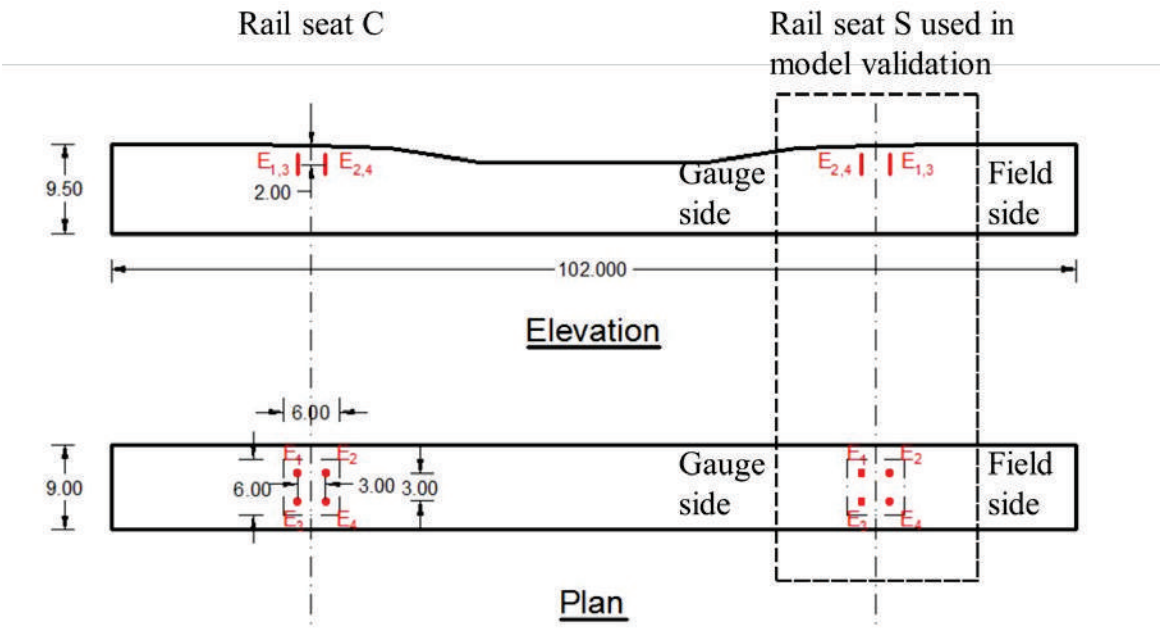

Figure 247. Position of the Embedded Strain Gauges Within Concrete Crosstie (Dimensions in Inches)

Of the four strain gauges, strain gauge 2 was damaged and only the data from strain gauges 1, 3 and 4 were collected. Figure 234 and Figure 235 show the change of strain measurement under increasing vertical and lateral wheel load along with the corresponding prediction of the FE model. Under vertical wheel load, which was applied onto the rail head with eccentricity to the gauge side, the vertical reaction in the rail seat region was concentrated on the gauge side (strain gauge 1 and 3). As a result, under the same vertical wheel load the strain measurement of gauges 1 and 3 is larger than that of gauge 4. Under increasing lateral wheel load, the strain measured on the field side (strain gauge 4) continued to increase, while the strain measured on the gauge side gradually decreased. This was because the lateral wheel load applied moment to the rail, which balanced the eccentricity moment due to vertical wheel load, and continued to rotate the rail head to the field side.

Embedded strain gauges were placed symmetrically about the centerline of the crosstie. Theoretically, identical measurements should be observed between strain gauges 1 and 3. However, under the same loading scenario the strain measured from strain gauge 3 is considerably larger than that of strain gauge 1. The difference between concrete vertical strains measured from strain gauge 1 and 3 could be due to the asymmetric support condition at the bottom of crosstie. Under field experimental conditions, concrete crossties were supported on the uneven surface of ballast, thus the symmetry of crosstie-ballast support about the centerline of the crosstie is not guaranteed. In addition, the dislocation of embedded strain gauges in the casting process could also contribute to the observed difference.

As a comparison with FE model data, identical concrete vertical strain values were predicted at gauges 1 and 3 as well as gauges 2 and 4. This was due to the track substructure modeled as continuous material with a flat surface that is symmetric about the centerline of the crosstie. In general, the FE model was able to capture the rotation of rail under vertical and lateral wheel load, as good correlation was observed between the change of concrete vertical strain in the

model output and that in the field measurement. The magnitude of strain in field measurement is close to that of model output, indicating that the model is able to capture the distribution of vertical and lateral wheel load among multiple rail seats. For strain gauges 1 and 3, the corresponding model output was between the field measurements of the two strain gauges. This supports the assumption that uneven support condition existed under the crosstie. In addition, as the strain measured at strain gauges 3 and 4 are both higher than that in the FE model output, it is most likely that the support stiffness under the corresponding side of the crosstie was higher than that of the other side.

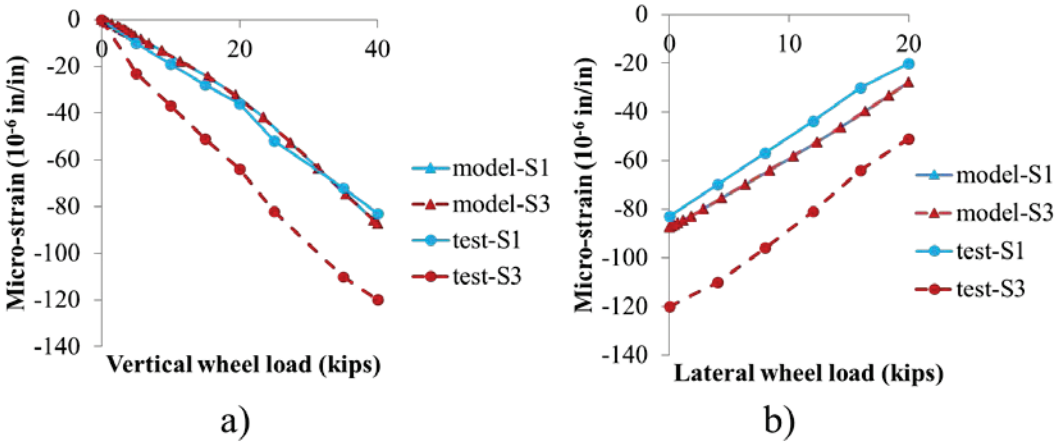

Figure 248. The Relationship Between the Measurements of Embedded Strain Gauges 1 and 3 and a) Vertical Wheel Load (Lateral Wheel Load = 0), and b) Lateral Wheel Load (Vertical Wheel Load = 40 kips)

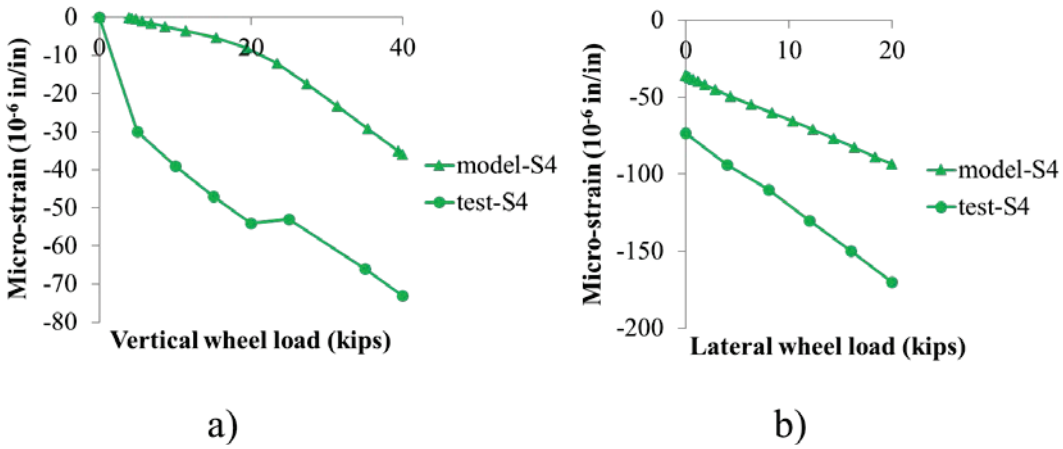

Figure 249. The Relationship Between the Measurements of Embedded Strain Gauge 4 and a) Vertical Wheel Load (Lateral Wheel Load = 0), and b) Lateral Wheel Load (Vertical Wheel Load = 40 kips)

8.7.4 External Crosstie Strain

As a part of field experimentation, concrete surface strain gauges were attached on multiple crossties (Figure 250). The strain measurement of crosstie C-S was used for model validation. Six surface strain gauges were attached in the longitudinal direction of the crosstie to measure

the flexural strain of concrete under wheel loads. As strain gauges 1 and 2, and 5 and 6 were attached at symmetric positions, only one pair (strain gauges 1 and 2) was used in the model validation.

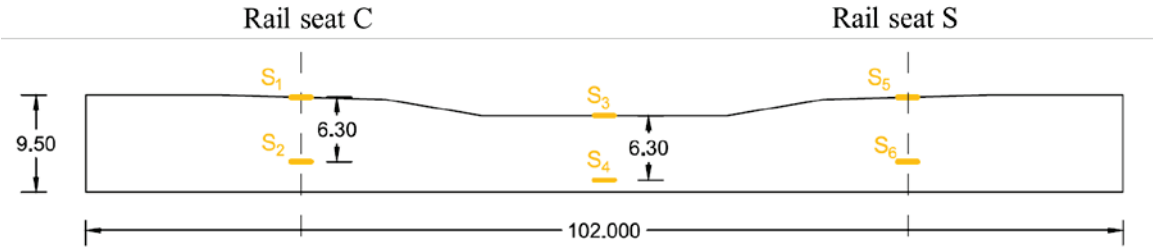

Figure 250. Profile View Showing Positions of Concrete Surface Strain Gauges (Dimensions in Inches)

The comparison of concrete surface strain between field experimentation and FE model output is shown in Figure 251 and Figure 252. Under vertical wheel load, positive bending was observed at the rail seat and negative bending was observed at the crosstie center. As symmetric lateral wheel loading was applied, the crosstie tensile strain increased and concrete compressive strain decreased with higher lateral wheel load. At the rail seat region (strain gauges 1 and 2), the concrete surface strain predicted by the FE model was slightly higher than that measured in the field. At the midspan of crosstie (strain gauge 3 and 4), considerable difference was observed between the concrete surface strains based on model output and field measurements under low vertical wheel loads. However, the difference gradually reduced at higher vertical and lateral wheel loads. This observed difference should be related to the interaction between crosstie and ballast. In the FE model, a flat interface was assumed between the crosstie and the ballast. However, in the field, gaps could exist beneath the crosstie and the crosstie could be partially supported before the application of wheel load. As a result, the concrete flexural strain increased considerably at the crosstie center under small vertical wheel loads. As higher vertical wheel loads were applied, the gaps were gradually closed and better agreement was observed between FE model output and field measurement under higher vertical wheel loads. In this comparison, it is shown that the FE model was able to accurately capture the support conditions measured in the field.

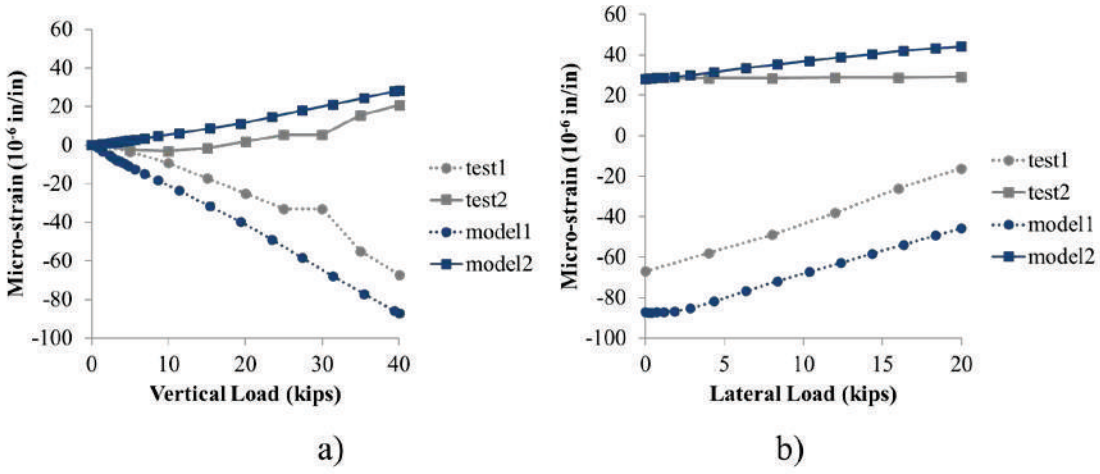

Figure 251. Comparison of FE Model and Field Data of Concrete Surface Strain in the Rail Seat Region Under a) Increasing Vertical Wheel Load and b) Increasing Lateral Wheel Load

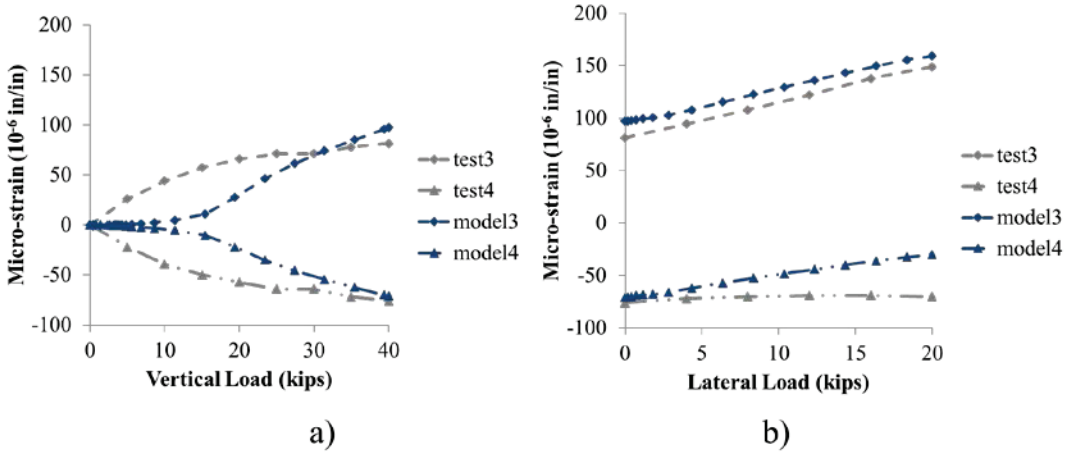

Figure 252. Comparison of FE Model and Field Data for Concrete Surface Strain at Crosstie Center Under a) Increasing Vertical Wheel Load and b) Increasing Lateral Wheel Load

8.7.5 Rail Pad Lateral Displacement

As shown in Figure 253a, linear potentiometers were installed on concrete crossties to measure the rail pad lateral displacement (RPLD) at different rail seats. In addition, RPLD s at different rail seats were compared for vertical and lateral loads applied to crosstie C-S (Figure 253b). The lateral displacement of the rail pad increased rapidly under low lateral wheel load magnitudes, and the incremental displacement decreased under higher magnitudes of lateral wheel load. The change of sliding stiffness is likely since the field-side shoulder restrained the lateral translation of the rail pad after the gap between the rail pad and field-side shoulder was closed.

Considerable variability was observed among the data from different rail seats. When the wheel load was applied over crosstie C-S, the largest RPLD was observed at rail seat E, which was

adjacent to the loaded crosstie. As negligible lateral load was measured at the field-side shoulder at rail seat E, the measurement indicated that a larger gap existed at rail seat E than other rail seats. The comparison of RPLD between the FE model output and field data is shown in Figure 254. The magnitude of RPLD in the FE model output is close to that measured in the field, however some difference is observed. The difference may be related to the geometric simplification in the FE model, which affected the local response of the rail pad close to the location of measurement. In addition, the difference between the pad-shoulder gap that was assumed in the FE model and the actual field conditions contributed to the difference.

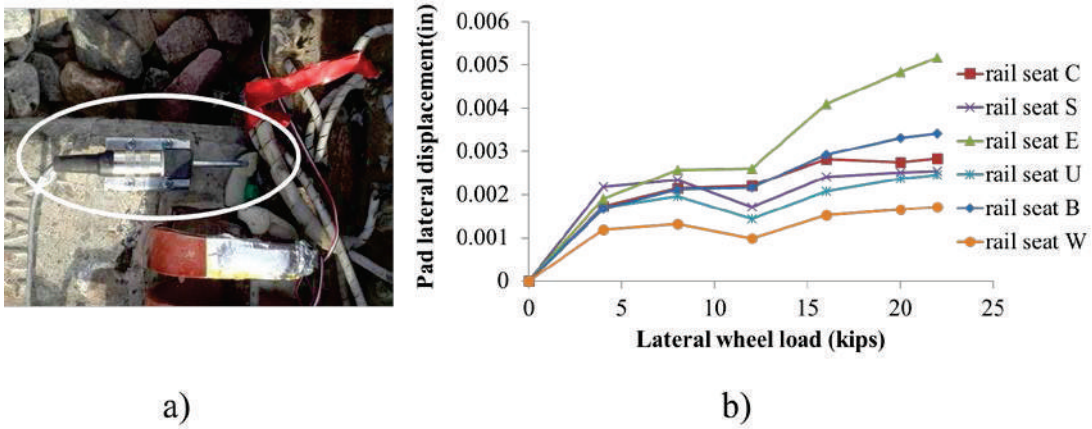

Figure 253. a) Linear Potentiometer Installed on Concrete to Measure Rail Pad Lateral Displacement and b) Measured Rail Pad Lateral Displacement at Different Rail Seats

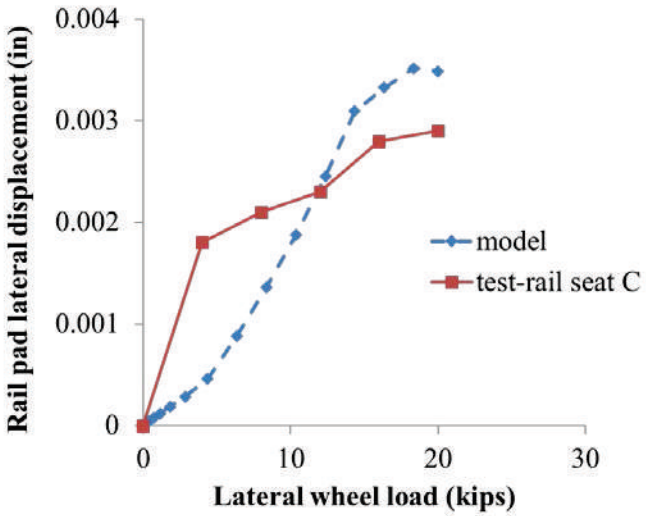

Figure 254. Comparison of FE Model and Field Data for Rail Pad Lateral Displacement

8.8 Calibration of Multiple-Crosstie Model Based on Full-scale Laboratory Experimentation

In the model validation based on field experimentation, it was proven that the FE model was able to capture the distribution of vertical and lateral wheel load among multiple rail seats. However, in the field experimentation, symmetric lateral wheel load (gauge-widening load) was applied using the TLV whereas lateral wheel loads toward one side of the track are more frequently observed on curved track. To more realistically evaluate the performance of concrete crosstie track on curved track, laboratory experimentation of concrete crosstie track was performed using the TLS at the RailTEC's Research and Innovation Laboratory (RAIL).

As shown in Figure 255a, a segment of concrete crosstie track that includes 11 crossties at a spacing of 24 inches was constructed within a steel frame for laboratory experimentation. The five concrete crossties in the middle of the track segment were instrumented, and a detailed instrumentation plan is provided in Chapter 3 of Volume 2. In the TLS, a wheel set was placed on the track segment, and actuators in the vertical and lateral directions were mounted on the wheel set to apply defined vertical and lateral wheel load. During experimentation, a constant vertical wheel load of 40 kips was applied to each wheel, and a lateral load increased from 0 to 24 kips was applied to the wheel set. The wheel set was moved over the five instrumented crossties, and the same loading procedure was repeated for each of them. The naming convention for the five instrumented crossties is shown in Figure 255b.

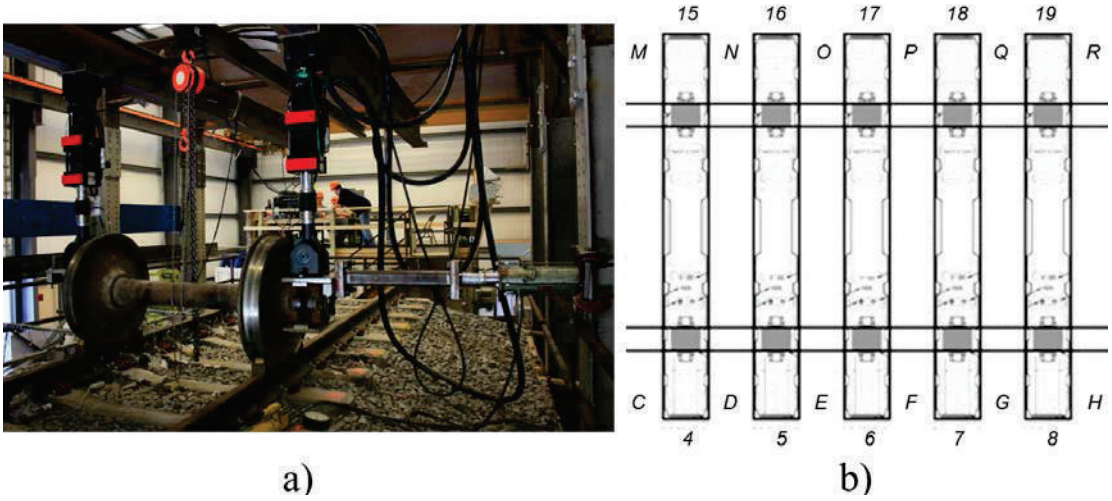

Figure 255. a) Track Loading System and b) the Naming Convention for TLS Rail Seats

As the loading scenario in the laboratory experimentation was asymmetric, full-scale FE models were used in model calibration and validation, as shown in Figure 256. The material property, component geometry, and interaction definitions used in the full-scale FE models are mostly the same as what is defined in the symmetric FE models. In the FE model, the wheel set was not simulated and wheel loads were directly applied on the rail head. While identical vertical wheel loads were applied on both rails, the distribution of the lateral wheel loads between the two rails was not clear. The lateral wheel load defined on the instrumented rail was based on the measurement of the lateral strain gauge bridge attached on the rail, which is described in detail in Chapter 3 of Volume 2. The lateral wheel load defined on the other rail was determined based on the lateral equilibrium of the wheel set. In addition, discrete springs that connects the

crossties to the ground was defined on the crosstie surfaces in the FE model to simulate the resistance of crib and shoulder ballast to the lateral displacement of the crossties, and the stiffness of the springs were defined based on single-crosstie push tests. The full-scale FE models were defined considering the laboratory measurement of different loading scenarios (wheel loads applied on different crossties), and the comparison between model output and experiment data when the wheel loads were applied over crosstie 6-17 is shown as an example for the model calibration and validation process in the following sections.

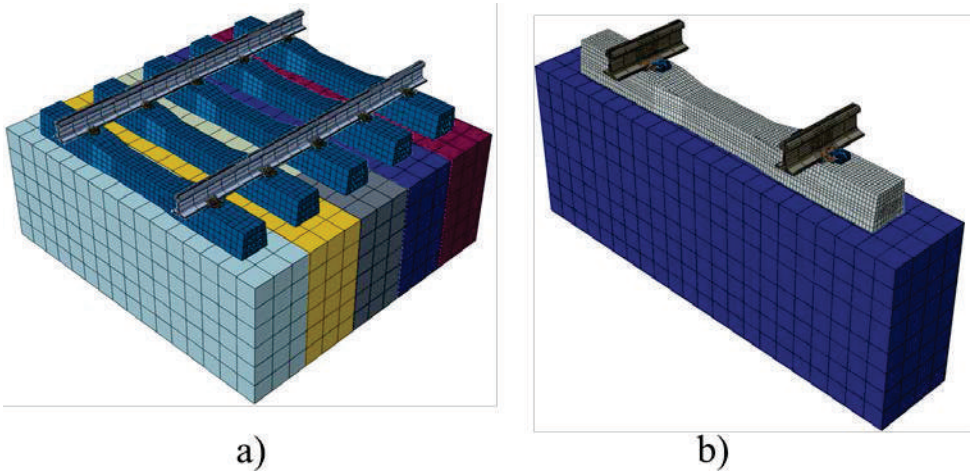

Figure 256. The Full-scale a) Global Model and b) Detailed Model Used for Laboratory FE Model Validation

8.8.1 Calibration of Vertical Support Stiffness

As indicated by Kish in 2011, a significant portion of the lateral load on a concrete crosstie is resisted by the friction between the crosstie and ballast below the base of the tie (Kish, 2011). As a result, it is critical to ensure that the FE model is able to capture the distribution of vertical wheel load in the laboratory experimentation before further analysis of the track structure under lateral wheel load. As shown in Figure 257a, strain gauge bridges were attached to the rail to determine the vertical rail seat load. The vertical rail seat load of the loaded rail seat in different loading scenarios is shown in Figure 257b. In comparison, the vertical response of different rail seats varied significantly, and no vertical rail seat load was observed at rail seat 6 and 8 when vertical wheel load increased from 0 to 40 kips. In addition, linear potentiometers were installed on the ends of crossties to measure the vertical crosstie displacement, as shown in Figure 258a. The measurement of vertical crosstie displacement at the loaded crosstie in different loading scenarios is shown in Figure 258. Under identical vertical wheel load, the vertical displacement of different crossties also varied significantly. Additionally, the vertical displacement of rail seat 6 and 8 are larger than other rail seats, which corresponds with the measurement of vertical rail seat load.

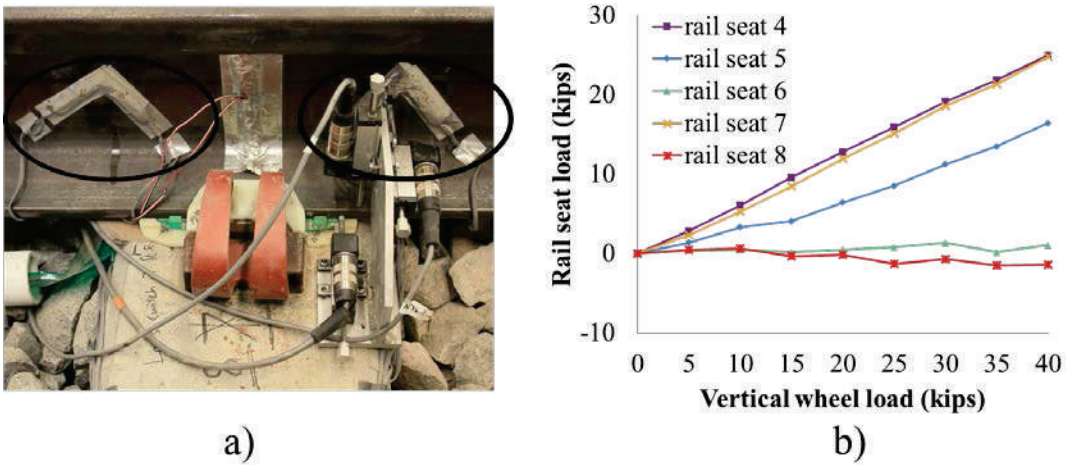

Figure 257. a) Strain Gauges Attached to Determine the Vertical Rail Seat Load, and b) the Vertical Rail Seat Load of the Loaded Rail Seat in Different Loading Scenarios (Lateral Wheel Load = 0 kips)

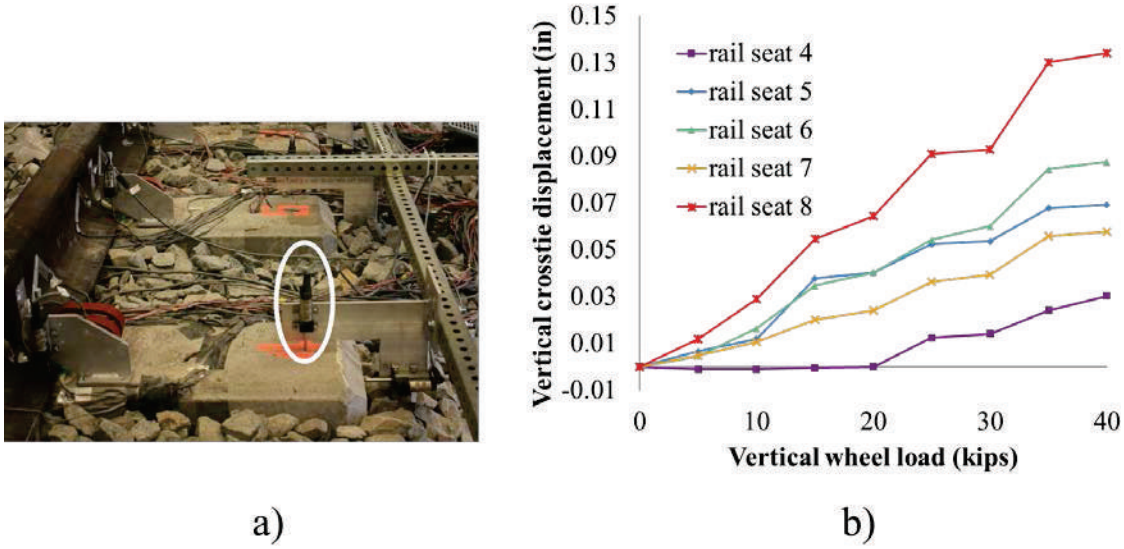

Figure 258. a) Linear Potentiometers Installed to Measure the Vertical Crosstie Displacement and b) the Vertical Crosstie Displacement of the Loaded Crosstie in Different Loading Scenarios (Lateral Wheel Load = 0 kips)

Based on the data collected, it is assumed that there were gaps between the crossties and ballast under rail seat 6 and 8, and the gaps were not closed even under a vertical wheel load of 40 kips. As both the rail seat load and the vertical crosstie displacement increased linearly with the applied vertical wheel load, a linear elastic material property model was defined for the support blocks underneath the crossties. In addition, the vertical support stiffness of different rail seats in the FE model were calibrated individually based on the measurement of vertical crosstie displacement to consider the difference among different rail seats. As gaps existed under rail seats 6 and 8, and the gaps were not closed under maximum vertical wheel load, negligible elastic modulus was assigned to the support block under rail seat 6 and 8. Figure 259 is shown as an example for the agreement after calibration, which includes the numerical versus

experimental comparison on the vertical crosstie displacement when the wheel loads were applied over crosstie 6-17. In this loading scenario, the vertical crosstie displacement at rail seat 5 and 7 in the model output agreed well with that in the laboratory experiment, and the vertical crosstie displacement at rail seat 6 is slightly higher than the laboratory measurement. Overall, the comparison shows that the vertical crosstie displacements based on the calibrated FE model agrees well with laboratory data.

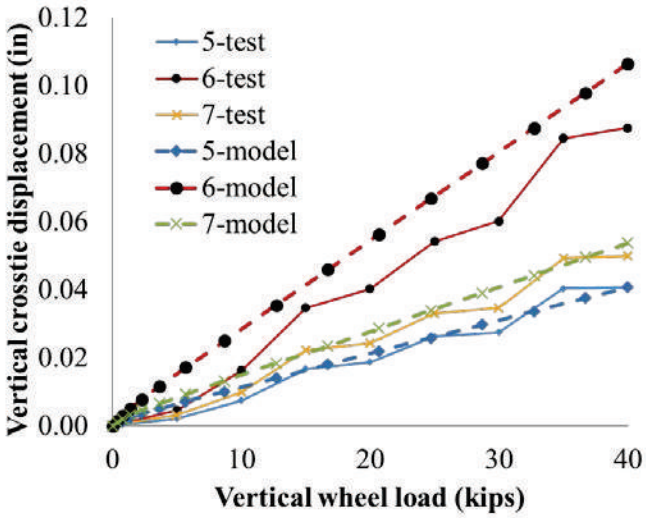

Figure 259. Numerical Versus Experimental Comparison on the Vertical Crosstie Displacement When the Wheel Loads were Applied Over Crosstie 6-17 (Lateral Wheel Load = 0 kips)

8.8.2 Calibration of Lateral Crosstie Displacement

In the laboratory, linear potentiometers were installed to measure the lateral crosstie displacements of the five instrumented crossties, as shown in Figure 260a. The relationships between the lateral crosstie displacement of the loaded crosstie and the lateral wheel load in different loading scenarios are summarized in Figure 260b. Based on the comparison, it is shown that under identical lateral wheel load, the lateral responses at different rail seats are quite different.

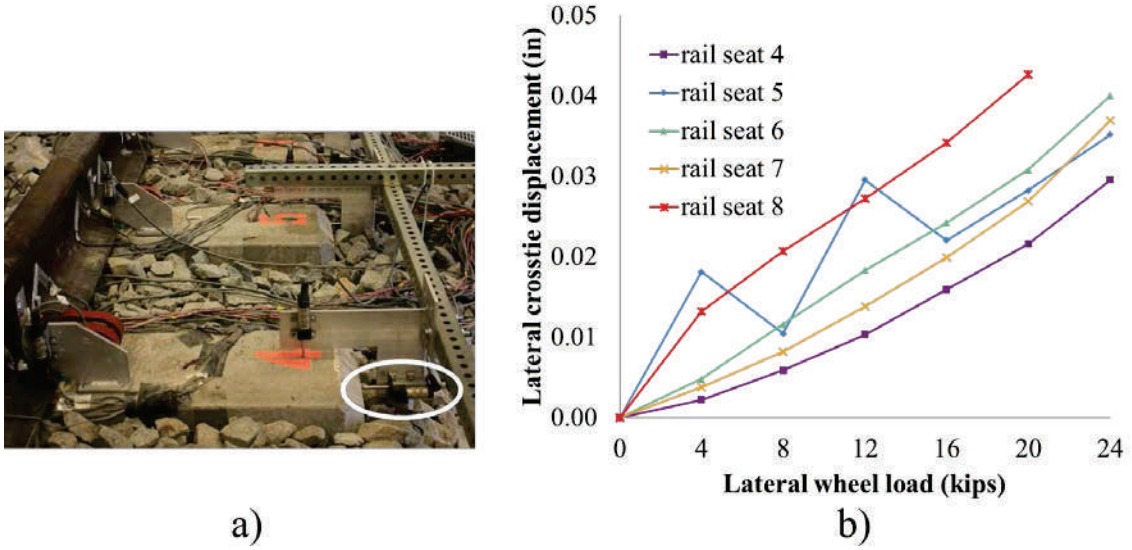

Figure 260. a) Linear Potentiometers Installed to Measure the Lateral Crosstie Displacement and b) the Lateral Crosstie Displacement of the Loaded Crosstie in Different Loading Scenarios (Vertical Wheel Load = 40 kips)

Figure 261 shows the lateral crosstie displacement of the instrumented crossties when the wheel loads were applied over crosstie 6-17. When symmetric lateral wheel load (gauge-widening load) was applied in the field experimentation, the lateral wheel load was primarily distributed among the three closest rail seats. However, when the single-side lateral wheel load was applied to the test track segment, lateral crosstie displacement was measured on the five closest rail seats (rail seat 4 to 8), which could suggest a different distribution of the lateral wheel load that involves more rail seats. However, due to the potential gaps under rail seat 6 and 8, it is hard to distinguish between the effects of different loading scenarios (symmetric or single-side lateral wheel load) and track anomalies.

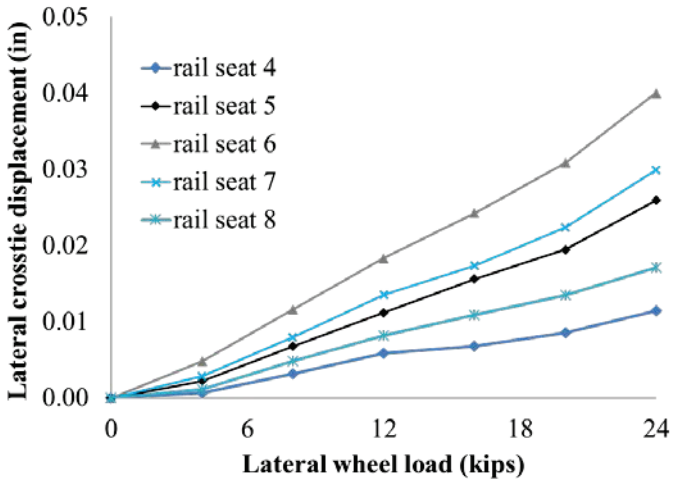

Figure 261. Lateral Crosstie Displacement of the Instrumented Crossties When the Wheel Loads Were Applied on Crosstie 6-17 (Vertical Wheel Load = 40 kips)

In the FE model, the resistance of crib and shoulder ballast to the lateral displacement of the crossties was simulated with connectors that connect the crossties to the ground. The resistance

of ballast beneath the crosstie to the lateral displacement of the crossties was simulated with frictional interactions defined between the crossties and the ballast. To capture the variability of the crosstie lateral responses at different rail seats, the frictional stiffness between different crossties and the ballast were individually calibrated in the FE model. Figure 262 summarizes the numerical versus experimental comparison of the lateral crosstie displacement when the wheel loads were applied over crosstie 6-17. In general, the model output agrees well with the measured crosstie displacements.

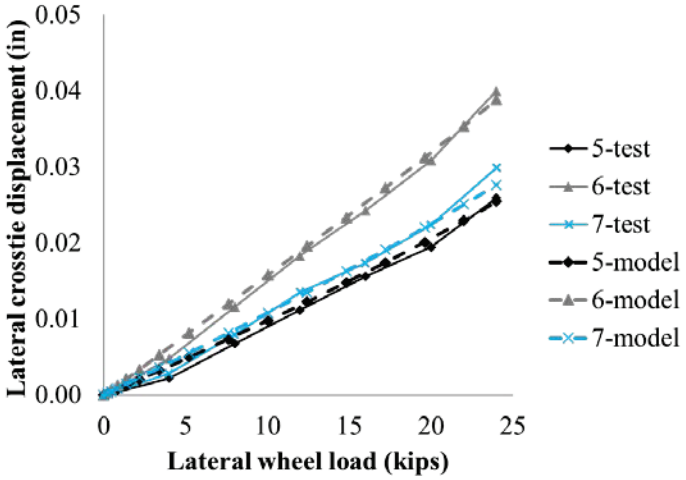

Figure 262. Numerical Versus Experimental Comparison on the Lateral Crosstie Displacement When the Wheel Loads Were Applied over Crosstie 6-17 (Vertical Wheel Load = 40 kips)

8.9 Validation of Multiple-Crosstie Model Based on Full-scale Laboratory Experimentation

To accurately simulate the laboratory experiment setup, the full-scale global and detailed models were calibrated based on some experimental data. To further prove that the FE models are able to capture the distribution of vertical and lateral wheel load among multiple rail seats and within the fastening system, the calibrated FE models were validated with the measurement of vertical rail seat load and shoulder bearing force, and the validation is discussed in the following sections.

8.9.1 Vertical Rail Seat Load

As previously mentioned, strain gauge bridges were attached to the rail to determine the vertical rail seat load. Figure 263 summarizes the comparison between the model output and the laboratory measurement on the vertical rail seat load when the wheel loads were applied on crosstie 6-17. In the laboratory measurement, the vertical rail seat load at rail seat 6 remains zero when the vertical wheel load increased from 0 to 40 kips. In addition, the vertical rail seat load at rail seats 5 and 7 gradually increased to approximately 20 kips at the maximum vertical wheel load, and the vertical rail seat load at rail seat 7 was slightly higher than that at rail seat 5. The difference in vertical rail seat load at the two rail seats agreed with the previous assumption that gaps existed under rail seat 8 while rail seat 4 was well supported. In the FE model output, the vertical rail seat load at rail seat 6 is slightly higher than the laboratory measurement, and

correspondingly, the vertical rail seat load at rail seat 5 is slightly lower than the laboratory measurement. However, the model output is quite close to the laboratory measurement, which proves that the calibrated FE model is able to capture the distribution of vertical wheel load in the laboratory experiment.

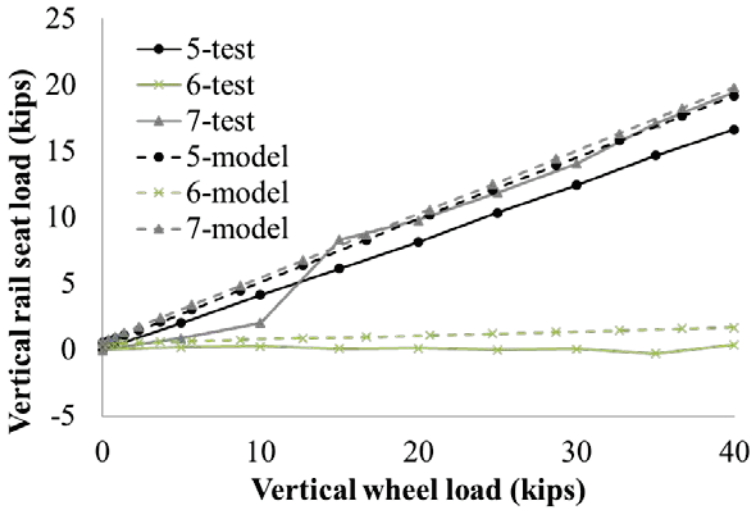

Figure 263. Numerical Versus Experimental Comparison on the Vertical Rail Seat Load When the Wheel Loads Were Applied on Crosstie 6-17 (Lateral Wheel Load = 0 kips)

8.9.2 Shoulder Bearing Force

A portion of the field-side shoulders on the instrumented crossties was removed and LLEDs were installed to measure the shoulder bearing force, as shown in Figure 264a. More details about the design and instrumentation of the LLED are provided in Chapter 3 of Volume 2. Figure 260b shows the shoulder bearing force at the loaded rail seat in different loading scenarios, and the lateral load on the field-side shoulder of the loaded rail seat varied considerably under identical lateral wheel load. Compared to the shoulder bearing force measured in the field experimentation, the measurements in the laboratory experiment were relatively small. This could be due to the part of the lateral load applied to the wheel sets was resisted by the other rail that was not instrumented.

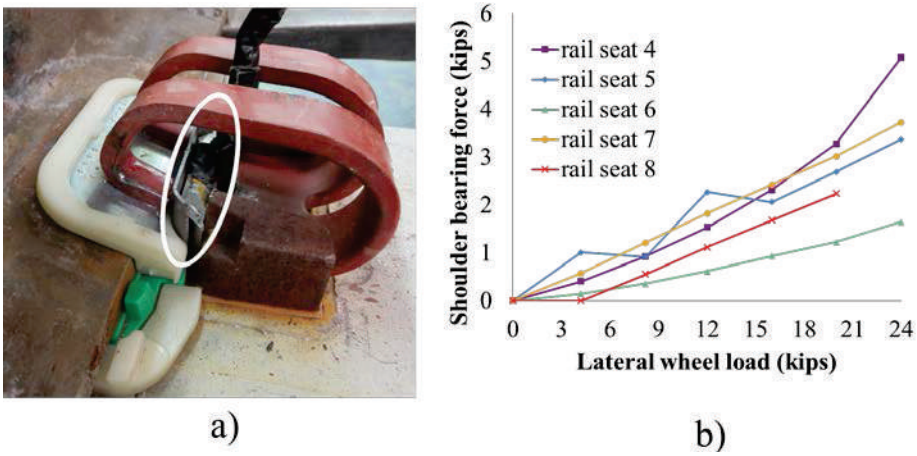

Figure 264. a) Lateral Load Evaluation Device Installed on the Field-side Shoulder and b) the Shoulder Bearing Force at the Loaded Rail Seat in Different Loading Scenarios (Vertical Rail Seat Load = 40 kips)

Figure 265 summarizes the comparison between model output and laboratory measurement on the shoulder bearing force when the wheel loads were applied on crosstie 6-17. While the lateral wheel load was applied on rail seat 6, the largest shoulder bearing force was measured at rail seat 7. The measurement also supports the previous assumption that due to the gaps beneath rail seat 6 and 8, rail seats 6 and 8 had limited lateral stiffness and the lateral wheel load was mainly resisted by rail seat 5 and 7. The calibrated FE model was able to capture the relative magnitude of the shoulder bearing forces at the three rail seats, that the largest shoulder bearing force was observed at rail seat 7 and the smallest shoulder bearing force was observed at rail seat 5. However, shoulder bearing force predicted by the FE models was slightly higher than the laboratory measurement, and the difference could be related to some gaps between the insulators and field-side shoulders on the instrumented crossties. In general, the calibrated FE models are able to capture the distribution of lateral wheel load among multiple rail seats and within the fastening system.

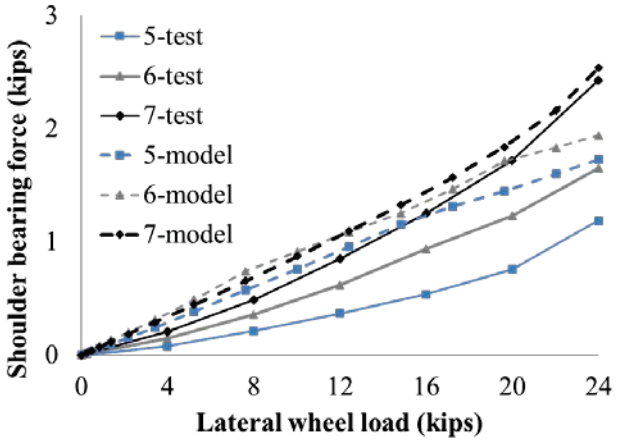

Figure 265. Numerical Versus Experimental Comparison on the Shoulder Bearing Force When the Wheel Loads Were Applied on Crosstie 6-17 (Vertical Wheel Load = 40 kips)

8.10 Parametric Studies of Critical Design Parameters

To investigate the effect of and interaction between a subset of critical design parameters on the performance of the concrete crosstie and fastening system, the field-validated FE model was used to execute a series of parametric studies. The design of parametric study is summarized in Table 48.

Three loading scenarios were considered to simulate the loading conditions on curved track with varying degrees of curvature. Considering a 315-kip gross rail load (GRL) rail car with a vertical wheel load of 40 kips, a variable lateral wheel load was defined for each of the three loading scenarios. The COF at the rail-pad interface and plate-concrete interface were combined and is discussed in detail in the following section. The ranges of input parameters were determined based on reference about tribology and polymer material property (Yamaguchi 1990, Hepburn 1982, Harper 1996) and conversations with experts in track component engineering. The same input and output parameters were studied under different loading scenarios, and the parameters that were not included in list of inputs were held constant at the same level that was observed in our field experimentation. Examples of constant parameters were track substructure stiffness and crosstie pre-stressing strand distribution. The definitions of output are shown in Figure 266. To evaluate the interactions of the design parameters (i.e. input) that were potentially significant, the parametric study was divided into two phases for each loading scenario. In the first phase, a full factorial design of cases was generated at reasonable maximum and minimum values of the design space. Based on the FE model output, an analysis of variance (ANOVA) was used to determine the interaction of design parameters that are statistically significant. In the second phase of this work, more cases were generated to further investigate significant input interactions.

Table 48. Design of the Parametric Study of Critical Design Parameters

		Range	Base value
Input	Crosstie spacing (in)	20~30	24
	Rail-pad and plate-concrete COF	0.12~1.0	0.3
	Pad elastic modulus (psi)	4,000~400,000	7,500
	Insulator elastic modulus (psi)	400,000~2,000,000	440,000
Output	Rail head lateral displacement		
	Shoulder bearing force at the loaded rail seat		
	Pad friction force at the loaded rail seat		
	Vertical rail seat load		
Loading scenarios	Loading scenario 1: V=40 kips, L=10 kips		
	Loading scenario 2: V=40 kips, L=20 kips		
	Loading scenario 3: V=40 kips, L=30 kips		

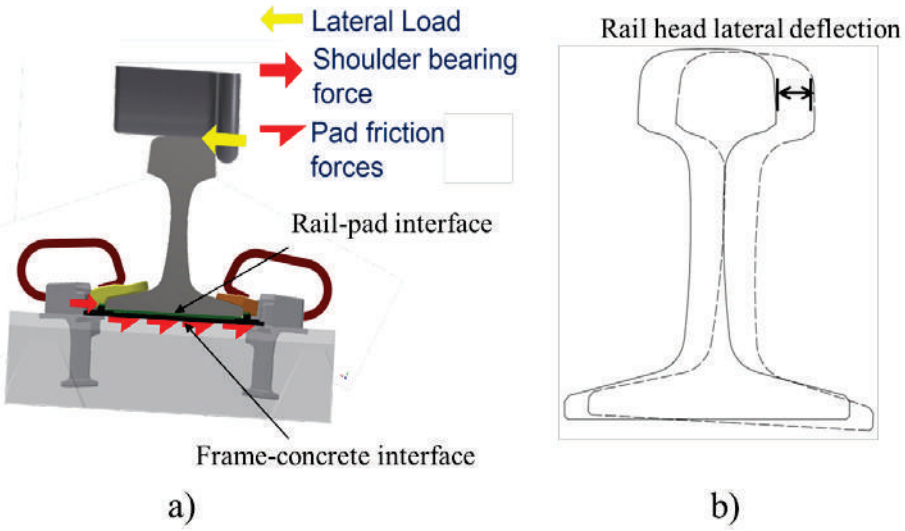

Figure 266. Illustration of FE Model Output in the Parametric Study: a) Shoulder Bearing Force and Rail Pad Friction Force at the Loaded Rail Seat and b) Rail Head Lateral Deflection

8.11 Preliminary Parametric Study of the Frictional Interaction and Behavior of the Fastening System and Its Components

Before the comprehensive parametric study was performed, the field-validated FE model was used in a preliminary parametric study of the effect of frictional interactions in the fastening system on the lateral load path. The COF at the rail-pad interface and the plate-concrete interface were used as input variables, and select outputs related to the fastening system performance under lateral wheel loads were extracted, as shown in Table 49. A vertical wheel load of 40 kips and a lateral wheel load of 20 kips was used for all cases.

Table 49. Design of Preliminary Parametric Study on Frictional Interaction

		Range	Base value
Input	Pad-rail COF	0.12～1.00	0.3
	Frame-concrete COF	0.15～1.00	0.3
Output	Rail head lateral displacement Shoulder bearing force at the loaded rail seat Pad friction force at the loaded rail seat		
Loading scenario	V=40 kips, L=20 kips		

Two sets of cases were generated to investigate the effect of rail-pad COF and frame-concrete COF on the performance of the fastening system under lateral wheel loads. In the first set, one COF varied within the defined range, and the other COF remained at the default value (single-variable cases). In the second set, both COF at the two interfaces were varied to evaluate their interaction (two-variable cases). The result of single-variable cases is summarized in Figure 267.

In each figure, the two lines represented the cases in which rail-pad or frame-concrete COF was the variable, and the other COF remained constant. In Figure 267, it can be observed that within a range, the rail pad frictional force increased with higher COF, and both the shoulder bearing force and rail-head lateral deflection decreased with higher COF. At higher COF, the model output was not as sensitive to the change in COF. In all cases, the threshold COF value for the sensitivity of system response was 0.3, which was the default value of the COF at the two interfaces. In addition, identical response of the shoulder bearing force, rail pad frictional force, and rail head lateral deflection was observed when the varying COF was at the same magnitude.

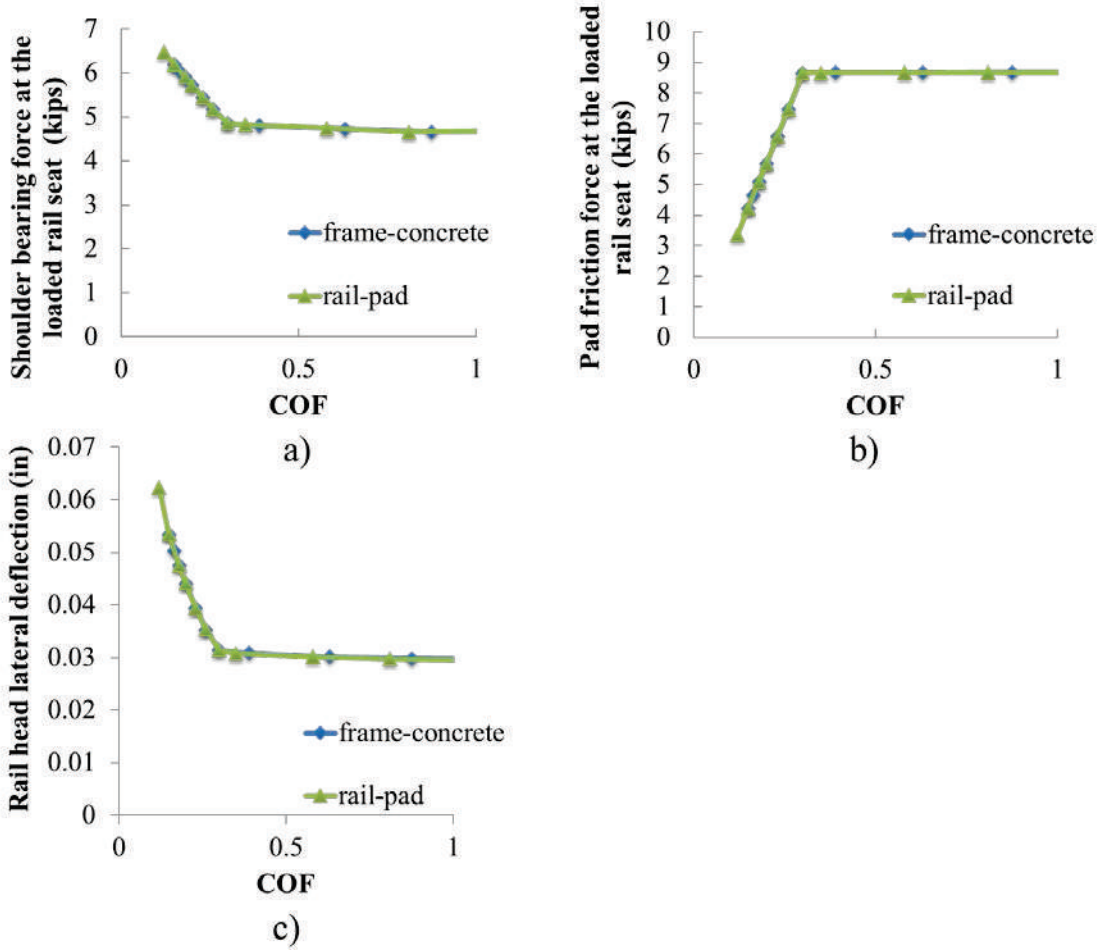

Figure 267. Results of Single-variable Parametric Analysis of a) Shoulder Bearing Force, b) Rail Pad Friction Force and c) Rail Head Lateral Deflection

Under lateral wheel loads, the relative sliding between rail base and concrete could be divided into three parts: 1) the relative sliding between rail and the rail pad, 2) between the abrasion plate and concrete, and 3) the shear deformation of the entire rail pad assembly. As the rail pad was embedded into the abrasion plate, the relative sliding between the rail pad and abrasion plate was assumed to be insignificant. The COF at the two interfaces served as the threshold for the linear friction-sliding relationship. Under higher lateral load, the frictional force remained at the maximum magnitude while the relative sliding continued to increase. As a result of this behavior, it was reasonable to approximate the frictional stiffness at the bottom of rail base as springs in series, and the threshold of linear behavior was determined (i.e. governed) by the

lower COF of the two interfaces. To validate this assumption, the two-variable cases were generated and the result was summarized in Figure 268.

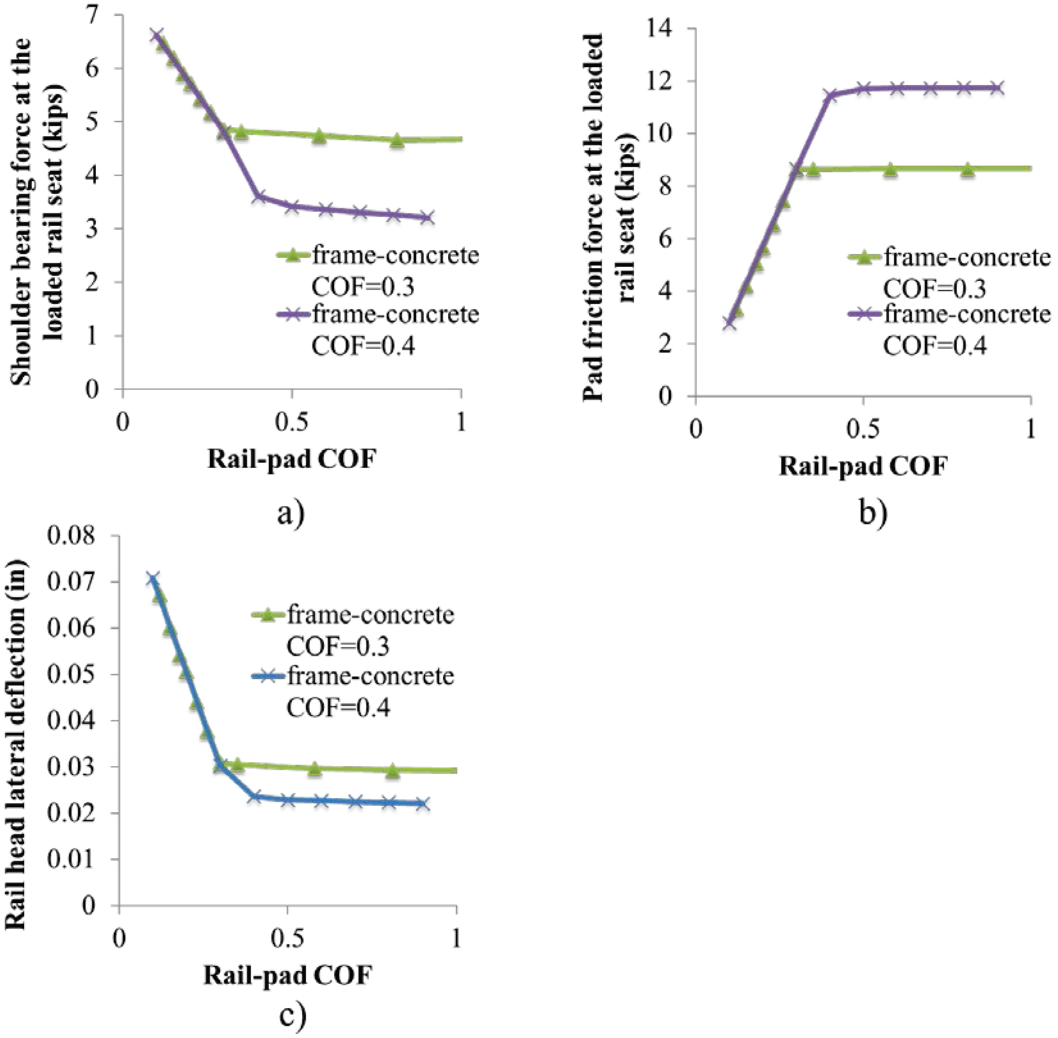

Figure 268. Results from Two-variable Parametric Studies Focusing on a) Shoulder Bearing Force, b) Rail Pad Friction Force, and c) the Rail Head Lateral Deflection

The two lines in each figure included in Figure 268 indicate the cases with different frame-concrete COF. Each line represents a case of varying rail-pad COF within the defined range. In Figure 268, the relationship between different responses and varying COF was similar to the behavior shown in Figure 267. In addition, the slopes of the two lines changed at different COF magnitude, which were 0.3 and 0.4, respectively. The location of different thresholds agreed with the frame-concrete COF of the cases, which support the assumption stated earlier. When the rail-pad COF was lower than the frame-concrete COF, it governed the system response, and identical response was observed between cases of different frame-concrete COF. However, when the rail-pad COF exceeded the frame-concrete COF, the frame-concrete COF governed the system response, which was not sensitive to the change of rail-pad COF. Considering this effect, the rail-rail pad COF and frame-concrete COF were combined into one variable, and identical COF were defined at the two interfaces for further parametric study.

8.12 Determination of Critical Input Interaction

To determine the input interactions that were statistically significant, the field-validated FE model was used to run model iterations that were generated using a full factorial design. In total, four input variables were included in the parametric study under each loading scenario, and 48 cases ($2^4 * 3 = 48$) were generated. Two levels were considered for each input variable, representing its minimum and maximum value.

After the cases were generated, the statistical software R (Venables et al. 2002) was used for ANOVA. A statistical model was built for each output, and through an ANOVA, p-values (Walpole et al. 1993) were calculated for each input variable and its interactions. Lower p-values indicate that the corresponding input or input interaction is more statistically significant for a certain output, and the threshold p-value to study the input interaction was determined as 0.05 (Walpole et al. 1993). In addition, the statistical models were built considering the hierarchy of variables (Faraway 2002). The input variables were defined as factorial, and they were first introduced in the statistical model without their interaction terms. Based on the result of ANOVA, the input variables with a p-value larger than 0.05 were deemed insignificant and were removed from the model. After this step, only the second-order interactions of existing input variables were added to the model and tested for significance. After the insignificant terms were removed from the statistical model, higher-order interaction terms were added until all the combinations were exhausted.

The results of ANOVA for the three loading scenarios are summarized in Table 50. The p-values of significant interactions are marked in bold. Some p-values were left blank as the corresponding input or lower-order input interaction was not significant for the given output. It can be observed that all the second-order interactions of input variables were significant for at least one of the outputs, and none of the third-order interactions were significant to any of the output. The elastic modulus of the insulator and its interaction with other input were not included as they were not statistically significant for any of the four outputs. Considering this result, more cases were generated to investigate all the second-order interactions of the three input variables.

Table 50. ANOVA Results for Three Loading Scenarios

Loading Scenario 1 Vertical load = 40 kips, Lateral load = 10 kips				
Interaction	P-value			
	Rail head lateral deflection	Shoulder bearing force	Rail pad frictional force	Vertical rail seat load
Spacing:COF	2.5E-01	1.1E-01	**3.7E-02**	**4.0E-03**
Spacing:Pad modulus	**4.9E-04**	**4.6E-03**	**7.1E-04**	1.6E-01
COF:Pad modulus	**4.8E-06**	**6.7E-07**	**3.7E-10**	**2.0E-03**
Spacing:COF:Pad modulus	N/A	N/A	N/A	N/A
Loading Scenario 2 Vertical load = 40 kips, Lateral load = 20 kips				
Interaction	P-value			
	Rail head lateral deflection	Shoulder bearing force	Rail pad frictional force	Vertical rail seat load
Spacing:COF	**1.3E-04**	N/A	N/A	**7.0E-05**
Spacing:Pad modulus	**1.6E-03**	N/A	N/A	4.7E-01
COF:Pad modulus	**5.1E-06**	**4.2E-06**	**6.7E-06**	**3.5E-09**
Spacing:COF:Pad modulus	7.7E-02	N/A	N/A	N/A
Loading Scenario 3 Vertical load = 40 kips, Lateral load = 30 kips				
Interaction	P-value			
	Rail head lateral deflection	Shoulder bearing force	Rail pad frictional force	Vertical rail seat load
Spacing:COF	**4.4E-08**	N/A	N/A	**3.6E-07**
Spacing:Pad modulus	**1.7E-04**	N/A	N/A	7.9E-01
COF:Pad modulus	**4.2E-06**	**2.2E-10**	**4.1E-06**	**1.2E-12**
Spacing:COF:Pad modulus	1.9E-01	N/A	N/A	N/A

Spacing: Concrete crosstie spacing
COF: The coefficient of friction at the rail-pad interface and the frame-concrete interface
Pad modulus: The elastic modulus of rail pad

8.12 Results from Loading Scenario 1: V = 40 kips, L= 10 kips, L/V = 0.25

Under loading scenario 1, nine input interactions were determined to be significant, and 64 cases (i.e. FE model runs) were generated to investigate the interaction of input variables. The results are summarized by relevant output variables in the following sections

8.12.1 Output: Rail Head Lateral Deflection

The rail head lateral deflection varied with respect to the interactions of rail pad elastic modulus and COF, and rail pad elastic modulus and crosstie spacing (Figure 269). Rail head lateral deflection generally decreased with higher rail pad elastic modulus, higher COF, and closer crosstie spacing. Compared to COF and rail pad elastic modulus, crosstie spacing had relatively little effect on the variation of rail head lateral deflection. The COF defined in the FE model affected the threshold of the linear friction-sliding relationship at the rail base, and minor differences in rail head deflection were observed between cases of high COF as the ratio between the rail pad friction force and the normal force at the loaded rail seat was smaller than the defined COF. In addition, the rail head lateral deflection gradually converged to a set number at high values rail pad elastic modulus. More significant interaction was observed between rail pad elastic modulus and COF than between rail pad elastic modulus and crosstie spacing. This agreed with the fact that the COF-pad modulus interaction had a smaller p-value than the pad modulus-spacing interaction.

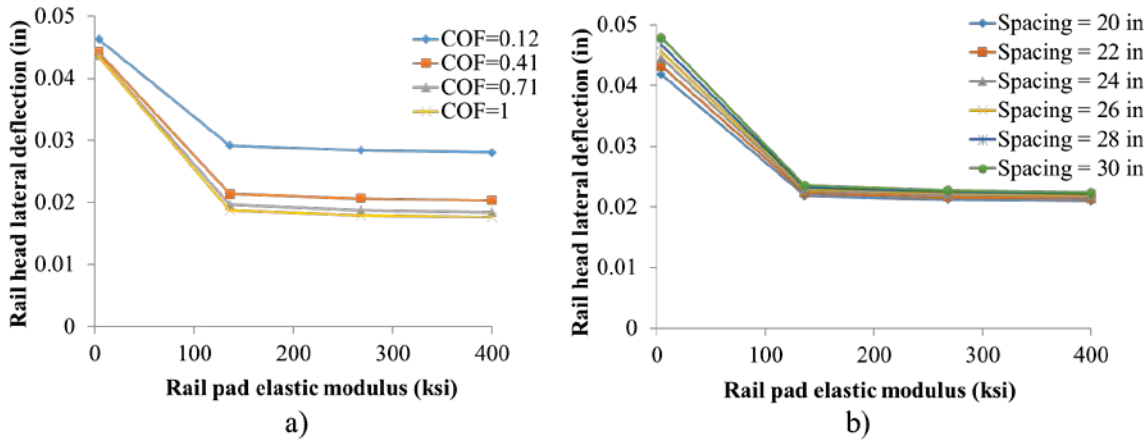

Figure 269. Variation of Rail Head Lateral Deflection with Respect to the Interaction of a) Rail Pad Elastic Modulus and COF, and b) Rail Pad Elastic Modulus and Crosstie Spacing (Loading Scenario 1: V=40 kips, L=10 kips)

8.12.2 Output: Shoulder Bearing Force at the Loaded Rail Seat

The variation of shoulder bearing force at the rail seat under the point of load application with respect to the interaction of rail pad elastic modulus and COF, and rail pad elastic modulus and crosstie spacing is shown in Figure 270. The shoulder bearing force at the loaded rail seat gradually decreased with higher rail pad elastic moduli, higher COF, and closer crosstie spacing. The crosstie spacing had relatively small impact on the variation of the shoulder bearing force, when compared to the other two input variables (rail pad elastic modulus and COF). In other words, the shoulder bearing force at the loaded rail seat is affected by the design of the fastening system (COF and rail pad elastic modulus) more than the global system configuration (crosstie spacing). In addition, the shoulder bearing force gradually converged to a set value at high rail pad elastic moduli and high COF. At the same time, more significant interaction was observed between the rail pad elastic modulus and the COF than between the rail pad elastic modulus and crosstie spacing. Both the rail pad elastic modulus and the COF determined the lateral frictional

stiffness at the bottom of rail base, and crosstie spacing had minimal impact on the lateral load path through the fastening system.

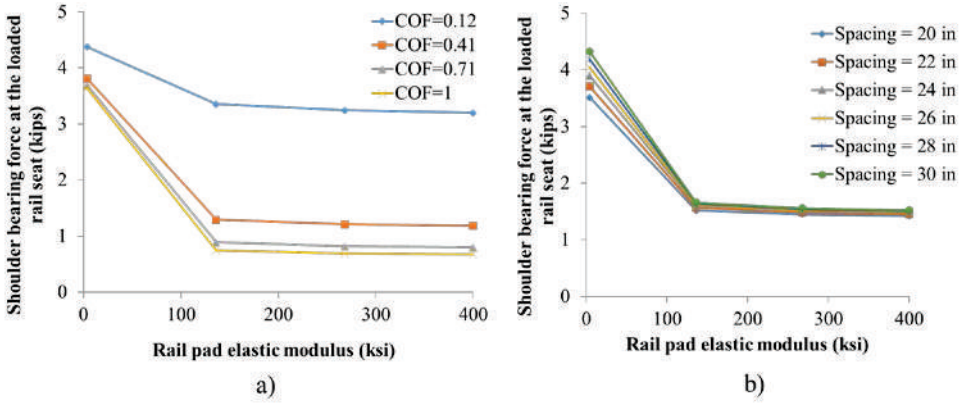

Figure 270. Variation of Shoulder Bearing Force at the Loaded Rail Seat with Respect to the Interaction of a) Rail Pad Elastic Modulus and COF, and b) Rail Pad Elastic Modulus and Crosstie Spacing (Loading Scenario 1: V=40 kips, L=10 kips)

8.12.3 Output: Rail Pad Friction Force at the Loaded Rail Seat

The variation of rail pad friction force at the rail seat under the point of load application with respect to the interaction of rail pad elastic modulus and COF, rail pad elastic modulus and crosstie spacing, and COF and crosstie spacing is shown in Figure 271. The rail pad friction force gradually decreased with lower rail pad elastic modulus, lower COF, and closer crosstie spacing. ANOVA indicated that the rail pad friction force at the loaded rail seat was significantly affected by all three second-order input interactions. However, it was also observed that the relationship between crosstie spacing and rail pad friction force was linear, and crosstie spacing had minor interaction with the other two input variables (rail pad elastic modulus and COF). The rail pad elastic modulus and COF had larger impact on the rail pad friction force at low load magnitudes, and the impact gradually reduced at higher load magnitudes.

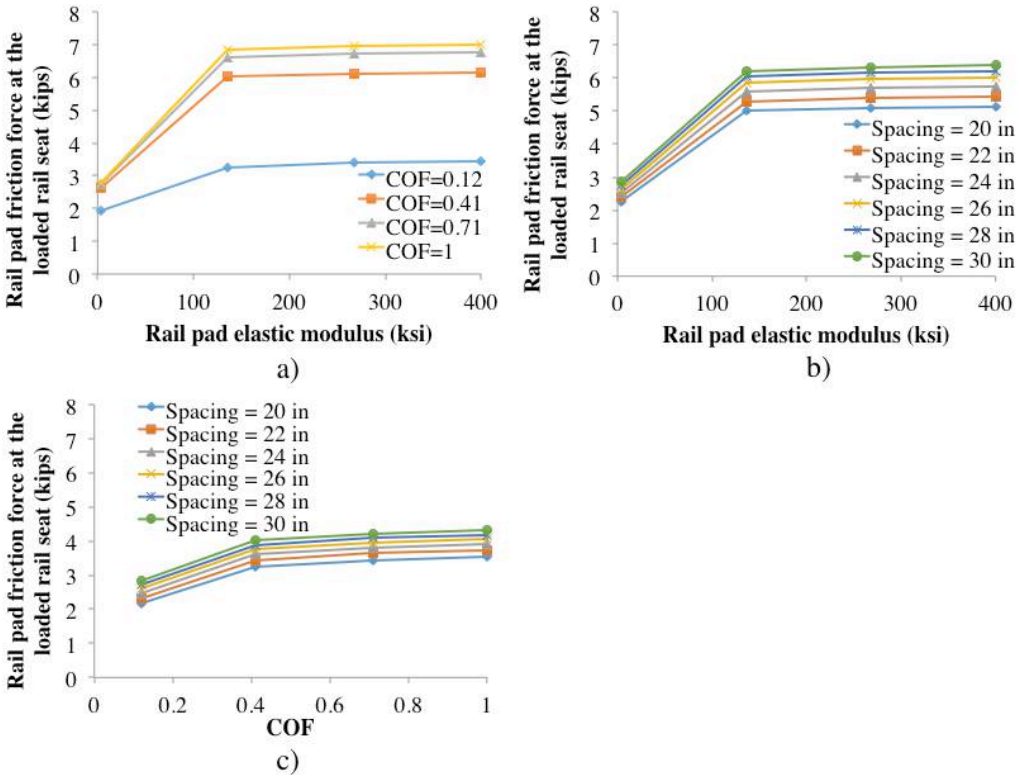

Figure 271. Variation of Rail Pad Friction Force at the Loaded Rail Seat with Respect to the Interaction of a) Rail Pad Elastic Modulus and COF, b) Rail Pad Elastic Modulus and Crosstie Spacing, and c) COF and Crosstie Spacing (Loading Scenario 1: V=40 kips, L=10 kips)

8.12.4 Output: Vertical Rail Seat Load

The variation of vertical rail seat load at the rail seat under the point of load application with respect to the interaction of rail pad elastic modulus and COF, and COF and crosstie spacing, is shown in Figure 272. The vertical rail seat load gradually decreased with smaller rail pad elastic modulus, lower COF, and closer crosstie spacing. It was observed that the relationship between crosstie spacing and vertical rail seat load was linear, and the crosstie spacing had a greater impact on the vertical rail seat load than the other two input variables. The rail pad elastic modulus affected the vertical rail seat load as it determined the vertical compression of the rail pad. The COF also affected the vertical rail seat load as the friction forces at the rail-pad interface and plate-concrete interface restrained the lateral expansion of the pad assembly and altered the effective compressive stiffness of the rail pad assembly.

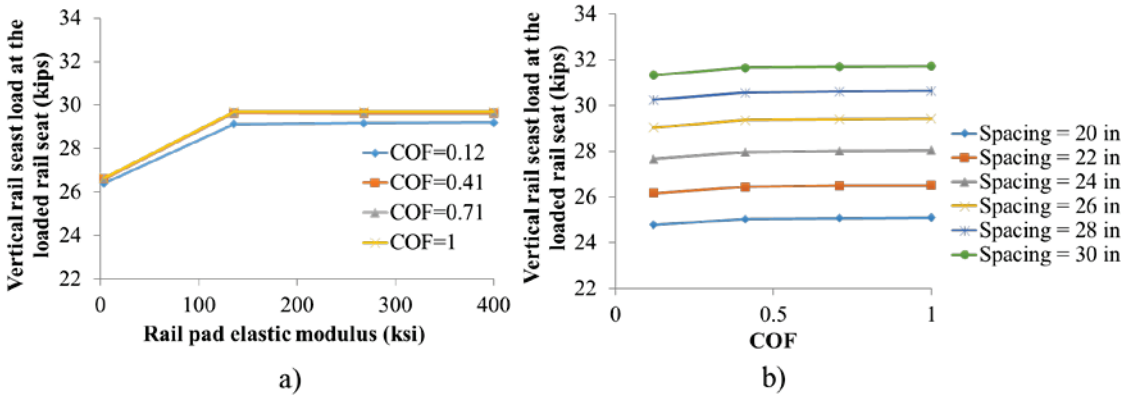

Figure 272. Variation of Vertical Rail Seat Load at the Loaded Rail Seat with Respect to the Interaction of a) Rail Pad Elastic Modulus and COF, and b) COF and Crosstie Spacing (Loading Scenario 1: V=40 kips, L=10 kips)

8.13 Results from Loading Scenario 2: V = 40 kips, L= 20 kips, L/V=0.5

Under loading scenario 2, 7 interactions were determined as significant, and 64 cases were generated investigate the interactions using the field-validated FE model. The results are summarized by relevant outputs in the following sections.

8.13.1 Output: Rail Head Lateral Deflection

The variation of rail head lateral deflection with respect the interaction of rail pad elastic modulus and COF, rail pad elastic modulus and crosstie spacing, and COF and crosstie spacing, is shown in Figure 273. For loading scenario 2, the interaction of various inputs on rail head lateral deflection was similar to what was noted in loading scenario 1. The rail head lateral deflection decreased with higher rail pad elastic modulus, higher COF, and closer crosstie spacing. The rail head lateral deflection gradually converged to a set value at high rail pad elastic moduli and high COF. The major interaction of input variables was observed between the rail pad elastic modulus and COF, and minor interaction was observed between the crosstie spacing and the other two input variables.

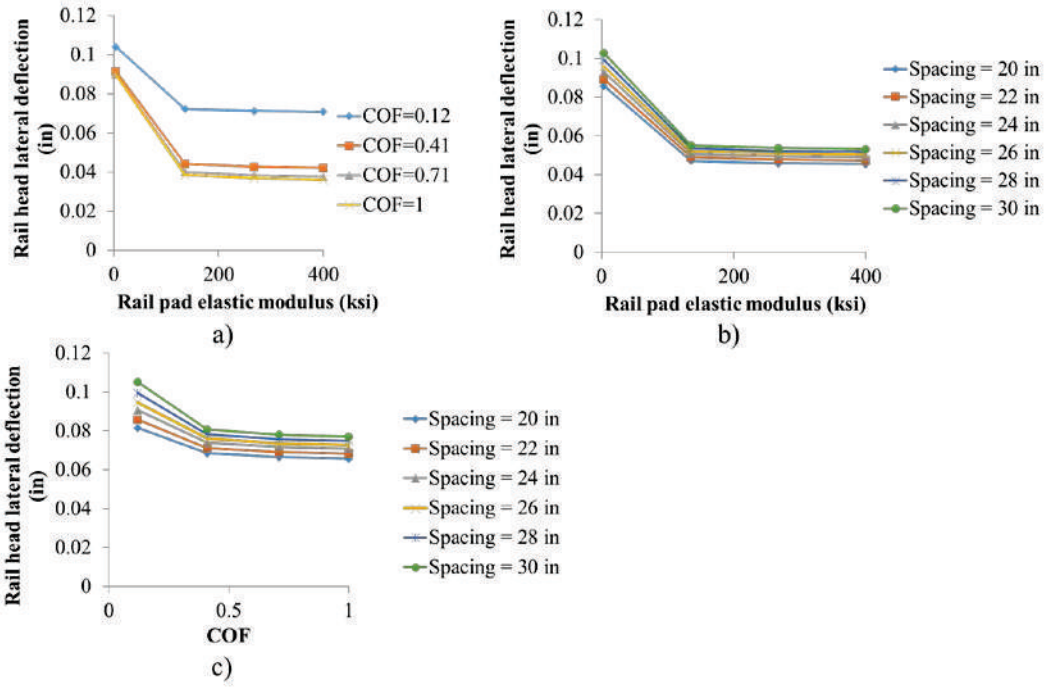

Figure 273. Variation of Rail Head Lateral Deflection with Respect to the Interaction of a) Rail Pad Elastic Modulus and COF, b) Rail Pad Elastic Modulus and Crosstie Spacing, and c) COF and Crosstie Spacing (Loading Scenario 2, V=40 kips, L=20 kips)

8.13.2 Output: Shoulder Bearing Force at the Loaded Rail Seat

Unlike loading scenario 1, the only significant interaction of input related to shoulder bearing force at the loaded rail seat in loading scenario 2 was between the rail pad elastic modulus and COF (Figure 274). The shoulder bearing force at the loaded rail seat decreased with higher rail pad elastic moduli and higher COF. In addition, the rail pad elastic modulus had larger impact on the shoulder bearing force at higher COF values. At a lower COF, limited friction force developed at the rail-pad interface and the plate-concrete interface, and as a result little difference in rail pad shearing existed between cases of different rail pad elastic moduli. Therefore, the shoulder bearing force was not significantly affected. At a higher COF, linear friction-sliding relationship existed at the surfaces of the rail pad assembly, and the shearing of rail pad varied through a larger range of values, which affected the shoulder bearing force.

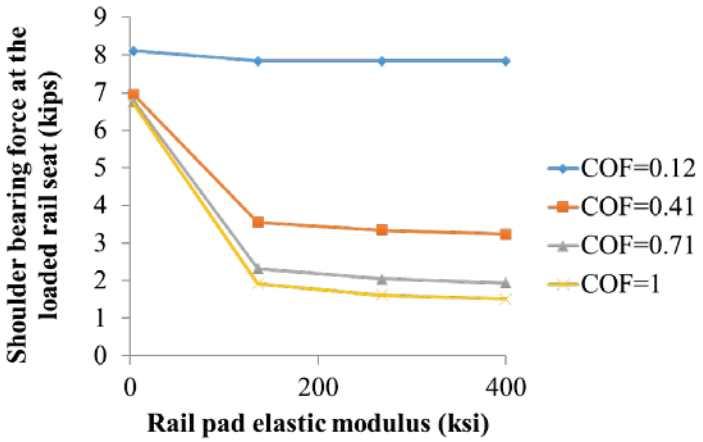

Figure 274. Variation of Shoulder Bearing Force at the Loaded Rail Seat with Respect to the Interaction of Rail Pad Elastic Modulus and COF (Loading Scenario 2, V=40 kips, L=20 kips)

8.13.3 Output: Rail Pad Friction Force at the Loaded Rail Seat

The variation of rail pad friction force with respect to the interaction of rail pad elastic modulus and COF is shown in Figure 275. The result of ANOVA indicated that in loading scenario 2 the only significant input interaction about rail pad friction force was between the rail pad elastic modulus and COF. The result of input interaction about rail pad friction force was closely aligned with those relating to shoulder bearing force. The rail pad friction force at the loaded rail seat decreased with lower rail pad elastic modulus and COF. In addition, the rail pad elastic modulus had larger impact on the rail pad friction force at high COF, and the impact decreased at lower COF.

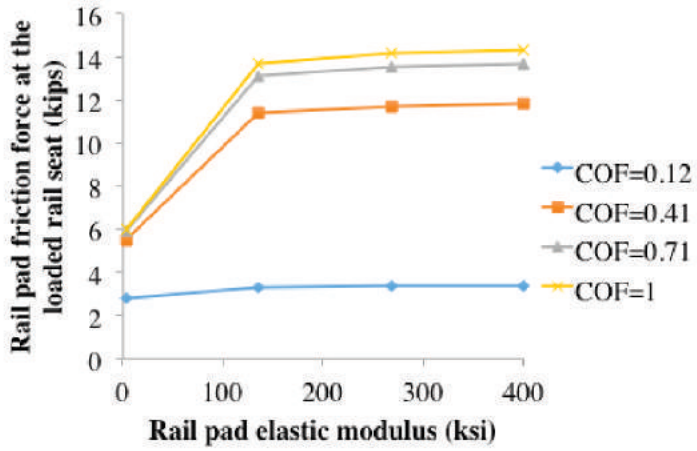

Figure 275. Variation of Rail Pad Friction Force at the Loaded Rail Seat with Respect to the Interaction of Rail Pad Elastic Modulus and COF (Loading Scenario 2, V=40 kips, L=20 kips)

8.13.4 Output: Vertical Rail Seat Load

The variation of vertical rail seat load with respect to the interaction of rail pad elastic modulus and COF, and COF and crosstie spacing is shown in Figure 276. The vertical rail seat load decreased with lower rail pad elastic modulus, lower COF, and closer crosstie spacing. In addition, the crosstie spacing had a larger impact on the vertical rail seat load than the other two input variables. Although the two interactions in Figure 276 were determined as statistically significant, they were not as significant as other interactions that were studied. The vertical rail seat load converged to a set value at high rail pad elastic modulus and high COF. In addition, it was observed that the relationship between crosstie spacing and the vertical rail seat load was linear, and minor interaction was noted between it and other input variables.

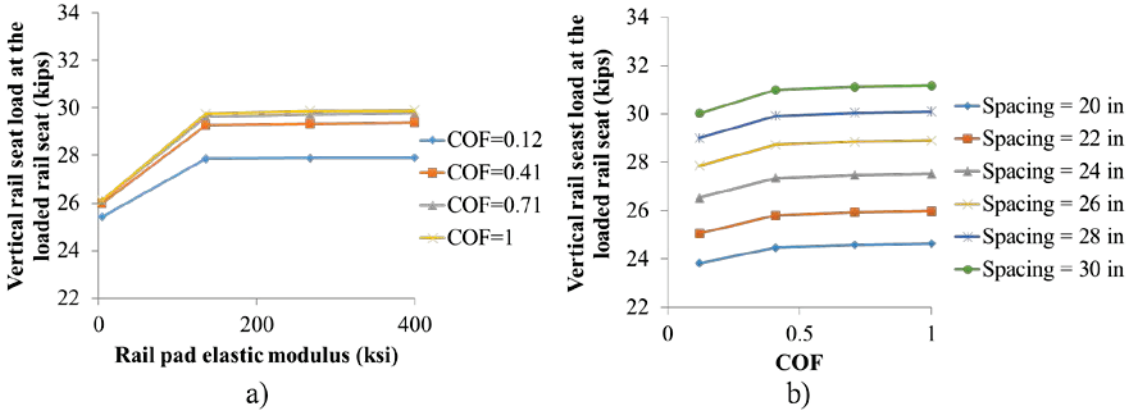

Figure 276. Variation of Vertical Rail Seat Load at the Loaded Rail Seat with Respect to the Interaction of a) Rail Pad Elastic Modulus and COF, and b) COF and Crosstie Spacing (Loading Scenario 2, V=40 kips, L=20 kips)

8.14 Results from Loading Scenario 3: V = 40 kips, L= 30 kips, L/V=0.75

Under loading scenario 3, seven interactions were determined to be statistically significant; the same as in loading scenario 2. Sixty-four cases were generated based on the field-validated FE model to investigate the interaction of the input, and the results were summarized based on the relevant output variables in the following sections.

8.14.1 Output: Rail Head Lateral Deflection

The variation of rail head lateral deflection with respect to the interaction of rail pad elastic modulus and COF, rail pad elastic modulus and crosstie spacing, and COF and crosstie spacing, is shown in Figure 277. The rail head lateral deflection decreased with higher rail pad elastic modulus, higher COF, and closer crosstie spacing. The result of rail head lateral deflection in loading scenario 3 was quite similar to loading scenario 2 except for a difference in magnitude. The rail head lateral deflection converged to a set value at high rail pad elastic moduli and high COF values. In addition, the crosstie spacing had minor interaction with rail pad elastic modulus and the COF, and the relationship between crosstie spacing and the rail head lateral deflection was linear.

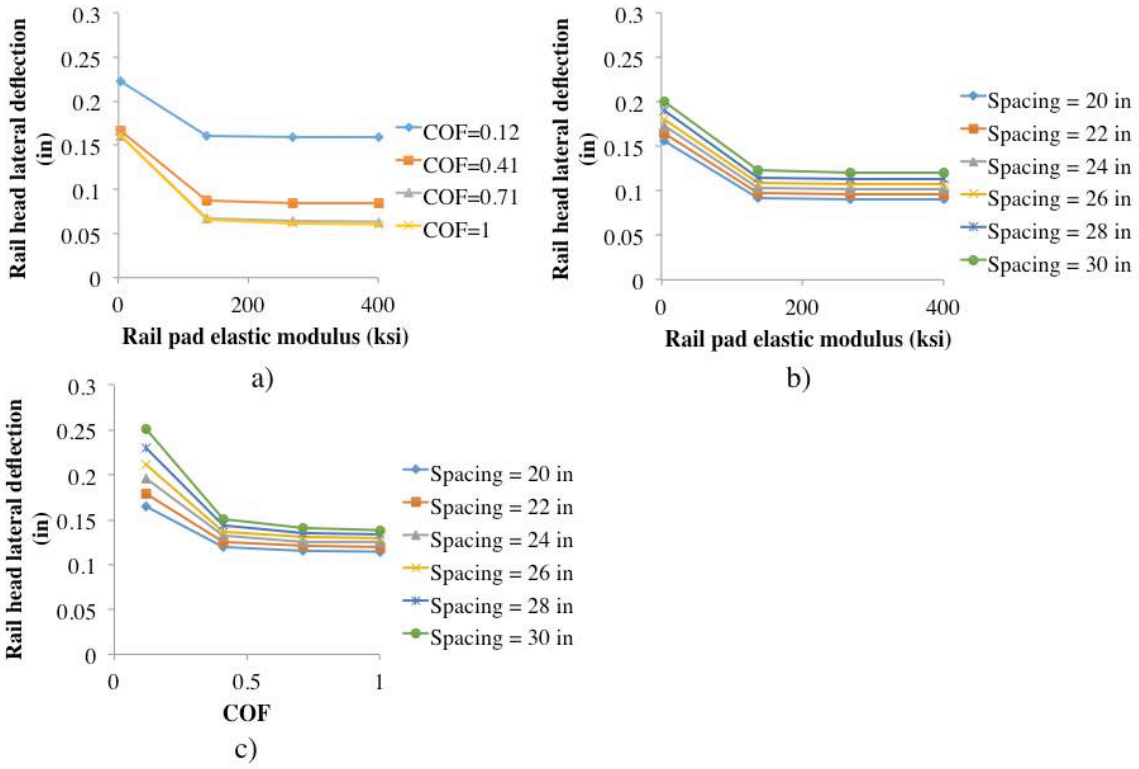

Figure 277. Variation of Rail Head Lateral Deflection with Respect to the Interaction of a) Rail Pad Elastic Modulus and COF, b) Rail Pad Elastic Modulus and Crosstie Spacing, and c) COF and Crosstie Spacing (Loading Scenario 3, V=40 kips, L=30 kips)

8.14.2 Output: Shoulder Bearing Force at the Loaded Rail Seat

The variation of shoulder bearing force with respect to the interaction of rail pad elastic modulus and COF is shown in Figure 278. The shoulder bearing force at the loaded rail seat decreased with higher rail pad elastic moduli and higher COF values. In addition, the shoulder bearing force gradually converged to a set value at high rail pad elastic moduli and high COF values. It can be observed that the rail pad elastic modulus had a larger impact on the shoulder bearing force at higher COF values.

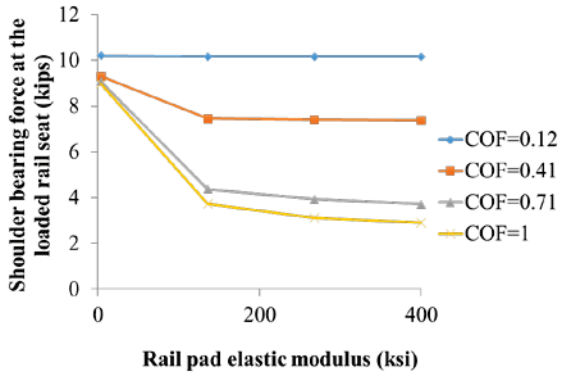

Figure 278. Variation of Shoulder Bearing Force at the Loaded Rail Seat with Respect to the Interaction of Rail Pad Plastic Modulus and COF (Loading Scenario 3, V=40 kips, L=30 kips)

8.14.3 Output: Rail Pad Friction Force at the Loaded Rail Seat

The variation of rail pad friction force with respect to the interaction of rail pad elastic modulus and COF is shown in Figure 279. The rail pad friction force decreased with lower rail pad elastic moduli and lower COF values. In addition, the rail pad friction force converged to a set value at high rail pad elastic moduli and high COF values. Similar to the result regarding shoulder bearing force in loading scenario 3, the rail pad elastic modulus had larger impact on the rail pad friction force at higher COF.

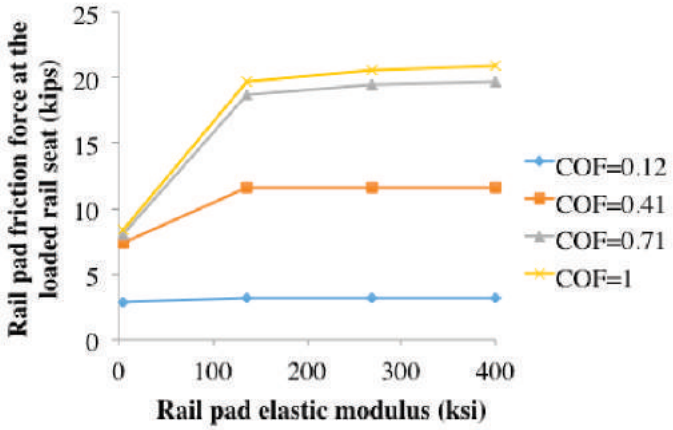

Figure 279. Variation of Rail Pad Friction Force at the Loaded Rail Seat with Respect to the Interaction of Rail Pad Elastic Modulus and COF (Loading Scenario 3, V=40 kips, L=30 kips)

8.14.4 Output: Vertical Rail Seat Load

The variation of vertical rail seat load with respect to the interaction of rail pad elastic modulus and COF, and COF and crosstie spacing, is shown in Figure 280. The vertical rail seat load decreased with lower rail pad elastic modulus, lower COF, and closer crosstie spacing. In addition, the vertical rail seat load converged to a set value at high rail pad elastic moduli and high COF values. Similar to other loading scenarios, the crosstie spacing had a larger impact on

the vertical rail seat load than the rail pad elastic moduli and COF values, but it had limited interaction with the other two input variables.

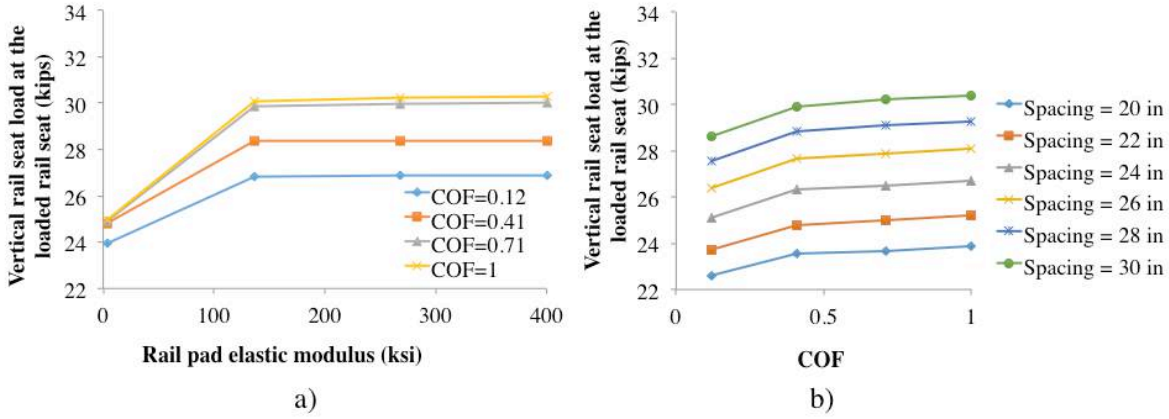

Figure 280. Variation of Vertical Rail Seat Load at the Loaded Rail Seat with Respect to the Interaction of a) Rail Pad Elastic Modulus and COF, and b) COF and Crosstie Spacing (Loading Scenario 3, V=40 kips, L=30 kips)

8.15 Summary

This chapter presented the detailed procedure for model validation at multiple levels (i.e. materials, component, and system) as well as results from parametric studies based on the field-validated FE model. Based on the results presented in this chapter, the following conclusions can be drawn:

- The detailed FE model was validated at multiple levels with manufacturer's data and experiment in laboratory and in the field. The FE model was proven successful in capturing critical mechanisms including the distribution of wheel loads and the flexure of concrete crosstie.
- The frictional behavior (frictional force and relative sliding) at the bottom of the rail seat is primarily governed by the interface (i.e. rail-pad interface and plate-concrete interface) with the lowest value of COF.
- The elastic modulus of the fastening system insulator has little effect on the lateral load path through the fastening system.
- Compared to the COF at the rail-pad and plate-concrete interfaces, and the elastic modulus of rail pad, crosstie spacing has a very minimal impact on the performance of the fastening system under lateral wheel load.
- The COF at the rail-pad and the plate-concrete interfaces, and the elastic modulus of the rail pad significantly affect the performance of the fastening system under lateral wheel load.
- Crosstie spacing significantly affects the distribution of vertical wheel load among multiple rail seats, and the relationship between crosstie spacing and the vertical rail seat load under the point of load application is approximately linear.

These conclusions are based on the cases generated for this parametric study, and are only valid within the range of input parameters considered in the parametric study. However, as the range of input parameters in this study covers what is typically used for track design in North America, the conclusions provide useful insights regarding the future design and optimization of the concrete crosstie and fastening system.

Chapter 9: Analytical Tool for Track Component Response Measurement (I-TRACK)

9.1 Motivation to Develop a Track Component Response Calculation Tool

The quality and state-of-repair of the track infrastructure and its components determines the permissible wheel loads, speeds, safety, and reliability of railroad operations (Hay 1982). With the development of high and higher-speed rail corridors and increasing axle loads in North America, there is increased demand on the railroad track components. This is especially true with concrete crosstie and fastening systems, which tend to be located in some of the most demanding operating environments. Despite the fact that the mechanics of the railroad track structure has been object of extensive investigation for many years (Chen et al. 2012, Shin et al. 2013), the historically dominant design approach adopted by track component manufacturers has been largely empirical.

As part of this study, researchers from UIUC have undertaken a major effort to develop a detailed 3D FE model of the concrete crosstie and fastening system (Figure 281). The model, largely described in Volume 2, Chapter 5 of this report, has been validated with both laboratory and field data, and proved to be a valuable tool for theoretical comparison between realistic loading cases and experimental testing. Additionally, the FE model facilities conducting parametric studies varying component material and geometric dimensions can assist in the development of recommended mechanistic design criteria for the concrete crosstie and fastening system (Chen 2012, Chen 2013, Shin 2013).

The FE model is a powerful tool capable of accurately representing the loading environments, support conditions, component interactions, load path, and system behavior. Nevertheless, there are accessibility and computational limitations that make its use impractical for the general user. The intensive computational effort needed to conduct each iteration of the model, combined with the high level of expertise demanded from the user when programming experimental runs, motivated UIUC researchers to develop a track component response calculation tool (I-TRACK).

I-TRACK is a software based on statistical analyses of data from the FE model, where the mechanical behavior of track components is modeled using a neural network that is capable of predicting mechanical outputs with respect to certain user-defined inputs (e.g. wheel loads, components material properties, etc.). In other words, the FE model is used to generate a broad set of outputs that are correlated with different inputs, allowing the development of a statistical model that reproduces the effects of the variation of inputs on the magnitude of outputs. I-TRACK is a tool that will play a role in improving the current design process for track components and will aid in developing mechanistic design practices focused on optimized component and system performance.

9.2 Characterization of I-TRACK – Features and Capabilities

Current concrete crosstie and fastening system design recommendations are primarily based on empirical approaches, and there is a lack of clarity behind some of the critical design limits. This is due, in part, to the fact that design load specifications related to speed and traffic at the AREMA were developed empirically, with input loads and forces distribution not clearly addressed as part of the design methodology (Chen et al. 2012, Van Dyk 2013). In particular, the fastening system component design recommendations present an inconsistent level of detail,

and many of the requirements do not represent the realistic loading demands and environments (Van Dyk 2013). Improvements to current design processes are difficult to implement without understanding the complex behavior of the track structure. Therefore, the development of an analytical tool to predict the mechanical behavior of the track system and its components can be a powerful asset in a mechanistic approach to designing the track, where the responses of these components (e.g. maximum stresses, relative displacements, deformations, etc.) are used to optimize their geometry and materials requirements (e.g. strengths, wear resistance, etc.).

I-TRACK has been designed as a practical and adaptable tool capable of quickly estimating the system and component performance based on a set of user defined input conditions. I-TRACK was developed with a degree of sophistication that does not demand proficiency in computer coding or knowledge in FE modeling. The primary functional objective of this tool is to provide both user accessibility and adaptability that facilitate rapid access to track component responses. When fully developed, I-TRACK can be used to assist manufacturers in improving the design of components and railroad track engineers in assessing the conditions, safety, and expected performance of the track structure.

The development of I-TRACK follows a systematic process, with its release divided into three versions, where each version adds additional capabilities and features to the tool. This approach expedites the development process, allows the accuracy and functionality of the model to be tested on a continuous basis, and provides interim utility to users.

First, input and output parameters were prioritized for each project phase. A Design of Experiments (DOE) based on Half Fractional Factorial Design was used to reduce the number of model iterations that were required to develop I-TRACK. DOE is a strategic way of extracting the system's behavior, optimizing the quality of the information and the effects of a response variable due to one or more factors (Krishnaiah 2012). Section 9.5 of this chapter will provide a detailed description of the techniques used to define the DOE. After the experimental matrix was completed using the DOE, the experiments were coded in the FE model, which was used to generate the track outputs. The matrix of results from the FE model runs was the database used to generate the radial basis function neural network model. This technique correlates the inputs to the output parameters with no error in the training data, allowing the correlation between input variations and their effects on the outputs magnitudes with good accuracy. Other methodologies based on multivariate regression analysis were tested in the development of the statistical model. Higher order effects and the inability to predict most of the correlations between inputs and outputs led to large errors in the results. Therefore, a neural network model approach was chosen as opposed to the aforementioned technique. The final model was embedded into a spreadsheet software, while in the future, researchers intend to launch I-TRACK on different platforms, possibly as cellular phone applications and open-source software.

9.3 I-TRACK Development

I-TRACK's initial development involved determining the key inputs to be analyzed in the FE model and choosing the primary outputs to be monitored. The inputs were selected based on their capability of affecting the track and fastening system component's mechanical responses. Additionally, the ease of coding them in the model has also contributed in their selection. The limitation on the number of inputs is due to the amount of experiments that must be carried out in the FE model when extracting their effects in the monitored outputs. The experiments that are

required for I-TRACK development grow exponentially with the amount of inputs and significantly increases the total computational effort that is required.

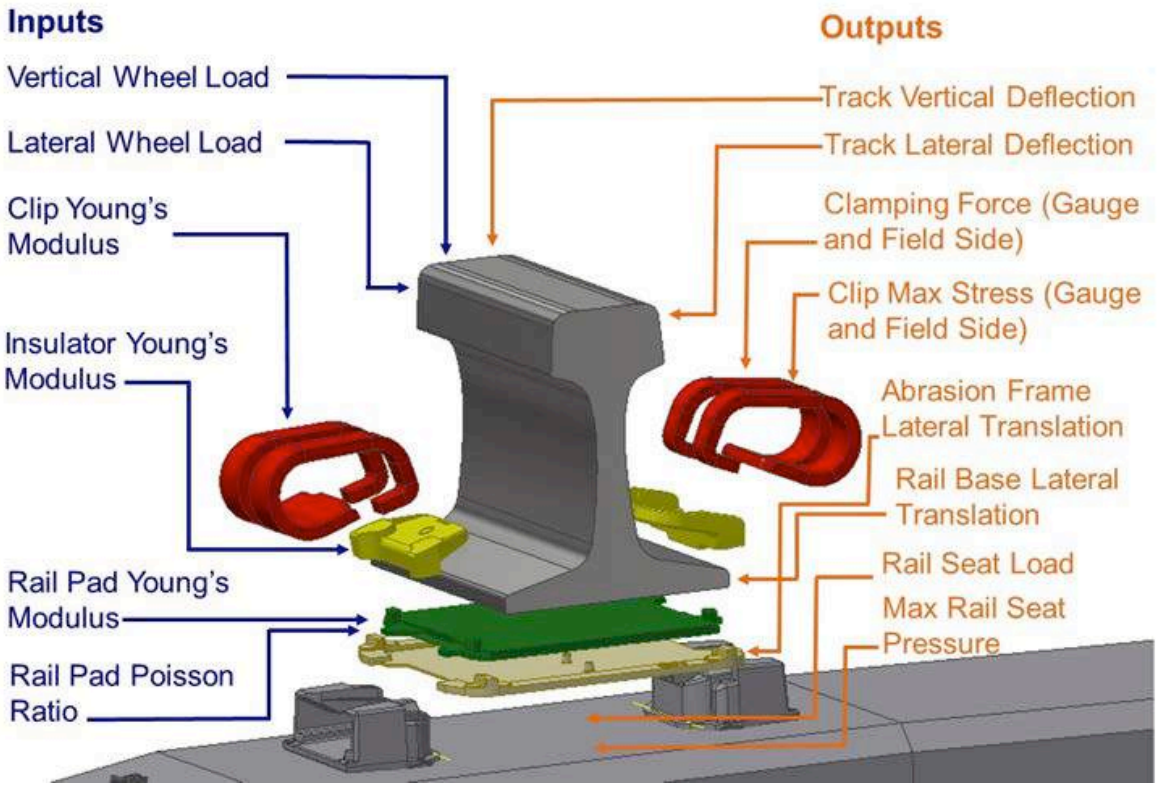

Figure 281. List of Inputs and Outputs Included in I-TRACK Version 1.0

For I-TRACK Version 1.0, static wheel loads (vertical and lateral) and some of the fastening system component's material properties were prioritized as inputs (Figure 282). The first set of outputs (Table 51) was selected to capture the general behavior of the track, giving the user insight about the behavior of key fastening system components. Figure 282 and Table 51 present the inputs and outputs captured for this version of the project and explain the relative location in which these outputs where measured in the FE model. It is important to note that the development of I-TRACK is a continuous process dependent on the FE model capabilities and is subject to a level of accuracy and variability that is related to the number of FE model runs. I-TRACK Versions 2.0 and 3.0 are still under development and additional details of these versions can be found in the next section of this chapter.

Table 51. Definition and Relative Position of Outputs Monitored in I-TRACK Version 1.0

Output	Definition and Relative Position
Track Vertical Deflection	The global vertical deflection at the top of the rail head
Track Lateral Deflection	The global lateral deflection measured at right-angles to the rail in a plane 5/8" below the top of the rail head. Positive value indicates the railhead moved to the gauge side, and negative value indicates the rail head moved to the field side
Rail Base Lateral Translation	The lateral translation measured at the middle of the rail base edge. Positive value indicates the rail base moved to the gauge side, and negative value indicates the rail base moved to the field side
Abrasion Frame Lateral Translation	The lateral translation measured at the field side edge of the abrasion frame. Positive value indicates the abrasion frame moved to the gauge side, and negative value indicates the abrasion frame moved to the field side
Rail Seat Load	The vertical component of the force resultant from the interaction between rail and rail pad on the loaded crosstie
Gauge Side Clamping Force	The vertical component of the force resultant from the interaction between the insulator and the gauge side clip
Field Side Clamping Force	The vertical component of the force resultant from the interaction between the insulator and the field side clip
Gauge Side Clip Maximum Stress	The maximum principal stress in the gauge side clip
Field Side Clip Maximum Stress	The maximum principal stress in the field side clip

9.4 I-TRACK – Versions 2.0 and 3.0

The second and the third versions of I-TRACK will allow the user to modify a larger number of inputs and the software will provide additional output parameters. I-TRACK Version 2.0 is designed to enable the modification of surface interactions and support conditions that will be used as inputs. Therefore, the COF between components and the track stiffness will be added as user-defined parameters (Table 52). The monitored outputs will consist of a set of 39 parameters (Table 53), which will permit a detailed understating of the track behavior and its components. Researchers at UIUC believe these are the main values that are likely to be the most significant from a mechanistic design standpoint, since they encompass macro and micro characteristics of the track mechanical response.

Table 52. Input Capabilities for I-TRACK Versions 2.0 and 3.0

Version	Inputs
I-TRACK 2.0	All the inputs considered in version 1.0
	Coefficient of Friction between rail seat and abrasion frame
	Coefficient of Friction between insulator and shoulder
	Coefficient of Friction between rail pad and rail
	Track Stiffness
	Concrete Compressive Strength
I-TRACK 3.0	All the inputs considered in versions 1.0 and 2.0
	Insulator Post Thickness
	Rail Pad Thickness
	Abrasion Frame Thickness
	Concrete Crosstie Dimensions
	Rail Section (Size)

I-TRACK Version 3.0 will incorporate component geometry into the existing set of input capabilities. Therefore, it will allow the modification of track components, concrete crosstie, and rail dimensions. However, the variation in geometry adds a significant computational challenge when running the DOE, since the relative position between components change in every run. The current FE model uses the Safelok I fastening system, the most prevalent system on concrete crossties in North America. Even though the incorporation of different fastening systems in I-TRACK would be extremely beneficial with respect to broadening its analyses capabilities, this is a limitation of the current FE model that will not be overcome and implemented in I-TRACK in the near term.

Table 53. Outputs for I-TRACK Versions 2.0 and 3.0

Component	Outputs
Track	Track Vertical Deflection Track Lateral Deflection
Rail	Rail Base Lateral Deflection Rail Base Rotation Maximum Stress in the Rail
Rail Pad Assembly	Abrasion Frame Lateral Deflection Rail Relative Lateral Displacement (Relative to Rail Seat) Abrasion Frame and Rail Pad Relative Lateral Displacement (Rel. to Rail Seat) Rail Pad Lateral Load
Insulator	Field Side and Gauge Side Insulator-Shoulder Relative Vertical Displacement Field Side and Gauge Side Insulator-Clip Relative Lateral Displacement Gauge Side Insulator-Shoulder Relative Lateral Displacement Field Side Insulator and Rail Relative Vertical Displacement (Relative to Rail) Gauge Side Insulator and Rail Relative Vertical Displacement
Clips	Gauge Side and Field Side Clamping Force Gauge Side Clip Maximum Stress Field Side Clip Maximum Stress
Shoulder	Contact Pressure between Shoulder and Insulator Field Side and Gauge Side Shoulder Lateral Force Shoulder Lateral Load
Concrete Crosstie	Maximum Rail Seat Pressure Rail Seat Pressure at 0.5, 2.0, 4.0, and 5.5 inches from Shoulder Concrete Crosstie Maximum Compressive Stress Concrete Crosstie Maximum Compressive Stress at Center Concrete Crosstie Maximum Tensile Stress at Center Moment at Concrete Crosstie Rail Seat Moment at the Center of the Concrete Crosstie Rail Seat Vertical Deflection at Center Concrete Crosstie Vertical Deflection at Center Lateral Rail Seat Load at Center Rail Seat Load at Adj. Crosstie (Including Clamping Force) for 3 Crossties Rail Seat Load at Center

9.5 Design of Experiments and Radial Basis Function Neural Network

The DOE is developed to allow an estimate for the interactions resulting from input variation in the output behavior. The intent of this modeling technique is to obtain the local shape of the response surface that is investigated. Under some circumstances, a model only involving main effects and interactions may be appropriate to describe a response surface when the analysis of results reveals no evidence of pure quadratic curvature in the output of interest (e.g. the response at the center is approximately equal to the average of the responses at the factorial runs). In other circumstances, a complete description of the output behavior may require higher order interactions, such a cubic model for example.

If a response behaves linearly, the design matrix to quantify this behavior only needs to contain factors with two levels (high and low). This model is a basic assumption of simple two-level factorial and fractional factorial designs. If a response behaves as a quadratic function, the minimum number of levels required for a factor to quantify this behavior is three. In this case, a Central Composite Design (CCD) based on factorial or fractional factorial design facilitates estimation of the responses' curvature.

I-TRACK's DOE used face centered CCF with an embedded Half Fractional Factorial Design (HFFD) to augment the experiments and capture the behavior of the track components responses. First, 32 experiments were developed based on HFFD and were analyzed in the FE model. Another 13 runs were included to capture the curvature of the outputs that presented a strong indication of nonlinear behavior. Additionally, the final DOE matrix considered extra 56 runs used to improve the accuracy of the outputs results and reduce errors. Ten of these runs were not used to train the model, and they were later applied to verify the accuracy of the results.

For the development of I-TRACK, a Radial Basis Function Network (RBFN) was trained using the function approximation method. A RBFN is an artificial neural network that uses radial basis functions as activation functions, which are the functions that define the outputs of a network node for a given set of inputs. The outputs are linear combinations of radial basis functions of the inputs and neuron parameters.

All the data points in the training set (95 observations obtained from the FE model) were taken as the centers of the radial basis functions. For each new input value, its Euclidean distance from the all the training points was calculated and the output was predicted based on their weights.

A total of 111 observations were obtained from the FE model. From this data matrix, 95 runs were used for training the model and 16 were used for testing it. The 95 observations used for training included 45 observations created using DOE. These output values were specifically chosen at the bounds of the input points and at central points. Inclusion of these observations in the model ensured high accuracy for the test data as the function approximation methodology requires output values at the extreme values of the input points. The model results have an average error of less than 20% for all the output values and highest error was less than 30%.

9.6 I-Track Features

9.7 Functionality

The primary objective behind the development of I-TRACK is to give users the capability of analyzing track mechanics and behavior using an accessible and accurate tool that runs on a commonly supported platform. For this reason, a series of functions were developed to intuitively guide users through the analysis process, including tutorials and a graphing tool that relates inputs to outputs. These features allow I-TRACK to provide reasonable approximations of the actual response (e.g. stresses, displacements, forces) of track components under different loading conditions.

9.8 Tutorial

I-TRACK includes a tutorial tab explaining how to use the software. This tutorial also contains output specifications detailing the meaning of positive and negative values, direction of axes, and the specific location in the FE model where the outputs were extracted. Additionally, an example analysis routine is provided.

9.9 Selection of Baselines

During the analysis process, users have the option to choose from several baseline scenarios for comparing the outputs that are calculated for each combination of inputs. This feature allows users to understand how the set of inputs they choose affects the behavior of the track and its components as compared to baseline values for these inputs. Table 54 shows results extracted from I-TRACK Version 1.0 where baseline values are compared to the results given for a specific set of inputs.

Table 54. Use of Defined Baseline Values for Results Comparison

	Baseline	User's Inputs	Variation (%)
Inputs			
Vertical Load (lb)	37,500	40,000	6%
Lateral Load (lb)	12,500	20,000	38%
Insulator Young's Modulus (psi)	400,000	1,000,000	60%
Rail Pad Modulus (psi)	202,000	20,000	-910%
Rail Pad Poisson Ratio	0.380	0.490	22%
Clip Young's Modulus (psi)	25,000,000	23,000,000	-9%
Outputs			
Track Vertical Deflection (in)	0.052	0.055	6%
Track Lateral Deflection (in)	-0.010	-0.043	312%
Rail Base Lateral Translation (in)	-0.010	-0.029	198%
Clamping Force Gauge Side (lb)	2,682	2,616	-2%
Clamping Force Field Side (lb)	2,919	2,748	-6%
Clip Maximum Stress Gauge Side (psi)	188,830	197,974	5%
Clip Maximum Stress Field Side (psi)	189,690	187,880	-1%
Rail Seat Load (lb)	28,819	25,845	-10%
Abrasion Frame Lateral Translation (in)	-0.006	-0.010	73%

9.10 User Interface

I-TRACK relies on a Visual Basic for Application (VBA) code embedded in a spreadsheet software (Figure 282 and Figure 283). "Macro" functions were added to the interface of I-TRACK to guide the analysis and automate the calculations involved in the process. When possible, figures were introduced to assist users in visualizing the track components and loading application points. Once the I-TRACK spreadsheet is opened, users can access a tutorial that explains how to use the tool or to tabs where the necessary inputs are added. The outputs are accessed in a similar manner, which takes place after the user initiates the calculations. Additionally, there is the option to generate a word processing document summary report, containing the magnitude of the values of all outputs available in a particular run of I-TRACK.

To prevent unintended changes to the configuration of the spreadsheet, all cells in the I-TRACK spreadsheet are blocked except the ones where inputs are entered. However, users have the option to unblock these cells, thereby accessing the code and making modifications. Since the code can be easily accessed, modifications in the program can be made to adapt its interface and features to the specific needs of users.

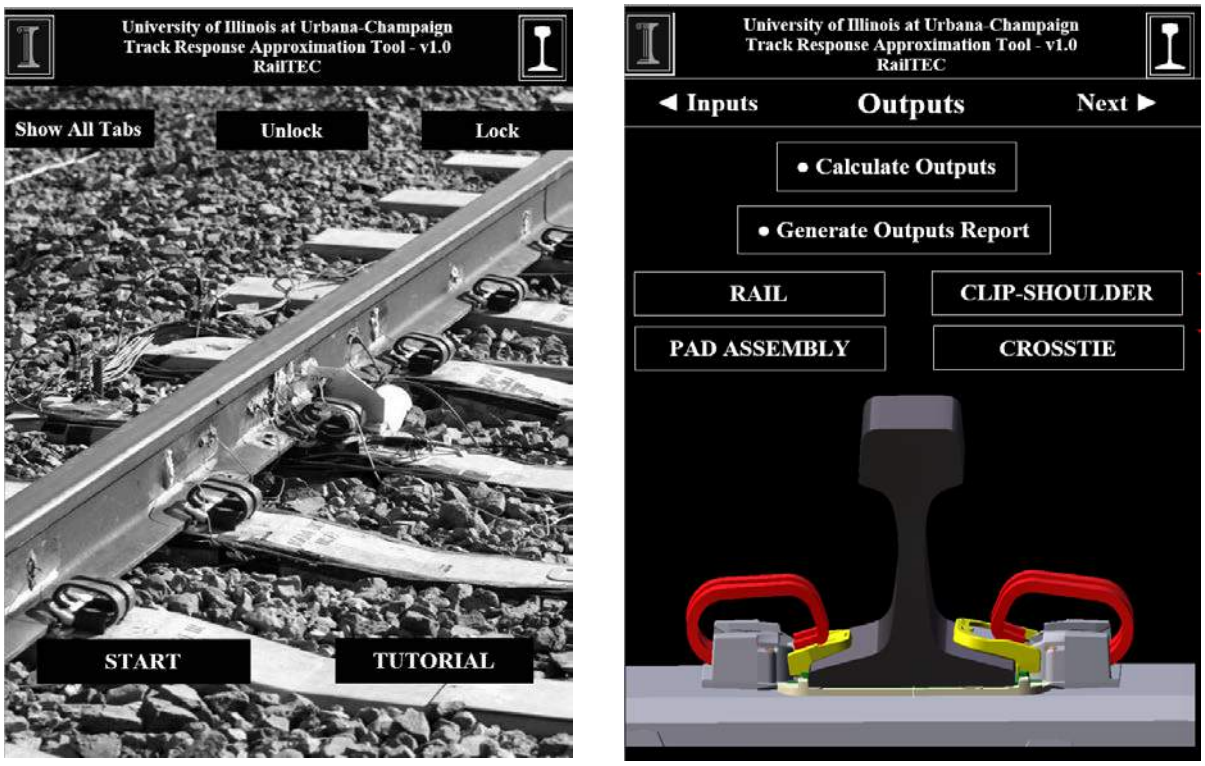

Figure 282. I-TRACK Version 1.0 Interface - Main Page and Outputs Page

9.11 Analysis Report

At the end of the analysis process, users have the option to generate a word-processed document summary report containing the results for the calculated parameters. Once generated, this file is automatically saved in the same folder where the software is located. This is a useful tool for comparing multiple results from I-TRACK, and documenting results for future use.

9.12 Automated Generation of Inputs vs Outputs Graphs

I-TRACK includes a "macro" that automatically generates Input vs Output graphs. After defining a set of base values, which are the inputs that will be used to generate these graphs, users may choose specific input and output combination to be plotted. If a certain input is chosen, all the other inputs of the analysis will assume the base values.

This tool assists in the visualization of the behavior of outputs when one input is varied and all the others are held constant. Using these graphs, the user can determine how sensitive individual outputs are with respect to the variation of each input. Therefore, an analysis process may determine how track vertical deflection (TVD) is affected by rail pad stiffness, for example, providing valuable information in a future mechanistic design process of this component.

Figure 284 shows an analysis routine where baseline values were chosen according to the inputs used by Chen in 2012 and a graph plotting vertical load with respect to TVD was selected (Chen 2012). Any graph can be plotted using the combination of the available inputs. However, the shape of the curves is not always intuitive due to a variety of reasons, including secondary effects from other inputs and the inherent mechanical complexity existent in some of the components interactions.

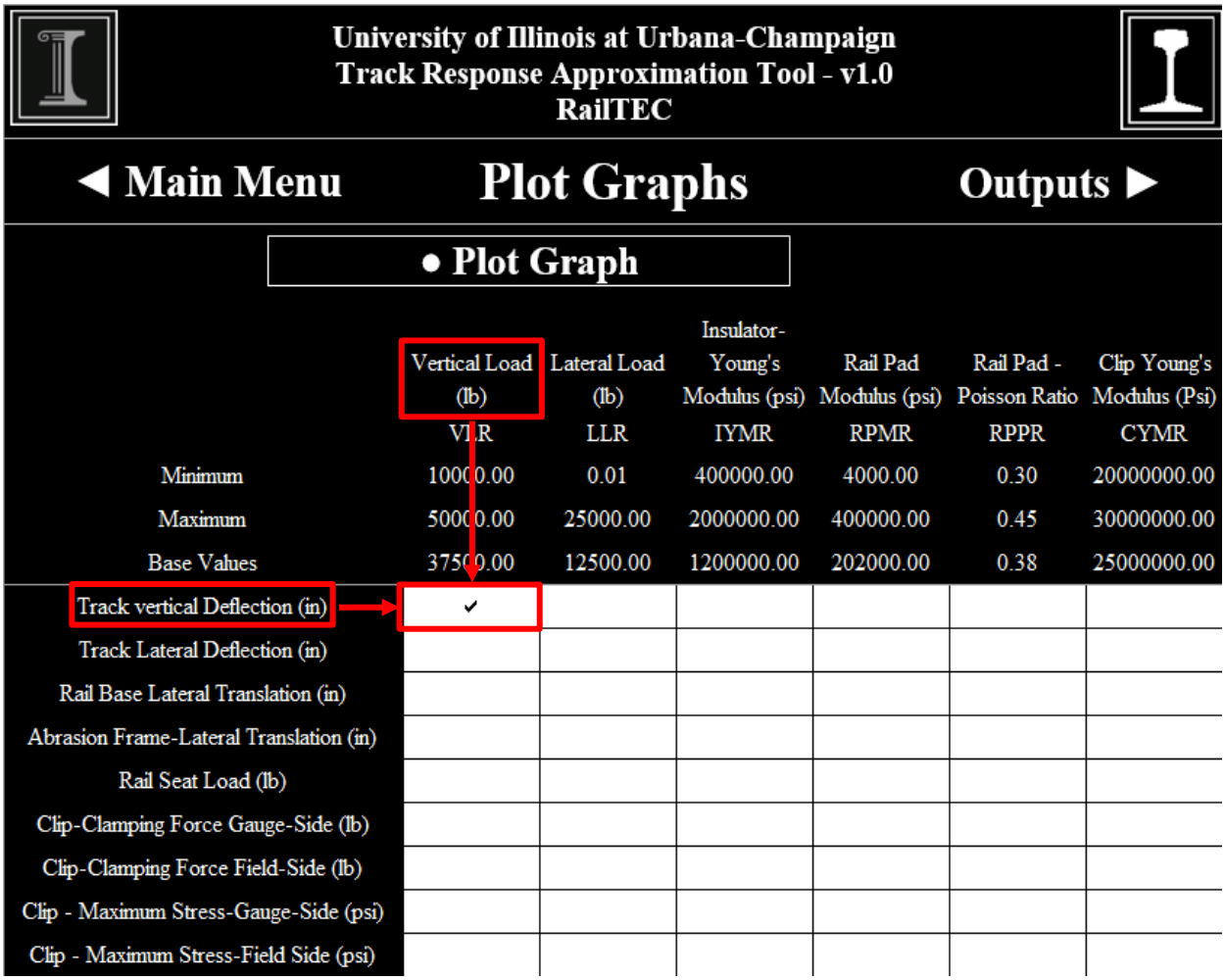

Figure 283. I-TRACK Version 1.0 Interface – Plot Graphs

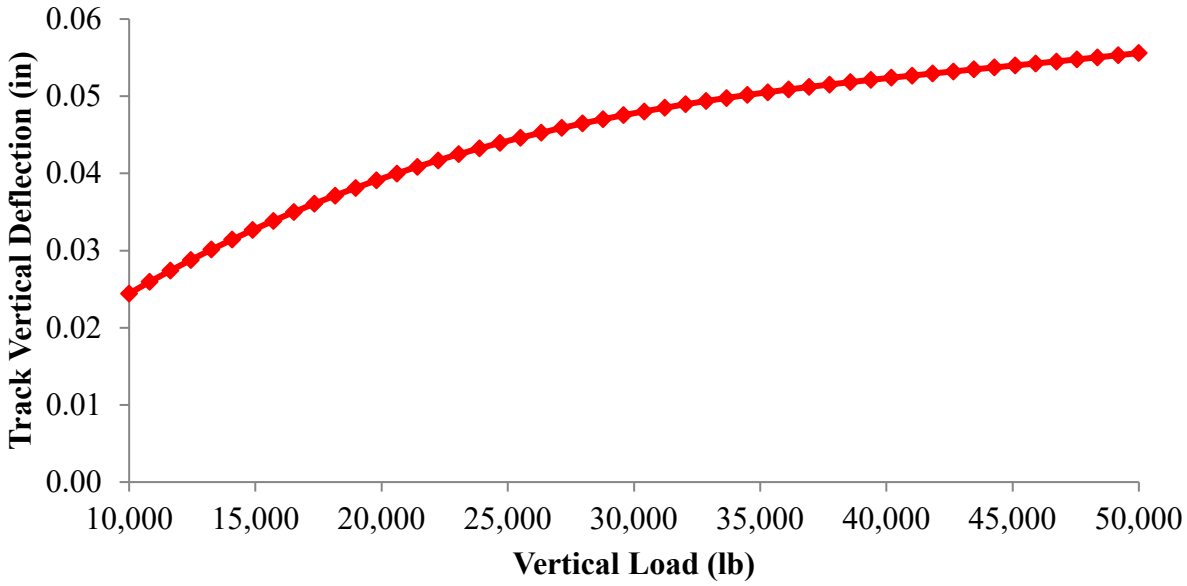

Figure 284. Automated Generation of Graphs Relating User Defined Inputs and Outputs

9.13 Validation of I-TRACK

This section is focused on the validation of I-TRACK results when compared to the FE model outputs. Additionally, a case study of rail pad assembly mechanical behavior was conducted and is included as a part of this section. The main intent is to test the accuracy of I-TRACK's outputs and demonstrate how this tool can be used when developing improved design methodologies for fastening system components. The standard wheel loads and components properties used for the analyses are specified in Table 55. They are the same properties used for the FE model parametric study described by Chen et al. (2013).

Table 55. Wheel Loads and Components Properties Used to Conduct the Case Study

Input	Magnitude
Vertical Load (lbs)	30,000
Lateral Load (lbs)	7,500
Insulator Young's Modulus (psi)	440,000
Rail Pad Young's Modulus (psi)	7,500
Rail Pad Poisson Ratio	0.49
Clip Young's Modulus (psi)	23,000,000

The accuracy of the statistical model embedded in I-TRACK was compared to the FE model results to ensure its credibility and accuracy. Using the material properties from Table 55 and vertical load equal to 40 kips, the lateral displacement of the track and the rail base was plotted for increasing lateral wheel loads. Good agreement is found between the results, with the magnitude of displacements close to each other. Error is present for all the simulated data points, but this factor is due to the amount of variables in the system and the reduced number of experiments used to develop the statistical model. Overall, I-TRACK was successfully able to capture the FE model behavior, providing results with satisfactory accuracy with R^2 value of

around 0.98 for both outputs. However, the high level of adaptability of the tool brings inherent constraints of a statistical model representation of the FE model output. For the purposes for which I-TRACK was developed, the results provide reasonable correlation with the FE model.

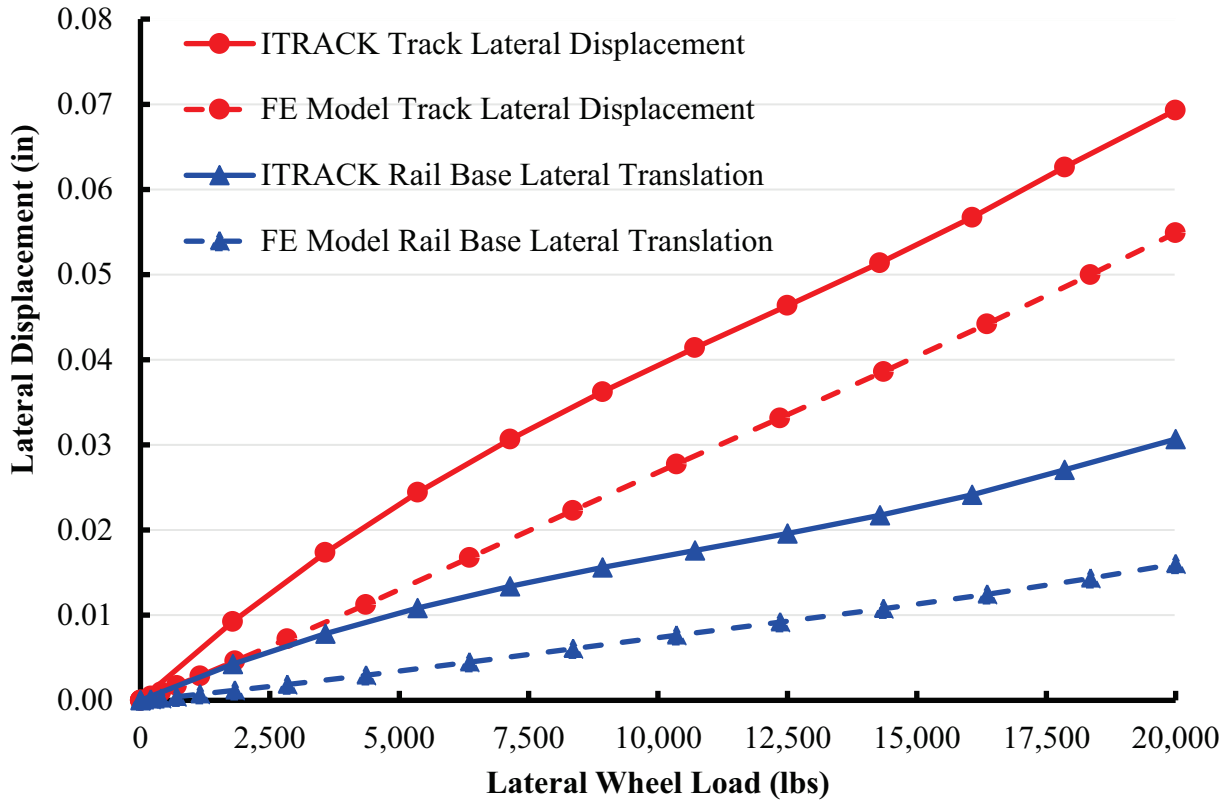

Figure 285. Comparison Between Track and Rail Base Lateral Displacement for Increasing Lateral Wheel Load

9.14 Rail Pad Assembly Mechanical Behavior Investigation Using I-TRACK

There are two system parameters that can be assessed using I-TRACK Version 1.0. The first is TVD, a global measurement of the of the rail head displacement when wheel loads are applied. This output is important to predict the general condition of the track structure, since large displacements must be prevented in order to maintain proper track geometry and adequate service levels. AREMA (2012) states that TVD is related to track performance and a poor performance equates to excessive maintenance and slow orders. The recommended maximum desirable range for TVD to ensure a proper balance between flexibility and stiffness is between 0.125 in (3.18 mm) and 0.25 in (6.35 mm) (AREMA 2012). Deflections smaller than the ones specified in this range may be desired to maintain adequate track geometry but are likely to cause larger loading demands on the fastening system components due to increased stiffness.

The Young's modulus of the rail pad assembly (RPM) affects the total TVD to a limited extent (Figure 285). An increase in the RPM from 7,500 psi to 400,000 psi was able to reduce up to 0.01 in (0.25 mm) of the total TVD, which corresponds to 4% of the maximum deflection

allowed in AREMA 2012. Even though it may seem to be a small difference in a system parameter, this change in RPM can affect component responses, especially the load distribution in the crosstie rail seat area (Rapp 2013). Strains at the bottom of the concrete crosstie and the vertical load path are also other parameters that are directly affected by the rail pad assembly elastic modulus.

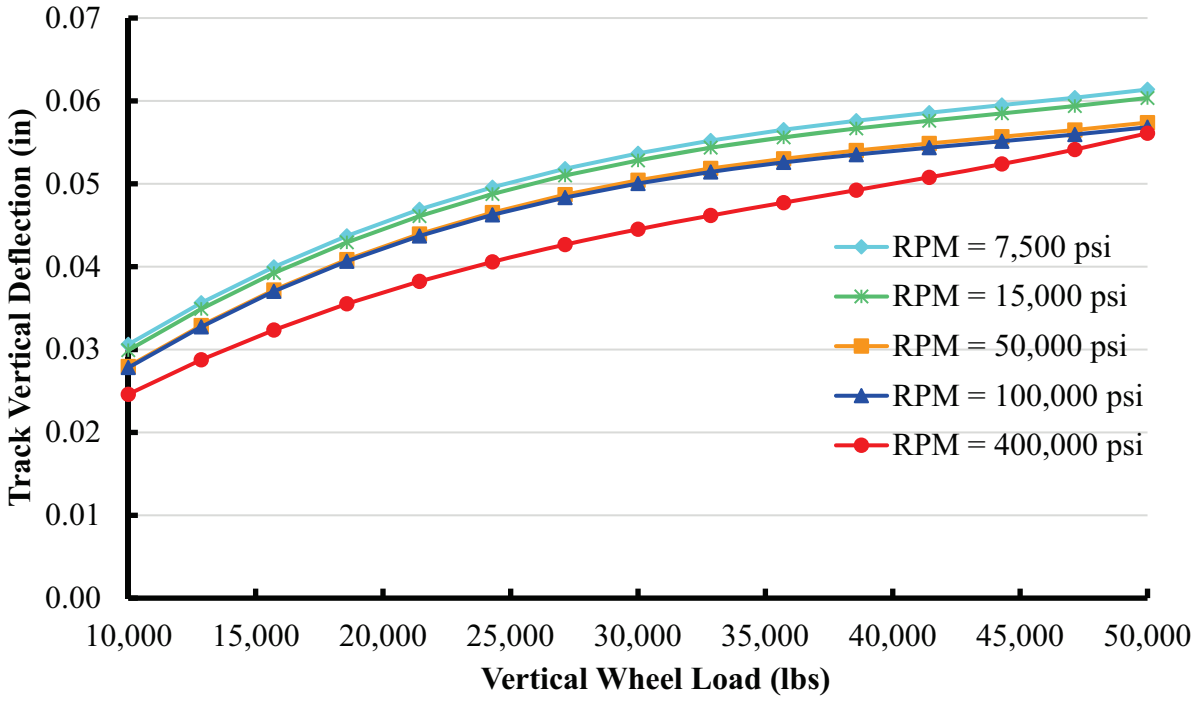

Figure 286. Relationship Between TVD and Vertical Wheel Load for Increased RPM

The other system parameter that can be analyzed through I-TRACK is the track lateral deflection (TLD), a global measurement of the rail head lateral displacement when wheel loads are applied to the rail. This parameter is not currently used in track design, even though researchers have indicated the significant influence of lateral load distribution and fastening system lateral stiffness in track components responses (Bizarria 2013, Williams 2013). This output can also be used to assess the overall performance of the track structure, since large displacements may indicate the occurrence of insufficient frictional forces in the system and relative slip between components.

I-TRACK analyses have shown that increased lateral wheel loads cause larger TLDs (Figure 286). The increase of vertical wheel loads affected the magnitude of this output, leading to smaller displacements. A 40 kip increase in the vertical load was capable of reducing the TLD by 40%, indicating the significant difference in track behavior when the system is subjected to heavier axle loads. Higher vertical loads significantly change frictional forces in the fastening system interfaces, reducing the component's lateral displacements (Kernes 2013, do Carmo 2013a, do Carmo 2013b). The development of shared passenger and freight train corridors imposes design challenges in the track infrastructure that must be overcome in order to guarantee adequate track geometry and desired service levels. Therefore, the current railroad trend to increase axle loads and combine passenger and heavy haul operations in the same infrastructure must take into consideration the impact of such loading environment in the infrastructure

responses. I-TRACK can be a useful tool to predict components behavior and provide insightful data to answer questions related to the structural design of shared corridors.

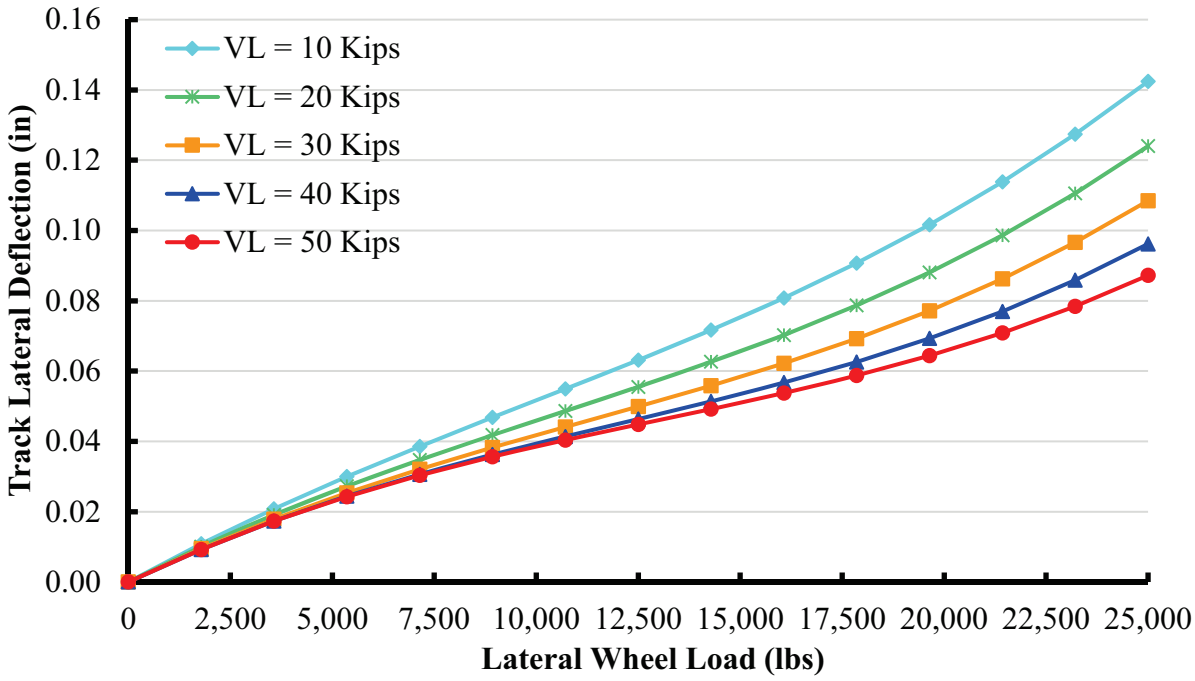

Figure 287. TLD for Increasing Lateral Wheel Loads Considering Different Vertical Wheel Loads

As observed in the outputs provided by I-TRACK, RPM is another parameter affecting TLD. A 5,200% increase in the RPM, from 7,500 psi to 400,000 psi, reduced the initial TLD by 15%. This result is likely due to the softer pads allowing more rail head rotation, which is the point where TLD was measured. Additionally, softer rail pads are able to undergo higher shear deformation, which also contributes to an increased magnitude of this output. Both system parameters analyzed in I-TRACK indicate that RPM may be used as a guiding parameter for track geometry. Even though its effects on TVD and TLD are limited, this is a component that can be altered to modify and achieve desired track performance parameters.

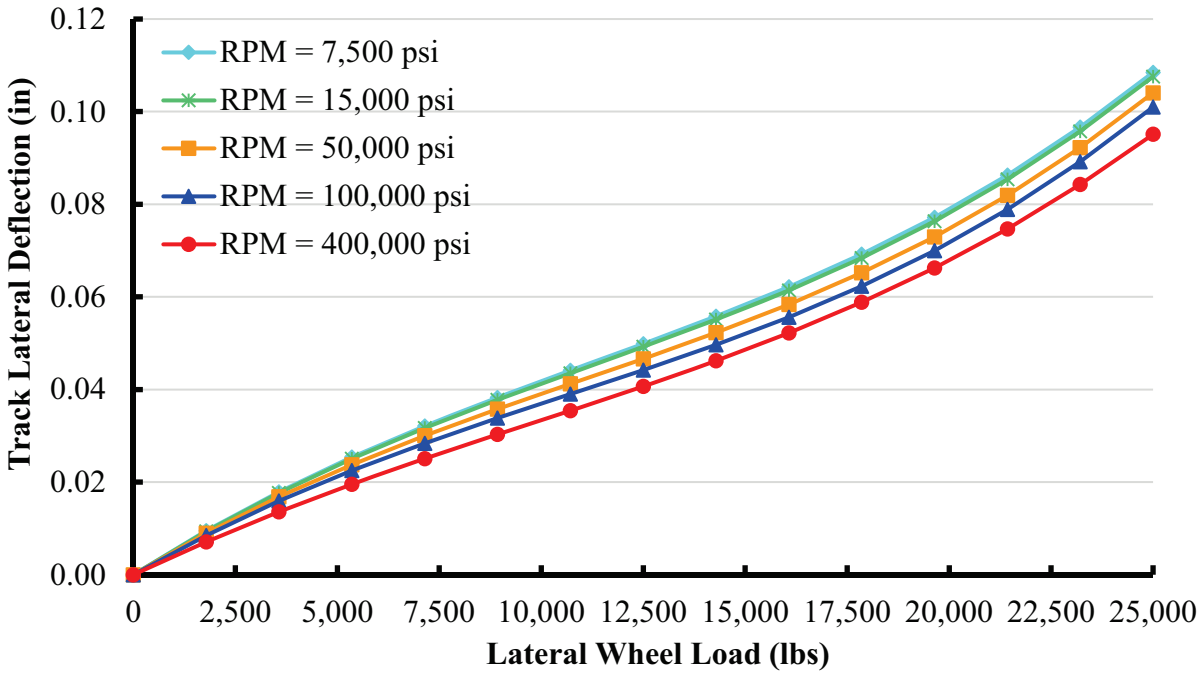

Figure 288. Influence of RPM in TLD for Increasing Lateral Wheel Loads

Another important capability of I-TRACK is related to the analysis of the wheel load path throughout the system, allowing the identification of key inputs that influence the stresses distribution throughout the system. The rail seat load has been the objective of several studies, especially after deterioration of the concrete surface on this interface was identified and related to crushing mechanisms (Rapp 2012, FRA 2012).

Using I-TRACK, it is possible to predict the rail seat load for increasing vertical wheel loads when different rail pad moduli are considered. For vertical wheel loads higher than 30 kips, which corresponds to HALs, the approximate 5,200% increase in RPM resulted in a 20% increase of loads being transferred to the rail seat. These results support the studies conducted by Rapp (2012) in which the author indicates that higher modulus rail pads distribute rail seat loads in more highly concentrated areas, possibly leading to localized crushing of the concrete surface under extreme loading events. For vertical wheel loads lower than 30 kips a trend in rail seat load with respect to RPM cannot be identified. Even though results indicate that lower RPM induce higher rail seat loads, this behavior is not clear. For lower vertical wheel loads the system possibly settles before forces start to be distributed from the rail through the rail pad assembly to the crosstie rail seat. Higher RPM may settle first and start distributing loads earlier, leading to the behavior presented in Figure 289.

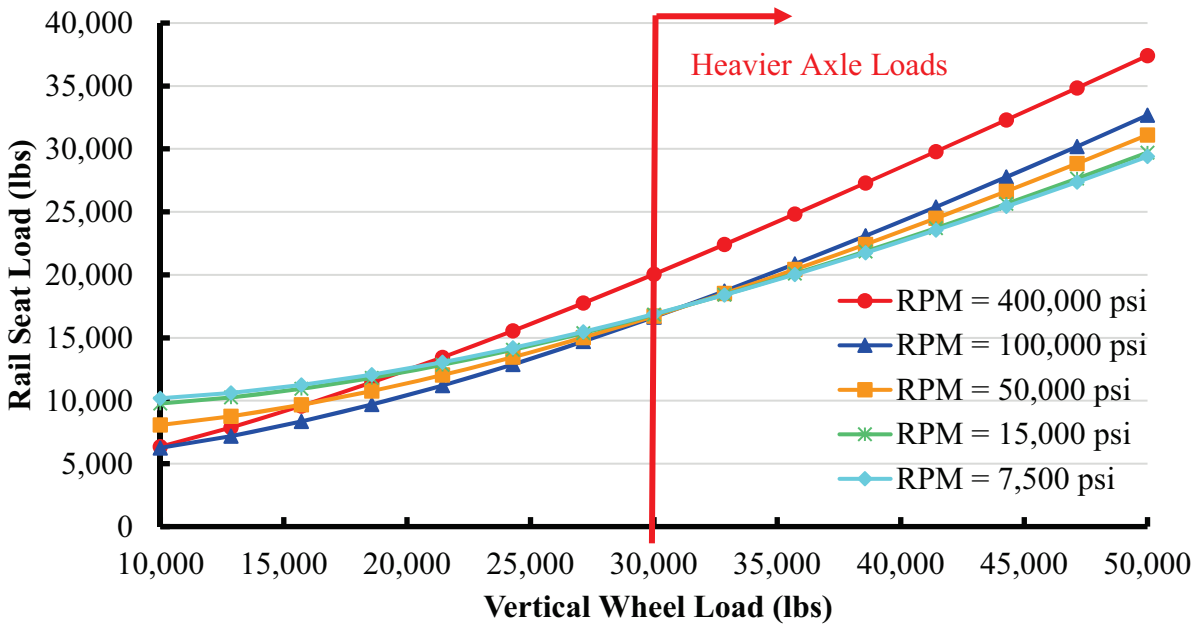

Figure 289. Effects on RPM on Rail Seat Loads for Increasing Vertical Wheel Loads

During the field experimentation, the rail base lateral translation (RBLT) at several rail seats was measured and compared to the rail pad assembly lateral displacement (RPLD). This comparison was important to verify the possible occurrence of shear slip in this interface. It was also capable of pointing out new areas in which future studies could be focused when investigating the mechanical behavior of rail pad assemblies.

The RBLT is a good proxy to measure fastening system lateral stiffness, a property that has been proved to significantly affect the track lateral load distribution (Williams 2013). Taking advantage of I-TRACK's capabilities, it is possible to observe the influence of vertical loads in RBLT. A 400% increase in the vertical wheel load decreased the magnitude of this output by almost 50% (Figure 290). For all the cases considered, the increase in lateral wheel loads was directly correlated to the increase in RBLT. This result also points out the difference in stiffness the fastening system may demonstrate when subjected to different magnitudes of vertical wheel loads. Improved design methodologies for the fastening system should take this difference in responses into account in order to provide adequate track geometry and maintain desired service levels throughout the life cycle of components.

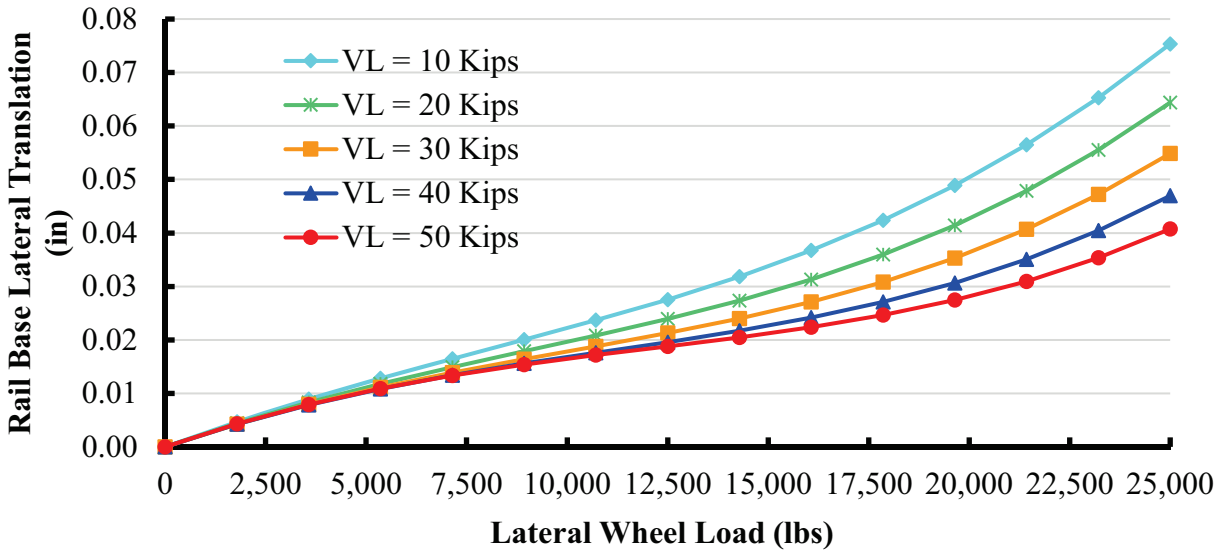

Figure 290. Rail Base Translation for Increasing Lateral Wheel Loads Considering Different Vertical Wheel Loads

An important step in validating the reliability and usefulness of I-TRACK is the comparison between the software output results and field measurements (Figure 291). By analyzing the data related to RBLT presented in Volume 2, Chapter 3 and simulating these results in I-TRACK using the same components properties, it is possible to observe a good correlation. The trend of the output to increase with the increase of lateral wheel load was successfully captured by the model. The magnitudes of the output were also close to the field measurements, even though an error close to 100% was observed for higher lateral wheel loads. It is important to note that a variety of factors are related to the difference in translation magnitudes measured in the field and the ones extracted from I-TRACK. The model is based on a static analysis of the track behavior, whereas the field results presented in Figure 291 are related to maximum track responses generated from dynamic freight train passes. The dynamic response of the track has already been shown to present a smaller magnitude of displacements when compared to static loading cases (Grassé 2013). A possible explanation for this phenomenon is the transient characteristic of the loads, and the fact that they don't allow enough time for the components to fully respond to the demands. Additionally, variability in rail seat geometry, cast-in shoulder spacing, and clamping force are also other factors that may have contributed to the differences observed between the field experimentation results for RBLT and the results provided by I-TRACK.

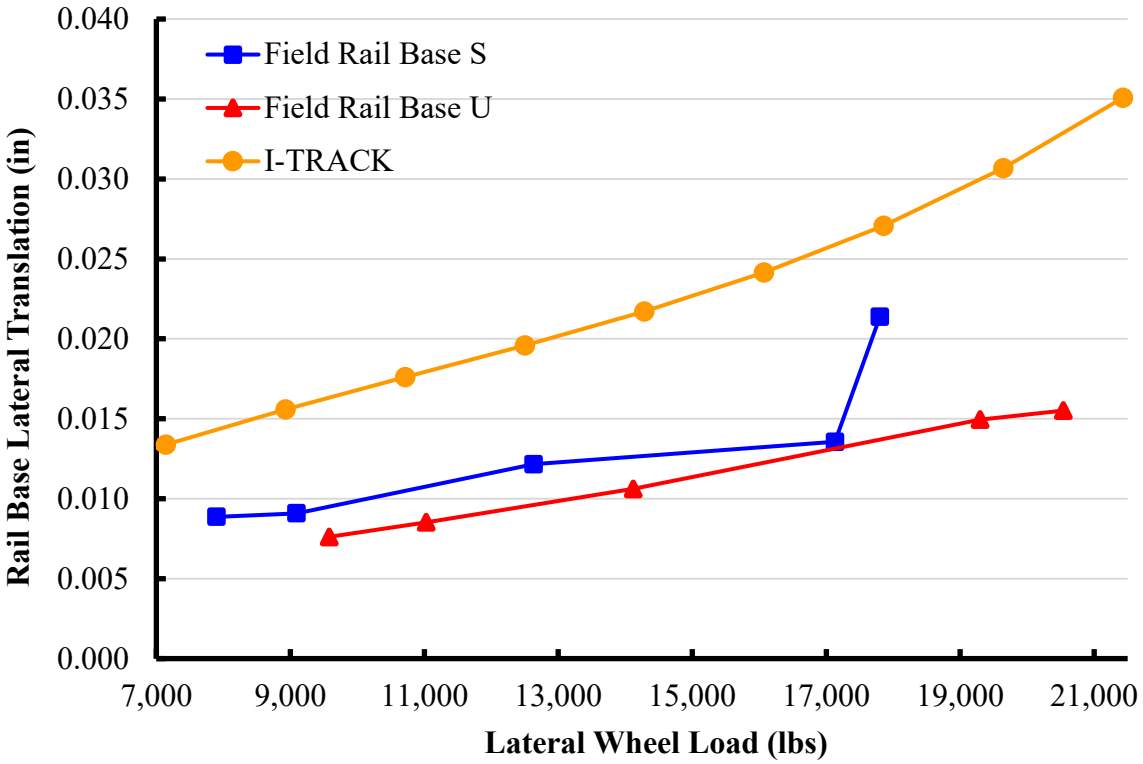

Figure 291. Comparison Between Rail Base Translations from I-TRACK and Field Experimental Results Considering a 40-kip Vertical Wheel Load

9.15 Summary and Future Work

The development of I-TRACK is still in its early stages, but this tool has already proven to be useful in assisting with the development of mechanistic design practices focused on component performance. The ease of use, coupled with the capability to analyze a broad set of outputs considering multiple loading cases and different components properties, is one of the greatest advantages of this software. After it is fully developed, I-TRACK will allow track component manufacturers and railroad engineers to rapidly assess the loading conditions, safety, and expected performance of the track infrastructure.

The case studies presented in this report demonstrated good correlation between the results extracted from I-TRACK and the expected behavior for these parameters. The RBFN successfully demonstrated the FE model results when used for this purpose. It is important to mention that I-TRACK provides estimates for the realistic behavior of the track and its components, but the user should be aware that analyses are based on static loading cases. When comparing to the dynamic loading environment, errors should be expected due to variability in the manner by which wheel loads are applied in the field, the differences in each individual fastening system configurations, and external factors such as magnitude of clamping force and presence of fines and moisture between components.

Researchers at UIUC will continue to develop and refine I-TRACK's features, and the second and third versions of the software will contain additional inputs and outputs to further improve

the current analysis capabilities. The ultimate goal of I-TRACK is to provide component manufacturers and track engineers with a powerful and adaptable tool to analyze the track responses and assist the development of improved fastening system components.

Chapter 10: Mechanistic Design of Concrete Crossties and Fastening Systems

10.1 Overview of Mechanistic Design

10.2 Introduction

The design of North American concrete crosstie and fastening systems has been based on practical knowledge, without a clear understanding of failure mechanisms, their causes, and the loading environment. This design methodology led to performance challenges and service failures that cannot be adequately explained or predicted. Without a clear framework for the design of concrete crossties and fastening systems, inefficiencies in component design may exist, negatively impacting the economies of using concrete crossties and fastening systems. Improvements in the design of these systems will provide a more robust railway superstructure, where the loading environment is more fully considered, failures are reduced, and the possibility of predicting performance metrics (e.g. wear rates) exists.

Based on a survey that polled railroads and fastening system manufacturers, both domestic and international, a list of the primary failures experienced in the field was developed (Van Dyk 2013). Table 56 provides a list of the survey results for critical concrete crosstie and fastening system problems in the United States.

Table 56. Concrete Crosstie Critical Failures

Most Critical Concrete Tie Problems
Rail seat deterioration
Shoulder/fastener wear or fatigue
Derailment damage
Cracking from center binding
Cracking from dynamic loads
Tamping damage
Other (ex: manufactured defect)
Cracking from environmental or chemical degradation

The problems listed in bold in Table 56 are issues that can potentially be mitigated by improving the design process for concrete crossties and fastening systems. These failures occur due to problems with the infrastructure or rolling stock, or result from severe loading conditions. Some failures may exist due to incorrect design assumptions and procedures, or a lack of understanding of the failure modes. A mechanistic design process will reduce the occurrence of these failures by understanding how and why they occur and by altering the design of the system to prevent similar occurrences. There will still be cases where damage and failures will occur, but a mechanistic design process can minimize this risk and allow railroads to understand the capacity of their infrastructure and its components.

The current design process found in the AREMA Manual on Railway Engineering has several areas that are in need of improvement (AREMA 2014). Some limit states are not justified, nor is there an explanation of their origin. For example, the origin of AREMA maximum allowable moments for concrete crossties is not explained, making it difficult to understand why these values were chosen. This knowledge is critical in understanding potential failures that might occur, and for developing new designs based on changing axle loads. Additionally, while it is possible that some elements of the previous design methods were mechanistic, the lack of documentation leads to uncertainty. Revised values developed as a part of the new design process will include appropriate references. This will allow interested parties to both understand the origin of the methodology, and make further improvements to the process.

An additional objective of the new design process is to provide limits for all critical properties. As an example, the AREMA recommended practices do not specify a limit on lateral rail base displacement for insulators (AREMA 2014). This value is critical to the design of the system, as too much displacement could result in a loss of gauge, causing a derailment. A goal of new design approach presented here is to provide limits for all properties that affect the performance of the crosstie and fastening system in order to minimize the risk of derailments and to reduce maintenance requirements.

The final way in which a mechanistic design process can improve the current recommended practices for design is by developing a comprehensive design process for all components. Currently, AREMA does not outline a design process for several crossties and fastening system components, including the rail pad. Several choices of rail pad material and thickness are discussed, but there is no process for designing a new rail pad. The design of a rail pad can depend on factors such as the type and speed of traffic. A comprehensive design approach will allow location specific optimization of component designs. A mechanistic design approach permits component design to be optimized based on track geometry, traffic characteristics, and other specific features.

10.3 Mechanistic Design Principles

The mechanistic design process is derived from analytical and scientific principles with consideration of field loading conditions and other performance requirements. Representative input loads and load distribution factors are used to determine the required component, geometric and material properties. This approach is based measured track loads and the necessary material properties of the components used to withstand or transfer these loads. Component responses to items such as contact pressure or relative displacement to optimize component geometry and material requirements. Since a mechanistic design requires a thorough understanding of the load path and distribution it allows for the development of load factors. By understanding exactly how loads transfer through the system, one can determine the failure points in the system and a load factor can be developed to ensure that these failures are eliminated. This load factor can change based on location and traffic composition. Mechanistic design has been used in other disciplines, such as the design of rigid and flexible highway pavements using particular input values, performance analyses, and alternative evaluations (Applied Research Associates Inc. 2004).

UIUC is developing a mechanistic design process that uses the existing loading environment to optimize the design of the concrete crosstie and fastening system. The approach chosen by UIUC begins by defining the vertical, lateral, and longitudinal input loads, and noting how these loads are passed through the system. The next step is defining load thresholds, which are limits of critical properties for the materials used to build the components, the components themselves (i.e. considering their geometry in addition to material properties), and the fully assembled fastening system. After the criteria for loading thresholds are defined, the components are designed using a set of pre-defined criteria. The last step is to verify that the system as a whole is performing according to expectations, primarily by installing the system in the field and measuring critical performance properties. The overall design process that will be followed can be seen in Figure 292 and will be discussed in detail in the next section of this chapter.

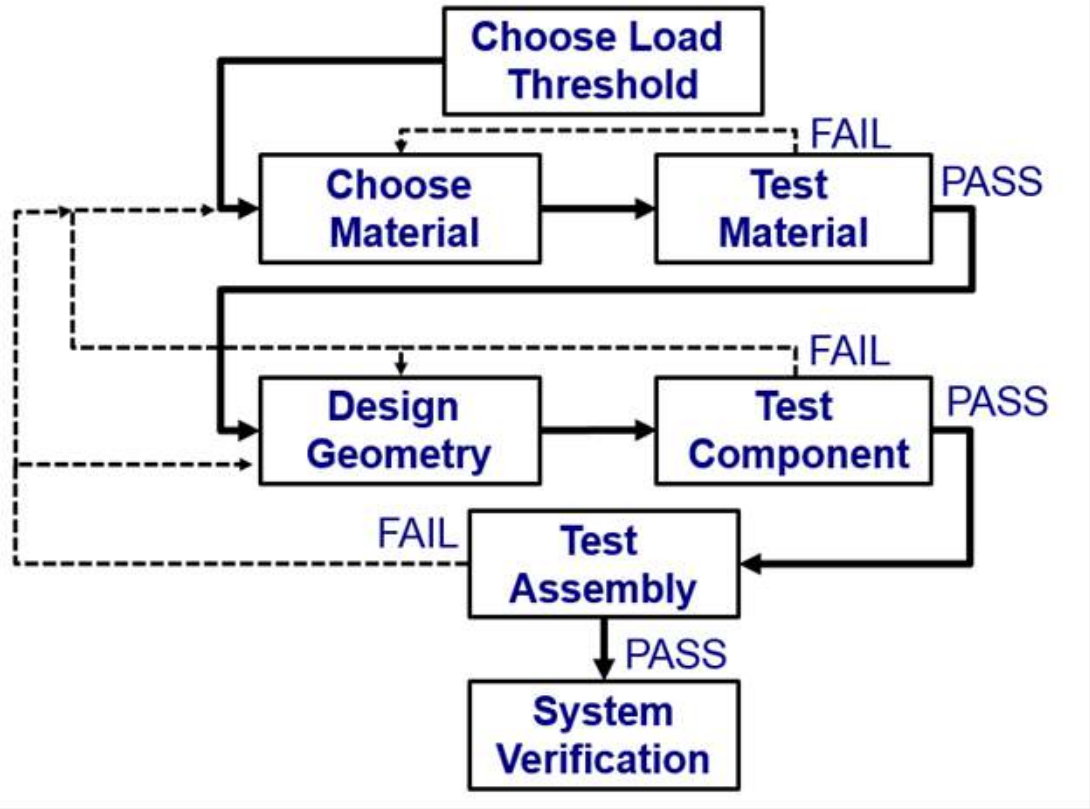

Figure 292. Mechanistic Design Process Flow Chart

10.4 Concrete Crosstie and Fastening Systems Design Process

10.5 Define Wheel Load Inputs

The first step in the mechanistic design process is to characterize the wheel loads that are applied to the track structure to ensure that appropriate design strengths for the system and its components can be determined. The magnitude and distribution of loading is primarily determined by traffic type, train speed, track geometry requirements and condition, and vehicle health. The railway operating environment in North America has a wide variety of train types sharing the same infrastructure. The most apparent difference is the diverging characteristics of passenger trains and freight trains. Passenger trains have much lower axle loads than typical

freight trains, but they tend to run at much higher speeds. Even within each train type, there is ae large distribution of wheel loads (e.g. loaded and empty freight cars).

Based on the prevalence of different traffic types and track strength requirements, the input loads used for the design of a system are quite variable. Train speed affects the magnitude of wheel loads, with the greatest effect seen in conjunction with impact loads occurring at high speeds. Impact loads are typically caused by characteristics of the vehicle or wheels, or due to certain infrastructure components (e.g. joints) or geometric defects. Track geometry also plays a large role in the magnitude of wheel loads, particularly in the significance of lateral versus vertical loads. In curves, the lateral wheel loads are much higher than in tangent track segments. The final factor is vehicle and track condition. Variations in the wheel profile can cause high impact loads that may result in wear and/or fracture components. Poor track condition can lead to similar problems, but with different root causes. Track warp, cross-level deviations, and any other deviation or combination of deviators can affect the loading environment.

It is important to be able to accurately characterize the range of loading conditions for the design process. The wheel loads selected for design will determine the loading demands on the system and its components. Given that there is a distribution of axle loads, it is not reasonable to use the maximum load for design, since it may not be indicative of the overall load distribution. Instead, a load bounding approach should be used. For example, a railroad may choose to use a 99.5% design approach. This results in selecting a wheel load representing a value that is equal to or greater than 99.5% of wheel loads. A small percentage of the wheel of wheel loads will exceed the design value. This approach will allow railroads to weigh the tradeoffs between first costs and operating costs with respect to the component design. Using a conservative threshold will result in a more durable system, and will lower the risk of damage to the system based on the expected wheel load environment, but may be too expensive to build. A less-conservative approach will have a higher percentage of loads that exceed the design value, which could result in an increased number of component failures and wear to the system.

Three load threshold levels are proposed, 99.5%, 97.5%, and 95%. The final choice will vary depending on the preference of the company performing or paying for the design. The reason that these percentiles are so high is due to the quantity of wheel loads that occur. Consider a typical freight train with 100 or more cars. Each car typically has eight wheel loads, so even at the most conservative threshold level (99.5%) a single train will have an average of four wheel loads that exceed the design value. Due to the high quantity of wheel load repetitions that will be experienced by the crosstie and fastening system over the course of its service life, high percentile load thresholds should be used.

To fully describe the wheel load distribution, the wheel loads are decomposed into three categories: vertical, lateral, and longitudinal wheel loads.

10.5.1 Vertical Wheel Loads

UIUC has acquired WILD data from both Amtrak's Northeast Corridor and UP to better understand the range of vertical loads applied to the track infrastructure. Vertical wheel loads can depend on a variety of factors. Some of the factors that are believed to have the greatest effect on their magnitude are train speed, track geometry, vehicle characteristics, curvature,

grade, position of the wheel within the train, geographic location, and temperature. WILD site data can be used to determine the effect of many of these factors, most importantly looking at the effect of train speed and vehicle characteristics.

WILD sites are typically constructed on well-maintained tangent track with concrete crossties, premium ballast, and well compacted subgrade (possibly with hot mix asphalt underlayment) to reduce sources of load variation within the track structure. Although loads experienced elsewhere on the network will vary and may have a higher magnitude due to track geometry deviations, these data still provide insight to the varied loading landscape at representative sites throughout North America. Specific loading properties such as peak vertical load, peak lateral load, impact factor, and speed are analyzed by creating various distributions of these properties and determining relationships between them. An example of this type of distribution is shown in Figure 293.

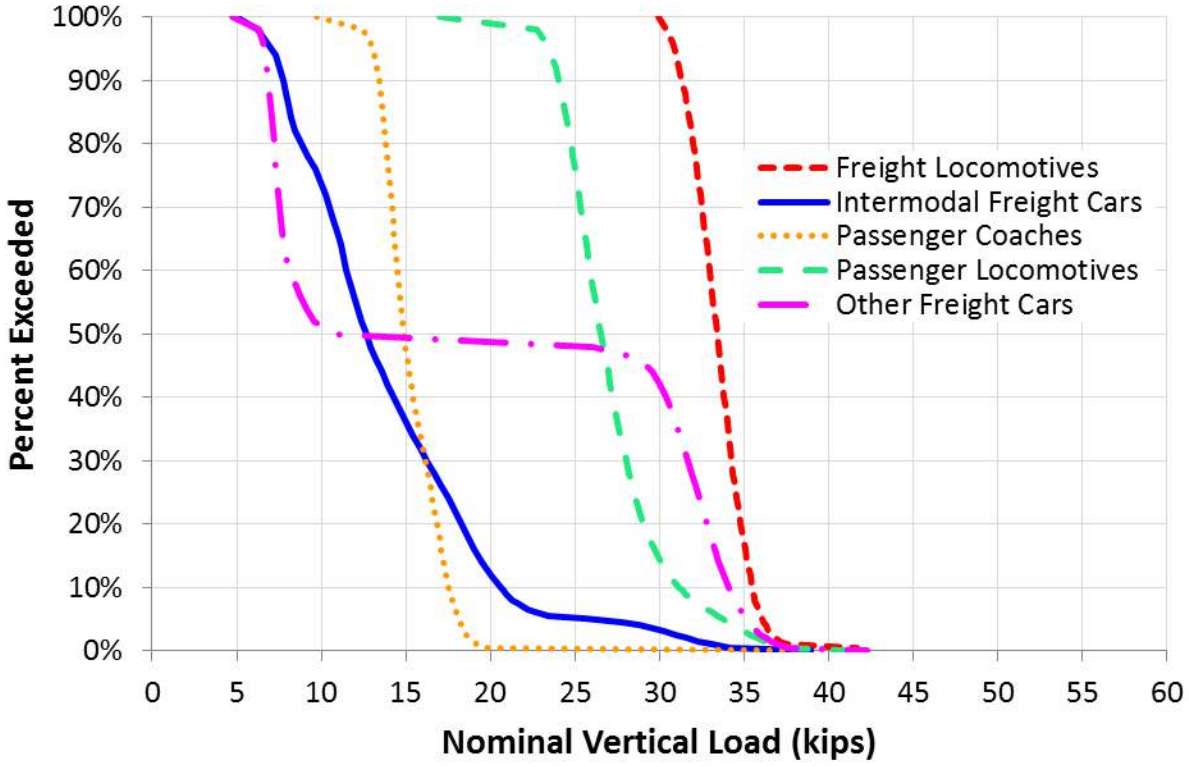

Figure 293. Percent Exceeding Particular Nominal Vertical Loads on Amtrak at Edgewood, Maryland (WILD data from November 2010) (Van Dyk 2013)

As seen in Figure 293 Amtrak's locomotives, freight cars, and passenger coaches all impart different magnitudes of vertical load into the track structure. Once the loading spectrum is adequately determined, one must decide how to effectively design the system and its components accordingly. The relationship between extreme loading events (e.g. wheel impact loads) and failure mechanisms is not well-defined, so it is difficult to sufficiently determine the required robustness of design. Probabilistic considerations must be made throughout the design process, reflecting safety, financial, and capacity decisions. The disparity in the magnitude of loads between passenger and freight traffic and their respective weighted traffic volumes must also be addressed in designing for specific loading environments.

Results from the 2012 UIUC International Survey described in Volume 2, Chapter 1 of this report provide a comparison of the North American and international loading environments and are summarized in Table 57. According to both the international and North American responses, the average maximum freight static axle load exceeds the design axle load based on responses from the concrete crosstie manufacturers. The load and tonnage values are, on average, substantially higher in North America than in the remainder of the world.

Table 57. Loading Environment Summary (Average of Responses) (Van Dyk 2013)

	International Responses	North American Responses
Maximum freight axle load*	29.5 tons (26.8 tonnes)	39.1 tons (35.4 tonnes)
Maximum passenger axle load*†	21.6 tons (19.6 tonnes)	29.1 tons (26.4 tonnes)
Concrete crosstie design axle load	27.6 tons (25.0 tonnes)	37.4 tons (33.9 tonnes)
Annual tonnage (per track)	38.7 million gross tons (35.1 million gross tonnes)	100.0 million gross tons (90.8 million gross tonnes)

*Interpreted from responses due to discrepancies in axle or wheel loads
†Light rail response excluded

Both the WILD data and survey results provide a better understanding of the loads imparted into the superstructure, but this understanding is not sufficient for the design of concrete crossties and elastic fastening systems. The load's attenuation and progression through the track provides information critical to the design of the superstructure components.

Before designing the individual components, the vertical wheel loads must be quantified to determine the magnitude of the loads that will be distributed to the rest of the system. To quantify these loads, WILD data was used to examine average and peak loads imparted by different types of cars, and then use knowledge of the specific route to determine what vehicles are expected. Several load thresholds were quantified to allow the choice of what design load to utilize. Table 58, Table 59, and Table 60 describe the loads gathered from WILD sites, which were used to determine the threshold values for vertical loads based on different traffic types.

Table 58. Distribution of Static Vertical Wheel Loads (Van Dyk 2013)

	Nominal Load (kips)				
Car Type	Mean	95%	97.5%	99.5%	100%
Unloaded Freight Car[1]	7	10	11	14	15
Loaded Freight Car[1]	34	40	41	42	46
Intermodal Freight Car[1]	21	36	37	40	51
Freight Locomotive[1]	34	37	38	39	44
Passenger Locomotive[2]	27	36	38	40	43
Passenger Coach[2]	15	19	19	21	46

Table 59. Distribution of Peak Vertical Wheel Loads (Van Dyk 2013)

		Peak Load (kips)			
Car Type	Mean	95%	97.5%	99.5%	100%
Unloaded Freight Car[1]	11	21	27	40	101
Loaded Freight Car[1]	43	57	66	85	157
Intermodal Freight Car[1]	28	47	55	75	142
Freight Locomotive[1]	43	54	58	69	110
Passenger Locomotive[2]	39	50	54	64	94
Passenger Coach[2]	24	36	43	59	109

Table 60. Peak Vertical Load to Static Vertical Load Ratio

		Peak Load / Nominal Load			
Car Type	Mean	95%	97.5%	99.5%	100%
Unloaded Freight Car[1]	1.6	2.1	2.5	2.9	6.7
Loaded Freight Car[1]	1.3	1.4	1.6	2.0	3.4
Intermodal Freight Car[1]	1.3	1.3	1.5	1.9	2.8
Freight Locomotive[1]	1.3	1.5	1.5	1.8	2.5
Passenger Locomotive[2]	1.4	1.4	1.4	1.6	2.2
Passenger Coach[2]	1.6	1.9	2.3	2.8	2.4

[1] Source of data: Union Pacific Railroad; Gothenburg, NE; January 2010
[2] Source of data: Amtrak; Edgewood, MD, Hook, PA, and Mansfield, MA; November 2010

A key factor in design is the ratio that represents the difference between peak and static wheel loads. The majority of peak wheel loads are between 1.3 and 3 times larger than the static load for the respective vehicle type. Since WILD sites are built on well-maintained track, the impact loads recorded at these locations are largely due to problems with the shape of the wheels or other rolling stock conditions. By developing more stringent requirements for wheel geometry, the loads experienced by the track can be greatly diminished. Instead of requiring a design that considers peak loads, the lower magnitude static loads can be used. Some consideration should also be given to impact forces that are generated due to track irregularities.

Another major difference between nominal and peak loads is the amount of variability. For example, the nominal load imposed by a loaded freight car differs by only 2 kips from the 95% load threshold to the 99.5% threshold. However, when considering the peak load this difference increases to 28 kips. This greater variability suggests that when choosing a load threshold, the peak load will be more important for the design of infrastructure, as the nominal load will not change very much depending on which load threshold is chosen.

It should be noted that these data represent best-case loading scenarios. This data reflects variations in wheel and train condition, not track conditions. The effect of track condition on the magnitude of vertical wheel loads should be studied to determine the final vertical load thresholds to be used in design. However, it is likely the overall distribution of the loads will remain the same, and track health variability can be considered through the use of an additional

load factor. For example, poor track condition may result in 10% higher impact loads. This could be accounted for by multiplying the peak load determined from WILD sites by 1.1. Additional research needs to be undertaken to quantify the magnitude of this load factor.

10.5.2 Lateral Wheel Loads

In order to quantify the magnitude and distribution of lateral wheel loads, truck performance detector (TPD) data was utilized. TPD's are similar to WILD sites, but use strain gauges located in curves instead of tangent track. However, they provide less detailed information and do not differentiate between static and peak wheel loads. Instead of using strain gauges to collect data for the full rotation of the wheel, TPD sites only have two instrumented cribs per curve. Despite this limitation, the data collected can still provide the magnitudes of typical lateral wheel loads. Some of the factors that are believed to have the greatest effect on their magnitude are train speed, track geometry, vehicle characteristics, curvature, grade, position of the wheel within the train, geographic location, temperature, low vs. high rail, and rail surface condition. TPD site data can be used to determine the effect of many of these factors, in particular, the effect of train speed, curvature, and superelevation.

The lateral wheel load can exceed 50 percent of the vertical wheel load in curves. The lateral load will not only affect the design of components such as the shoulder or insulator, it also can change the load distribution in the entire crosstie and fastening system. The lateral load will have more variability than vertical load, due to the difference between load magnitudes in tangent track and curves. Finally, lateral loading is typically very low on tangent track, and as a result, it has very little effect on the design of components for those sections.

Figure 294 gives an example of the distribution of lateral loads measured by TPDs, categorized according to car type.

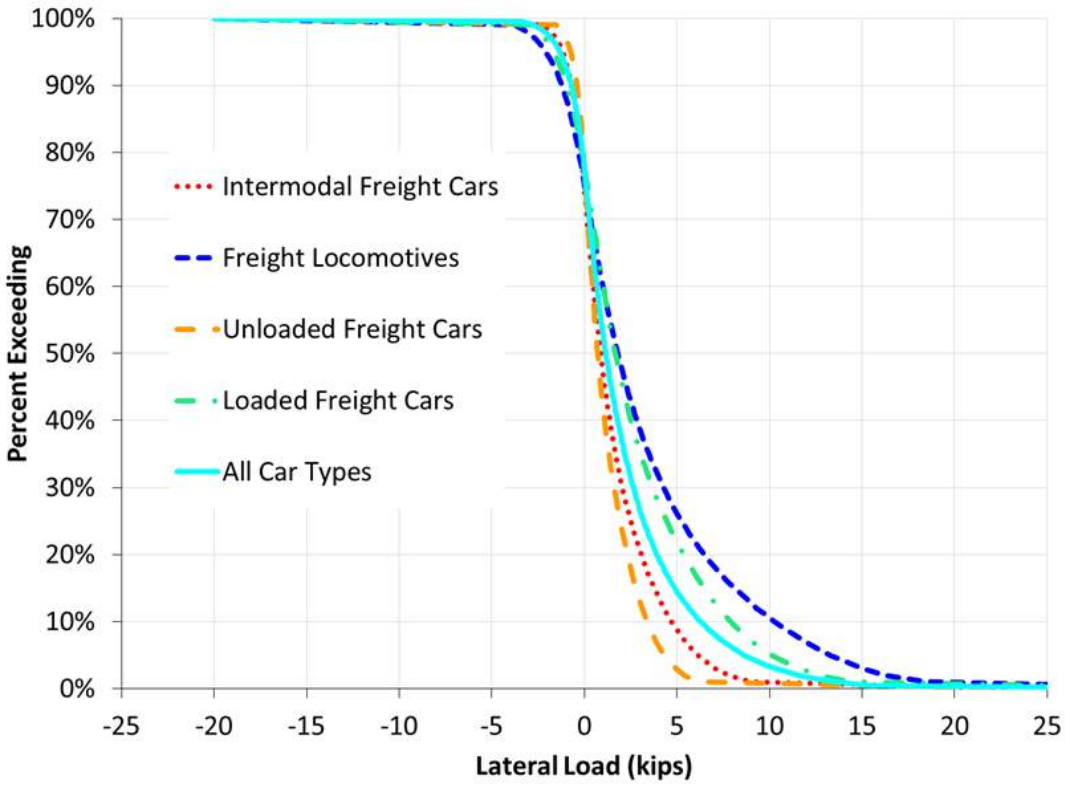

Figure 294. Lateral Load Variation with Car Type (Scheppe 2014)

Figure 294 illustrates that different car types impart different magnitude of lateral loads to the track structure. The TPD data sites were located all over the United States on curves with varying degrees of curvature and inches of superelevation. Many of the factors that were believed to affect the magnitude of lateral wheel load were analyzed, with car weight having the most significant impact.

Table 61 and Table 62 describe the wheel loads as measured by TPD sites. The categories are the same as used previously for quantifying vertical wheel loads.

Table 61. Distribution of Peak Lateral Wheel Loads (Scheppe 2014)

	Lateral Load (kips)				
Car Type	Mean	95%	97.5%	99.5%	100% (Max)
Unloaded Freight Car	1.1	4.4	5.2	6.9	22.4
Loaded Freight Car	2.7	10.1	12.1	15.9	33.5
Intermodal Freight Car	1.9	6.2	7.4	10.1	22.8
Freight Locomotive	3.9	13.3	15.6	20.5	34.4

Table 62. Distribution of Lateral/Vertical Load Ratios (Scheppe 2014)

	L/V				
Car Type	Mean	95%	97.5%	99.5%	100% (Max)
Unloaded Freight Car	0.15	0.44	0.50	0.64	4.00
Loaded Freight Car	0.11	0.35	0.41	0.52	1.46
Intermodal Freight Car	0.12	0.39	0.46	0.59	1.61
Freight Locomotive	0.11	0.38	0.44	0.56	0.81

Table 61 illustrates the fact that heavy railcars impart a larger lateral wheel load to the track. One exception is the load from freight locomotives compared to loaded freight cars. Even though freight locomotives have slightly lower static vertical wheel loads than loaded freight cars, they tend to have significantly higher lateral wheel loads. Based on TPD data, locomotives at the front of a freight consist show no difference in lateral wheel load distribution from locomotives at the middle or end of the consist. This suggests that the increased loading is solely due to the curving characteristics of the locomotives.

Table 62 contains the distribution of Lateral to Vertical (L/V) load ratio collected at TPD sites. At high values of L/V, the wheel can climb over the rail, causing a derailment. Instability of the rail can start to occur at L/V ratios of 0.68, and at a 1.29 ratio, rollover is nearly assured (Hay 1953). From the analysis of the data it is evident that the empty cars are the most prone to high L/V ratios.

As with WILD data discussed in the vertical wheel load section, this data represents a best-case scenario. TPD sites tend to be well maintained and free from issues that may occur elsewhere on the network, such as geometric defects or poor support conditions. These issues could result in higher magnitude lateral wheel loads than quantified here.

In the future, data will be collected from curves with higher degrees of curvature. The maximum degree of curvature in this study was 6 degrees, which is not the maximum for mainline tracks in the US. It is possible that more severe curves could cause lateral loads to increase, and change the way lateral wheel loads should be estimated. Additionally, TPD data from passenger trains will be measured and added to the lateral loading table for use as input loads for design.

10.5.3 Longitudinal Wheel Loads

The magnitude and distribution of longitudinal loads is not well understood compared to the other two loading types. This is partially due to there being no wayside detectors that quantify the magnitude of longitudinal loads from passing trains. One technology that could be used to measure these loads is an IWS. An IWS is a wheel set that has strain gauges on the axle and wheel. An IWS can be deployed on any vehicle type and will measure vertical, lateral, and longitudinal forces. Since this technology is on the rail car rather than at a discrete wayside location, the nature of the data that is collected is different from TPD and WILD sites.

An IWS gives an in-depth understanding of the forces on a single wheel as it moves over a given route. However, to develop an understanding of a variety of car types, the number of wheel sets and the volume of data would be prohibitively large. Given how longitudinal load is transferred,

the use of an IWS may be the appropriate approach to quantifying loads, as longitudinal load might not be as closely tied to car weight as vertical and lateral loads are. Longitudinal load cannot be classified according to wheel loads like vertical and lateral loads. Longitudinal loads will vary according to the tractive effort of the locomotive and the braking characteristics of the train (e.g. condition of brakes, length of train, etc.). Longitudinal loads are also present without train-induced forces, due to thermal stress in the rail.

Because of these characteristics, simply examining the distribution of wheel loads and determining the appropriate threshold is not an appropriate method to determine the input load for design. It is also not completely understood how the longitudinal load is transferred through the fastening system and into the crosstie. Most previous research within the realm of longitudinal forces has focused on bridge approaches, examining braking load magnitudes. Some of the factors that are believed to have the greatest effect on longitudinal load magnitude are train speed, track geometry, vehicle characteristics, curvature, grade, position of the wheel within the train, geographic location, and temperature. Of particular interest is the relationship between longitudinal load and track geometry (tangent vs. curve) as well as gradient. In the future, research should be conducted to investigate typical values of longitudinal load in tangent and curved track, varying the acceleration and braking characteristics of the train as well as the clamping force of the fastening system.

Absent other data, the values provided in Table 63 from AREMA (Table 30-1-1 in manual) can provide an estimate for longitudinal load magnitude.

Table 63. Longitudinal Wheel Loads

	Mainline Freight	Light Density Freight	High Speed Passenger
Longitudinal Load (kips)	50	30	25

10.6 Load Transfer

After establishing the distribution of the wheel load environment, the next step in the mechanistic design process is to determine how these wheel loads are transferred through the system. As the wheel loads from trains are transferred through the concrete crosstie and fastening system, each component attenuates and distributes the load to the next component in the system.

10.6.1 Qualitative Establishment of Load Path

At their core, mechanistic design practices use actual loading data to develop a design that functions adequately under the expected loading conditions. To better determine the demands on each component, an analysis of the static load path was conducted at UIUC. This analysis underwent several iterations with increasingly complex assumptions. This static analysis of interface loads and component deflections, described in the following sections, helped to establish the locations for load transfer that may require additional analysis.

Given a particular input loading condition and the appropriate simplifying assumptions, the magnitude of forces at each interface can be determined. UIUC is developing a I-TRACK that accepts particular input parameters, such as material and geometrical component properties, and

calculates forces at interfaces and deflections of components and the system as a whole. Using I-TRACK, the spectra of loads such as those shown in Figure 293 can be traced throughout the remainder of the fastening system (and the crosstie, ballast, and subgrade), providing estimates of the magnitudes of forces to be measured at each interface given a particular traffic type.

In addition to this initial analysis, the effect of accelerating wheel loads and clamping force on longitudinal forces must also be considered in a comprehensive exploration. Because many simplifying assumptions were used to complete this initial investigation, its results should be considered as estimates, providing feasible values to be compared with other load quantification efforts. To evaluate the loads within the system more accurately, laboratory and field instrumentation and FE modeling techniques were employed. The detailed load path discussion and analysis culminated in the result shown in Figure 295.

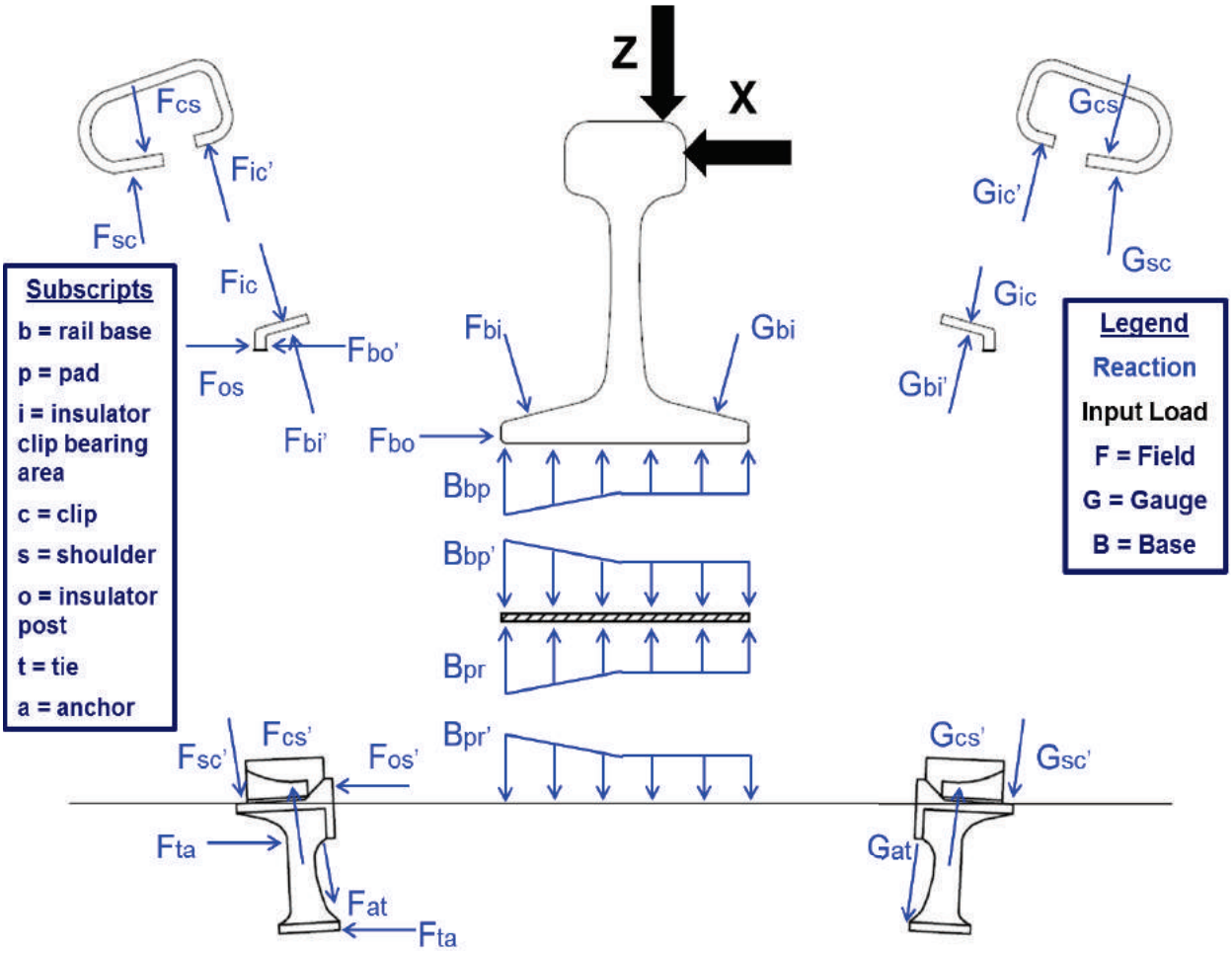

Figure 295. Concrete Crosstie Fastening System Load Path Map and Component Free Body Diagram

10.6.2 Laboratory Experimental, Field Instrumental, and Analytical Modeling

After identifying locations where the load is transferred throughout the system, it is necessary to quantify the loads that were previously derived through a qualitative method. This quantification

process defines the demands on each component, focusing primarily on determining the magnitude of forces that are transferred at component interfaces.

Given the continuous and elastic nature of the track structure, each component in the system will not be subjected to the full wheel load. As the wheel load is distributed throughout the system it will be transferred to multiple components longitudinally and will be attenuated as it transfers through components. Thus, each component will have its own input load that will be some percentage of the initial wheel load that is measured at the wheel-rail interface. Determining what portion of the input wheel load is imparted on each component is challenging due to the variability of many factors such as track stiffness. As the component geometry varies, either due to design changes or wear, the load path will also change. A change in the load path could result in the magnitude of the force on each component changing, thus changing the requirements for the strength. This creates a circular relationship within component design. The load distribution will guide the design of a component, but as the design (e.g. geometry) changes the load distribution will further change.

Given these conditions, determining what load is actually imparted on each component of the crosstie and fastening system is not as simple as quantifying the initial distribution. Laboratory experimentation, field experimentation, and FE modeling can be used to quantify the variables. Laboratory experimentation is discussed in Volume 2, Chapters 3 and 4, field experimentation in Volume 2, Chapters 5 and 6, and analytical modeling in Volume 2, Chapters 7 and 8. The results of all three of these methods are summarized in Volume 1, Section 3.

10.7 Define Design Criteria

After gaining an improved understanding of the loading environment, the current geometry and material properties of the components must be evaluated to determine whether those properties are appropriate for the expected loading environment. If not, alternative component geometries or materials that perform better in response to the loading demands should be pursued.

The proposed design process is referred to as a limit state design. In limit state design, the design of each component is based on load-related failure modes. Each type of failure can be traced to the component loads and the specific properties that were exceeded. A failure is defined as a change in the behavior of an object such that it can no longer perform its intended function. For example, failure of a rail clip would be any condition that causes the rail clip to no longer provide the desired amount of clamping force.

In order to prevent failures from occurring, certain design criteria must be developed. These design criteria will be defined for various material properties, such as tensile strength or compressive strength. The appropriate value of the criteria will be determined based on safe system operation. Safe system operation refers to the process of reducing the probability of a failure in order to minimize the chance of an accident. Each component will have an associated probability of failure. Depending on the severity of a failure occurring, the acceptable probability of failure may change, with a severe failure requiring a lower probability of failure.

Limit states can be divided into two primary categories; ultimate and fatigue. An ultimate limit state is defined by a failure that can be caused by a single loading event that exceeds a certain

threshold. For example, a very high impact load could result in the cracking of a crosstie. This category of failure would require a low probability of failure, to ensure that this type of failure is unlikely to occur during the design life of a component. For example, if a concrete crosstie has a 50-year design life, the chance of a load occurring that would cause that crosstie to crack should be less than once in 50 years. Fatigue limit states are time-dependent failures where repeated loading over a period of time can result in the failure of a component through wearing or other mechanisms. For example, a concrete crosstie rail seat could gradually abrade over time until it reaches a level that causes the rail to roll. This would require an estimation of the amount of tonnage that the track will experience during the component's lifetime in order to determine the total fatigue demands (Kaewunruen 2011).

To test that the various design criteria are met, an approach using both nominal and required strength will be used. The nominal strength is an approximation of the actual strength of a component. This can be determined by performing laboratory tests and stressing the component until failure occurs. In this stage, a reduction factor should be included to account for the acceptable probability of failure of the failure mode type. A more critical failure will have a higher reduction factor, which reduces the estimated strength of the component. This reduction factor should also consider the variability of test results, which are largely a function of the type of material being tested or variation of component geometry.

To determine if the nominal strength is adequate, the required strength needs to be determined. The required strength refers to the amount of strength required to resist the load. This required strength depends on the input wheel load, and is a function of different load thresholds. The input load used will also depend on the type of limit state that is being tested. Ultimate limits will require a high percentile load, while fatigue limits will require a load closer to the average, as it is based on a failure that occurs over a longer time scale. Based on the load imparted on the object, the required strength can be determined. This required strength must be less than or equal to nominal strength multiplied by the reduction factor. This ensures that the tested strength of the object meets the predicted demands and will be unlikely to fail given the operating conditions. This approach is similar to the Load and Resistance Factor Design (LRFD) process used in structural design.

The proposed design criteria will be split into categories based on where the design fits into the overall process of designing a concrete crosstie and fastening system. There will be different critical properties and acceptable limit states based on what aspect of the component and system is being designed. The design criteria can be split into three categories: material, geometric, and assembly.

10.7.1 Material Design Criteria

Material design criteria are design properties that are based solely on the material that is used to in the fabrication of components. The critical material properties in need of specified criteria are compressive strength, tensile strength, flexural strength, shear strength, stiffness, wear resistance, and fatigue strength. These tests should be the same for all types of fastening systems, as they do not depend on the geometry of the components or the load path in the system. These material criteria will depend on a variety of factors, such as the environment and the tonnage. The environment can affect required wear resistance based on the prevalence of moisture and fines.

For instance, environments with a high likelihood of moisture intrusion of moisture and fouling fines will require more strict wear resistance requirements. Tonnage (e.g. both axle load and number of load applications) will help determine how critical fatigue is, as it will determine the number of cycles per year that the components experience. Higher traffic levels will increase the likelihood of fatigue failure occurring before the design life of the component is reached.

10.7.2 Geometric Design Criteria

Geometric design criteria are design properties based on the geometry of the components. The critical properties are the same as the material design criteria, and include compressive strength, tensile strength, flexural strength, shear strength, stiffness, wear resistance, and fatigue strength. However, the acceptable limits of the design criteria will change, as the strength will depend on both the material properties and geometry of the component. This stage of design criteria will consider the load distribution and what percentage of a typical wheel load will be imparted on each component. This can be used to calculate the input load and therefore determine the stresses and strains on each component. These stresses and strains can then be used to determine the required strength for each property.

10.7.3 Assembly Design Criteria

Assembly design criteria are design properties that are based on the performance of the fully assembled crosstie and fastening system. This system design testing should be conducted in a laboratory setting, to avoid variation due to support conditions. Critical properties to develop design criteria for include contact pressure, relative displacement, and wear resistance. These should be measured at interfaces between components, to determine if the system is behaving in a way that will result in good long-term performance. For example, high pressures between two interfaces can result in damage to the components and require that they be replaced. These design criteria will limit the contact pressure to a level that will not cause excessive damage for the design life of the component. As different types of fastening systems will have different components, the interfaces will also vary, thus these criteria are fastening system dependent.

10.8 Design Process

After the aforementioned design criteria are selected, the component design process can begin (Figure 292). The first step is to select the desired load threshold. This will determine the value for the required strength. The required strength is then compared to nominal strength. A material is selected and tested according to the defined material design criteria. If all material-level design criteria are not met, then a new material will need to be chosen or the existing material modified until all material design criteria are met. After the material passes, the geometry of the component should be designed. The component will then be tested for all geometric design criteria. If any criteria are not met, either a new material should be chosen, or the geometry should be modified. If a new material is chosen, the material criteria will need to be checked again before continuing. After passing the geometric criteria, the assembly criteria will need to be tested. If any assembly criteria are not met, a new material or geometry should be chosen, retesting material or geometric criteria if changes occur. Following successful completion of all assembly design criteria, the crosstie and fastening system can move to the system verification process.

10.8.1 System Level Verification

The system verification stage of the design process confirms that the design is adequate and will perform as expected in revenue service. In this stage, representative support conditions are included to account for all possible forms of variability that could affect the performance of the system. Critical properties to consider include maximum ballast pressure, maximum subgrade pressure, total track deflection, and track modulus. Historically, this is accomplished by installing the fastening system in a section of revenue service track, to test whether the system will perform well over time. Another way to test this would be using an analytical model, such as the FE model developed by UIUC, which would have the capability of checking the values of critical system properties. This approach would be more cost effective than field testing as the physical components would not need to be manufactured. It also would be faster, as producing the components requires more time as compared to a simulated setting. If the critical properties were exceeded, then the fastening system could be further modified until it exceeds the required system level design thresholds. The system will still need to be tested in the field, but this approach should avoid the costly process of physical design iterations. Once the system passes all the tests in a simulated setting it can be deemed ready for revenue service.

Another possibility for testing a given design would be to install it in the TLS at UIUC (see Volume 2, Chapters 3 and 4 for additional information). The TLS has representative ballast and subgrade conditions, as well as realistic loading conditions. Once the concrete crosstie and fastening system has been produced, the TLS can be used to measure critical system properties, and test whether system level design thresholds are exceeded.

10.9 Design Process Examples

To illustrate the mechanistic design process that was introduced in this chapter, several examples using existing fastening system components are presented. These examples will demonstrate how the new design approach works, and will describe ways that this new process can improve the performance of the system. These examples are not meant to be a comprehensive set of all possible applications of mechanistic design for concrete crossties and fastening systems, but are intended to provide examples of potential ways to mechanistically design select components. Each component design section will follow a general outline as described below:

1. Description of the current design process
2. Design example using the current design process
3. Discussion of potential improvements to the current design process
4. Design example using the revised current design process
5. Discussion of future work to meet a fully mechanistic design

The four design examples are the rail pad assembly, insulator, concrete crosstie, and rail seat load distribution. The final example is intended to provide a new mechanistically-derived design test for verifying the performance of the rail seat area.

10.10 Resilient Rail Pad Assembly

10.10.1 Current Status

A variety of rail pad designs are used throughout the world and new types are added regularly to keep up with changes in design requirements, loading demands, and material supply. In North America, the rail pad assembly is typically composed of a resilient rail pad on top of an abrasion resistant plastic frame. This sub-system has already seen significant design variation through attempts to solve failures mostly related to wear and degradation of the fastening system. Previous single layer rubber pads were superseded by multiple layered plastic pads to withstand the increasing loading demands by attenuating the cyclic wheel loads without compromising the integrity of the fastening system and concrete crosstie.

The majority of railway design codes and recommended practices typically contain a section dedicated to specifications and design qualification testing for the rail pad assembly. Despite some performance requirements and other specific testing protocols, none of them provide a mechanistic approach to evaluate the behavior of this component. For instance, the AREMA recommended practices lack information regarding threshold choices that are key parameters in understanding the performance of the rail pad assembly. As an example, rail pads are not classified according to their stiffness, which is a property that dictates their capacity to attenuate the loads transferred from the rail to the crosstie. As a result, there is no standard specifying the amount of damping the fastening system should provide for different loading environments and track geometries. Moreover, no pass/fail criteria are specified for some of the suggested qualification testing, and the standards only provide a description of the experiment to be conducted.

The portion of the AREMA recommendations focusing on rail pads is classified into sections on material properties and evaluative tests. The material properties are related to American Society for Testing and Materials (ASTM) tests that should be performed for the evaluation of suitable materials to be used in the manufacture of rail pad assemblies. However, not all of the tests were made for plastics, as they only contain specifications for rubber materials, which are rarely used. The evaluative tests attempt to qualify the performance of the rail pad when subjected to standardized loading environments. They provide an initial evaluation of the stiffness, resilience, and damping capabilities of the component, but they do not address important factors that contribute to rail pad assembly performance. Supporting conditions of the crosstie, effects of lateral and longitudinal loads, and the variation of the COF between components are parameters that greatly contribute to the system behavior, controlling the transfer and distribution of loads. Addressing these conditions is of paramount importance when developing mechanistic design recommendations for a component that will be subjected to severe loading environments during its service life.

10.10.2 Design Process Overview

The design process for rail pad assemblies is not directly addressed in AREMA. AREMA imposes material properties and performance requirements that should be complied with by the different designs of this component. These requirements are divided into two main sections: material properties and evaluative tests.

The material properties section specifies the ASTM tests that should be performed on the materials considered to be used in the manufacture of this component. Further details can be found in Section 1.7.3.4 of AREMA Chapter 30. These tests primarily cover the following properties: hardness, compression, tensile strength, ozone resistance, abrasion resistance, volume resistivity, resistance to fluids, and Vicat softening temperature. The second section on evaluative tests describes qualification tests for the rail pad assembly and provides some geometry requirements. The crosstie rail pad test measures the load-deflection properties of the rail pad assembly. The experimentation consists of applying dynamic and static loads to a fastening system setup, while measuring the rail pad deflection. The test criteria is specified in Section 4.9.1.15 of AREMA Chapter 30 and requires that the pad assembly should return to within 0.002 in (0.051 mm) of its original position after the load is removed. Additionally, the spring rate calculated from three different specimens should not vary more than 25%. No explanation is given regarding the choice of these thresholds or possible effects on the track components if these criteria are not met. Even though this test is able to provide a simple evaluation of the rail pad assembly's stiffness and resilience, it fails to provide a deeper understanding about the load distribution and behavior of the component under realistic loading scenarios, where lateral loads and shear forces are present.

The rail pad attenuation test was designed to determine the ability of the rail pad assembly to attenuate the effects of impact loads. In this test, strain gages are attached close to the bottom of the crosstie to measure the strain resultant from a 115 lb weight dropped from a height of 12 in, simulating an impact load on the head of the rail. Further details about the test set up can be found in Section 2.5.2 of AREMA Chapter 30. The result is presented relative to a measured control strain when a 5 mm ethylene vinyl acetate flat rail pad is used on the fastening system. There are no criteria for the results obtained from this specific test. Therefore, these tests simply provide an initial evaluation of the stiffness, resilience, and damping capabilities of this component, without addressing important factors that contribute to the rail pad assembly performance.

The development of recommended practices based on a mechanistic design approach would significantly contribute to improved performance and life cycle of components. Factors including pressure distribution, load path, energy dissipation, and geometry tolerances must be addressed in the codes, especially after recent studies having demonstrated the high capability of these parameters to change the behavior of the track structure and fastening system components (Rewczuk 2012).

According to AREMA, rail pad assemblies do not have a specific design process. They must have a minimum 5 mm thickness and should comply with the material properties and evaluative test requirements described in the "Tie Pad Test" and "Impact Attenuation Test" sections (AREMA Chapter 30 Sections 2.5.1 and 2.5.2). Manufacturers usually take into consideration traffic characteristics, train speed, and maximum track deflection to choose the appropriate material and stiffness. However, this is generally an empirical process, based on trial and error given the lack of guidance in the current AREMA recommended practices.

10.10.3 New Design Methodology

Uncertainties related to the cause of fastening system deterioration due to a lack of understanding regarding the mechanical interactions among components has led the rail industry to pursue design modifications. Attempts to enhance the life cycle performance of components were developed based on empirical design approaches. These approaches usually rely on increased robustness and stiffness to overcome the loading demands and withstand wear rates. An improved design methodology for rail pad assemblies should be based on a mechanistic approach, where material properties, relative displacements, stress distribution, and component deformation are taken into consideration when optimizing its geometry and performance. The following topics present suggestions for modifications AREMA Chapter 30 that would contribute to the development of improved rail pad assemblies.

Materials Choice

The materials choice should be based on stress capacity (compressive and shear), abrasion resistance, and damping properties. FE model analyses and field experimentation are capable of determining peak loads and stresses distribution for a variety of loading cases. Computer simulations can assist component manufacturers to choose the appropriate rail pad assembly compressive and shear strength according to the intended service level and loading demands.

The material's abrasion resistance should be able to withstand the usual wear rates measured for the intended type of application. For this reason, it would be helpful for railroads to collect data regarding rail pad assembly wear rates. A correlation between wear rates and track service conditions such as tonnage, degree of curvature, and grade would be extremely beneficial when determining appropriate abrasion resistance each rail pad should have for specific operating environments. For example, the desired damping properties can be assessed using dynamic tests of energy dissipation, which would determine the materials that are more efficient in absorbing and distributing cyclic vertical and lateral wheel loads.

Design Specifications

Rail pad designs should minimize the relative displacements of the rail pad with respect to the rail seat surface and rail base. Previous studies indicate that this will reduce the risk of abrasive wear and premature deterioration of materials (Kernes 2013). Incorporating stricter geometric tolerances for the manufacture of track components (e.g. concrete crosstie rail seat profile, shoulder spacing, etc.) will provide a tighter fit of the components assembly, preventing the occurrence of gaps and displacements in the fastening system. Excessive moisture and fines may occur in such gaps, contributing to the deterioration of components.

The shear deformation of rail pad assemblies should also be investigated as a viable way of dissipating the energy that goes into the system without generating potentially damaging displacements between components. Finally, new recommended practices should be created in order to address the desired characteristics for this component behavior, optimizing its performance and life cycle.

Improved Evaluative Tests

Improved evaluative tests would enhance the current methods for assessing rail pad assembly performance and prevent possible failure modes from occurring in revenue service. The recommended practices should contain tests with additional details and specifications on rail pad stiffness, impact load attenuation, and rail seat pressure distribution. The rail pad assembly stiffness test can be improved with the inclusion of stiffness thresholds, to classify the components according to their load-deflection properties (soft, medium, hard). This specific action would allow for unique designs for different service applications and would also provide valuable information related to the material's resilience. The load magnitude and frequency should represent the usual demands encountered for each specific application (e.g. heavy haul, high speed passenger rail, shared corridors, etc.) with cycles representing the repetitive axial loads acting on the rail head for a standardized train pass

The impact attenuation test can also be modified in order to consider more realistic support conditions, using ballast to guarantee an adequate representation of bearing forces. The Australian and European Standards (AS, EN) give the option of using aggregate to support the crosstie. This should also be included in AREMA as a test parameter. More realistic support conditions would provide a better sense of the strains generated at the bottom of the crosstie when impact loads are imposed on the rail. Additional recommendations should also be made on the loads applied to the rail head. These loads need to be more representative of the IF observed in the field, for both vertical and lateral directions. WILD data analysis is a good source to extract realistic impact loads for an improved impact attenuation test.

The rail seat load distribution should be assessed in a standardized test, which could make the use of pressure sensors to determine how effective the rail pad is in distributing the forces in the rail seat area. Researchers at UIUC have proposed a novel index for this measurement, which could be an innovative parameter to evaluate the effectiveness of rail pad designs in distributing the wheel loads.

Path Forward

The study of rail pad assembly mechanical behavior presents several challenges to relating the component responses to the failure modes observed in the field. Usually described as one of the driving mechanisms of RSD, abrasion has been correlated to the occurrence of relative motion at the rail seat, specifically rail pad relative displacements. Even though this study was able to successfully quantify the magnitude of displacements, further investigation must be conducted to establish their relationship to wear rates generated at the concrete crosstie rail seat. Laboratory tests similar to the improved AREMA Test 6 (Tie and Fastener System Wear/Deterioration Test) proposed by Kernes (Kernes 2013) could be a starting point to determine how wear rates are related to rail pad assembly displacement magnitude and loading cycles.

Field research conducted under this program provided results with a strong indication of shear slip taking place at the rail pad, since significant differences in translation magnitude were observed for this component when compared to the rail base displacements (Do Carmo 2014). In this study, it has been hypothesized that increased rail pad assembly shear slip may induce reduced forces being transferred to the insulator and cast-in shoulder in the lateral direction, since the deformation of the rail pad could absorb part of the energy that would be otherwise

transferred to other fastening system components. Future work could make the use of the LLED developed by Williams (Williams 2015) to determine if rail pad assemblies with different elastic moduli present variation in the lateral loads being transferred to the cast-in shoulder. If confirmed, this property could be used as a design parameter, taking the shear modulus and strength of materials into consideration during the development of improved rail pad assembly designs.

10.11 Insulator

10.11.1 Current Status

There are no component-specific tests for the insulator provided in AREMA Chapter 30. Instead, system-level tests are specified to ensure reasonable wear characteristics of the system. Electrical properties of the entire crosstie and fastening system are also tested and limited to a specified threshold. Tests for wearing properties (i.e. AREMA Test 6, Tie and Fastener System Wear/Deterioration Test) include visual inspection and measurements of each component before and after the test while tests for electrical properties (i.e. AREMA Test 7, Fastener Electrical Impedance Test) involve determining the ability of the tie and fastening system to resist conducting electrical current under wet conditions.

Under AREMA, the only design requirement for a new insulator involves running ASTM D257 to measure the material's electrical resistivity. Otherwise, no geometric parameters are specified nor are load-related specifications. As long as thresholds for AREMA Tests 6 and 7 are met (i.e. displacements do not exceed a maximum specified value and impedance values are above a specified minimum value), the insulator is considered acceptable.

10.11.2 Overview of Current Design Process

Under the current AREMA recommended practices, the first test would run under ASTM D257. This test is run on the insulator material to ensure the component has necessary electrical properties. This test has no threshold values, and is used to provide general information of the electrical resistance properties of the material and the resulting component.

AREMA Test 7 is the next step in testing the insulator. In this test, minimum electrical impedance values would be measured by applying a known electrical current between the two rails. Electrically isolating the rail from the shoulder and crosstie is a primary function of insulator, and this test is run to ensure proper electrical isolation is achieved. This is an appropriate test to run considering the most important function of the insulator is to electrically isolate the rail from the shoulder and crosstie. The component-level test that is run to ensure adequate electrical resistivity of the insulator (as well as the tie pad) should provide a good indication of whether this test will pass or fail. Regardless, this test should still be run to provide traceability through the entire mechanistic design process.

AREMA Test 6 is the next step in after the geometric design of the system is complete. In this test, maximum lateral rail head displacements are measured. In addition to protecting the cast shoulder and electrically isolating the rail from the shoulder and crosstie, lateral rail restraint is also a primary function of the insulator. Thus, lateral rail displacements are an indicator of

insulator performance, yet they are not specified in AREMA. Lateral displacements are a system performance indicator.

As a sample calculation, if the lateral rail head displacement is less than 0.25 inches, the insulator would pass the test and be considered an adequate component design, assuming allowable wear of the component is determined through visual inspection of the insulator. Missing from this test is a measurement of the lateral rail base displacement. Given the insulator is in direct contact with the rail base, this measurement would give valuable insight into the demands placed on the insulator. A maximum value would be the limiting factor with this measurement. This test is *not* rooted in mechanistic design because it is a wear and deterioration test of a fastening system that has already been designed. AREMA Test 6 is very much used in an empirical approach to designing fastening systems.

The combination of these tests is used for validation and comparison. The values for allowable wear and rail displacements as measured during Test 6 appear to be empirically derived from industry experience and not from a calculated, mechanistic approach. If a true mechanistic component design approach were to be used for the insulator, the electrical properties of the insulator material would be determined before any geometric design aspects were considered. However, because there should be an applied load test to test the ability of the insulator to withstand a specified load for a specified duration, material selection must be carefully considered. A proper balance of electrical resistivity and ability to withstand an applied load must be determined for insulator mechanistic design.

10.11.3 New Design Methodology

A mechanistic component design process for the fastening system insulator has four steps: selecting load thresholds, selecting component material; designing component geometry, and verifying component performance at the system level.

Load Threshold Selection

Using lateral fastening system force measurement data obtained from both field and laboratory experiments and FE modeling results, load thresholds (i.e. low, medium, high) should be designated. Applied wheel loads should also be designated for system level verification tests. Load threshold selection includes designating the magnitudes of applied forces on the component and system that a given percentage of all applied forces will statistically fall below (i.e. confidence level) the load.

Material Selection

Material selection should be made based on specific material properties. For an insulator, relevant material properties include electrical resistivity, compressive strength, tensile strength, flexural strength, shear strength, stiffness, wear resistance, and fatigue characteristics. The material properties should take into consideration the lateral force data described earlier. Tests for material properties should be conducted on samples of the material to ensure the material withstands applied stresses and displacements up to maximum values defined by either the fastening system manufacturer or end user (i.e. railroads).

Geometric Design

Once the material is selected, the geometry of the component can be designed. The geometric characteristics should take into consideration the applied forces and optimize necessary bearing areas to stay below maximum limits of the material (e.g. compressive strength, tensile strength, etc.). Although the component material has already been tested, component tests should be run to ensure proper bearing areas and stresses are as designed now that geometry has been selected.

System Level Verification

Once material selection and component geometry design are complete, verification of the component through system level testing can be conducted. The verification test should be conducted on a fastening system installed on a concrete crosstie. The applied loads should be based on the selection of the load threshold from step one.

10.11.4 Example

Load Bounding Method

The design load for the component should be based on lateral fastening system (FS) force data selected from Table 64 that was obtained through field experimentation. A threshold should be chosen using the field data and based on the probability that a certain percent of anticipated loads will fall under a specific load.

Table 64. Lateral fastening system forces - Peaks

	Peak Load (lbf)				
	Mean	95%	97.50%	99.50%	100%
Force on Shoulder[1]	2,020	5,501	6,414	7,408	7,883

[1] Source of data: Transportation Technology Center, Pueblo, CO, May 2013

Sample selection:

- Choose 95% confidence threshold
- 95% of lateral FS forces fall below 5,500 lbf (based on field data)
- Design FS force → 8,000 lbf

The design load for the system level verification tests should be based on lateral wheel load data obtained in the field (Table 64). A threshold should be chosen using the field data and based on the probability that a certain percent of loads will fall under a specific load magnitude.

Sample selection:

- Choose 95% confidence threshold
- 95% of lateral wheel loads fall below 26,000 lbf (based on field data)
- Design wheel load → 26,000 lbf

Material Selection – Electrical Resistivity

A sample of the material used in the insulator should be tested to meet necessary electrical resistivity. Apply 10 volts AC 60 Hz potential between each end of the sample piece of material. After measuring the current flow between the two points, the calculated resistance of the material should be greater than or equal to 10,000 Ω.

As a sample calculation, if the electrical impedance between the two rails is measured to be greater than 10,000 Ω, the insulator would pass the test and be considered an adequate component design.

Sample calculation:

$$\frac{\text{Applied Voltage (V)}}{\text{Current Flow (A)}} = \text{R}$$

$$\frac{10{,}000\ \text{V}}{0.00094\ \text{A}} = 10{,}638\ \Omega \rightarrow \text{Pass}$$

Material Selection - Applied Load

A sample of the material used in the insulator should be tested to meet necessary load vs. deflection requirements. Apply 10,000 lbf to a 0.5" x 4" x 0.25" (L x W x H) sample piece of material and measure displacement in direction of applied load. After applying load 10 times for one second each, generate a load versus displacement curve. The slope of the linear trend line should be less than 150,000 lb/in (defined by either the fastening system manufacturer or end user (e.g. railroads)).

Sample calculation:

$$\frac{\text{Applied Load (lbf)}}{\text{Displacement (in)}} = \text{S}$$

$$\frac{10{,}000\ \text{lbf}}{0.0714\ \text{in}} = 140{,}000\ \text{lbf/in} \rightarrow \text{Pass}$$

Geometric Design – Stress on Bearing Areas

The insulator bearing area on the shoulder should be designed in a way to ensure stress limits are not exceeded. Based on the design applied load (8,000 lbf) and the material's compressive strength (e.g. 25,000 psi), the bearing area of the applied load should be designed to ensure stresses fall under the material's limits. A safety factor could be used in the process to add an additional assurance to ensure stress limits are not exceeded.

Sample calculation:

$$\frac{\text{Applied Load (lbf)}}{\text{Compressive Strength (psi)}}(\text{S.F.}) = A$$

$$\frac{8{,}000 \text{ lbf}}{25{,}000 \text{ psi}}(2) = 0.64 \text{ in}^2$$

System Level Component Verification

Methods of measuring bearing areas and forces on the insulator should be developed to ensure the design values and actual values are equivalent. The measurements could be implemented on tests such as AREMA Test 6 to evaluate insulator design and actual performance in parallel with wear and abrasion testing.

Sample calculation:

$$\frac{\text{Measured Force (lbf)}}{\text{Bearing Area (in}^2\text{)}} = \sigma$$

$$\frac{7{,}250 \text{ lbf}}{0.68 \text{ in}^2} = 10{,}662 \text{ psi} > 25{,}000 \text{ psi} \rightarrow \text{Pass}$$

10.11.5 Path Forward for Insulator

More validation data from the field as well as from the FE model should be used and analyzed to make the revised design process a reality. An in-depth understanding of solid materials is necessary to finish the design process given that material selection is such an important factor in the design of fastening system components. Further full-scale testing on lateral loads and load distribution must be conducted to obtain more data that can be used for validation. Likewise, field full-scale testing should be conducted in parallel with FE modeling to expedite data analysis.

10.12 Concrete Crosstie

10.12.1 Current Concrete Crosstie Design Practices

Chapter 30 of AREMA 2014 (AREMA 2014) contains the current recommended design practices for concrete crossties. Section 4 of AREMA Chapter 30 provides considerations for materials, physical dimensions, flexural strength, longitudinal rail restraint, lateral rail restraint, electrical properties, testing, ballast, special track, and repair. Section 4 also includes recommended practices for shipping, handling, application and use of concrete crossties. Flexural strength and testing are separated by type of concrete crosstie, prestressed monoblock, and two-block. The following text will focus exclusively on the current methods of determining flexural strength of standard prestressed monoblock concrete crossties, found in Section 4.4. Section 4 starts with general considerations and assumptions, these will be explained further below.

Crosstie Spacing

Crosstie spacing affects rail and crosstie flexural stresses and the bearing stress on ballast (or other support). If crosstie dimensions and ballast conditions are held constant, an increase in crosstie spacing results in a decrease in track modulus (larger track deflection upon loading). Recommended crosstie spacing in AREMA Chapter 30 is between 20 and 30 inches.

Crosstie Dimensions

Section 4 of AREMA Chapter 30 specifies minimum dimensions for crossties. Length increase generally increases track modulus and provides larger distance for prestressing force to transfer from steel to concrete within the rail seat. Width increase also serves to increase track modulus and also provides larger bearing area on ballast, thereby reducing ballast bearing stress. An increase in depth often increases the flexural strength of the crosstie and the frictional area of ballast. The design criteria contained in Section 4 are valid for crossties between the minimum and maximum requirements shown below in Table 65. This report only focuses on the design of concrete crossties when the requirements in Table 65 are met.

Table 65. Dimensional Requirements for Pre-tensioned Concrete Crossties (AREMA)

	Minimum	Maximum
Length	* 7’-9”	9’-0”
Width	6” (top) / 8” (bearing)	13”
Depth	6”	10”
Rail Cant	1/45”	1/35”

* 8’-0” if no additional provisions to ensure adequate prestress transfer

Load Distribution

AREMA Chapter 30 states that wheel loads applied to the rail will be distributed to several crossties. Field investigations have been used to develop a conservative estimate of load distribution to a single crosstie. This is shown in Figure 296 below.

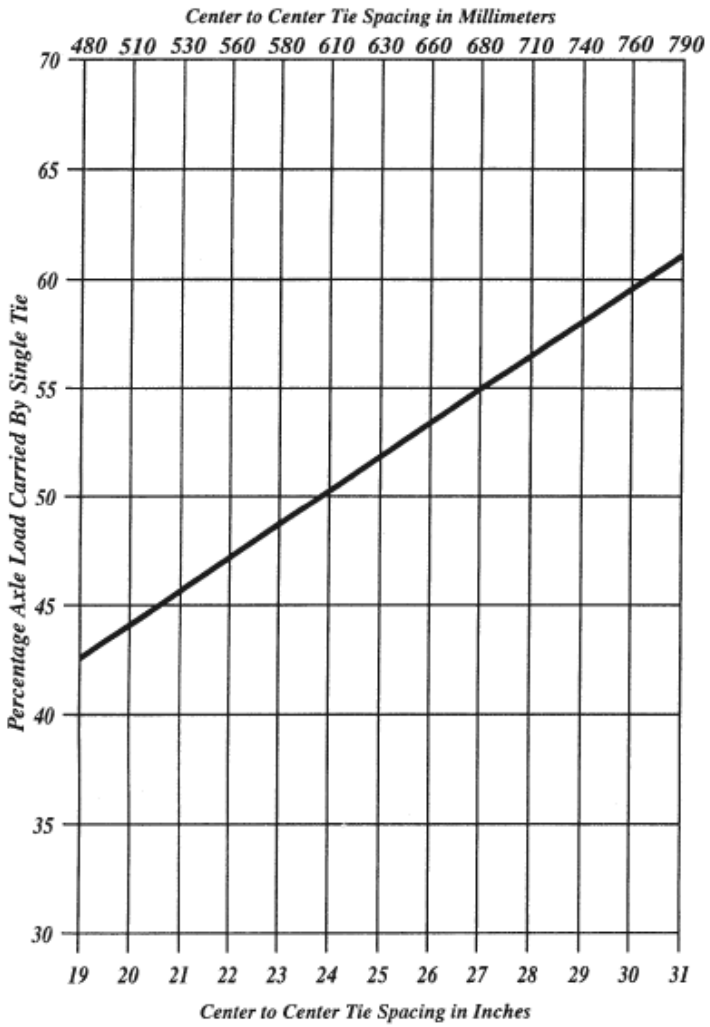

Figure 296. Estimated Distribution of Loads (AREMA 2014 Fig. 30-4-1)

Impact Factors

AREMA bases the design specifications listed in Chapter 30 on an assumed impact factor of 200%. In the calculation of rail seat load, this impact factor is added to 1, making the total impact factor 300% (static load multiplied by 3). The impact factor accounts for the increased loadings caused by track dynamics and wheel imperfections.

Flexural Strength/Design for Flexure

The mechanistic design of prestressed monoblock crossties for flexure is the main focus of the mechanistic design practices that are contained within this report. The design of any structure must begin with a structural analysis to determine the loadings that the structure will experience. In AREMA Chapter 30, this analysis takes the form of the empirically-derived factored design flexural strength values. There are four key locations on the crosstie: the rail seat positive bending moment, the rail seat negative bending moment, the center positive bending moment, and the center negative bending moment. These positions are shown below in Figure 297.

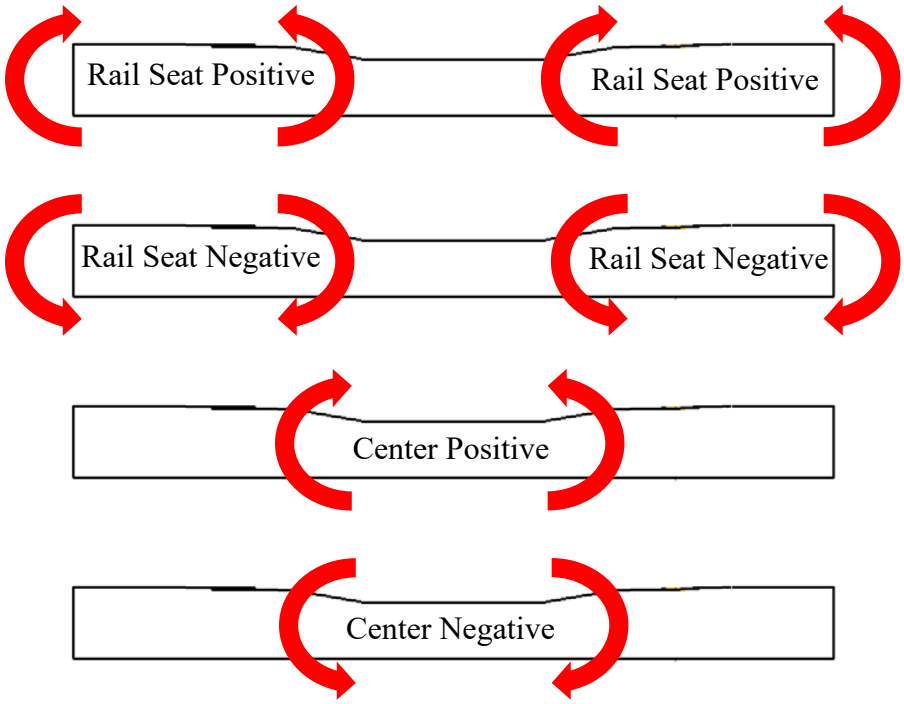

Figure 297. Critical Moment Locations

First, to determine the factored design bending moment for a given loading condition, Figure 298 is used. By specifying the crosstie spacing and the crosstie length, an unfactored rail seat positive bending moment can be found from Figure 298. Figure 299 is then used to determine the speed and tonnage factors, which are based on expected track speed and tonnage, respectively. These three values are then multiplied together according to Equation 1. For each figure, linear interpolation can be performed between two specified points.

$$\mathrm{M} = B \cdot V \cdot T \tag{1}$$

Where:

M = factored rail seat positive bending moment (kip · in)

B = unfactored rail seat positive bending moment (kip · in)

V = speed factor

T = tonnage factor

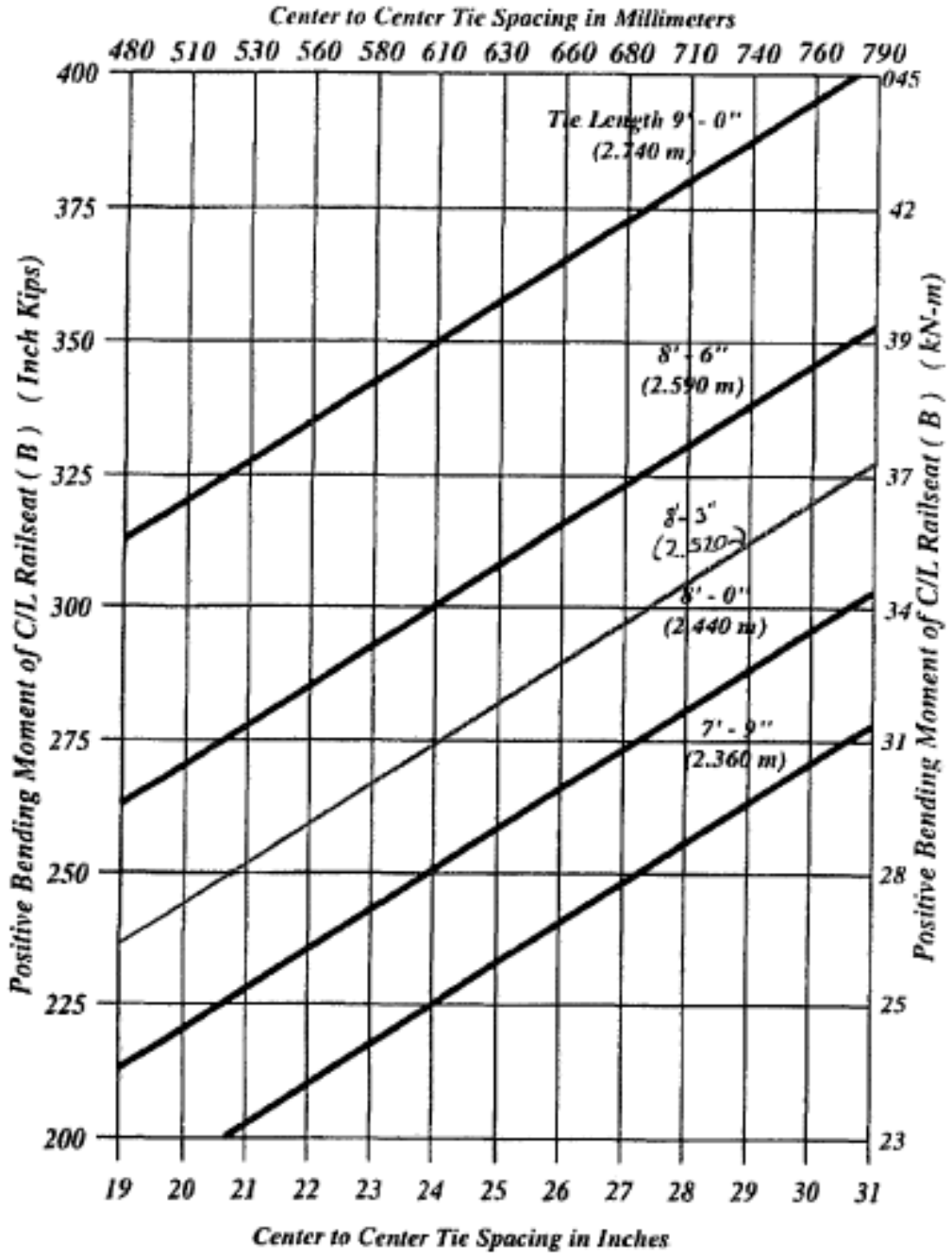

Figure 298. Unfactored Bending Moment at Rail Seat Center (AREMA 2014 Figure 30-4-3)

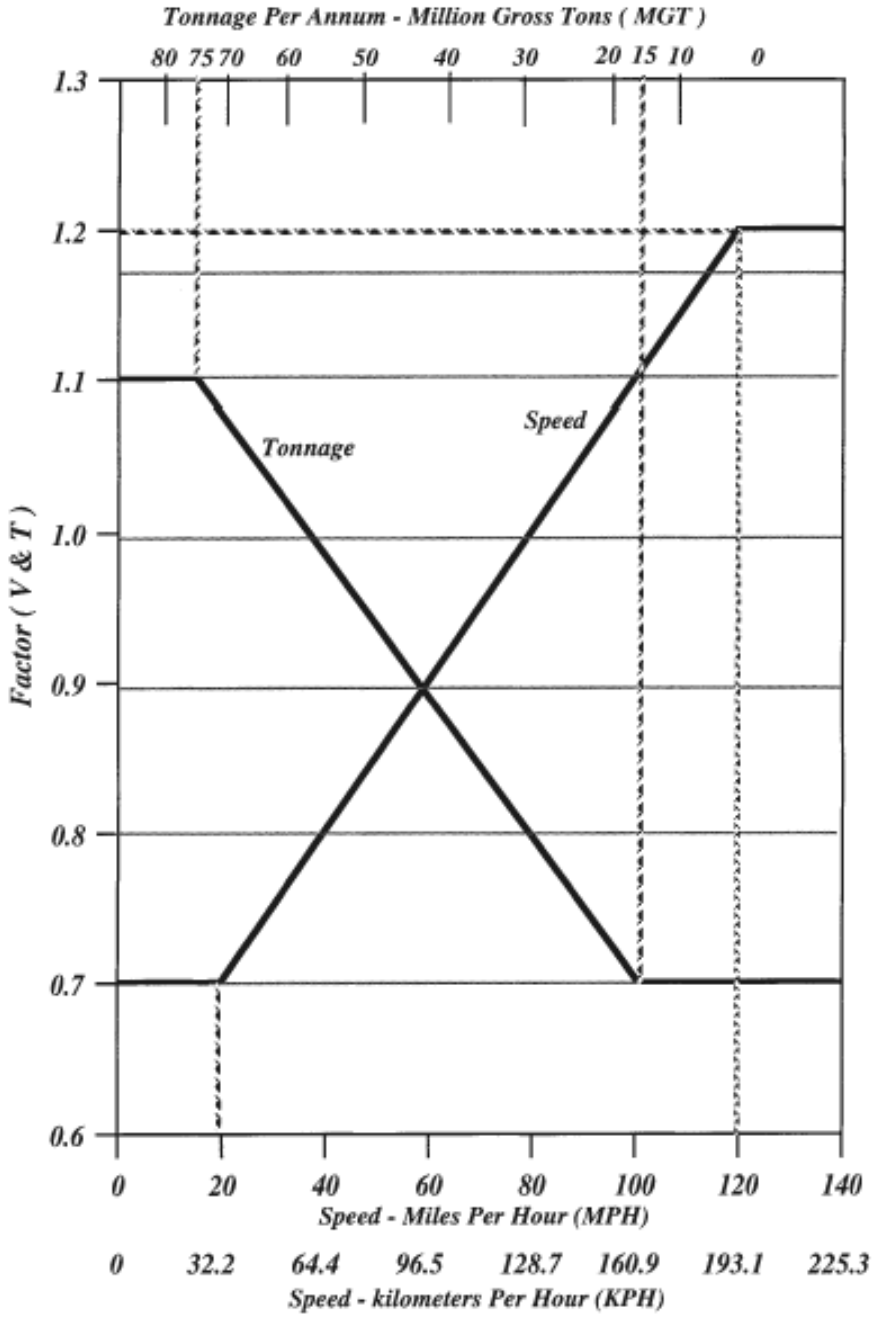

Figure 299. Tonnage and Speed Factors (AREMA 2014 Figure 30-4-4)

Once the factored rail seat positive bending moment is determined, it is further factored to determine factored bending moments at the other key locations. The factors are based on crosstie length and can be linearly interpreted, and are shown in Table 66 below.

Table 66. Bending Moment Factors (AREMA 2014 Table 30-4-1)

Tie Length	Rail Seat Negative	Center Negative	Center Positive
7′-9″ (2.360 m)	0.72M	1.13M	0.61M
8′-0″ (2.440 m)	0.64M	0.92M	0.56M
8′-3″ (2.520 m)	0.58M	0.77M	0.51M
8′-6″ (2.590 m)	0.53M	0.67M	0.47M
9′-0″ (2.740 m)	0.46M	0.57M	0.40M

Throughout Section 4.4 of AREMA Chapter 30 there are notes that allow for some freedom in crosstie design. AREMA allows for the factored design positive bending moment to be reduced due to the use of attenuating crosstie pads, which have been shown to reduce crosstie bending moment. AREMA also states that crossties with a larger bottom width at the rail seat than at the center (wasted section) will experience higher moments at the rail seat and lower moments at the center compared to constant bottom width crossties, which must be either considered in analysis or by increasing bending moment requirement by 10% at the rail seat positive and reducing by 10% at the center negative. AREMA recommends a maximum prestress after losses of 2,500 psi at all points in the tie. Furthermore, AREMA specifies a minimum prestress after losses and without any applied load of 500 psi.

In the design section, AREMA defines failure for two-block designs as cracks exceeding AREMA-specified allowable crack widths in Table 30-4-3. However, there are no explicit recommendations or specifications for failure of prestressed monoblock crossties. Instead, AREMA states that prestressed monoblock crossties must comply with ACI 318, “Building Code Requirements for Structural Concrete” specifications (ACI 2011). In ACI 318-11 prestressed concrete design requirements are included in Chapter 18. Serviceability design requirements for prestressed concrete for ACI 318-11 are shown in Table 67 below. From the table, it is assumed that prestressed concrete monoblock crossties are considered as Class U. Design of Class U prestressed concrete assumes uncracked behavior, allowing the gross section of the concrete to be used in calculation of the flexural strength capacity. Considering this, failure of a prestressed monoblock crosstie must be defined as cracking. In the testing methods section AREMA defines failure of the crosstie to be cracking extending to the first layer of reinforcement.

Table 67. Serviceability Design Requirements (ACI 318-11 Table R18.3.3)

	Prestressed			
	Class U	Class T	Class C	Nonprestressed
Assumed behavior	Uncracked	Transition between uncracked and cracked	Cracked	Cracked
Section properties for stress calculation at service loads	Gross section 18.3.4	Gross section 18.3.4	Cracked section 18.3.4	No requirement
Allowable stress at transfer	18.4.1	18.4.1	18.4.1	No requirement
Allowable compressive stress based on uncracked section properties	18.4.2	18.4.2	No requirement	No requirement
Tensile stress at service loads 18.3.3	$\leq 7.5\sqrt{f_c'}$	$7.5\sqrt{f_c'} < f_t \leq 12\sqrt{f_c'}$	No requirement	No requirement
Deflection calculation basis	9.5.4.1 Gross section	9.5.4.2 Cracked section, bilinear	9.5.4.2 Cracked section, bilinear	9.5.2, 9.5.3 Effective moment of inertia
Crack control	No requirement	No requirement	10.6.4 Modified by 18.4.4.1	10.6.4
Computation of Δf_{ps} or f_s for crack control	—	—	Cracked section analysis	$M/(A_s \times \text{lever arm})$, or $0.6f_y$
Side skin reinforcement	No requirement	No requirement	10.6.7	10.6.7

Testing of Flexural Strength

For a prestressed concrete monoblock crosstie design to be approved, there are a series of design validation tests that the crosstie must pass. These tests are explained extensively in AREMA Chapter 30, Section 4.9, "Testing of Monoblock Ties".

10.12.2 Numerical Example of Current Concrete Crosstie Design Process

The following section includes a sample calculation demonstrating the current design process specified by AREMA 2014 and explained in detail in the previous section. This system will be designed for a prestressed concrete monoblock crosstie 8'-6" in length, spaced at 24" on center for a corridor with an annual tonnage of 55 MGT and average train speed of 80 mph. This scenario is solely for example purposes.

1. Use pre-determined crosstie length of 8'-6" and spacing of 24" to determine the unfactored positive bending moment at the rail seat. This value can be determined from Figure 298. Figure 300 shows how this value is found. In this example, the rail seat positive bending moment is found to be 300 kip-in.

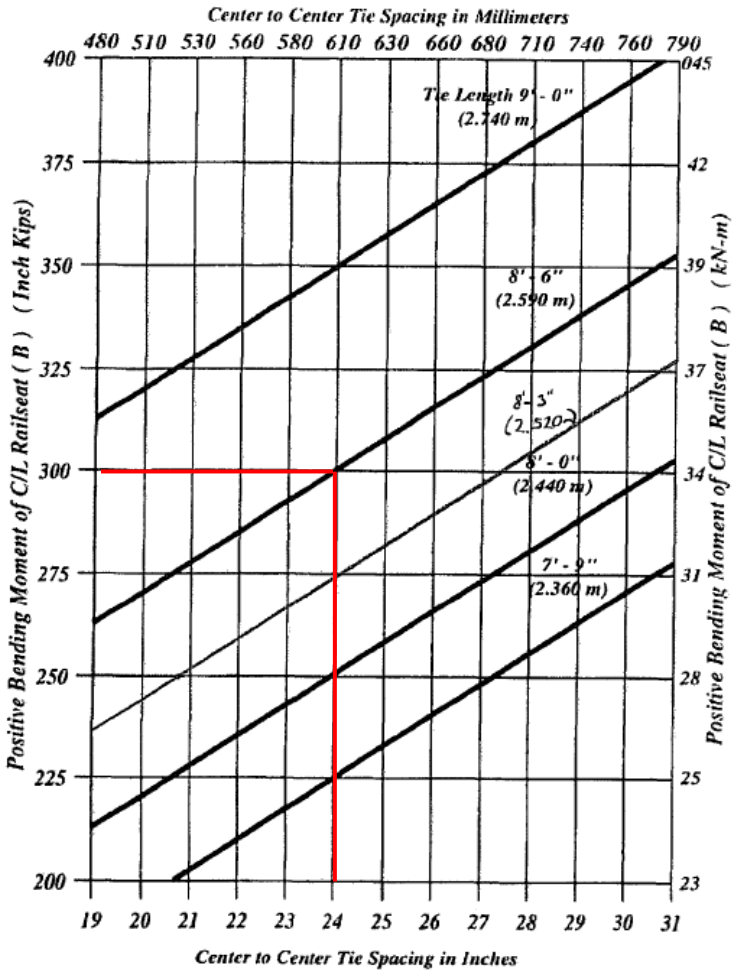

Figure 300. Determination of Unfactored Rail Seat Bending Moment

2. Next, the velocity (V) and tonnage (T) factors are determined using Figure 298. This determination is illustrated in Figure 305 below. In this example, the velocity factor (for 80 mph) is found to be 1.0 and the tonnage factor (for 55 MGT) is found to be 1.0.

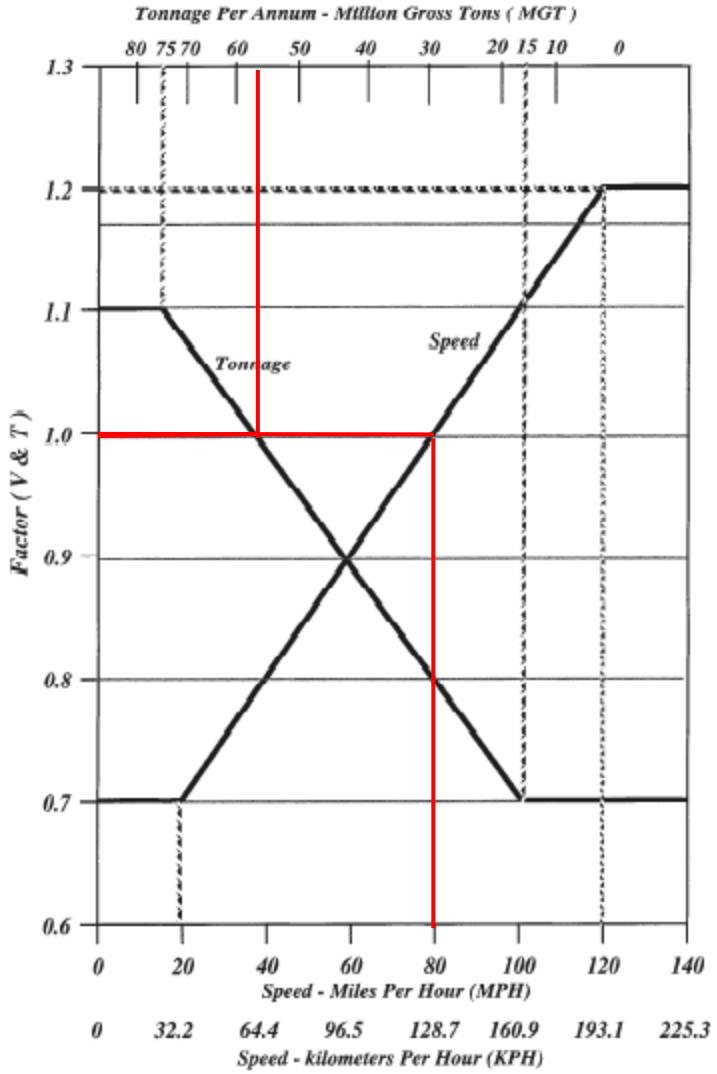

Figure 301. Determination of Velocity and Tonnage Factors

3. Next, factored design rail seat positive moment can be calculated. Using Equation 2, this value can be computed.

$$\mathrm{M} = B \cdot V \cdot T \tag{2}$$

$$\mathrm{M} = (300\ \mathrm{kip} \cdot \mathrm{in})(1.0)(1.0) = \mathbf{300\ kip \cdot in}$$

4. Next, the factored design bending moments can be determined using the crosstie length and the computed factored design rail seat positive moment (M) following Table 66. The sample calculations and results are shown in Table 68 below.

Table 68. Factored Design Bending Moment Calculations

	Positive	Negative
Rail seat	1.00M = 300 kip-in	0.53M = 159 kip-in
Crosstie center	0.47M = 141 kip-in	0.67M = 201 kip-in

5. The factored design moments listed in Table 68 can now be used to design a prestressed concrete monoblock crosstie. AREMA does not provide any recommendations on this process, other than specifying the minimum and maximum dimensions (shown in Table 65) and setting a minimum and maximum amount of prestress after losses. Instead, AREMA relies on empirical tests to validate the design. Thus, a crosstie designer must go through the design process unaided to design a crosstie that will pass the tests explained earlier in this report. Using the CXT 505S crosstie specifications as an example, the flexural strength values are given as applied loads, shown in Table 69 below. Below, these applied loads are converted to bending moments per AREMA to check that they exceed the factored design bending moments. CXT did not provide flexural strengths for rail seat negative or center positive, likely because rail seat positive and center negative are the most critical cases and often limit the design.

Table 69. CXT Test Loads

Section	Rail Set Load
Rail Seat Positive	61 kips
Center Negative	15 kips

Rail Seat Positive Flexural Capacity

The CXT-specified test load for rail seat positive bending is 61 kips. In the below equation, this is denoted as P, where M is the factored rail seat positive flexural strength, and x is the distance from the end of the crosstie to the center of the rail seat (for the CXT 505S, this distance is 21.16 inches).

$$\mathrm{P} = \frac{2M}{\frac{2X}{3} - 2.25"} \tag{3}$$

Solving the above equation for M,

$$\mathrm{M} = \frac{\mathrm{P}\left(\frac{2X}{3} - 2.25"\right)}{2} \tag{4}$$

Solving this equation for a CXT 505S, rail seat positive bending moment capacity can be found.

$$\mathrm{M} = \frac{61\left(\frac{2(21.16")}{3} - 2.25"\right)}{2} = \mathbf{362\ kip \cdot in}$$

This capacity exceeds the required bending moment found in Table 68, and theoretically should pass all tests related to flexural strength prescribed by AREMA.

Center Negative Flexural Capacity

A similar process is followed to compute the factored center negative flexural capacity. The CXT-specified test load for center negative bending is 15 kips. In the below equation, this is denoted as P and M is the factored center negative flexural strength.

$$\mathrm{P} = \frac{2\mathrm{M}}{27"} \tag{5}$$

Solving the above equation for M,

$$M = \frac{27P}{2} \tag{6}$$

Solving this equation for a CXT 505S, rail seat positive bending moment capacity can be found.

$$M = \frac{27(15)}{2} = \mathbf{203\ kip \cdot in}$$

This capacity exceeds the required bending moment found in Table 68, and theoretically should be pass all tests related to flexural strength prescribed by AREMA.

6. Finally, after the crosstie is designed, it must pass all tests specified by AREMA Section 4.9.

10.12.3 Comments on Current Concrete Crosstie Design Process

The design process specified by AREMA does not follow a mechanistic framework. There are also several very important factors that are either not considered or not specified. Below is a list of factors with a brief explanation of the factor and its importance.

- *No modifiable or justified dynamic amplification factor*:

  In Chapter 30, Section 4.1.2.4, a constant 200% impact factor is assumed. This value could change based on vehicle dynamics and track structure. As train tonnage and speed increase, this DAF could prove to be even greater (for example, see Table 60). This amplification factor needs to be adjustable so that designers and railroads can determine the factor of safety they want to include in the system. To consider the wheel load and wheel-rail dynamic interaction into design, AREMA uses another design chart (Figure 298) to scale the calculated unfactored bending moment. In this chart, AREMA uses train speed and annual tonnage as the two parameters to scale the design crosstie bending capacity; however, this is based more on statistics than dynamics and predicts a more general case. Wheel-rail dynamic interaction depends on more factors than just train speed and annual tonnage. For example, wheel profile, contact condition, and railcar suspension system all play a factor in dynamic and impact loading cases. In short, there needs to be more inputs in calculating DAF. The current design methodology may reach the requirement of the common case, but it neglects the destructive force of extreme impact loading, which could cause the failure of the track system.

- *Origin and assumptions for determination of bending moments is unclear:*

  Bending moments determined by AREMA 2014 Figure 30-4-3, speed and tonnage factors from Figure 30-4-4, and bending moment scaling factors found in Table 30-4-1 are all presented without explanation of origin. There is no indication of how these moments or factors were derived and what they are based on. After much review, it was found that the values in Figure 30-4-3 are likely found according to a 1983 P.J. McQueen paper titled “Introduction to Concrete Tie Systems” for an 82 kip axle load and uniform ballast reaction (McQueen 1983). However, the origins of Figure 30-4-4 and Table 30-4-1 remain unknown.

- *There is no consideration of the pad attenuation or the ballast support conditions:*

  Quantifying or assigning values to reflect these factors is very difficult, but not including them at all or even providing an assumption is unacceptable. Pad attenuation has been shown to significantly affect the loadings experienced by the crosstie along with its dynamic response. Ballast conditions, such as rail seat bound and center bound are not considered, instead opting for the improbable assumption of perfect ballast contact with the bottom of the crosstie.

- *There are no equations, recommendations, methods, or even defined limit states for crosstie design:*

  AREMA has put all the design responsibility on crosstie manufacturers. Chapter 30 does not suggest an equation or a method for determining the theoretical flexural strength of a crosstie, only providing a method of analysis. A limit state (i.e. cracking) is not explicitly stated in the design section.

10.12.4 New Design Methodology

Examples of design methodologies that are based in mechanics are seen in many other design codes worldwide. The two best examples of these mechanistic design methodologies are the UIC 713R specification and the Australian Standard (AS) 1085, Part 14 (Standards Australia 2003). As discussed previously, the AREMA determination of bending moments is empirically driven and difficult to follow and modify. The unfactored positive rail seat bending moment values shown in Figure 298 are likely based on the calculations found in McQueen's 1983 paper "Introduction to Concrete Tie Systems" (McQueen 1983). The origin of the speed and tonnage factors found in Figure 299 is unknown. Additionally, the origin of the factors presented in Table 11 is not officially stated, but they could be based on empirical data presented in McQueen's 2006 paper "Flexural Performance Requirements for Prestressed Concrete Ties by Factoring" (McQueen 2006).

To move toward a more mechanistic design framework, the AREMA analysis must shift from the current factored method to a mechanically-based analysis. UIC 713 and AS 1085.14 provided good examples for this, and both methods served as a template for the following proposed methodology. It is important to note that no current railroad design standard provides any recommendation for crosstie *design*, instead presenting only a recommendation for *analysis*.

Determine rail seat load

Following the current AREMA methodology for determining rail seat load, use Figure 296 to determine the distribution factor. The end user can define the unfactored wheel-rail load and impact factor or the designer can use the wheel-rail loads given in Table 58. It is important to note that the wheel-rail loads given in Table 58 already account for impacts, thus an impact factor of 0% should be used with these values. The design rail seat load (R) can be calculated using Equation 7.

$$R = WL \times DF \times (1 + IF) \tag{7}$$

where:

$$R = \text{design rail seat load (kip)}$$

WL = unfactored wheel-rail load (kip)
DF = distribution factor
IF = impact factor

Calculate design rail seat positive bending moment

For the rail seat positive bending moment, it is assumed that the crosstie is supported only at the rail seats, as seen in Figure 303. This represents a feasible worst-case scenario for rail seat positive bending and approximates the ballast reaction seen for newly-tamped track. These are the same support conditions used in Part 14 of the 2003 AS (Standards Australia 2003).

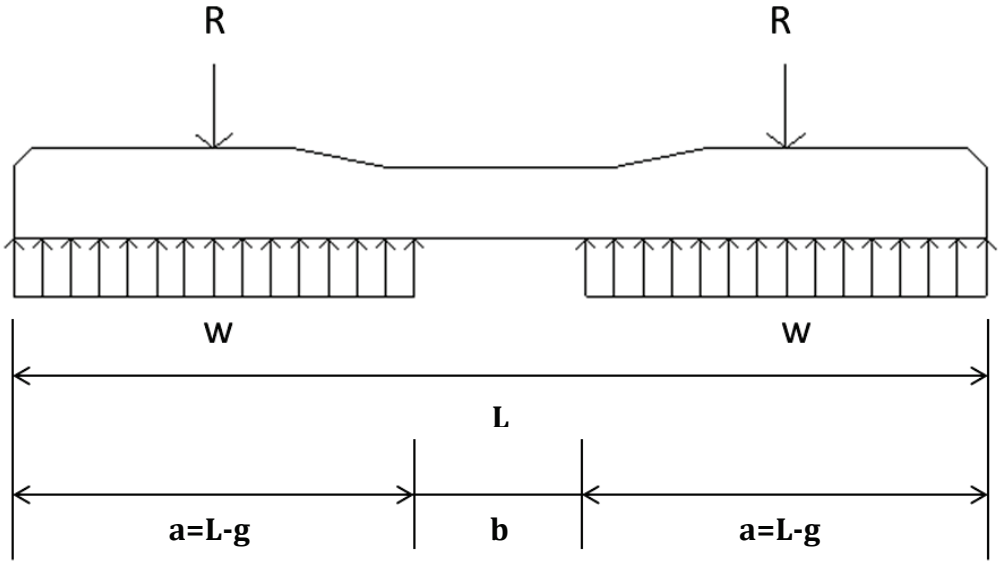

Figure 303. Support Conditions for Rail Seat Positive Bending Moment

To calculate the design rail seat positive bending moment, the rail seat section shown in Figure 303 can be modeled as a beam with a uniform distributed load bending about a centered point load (shown in Figure 304). The equation for the rail seat positive bending moment is given by Equation 8.

$$M_{RS+} = \frac{Ra}{8} \tag{8}$$

where:

M_{RS+} = design rail seat posititve bending moment (kip · in)
R = design rail seat load (kips)
a = rail seat support reaction (in)

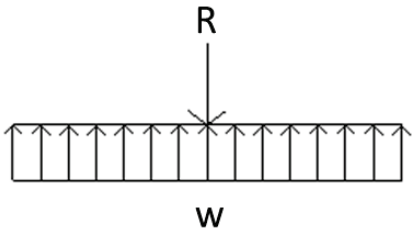

Figure 304. Simplified Beam Model for Rail Seat Positive Bending Moment

Calculate design center negative bending moment

For the center negative bending moment analysis, it is assumed that the crosstie is uniformly supported, as shown in Figure 305. This uniform ballast reaction can be found by dividing the design axle load (2R) by the crosstie length (L). This approximates the ballast reaction after heavy train traffic and ballast fouling. The equation for the center negative bending moment is given in Equation 9.

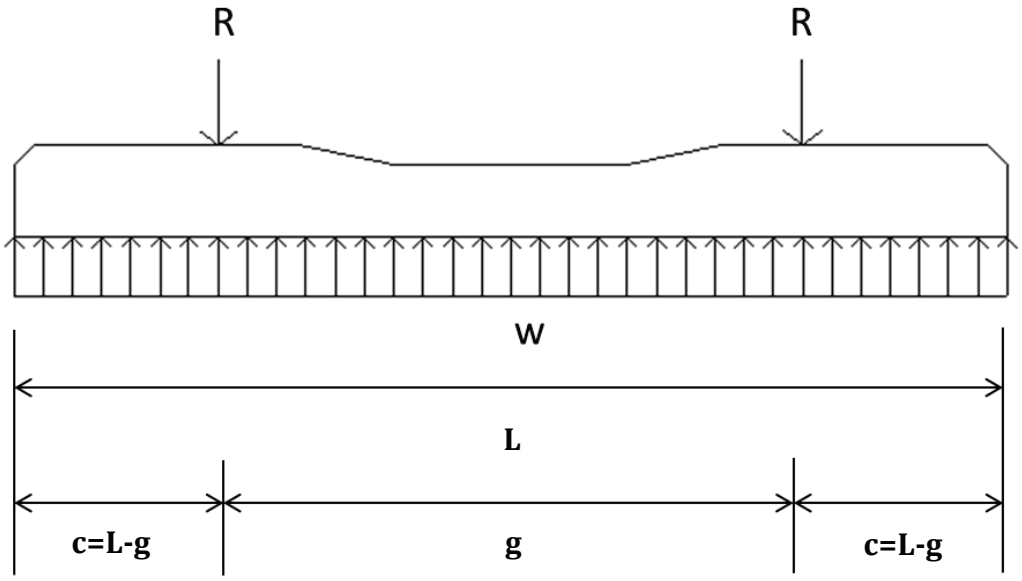

Figure 305. Support Conditions for Center Negative Bending Moment

$$M_{C-} = \frac{w(0.5L)^2}{2} - \frac{Rg}{2} \tag{9}$$

where:

M_{C-} = design center negative bending moment (kip · in)
w = distributed ballast reaction (kips/in)
L = crosstie length (in)
R = design rail seat load (kips)
g = rail center spacing (in)

This equation is found by modeling the crosstie as a beam cantilevered at the center, as shown in Figure 306.

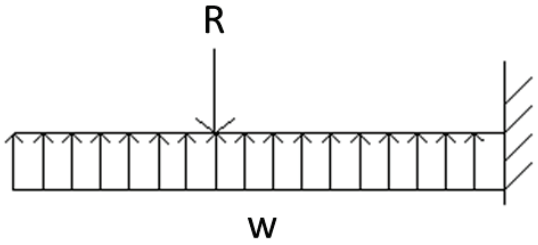

Figure 306. Simplified Beam Model for Center Negative Bending Moment

After speaking with many concrete crosstie manufacturers and designers, it became clear that they design only for rail seat positive and center negative bending. This is due to the eccentricity of the prestressing steel. If the crosstie is designed to withstand the positive flexural demand at the rail seat, then the crosstie should also be sufficient for center positive bending. The same philosophy holds true for negative bending; if the crosstie is designed to satisfy the center negative bending, it too should be adequate for rail seat negative bending. Therefore, no mechanics-based analysis is proposed to calculate the rail seat negative or center positive bending moments.

AREMA, UIC 713, and AS 1085.14 are similar in that they both stop after the analysis of the crosstie. It must be remembered that this is only half of the design process, and a methodology for the physical design of the crosstie must also be included. There are many parameters that affect both the cracking and ultimate flexural strength of a crosstie. Some examples are provided below but not limited to:

- Prestress jacking force
- Number of prestressing wires or strands
- Arrangement of prestressing wires or strands
- Concrete strength
- Concrete cross section at rail seat and center

There must be some method or equation to give crosstie manufacturers an idea of what parameters can be changed and how these changes will affect the crosstie flexural strength.

10.12.5 Numerical Example of New Design Process

For this example, flexural analysis will be performed for a prestressed concrete crosstie that is 8’-6” long, has a 60” gauge length, is spaced at 24”, and must withstand an 82-kip axle load.

Determine Rail Seat Load

Using Figure 247, for 24” crosstie spacing, 50% of the wheel load is carried by a single rail seat immediately under the point of load application. Using Equation 10, and the AREMA-specified 200% impact factor, the design rail seat load can be calculated.

$$R = WL \times DF \times (1 + IF) \tag{10}$$

$$R = \left(\frac{82\text{ k}}{2}\right) \times 0.50 \times (1 + 2.00) = \mathbf{61.5\ kips}$$

Calculate Rail Seat Positive Bending Moment

From the assumptions stated in the previous section and illustrated in Figure 304, Equation 11 can be used to calculate the rail seat positive bending moment.

$$M_{RS+} = \frac{Ra}{8} \tag{11}$$

$$M_{RS+} = \frac{(61.5\text{ k})(102" - 60")}{8} = \mathbf{323\ kip \cdot in}$$

Calculate Center Negative Bending Moment

From the assumptions stated in the previous section and illustrated in Figure 306, Equation 12 can be used to calculate the center negative bending moment.

$$M_{C-} = \frac{w(0.5L)^2}{2} - \frac{Rg}{2} \tag{12}$$

$$M_{C-} = \frac{\left(\frac{2 \cdot 61.5\text{ k}}{102"}\right)(0.5 \cdot 102")^2}{2} - \frac{(61.5\text{ k})(60")}{2} = \mathbf{277\ kip \cdot in}$$

This completes the proposed procedure for performing flexural analysis on a prestressed concrete crosstie. These moments are compared with the numerical AREMA example in Table 70 below.

Table 70. Comparison Between Current AREMA and Proposed Flexural Analysis Methods

Method	AREMA	Proposed	Difference
M_{RS+} (kip-in)	300 kip-in	323 kip-in	+8%
M_{C-} (kip-in)	201 kip-in	277 kip-in	+38%

10.12.6 Future Work for Concrete Crosstie Mechanistic Design

For this methodology to be implemented agreement must be reached between crosstie manufacturers, railroads, researchers, and AREMA. The new analyses discussed in the previous section require higher flexural strength of crossties, which will result in designs that while currently acceptable according to AREMA standards will become inadequate. A large part of this discussion is related to limit states and DAFs. If these parameters are accepted, the design process can be revised.

Listed below are the next steps necessary to continue refining this process and the methods for testing them:

- All assumptions and factors made in the new design procedure need to be verified (from field and laboratory experiments as well as FE modeling results). This can be

accomplished by conducting more tests in the field and more iterations of the FE model. The factor of greatest concern and need of review is the DAF associated with extreme loading. Further investigation into WILD data can shed light on probabilistic loadings that incorporate dynamic amplification effects.

- Bending moment distribution of the crosstie under different ballast conditions needs to be further investigated. Currently, even with the proposed changes, the ballast conditions are almost completely neglected when determining the required bending moments at the critical sections of the crosstie. Changes to support conditions including ballast consolidation and ballast stiffness are factors that significantly affect the forces and moments experienced by the crosstie. This can be further investigated by calculating the bending moments under changing ballast reactions using linear-elastic analysis as shown in the proposed section.
- The acceptable prestressing transfer length must be considered in the crosstie design process. It is not currently mentioned in the proposed new method, but should be considered by crosstie manufacturers. Researchers at Kansas State University have done extensive research in the required transfer length of different prestressing wires and strands (Haynes 2013, Bodapati 2013). Findings from their work could be used to provide crosstie manufacturers guidance on this issue. The same researchers have also developed a non-contact method of measuring the prestressing forces in a crosstie, which could be implemented by manufacturers as a method of quality control (Zhao 2013).

10.13 Rail Seat Load Distribution

10.13.1 Current Status

AREMA Chapter 30 does not contain any design considerations for the distribution of load at the crosstie rail seat. For design purposes, the rail seat load is regarded as uniformly distributed across the entire rail seat. This assumption, however, does not accurately describe the behavior of the rail seat load at high L/V force ratios (Greve 2014). Figure 307 compares the qualitative effect of L/V force ratio under a constant 40 kip (178 kN) vertical load for three separate cases. The first case represents the common design assumption that the rail seat load is distributed uniformly across the entire rail seat. By definition, this distribution is not affected by L/V force ratio. The second case represents a typical rail seat load distribution for a rail seat with new fasteners, as illustrated by data from experimentation on the TLS. Although there is some concentration of load on the field side of the rail seat, the fasteners are able to restrict rail rotation to 0.31 degrees or less. This results in very little change in rail seat load distribution. The final case represents a typical rail seat load distribution for a rail seat with worn fasteners, as illustrated by data from experimentation on the RTT using the TLV. The ability of the clips to restrict rail rotation is reduced, allowing rail rotations up to 0.52 degrees, which results in significant concentration of the rail seat load along the field side of the rail seat. This excessive rail rotation results in a complete unloading of the gauge side of the rail seat at high L/V ratios. Figure 307 also shows the change in pressures exerted on the rail seat: the increased rail rotation in the worn fastener case results in higher pressures than the new fastener case, as illustrated by the accompanying pressure scale.

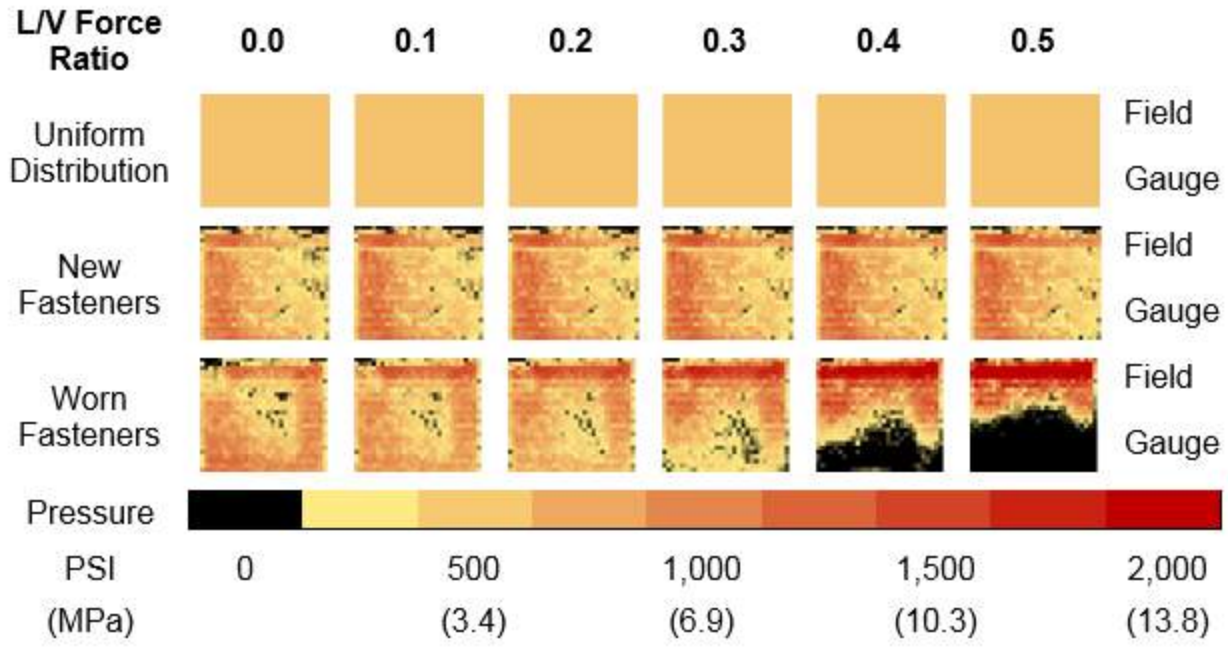

Figure 307. Three Rail Seat Pressure Distributions under 40 Kip (178 kN) Vertical Wheel Load at Varying L/V Force Ratios

Figure 308 illustrates the quantitative effect of L/V force ratio and fastener health on contact area, the area of the rail seat that is engaged in load transfer. The data has been normalized to the contact area seen under a 40 kip (178 kN) vertical and 0 lb lateral loading environment. Therefore, the percent of contact area at a 0.0 L/V force ratio describes the effect of vertical load, while the change in percent contact area for each data series describes the effect of L/V force ratio for each vertical load magnitude. The new fastener case results in a consistent increase in contact area for all vertical load magnitudes between 0.58% and 1.75%. It is hypothesized that this increase is due to deformation of the rail pad assembly as the rail rotates under higher L/V force ratios. By contrast, the worn fastener case exhibits a loss of up to 42% of initial contact area once the L/V force ratio exceeds a critical threshold value (Greve 2014). These data support the hypothesis that the ability of the worn fasteners to restrict rail rotation was reduced, which resulted in the observed lower contact areas under worn fasteners.

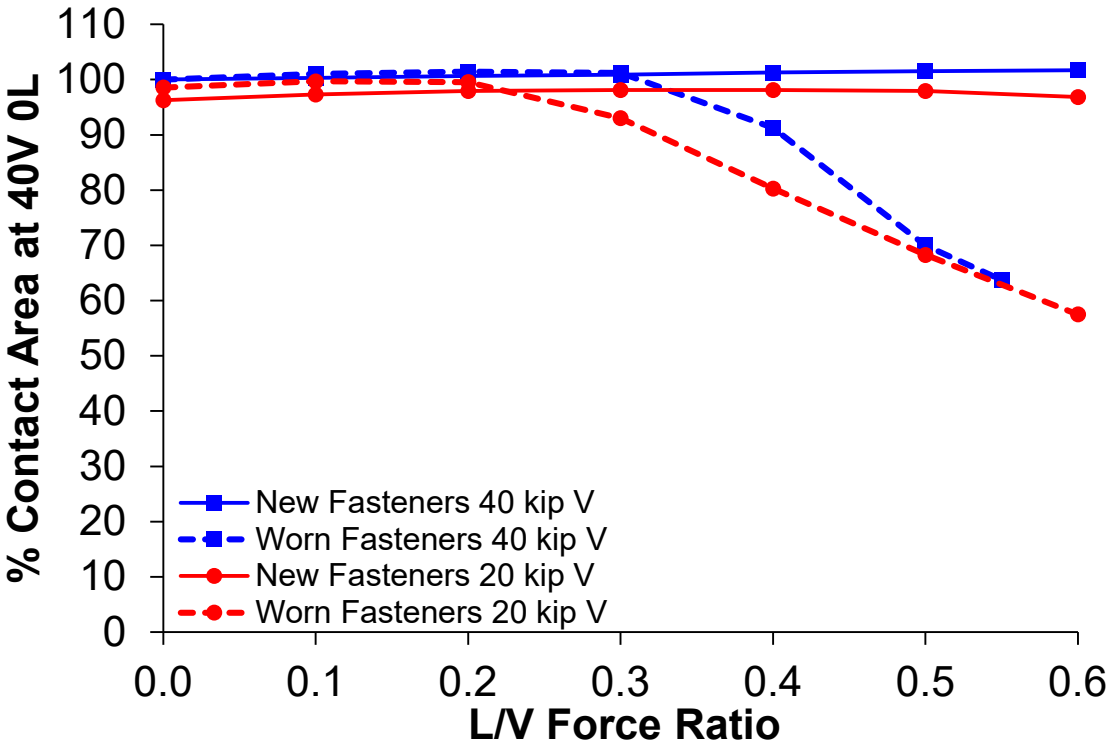

Figure 308. Effect of L/V Force Ratio on Contact Area

Figure 309 and Figure 310 illustrate the effect of loading environment on the pressures exerted on the crosstie rail seat. There are three primary metrics used to characterize the pressures at the rail seat interface. The first is the theoretical uniform pressure, which represents conventional design methodology. It assumes that the rail seat load is evenly distributed across the rail seat and is not affected by L/V force ratio, analogous to the uniform pressure distribution case illustrated in Figure 297. The second is the average pressure, which is calculated by dividing the rail seat load by the measured contact area. The third pressure metric is the maximum pressure observed for a given combination of vertical load and L/V force ratio.

Figure 309 compares the uniform, average, and maximum pressures for the new and worn fastener cases under a 20 kip (88.9 kN) vertical load, and Figure 310 compares the uniform, average, and maximum pressures for the same cases under a 40 kip (178 kN) vertical load. In both figures, the new fastener average pressures plot within 50% of the theoretical uniform pressure, even under L/V force ratios as high as 0.6. This indicates that almost all the contact area is utilized in load transfer. The worn fastening system average pressures plot close to the theoretical uniform pressure below the aforementioned "threshold" L/V force ratio.

Above this critical point, the reduction of contact area increases these pressures by up to 80% of their original value. The maximum pressures observed for the new fastener case were approximately 325% higher than the theoretical uniform pressure under a 20 kip (88.9 kN) vertical wheel load, experiencing no net change from 0 to 0.6 L/V. Under a 40 kip (178 kN) vertical wheel load, the new fastener maximum pressures are inversely related to L/V force ratio, ranging from 211% to 177% higher than the theoretical uniform pressure. By contrast, the maximum pressures observed in the worn fastening system case for both vertical wheel load

magnitudes exhibited strong positive correlation with L/V force ratio. Again, the magnitude of maximum pressure relative to the theoretical uniform pressure is greater under the 20 kip vertical load, ranging from 350% to 660% greater than the theoretical uniform pressure, than under the 40 kip vertical wheel load, ranging from 160% to 370% greater than the theoretical uniform pressure. Figure 311 shows a higher maximum pressure for the new fastening system case than was observed in the worn fastener case under a 40 kip (178 kN) vertical wheel load. It is hypothesized that this is due primarily to increased rail seat load on the instrumented rail seats resulting from stiffer support conditions relative to adjacent crossties.

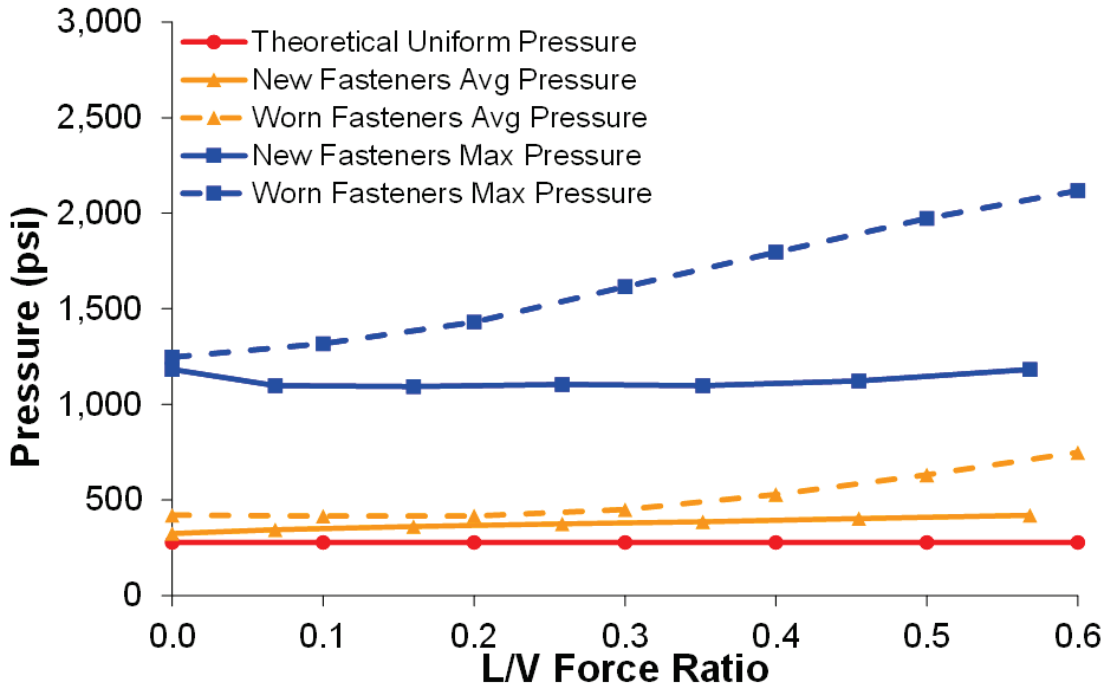

Figure 309. Effect of L/V Force Ratio on Pressure (20 Kip (88.9 kN) Vertical Wheel Load)

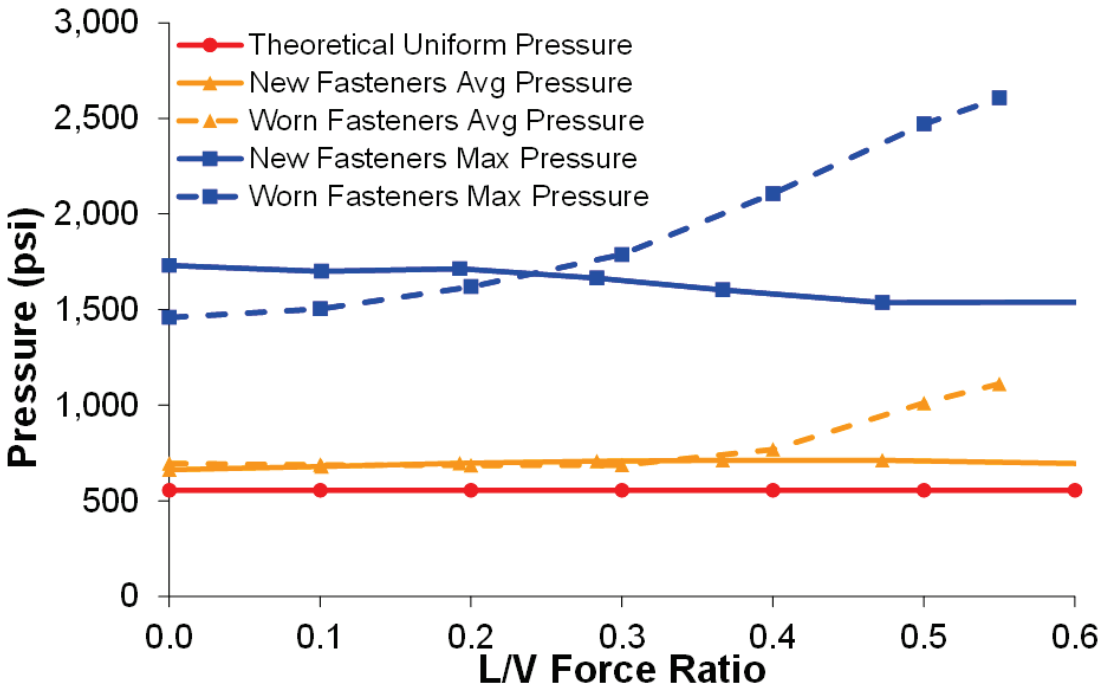

Figure 310. Effect of L/V Force Ratio on Pressure (40 Kip (178 kN) Vertical Wheel Load)

Figure 312 shows the distribution of rail seat load in the worn fastener case as a function of the distance from the field side shoulder. The data series were calculated by summing the load applied to each sensor row, which are 0.22 inches (5.59 mm) in width, at each L/V force ratio. As the L/V force ratio increases, the data show significant concentration of the rail seat load on the field side of the rail seat, and an unloading of the gauge side of the rail seat, which agrees with the analysis detailed in this report. The area of the rail seat 1 inch (25.4 mm) or less from the field side shoulder, illustrated by the area left of the dashed line in Figure 10, exhibits the highest sensitivity to changes in the L/V force ratio, and consistently exhibits significantly higher loads than the remainder of the rail seats. Figure 312 also shows the effect of the rail pad texture. The micro-level variations in each data series are due to studs on the bottom of the rail pad designed to allow water to drain from the rail pad-abrasion frame interface, with higher loads occurring under the studs. Although the variation in load due to rail pad texture are not as significant as those due to changes in the loading environment, it is interesting to note that the effect of rail pad texture does have a visible impact on the rail seat load distribution.

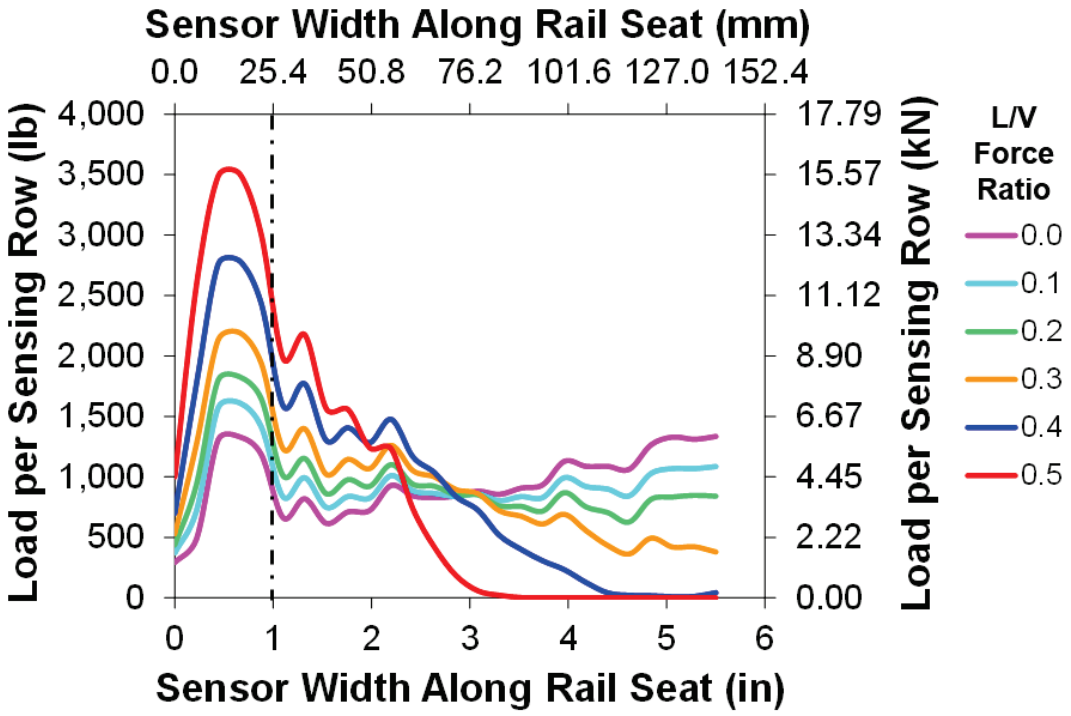

Figure 311. Lateral Distribution of Rail Seat Load at Varying L/V Force Ratio (40 Kip (178 kN) Vertical Wheel Load)

It is important to note that although none of the observed pressures approach the design compressive strength of the concrete (i.e. 7,000 psi [9]), the increase in pressure will change the characteristics of failure mechanisms associated with RSD (e.g. increased frictional force leading to more severe abrasion). It is hypothesized that RSD first develops in regions of extreme pressure and then spreads as the loss of material becomes more severe. Therefore, a design check ensuring that the rail seat load distribution does not generate these critical higher pressures would lead to fastening systems with a greater inherent resistance to RSD.

10.13.2 New Design Methodology

The Rail Seat Load Index (RSLI) is proposed as a quantifiable design value which describes the sensitivity of the rail seat load distribution to changes in the L/V force ratio. The RSLI of a rail seat describes the portion of the total rail seat load that is imparted onto a critical region of the rail seat, normalized to a theoretical uniform distribution, as described in Equation 13. Because the RSLI is calculated from a ratio of loads, RSLI can be applied to any units of load, provided that the same units are used for both the vertical load applied to the critical area and the total vertical rail seat load. This critical region is defined as the area of the rail seat not more than 1 inch (25.4 mm) from the field side shoulder and this region of the rail seat is the most sensitive to changes in the L/V force ratio. Therefore, for a 6-inch (152.4 mm) rail base, one sixth of the total rail seat load will be imparted onto the critical region in a uniform loading case.

$$RSLI = \frac{\frac{[Load\ in\ Critical\ Area]}{[Total\ Rail\ Seat\ Load]}}{1/6} = 6 * \frac{[Load\ in\ Critical\ Area]}{[Total\ Rail\ Seat\ Load]} \quad (13)$$

To further explain this metric, RSLI values can be calculated for the data presented in this section (Figure 314). The average effect of increasing L/V force ratio on RSLI for both the new and worn fastener cases are shown for a 40 kip (178 kN) vertical wheel load. At 0.0 L/V force ratio, both the new and worn fastener cases achieve an RSLI near 1, indicating a proportionate amount of the rail seat load is imparted to the critical area. The new fastener RSLI increases to 1.4 at a 0.6 L/V force ratio; by Equation 13, this indicates that slightly less than one quarter of the total rail seat load is applied to the one inch closest to the field side shoulder. By contrast, the worn fastener case experiences a significant increase in RSLI, with a maximum RSLI of 3.1 at 0.55. By Equation 13, this means that more than half of the rail seat load is concentrated in the critical area of the rail seat, indicating a severely nonuniform load confirmed by the analysis detailed in this paper. Lastly, Figure 312 also includes RSLI data from joint experimentation with TTCI examining the effect of rail seat deterioration on the rail seat load distribution (Greve, 2015). This data is representative of extreme RSLI that may occur in the field as a result of 0.75 inches (19.1 mm) of RSD: at 0.0 L/V, the data shows an RSLI of 2.8 and increases to 4.1 under a 0.6 L/V force ratio. This represents two thirds of the rail seat load applied to the one inch closest to the field side of the rail seat.

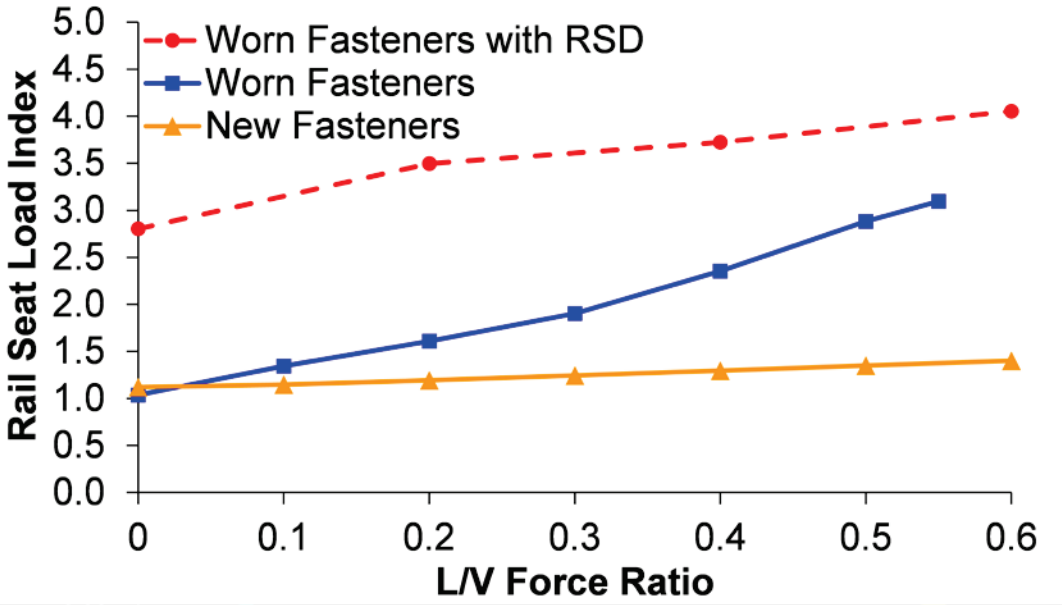

Figure 312. Effect of L/V Force Ratio on RSLI (40 Kip (178 kN) Vertical Wheel Load)

To determine the maximum RSLI of a fastening system, an experimental testing procedure has been developed. This RSLI test would be performed on a single rail seat in conjunction with AREMA Test 6 (Wear and Abrasion) to examine both new and worn fastening system component conditions. The test utilizes a loading frame capable of applying controlled vertical and lateral loads of independently varying magnitude to the rail head. A section of 136RE rail 18 inches (457 mm) in length should be affixed to a single rail seat with a typical fastening system, with MBTSS installed between the fastening system and crosstie rail seat as shown in Figure 313. The assembly should then be subjected to the design vertical load. Once the design vertical load is reached, the lateral load should be increased until the design L/V force ratio is achieved. MBTSS is then removed, and the same fastening system components are reassembled and subjected to AREMA Test 6. Following Test 6, the fastening system is disassembled,

MBTSS is reinstalled, the fastening system is reassembled once more, and is then again subjected to the design loading environment. Failure criteria for the test would be established based on both the change in RSLI as a result of AREMA Test 6, and the absolute maximum RSLI recorded during the test.

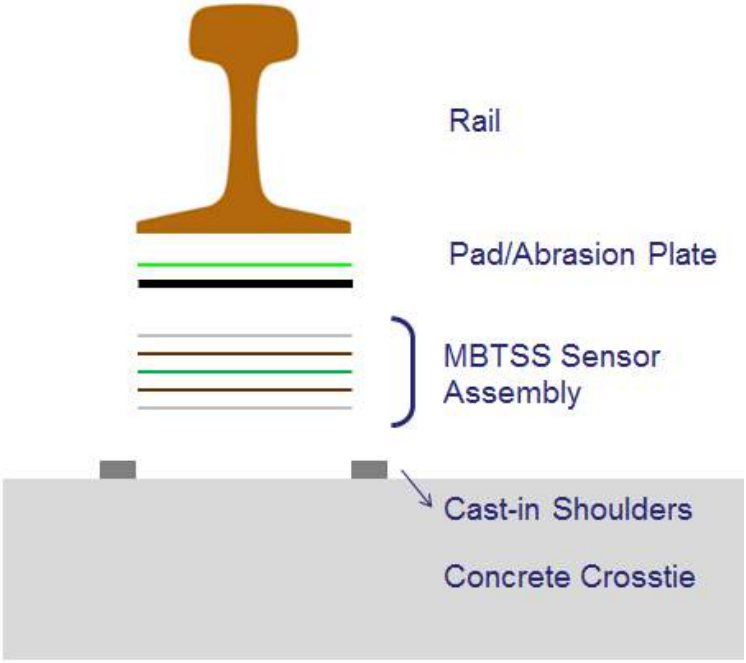

Figure 313. Profile View of Example Sensor Installation for RSLI Test

Although no criteria for maximum permissible RSLI has been established, it is theorized that a maximum RSLI exists which permits limited concentration of the rail seat load, but prohibits excessive loading on the field side of the rail seat. This would result in accelerated wear of the fastening system and an increased potential for RSD. Figure 314 illustrates this hypothetical range, which is not affected by L/V force ratio. Instead, the fastening system should be designed to meet the maximum permissible RSLI at the design L/V; this will result in stiffer fastening system designs for loading environments in which high L/V force ratios are common. Further, this allows for fastening systems to be optimized for their design application, rather than designing all fastening systems to the same standard regardless of application.

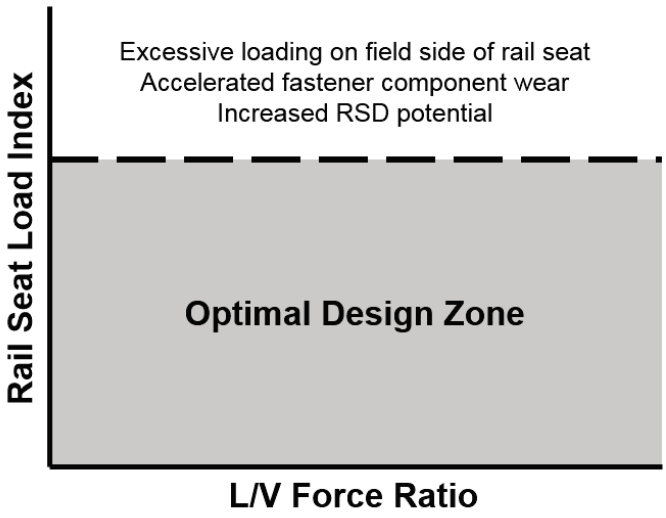

Figure 314. Conceptual RSLI Design Limit Philosophy

10.13.3 Sample calculations

This section utilizes data from lab experimentation to perform a sample calculation of the RSLI at 0.6 L/V force ratio for an example rail seat with an Amsted RPS P2000 fastening system. Figure 315 shows the load distribution of a P2000 rail seat subjected to a vertical load of 32.5 kip (144.6 kN) and a lateral load of 19.5 kip (86.7 kN), which will be used to calculate the RSLI. The critical portion of the rail seat is highlighted in blue.

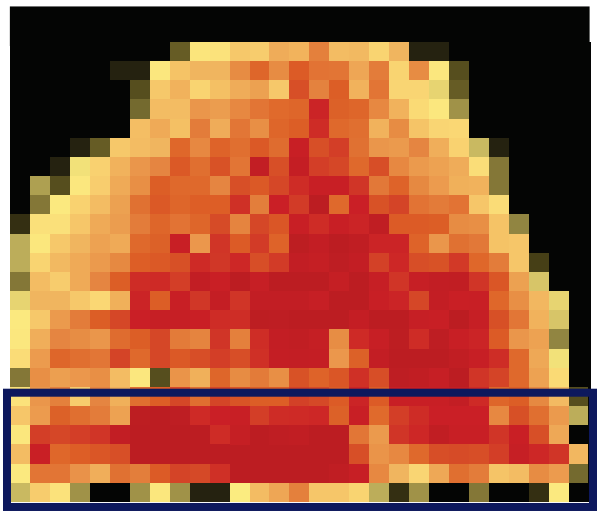

	Pounds	(kN)
Load in Critical Area	9,449	(42.0)
Total Rail Seat Load	32,500	(144.6)

Figure 315. Sample Rail Seat Load Distribution

Thus, we can now calculate the RSLI by Equation 14, below:

$$RSLI = \frac{\frac{[Load\ in\ Critical\ Area]}{[Total\ Rail\ Seat\ Load]}}{1/6} = \frac{\frac{9{,}449}{32{,}500}}{1/6} = 1.74 \tag{14}$$

10.13.4 Path Forward

RSLI can be readily defined and evaluated for existing fastening systems with currently available testing equipment. However, a study comparing the RSLI of common fastening systems both in the new and worn case would further the understanding of the practical design zone for RSLI, and experimentation characterizing the relationship between RSD failure mechanisms and rail seat load non-uniformity would aid in the development of mechanistic thresholds for RSLI. Further, experimentation to establish a relationship between RSLI and a measurement presently obtained from AREMA Test 6 experiments would allow for more widespread adaptation of the concept behind RSLI without necessitating the acquisition of specialized instrumentation. Ultimately, the consideration of rail seat load non-uniformity in the design of concrete crossties and fastening systems will lead to designs with a greater inherent resistance to RSD.

10.14 Summary

This chapter provided a review of the existing design process for concrete crosstie and fastening systems, and the method by which a mechanistic design process can be achieved. A mechanistic design process will provide many benefits that are not currently achieved by the iterative design process outlined in AREMA. Table 71 compares the two methods to highlight the areas where a mechanistic design process would provide the greatest benefit.

Table 71. Qualitative Comparison of Iterative and Mechanistic Design Processes

Category	Iterative Design (Current)	Mechanistic Design (Proposed)
Ease of development	Already developed	Will require large amounts of capital investment and time
Time required to run analysis	Relatively quick	Requires lengthy analysis process
Accuracy of demand estimates	Variable, could be inaccurate	Highly accurate, based on system specific analysis
Ability to account for specific failure modes	Limited, mostly focused on crosstie failure modes	Design specifically accounts for each failure mode of every component
Potential for design of new systems	Low, may not be accurate	High, very flexible for material or geometry chosen for the system
Safety factor of design	Relatively conservative	More variables according to choice of designer

The primary difference between the two design processes is that while mechanistic design will provide more accurate predictions of the load experienced by components, it will require a large amount of capital and time to develop the process. Also, even if both processes were fully developed, designing a system using mechanistic design will take more time as the full load path will need to be determined. As FE models become more robust, it should be possible to determine the load path and distributed forces more quickly, but currently this is a time-consuming process. Once a mechanistic design is developed it will provide much more flexibility than the iterative design process, allowing for variable factors of safety for each failure mode, as well as allowing multiple types of fastening systems while still producing reliable predictions of performance.

We have provided a framework for a mechanistic design process that can provide some immediate changes to the design process outlined in the AREMA recommended practices. However, the more important purpose is to highlight the areas that need the most improvement, so that future research projects will have clear goals that can positively impact the rail industry.

References

ACI Committee 318. (2011). *Building Code Requirements for Structural Concrete (ACI 318-11) and Commentary*. American Concrete Institute. Farmington Hills, MI.

Ahlbeck, D.R., Tuten, J.M., Hadden, J.A., and Harrison, H.D. (1986). *Development of Safety Criteria for Evaluating Concrete Tie Track in the Northeast Corridor Volume 1*. Remedial Projects Assessment. Columbus, OH: Battelle's Columbus Laboratories.

American Railway Engineering and Maintenance-of-Way Association. (2014). *AREMA Manual for Railway Engineering*. American Railway Engineering and Maintenance-of-Way Association. Landover, MD.

American Railway Engineering and Maintenance-of-Way Association. (2012). *AREMA Manual for Railway Engineering*. Vol. 1, Ch. 30. Landover, MD: American Railway Engineering and Maintenance-of-Way Association.

Andersson, E. Berg, M., and Stichel, S. (2013). *Rail Vehicle Dynamics*. Stockholm, Sweden: KTH, Royal Institute of Technology.

ARA, Inc. (2004). *Guide for Mechanistic-Empirical Design of New and Rehabilitated Pavement Structures.* ERES Consultants Division. Champaign, IL.

Armstrong, J. (2008). *The Railroad: What It Is, What It Does,* Fifth Edition. Simmons-Boardman Books. New York, NY.

Bayer, R.G. (2004). *Mechanical wear fundamentals and testing*. New York, NY: Marcel Dekker.

Bodapati, N.N.B., Zhao, W., Peterman, R.J., Wu, C.H.J., Beck, B.T., Haynes M., and Holste, J.R. (2013, April). Influence of Indented Wire Geometry and Concrete Parameters on the Transfer Length in Prestressed Concrete Crossties. In: *Proceedings: 2013 Joint Rail Conference*. Knoxville, TN.

Chambers, S.K. (1980). Stresses in Railroad Track. *The Talbot Reports*. Washington, DC: American Railway Engineering Association.

Chen, Z., Shin, M., and Andrawes, B.O. (2013, February). Finite Element Modeling of the Fastening Systems and Concrete Sleepers in North America. In: *Proceedings: 10th International Heavy Haul Association Conference*, (p. 139–144). New Delhi, India.

Chen, Z., Shin, M., and Andrawes, B.O. (2012). Numerical Simulation of Presstressed Concrete Crosstie and Fastening System. *Accepted, Precast/Prestressed Concrete Institute and National Brigde Conference.*

Dassault Systemes Simulia Corp. (2011). *ABAQUS Analysis User's Manual: Version 6.11*. Dassault Systemes Simulia Corp.

Do Carmo, T.B. (2014). *Multifaceted approach for the analysis of rail pad assembly response.* Department of Civil and Environmental Engineering, University of Illinois at Urbana-Champaign, Graduate College. Urbana, IL.

Du, M.M., Su, X.Z., and Zhao, Y. (2010). Experimental study on bond behavior of ribbed bar and strand. *Jianzhu Cailiao Xuebao – Journal of Building Materials, 13*(2), p. 175–181.

Esveld, C. (2001). *Modern Railway Track, Second Edition*, (p. 84, 91). The Netherlands: MRT-Productions, Zaltbommel.

Faraway, J.J. (2002). Practical regression and ANOVA using R. Bath, England: University of Bath.

Federal Railroad Administration. (2002). *Track and Rail and Infrastructure Integrity Compliance Manual: Volume II - Chapter 1*. Available at https://www.fra.dot.gov/eLib/details/L18604#p1_z50_gD_kcompliance%20manual.

Filho, A., Menezes, F., El Debs, M.K., and El Debs, A.L.H.C. (2007). Bond-slip behavior of self-compacting concrete and vibrated concrete using pull-out and beam tests. *Materials and Structures, 41*(6), 1073–1089.

Friedrich, K. (1986). *Friction and wear of polymer composites*. Elsevier.

Gambarova, P.G., and Rosati, G.P. (1996). Bond and splitting in reinforced concrete: Test results on bar pull-out. *Materials and Structures/Materiaux et Constructions, 29*(189), p. 267–276.

Giannakos, K., and Loizos, A. (2010). Evaluation of actions on concrete sleepers as design loads - influence of fastenings. *International Journal of Pavement Engineering, 11*(3), p. 197–213.

Grassé, J., and Lange, D. (2013). Field Testing of Concrete Crossties and Fastening Systems for the Understanding of Mechanistic Behavior. In: *Proceedings: 2013 Joint Rail Conference*. Knoxville, TN.

Greve, M.J., Dersch, M.S., Edwards, J.R., Barkan, C.P.L., Mediavilla, J., and Wilson, B. (2014). Analysis of the Relationship Between Rail Seat Load Distribution and Rail Seat Deterioration in Concrete Crossties. In: *Proceedings: 2014 Joint Rail Conference*, Colorado Springs, CO.

Greve, M. J., Dersch, M.S., Edwards, J.R., Barkan, C.P.L., Thompson, H., Sussman, T., and McHenry, M. (2015). Examiniation of the Effect of Concrete Crosstie Rail Seat Deterioration on Rail Seat Load Distribution. Accepted *Transportation Research Record: Journal of the Transportation Research Board*. Washington, DC: Transportation Research Board of the National Academies.

Hay, W. (1982). *Railroad Engineering, Second Edition*. New York, NY: John Wiley & Sons.

Haynes, M., Wu, C.H.J., Beck, B.T., Bodapati, N.N.B., and Peterman, R.J. (2013, April). Prestressing Steel Reinforcement Wire Bond Index Number. In: *Proceedings: 2013 Joint Rail Conference*. Knoxville, TN.

Harper, C.A. (1996). Handbook of Plastics, Elastomers, and Composites. *McGraw-Hill Inc*, *2*(2), p. 41.

Harrison, H D., Dean, F.E., Selig, E.T., and Stewart, H.E. (1984). *Correlation of Concrete Tie Track Performance in Revenue Service and at the Facility for Accelerated Service Testing.* Volume I. Columbus, OH. Battelle Columbus Laboratories.

Hepburn, C. (1982). *Polyurethane elastomers*. London, England: Applied Science Publishers.

Huang, H., and Tutumluer, E. (2011). Discrete Element Modeling for fouled railroad ballast. *Construction and Building Materials, 25*(8), p. 3306–3312.

International Union of Railways. (2002). *Design of monoblock concrete sleepers, UIC 713*. International Union of Railways.

Iwnicki, S. (2006). *Handbook of Railway Vehicle Dynamics*, (p. 212), Boca Raton, FL: CRC Press, Taylor and Francis Group.

Jimenez, R., and LoPresti, J. (2004). Performance of Alternative Tie Material under Heavy-Axle-Load Traffic. *Railway Track & Structures*, *100*(1), (p.16–18).

Kaewunruen, S., and Remennikov, A.M. (2007). Investigation of Free Vibrations of Voided Concrete Sleepers in Railway.

Kennedy, Jr., J.C., and Prause, R.H. (1978). Development of a Multilayer Analysis Model for Tie/Ballast Track Structures. In: *Proceedings: 57th Annual Meeting of the Transportation Research Board*. Washington, DC.

Kerchof, B, and Huimin, W. (2012). Causes of Rail Cant and Controlling Cant Through Wheel/Rail Interface Management. In: *Proceedings: 2012 Annual AREMA Conference*. Chicago, IL.

Kernes, R.G., Edwards, J.R., Dersch, M.S., Lange, D.A., and Barkan, C.P.L. (2012, January). Investigation of the Dynamic Frictional Properties of a Concrete Crosstie Rail Seat and Pad and its Effect on Rail Seat Deterioration (RSD). In: *Proceedings: 91st Annual Meeting of the Transportation Research Board*. Washington, DC.

Kernes, R. G. (2013). *The mechanics of abrasion on concrete crosstie rail seats*. Urbana, Illinois: Department of Civil and Environmental Engineering, University of Illinois at Urbana-Champaign, Graduate College.

Kerr, A.D. (2003). *Fundamentals of Railway Track Engineering*, 1st Ed., Simmons-Boardman Books, Inc. Omaha, NE.

Kish, A. (2011). *On the fundamentals of track lateral resistance.* American Railway Engineering and Maintenance-of-Way Association.

Koch, K. (2007). *Measurement of Wheel Load and Axle Strain Environment, 286,000-pound Gross Rail Load Coal Train Service; Powder River Basin to New York, March 2006; Powder River Basin to Georgia, May 2006*, R-983. Association of American Railroads, Pueblo, CO.

Krishnaiah, K., and Shahabudeen, P. (2012). *Applied Design of Experiments and Taguchi Methods,* First Edition. New Dheli, India: PHI Learning.

Kumaran, G., D. Menon, and Nair, K.K. (2002). Evaluation of dynamic load on railtrack sleepers based on vehicle track modeling and analysis. *International Journal of Structural Stability and Dynamics, 2*(3), p. 355–74.

Leong, J., and Murray, M.H. (2008). Probabilistic analysis of train-track vertical impact forces. In: *Proceedings: Institution of Civil Engineers*. London, United Kingdom.

Lu, S., Arnold, R., Farritor, S., Fateh, M., and Carr, G. (2008). On the Relationship between Load and Deflection in the Railroad Track Structure. In: *Proceedings: 2008 Annual AREMA Conference*. Salt Lake City, UT.

Marquis, B P., Muhlanger, M., and Jeong, D.Y. (2011). Effect of Wheel/Rail Loads on Concrete Tie Stresses and Rail Rollover. In: *Proceedings: ASME 2011 Rail Transportation Division Fall Technical Conference*. Minneapolis, MN.

McQueen, P.J. (1983). *Introduction of Concrete Tie Systems*. San Rafael, CA.

McQueen, P.J. (2006). *Flexural Performance Requirements for Prestressed Concrete Ties by Factoring*. San Rafael, CA.

Mitchell, D.W. and H. Marzouk. (2007). Bond characteristics of high-strength lightweight concrete. *ACI Structural Journal, 104*(1), p. 22–29.

Rapp, C.T., Dersch, M.S., Edwards, J.R., Barkan, C.P.L., Wilson, B., and Mediavilla, J. (2012.) Measuring Concrete Crosstie Rail Seat Pressure Distribution with Matrix Based Tactile Surface Sensors. In: *Proceedings: AREMA 2012 Annual Conference*. Chicago, IL.

Read, D.M. (1990). *FAST/HAL Concrete Tie and Fastener Experiment*. Preprints of AAR 1990 Workshop on Heavy Axle Loads. Pueblo, CO.

Rewczuk, C. (2012, June). Union Pacific's Concrete Tie Design Requirements and Research Outlook. In: *Proceedings: International Concrete Crosstie and Fastening System Symposium*. Urbana, IL.

Rhodes, D., and Cox, S.J. (2013). Rail Fastenings for Heavy Haul and Extreme Longitudinal Forces. In: *Proceedings: 10th International Heavy Haul Association Conference*, New Delhi, India.

Rhodes, D. (2005). Designing Track for High Traction Forces. *International Railway Journal, 45*(5), (p. 34). Available at: https://trid.trb.org/view.aspx?id=756747.

Scheppe, A.J., J.R. Edwards, M.S. Dersch and C.P.L Barkan. (2015). Quantifying Lateral Wheel Loading Variation Using Truck Performance Detectors. In: *Proceedings: Transportation Research Board (TRB) 94th Annual Meeting*. Washington, DC.

Selig, E.T., and Li, D. (1994). Track Modulus: Its Meaning and Factors Influencing It. *Transportation Research Record*, (1470), p. 47–54.

Standards Australia. (2003). *Australian Standard,* 3rd Ed. Sydney, Australia: Standards Australia International, AS 1085.14.

Stewart, H.E., and Selig, E.T. (1984). *Correlation of Concrete Tie Track Performance in Revenue Service and at the Facility for Accelerated Service Testing: Volume II*. University of Massachusetts. Amherst, MA.

Track Train Dynamics Research Program in Cooperation with the FRA. (1973). *Track Train Dynamics*. AAR-R.P.I.

Van Dyk, B.J., Dersch, M.S., Edwards, J.R., Ruppert, C.J., and Barkan, C.P.L. (2013). Evolution of Dynamic and Impact Wheel Load Factors and their Application for Design. *Accepted, Transportation Research Record – Journal of the Transportation Research Board.*

Van Dyk, B.J., Dersch, M.S., Edwards, J.R., Ruppert, C.J., and Barkan, C.P.L. (2014). Load Chacterization Techniques and Overview of Loading Environment in North America. *Accepted, Transportation Research Record – Journal of the Transportation Research Board.*

Van Dyk, B.J., et al. (2013). Quantifying Shared Corridor Wheel Loading Variation Using Wheel Impact Load Detectors. In: *Proceedings: 2013 Joint Rail Conference*. Knoxville, TN.

Venables, W.N., Smith, D.M., and R.D.C. Team. (2002). *An Introduction to R: Notes on R: a Programming Environment for Data Analysis and Graphics: Version 1.4.1*. Network Theory Limited.

Wang, W.J., P. Shen, Song, J.H., Guo, J., Liu, Q.Y., and Jin, X.S. (2011). Experimental study on adhesion behavior of wheel/rail under dry and water conditions. *Wear, 271*(9–10), p. 2699–2705. Available at https://doi.org/10.1016/j.wear.2011.01.070.

Walpole, R. E., Myers, R.H., Myers, S.L., and Ye, K. (1993). *Probability and statistics for engineers and scientists*. New York, NY: Macmillan.

Weber, J.W., and Ball, C.G. (1976). *Performance Evaluation of Concrete Tie Test Section on the Santa Fe at Leeds, Illinois*. Portland Cement Association. Skokie, IL.

Williams, B., Dersch, M.S., Edwards, J.R., and Barkan, C.P.L. (2015, January). Quantification of Lateral Forces in Concrete Crosstie Fastening Systems. In: *Proceedings: Transportation Research Board (TRB) 94th Annual Meeting*. Washington DC.

Williams, J.A. (1997). The laboratory simulation of abrasive wear. *Tribotest Journal, 3*(3), p. 267–306.

Wolf, H.E., Mattson, S., Edwards, J.R., Dersch, M.S., and Barkan, C.P.L. (2015, January). Flexural Analysis of Prestressed Concrete Monoblock Crossties: Comparison of Current Methodologies and Sensitivity to Support Conditions. In: *Proceedings: Transportation Research Board 94th Annual Meeting*. Washington, DC.

Yamaguchi, Y. (1990). *Tribology of Plastic Material: Their Characteristics and Applications to Sliding Components, Vol. XVI.* Elsevier Science.

Zakeri, J. A., Xia, H., and Fan, J.J. (2009). Dynamic responses of train-track system to single rail irregularity. *Latin American Journal of Solids and Structures, 6*(2), p. 89–104.

Zeman, J.C. (2010). Hydraulic Mechanisms of Concrete-Tie Rail Seat Deterioration, M.S. Thesis. University of Illinois at Urbana-Champaign. Urbana, IL.

Zhao, W., Beck, B.T., Peterman, R.J., Murphy, R., Wu, C.H.J., and Lee, G. (2013, April). A Direct Comparison of the Traditional Method and a New Approach in Determining 220 Transfer Lengths in Prestressed Concrete Railroad Ties. In: *Proceedings: 2013 Joint Rail Conference*. Knoxville, TN.

Appendix A: Infrastructure Owner, Operator, or Maintainer Responses

3. Please identify a representative route within your network that best fits the following criteria:- Mainline with higher than average tonnage- Concrete sleepers and elastic fastening systems in place for at least fifteen years- High curvature and grade relative to the rest of the network- In general, offers demanding operating conditionsHereafter, this route will be referred to as the "typical route".

8 Responses

4. Freight Train Loading

	Question 4: What are the maximum gross static wheel loads?	Question 4: What is the typical dynamic load impact factor? (%) (e.g. 200% = 2 x static loading)
INTL	24.8 tons (22.5 tonnes)	not of concern
	24.8 tons (22.5 tonnes)	
	18.7 tons (17.0 tonnes)	Velocity(km/h)×0.5/100
	38.6 tons (35.0 tonnes)	200
	29.2 tons (26.5 tonnes)	200
	30.3 tons (27.5 tonnes)	250
US	44.0 tons (39.9 tonnes)	150
	18.0 tons (16.3 tonnes)	?
	17.9 tons (16.2 tonnes)	220

5. Passenger Train Loading

	Question 5: What are the maximum gross static wheel loads?	Question 5: What is the typical dynamic load impact factor? (%) (e.g. 200% = 2 x static loading)
INTL	24.8 tons (22.5 tonnes)	not of concern
	22.0 tons (20.0 tonnes)	
	13.2 tons (12.0 tonnes)	Velocity(km/h)×0.5/100
	33.1 tons (30.0 tonnes)	200
	22.6 tons (20.5 tonnes)	204
US	N/A	
	12.5 tons (11.3 tonnes)	180

6. What is the average speed of trains?

	30-60 miles per hour (50-100 kilometers per hour)	5	56%
	60-90 miles per hour (100-150 kilometers per hour)	2	22%
	90-120 miles per hour (150-200 kilometers per hour)	1	11%
	120-150 miles per hour (200-250 kilometers per hour)	0	0%
	150-180 miles per hour (250-300 kilometers per hour)	0	0%
	Other, please specify	1	11%
	Total	9	100%
US	90-150 mph passenger, 30-50 mph freight		

7. Please provide the following axle spacings.

	Question 7: What is the minimum axle spacing on freight wagons?	Question 7: What is the average axle spacing on freight wagons? (i.e. length of most common wagon divided by number of axles)	Question 7: What is the minimum axle spacing on passenger carriages?	Question 7: What is the average axle spacing on passenger carriages? (i.e. length of most common carriage divided by number of axles)
INTL	5.9 feet (1.8 meters)		6.6 feet (2.0 meters)	26.4 feet (8.0 meters)
	26.4 feet (8.0 meters) for bogie wagons, 32.8 feet (10.0 meters) for axle wagons	55.8 feet (17.0 meters)	50.5 feet (15.4 meters) between bogies and 6.9 feet (2.10 meters) between axles	
	5.2 feet (1.6 meters)	6.2 feet (1.9 meters)	6.9 feet (2.1 meters)	6.9 feet (2.1 meters)
	I do not know	I do not know	I do not know	I do not know
	32.5 feet (9.9 meters)	39.3 feet (12.0 meters)		
	5.2 feet (1.6 meters)	6.2 feet (1.9 meters)	7.9 feet (2.4 meters)	8.2 feet (2.5 meters)
US	Unknown	Unknown	Unknown	Unknown
	Standard freight and coal equipment			
		10 feet (3.0 meters)		10 feet (3.0 meters)

8. Is locomotive sand used on your network to increase wheel adhesion and prevent wheels from slipping?

Yes	9	100%
No	0	0%
Total	9	100%

9. What is the annual tonnage per track?

INTL	2.2 million tons (2.0 million tonnes)
	3.9 million tons (3.5 million tonnes)
	22.0 million tons (20.0 million tonnes)
	88.2 million tons (80.0 million tonnes)
	71.7 million tons (65.0 million tonnes)
	33.1 - 55.1 million tons (30 - 50 million tonnes)
US	varies widely from 50.0 - 250.0 million tons (45.4 - 226.8 million tonnes)
	50.0 million tons (45.4 million tonnes)
	10.0 - 45.0 million tons (9.1 - 44.8 million tonnes)

Sleepers

10. Please provide the typical sleeper spacing for the following track segments.

	Question 10: Tangent	Question 10: Curve	Question 10: Grade Crossing
INTL	23.6 inches (60.0 centimeters)	23.6 inches (60.0 centimeters)	23.6 inches (60.0 centimeters)
	23.6 inches (60.0 centimeters)	23.6 inches (60.0 centimeters)	
	23.6 inches (60.0 centimeters)	22.8 inches (58.0 centimeters)	22.8 inches (58.0 centimeters)
	24.0 inches (61.0 centimeters)	24.0 inches (61.0 centimeters)	24.0 inches (61.0 centimeters)
	27.0 inches (68.5 centimeters)	27.0 inches (68.5 centimeters)	27.0 inches (68.5 centimeters)
	23.6 inches (60.0 centimeters)	23.6 inches (60.0 centimeters)	19.7 - 23.6 inches (50.0 - 60.0 centimeters)
US	24.0 inches (61.0 centimeters)	24.0 inches (61.0 centimeters)	18.0 - 24.0 inches (45.7 - 61.0 centimeters)
	24.0 inches (61.0 centimeters)	24.0 inches (61.0 centimeters)	
	24.0 inches (61.0 centimeters)	24.0 inches (61.0 centimeters)	24.0 inches (61.0 centimeters)

11. What is the typical area of your rail seat?	
INTL	23.3 square inches (150.0 square centimeters)
	44.6 square inches (288.0 square centimeters)
	46.5 square inches (300.0 square centimeters)
	1020.0 square inches (6580.0 square centimeters)
	40.3 square inches (260.0 square centimeters)
	44.6 square inches (288.0 square centimeters)
US	54.6 square inches (352.4 square centimeters)
	standard
	29.5 square inches (190.3 square centimeters)

12. What is the specified rail seat inclination (referred to as cant in North America)? (e.g. 1:40)	
INTL	1:40
	1:20
	1:40
	1:40
	1:20
	1:20
US	1:30 (pre 2007), 1:40 (post 2007)
	1:40
	1:40

13. Which companies and facilities manufacture the sleepers on your typical route? (manufacturer, city, and country of facility)	
INTL	Local Swiss concrete suppliers
	SATEBA, France
	There are many manufacturers
	ROCLA Concrete Tie, Denver, CO, USA
	Austrak, Rockhamption, Australia
	ROCLA, Bowral, NSW Australia
US	CXT, Grand Island/Tucson/Spokane, USA; Rocla, Amarilo, USA; NorTrak, Cheyenne, USA
	KSA, Sciotoville, OH, USA
	Rocla, Bear, DE, US

Fastening Systems

14. Fastening System Trends

	Question 14: Historically, what types of fasteners have been most commonly used? (brand and model, e.g. Pandrol e-CLIP)	Question 14: Currently, what types of fasteners are most commonly installed? (brand and model, e.g. Pandrol e-CLIP)	Question 14: If these two answers are different, please explain the design and performance advantages of the system that is currently installed.
INTL	Vossloh K12 etc	Several different Vossloh types, depending on sleeper.	
	NABLA System	NABLA System	
	According to Japan Industrial Standard (JIS)	JIS Type 5 (tangent) or Type 9 (curved)	
	e-clip 78-late 80s Safelok 87-2008 Vossloh 2008 and current	Safelok has the largest population- about 10 Million ties.	Evolution changes: Clip fatigue drove the change from e-clip to Safelok. Shoulder and insulator wear drove the change from Safelok to Vossloh.
	Pandrol e-clip	Pandrol e-clip	
	Pandrol e-Clip	Pandrol e-Clip	
US	In order of quantity: Pandrol Safelok III Pandrol Salelok I Pandrol e-clip Vossloh	Pandrol Safelok III	The vast majority of fasteners installed on concrete ties on our territory are Pandrol Safelok III. This remains our standard as the fastener provides improved toe loads versus all previous Pandrol products. The Vossloh fastening system is currently under test.
	e Fast Clip	Fast Clip	Captive Fast Clip design for initial installation.
	Pandrol fast clip, Pandrol e-clip	Pandrol fast clip	Ease of installation of fast clip

15. What is the fastener clamping force (toe load)?

INTL	2248 pounds force (10.0 kilonewtons)
	According to track structure (ballasted/slab)
	4496 pounds force (20.0 kilonewtons)
	6774 pounds force (30.0 kilonewtons)
	2360 pounds force (10.5 kilonewtons) per clip
US	2500 - 2900 pounds force (11.1 - 12.9 kilonewtons)
	2250 pounds force (10.0 kilonewtons)

16. What is the rail pad material?

	Polyurethane	6	67%
	Rubber	2	22%
	Other, please specify	1	11%
	Total	9	100%
US	HDPE		

17. What is the rail pad geometry?

	Dimpled	2	25%
	Grooved	0	0%
	Studded	1	13%
	Flat	1	13%
	Other, please specify	4	50%
	Total	8	100%
INTL	Ribbed		
	Dimpled and corrugated can yield the same results. We use both.		
US	Proprietary info		
	All four pad styles are presented.		

18. What is the material of the component in the fastening system that provides electrical insulation?

INTL	polyamid
	plastic
	polyurethane tie pad and nylon insulator or angle guide plate plus plastic insert
	polyurethane
	HDPE
US	polyurethane & nylon
	polyurethane & nylon
	nylon

19. Is a frame or plate used between the rail pad and sleeper?

Yes	3	43%
No	4	57%
Total	7	100%

20. If so, from what material is it constructed?

INTL	steel
	We are still testing frames vs conventional gasket, steel plate + tie pad
US	plastic or steel

21. How many years have concrete sleepers and fastening systems been used by your railroad?

INTL	90
	about 60
	34
	30
	25 - 35
US	22
	28
	34

Effectiveness

22. Concrete Sleeper Life

	Question 22: What is the design life of the concrete sleepers? (years)	Question 22: What percentage of your concrete sleepers remain in service beyond their design life?	Question 22: Of the concrete sleepers that do not achieve their design life, what is their average service life?	Question 22: What is the most common reason for replacing concrete sleepers prior to achieving their design life?
INTL	35 estimated for these old sleepers (no design life fixed)	10%		fastening system disorders
	25	0%		Defect of screw
	30	less than 1 %. After all only 10 miles have been in track that long.	Not known.	shoulder wear.
	50	not there yet	don't know yet	fist fastener sleepers
	50	0%	3 years	impact force (from various sources); severe sleeper or rail seat abrasion
US	50 years is the desired tie life, with the maximum actual tie life currently at 22 years	We have not reached the desired tie life on any of our ties.	5-10 years	bond loss
	?	0%	15 years	failed
	50	haven't reached design life yet	unkown	failure due to mechanical breakage or ASR

23. Fastening System Life

	Question 23: What is the design life of the fastening systems? (years)	Question 23: What percentage of your fastening systems remain in service beyond their design life?	Question 23: Of the fastening systems that do not achieve their design life, what is their average service life?	Question 23: What is the most common reason for replacing fastening systems prior to achieving their design life?
INTL	> 30	?	?	fastening system disorders (anchoring)
	25	Large lateral force	Defect of spring	
	life of the rail	None		insulator wear
	30 so far	n/a	25	fist fastener sleepers due to corrosion of pin
	50	10	n/a	damage, unfit, electrical resistance
US	Not measured in years, but in tonnage which is 1.2 BGT (high curvature) - 3 BGT (tangent)	Unknown	Loss of toe load	Capital project rail change outs
	Life of rail	0	5	failed or wide gage
	same as tie life			mechanical breakage

24. Do you perform any maintenance (replacement, repair, etc.) on your concrete sleepers and fastening systems?

Yes	8	100%
No	0	0%
Total	8	100%

31. Please rank the following concrete sleeper and fastening system problems on your network from most to least critical.

Top number is the count of respondents selecting the option. Bottom % is percent of the total respondents selecting the option.

	1	2	3	4	5	6	7	8
Derailment damage	0	0	3	0	4	0	0	0
	0%	0%	43%	0%	57%	0%	0%	0%
Cracking from center binding	1	1	0	3	1	0	0	0
	17%	17%	0%	50%	17%	0%	0%	0%
Cracking from dynamic loads	1	1	1	1	1	1	0	0
	17%	17%	17%	17%	17%	17%	0%	0%
Cracking from environmental or chemical degradation	0	0	0	1	0	1	3	1
	0%	0%	0%	17%	0%	17%	50%	17%
Deterioration of concrete material beneath the rail	1	2	0	1	0	1	1	1
	14%	29%	0%	14%	0%	14%	14%	14%
Shoulder/fastening system w ear or fatigue	3	1	1	0	0	2	0	0
	43%	14%	14%	0%	0%	29%	0%	0%
Tamping damage	0	2	2	0	1	1	1	0
	0%	29%	29%	0%	14%	14%	14%	0%
Other (e.g. manufactured defect)	2	0	0	1	0	1	0	2
	33%	0%	0%	17%	0%	17%	0%	33%

32. Of the following potential failure causes, please select any and all that have resulted in deficiencies of your concrete sleepers and fastening systems.

	Deficient concrete strength	3	60%
	Improper prestress force	2	40%
	Poor material quality or behavior (of clamp, insulator, rail pad, or sleeper)	5	100%
	Poor environmental conditions (e.g. moisture or fines intrusion)	1	20%
	Manufacturing flaw s	5	100%
	Improper component design (of clamp, insulator, rail pad, or sleeper)	5	100%
	Fastening system damage	3	60%
	Concrete deterioration beneath the rail	4	80%
	Poor bonding of concrete to prestress	3	60%
	Other, please specify	2	40%
INTL	Ranking orger: Insulator loads exceed capacity w hich can result in shoulder w ear		
US	ASR		

Practices

33. What set of standards or industry-recommended practices do you follow for the design, manufacture, testing, and installation of concrete sleepers and fastening systems?

INTL	Euro Norms + Internal standards
	according to Japanese Industrial Standard
	Internal standards considering AREMA and Euro-Norm
	australian standards
	RailCorp Standards/Specifications and Australian Standard
US	many
	AREMA
	Internal specifications, AREMA, ASTM

34. What types of tests do you execute on concrete sleepers and fastening systems? Please refer to specific sections in the standard stated in the previous answer, when applicable.

INTL	Euro Norms + Internal standards
	according to Japanese Industrial Standard
	We have a long list of concrete tie specifications.
	visual inspection and concrete testing of compressive strength
	Many tests as per RailCorp Specifications and Australian Standards
US	many from ASTM, ACI, PCI
	none except mfg. required by AREMA
	refer to Amtrak Concrete Tie specification

35. What additional general comments do you have on concrete sleeper and fastening system design, manufacture, testing, and installation?

INTL	Complex problem. We believe that we have a pretty good structural tie design. We are ALWAYS looking for improvements. The fastening area have the most opportunities for improvement. WE want the fastener and rail life to match without maintenances!
	sleepers need reduced thickness
	High speed rails require a proper design of fastening system. Urban rails and Frieghts require a very good maintenance of rail system.
US	make stronger field shoulder; avoid sharp curves or decrease spacing
	We need to continue research. We can do better. We need to better understand the dynamic loading environment, how the tie responds to these loads and how we can improve our testing procedures to better match what the ties will see in the field.

Research

36. In your opinion, what are the most important topics of research regarding concrete sleepers and fastening systems? Please rank the following areas of concrete sleeper and fastening system research from most to least beneficial.

Top number is the count of respondents selecting the option. Bottom % is percent of the total respondents selecting the option.

	1	2	3	4	5
fastening systems design: clamps, insulators, inserts, rail pads	3 38%	4 50%	0 0%	1 13%	0 0%
materials design: concrete mix, prestress strand arrangement	1 13%	1 13%	1 13%	4 50%	1 13%
optimize sleeper design: spacing, cross-section, body shape, for specific uses (curves, grades, etc.)	0 0%	1 13%	5 63%	2 25%	0 0%
prevention of concrete deterioration under the rail or repair of abraded sleepers	1 13%	1 13%	1 13%	1 13%	4 50%
track system design: determining the track service environment and required sleeper characteristics	3 38%	1 13%	1 13%	0 0%	3 38%

37. Has concrete sleeper and fastening system research been performed by your railroad or other parties on your sleepers and fastening systems?

Yes	8	100%
No	0	0%
Total	8	100%

38. If so, on what primary topics has research been conducted?

INTL	Life cycle (cost and remaining strength)
	ladder type sleeper
	RSD
	toe loads
	impact loading, strength and serviceability, design concept, reliability and safety, noise & vibration, railseat abrasion, void and pocket, dynamic characteristics, integrated sensors, etc.
US	concrete tie life cycle, fastener life cycle, pad life cycle, rail seat repair, etc.
	lateral loads
	premature failures

39. Please provide references to literature published by your railroad or by outside parties on your railroad.

INTL	There are many papers. Please search the author "Hajime WAKUI".
	Private.
	nil
	Published data available in http://www.ro.uow.edu.au Internal data (+100 tech reports) has been internally available (also available to our academic researchers via RailCRC). Not available to public.
US	TTCI, otherwise all other research is witheld
	N/A

40. If unpublished test results have been documented regarding the research conducted by your railroad, would you be willing to share relevant information with the University of Illinois at Urbana-Champaign research team?

Yes	5	63%
No	3	38%
Total	8	100%

190. Please enter the following general information. Any information obtained on this page will remain confidential and will not be released.

8 Responses

191. Please briefly describe the technical responsibilities related to your position.

8 Responses

192. If you are aware of any other individuals who would be able to offer relevant information, please provide their names and e-mail addresses.

4 Responses

193. What proprietary restrictions exist with the information you have provided in this survey?

7 Responses

Appendix B: Academic, Industry, or Industrial Researcher Responses

41. Concentration of Research

	Question 41: What are your specific areas of research? (e.g. infrastructure components, subgrade, structures)	Question 41: Specifically, how are you involved with concrete sleepers and fastening systems? (e.g. instrumenting sleepers, modeling of fastening systems)
INTL	Infrastructure components, stiffness, actions, fastenings, sleepers	Modeling of: track, fastenings, sleepers. Sleepers' testing. To propose a reliable method for calculating the actions on track.
	Studying Master of Engineering (Rail Infrastructure) at QUT	Current course unit UDN500 Ballast & Sleepers
	track structures and components incluing fastening, sleeper and concrete slab	modeling and analysis, experiment and on-site testing on sleeper and fastening systems
	Concrete railway sleepers and bridges. Our university track research group is dealing also with all the other components of railway track (subsoil, subballast, ballast, rail, wheel-rail interaction)	general research on concrete sleepers
	infrastructure components and systems	theoretical design, modelling, component tests, field measurements
	Materials for especially concrete sleepers, subgrade improvement	development of new eco-friendly PC sleeper
	Railway track mechanic and dynamic infrastructure engineering	Field research on sleepers and CWR, lab research on fastening systems and rail joints
	concrete sleepers and railway track dynamics	experimental and numerical investigation of sleepers
	track degradation and component life, track dynamics, track stiffness, track modelling, wheel-rail forces	limit states design and rating of concrete sleepers, static and fatigue testing of sleepers, sleeper life modelling, study of impact forces on sleepers
US	track structure	modeling, insrumenting and testing of cross ties

Based on your expertise as described in the previous answers, please answer the following questions to the best of your ability as they apply in your country.If railroads in your country have different types of concrete sleepers and fastening systems in their networks, please respond to this survey based on the sleeper and fastening system most commonly used in demanding operating conditions.

42. What operating conditions would you consider to be demanding?

INTL	Mixed traffic passenger and freight in High-Speed lines (Vmax=200-250 km/h), axle-load 22.5 t/axle
	Heavy haul traffic, High speed passenger traffic
	Freight trains with flat wheels running on the same track as passenger trains
	High Speed, Heavy Haul
	conventional railway under the speed of 200km/hr
	durability of concrete sleepers, optimizing dimensions, life cycle, reliability analysis, vibration noise absorption
	High speed 120-150 km/h, high axle loads
	heavy axle loads, dirty environment (dust or sand from the ground or from mineral payloads, borne by air or water), poor maintenance of the rail head or of the wheel treads, high speed trains
US	315k lbs cars, sharp curves, hilly and/or rainy areas.
	Mainline coal routes, mountainous terrain

43. Freight Train Loading

	Question 43: What are the maximum gross static wheel loads?	Question 43: What is the typical dynamic load impact factor? (%) (e.g. 200% = 2 x static loading)
INTL	24.8 tons (22.5 tonnes)	Depending on the case it maybe arrive 3 times the static load and if there is fault on the rail's running surface even higher
	16.5 tons (15 tonnes)	Unknown
	12.1 tons (11.0 tonnes)	250%
	13.8 tons with 62 mile per hour speed (12.5 tonnes with 100 kilometers per hour speed)	highly dependent on flat wheels, but for a sleeper typically maybe around 150-200%
	27.6 tons (25.0 tonnes)	150%
	44.1 tons (40 tonnes)	200%
	24.3 tons (22.0 tonnes)	130-150%
	27.6 tons (25.0 tonnes)	133%
	35.3 tons (32.0 tonnes)	200-250%
	22.0 tons (20.0 tonnes) per wheel for heavy axle wagons containing coal or iron ore; 14.3 tons (13.0 tonnes) per wheel for ordinary freight	250%
US	19.5 tons (17.7 tonnes)	150%
	41 tons (37.2 tonnes)	

44. Passenger Train Loading

	Question 44: What are the maximum gross static wheel loads?	Question 44: What is the typical dynamic load impact factor? (%) (e.g. 200% = 2 x static loading)
INTL	24.8 tons (22.5 tonnes)	as in freight, a little bit less perhaps
	8.7 tons (7.9 tonnes)	Unknown
	12.1 tons (11 tonnes) for conventional lines and 13.8 tons (12.5 tonnes) for high-speed lines in design (but actual wheel load of Korean high speed train is 9.4 tons (8.5 tonnes))	200% for ballasted and 150% for slab track
	8.8 tons with 137 miles per hour speed (8.0 tonnes with 220 kilometers per hour speed)	highly dependent on flat wheels, but for a sleeper typically maybe around 150-200%
	24.8 tons (22.5 tonnes)	150%
	28.7 tons (26.0 tonnes)	150%
	18.7 tons (17.0 tonnes)	150-160%
	27.6 tons (25.0 tonnes)	133%
	N/A	N/A
	12.1 tons (11 tonnes) per wheel	250%
US	20 tons (18.1 tonnes) (light rail)	

45. What is the maximum allowable speed under such demanding operating conditions?

	30-60 miles per hour (50-100 kilometers per hour)	3	25%
	60-90 miles per hour (100-150 kilometers per hour)	0	0%
	90-120 miles per hour (150-200 kilometers per hour)	4	33%
	120-150 miles per hour (200-250 kilometers per hour)	1	8%
	150-180 miles per hour (250-300 kilometers per hour)	2	17%
	Other, please specify	2	17%
	Total	12	100%

INTL	(100-105 mph (160-170 kph) in track designed for operational 120-150 mph (200-250 kph))
	Passenger: 60-120 mph (100-200 kph); Freight: 30-60 mph (50-100 kph)

46. Please provide the typical sleeper spacing for the following track segments.			
	Question 46: Tangent	Question 46: Curve	Question 46: Grade Crossing
INTL	23.6 inches (60.0 centimeters)	23.6 inches (60.0 centimeters)	23.6 inches (60.0 centimeters)
	24.0 inches (61.0 centimeters)	24.0 inches (61.0 centimeters)	24.0 inches (61.0 centimeters)
	24.6 inches (62.5 centimeters) for ballasted track and 25.6 inches (65.0 centimeters) for slab track	same	same
	24.0 inches (61.0 centimeters)	24.0 inches (61.0 centimeters)	24.0 inches (61.0 centimeters)
	23.6 inches (60.0 centimeters)	23.6 inches (60.0 centimeters)	23.6 inches (60.0 centimeters)
	23.6 inches (60.0 centimeters)	23.6 inches (60.0 centimeters)	23.6 inches (60.0 centimeters)
	24.6 inches (62.5 centimeters)		
	23.6 inches (60.0 centimeters)		
	23.6-24.4 inches (60.0-62.0 centimeters)		
	23.6-27.6 inches (60.0-70.0 centimeters)	23.6-27.6 inches (60.0-70.0 centimeters)	23.6-27.6 inches (60.0-70.0 centimeters)
US	24.0 inches (61.0 centimeters)	24.0 inches (61.0 centimeters)	24.0 inches (61.0 centimeters)
	24.0 inches (61.0 centimeters)	24.0 inches (61.0 centimeters)	24.0 inches (61.0 centimeters)

47. What are the five (5) most common concrete sleeper designs used in your country? (manufacturer and sleeper identification) (e.g. RAIL.ONE NS 90)	
INTL	Twin-block U2, Twin-block U3, Twin-block U31 (all of them French design and Greek production meeting absolutely the pre-scriptions) patent and license agreement and know-how transfer SATEBA Monoblock pre-stressed B70 (German design and Greek production meeting absolutely the pre-scriptions) patent and license agreement and know-how transfer in three factories: Dywidag, Pfleiderer (now RAILONE), Walterbau. Monoblock pre-stressed for metric gauge line license Moll (German)
	Austrak
	KNR 60kg rail PC sleeper(Korean standards) High speed railway sleeper(Korean standards) Rail.One concrete sleeper for Rheda2000 track
	Only 3 new designs available (2 Finnish manufacturers): Parma BP 99, Parma BP 89 (minor amount) and Luja B97
	Two kinds of Korean sleepers (50kg N and 60kg K) are manufactured by Taemyung industry, Samsung industry, Is dongseo, Jeail con, Sampyo.
	B 70 B58
	AUSTRAK and ROCLA
	Austrak and Rocla are the two main manufacturers and their most common size of heavy duty sleepers are 22cm deep, 20-25cm wide, and 250cm long. Both companies also manufacture low profile sleepers around 17cm deep, 20-22cm wide, and 250cm long.
US	CXT, Rocla, Koppers
	Rocla

48. What are the five (5) most common fastening system designs used in your country? (manufacturer and fastening system identification) (e.g. Vossloh W 14 HH)	
INTL	RN, Nabla designer French company STEDEF W14 German company Vossloh Gmbh
	Pandrol e clip Pandrol Fastclip Fist BTR
	Pandrol e-Clip Pandrol SFC with FC 1501 Vossloh System 300
	Vossloh W 14, Pandrol E-CLIP for replacement of old similar fasteners.
	Vossloh W3, Vossloh W14, Vossloh System 300,
	Railtech Fastclip - e clip Vossloh W21 - W14
	Pandrol products are common in Korea for the conventional line under the speed of 150km/hr Several products are installed for the high-speed line
	Vossloh Pandrol SKL 12
	Pandrol e-clip and Pandrol fast-clip
	Pandrol, Vossloh, e-clip, fastclip, fistclip
US	Saflok I and III e-clips Vossloh
	Vossloh 101L Safelok 101L

49. How many years have concrete sleepers been used in your country?	
INTL	since 1972
	30 plus
	about 40
	monoblock sleepers from year 1964 (at first a German type)
	> 55
	25
	about 50
	20
	40
	40
US	30-40
	+/- 35

Effectiveness

50. What is the most common cause of early replacement of concrete sleepers in your country?	
INTL	Not sufficient strength, not correct design
	Derailment damage
	flexural failure due to unsupported condition and longitudinal cracking
	In general, the need for early replacement has not been significant. Frost weathering. Transversal cracks in sleepers.
	chemical influences
	Derailment
	to increase its weight for track's stability
	longitudinal cracks inside sleepers, cracks under the sleeper due to durability problems
	cracking in rail seat zone
	Derailment damage
US	Generally concrete ties do not complete service life cycle. They are replaced after the lessons are learnt.
	Cracking and spalling

51. What is the most common cause of early replacement of fastening systems in your country?	
INTL	Not correct toe-load, not correct design, high value of static stiffness meaning high value of actions on track
	Fastener corrosion
	broken clip and early hardening of railpad
	Loose fastening
	elasticity
	Clip breakage
	noise and vibration
	failure
	fatigue
US	broken fasteners
	Broken fasteners

52. Have railroads in your country ever experienced the type of deterioration in the sleeper as shown in the images below?		
Yes	4	36%
No	7	64%
Total	11	100%

53. If so, what term would you use to identify this deterioration?

INTL	RSD
	Rail Seat Abrasion
	wear - indentation
	to need to estimate the train loading in order to design the sleeper
US	rail seat abrasion

54. Please briefly describe the characteristics of this deterioration, in terms of where it occurred, at what rate it occurred, to what depth it occurred, etc.

INTL	I cannot see clearly, could you please send me more clear and detailed photos?
	depth: 0.02 to 0.04 inches (0.5 to 1.0 millimeters)
	Although rail seat abrasion is perceived to be a big problem in the USA, it's relatively rare in Australia despite many 1000s of kilometres of concrete sleepered track, and it generally occurs only in very dirty environments; abrasion of the underside of the sleeper (due to tamping damage and abrasion from ballast forces due to heavy axle load traffic) is far more common and over a period of 30 years up to 2cm can be lost that way.
US	In general, US railroads have this problem. I do not have direct exposure to this issue.

55. Please rank the following concrete sleeper and fastening system problems in your country from most to least critical.

Top number is the count of respondents selecting the option. Bottom % is percent of the total respondents selecting the option.

	1	2	3	4	5	6	7	8
Derailment damage	2	0	1	1	1	3	2	1
	18%	0%	9%	9%	9%	27%	18%	9%
Cracking from center binding	0	3	2	1	0	2	0	0
	0%	38%	25%	13%	0%	25%	0%	0%
Cracking from dynamic loads	2	2	3	1	1	1	1	0
	18%	18%	27%	9%	9%	9%	9%	0%
Cracking from environmental or chemical degradation	4	0	1	1	2	0	1	0
	44%	0%	11%	11%	22%	0%	11%	0%
Deterioration of concrete material beneath the rail	0	1	1	0	0	2	1	4
	0%	11%	11%	0%	0%	22%	11%	44%
Shoulder/fastening system w ear or fatigue	0	2	0	4	3	0	0	0
	0%	22%	0%	44%	33%	0%	0%	0%
Tamping damage	2	2	1	2	1	1	1	0
	20%	20%	10%	20%	10%	10%	10%	0%
Other (e.g. manufactured defect)	1	1	2	0	1	0	2	2
	11%	11%	22%	0%	11%	0%	22%	22%

56. Of the following potential failure causes, please select any and all that have resulted in deficiencies of concrete sleepers and fastening systems in your country.

Deficient concrete strength	1	9%
Improper prestress force	0	0%
Poor material quality or behavior (of clamp, insulator, rail pad, or sleeper)	4	36%
Poor environmental conditions (e.g. moisture or fines intrusion)	5	45%
Manufacturing flaw s	4	36%
Improper component design (of clamp, insulator, rail pad, or sleeper)	3	27%
Fastening system damage	5	45%
Concrete deterioration beneath the rail	3	27%
Poor bonding of concrete to prestress	2	18%
Other, please specify	4	36%

INTL	poor bonding of concrete to reinforcement rods in "normal" concrete tw in-block sleepers
	corrosion of fasteners and attrition of concrete from underside of sleeper due to pumping track
	insufficient support from ballast/embankment
	longitudinal cracks on the surface of sleeper

Research

57. In your opinion, what are the most important topics of research regarding concrete sleepers and fastening systems? Please rank the following areas of concrete sleeper and fastening system research from most to least beneficial.

Top number is the count of respondents selecting the option. Bottom % is percent of the total respondents selecting the option.

	1	2	3	4	5
fastening system design: clamps, insulators, inserts, rail pads	2	1	4	4	0
	18%	9%	36%	36%	0%
materials design: concrete mix, prestress strand arrangement	0	1	3	4	2
	0%	10%	30%	40%	20%
optimize sleeper design: spacing, cross-section, body shape, for specific uses (curves, grades, etc.)	4	5	2	0	0
	36%	45%	18%	0%	0%
prevention of concrete deterioration under the rail or repair of abraded sleepers	1	1	1	1	5
	11%	11%	11%	11%	56%
track system design: determining the track service environment and required sleeper characteristics	4	3	1	1	1
	40%	30%	10%	10%	10%

58. Has concrete sleeper and fastening system research been performed by your organization?

Yes	10	83%
No	2	17%
Total	12	100%

59. If so, on what primary topics has research been conducted?

INTL	stiffness, toe-load, actions on track, life-cycle, compatibility of clip and pad
	deisgn and perfomance verification of rail fastening design
	Field tests, several types of tests. Loading tests at our university, static and cyclic. Structural calculations. Literature review. Interviews.
	Sleeper design, Fastenings Elasticity,
	loads and deflection
	to design new fastening system and sleeper for high-speed railway and the reduction of noise and vibration
	durability of concrete, sleeper optimization, reliability analysis and design of sleeper and fastening systems
	resistance of concrete sleepers to severe impact loads
	these topics were all laid out in my responses at the start of this survey
US	primary focus is to reduce the life cycle cost.

60. Please provide references to literature published by your organization regarding concrete sleepers and fastening systems.

9 Responses - available upon request

61. If unpublished test results have been documented regarding the research conducted by your organization, would you be willing to share relevant information with the University of Illinois at Urbana-Champaign research team?

Yes	9	90%
No	1	10%
Total	10	100%

190. Please enter the following general information. Any information obtained on this page will remain confidential and will not be released.

12 Responses

191. Please briefly describe the technical responsibilities related to your position.

12 Responses

192. If you are aware of any other individuals who would be able to offer relevant information, please provide their names and e-mail addresses.

4 Responses

193. What proprietary restrictions exist with the information you have provided in this survey?

6 Responses

Appendix C: Concrete Crosstie Manufacturer Responses

If your organization manufactures different types of sleepers, please respond to this survey based on the most commonly-used sleeper for primary lines, hereafter referred to as the "typical sleeper".

62. What is your typical sleeper? (manufacturer and sleeper identification) (e.g. RAIL.ONE NS 90)

7 Responses

Concrete

63. What is the concrete design mix?

5 Responses

64. What is the design air content of the concrete mix? (% or range of %)

INTL	confidential
	1.0 - 1.3 %
	4.50%
US	5.50%
	3 - 6 %
	3 - 5 %

65. What type of cement is used? (e.g. Type III cement)

INTL	confidential
	CEM II/A-S42,5R WT38
	high early strength (in spec)
US	Type III low alkali
	fine grind type II
	TYPE III
	Type II LA

66. What type of aggregate is used?

	Limestone	1	14%
	Dolomite	0	0%
	Granite	2	29%
	Basalt	0	0%
	Other, please specify	4	57%
	Total	7	100%

INTL	confidential
	Moraine gravel, crushed (limestone-rich)
	river rock, traditionally; now from foot of mountains

67. What is the shape of the aggregate?

Rounded	0	0%
Crushed	6	100%
Total	6	100%

68. What is the average slump of your concrete at placement?

INTL	confidential
	not applicable C0
	4.7 inches (120 millimeters)
US	9.0 inches (229 millimeters)
	7.0 inches (178 millimeters)
	3.0 inches (76 millimeters)

69. What consolidation method is used?

	Vibration mechanism	5	71%
	Self-consolidating concrete	1	14%
	Physical compaction of concrete	0	0%
	Other, please specify	1	14%
	Total	7	100%

INTL	confidential

70. What methods are used to control concrete curing? Please select all that apply.

	Curing membrane (e.g. w et burlap)	3	43%
	Liquid curing compound	0	0%
	Steam	3	43%
	None	0	0%
	Other, please specify	5	71%

INTL	confidential
	water basin under air-tight curing stack
US	oil
	Radiant Heat

71. What is the maximum allowable internal temperature of the typical sleeper during curing?

INTL	confidential
	113 °F (45 °C)
	122 - 140 °F (50 - 60 °C)
US	140 °F (60 °C)
	158 °F (70 °C)
	140 °F (60 °C)
	140 °F (60 °C)

72. What is the minimum allowable concrete strength at prestress transfer?

INTL	confidential
	7000 pounds per square inch (48 megapascals)
	6000 pounds per square inch (41 megapascals)
US	5000 pounds per square inch (34 megapascals)
	5000 pounds per square inch (34 megapascals)
	4200 pounds per square inch (29 megapascals)
	4500 pounds per square inch (31 megapascals)

73. What is the average time that elapses between concrete placement and transfer of prestress forces to the concrete? (hours)

INTL	confidential
	36
	17 (17-24 hours for turning beds; 1 per day)
US	8.25
	17
	8 - 14

74. Is the surface of the rail seat treated in any way?

	Yes	2	40%
	No	3	60%
	Total	5	100%

75. If so, how is it treated? (e.g. polished, added polyurethane, etc.)

INTL	confidential
US	epoxy
	Approx 50% of ties are epoxy railseats

76. What is the design 28-day compressive strength of your concrete mix?

	3 - 4.5 kips per square inch (20-30 megapascals)	0	0%
	4.5 - 6 kips per square inch (30-40 megapascals)	0	0%
	6 - 7.5 kips per square inch (40-50 megapascals)	1	14%
	7.5 - 9 kips per square inch (50-60 megapascals)	3	43%
	9 - 10.5 kips per square inch (60-70 megapascals)	2	29%
	Other, please specify	1	14%
	Total	7	100%
INTL	confidential		

Prestressing

77. Are the sleepers pretensioned or post-tensioned?

	Pretensioned	8	100%
	Post-tensioned	0	0%
	Total	8	100%

78. What form of steel is used in the typical sleeper?

	Wires	4	50%
	Strands	1	13%
	Bars	1	13%
	Other, please specify	2	25%
	Total	8	100%
INTL	confidential		
US	indented strand		

79. How many wires, strands, or bars pass through the centerline section of your concrete sleepers?

INTL	confidential
	8
	20
US	20
	8
	18

80. What is the diameter of the wires, strands, or bars used?

INTL	confidential
	0.30 inches (7.5 millimeters)
	0.11 inches (2.9 millimeters)
US	0.2094 inches (5.3 millimeters)
	3.0 - 8.0 inches (76.2 - 203.2 millimeters)
	5.32 inches (135.1 millimeters)

81. What is the jacking force introduced in the wires, strands, or bars?

INTL	confidential
	12.6 kips (56.0 kilonewtons); wires: 211.8 kips per square inch (1460 newtons per square millimeter)
	80% of f_{pu}
US	7.0 kips (31.1 kilonewtons)
	100.1 kips (445.3 kilonewtons)
	6.8 kips (30.2 kilonewtons)

82. What is the yield strength of the wires, strands, or bars?

INTL	confidential
	247 kips per square inch (1700 megapascals)
	270 kips per square inch (1862 megapascals)
US	265 kips per square inch (1827 megapascals)
	270 kips per square inch (1862 megapascals)
	260 kips per square inch (1793 megapascals)

Production

83. How are the concrete sleepers manufactured?

Carousel	2	29%
Long line	5	71%
Other, please specify	0	0%
Total	7	100%

84. Is your typical sleeper manufactured to incorporate a specific fastening system?

Yes	6	86%
No	1	14%
Total	7	100%

85. If so, what is that fastening system?

INTL	Vossloh W14, Pandrol is also possible
	JR Central, JR Standard (drawings in spec)
US	any
	Pandrol Safelok III
	Fast clip / E clip
	Vossloh and Safelok III

86. How many sleepers did you produce last year?

INTL	> 2 million
	180,000
	60,000
US	> 1 million
	15,000

87. What is your average daily production rate over the last five years?

INTL	1200 in 3 shifts, 800 in 2 shifts
	200 (pretensioned)
US	3000
	50,000

Sleepers

88. Which infrastructure owners use your concrete sleepers?

INTL	see our reference list
	ÖBB, Wiener Linien, several private companies
	JR East, JR West, JR Central, Hokido North, South Kyushu, JR Shikoku
US	Public and private
	uprr
	CSX - LIRR
	BNSF UPRR

89. What is the design life of your concrete sleepers? (years)

INTL	it's more important what is the REAL life of the concrete sleeper
	50
	30 (often last 40)
US	50+
	25
	NA

90. Please provide design loads for your concrete sleeper.

	Question 90: What is the design axle load?	Question 90: What are the maximum design bending moments?	Question 90: What is the shear design load?
INTL	various	confidential	confidential
	27.6 tons (25.0 tonnes)	177.0 inch-kips (20.0 kilonewton-meters)	no issue
	27.6 tons (25.0 tonnes)	-	-
US	35.8 tons (32.4 tonnes)	381.0 inch-kips (43.0 kilonewton-meters)	-
	39.0 tons (35.4 tonnes)	Varies	-

Effectiveness

91. Have your sleepers ever experienced the type of deterioration as shown in the images below?

Yes	4	80%
No	1	20%
Total	5	100%

92. If so, what term would you use to identify this deterioration?

INTL	rail seat abrasion
US	rsa / rsd
	RSD
	Cavitation, Degradation

93. Please briefly describe the characteristics of this deterioration, in terms of where it occurred, at what rate it occurred, to what depth it occurred, etc.

INTL	Generally, rail seat abrasion is not a big issue in the EU. The abrasion on the pictures is not typical for us and we guess the reason are hard/stiff rail pads. The Austrian rail road company ÖBB is only using soft pads. Rail seat abrasion by rail is possible, but at first the pad be have been destroyed.
	Most of track is electrified (and signalled); stray currents jumping, affecting concrete, wires, and fastening
US	Elevated curves,deep south, unmaintained track, up to 1 inch (25.4 millimeters)

94. Please rank the following concrete sleeper and fastening system problems from most to least critical.

Top number is the count of respondents selecting the option. Bottom % is percent of the total respondents selecting the option.

	1	2	3	4	5	6	7	8
Derailment damage	0	1	1	0	1	0	0	0
	0%	33%	33%	0%	33%	0%	0%	0%
Cracking from center binding	0	0	0	0	1	1	0	1
	0%	0%	0%	0%	33%	33%	0%	33%
Cracking from dynamic loads	0	0	0	0	1	1	1	0
	0%	0%	0%	0%	33%	33%	33%	0%
Cracking from environmental or chemical degradation	0	0	0	1	0	0	2	0
	0%	0%	0%	33%	0%	0%	67%	0%
Deterioration of concrete material beneath the rail	2	1	0	1	0	0	0	0
	50%	25%	0%	25%	0%	0%	0%	0%
Shoulder/fastening system w ear or fatigue	1	2	1	0	0	0	0	0
	25%	50%	25%	0%	0%	0%	0%	0%
Tamping damage	2	0	1	0	0	1	0	0
	50%	0%	25%	0%	0%	25%	0%	0%
Other (e.g. manufactured defect)	0	0	0	1	0	0	0	2
	0%	0%	0%	33%	0%	0%	0%	67%

95. Of the following potential failure causes, please select any and all that have resulted in deficiencies of your concrete sleepers and fastening systems.

Deficient concrete strength	0	0%
Improper prestress force	0	0%
Poor material quality or behavior (of clamp, insulator, rail pad, or sleeper)	0	0%
Poor environmental conditions (e.g. moisture or fines intrusion)	1	25%
Manufacturing flaw s	0	0%
Improper component design (of clamp, insulator, rail pad, or sleeper)	0	0%
Fastening system damage	3	75%
Concrete deterioration beneath the rail	4	100%
Poor bonding of concrete to prestress	2	50%
Other, please specify	0	0%

190. Please enter the following general information. Any information obtained on this page will remain confidential and will not be released.

7 Responses

191. Please briefly describe the technical responsibilities related to your position.

6 Responses

192. If you are aware of any other individuals who would be able to offer relevant information, please provide their names and e-mail addresses.

2 Responses

193. What proprietary restrictions exist with the information you have provided in this survey?

4 Responses

Appendix D: Definition of Critical Model Outputs

Track vertical deflection	The vertical displacement at the top of railhead.
Track lateral deflection	The lateral displacement measured at right-angles to the rail in a plane five-eighths of an inch below the top of railhead. Positive value indicates the railhead moved to the gage side, and negative value indicates the railhead moved to the field side.
Rail-base lateral displacement	The lateral displacement measured at the middle of rail-base edge. Positive value indicates the rail base moved to the gage side, and negative value indicates the rail base moved to the field side.
Abrasion frame lateral translation	The lateral displacement measured at the field-side edge of abrasion frame. Positive value indicates the abrasion frame moved to the gage side, and negative value indicates the abrasion frame moved to the field side.
Vertical rail-seat load	The vertical component of interaction force from the interaction between rail and rail pad at the loaded rail seat.
Lateral rail-seat load	The summation of shoulder bearing force and rail pad friction force at the loaded rail seat.
Gauge-side clamping force	The vertical component of interaction force between insulator and gauge-side clip.
Field-side clamping force	The vertical component of interaction force between insulator and field-side clip.
Maximum rail-seat pressure	The maximum pressure between rail seat and rail pad.
Rail base rotation	The rotation of rail base is calculated by assuming the rail base remain plane under the loadings. The vertical displacement of the four corners in loaded rail seat is measured, and the averaged difference is used to calculate rail base rotation.
Shoulder bearing force	The lateral component of the interaction force between field-side shoulder and insulator.
Rail pad frictional force	The lateral and longitudinal components of the frictional force between the rail base and the rail pad.
Crosstie rail-seat moment	The crosstie-substructure interaction is divided into four segments: segment one covers from crosstie end to the center of rail seat; segment two covers from center of the rail seat to the center of crosstie. Segment three and four covers symmetric parts on the other half of the crosstie. Based on the magnitude and position of the resultant

	interaction force of each segment and the vertical and lateral rail seat load, the moment at the center of the rail seat is calculated.
Crosstie center moment	The crosstie-substructure interaction is divided into four segments: segment one covers from crosstie end to the center of rail seat; segment two covers from center of the rail seat to the center of crosstie. Segment three and four covers symmetric parts on the other half of the crosstie. Based on the magnitude and position of the resultant interaction force of the four segments and the rail seat load, the moment at the center of the crosstie is calculated.
Vertical rail-seat load at adjacent crossties	The vertical rail-seat load at the four closest crossties around the loaded crosstie.
Lateral rail-seat load at adjacent crossties	The lateral rail-seat load at the four closest crossties around the loaded crosstie.
Relative sliding between abrasion frame and rail seat	One node at the field-side edge of abrasion plate is selected for displacement output, and the coincident concrete node is also selected. The difference of lateral displacement of the two nodes before and after the loadings is used as the relative sliding between abrasion frame and rail seat.
Relative sliding between rail and rail pad	One node at the field-side edge of rail base is selected for displacement output, and the coincident rail pad node is also selected. The difference of lateral displacement of the two nodes before and after the loadings is used as the relative sliding between rail base and rail pad.

Abbreviations and Acronyms

ACI	American Concrete Institute
AREA	American Railway Engineering Association
AREMA	American Railway Engineering and Maintenance-of-Way Association
ASTM	American Society for Testing and Materials
ANOVA	Analysis of Variance
AAR	Association of American Railroads
AS	Australian Standard
BAA	Broad Agency Announcement
BNSF	Burlington Northern Santa Fe Railway
CCD	Central Composite Design
COF	Coefficient of Friction
cDAQ	Compact Data Acquisition
DOF	Degrees of Freedom
DEM	Discrete Element Method
DAF	Dynamic Amplification Factor
DGL	Lateral Crosstie Global Displacement
DGV	Vertical Crosstie Global Displacement
FAST	Facility for Accelerated Service Testing
FRA	Federal Railroad Administration
FEA	Finite Element Analysis
FE	Finite Element
GRL	Gross Rail Load
HFFD	Half Fractional Factorial Design
HAL	Heavy Axle Load
HTL	High Tonnage Loop
IF	Impact Factors
IWS	Instrumented Wheel Set
UIC	International Union of Railways
Kip	Kilopound
LSAT	Large Scale Abrasion Test
LAM	Lateral Axial Measurement

LLED	Lateral Load Evaluation Device
LLF	Lateral Load Frame
L/V	Lateral/Vertical
LVDT	Linear Varying Displacement Transducers
LRFD	Load and Resistance Factor Design
MBTSS	Matrix-Based Tactile Surface Sensor
ms	Micro-strain
MGT	Million Gross Tons
NI	National Instruments
PLTM	Pulsating Load Testing Machine
PLTF	Portable Track Loading Fixture
RBFN	Radial Basis Function Network
RBLT	Rail Base Lateral Translation
RPLD	Rail Pad Lateral Displacement
RPM	Rail Pad Modulus
RSD	Rail Seat Deterioration
RSLI	Rail Seat Load Index
RailTEC	Rail Transportation and Engineering Center
RTT	Railroad Test Track
RAIL	Research and Innovation Laboratory
SLTM	Static Load Testing Machine
STT	Static Tie Tester
I-TRACK	Track Component Response Calculation Tool
TLD	Track Lateral Deflection
TLS	Track Loading System
TLV	Track Loading Vehicle
TVD	Track Vertical Deflection
TTC	Transportation Technology Center
TPD	Truck Performance Detector
UIUC	University of Illinois at Urbana-Champaign
UP	Union Pacific Railroad
WILD	Wheel Impact Load Detector